國立中央大學天文研究所
鹿林天文台年報

2013

No.11

國立中央大學天文研究所 編

目錄

研究論文

工作報告

新聞報導

研究論文

The Astrophysical Journal, 770:97 (7pp), 2013 June 20 doi:10.1088/0004-637X/770/2/97

DETECTION OF COMA ACTIVITY OF THE ACO/QUASI-HILDA OBJECT 212P/2000YN$_{30}$

Y.-C. Cheng[1] and W.-H. Ip[1,2,3]

[1] Institute of Astronomy, National Central University, No. 300, Jhongda Road, Jhongli City, Taoyuan County 32001, Taiwan (R.O.C.); m969005@astro.ncu.edu.tw

[2] Institute of Space Science, National Central University, Taiwan

[3] Space Science Institute, Macau University of Science and Technology, Macau

Received 2011 November 22; accepted 2013 April 24; published 2013 May 29

ABSTRACT

The quasi-Hilda object 212P/2000YN$_{30}$, which has a cometary-like orbit, was found to display a dust tail structure between 2009 January and March. From orbital calculations, it is shown that this object could have been an active comet in the past before being transported to its current orbital configuration in quasi-stable 3:2 resonance with Jupiter.

Key words: comets: general – Kuiper belt: general – minor planets, asteroids: general

1. INTRODUCTION

One basic question in connection to the origin of life and the development of a biosphere has to do with the source of the terrestrial ocean. For exogenic sources, ocean water could have come from either comets or asteroids. The idea that cometary water ice could be the main contributor (Chyba 1987; Ip & Fernandez 1988) has suffered a setback because the D/H isotope ratios measured in several comets are about a factor of two larger than the standard value $1.49 \pm 0.03 \times 10^{-4}$ for ocean water (Eberhardt et al. 1995; Meier et al. 1998; Crovisier et al. 2004; Jehin et al. 2009).

However, the recent report of the D/H ratio ($=1.61 \pm 0.24 \times 10^{-4}$) of the Jupiter family comet (JFC) 103P/Hartley 2 determined from *Herschel* observations has shed new light on the old issue of terrestrial water (Hartogh et al. 2011). The most recent report of a D/H ratio of $2.06 \pm 0.22 \times 10^{-4}$ for the Oort cloud comet C/2009 P1 (Garradd) by Bockelee-Morvan et al. (2012) has further underscored the point that comets could have a wider range of D/H ratios than previously thought. In any event, they could still make a contribution to the terrestrial water source reservoir within the dynamical constraint of being no more than 10% in total, as estimated by Morbidelli et al. (2000). We note that among the seven other comets for which D/H ratios have been measured by pre-*Herschel* spacecraft observations or ground-based observations, C/1995 O1 Hale-Bopp, C/1996 B2 Hyakutake, C/2001 Q4 NEAT, and C/2002 T7 LINEAR are all long-period comets from the Oort cloud, and 1P/Halley, 8P/Tuttle, and 81P/Wild2 are short-period comets (see Jehin et al. 2009). The D/H ratios of the long-period comets—which presumably have a different condensation region from that of the Jupiter-family comets—now range from 2.06×10^{-4} (Bockelee-Morvan et al. 2012), $3.3 \pm 0.8 \times 10^{-4}$ (Meier et al. 1998) to $4.6 \pm 1.4 \times 10^{-4}$ for C/2001 Q4 NEAT (Weaver et al. 2008). These values overlap with the range between $1.49 \pm 0.03 \times 10^{-4}$ for 103P/Hartley 2 (Hartogh et al. 2011) and $4.09 \pm 1.45 \times 10^{-4}$ for 8P.Tuttle (Villanueva et al. 2009).

Another basic question of equal importance is, therefore, how would JFCs that presumably originated from the trans-Neptunian region (Duncan et al. 1989; Ip & Fernandez 1991; Volk & Malhotra 2008) have such large differences in the D/H ratios? Could they have formed in different orbital positions in the outer solar nebula before being swept up by planet migration (Fernandez & Ip 1984; Malhotra 1995)? Tiscareno & Malhotra (2003), Di Sisto & Brunini (2007), and Volk & Malhotra (2008) considered the dynamical transformation of the trans-Neptunian objects into Centaur populations with orbits in the Jovian and Saturnian zones and then short-period comets in the inner solar system. Or, some of them could have formed in the asteroidal region but were later implanted in the Kuiper Belt after following a complex history of dynamical evolution. Di Sisto et al. (2005) studied the interesting issue of whether JFCs could be mixed with the Hilda asteroids and vice versa by performing numerical orbital calculations on a stably trapped population in 3:2 resonance with Jupiter and those quasi-stable populations. They found that the majority (∼99%) of the escaping Hildas would be perturbed into JFC-like orbits but with perihelia $q > 2.5$ AU. This means that only a small fraction (∼1%) of them would become near-Earth objects with the possibility of hitting the Earth, according to this study. Whether the Hilda population could have significantly contributed to terrestrial ocean water thus depends very much on the total mass of the original population. Di Sisto et al. (2005) further estimated that at the present time the expected number of comet-sized Hilda asteroids in cometary-like orbits should be on the order of 143, in comparison to about 2800 dormant JFCs.

In a series of papers, Dahlgren & Lagerkvist (1995) and Dahlgren et al. (1997, 1999) reported on their photometric survey of the color distribution of the Hilda asteroids. In one study, they showed that about 36% of the Hildas could be classified as D-type, 28% as P-type, and only 2% as C-type (Dahlgren et al. 1999). The fact that both JFCs and Hilda asteroids share many of the characteristics of the D-type taxonomic class is another possible piece of evidence for a link between these two populations of small bodies. From this point of view, we might pose the hypothesis that comet 103P/Hartley 2 could be an escapee from the Hilda group if the D/H ratio of the Hildas is found to be the same as those of the CI–CM chondrites (Robert 2006).

The above discussion shows the new impetus in the study of asteroids in cometary orbits (ACOs) since they can provide hints on the nature and relationship between terrestrial water and plantesimals formed in the early solar system. This is also why the recent discovery of a small population of main-belt comets or active asteroids (Hsieh & Jewitt 2006; Jewitt 2012) has drawn so much attention. The main belt objects discovered by these authors are all located at the outer edge of the main asteroidal belt with semi-major axes between 3.156 AU and 3.196 AU and near-zero eccentricity. The detection of water ice and organics

Table 1
The Observation log of 212P by Using the LOT Telescope at Lulin Observatory

Date		R_h (AU)	Δ (AU)	α (deg)	V	Remark
2009 Jan	2	1.683	0.959	30.4	19.594 (±0.064)	
	5	1.688	0.948	29.6	19.548 (±0.070)	Close to a BG stellar
	6	1.690	0.944	29.4	20.027 (±0.094)	Not photometric night
	7	1.693	0.941	29.1	19.762 (±0.079)	
2009 Mar	17	1.950	1.107	20.7	20.700 (±0.130)	
	18	1.955	1.115	20.8	20.512 (±0.129)	
	19	1.960	1.123	20.9	20.504 (±0.132)	

on the surface of the asteroid 24 Themis has further heightened the interest in this issue (Campins et al. 2010; Rivkin & Emery 2010).

In our observational program at Lulin, the Tisserand parameter,

$$T_J = a_J/a + 2 \cdot \sqrt{(a/a_J)(1 - e^2)} \cos i,$$

has been used to select the targets. In the above equation, a_J is the semi-major axis of Jupiter, and e and i are the eccentricity and inclination, respectively, of the object in question. Vaghi (1973) examined the T_J values of the 73 JFCs known at the time and found that the majority of them fall in the range of $2.450 < T_J < 3.032$, and further concluded that those with $T_J > 2\sqrt{2}$ must have originated from elliptical orbits instead of parabolic orbits. Kresak (1980) discussed the variation of the values of the Tisserand parameter among different groups of solar system small bodies and showed that the Hilda asteroids shared the same dynamical characteristics as those of the JFCs, even though not a single asteroidal-like object could be definitely identified as an ex-comet at that time. A recent study by Fernandez et al. (2005) comparing the albedos (p_V) and T_J values of 26 asteroids in cometary orbits (including 6 Damocloids and 6 near-Earth asteroids) found the interesting result that there is a discontinuity in the albedo distribution as a function of T_J. That is, those with $T_J < 3.0$ would tend to have $p_V \sim 0.04$ and those with $T_J > 3.0$ would have $p_V > 0.2$, thus suggesting different physical origins. For these reasons, we are mainly interested in objects with $T_J < 3$.

In addition to the ACOs and Hilda asteroids, many objects called quasi-Hildas moving in the orbital region of the Hildas but without being stably trapped in the 3:2 mean motion resonance with Jupiter are also included in the Lulin target list according to their T_J values. While Di Sisto et al. (2005) suggested that the Hildas and quasi-Hildas could be closely related to JFCs according to their dynamical behavior, Toth (2006) gave an update on the orbital properties of ecliptic comets in Hilda-like orbits and quasi-Hilda asteroids. Subsequently, Ohtsuka et al. (2008) showed that some of the quasi-Hildas (i.e., 147P/Kushida-Muramatsu) could be the progenitors of temporarily captured irregular satellites of Jupiter. Along the same line, Fernandez & Gallardo (2002) used an orbital integration method to trace the dynamical evolution of inactive JFCs and estimated that up to 20% of the near-Earth asteroid population with $T_J < 3$ could be of cometary origin. Thus, the intercomparison of the surface color variations and size distributions of Hildas/quasi-Hildas, JFCs, and ACOs might give us some hints on the evolution of the surface material and structures of cometary nuclei, namely, from youth to old age in case the ACOs are representative of defunct (i.e., inactive) cometary nuclei. The aim of our observational project is therefore to establish a comprehensive database of the sizes and surface colors of these populations of small bodies with the intention of comparing them to those of the JFCs (Lamy & Toth 2009).

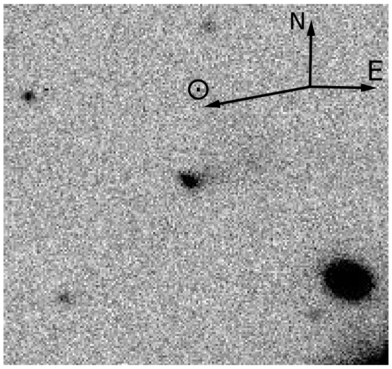

Figure 1. Discovery image of 212P taken at Lulin Observatory (*B*-band image with 300 s exposure).

In this work, we bring attention to the serendipitous discovery of the coma activity of an ACO. This object, previously known as 2000 YN_{30} (212P hereafter), was a target in our survey program of ACOs using the LOT 1 m telescope at Lulin Observatory. It was first discovered by the NEAT (Near Earth Asteroid Tracking) group on 2000 December 1 as an asteroid when it was at a solar distance of 1.86 AU just before perihelion. Its orbital parameters of $a = 3.929$ AU, $e = 0.579$, and $i = 22^\circ\!.398$ with $T_J = 2.635$ make it a member of the ACOs. With an absolute magnitude $H = 16.76$ and an R-band geometric albedo p_R of 0.096 ± 0.032, its size can be estimated to be $D = 1.7 \pm 0.3$ km (Fernandez et al. 2005). The fact that 212P has a larger eccentricity and higher inclination than the quasi-Hildas or the outliers listed in Toth (2006) might mean that it could actually be a weakly outgassing comet in transition to an inactive cometary nucleus. On the other hand, we note that two quasi-Hilda asteroids, 2004 FM_{24} and 2002 CF_{140} in Toth (2006), can be shown by numerical calculations to evolve into cometary-like orbits within a million years. Comet 212P might share the same dynamical origin as these two quasi-Hildas.

This paper is organized as follows. In Section 2, we will describe observations and images obtained at Lulin. Section 3 will be dedicated to the discussion of the orbital evolution of 212P. Finally, the summary and discussion will be given in Section 4.

2. OBSERVATIONS

The LOT telescope used in this project was equipped with the PI 1300B 1340 × 1300 pixels CCD camera. The image scale is $0''.516$ pixel^{-1}. The standard Asahi *BVRI* broadband filters were used in the photometric measurements. The observational log is given in Table 1. Figure 1 shows the discovery image of 212P's outgassing activity taken on 2009 January 2 (Cheng et al. 2009). A faint dust tail with a length of about 20″ or 14,000 km appeared in the anti-sunward direction. Note that 6.5 hr prior to our observation, Gibbs (2009) detected the presence of a diffuse coma surrounding this object that was not there in the previous observational report in 2008 December (Marsden 2008). After confirmation by IAU Circulars, this object was renamed 212P/2000 YN_{30} (NEAT) to reflect its cometary nature.

Since the first detection of the dust tail feature, 212P was routinely monitored at Lulin until March of the same year. As

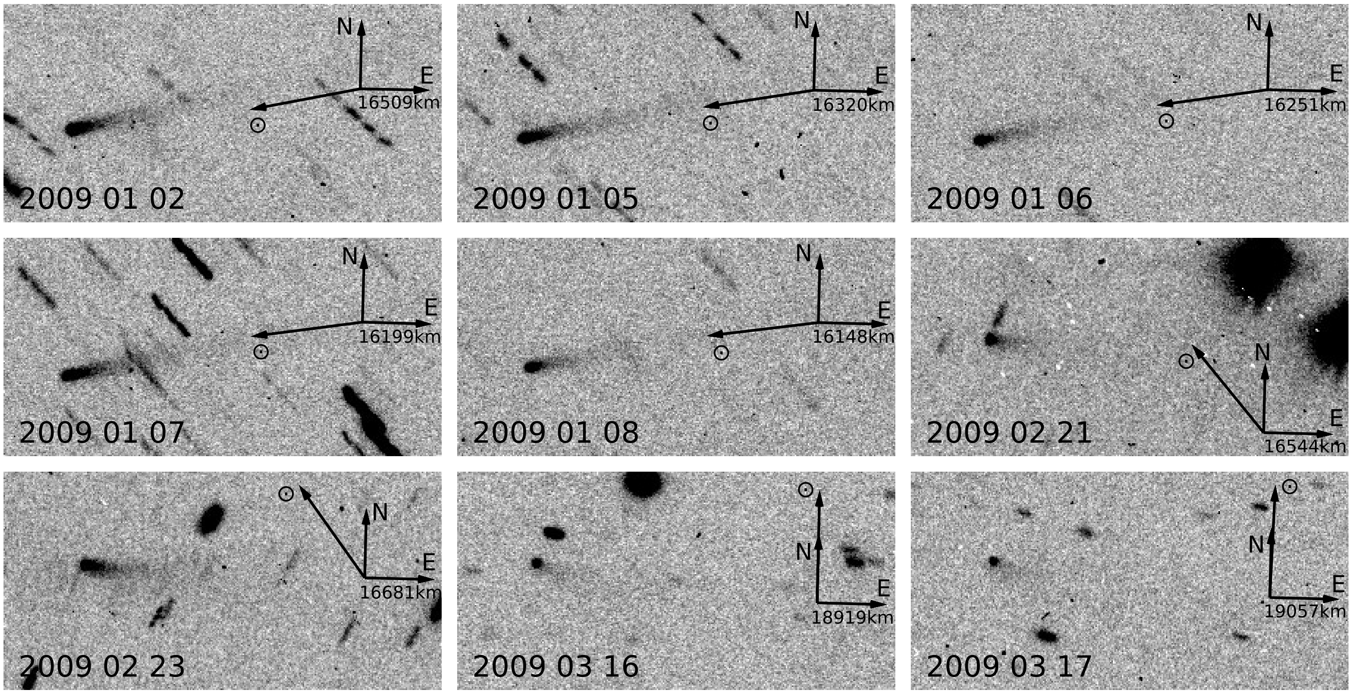

Figure 2. Follow-up images of 212P from 2009 January 2, until March 17. All the images were composites of three *R*-band images of five minute exposure. North is up and east is to the right. The direction of the Sun is also indicated.

Table 2
The Time Variation of the Afρ Values of 212P over the Period of the Lulin Observations in 2009

Date		*rh* (AU)	Δ (AU)	α (deg)	Afρ, 3.″5 (cm)
2009 Jan	2	1.683	0.959	30.4	5.341
	5	1.688	0.948	29.6	4.712
	6	1.690	0.944	29.4	4.410
	7	1.693	0.941	29.1	4.927
	8	1.695	0.938	28.8	4.573
2009 Feb	17	1.822	0.945	20.0	4.113
	21	1.839	0.961	19.7	3.385
	23	1.848	0.969	19.6	4.461
2009 Mar	16	1.945	1.099	20.6	2.861
	17	1.950	1.107	20.7	2.844
	18	1.955	1.115	20.8	3.275
	19	1.960	1.123	20.9	2.707
	20	1.965	1.132	21.1	2.846

shown in Figure 2, the images consistently show the formation of a faint dust tail. Morphologically speaking, the dust tail appears to have the same length between January 2 and 7 and then becomes shorter and fainter afterward. At the end of the Lulin observation in 2009 March, only a very diffuse structure could be recognized. An important question is thus whether the observed outgassing process could have existed for more than just a few days.

This interpretation is also consistent with the finding that the Afρ (cm) value as determined according to A'Hearn et al. (1984) varies from 4.6 to 5.3 at the beginning of January to 3.4–4.6, and finally to about 2.8 in March as the comet moved away from the perihelion (see Table 2). The continuous presence of the dust tail between 2009 January and March suggests an uninterrupted emission process through this time interval according to the synchrone approach (Finson et al. 1968). However, we are unable to determine whether or not the dust emission was triggered by the recent excavation of some fresh active region by an impact event.

Next we check the colors of the dust coma. The aperture size of our photometric study is about 6–8 pixels (4200–5600 km) depending on the seeing conditions. The measured values of $B-V$ (0.995 ± 0.189), $V-R$ (0.678 ± 0.092), and $V-I$ (1.008 ± 0.106) at the optical center are consistent with those of the nuclei of JFCs (Lamy & Toth 2009). Because of the faintness of the dust tail, it is not possible to accurately estimate the color of the dust. In any event, the $B-R$ color at a location several arcseconds away from the central nucleus in the tailward direction can be estimated to be about 1.1 ± 0.1 (see Figure 3). This is consistent with the average value of about 1.1 ± 0.3 for cometary dust as summarized in Kolokolova et al. (2004) and the $B-R$ value of the dust tail of comet P/2010 TO20 LINEAR-Grauer which was found to be about 1.2 ± 0.2 (Lacerda 2013). Because the color remains nearly the same along the tail, where the brightness distribution has a much smaller slope as a function of the cometocentric distance than that of the gas coma, we believe that our measurements are not subject to strong contamination by gas emission.

Figure 4 summarizes the orbital positions of 212P during the Lulin observations. The orbits of a number of main-belt comets are also shown for comparison. It can be seen that the coma activity occurred a few days after perihelion and the dust coma remained detectable with LOT for the next two months. An enhanced level of solar heating for the nucleus surface could be the triggering mechanism of the dust tail formation. Other effects might also play a role. For example, the absence of a dust coma when 212P was discovered as an asteroid might have two possible reasons. First, the appearance of a diffuse coma and dust tail in 2009 January could be associated with an outburst of a pocket of volatile material similar to that of comet 17P/Holmes (Lin et al. 2009; Reach et al. 2010) but on a smaller

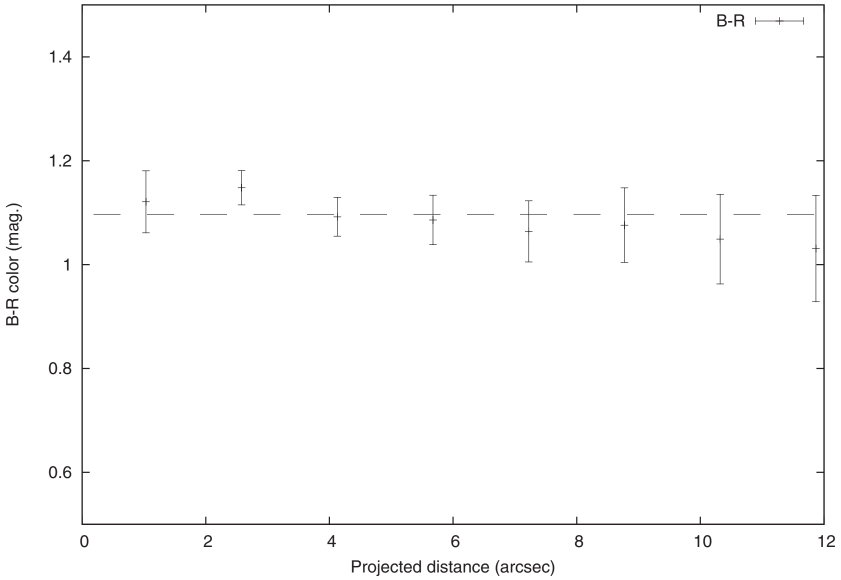

Figure 3. $B - R$ color of 212P along its dust tail on 2009 January 2.

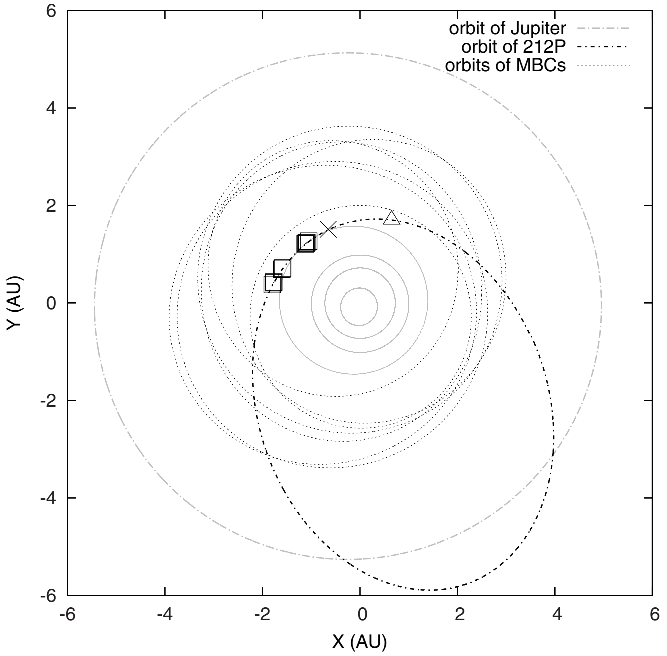

Figure 4. Orbit of 212P with some important positions identified: □ indicates the positions of our observations in 2009; Δ is for the orbital position of the first discovery in 2000 December. The orbits of several main-belt comets are also shown for comparison.

scale. Alternatively, the disappearance/non-detection of the dust features in earlier observations could be the result of a seasonal effect connected to the obliquity of the rotating nucleus (Hsieh et al. 2010). It is therefore interesting to know whether 212P is basically a defunct comet with its nucleus surface covered by a dust mantle or if it is of the nature of a new comet that has only recently reached the present perihelion distance. We used numerical computation to trace the dynamical history of 212P.

3. ORBITAL EVOLUTION

Table 3 shows the orbital parameters of 212P from the Jet Propulsion Laboratory (JPL-SBD). We used the Mercury integrator of the Bulirsch–Stoer algorithm (Chambers 1999) for the numerical orbit integrations. All planets from Mercury to Neptune are included in the computation. The step size employed was 0.05 days. The orbital evolution of 212P was traced backward and forward for 100,000 yr in each direction.

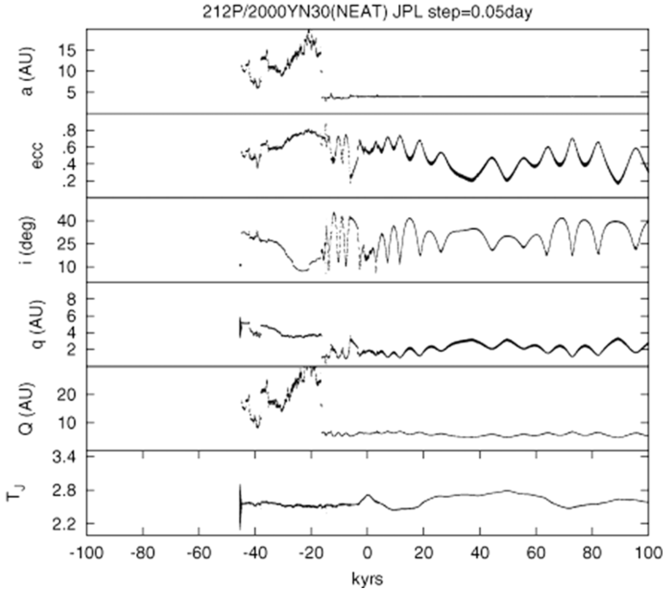

Figure 5. Time variations of the orbital parameters of 212P obtained by using initial values from JPL.

Table 3

Orbital Parameters of 212P from the NASA Jet Propulsion Laboratory

	JPL_SBD
Perihelion, q (AU)	1.654234
Eccentricity, e	0.578748
Inclination, i (deg)	22.3980
Argument of pericenter (deg)	15.0710
Ascending node (deg)	98.9294
Epoch of pericenter, T_p (JD)	2454803.81008
Orbital epoch (JD)	2454481.5

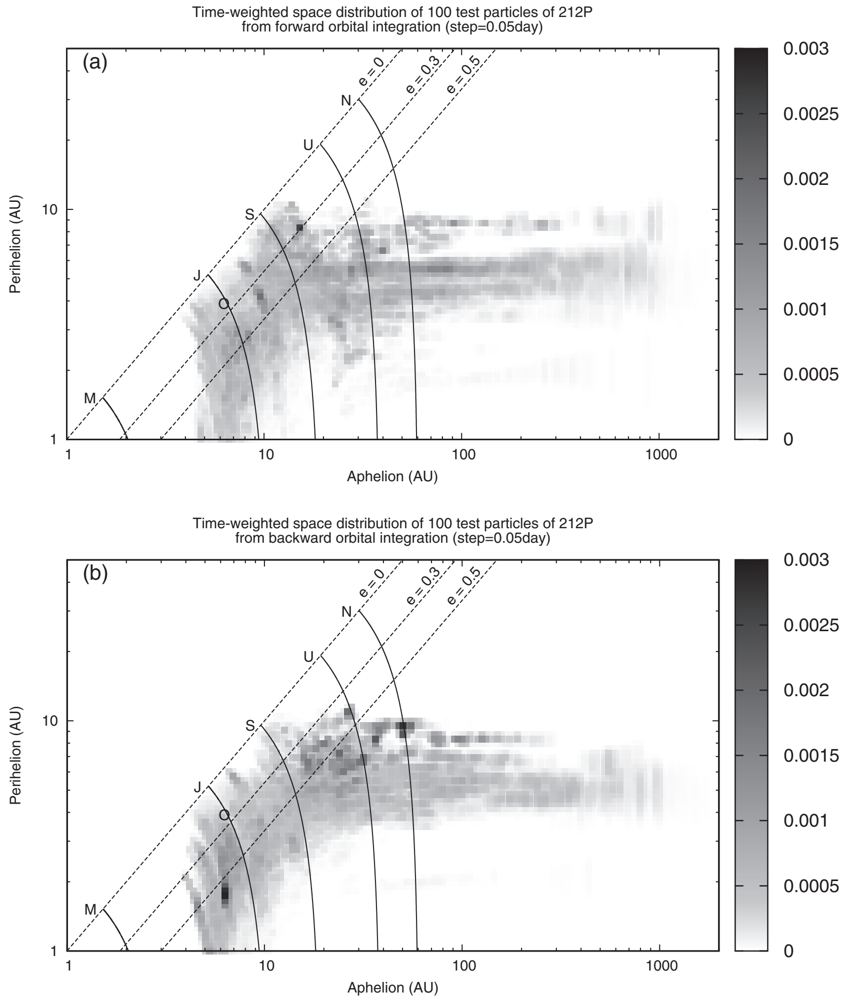

Figure 6. Probability distribution of the footprints of the 100 212P clones in the aphelion and perihelion distances. For our 1 Myr integration, about 10% of the orbital duration would have perihelion distances reaching below 2 AU. The current position is denoted by the black dot: (a) from backward orbital integration over the last 10^6 yr; (b) from forward orbital integration over the next 10^6 yr.

Figure 5 shows an example of the pattern of orbital evolution according to the JPL ephemeris. In the case of backward integration, 212P was captured into a "short-period" orbit with $a < 20$ AU at $T = -46{,}802$ yr ago as a result of a close encounter with Jupiter at a distance of 0.0063 AU. Its perihelion (q) stays at about 4 AU and aphelion (Q) at about 15 AU. Another close encounter with Jupiter at $T = -18{,}250$ yr ago at a distance of 0.021 AU transforms the orbit into a quasi-Hilda orbit with the semi-major axis remaining at about 4 AU. Our calculation shows that repeated planetary perturbations will lead to long-term oscillations in the eccentricity and inclination, with periods varying between a few hundred years to about ten thousand years. At about $t \sim -18{,}250$ yr ago, the eccentricity reaches values as high as 0.8, allowing 212P to attain a perihelion distance as close as 0.8 AU to the Sun. It is probably in this time interval that 212P begins its career as a short-period comet. This phase lasts about 250 yr. Subsequently, the orbit of 212P will be transformed to one that increasingly resembles that of a quasi-Hilda asteroid, with q being raised to larger values between 1 and 3.5 AU. At the present time, the orbital evolution of 212P is in transition from a punctuated long-term 3:2 libration to a relatively smooth long-term libration in e and i for the next 10^5 yr. According to this sample calculation with the JPL orbital data, 212P will be a very stable quasi-Hilda object from now on.

The study of the orbital evolution of this test particle gives us some idea of the possible origin and fate of an object like 212P. For example, it tells us how an object with a perihelion distance originally outside the orbit of Jupiter could be transformed into a quasi-Hilda in long-term stable 3:2 resonance with Jupiter. However, the orbital elements given in the JPL ephemeris have numerical uncertainties. Furthermore, additional numerical effects could be introduced in the direct integration scheme. It is therefore important to study the statistical pattern of the orbital evolution of 212P by running a number of its clones. The Monte Carlo simulation of the orbital histories of 100 clones of 212P was done by following the description in Bernstein & Khushalani (2000).

The global pattern of the dynamical evolution of 212P-like objects could be formulated by computing the relative fractions of time in the lifetimes of individual test particles (clones) spent in different combinations of orbital parameters. One method that is often used is the statistical distribution of the time intervals in the q (perihelion) and Q (aphelion) coordinate system divided into many grids with $\Delta q = 1$ AU and $\Delta Q = 1$ AU. The sum of the total time of duration in each grid therefore constitutes the probability, namely, the distribution of residence time or "footprint," of the object during its orbital evolution.

Figure 6 compares the statistical distributions of the "footprints" of the 212P clones in the orbital space for the past and

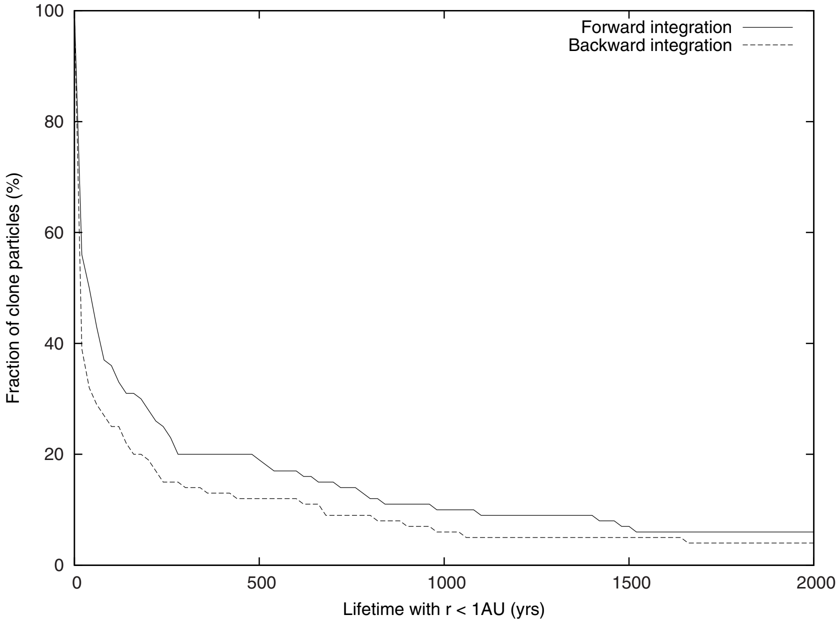

Figure 7. Statistical distributions of the cumulative time of the test bodies inside a certain heliocentric distance during their dynamical evolution in the backward (dashed lline) and forward (solid line) orbital integrations.

future one million years, respectively. The gravitational influences of Jupiter and Saturn are clearly seen. In the cases of the backward and forward integrations, we find several strips and clusters confined within the q–Q curve of Jupiter and then some others between those of Jupiter and Saturn, respectively. Similar features can be found between the q–Q curves of Saturn and Uranus. Those are objects that are being temporarily trapped between the orbits of these two outer planets. In the forward integration, there are also two horizontal patterns, one has q nearly being fixed at about 5 AU but Q moving from $<$10 AU to $>$1000 AU, and the other one has q being fixed at about 9 AU and Q ranging from 10 AU to beyond 1000 AU. These two tracks are produced by the gravitational scattering of the test particles by Jupiter and Saturn, respectively, to large aphelion distances. Similar "footprint" structures in the backward integration can be understood in the same manner. Because of their large gravitational scattering effect, both Jupiter and Saturn effectively form barriers for further outward diffusion of the test particles to the orbital region of Uranus and Neptune. In the numerical simulations of the injection of trans-Neptunian objects into the inner solar system (see Tiscareno & Malhotra 2003), we would find the presence of "footprints" between the orbit of Neptune and that of Uranus simply because the source region is located in the vicinity of the trans-Neptunian region while Jupiter and Saturn form barriers to inward diffusion.

Therefore, the evolutionary behavior as shown in Figure 6 is what would be expected of short-period comets that are injected from the trans-Neptunian region. However, in our backward integration, random planetary encounters tend to produce a cutoff at Jupiter's orbit, thus curtailing the reverse paths returning to the trans-Neptunian region and the transitory zone occupied by Centaurs (Tiscareno & Malhotra 2003). The orbital footprints from the forward integration show a pattern similar to that of the backward integration.

These results also indicate that the exact evolutionary histories of quasi-Hilda asteroids are very sensitive to the starting values of the orbital elements. Even small differences could lead to very different outcomes in the orbital integrations. On the other hand, it is interesting to note that in a statistical sense, some of the quasi-Hildas could have originated from the outer solar system via gravitational scattering by Jupiter. In this process, these objects, including 212P, would have moved in orbits with perihelia of less than 1 AU for some short intervals. This means that there is a fair chance that 212P had experienced ice sublimation and gas outgassing from its surface material.

According to estimates of the average physical lifetime of short-period comets (Fernandez 1984; Hughes 2003), the outgassing activity of those with perihelion $q < 1$ AU should decay away with a physical lifetime of 10^3–10^4 yr due to of the buildup of a dust mantle. For a short-period comet orbit of $a = 3$ AU and $e = 0.8$, the time spent inside 1 AU is about 0.4 yr per orbit with an orbital period of 5.2 yr. This means that objects with a cumulative time of $\Delta t >$ 80–800 yr with $q < 1$ AU over their past orbital evolution would have a high probability of becoming inactive.

Figure 7 shows the statistical distribution of the cumulative time of the 212P clones as a function of heliocentric distance during their individual dynamical evolutions. Note that in our sample of "backward" test runs, a fraction ($\sim$30%) of the objects spend more than a total of $\Delta t \sim 100$ yr inside a 1 AU heliocentric distance. From this point of view, it is possible that 212P could have developed a partial dust mantle in its past history as a short-period comet.

4. SUMMARY AND DISCUSSION

In the present work, we report the serendipitous discovery of the coma activity of 212P, which is a quasi-Hilda object in cometary-like orbit. This object, with a diameter of $D = 1.7 \pm 0.3$ km, is the size of a cometary nucleus. The results of our orbital integration show that it could have been captured into a short-period orbit from a Centaur-like orbit. Subsequent close encounters with Jupiter could have transformed its orbit into that of a quasi-Hilda characterized by a 3:2 mean motion resonance. The exact dynamical origin and its fate depend sensitively on the starting orbital elements. Our study therefore shows that ACOs/quasi-Hilda asteroids are potentially important in tracing the transport process of volatile materials from the outer solar system to the inner solar system via planetary orbital migration and scattering. 212P will return to perihelion in 2016. Its brightness variation and the possible reappearance of the dust coma activity will be closely monitored so that we can know for sure whether its observed dust tail structure from last time was related to thermal sublimation or not. As for the larger issue of the Hildas and quasi-Hildas (and other classes of objects like the main-belt comets) as potential contributors to terrestrial oceans, we intend to follow up with model calculations of their orbital evolution with and without the possible effects of planetary orbital migration. The definite answer would probably need to wait for in situ (D/H) measurements (or sample returns) from these objects.

We thank the reviewer for many useful and constructive comments which improved the scientific content of this work. We thank Yingtung Chen and Hsingwen Lin for useful discussions. This work was partially supported by NSC grant NSC 101-2119-M-008-007-MY3 and Ministry of Education under the Aim for Top University Program NCU, and Project 019/2010/A2 of Science and Technology Development Fund MSAR No. 0166.

REFERENCES

A'Hearn, M. F., Schleicher, D. G., Millist, R. L., Feldman, P. D., & Thompson, D. T. 1984, AJ, 89, 579
Bernstein, G., & Khushalani, B. 2000, AJ, 120, 3323
Bockelee-Morvan, D., Biver, N., Swinyard, B., et al. 2012, A&A, 544, 15
Campins, H., Hargrove, K., Pinilla-Alonso, N., et al. 2010, Natur, 464, 1320
Chambers, J. E. 1999, MNRAS, 304, 793
Cheng, Y. C., & Hsiao, H. Y. 2009, IAUC, 9010, http://www.cbat.eps.harvard.edu/iauc/09000/09010.html
Chyba, C. F. 1987, Natur, 330, 632
Crovisier, J., Bockelee-Morvan, D., Colom, D., et al. 2004, A&A, 418, 1141
Dahlgren, M., & Lagerkvist, C.-I. 1995, A&A, 302, 907
Dahlgren, M., Lagerkvist, C.-I., Fitzsimmons, A., Williams, I. P., & Gordon, M. 1997, A&A, 323, 606
Dahlgren, M., Lahulla, J. F., & Lagerkvist, C.-I. 1999, Icar, 138, 259
Di Sisto, R. P., & Brunini, A. 2007, Icar, 190, 224
Di Sisto, R. P., Brunini, P., Dirani, A., Lorena, D., & Orellana, R. B. 2005, Icar, 174, 81
Duncan, M., Quinn, T., & Tremaine, S. 1989, Icar, 82, 402
Eberhardt, P., Reber, M., Krankowsky, D., & Hodges, R. R. 1995, A&A, 302, 301
Fernandez, J. A. 1984, A&A, 135, 129
Fernandez, J. A., & Gallardo, T. 2002, Icar, 159, 358
Fernandez, J. A., & Ip, W.-H. 1984, Icar, 58, 109
Fernandez, Y. R., Jewitt, D. C., & Sheppard, S. S. 2005, AJ, 130, 308
Finson, M. L., & Probstein, R. F. 1968, ApJ, 154, 327
Gibbs, A. R. 2009, IAUC, 9010, http://www.cbat.eps.harvard.edu/iauc/09000/09010.html
Hartogh, P., Dariusz, C. L., Dominique, B., et al. 2011, Natur, 478, 218
Hsieh, H. H., & Jewitt, D. C. 2006, Sci, 312, 561
Hsieh, H. H., Jewitt, D. C., Lacerda, P., et al. 2010, MNRAS, 403, 363
Hughes, D. W. 2003, MNRAS, 346, 584
Ip, W.-H., & Fernandez, J. A. 1988, Icar, 74, 47
Ip, W.-H., & Fernandez, J. A. 1991, Icar, 92, 185
Jehin, E., Manfroid, J., Hutsemekers, D., Arpigny, C., & Zucconi, J.-M. 2009, EM&P, 105, 167
Jewitt, D. 2012, AJ, 143, 66
Kolokolova, L., Hanner, M. S., Levasseur-Regourd, A.-Ch., & Gustafson, B. Å. S. 2004, in Comets II, ed. M. C. Festou, H. U. Keller, & H. A. Weaver (Tucson, AZ: Univ. of Arizona Press), 577
Kresak, J. 1980, M&P, 22, 83
Lacerda, P. 2013, MNRAS, 428, 1818
Lamy, P., & Toth, I. 2009, Icar, 201, 674
Lin, Z. Y., Lin, C. S., Ip, W.-H., & Lara, L. M. 2009, AJ, 138, 625
Malhotra, R. 1995, AJ, 110, 420
Marsden, B. G. 2008, MPEC-2008X77, http://www.minorplanetcenter.net/mpec/K08/K08V41.html
Meier, R., Owen, T. C., Mathews, H. E., et al. 1998, Sci, 279, 842
Morbidelli, A, Chambers, J., Lunine, J. I., et al. 2000, M&PS, 35, 1309
Ohtsuka, K., Ito, T., Yoshikawa, M., Asher, D. J., & Arakida, H. 2008, A&A, 489, 1355
Reach, W. T., Vaubaillon, J., Lisse, C. M., Holloway, M., & Rho, J. 2010, Icar, 208, 276
Robert, F. 2006, in Meteorites and the Early Solar System II, ed. D. S. Lauretta & H. Y. McSween, Jr. (Tucson, AZ: Univ. Arizona Press), 341
Rivkin, A. S., & Emery, J. P. 2010, Natur, 464, 1322
Tiscareno, M. S., & Malhotra, R. 2003, AJ, 126, 3122
Toth, I. 2006, A&A, 448, 1191
Vaghi, S. 1973, A&A, 24, 107
Villanueva, G. L., Mumma, M. J., Bonev, B. P., et al. 2009, ApJL, 690, L5
Volk, K., & Malhotra, R. 2008, ApJ, 687, 714
Weaver, H. A., A'Hearn, M. F., & Arpigny, C. 2008, LPICo, 1405, 8216

The Astronomical Journal, 146:14 (10pp), 2013 July
doi:10.1088/0004-6256/146/1/14

THE TAOS PROJECT: RESULTS FROM SEVEN YEARS OF SURVEY DATA

Z.-W. Zhang[1], M. J. Lehner[1,2,3], J.-H. Wang[1], C.-Y. Wen[1], S.-Y. Wang[1], S.-K. King[1], Á. P. Granados[4], C. Alcock[3], T. Axelrod[5], F. B. Bianco[6], Y.-I. Byun[7], W. P. Chen[8], N. K. Coehlo[9], K. H. Cook[1], I. de Pater[10], D.-W. Kim[11], T. Lee[1], J. J. Lissauer[12], S. L. Marshall[13], P. Protopapas[3,14], J. A. Rice[9], and M. E. Schwamb[15,16]
[1] Institute of Astronomy and Astrophysics, Academia Sinica. 11F of Astronomy-Mathematics Building,
National Taiwan University. No. 1, Sec. 4, Roosevelt Road, Taipei 10617, Taiwan; zwzhang@asiaa.sinica.edu.tw
[2] Department of Physics and Astronomy, University of Pennsylvania, 209 South 33rd Street, Philadelphia, PA 19104, USA
[3] Harvard-Smithsonian Center for Astrophysics, 60 Garden Street, Cambridge, MA 02138, USA
[4] Instituto de Astronomía, Universidad Nacional Autónoma de México, Apdo. Postal 106, Ensenada, Baja California 22800, Mexico
[5] Steward Observatory, 933 North Cherry Avenue, Room No. 204, Tucson AZ 85721, USA
[6] Center for Cosmology and Particle Physics, New York University, 4 Washington Place, New York, NY 10003, USA
[7] Department of Astronomy and University Observatory, Yonsei University, 134 Shinchon, Seoul 120-749, Korea
[8] Institute of Astronomy, National Central University, No. 300, Jhongda Road, Jhongli City, Taoyuan County 320, Taiwan
[9] Department of Statistics, University of California Berkeley, 367 Evans Hall, Berkeley, CA 94720, USA
[10] Department of Astronomy, University of California Berkeley, 601 Campbell Hall, Berkeley, CA 94720, USA
[11] Max Planck Institute for Astronomy, Königstuhl 17, D-69117 Heidelberg, Germany
[12] Space Science and Astrobiology Division 245-3, NASA Ames Research Center, Moffett Field, CA 94035, USA
[13] Kavli Institute for Particle Astrophysics and Cosmology, 2575 Sand Hill Road, MS 29, Menlo Park, CA 94025, USA
[14] Initiative in Innovative Computing, Harvard University, 60 Oxford Street, Cambridge, MA 02138, USA
[15] Department of Physics, Yale University, New Haven, CT 06511, USA
[16] Yale Center for Astronomy and Astrophysics, Yale University, P.O. Box 208121, New Haven, CT 06520, USA

Received 2013 January 16; accepted 2013 May 1; published 2013 June 14

ABSTRACT

The Taiwanese–American Occultation Survey (TAOS) aims to detect serendipitous occultations of stars by small (∼1 km diameter) objects in the Kuiper Belt and beyond. Such events are very rare ($<10^{-3}$ events per star per year) and short in duration (∼200 ms), so many stars must be monitored at a high readout cadence. TAOS monitors typically ∼500 stars simultaneously at a 5 Hz readout cadence with four telescopes located at Lulin Observatory in central Taiwan. In this paper, we report the results of the search for small Kuiper Belt objects (KBOs) in seven years of data. No occultation events were found, resulting in a 95% c.l. upper limit on the slope of the faint end of the KBO size distribution of $q = 3.34$–3.82, depending on the surface density at the break in the size distribution at a diameter of about 90 km.

Key words: comets: general – Kuiper Belt: general – occultations – planets and satellites: formation

1. INTRODUCTION

The size distribution of Kuiper Belt objects (KBOs) has been accurately measured down to diameters of $D > 30$ km (Fuentes et al. 2009; Fuentes & Holman 2008; Fraser & Kavelaars 2008; Fraser et al. 2008; Bernstein et al. 2004; Luu & Jewitt 2002), while Fraser & Kavelaars (2009) have provided measurements down to diameters $D \gtrsim 15$ km. The size distribution of large KBOs approximately follows a power law of the form:

$$\frac{dn}{dD} \propto D^{-q}, \tag{1}$$

where the slope $q = 4.5$ down to a diameter of $D \approx 90$ km. A clear break in the size distribution has been detected near 90 km (Fuentes et al. 2009; Fraser & Kavelaars 2009; Bernstein et al. 2004), giving way to a shallower distribution for smaller objects. Various models of the formation of the Kuiper Belt have been developed (Schlichting et al. 2013; Benavidez & Campo Bagatin 2009; Kenyon & Bromley 2001, 2004, 2009; Pan & Sari 2005; Benz & Asphaug 1999; Kenyon & Luu 1999a, 1999b; Davis & Farinella 1997; Stern 1996; Duncan et al. 1995) which predict this break in the size distribution, but these models make vastly different predictions on the size distribution for objects smaller than the break diameter. These models are based on different scenarios of the dynamical evolution of the solar system and the internal structure of the KBOs themselves. It is generally assumed that the outward migration of Neptune stirred up the orbits of objects in the Kuiper Belt, which subsequently underwent a process of collisional erosion, giving rise to a shallower size distribution. The simplest models also predict a small-end power-law size distribution as shown in Equation (1), where the slope q depends primarily on the internal strength of the KBOs. Solid objects held together by material strength give rise to larger slopes, while the weaker gravitationally bound rubble piles are more easily broken up and give rise to smaller values of q. A measurement of the size distribution of smaller objects (down to $D \gtrsim 100$ m) is needed in order to constrain these models. Furthermore, such a measurement would provide important information on the origin of short-period comets (Volk & Malhotra 2008; Tancredi et al. 2006; Duncan & Levison 1997; Levison & Duncan 1997; Morbidelli 1997; Holman & Wisdom 1993).

The direct detection of such objects is difficult because they are extremely faint, with typical magnitudes $R > 28$, and are thus invisible to surveys using even the largest telescopes. However, a small KBO will induce a detectable drop in the brightness of a distant star when it passes across the line of sight to the star (Chang et al. 2006, 2007, 2013; Schlichting et al. 2009, 2012; Wang et al. 2009, 2010; Bianco et al. 2009, 2010; Bickerton et al. 2008, 2009; Liu et al. 2008; Zhang et al. 2008; Nihei et al. 2007; Roques et al. 1987, 2003, 2006; Cooray 2003; Cooray & Farmer 2003; Roques & Moncuquet 2000; Brown & Webster 1997; Bailey 1976). High-speed photometry is needed to detect these events, given that we expect a typical event duration of about 200 ms. Detection of such events is

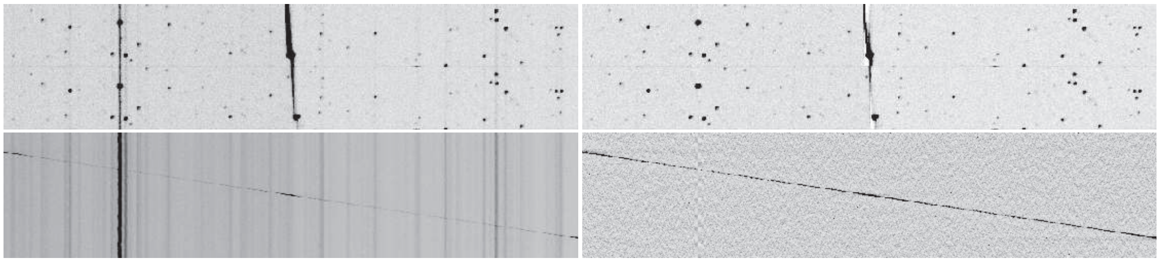

Figure 1. Top left: horizontal subsections of two consecutive rowblocks with a bright moving object in the center. (The boundary between the rowblocks is visible as a dark horizontal line bisecting the image. This is a slight excess in dark current from the edge of the CCD.) The vertical streaks (see the text) from the brighter stars are also evident. Top right: the same rowblock subsections after the background streak subtraction. While the streaks from the bright stars are removed, the moving object itself is not completely removed, and the background flux near the moving object is oversubtracted. Bottom left: gray-scale image representation of the background flux subtracted from the rowblocks near those shown in the top panels. Here, each row represents the flux subtracted from a single rowblock, while the columns correspond to those in the top panels. The vertical streaks in this image are the streaks left by the stars during the zipper-mode readout. The moving object in original data cause the background to be oversubtracted, and the oversubtracted flux clearly shows the trajectory of the moving object across the focal plane. Bottom right: the same background image from the bottom-left panel after applying the high-pass mean and variance filters to remove the streaks from the bright stars. The oversubtracted background flux from the moving object is clearly evident.

further complicated by the fact that the sizes of the objects of interest are on the order of the Fresnel scale (about 1.4 km for our median observed wavelength of about 600 nm and a typical object distance of 43 AU), and the resulting light curves exhibit significant diffraction features (Nihei et al. 2007). The goal of the Taiwanese–American Occultation Survey (TAOS) project is to detect such occultation events and measure the size distribution of KBOs with diameters $0.5\,\mathrm{km} < D < 30\,\mathrm{km}$.

To date, 18 events consistent with occultations by objects in the outer solar system have been detected. The three detections claimed by Roques et al. (2006), if they are occultations, are unlikely to have been caused by KBOs (the distances are inconsistent). On the other hand, two detections reported by Schlichting et al. (2009, 2012) are consistent with occultation events by 1 km diameter KBOs at 45 AU. Schlichting et al. (2012) found one additional event consistent with a KBO occultation, but they reject this event because of its high inclination (it was detected at an ecliptic latitude of $b = 81^{\circ}\!.5$). The remaining 12 possible events (Chang et al. 2007) were found in archival *RXTE* measurements of Sco X-1. However, the interpretation of these detections as occultation events has been challenged (Jones et al. 2008; Blocker et al. 2009).

TAOS has been in operation since 2005 February. The system is described in detail in Lehner et al. (2009). In summary, the survey operates four 50 cm telescopes at Lulin Observatory in central Taiwan. The telescopes are very fast ($F/1.9$), with a field of view of 3 deg^2. Each telescope is equipped with a camera which utilizes a single 2k × 2k CCD imager. All four telescopes monitor the same stars simultaneously at a readout cadence of 5 Hz (with the readout cadence synchronized among the four telescopes). We require that any events be detected simultaneously in each of the telescopes in order to minimize the false positive rate (Lehner et al. 2010).

High-speed cadence is achieved using a special CCD readout mode called zipper mode, which is described in detail in Lehner et al. (2009). To summarize, instead of taking repeated exposures, we leave the shutter open for the duration of a data run. At a cadence of 5 Hz, we read out a subimage comprising 76 rows, which we have called a rowblock. When the rowblock is read out, the remaining photoelectrons on the CCD are shifted down by 76 rows as well. If one considers starting with a rowblock at the far edge of the CCD, photoelectrons are collected and then shifted to the next rowblock. Photoelectrons are then collected in addition to those from the first rowblock, and then they are shifted to the next. By the time the original photoelectrons are read out, photoelectrons have been collected from every star on the focal plane in a single rowblock, although at different epochs.

While zipper-mode readout allows us to image every star in the focal plane, there are two characteristics of the data that reduce the signal-to-noise ratio (S/N). The first is that sky background that is collected as a rowblock is shifted across the focal plane, while photoelectrons from a single star are only collected at one location. Furthermore, it takes about 1.3 ms to read out a single row, corresponding to about 95 ms for an entire rowblock, so the actual exposure of a star is only 105 ms, while sky background is collected for a total of 5.4 s. Second, flux is also collected from the stars during the readout stage, and the brighter stars will leave significant numbers of photoelectrons in the pixels as they are being shifted. This flux will appear as bright vertical streaks in the images (see the upper left panel of Figure 1). Nevertheless, zipper mode is successful in collecting high S/N photometric data on enough stars for the project to successfully probe a significant fraction of the allowed size distribution parameter space.

In this paper, we report on the analysis of seven years of zipper-mode data collected by the TAOS system. In Section 2, we describe the data set used in this analysis. In Section 3, we provide a detailed discussion of the analysis pipeline. In Section 4, we present the results of the analysis of the data set, and finally in Section 5, we discuss our future plans for the survey.

Throughout the remainder of this paper, we use the following definitions. A data run is a series of high-cadence multi-telescope measurements on a single field, typically for 1.5 hr at a time. A light curve is a time series of photometric measurements of a single star from one telescope in one data run, and a light curve set is a set of multi-telescope photometric measurements of a single star during one data run. A flux tuple is a set of multi-telescope measurements (with a minimum of three telescopes) of one star at a single epoch. A light curve set is thus a time series of flux tuples.

2. THE SEVEN YEAR DATA SET

Earlier results from the TAOS search for small KBOs were reported in Zhang et al. (2008) and Bianco et al. (2010). These two papers describe results obtained from operating three telescopes. The data set used in Bianco et al. (2010) ended on 2008 August 2, when the fourth telescope became

Table 1
Data Set Parameters

Parameter	Zhang et al. (2008)	Bianco et al. (2010)	This Work
Start date	2005 Feb 7	2005 Feb 7	2005 Feb 7
End date	2006 Dec 31	2008 Aug 2	2011 Sep 8
Data runs	156	414	858
Light curve sets[a]	110,554	366,083	835,732 (209,130)
Total exposure (star hours)[a]	152,787	500,339	1,159,651 (292,514)
Photometric measurements[a]	7.8×10^{9}	2.7×10^{10}	6.7×10^{10} (2.1×10^{10})
Flux tuples[a]	2.6×10^{9}	9.0×10^{9}	2.1×10^{10} (5.3×10^{9})

Note. [a] Values for four-telescope data shown in parentheses.

operational. The addition of the fourth telescope to the array was beneficial in two ways. First, using four telescopes increases the significance of any candidate occultation events, while the false positive rate remains constant (Lehner et al. 2010). Second, we have experienced frequent problems with the reliability of our cameras and telescopes. With four telescopes, we can still operate with three telescopes when one of the systems is shut down for repair. Given that a minimum of three telescopes is necessary to keep the false positive rate low enough (Lehner et al. 2010), we can still collect useful data in the event that there is a problem with one of the systems. The overall operational efficiency of the survey thus improved significantly since we could still collect data when one telescope was offline.

The current data set is summarized in Table 1, along with the data sets used in Zhang et al. (2008) and Bianco et al. (2010). The current data set is more than 2.3 times larger than that used in Bianco et al. (2010). Ninety percent of the photometric data in this set were acquired within 6° of the ecliptic in order to maximize the event rate. The results quoted in this paper are thus applicable to both the hot (inclination $i > 5°$) and cold ($i < 5°$) KBO populations.

3. DATA ANALYSIS

The data analysis took place in three stages: photometric reduction of raw image data, the search for occultation events, and the detection efficiency simulation. These stages roughly follow the same procedures outlined in Bianco et al. (2010), but several improvements were made to the pipeline in this round of data analysis. The new pipeline is described in the following subsections.

3.1. Photometric Reduction

For the first step in the pipeline, a custom photometric reduction pipeline (Zhang et al. 2009) is used to measure the brightness of each star in the field at each epoch, and the resulting measurements are assembled into a time-series light curve for each star. For every star, the light curve from each telescope is combined into a light curve set. Next, bad data points (e.g., measurements where the star lies near the edge of the focal plane) are removed from the light curves (see Zhang et al. 2009, for details).

A significant improvement added to this stage in the process is the automated flagging of photometric measurements affected by bright objects (such as satellites or airplanes) moving across the field of view. As discussed in Bianco et al. (2010), several candidate events were found in the previous data set. Visual inspection of the relevant images revealed that these events were caused by bright moving objects passing near the star that appeared to be occulted. The new algorithm to detect these bright moving objects is described in Section 3.1.1.

3.1.1. Bright Moving Object Detection

As mentioned in Section 3.1, bright objects moving across the field of view during zipper-mode image collection can give rise to a large number of false positive events. This is caused by the background subtraction in the photometric reduction. As discussed in Section 1, the zipper-mode readout has the disadvantage that the brighter stars leave streaks along the columns in the images due to the finite time it takes to read out a row from the CCD. These streaks are removed during the photometric reduction by subtracting an estimate of the mode of the column from each pixel in the column, where the mode is calculated for each zipper-mode rowblock (Zhang et al. 2009). A bright moving object passing over a particular column causes the mode of that column to be overestimated, and the background is thus oversubtracted, causing an artificial drop in the measured brightness of any star whose aperture includes that column (see the top panels of Figure 1).

In order to detect these events, we save the 3σ-clipped column mean for each rowblock and column on all four cameras. These background data are stored in FITS format, and an example is shown in the bottom left panel of Figure 1. Note that each column in this image corresponds to an actual column on the CCD, but the row corresponds to a rowblock in the zipper-mode data. The pixel value is simply the column mean (after 3σ clipping) for that rowblock and column. The streaks from the bright stars are evident in the image. Also clearly visible is the object shown in the top panels moving across the image. We note that what appears as a moving object is actually the high value for the column average due to the moving object. Nevertheless, it is straightforward to identify which columns in which rowblocks are affected by the overestimated background.

First, we normalize the image by applying the same rolling clipped mean and variance filter to each of the columns we use to remove the slowly varying trends along the light curves (Lehner et al. 2010). That is, we replace each column average value b_{mn}, where m is the rowblock index and n is the column, with a normalized value d_{mn}, defined as

$$\begin{aligned} c_{mn} &= b_{mn} - \mu_{mn}, \\ d_{mn} &= \frac{c_{mn}}{\sigma_{mn}}, \end{aligned} \qquad (2)$$

where μ_{mn} is the local (3σ-clipped) mean within column n and σ_{mn} is the local variance within column n, calculated with window sizes of 21 rowblocks. Note that σ_{mn} is calculated after the mean has been subtracted from every rowblock background value along the column.

The bottom right panel of Figure 1 shows the resulting values of d_{mn} after application of this filter to the image shown in the bottom left panel. We then apply an algorithm (Lutz 1980)[17] to find objects in the normalized background image. We define an object as either a set of 20 or more adjoining pixels with values of d_{mn} larger than 1.5, or as a set of 5 or more pixels with values larger than 2.5. We then flag any photometric measurements where a column affected by a moving object lies within the aperture used in the photometry. The removal of all flagged data points results in the elimination of all false positive events caused by moving objects.

3.2. Event Search

3.2.1. Rank Product Statistic

Our event selection algorithm uses the rank product statistic, which is described in detail in Lehner et al. (2010). This statistic takes advantage of the multi-telescope data to give an exact value for the significance of any candidate event, even if the underlying distribution of the flux measurements is not known. Given that TAOS samples at a 5 Hz readout cadence, we cannot resolve the features of any candidate events in our light curves. Any occultation event we detect would typically appear as a small drop in the flux for one or two consecutive measurements (although occultation events by larger objects could contain up to five or six consecutively measured flux drops). We therefore need to have an accurate estimate of our false positive rate in order to report a credible result.

To search for events in the data, we calculate the rank product statistic on each tuple in the entire data set. To calculate this statistic, we take a time series of fluxes $f_1, f_2, \ldots, f_{N_\mathrm{P}}$ (where N_P is the number of points on the time series), and replace each measurement f_j with its rank r_j. The lowest measurement in the time series will be given a rank of 1, and the brightest measurement will be given a rank of N_P. For a given light curve set, we thus replace the time series of flux tuples with a time series of rank tuples of the form

$$(r_{1j}, \ldots, r_{Tj}),$$

where T is the number of telescopes used. We do not know the underlying distribution of the flux tuples in each light curve set, but, assuming the light curves meet the correct requirements (discussed in Section 3.2.2), we do know the exact distribution of rank tuples, and we can thus calculate the significance of any candidate event exactly.

The rank product statistic is calculated as

$$z_j = -\ln \prod_{i=1}^{T} \frac{r_{ij}}{N_\mathrm{P}}. \tag{3}$$

If one assumes that the rank distribution for a single light curve is continuous, then this statistic follows the gamma distribution. Given that the ranks are discrete, the approximation fails for large values of z; however, the probability distribution can be calculated exactly using simple combinatorics.

In the case of an occultation event, one expects the flux to drop below the nominal value simultaneously in each of the telescopes. The corresponding rank tuple would have lower values for all of the ranks, and the resulting rank product would be significantly smaller than average, leading to a large value of our test statistic z. We set a threshold z_t for event detection based on choosing an upper limit on the expected false positive rate, such that

$$P(Z > z_\mathrm{t}) = \frac{0.25}{N_\mathrm{T}}, \tag{4}$$

where Z is a random variable chosen from the rank product probability distribution, 0.25 is our limit on the expected number of false positive events in the data set, and N_T is the total number of tuples used in the event search.

3.2.2. Light Curve Filtering and Data Quality Checks

The rank product test statistic follows the expected distribution for an individual light curve set if and only if the following conditions are satisfied (Coehlo 2010).

1. The distribution of measurements in each light curve in the light curve set is stationary.
2. Each light curve in the light curve set is ergodic in mean.
3. Each light curve in the light curve set is independent of the other light curves in the light curve set.

However, none of the light curve sets in our data set meet these requirements. Changes in the transparency of the atmosphere throughout the course of our typical 1.5 hr data runs induce fluctuations in the light curves, rendering them non-stationary. Furthermore, these fluctuations are correlated between the different telescopes, so the light curves are not independent of each other. We therefore apply a rolling mean and variance filter to each point in the light curves, thus replacing each flux measurement f_j with h_j, given by

$$\begin{aligned} g_j &= f_j - \mu_j, \\ h_j &= \frac{g_j}{\sigma_j}. \end{aligned} \tag{5}$$

where μ_j is the local mean and σ_j is the local variance at point j, calculated with window sizes of 33 and 151, respectively. Note that the variance is calculated after the rolling mean was subtracted, as was done in Equation (2). In most cases, this filter removes all of the slowly varying trends, and the resulting filtered light curves h meet the requirements for the application of the rank product statistic.

However, there are still some data runs where fast moving cirrus clouds can induce simultaneous variations in the light curves that are not removed by the high-pass filter. We have therefore devised a pair of tests (Lehner et al. 2010) to identify light curve sets where the filtered light curves are not independent (and likely not stationary as well, given that the fluctuations in the light curves from the cirrus clouds are not constant over time). The tests are based on the fact that the rank tuples should be distributed uniformly over the T-dimensional rank space (recall that T is the number of telescopes used). For the first test, we divide the T-dimensional rank space uniformly into a T-dimensional grid. If the light curves are independent, we expect that each cell in the grid would contain the same number of rank tuples. We thus calculate the Pearson's χ^2 statistic on the number of tuples in each cell of the grid. For the second test, we only look at the number of rank tuples in the lowest ranked cell in each dimension. When looking at all of the light curve sets in a given data run, the results from the first test should follow the χ^2 distribution, and the results from the second test should follow the hypergeometric distribution. (However, this is only true if the light curves are independent and identically distributed, which is a stricter requirement than stationary. We have thus devised a blockwise bootstrap method to calculate

---

[17] This is the same algorithm used in SExtractor (Bertin & Arnouts 1996) to detect objects.

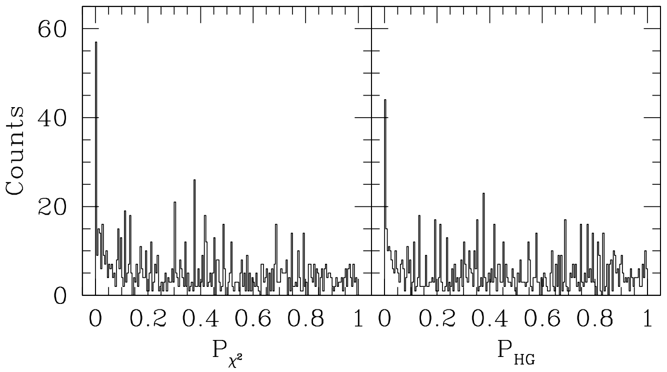

Figure 2. Histograms of p-values for the Pearson's χ^2 test (left panel) and hypergeometric test (right panel) for each of the data runs in the data set.

the expected distributions. We still call the tests the Pearson's χ^2 test and the hypergeometric test.) We can thus calculate a p-value for both tests for each data run to see how well the two test statistics match the expected distributions. Histograms of these p-values are shown in Figure 2 for each test. If the statistics match the distribution, we would expect a uniform distribution of p-values in the range of [0, 1]. The large spikes evident in the lowest bins of each histogram are the data runs that have correlated fluctuations in the light curves that are not removed by the high-pass filter. This leads to a non-uniform distribution of rank tuples, meaning that the test statistics for each of the light curve sets does not follow the expected distribution. We thus remove every data set with a p-value less than 0.01. Note that this means we would only expect to remove 1% of our data runs due to random chance.

In order to perform these tests, we require enough high S/N stars to accurately calculate these two test statistics. We thus set a minimum of 10 stars with $S/N > 10$ in the data run. Any data run that does not meet this requirement is excluded from further analysis. Visual inspection of light curves in such data runs indicate that there are very few stars, and the S/N is compromised, usually by very bright sky during a full moon. These data runs are not expected to contribute significantly to our effective sky coverage, so we lose little by excluding them from the final results. Furthermore, as will be discussed in Section 3.2.4, most of the stars in these data runs will end up being excluded anyway.

3.2.3. Detection of Multipoint Occultation Events

The rank product statistic described in Section 3.2.1 only works on one rank tuple at a time. This has the disadvantage of being inefficient at detection of longer duration occultation events (such as objects with $D \gtrsim 5$ km, scattered disk or Oort Cloud objects beyond 100 AU, or events measured at large opposition angles). However, as was shown in Coehlo (2010) and discussed in Lehner et al. (2010), if we replace a stationary light curve with a moving average of the form

$$a_j = \frac{1}{w}(h_j + \cdots + h_{j+w-1}), \qquad (6)$$

where h_j is the light curve after high-pass filtering and w is the rolling average window size, then the resulting light curve will also be stationary, and the rank product statistic will still be applicable. By applying a moving average, we can increase the significance of any candidate event since the average light curve will exhibit a more significant drop in the measured flux when the averaging window is centered on the event.

The effect of using different window sizes is illustrated in Figures 3 and 4, which show the results of the application of moving averages on actual light curves with simulated events added in. (Note that these simulated events include diffraction effects that are not strongly evident in the light curves due to the fact that they are integrated out with the 5 Hz sampling cadence.) We have used three different window sizes $w = 2$, 3, and 5, in order to optimize our detection efficiency. We also looked at the light curves with no average applied, which we will refer to as using a window size $w = 1$ in order to simplify the discussion. For the 1 km diameter simulated event, we detect the event using $w = 1$, 2, and 3. For such a small object, using $w = 5$ smoothes out the signal, while amplifying other small fluctuations, so that the event does not pass the cuts. For the 3 km and 8 km diameter objects, the events are detected only with $w = 1$ and 2. For the 30 km object, which is longer in duration than the other simulated events, the signal is not detectable for $w = 1$, but it is detected with $w = 2$, 3, and 5. (Note that for each diameter, we have used different light curve sets to add the simulated events. These example light curve sets have different S/N values, and thus no comparison should be made between the relative filter strengths among the different diameters.)

It is clear that the different window sizes increase the sensitivity to different size objects. However, while the effective sky coverage of the survey can be increased by using a wide array of window sizes, this will also increase the false positive rate (Lehner et al. 2010). Running each multiple window size on each light curve set is not an independent test, given that events can be detected using more than one window size, as demonstrated in Figures 3 and 4. It follows that any false positive event could be detected multiple times using different window sizes. However, given that we do not know the underlying distribution of flux values in the data set, we cannot estimate the rate at which this may occur. Therefore, instead of estimating the true false positive rate, we can only set an upper limit on the false positive rate by assuming that searching for events in a light curve set after applying the moving average is a completely independent test for each value of w. If we have a total of N_w window sizes, we thus modify Equation (4) as

$$P(Z > z_\mathrm{t}) = \frac{0.25}{N_\mathrm{T} N_\mathrm{w}}. \qquad (7)$$

So the more window sizes that are used, the tighter the detection threshold must be. The optimization of the selection of the window sizes used in this analysis will be discussed in Section 4.

Note that the data quality tests described in Section 3.2.2 must be reapplied for each window size w. As shown in Lehner et al. (2010), application of the moving average can highlight small correlations between the telescopes that are insignificant in the unaveraged data. Therefore, using larger window sizes will require removing more data runs from the analysis. In cases where we use more than one window size, we always choose to be conservative and remove the union of data sets that would be rejected using each value of w.

3.2.4. Signal-to-Noise Ratio Cuts

The final cut we apply to our data set is to set a threshold on S/N of each light curve set. The goal of this cut is to exclude stars which provide little sensitivity to occultation events, yet still contribute to the total number of tuples N_T, which tightens the selection threshold (see Equation (7)). This is illustrated in Figure 5, which shows the total distribution of S/N values

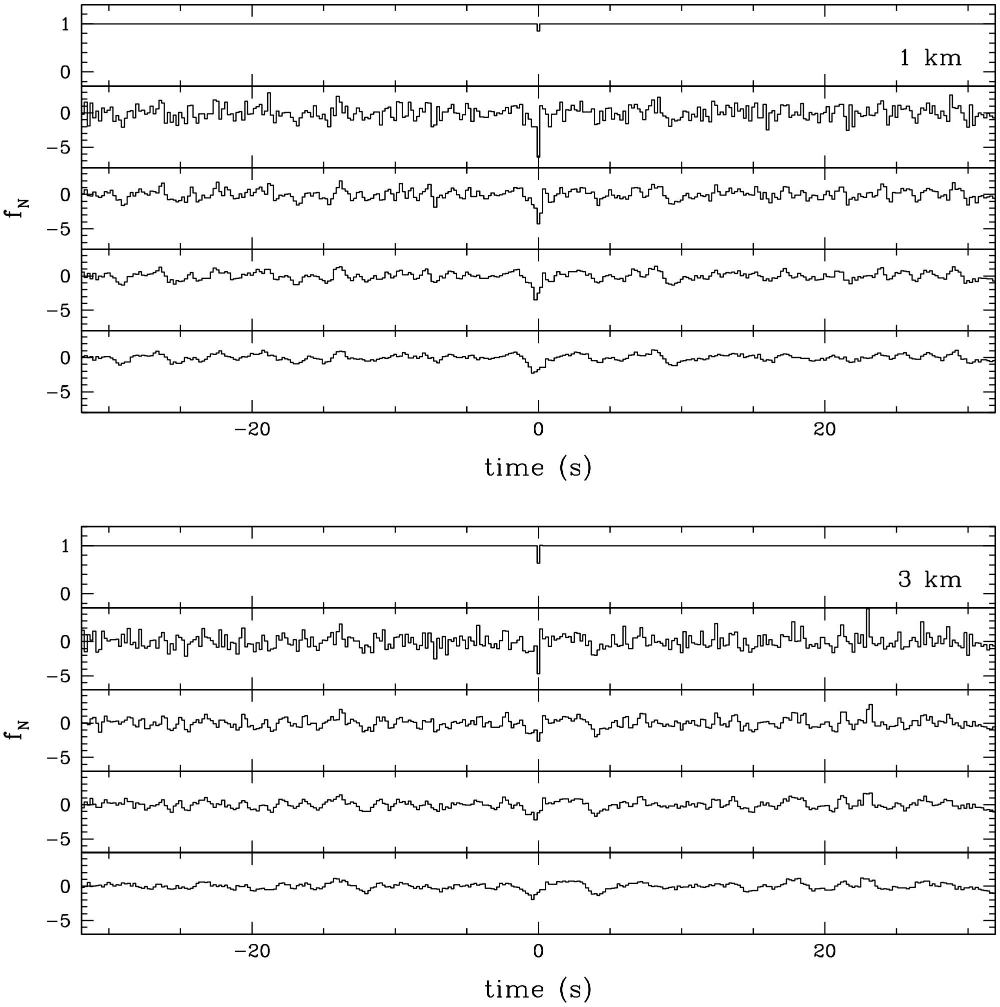

Figure 3. Light curves with simulated occultation events from 1 km (top) and 3 km (bottom) diameter objects added in, before and after application of the moving average. In each panel, the top light curve is the simulated event, the second light curve has no moving average applied, and the next three have moving averages with window sizes 2, 3, and 5, respectively.

for every light curve set in the data set, as well as the S/N distributions of stars for which simulated events are recovered for 1 km, 8 km, and 30 km objects. It is clear that there is little contribution to our effective sky coverage for S/N $\lesssim 5$. Also shown is the detection efficiency for the same diameter objects versus S/N. As expected, the detection efficiency drops off at low S/N values, especially for the smaller objects.

The exact value of S/N to use as a threshold depends on many factors, especially the set of moving average window sizes that will be used. This optimization is discussed in Section 4.

4. RESULTS

We searched through our data set, using moving average window sizes of 1, 2, 3, and 5 (and every combination thereof) as well as S/N cuts of 0, 1, 2, 3, 4, 5, 6, and 7. For each combination of window size and S/N threshold, the detection threshold $z_{\rm t}$ was calculated as shown in Equation (7). In all cases, no events were found in the data set so the next step in the analysis was to measure our effective sky coverage and optimize the selection of moving average window sizes and S/N cut.

The total number of events expected in the survey is given by

$$N_{\rm exp} = \int \frac{dn}{dD}\, \Omega_{\rm eff}(D)\, dD, \tag{8}$$

where dn/dD is the differential size distribution (the number of objects deg^{-2} km^{-1} along the ecliptic), and $\Omega_{\rm eff}$ is the effective sky coverage of the survey. We estimate $\Omega_{\rm eff}$ by implanting a simulated event into each light curve set and seeing if it is recovered by our selection criteria. For this simulation, we choose a set of diameters between 0.5 km and 30 km, and for each diameter, we implant exactly one event into each light curve set. We assume every object is at a geocentric distance of 43 AU, since the light curve shape does not depend critically on the distance for most objects (40–46 AU) in the Kuiper Belt. The tests for each diameter are performed independently, so there is never more than one event implanted into any light curve set at any time. The effective sky coverage is calculated as

$$\Omega_{\rm eff}(D) = \sum_{l \in {\rm rec}} \frac{H}{\Delta} \frac{v_{\rm rel}}{\Delta} E_l, \tag{9}$$

where the sum is over only those light curve sets l where the added event was recovered, E_l is the length of the light curve set in time, $v_{\rm rel}$ is the relative transverse velocity between the Earth and the KBO, Δ is the geocentric distance to the KBO (again, fixed to a constant value of 43 AU), and H is the event cross section. We estimate H as

$$H(D, \Delta, \theta_*) \approx \left[(2\sqrt{3}F)^{3/2} + D^{3/2}\right]^{2/3} + \theta_* \Delta, \tag{10}$$

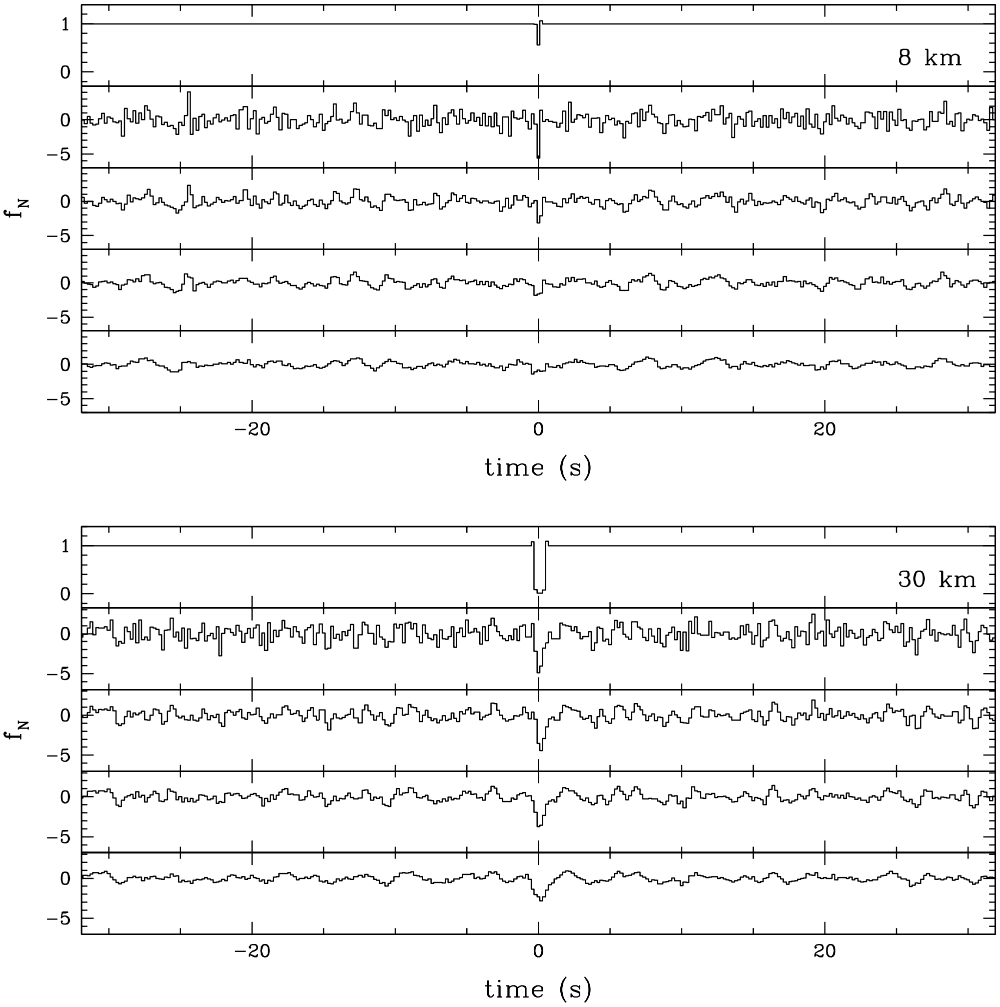

Figure 4. Same as Figure 3, but for 8 km (top) and 30 km (bottom) diameter objects.

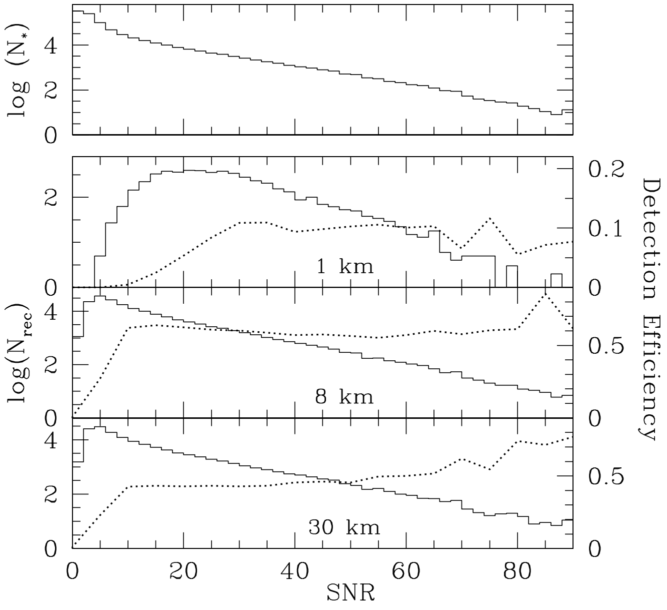

Figure 5. Top panel: histogram of S/N values for light curve sets in the entire data set. (For each light curve set, the minimum S/N among all telescopes is used for the histogram.) Lower panels: S/N values of recovered events from our efficiency simulation for 1 km, 8 km, and 30 km objects (solid histogram). Also shown, using the right vertical axis, is the detection efficiency vs. S/N (dotted lines).

where θ_* is the angular size of the target star and F is the Fresnel scale, which is included to account for the minimum cross section of an event due to diffraction (Nihei et al. 2007).

To optimize the selection of window sizes and S/N cut, we looked at the resulting values of $\Omega_{\rm eff}$ for every possible combination. There is no clear optimum set of cuts, so we decided to optimize our selection based on three criteria.

1. Minimize the upper limit of the slope q at the small end of the size distribution, assuming a power-law size distribution anchored at the break diameter of 90 km and a cumulative surface density at the break diameter of 5.4 deg^{-2} (Fraser & Kavelaars 2009; Schlichting et al. 2009).
2. Maximize the sensitivity at $D = 1$ km, where Schlichting et al. (2009, 2012) claimed the detection of two KBOs.
3. Maximize the sensitivity at $D = 30$ km in order to bring our upper limit as close as possible to the current direct detection limits (Bernstein et al. 2004; Fuentes et al. 2009; Fraser & Kavelaars 2009).

The best results came from using cuts on S/Ns of 3, 4, and 5. The results are summarized in Table 2. We found that the upper limit on the slope q did not vary significantly as long as we limited ourselves to two window sizes, and included $w = 1$. The combination of $w = 1$ and 2 and a minimum of S/N > 3 gave the largest effective sky coverage at 1 km; however, this was particularly bad at 30 km. The best result at 30 km came

Table 2
Results from Using Different Window Sizes and S/N Cuts

Window Sizes	S/N Cut	Tuples	z_t	q	$\Omega_{\rm eff}$ ($D = 1$ km)	$\Omega_{\rm eff}$ ($D = 30$ km)
1 and 2	3	9.49×10^9	1.32×10^{-11}	3.82	$(3.590 \pm 0.053) \times 10^{-7}$	$(2.788 \pm 0.011) \times 10^{-5}$
1 and 2	4	7.13×10^9	1.75×10^{-11}	3.81	$(3.703 \pm 0.054) \times 10^{-7}$	$(2.577 \pm 0.010) \times 10^{-5}$
1 and 2	5	5.63×10^9	2.22×10^{-11}	3.82	$(3.806 \pm 0.055) \times 10^{-7}$	$(2.277 \pm 0.010) \times 10^{-5}$
1 and 3	3	9.14×10^9	1.37×10^{-11}	3.82	$(3.467 \pm 0.053) \times 10^{-7}$	$(5.065 \pm 0.014) \times 10^{-5}$
1 and 3	4	6.87×10^9	1.82×10^{-11}	3.82	$(3.559 \pm 0.053) \times 10^{-7}$	$(4.430 \pm 0.013) \times 10^{-5}$
1 and 3	5	5.42×10^9	2.31×10^{-11}	3.82	$(3.657 \pm 0.054) \times 10^{-7}$	$(3.770 \pm 0.012) \times 10^{-5}$
1 and 5	3	8.60×10^9	1.45×10^{-11}	3.84	$(3.213 \pm 0.051) \times 10^{-7}$	$(5.594 \pm 0.015) \times 10^{-5}$
1 and 5	4	6.46×10^9	1.94×10^{-11}	3.84	$(3.301 \pm 0.052) \times 10^{-7}$	$(4.824 \pm 0.014) \times 10^{-5}$
1 and 5	5	5.08×10^9	2.46×10^{-11}	3.84	$(3.413 \pm 0.052) \times 10^{-7}$	$(4.071 \pm 0.013) \times 10^{-5}$

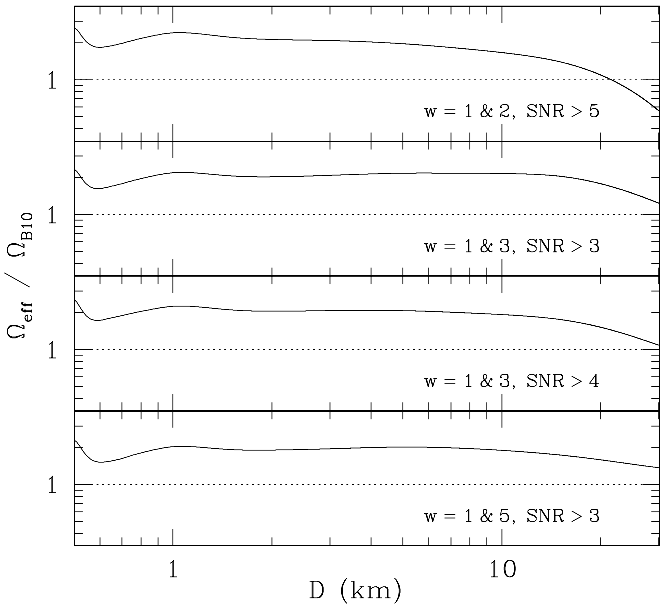

Figure 6. Plots of $\Omega_{\rm eff}$ vs. D for the optimum combinations of moving average window sizes and S/N cuts. The values are scaled by $\Omega_{\rm B10}$, which is $\Omega_{\rm eff}$ from Bianco et al. (2010), in order to highlight the differences.

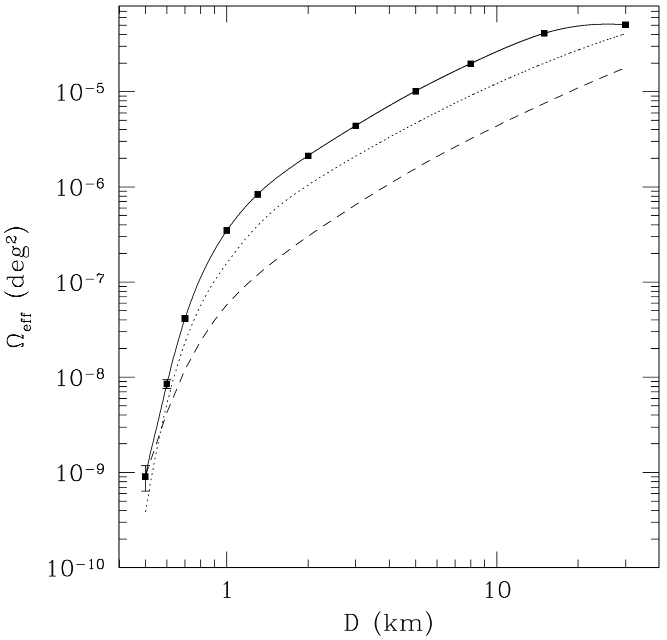

Figure 7. $\Omega_{\rm eff}$ vs. D using our final selection criteria of $w = 1$ and 3 and S/N > 3. Also shown for comparison are the previous TAOS results from Bianco et al. (2010; dotted line) and Zhang et al. (2008; dashed line).

from $w = 1$ and 5 with S/N > 3, but this combination was not very good for 1 km. The combinations that worked best for both diameters was using $w = 1$ and 3 with S/N cuts of 3 and 4. The resulting values of $\Omega_{\rm eff}$ for these four combinations are shown in Figure 6. In the end, we opted for using $w = 1$ and 3 with a threshold of S/N > 3 as this is better at 30 km, and not much worse at 1 km.

Given our final set of cuts, the resulting plot of $\Omega_{\rm eff}$ versus D is shown in Figure 7. The points on the curve indicate the diameters where we calculated $\Omega_{\rm eff}$ using our detection efficiency simulation, and the curve itself is a cubic spline fit to these values.

To set a model-independent upper limit, with no detected events we can eliminate any model which would lead us to expect more than three detected events at the 95% c.l. Our model-independent upper limit is shown in Figure 8 along with results from other occultation surveys and direct searches. We note that our upper limit at $D = 1$ km is a factor of 4.5 below that reported by Schlichting et al. (2012), but it is also a factor of 6.7 higher than their lower limit based upon their two reported events. Therefore, even though we found no events at 1 km (despite the fact that our efficiency simulation for 1 km diameter objects showed that we are in fact sensitive to events similar to those detected by the *Hubble Space Telescope* (*HST*) survey), our limit is thus still consistent with their published result.

We also calculate upper limits on the small KBO size distribution assuming it follows a power law anchored at the detected break at $D = 90$ km. We use Equation (8) to calculate the number of expected events as a function of slope q. The results are shown in Figure 9. We use two values for the surface density at $D = 90$ km, which normalize the size distribution for smaller diameters. Using the value reported by Fraser & Kavelaars (2009) of $N_{D>90\,{\rm km}} = 5.4$ deg^{-2} yields a 95% c.l. upper limit of $q = 3.82$. In comparison, Schlichting et al. (2009) report a slope of $q = 3.8 \pm 0.2$ based on their claim of two detections at $D = 1$ km, assuming the inclination distribution of small KBOs follows that of the larger ($D > 100$ km) objects (Elliot et al. 2005). The second value we use is $N_{D>90\,{\rm km}} = 38.0$ deg^{-2} as reported by Fuentes et al. (2009). This results in a 95% c.l. upper limit on q of 3.34.

5. FUTURE PLANS

After seven years of observations, it would only be of marginal value to continue the survey in its present form so at the end of the data set discussed in this paper, we shut down the

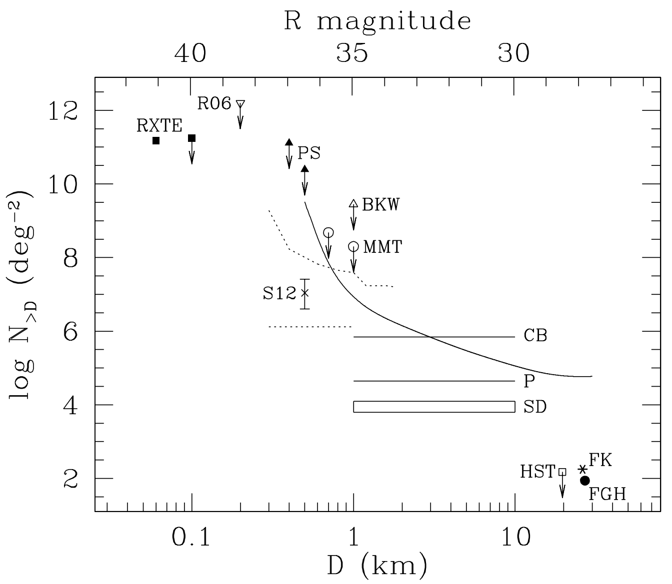

Figure 8. Solid line: 95% c.l. upper limit on cumulative surface density vs. diameter D (bottom axis) and R magnitude (top axis, assuming an albedo of 4% and a distance of 43 AU) from current TAOS data set. Dotted lines: 95% c.l. upper and lower limits on surface density from Schlichting et al. (2012). Cross and error bar (S12): surface density reported by Schlichting et al. (2012). (Note that this is not strictly model independent because it is based on a power-law model. However, the result does not depend very strongly on the assumed slope.) Solid squares (*RXTE*): upper limit (right point) reported by Liu et al. (2008) and the best-fit surface density (left point) reported by Chang et al. (2007) from an occultation search through *RXTE* observation of Sco X-1. Solid triangles (PS): upper limits reported by Wang et al. (2010) using Pan-STARRS guider images. Empty triangle (BKW): upper limit reported by Bickerton et al. (2008) using the 1.8 m telescope at DAO. Empty circles (MMT): upper limits reported by Bianco et al. (2009) from analysis of trailed images obtained with the MMT. Upside down empty triangle (R06): upper limit reported by Roques et al. (2006) from high-speed imaging using the 4.2 m Herschel Telescope. Empty square (*HST*): upper limit reported by Bernstein et al. (2004) from a direct survey using the *HST*. Solid circle (FGH): surface density reported by Fuentes et al. (2009) from a direct search using Subaru. Star (FK): surface density reported by Fraser & Kavelaars (2009) from a direct survey using Subaru. (Note that Fraser & Kavelaars (2009) assume an albedo of 6% and a distance of 35 AU, so they claim that the point plotted at $R = 27.875$ corresponds to a diameter $D = 15$ km.) Lines and box labeled CB, P, and SD: required surface density for the Classical Belt (Levison & Duncan 1997), Plutinos (Morbidelli 1997), and Scattered Disk (Volk & Malhotra 2008), respectively, to be the source for the observed distribution of Jupiter family comets.

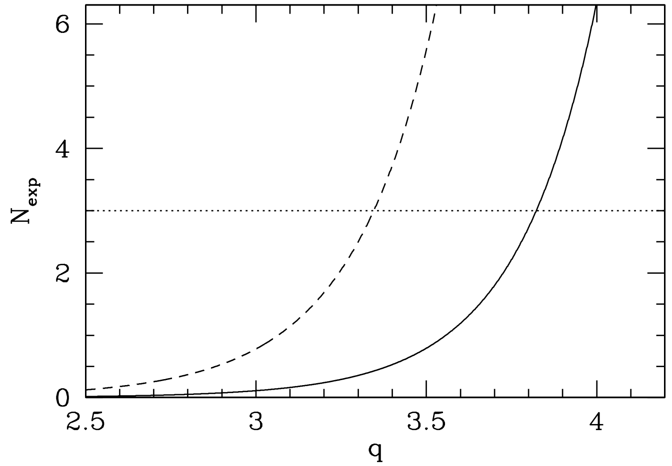

Figure 9. Number of expected events vs. slope q. Solid line: number of expected events using a surface density of $N_{D>90\,\mathrm{km}} = 5.4\ \mathrm{deg}^{-2}$, as reported by Fraser & Kavelaars (2009). Dashed line: number of expected events vs. slope q, using a surface density of $N_{D>90\,\mathrm{km}} = 38.0\ \mathrm{deg}^{-2}$, as reported by Fuentes et al. (2009). Since no events were found, any model predicting more than three events (dotted line) is excluded at the 95% c.l.

system for a camera upgrade. Each new camera, manufactured by Spectral Instruments, utilizes a CCD47-20 frame transfer CCD from e2v. With the new cameras, we can image with a readout cadence of just under 10 Hz if we use 2×2 binning. The CCDs are 1k×1k with 13 μm pixels, as opposed to the 2k×2k imagers with 13.5 μm pixels used to collect the current data set, so 77% of the field of view is lost. However, by moving away from zipper mode to full-frame imaging, our S/N increases significantly and we estimate that our limiting magnitude will increase from $R = 13.5$ to 15. We thus expect to be able to monitor a similar number of stars. Given the higher readout cadence, we become significantly more sensitive to objects with $D \lesssim 1$ km. Observations with these new cameras began in 2012 November.

Work at ASIAA was supported in part by the thematic research program AS-88-TP-A02. Work at NCU and at Lulin Observatory was supported in part by grant NSC101-2628-M-008-002. Work at the CfA was supported in part by the NSF under grant AST-0501681 and by NASA under grant NNG04G113G. Work at Yonsei was supported by the NRF grant 2011-0030875. Work at NCU was supported by the grant NSC 96-2112-M-008-024-MY3. Work at Berkeley was supported in part by NSF grant DMS-0636667. Work at SLAC was performed under USDOE contract DE-AC02-76SF00515. Work at NASA Ames was supported by NASA's Planetary Geology and Geophysics Program.

REFERENCES

Bailey, M. E. 1976, Natur, 259, 290
Benavidez, P. G., & Campo Bagatin, A. 2009, P&SS, 57, 201
Benz, W., & Asphaug, E. 1999, Icar, 142, 5
Bernstein, G. M., Trilling, D. E., Allen, R. L., et al. 2004, AJ, 128, 1364
Bertin, E., & Arnouts, S. 1996, A&AS, 117, 393
Bianco, F. B., Protopapas, P., McLeod, B. A., et al. 2009, AJ, 138, 568
Bianco, F. B., Zhang, Z.-W., Lehner, M. J., et al. 2010, AJ, 139, 1499
Bickerton, S. J., Kavelaars, J. J., & Welch, D. L. 2008, AJ, 135, 1039
Bickerton, S. J., Welch, D. L., & Kavelaars, J. J. 2009, AJ, 137, 4270
Blocker, A. W., Protopapas, P., & Alcock, C. R. 2009, ApJ, 701, 1742
Brown, M. J. I., & Webster, R. L. 1997, MNRAS, 289, 783
Chang, H.-K., King, S.-K., Liang, J.-S., et al. 2006, Natur, 442, 660
Chang, H.-K., Liang, J.-S., Liu, C.-Y., & King, S.-K. 2007, MNRAS, 378, 1287
Chang, H.-K., Liu, C.-Y., & Chen, K.-T. 2013, MNRAS, 429, 1626
Coehlo, N. K. 2010, PhD thesis, Univ. California, Berkeley
Cooray, A. 2003, ApJL, 589, L97
Cooray, A., & Farmer, A. J. 2003, ApJL, 587, L125
Davis, D. R., & Farinella, P. 1997, Icar, 125, 50
Duncan, M. J., & Levison, H. F. 1997, Sci, 276, 1670
Duncan, M. J., Levison, H. F., & Budd, S. M. 1995, AJ, 110, 3073
Elliot, J. L., Kern, S. D., Clancy, K. B., et al. 2005, AJ, 129, 1117
Fraser, W. C., & Kavelaars, J. J. 2008, Icar, 198, 452
Fraser, W. C., & Kavelaars, J. J. 2009, AJ, 137, 72
Fraser, W. C., Kavelaars, J. J., Holman, M. J., et al. 2008, Icar, 195, 827
Fuentes, C. I., George, M. R., & Holman, M. J. 2009, ApJ, 696, 91
Fuentes, C. I., & Holman, M. J. 2008, AJ, 136, 83
Holman, M. J., & Wisdom, J. 1993, AJ, 105, 1987
Jones, T. A., Levine, A. M., Morgan, E. H., & Rappaport, S. 2008, ApJ, 677, 1241
Kenyon, S. J., & Bromley, B. C. 2001, AJ, 121, 538
Kenyon, S. J., & Bromley, B. C. 2004, AJ, 128, 1916
Kenyon, S. J., & Bromley, B. C. 2009, ApJL, 690, L140
Kenyon, S. J., & Luu, J. X. 1999a, AJ, 118, 1101
Kenyon, S. J., & Luu, J. X. 1999b, ApJ, 526, 465
Lehner, M. J., Coehlo, N. K., Zhang, Z.-W., et al. 2010, PASP, 122, 959
Lehner, M. J., Wen, C.-Y., Wang, J.-H., et al. 2009, PASP, 121, 138
Levison, H. F., & Duncan, M. J. 1997, Icar, 127, 13
Liu, C.-Y., Chang, H.-K., Liang, J.-S., & King, S.-K. 2008, MNRAS, 388, L44
Lutz, R. K. 1980, CompJ, 23, 262
Luu, J. X., & Jewitt, D. C. 2002, ARA&A, 40, 63
Morbidelli, A. 1997, Icar, 127, 1

Nihei, T. C., Lehner, M. J., Bianco, F. B., et al. 2007, AJ, 134, 1596
Pan, M., & Sari, R. 2005, Icar, 173, 342
Roques, F., Doressoundiram, A., Dhillon, V., et al. 2006, AJ, 132, 819
Roques, F., & Moncuquet, M. 2000, Icar, 147, 530
Roques, F., Moncuquet, M., Lavillonire, N., et al. 2003, ApJL, 594, L63
Roques, F., Moncuquet, M., & Sicardy, B. 1987, AJ, 93, 1549
Schlichting, H. E., Fuentes, C. I., & Trilling, D. E. 2013, arXiv:1301.7433
Schlichting, H. E., Ofek, E. O., Sari, R., et al. 2012, ApJ, 761, 150
Schlichting, H. E., Ofek, E. O., Wenz, M., et al. 2009, Natur, 462, 895
Stern, S. A. 1996, AJ, 112, 1203
Tancredi, G., Fernández, J. A., Rickman, H., & Licandro, J. 2006, Icar, 182, 527
Volk, K., & Malhotra, R. 2008, ApJ, 687, 714
Wang, J.-H., Lehner, M. J., Zhang, Z.-W., et al. 2009, AJ, 138, 1893
Wang, J.-H., Protopapas, P., Chen, W.-P., et al. 2010, AJ, 139, 2003
Zhang, Z.-W., Bianco, F. B., Lehner, M. J., et al. 2008, ApJL, 685, L157
Zhang, Z.-W., Kim, D.-W., Wang, J.-H., et al. 2009, PASP, 121, 1429

The Astronomical Journal, 146:4 (9pp), 2013 July doi:10.1088/0004-6256/146/1/4

LONG-TERM MONITORING OF COMET 103P/HARTLEY 2*

Z.-Y. Lin[1], L. M. Lara[2], and W.-H. Ip[1]

[1] Institute of Astronomy, National Central University, Jhongli City, Taoyuan County 32001, Taiwan, Taiwan; zylin@astro.ncu.edu.tw

[2] Instituto de Astrofísica de Andalucía (CSIC), Glorieta de la Astronomía s/n, ES-18008 Granada, Spain; lara@iaa.csic.es

Received 2012 November 26; accepted 2013 April 4; published 2013 May 29

ABSTRACT

We report the spectrophotometric, photometric, and imaging monitoring results of comet 103P/Hartley 2 obtained at the Lulin (1 m), Calar Alto (2.2 m), and Beijing Astronomical (2.16 m) observatories from 2010 April to December. We found that a dust feature in the sunward direction was detected starting from the end of September until the beginning of December (our last observation from the Lulin and Calar Alto observatories). Two distinct sunward jet features in the processed images were observed on October 11 and after October 29 until November 2. In parallel, the CN images reveal two asymmetrical jet features which are nearly perpendicular to the Sun-nucleus direction, these asymmetrical features imply that the comet was in a nearly side-on view in late October and early November. In addition to the jet features, the average result of the C_2-to-CN production rate ratio ranges from 0.7 to 1.5, consistent with 103P/Hartley 2 being of typical cometary chemistry. We found that the r_h dependence for the dust production rate, Afρ (5000 km), is -3.75 ± 0.45 before perihelion and -3.44 ± 1.20 during the post-perihelion period. We detected higher dust reddening around the optocenter and decreased reddening along the sunward jet feature. We concluded that higher dust reddening could be associated with strong jet activity while lower dust reddening could be associated with the outburst or might imply changes in the optical properties. The average dust color did not appear to vary significantly as the comet passed through perihelion.

Key words: comets: individual (103P/Hartley 2) – dust, extinction

Online-only material: color figures

1. INTRODUCTION

Comet 103P/Hartley 2, hereafter referred to as Hartley 2, was first spotted by M. Hartley on 1986 March 16. It has a semimajor axis of $a = 3.47$ AU, eccentricity $e = 0.695$, inclination $i = 13.617$, and an orbital period of 6.46 yr. Its low eccentricity made it a suitable target for the extended mission of NASA's *Deep Impact* spacecraft after the impact experiment at comet 9P/Tempel 1 on 2005 July 4. The mission to Hartley 2 was renamed *EPOXI* and given two missions, Extrasolar Planet Observation and Characterization and Deep Impact Extended Investigation. The *EPOXI* flyby observations at a closest distance of 694 km on 2010 November 4 provided a wealth of information on the outgassing activity, shape, and surface structure of this small Jupiter-family comet (A'Hearn et al. 2011). For example, the strong outflows of the CO_2-rich jet from the Sun-lit end of the bowling-pin shape and the H_2O-rich jet in the waist region came as surprises. How are these out flows connected to the large-scale jet structures observed in the coma? How would the outgassing process be modulated by the rotation of the comet nucleus? In fact, based on the time variability of the CN coma morphology and millimeter/submillimeter spectra, the rotation period of Hartley 2 has been found to be increasing from 16.7 hr in 2010 August to 18.4 hr in the first half of November and then to nearly 19 hr in late November (Drahus et al. 2011; Samarasinha et al. 2011; Knight & Schleicher 2011; Meech et al. 2011; Waniak et al. 2012). Such time variations of the nucleus rotation period, together with the close-up measurements from the *EPOXI* mission, demonstrate the complex nature of the surface outgassing process.

In anticipation of the scientific opportunity to compare the large-scale coma structures and gas production rates of Hartley 2 with the *EPOXI* results, we conducted a long-term monitoring program from 2010 April to December using imaging with both broadband and narrowband filters, and long-slit spectrophotometry. This cooperative effort involved observations at the Lulin Observatory in Taiwan, the Calar Alto Observatory in Spain, and the Beijing Astronomical Observatory in China. The paper is organized as follows. In Section 2, we explain the observational procedures, instruments, and analysis methods. In Section 3, the derived morphology and gas production of the CN coma and jets are described. In Section 4, we describe the dust jets and the structure of the dust coma during this period. A summary of the major characteristics of the large-scale structures of the gas and dust comas of Hartley 2 is given in Section 5.

2. OBSERVATIONS, INSTRUMENTS, AND DATA ANALYSIS

Imaging. The bulk of the photometric imaging observations was done using the Lulin One-meter Telescope (LOT) at Lulin Observatory. In our first image of Hartley 2 on 2010 April 24 when the comet was 2.42 AU away from the Sun and 2.36 AU from the Earth, only a diffuse coma 5″ in diameter was visible in a 10 minute exposure. There was no tail feature. In the monitoring program, an Asahi *R* broadband filter and the narrowband filters of the *Rosetta* filter set were used. The specifications of these narrowband filters are given as $\lambda_c/\Delta\lambda$ both in nm, λ_c being the central wavelength and $\Delta\lambda$ the band width: CN (387/5 nm), C_2 (512.5/12.5 nm), blue continuum

---

* Based on observations collected at the Centro Astronómico Hispano Alemán (CAHA) at Calar Alto, operated jointly by the Max-Planck Institut für Astronomie and the Instituto de Astrofísica de Andalucía (CSIC), at Lulin Observatory operated by the Institute of Astronomy, National Central University in Taiwan, and at Xinglong Station inaugurated by the National Astronomical Observatory (BAO), Beijing.

Table 1
Log of Observations

Date	UT	r_h	Δ	PA	α	Pix Scale	Data	Obs.	Sky
Apr 24	19:56–20:17	2.424	2.363	256.2	24.2	884.4	*R*	Lulin	Phot.
May 11	18:39–18:48	2.283	2.026	252.1	26.3	758.2	*R*	Lulin	Phot.
May 15	18:58–19:10	2.249	1.948	251.0	26.7	729.1	*R*	Lulin	Part. cloudy
May 16	19:07–19:36	2.240	1.928	250.8	26.8	721.6	*R*	Lulin	Part. cloudy
May 20	18:34–18:56	2.206	1.851	249.7	27.1	692.7	*R*	Lulin	Part. cloudy
Jul 14	17:01–18:40	1.721	0.924	226.9	29.0	345.8	*R*	Lulin	Part. cloudy
Jul 14	23:00–23:49	1.719	0.921	226.7	29.0	354.0	*R*	CA	Phot.
Jul 22	01:25–02:36	1.656	0.825	221.7	29.0	316.1	*R*	CA	Part. phot.
Jul 30	02:22–02:55	1.585	0.725	215.2	29.2	278.7	*R*	CA	Phot.
Aug 1	17:30–18:42	1.562	0.694	212.9	29.3	259.7	*R*	Lulin	Phot.
Aug 19	14:00–20:15	1.409	0.503	195.5	31.1	188.3	*R*	Lulin	Part. cloudy
Aug 20	01:33–01:44	1.406	0.500	195.1	31.1	192.2	*R*	CA	Phot.
Aug 20	13:17–20:01	1.402	0.494	194.5	31.2	184.9	*R*	Lulin	Phot.
Aug 21	19:27–20:43	1.392	0.483	193.3	31.4	180.8	*R*	Lulin	Phot.
Aug 25	22:46–00:23	1.359	0.445	189.3	32.3	174.5	*R*, *S*	CA	Phot.
Aug 29	18:37–19:09	1.329	0.412	185.6	33.3	154.2	*R*	Lulin	Part. cloudy
Sep 2	02:23–02:27	1.304	0.384	182.7	34.2	147.6	*R*, *S*	CA	Part. phot.
Sep 14	00:35–00:57	1.219	0.293	175.1	38.3	109.2	*R*, *S*	CA	Phot.
Sep 29	14:45–20:51	1.130	0.192	182.1	44.2	71.9	*R*	Lulin	Phot.
Sep 30	13:55–20:06	1.125	0.186	183.8	44.6	69.6	*R*	Lulin	Phot.
Oct 2	17:55–18;05	1.116	0.175	188.3	45.3	65.5	*R*	Lulin	Part. phot.
Oct 3	15:21–15:30	1.112	0.170	191.1	45.6	63.6	*R*	Lulin	Part. phot.
Oct 9	14:40–17:55	1.090	0.143	211.7	47.7		*S*	BAO	Part. phot.
Oct 10	12:32–18:45	1.087	0.140	215.9	48.0	52.4	*R*+*N*	Lulin	Phot.
Oct 11	15:08–19:00	1.083	0.136	220.3	48.4		*S*	BAO	Phot.
Oct 11	13:05–21:08	1.083	0.136	220.3	48.4	50.9	*R*+*N*	Lulin	Phot.
Oct 15	00:28–02:18	1.077	0.129	230.9	49.4	48.8	*R*, *S*	CA	Part. cloudy
Oct 18	04:38–05:10	1.068	0.122	248.1	51.4	46.9	*R*, *S*	CA	Phot.
Oct 19	22:32–23:15	1.065	0.121	254.4	52.5	46.5	*R*, *S*	CA	Part. phot.
Oct 22	02:39–03:13	1.062	0.121	261.0	53.8	46.5	*R*, *S*	CA	Phot.
Oct 25	03:53–04:38	1.060	0.125	268.6	55.6	47.6	*R*	CA	Part. cloudy
Oct 25	18:09–18:39	1.059	0.126	269.8	55.9	47.2	*R*+*N*	Lulin	Phot.
Oct 26	16:09–21:24	1.059	0.128	271.8	56.4	47.9	*N*	Lulin	Phot.
Oct 27	16:24–26:56	1.059	0.130	273.7	56.5	48.7	*N*	Lulin	Phot.
Oct 28	17:50–21:28	1.059	0.132	275.3	57.4	49.4	*N*	Lulin	Phot.
Oct 29	03:06–03:20	1.059	0.133	275.9	57.5	51.1	*R*	CA	Part. cloudy
Oct 29	16:24–21:00	1.059	0.135	276.9	57.7	50.5	*R*+*N*	Lulin	Phot.
Nov 1	19:14–21:12	1.060	0.145	280.9	58.6	54.3	*R*	Lulin	Part. cloudy
Nov 2	17:58–20:31	1.061	0.150	282.0	58.7	56.1	*R*+*N*	Lulin	Phot.
Nov 3	16:04–16:28	1.061	0.149	281.9	58.7	55.7	*R*	Lulin	Part. cloudy
Nov 5	18:07–21:09	1.064	0.157	284.2	58.8	58.8	*R*	Lulin	Part. cloudy
Nov 5	01:25–05:45	1.065	0.162	285.4	58.8	62.3	*R*, *S*	CA	Part. phot.
Nov 16	01:18–01:47	1.090	0.210	294.0	56.1	80.3	*R*, *S*	CA	Part. phot.
Nov 21	19:07–19:37	1.112	0.239	298.8	53.2	60.3	*R*	Lulin	Phot.
Dec 2	16:24–18:48	1.116	0.295	308.9	46.4	74.5	*R*	Lulin	Part. cloudy
Dec 17	17:48–20:58	1.262	0.377	326.2	36.4	95.2	*R*	Lulin	Phot.
Dec 26	23:08–00:12	1.323	0.427	338.0	31.3	163.7	*R*, *S*	CA	Phot.

Notes. Δ and r_h are the geocentric and heliocentric distances in AU; PA is the extended Sun-target radius vector as seen in the observer's plane-of-sky, measured from north toward east. α is the phase angle (Sun-comet-observer angle). *R* is the broadband filter, *N* is the cometary filter set, and *S* refers to long-slit spectra.

(BC; 443/4 nm), and red continuum (RC; 684/9 nm). Because of the consideration of the signal-to-noise ratio (S/N), the narrowband filters were used only in October and on November 2 just before the *EPOXI* close encounter. The camera used on LOT from April to November was PI 1300B, which has a pixel scale of 0.516 arcsec and a field of view (FOV) of 11.2 × 11.6 arcmin. In 2010 late November, there was a cooling problem with PI1300B. We therefore switched to a U42 CCD which has 2k × 2k pixels and a FOV of 12.17 × 11.88 arcmin. The telescope was always operated with non-sidereal tracking so as not to produce a trail in the comet images. Typical integrations were 600 s–900 s for the narrowband filters and 30 s–300 s for the broadband *R* filter.

Table 1 is the observational log of our program. Standard data reduction procedures were applied, beginning with dark current subtraction and a flat-field correction of all image frames and followed by the subtraction of the night sky contribution. For the observations obtained before late September, the night sky levels were determined directly from areas of the CCD frames that did not contain contributions from the cometary emission. However, the sky-background of those images taken from late-September to early-November was influenced by the cometary coma. Therefore, we took sky background images positioned about 0.5 deg away from the comet center. The extinction coefficients of the narrowband and broadband *R* filters were determined for all nights with photometric sky conditions, using photometric stars like Feige 110 and GD71 observed at different air masses during the night. For example, the first order extinction coefficient (in units of magnitudes per air mass) measured with Feige 110 at air masses ranging from 1.1 to 1.7 for the *R* filter on October 29 is 0.10. For the CN and C_2 filters, the corresponding values are 0.39 and 0.14, respectively. These data were used to convert the measured counting rates into physical units; details are described in Lin et al. (2007b). Because the CN images contain a 29% contribution from the continuum in the blue range while the C_2 images contain as much as a 93% contribution, the net CN and C_2 gas coma images need to go through the subtraction procedure according to the following formulas: $\mathrm{CN} = \mathrm{CN}_{\mathrm{obs}} - 0.29\ \mathrm{BC}_{\mathrm{obs}}$, $\mathrm{C}_2 = \mathrm{C}_2^{\mathrm{obs}} - 0.93\ \mathrm{BC}_{\mathrm{obs}}$.

In addition to the Lulin observations, the coma activity of 103P/Hartley 2 was also monitored continuously in the *R*-band from the Calar Alto Observatory (near Almeria, Spain) from 2010 July 14 to December 26 (see Table 1). We used the CAFOS imaging camera (2k × 2k pixels, pixel size: $0\farcs53$, FOV $18' \times 18'$), which was mounted on the 2.2 m telescope. In our observations, only the central 1k × 1k pixels were used, thus providing an FOV of $9' \times 9'$. Appropriate bias and flat field frames were taken each night. If photometric conditions prevailed, photometric standard stars were observed at air masses similar to those of the comet observations. Table 1 contains the observations log for the complete data set. Note that a large number of nights listed in Table 1 were used for the $Af\rho$ estimation; some of these nights were not used to enhance the structures in the coma because the S/N was too low.

Spectroscopy. Spectroscopic measurements were planned once every month using CAFOS with the B400 grism (see http://www.caha.es/alises/cafos/cafos22.pdf) which renders a spectral range between 3200 and 8800 Å with a wavelength scale of 9.4 Å pixel^{-1}. The slit of the spectrograph was oriented in the north–south direction, giving dust and gas profiles at different cross-cuts through the coma, depending on the position angle (PA) of the Sun-comet vector on the sky. For absolute calibration, observations of appropriate spectrophotometric standard stars were acquired. All comet observations were done with telescope tracking on Hartley 2. With the exception of 2010 November 5, all observations were done in service mode of the Calar Alto Observatory. Details on the images and spectra reduction and calibration can be found in Lara et al. (2001, 2011b) and they will not be repeated here. If the gas coma covered the whole slit, the sky level was estimated from the edges of the frame. Otherwise, the background could be measured directly by using regions near the edges of the frame.

Besides spectra obtained from the Calar Alto Observatory, spectroscopic observations were also performed on October 9 and October 11 at the Beijing Astronomical Observatory using the 2.16 m telescope in the spectral range between 3600 Å and 8400 Å at a dispersion of 4.8 Å pixel^{-1}. The spectroscopic data were reduced following the standard procedures including bias and flat-field corrections and cosmic ray removal. Wavelength calibration was performed based on helium–argon lamps exposed at both the beginning and the end of the observations every night. Flux calibration of all spectra was conducted based on observations of at least one of the spectral standard stars, i.e., HD19445. The atmospheric extinction effect was corrected by the mean extinction coefficients measured by the Beijing–Arizona–Taiwan–Connecticut multicolor survey. See Lin et al. (2007a) for more detailed information.

3. GAS COMA MORPHOLOGY AND PROPERTIES

3.1. CN Jets

In order to study the visibility of faint structures of the gas coma of comet Hartley 2, an image enhancement technique was applied to the present set of images. The method used here is the azimuthally averaged profile division, a detailed description of which can be found in Lin et al. (2012). This method was applied to all images taken in the CN filter, in continuum filters, and in the *R*-band filter.

To estimate the rotational phase from the CN morphology, a lot of observing data have to be acquired on consecutive nights. However, the images obtained in our observing nights with less temporal coverage were not enough to estimate and display the rotational period due to snapshot observations, poor weather, and telescope tracking problems. We therefore use the known periodicity to estimate the rotational phase in our images. However, we face several problems: a non-principal axis rotation of comet Hartley 2 and a rapid change of the viewing geometry might cause different periodicities between rotational cycles. A specific phase is really only applicable to a short stretch of data if we adopt a known periodicity such as 18.15 hr in mid-October and 18.7 hr in early November from Knight & Schleicher (2011) or 18.22 hr around perihelion from Harmon et al. (2011). Note that those ground-based observations have error bars between 0.01 and 0.3 hr. The most robust rotation period at present is from the *EPOXI* spacecraft light curve given in Belton et al. (2013). This light curve gives a spin period of 18.40 hr at the spacecraft's encounter and states that the period was increasing by 1.3 minutes day^{-1}. As the data acquired with the Rosetta filter set spread around one month, it is appropriate to use the midpoint of the observational time interval for this period of time. We extrapolate the rotation period back to the midpoint assuming the rotation period was steadily changing during this time frame. Therefore, the rotation period quoted in this work is 18.11 hr on October 21.5 UT, which refers to the midpoint of the October 10–November 2 data. The zero phase is set at 11:40 UT on 2010 October 10.

In Figure 1, we can see that the morphology of the CN coma extended almost perfectly along the east–west direction in early October and along the north–south direction around Hartley 2's perihelion. The CN images all show clear asymmetries before performing the image enhancement. One of these unprocessed CN images is shown as a contour plot in Figure 1 (top left panel). The variations in the CN jet features in between early October and its perihelion are related to the spin period of the comet nucleus, the changing viewing geometry, and non-principal axis rotation, as has already been reported by Samarasinha et al. (2011), Knight & Schleicher (2011), Lara et al. (2011a) and Waniak et al. (2012). The processed CN images from the observations between October 11 and November 2 revealed two jets in the coma of comet Hartley 2. The CN jet features nearly perpendicular to the Sun-tail direction not only varied smoothly during a night but showed similar morphologies near the comet's perihelion even though the rotational state was different.

We compared the morphologies of the CN jet features with those presented by Knight & Schleicher (2011), and Samarasinha et al. (2011) and found that the CN jet features of Hartley 2 did not show the spiral-like structure in early October but were compatible with the observations obtained by Knight

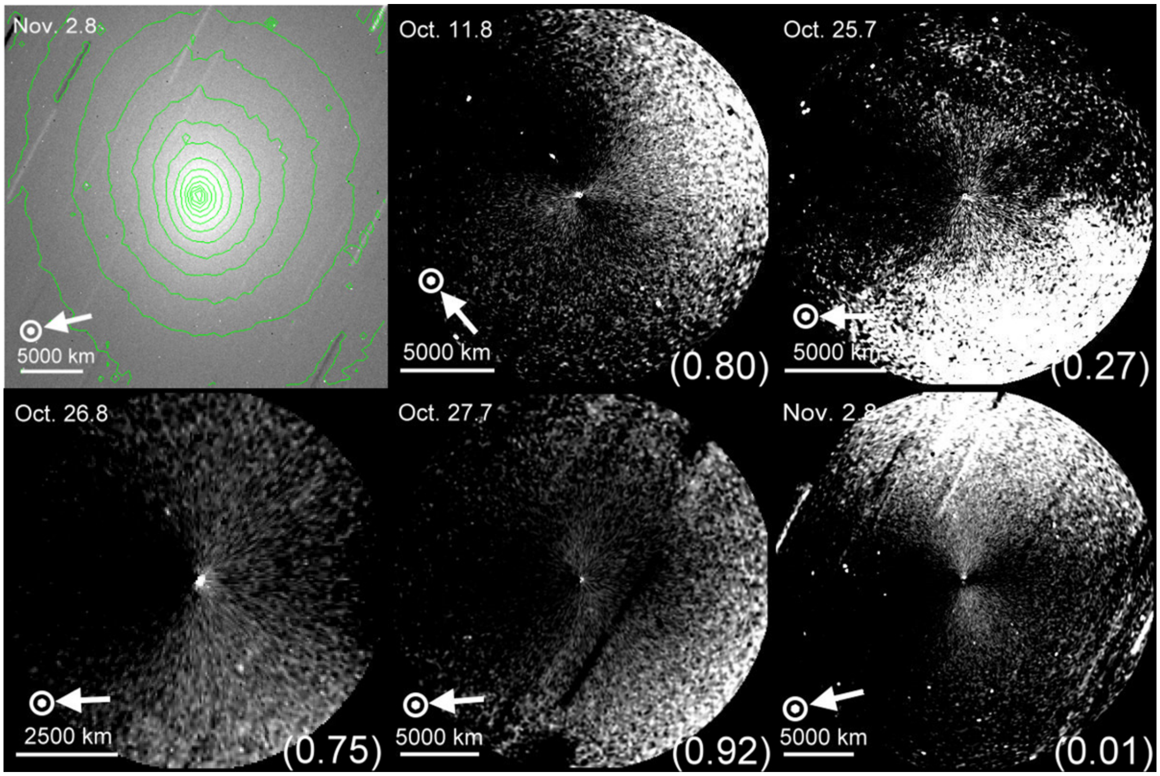

Figure 1. CN images after the dust continuum was removed were enhanced by dividing by an azimuthal median profile. The rotational phase is given in the bottom right corner of each image (see the text for details). The original image (top left) obtained on November 2 is shown with contours overplotted in green. The Sun symbol and arrow indicate the projected direction toward the Sun. North is up, east is to the left. The field of view is $3'.44 \times 3'.44$ and a scale bar is shown at the bottom left corner. The images are centered on the optocenter and the color code stretches to white representing the brightest areas and to black representing the darkest areas.

(A color version of this figure is available in the online journal.)

& Schleicher (2011) and Lara et al. (2011a) in late October. The reason could be the observing geometry, i.e., whether it is observed face-on or side-on. Knight & Schleicher (2011) confirmed this effect from images that revealed face-on spiral structures in August and September. Furthermore, we found these two CN jet features to be asymmetrical. One of them is always brighter than the other, possibly because it is facing toward the Earth. For example, the southern jet of the images obtained from October 25 to October 27 is slightly stronger than the northern jet of those images. Such asymmetrical features have also been reported in earlier works by Samarasinha et al. (2011), Lara et al. (2011a), and Waniak et al. (2012).

3.2. Gas Production Rates

In order to determine the gas production rates, the mean radial emission profiles of CN and C_2 were derived from the continuum-subtracted images. These profiles were also used with the spectra acquired at the Calar Alto Observatory and the Beijing Astronomical Observatory to investigate the CN, C_3, C_2, and NH_2 profiles in the north–south direction and to derive the production rates of these gaseous species. The spectral regions and the subtraction of the underlying continuum in the gas emission bands were done as described by Lara et al. (2001). The conversion of the emission-band fluxes into column densities made use of fluorescence efficiency factors (*g*-factors) for C_3, C_2, and NH_2 (A'Hearn et al. 1995), whereas the *g*-factors of the CN molecule were calculated for the heliocentric distance and velocity of 103P/Hartley 2 on every date from the set of values given by Schleicher (2010). The gas production rates were obtained by means of the (Haser 1957) model for isotropic emission of cometary neutral molecules and their daughter molecules and radicals. The parameter used for the parent velocity is $v_p = 0.85\, r_h^{-0.5}$ km s^{-1} (Fray et al. 2005) and for the daughter velocity it is 1 km s^{-1}. For the corresponding set of parameters in the Haser model, we produced theoretical column density profiles for each species by varying the production rate until the best match between observations and theoretical predictions was achieved. The results of nightly averages for Q(CN), Q(C_3), Q(C_2), and Q(NH_2) are summarized in Table 2. Table 2 also contains the average gas production rates obtained from the images acquired in one night together with the aperture size we have considered to derive Q. The variation of production rates seen in multiple measurements during a night were less than 5%; this variation is reflected in the uncertainties in Table 2. We have fewer measurements of Q(C_2) as there were tracking problems at LOT from October 10–11 to October 25–27. Long-slit spectroscopic measurements could provide Q(C_2) at other dates thus spanning larger heliocentric distances.

Our Lulin, BAO and CA results in Table 2 show that there is no significant variation in Q(CN) from mid-October to early November. This result is consistent with the Lara et al. (2011a) and Mumma et al. (2011) results that assumed that HCN is the main parent species of CN and that the expected variation of Q(HCN) around perihelion is not very large. Note that we used the mean radial profile to estimate the gas production rate from the images obtained from Lulin Observatory. However, if we averaged the radial profile in the north–south direction where the CN jet feature exists, the derived Q(CN) would be larger by a factor of two to three compared with the azimuthally averaged radial profile. Figure 2 shows the logarithm of the

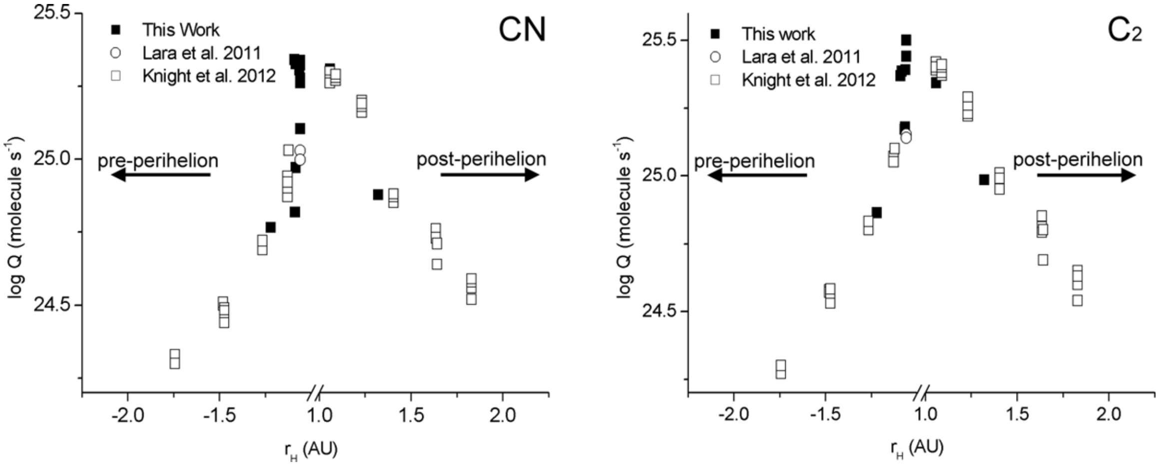

Figure 2. Log of production rates for CN (left) and C_2 (right) plotted as a function of the heliocentric distance. Different symbols come from different data sets: filled square symbols refer to results presented here; open square symbols are taken from results in Knight & Schleicher (2013); and the open circle symbols come from Lara et al. (2011b). "//" refers to a break in the heliocentric distance from −0.1 AU (pre-perihelion) to 0.99 AU (post-perihelion).

Table 2
Gas Production Rates of Comet 103P/Hartley 2

Date	UT	Observatory	Aperture	CN	C_2	C_3	NH_2	$Q(C_2)/Q(CN)$
Sep 14	00:35–00:57	CA		5.82 ± 0.13	7.28 ± 1.03	0.37 ± 0.05	X	
Oct 9	14:40–17:55	BAO		21.9 ± 4.78	23.4 ± 5.24	4.39 ± 0.94	44.4 ± 9.70	1.07 ± 0.11
Oct 10	12:32–18:45	Lulin	4.01	6.57 ± 0.93	X	X	X	
Oct 11	15:08–19:00	BAO		21.2 ± 3.57	24.3 ± 4.10	4.37 ± 0.74	44.0 ± 7.38	1.15 ± 0.11
Oct 11	13:05–21:08	Lulin	4.00	9.32 ± 1.37	X	X	X	
Oct 18	04:38–05:10	CA		21.4 ± 3.56	14.8 ± 1.57	1.34 ± 0.02	35.2 ± 1.41	0.69 ± 0.04
Oct 18	04:38–05:10	CA		21.2 ± 1.39	15.1 ± 3.99	1.33 ± 0.002	46.9 ± 0.97	0.71 ± 0.29
Oct 22	02:39–03:13	CA		20.2 ± 2.90	24.6 ± 1.57	1.56 ± 0.05	X	1.22 ± 0.05
Oct 25	18:09–18:39	Lulin	3.62	18.2 ± 3.1	X	X	X	
Oct 26	16:09–21:24	Lulin	3.66	20.1 ± 5.4	X	X	X	
Oct 27	16:24–26:56	Lulin	3.82	12.7 ± 2.7	X	X	X	
Oct 28	17:50–21:28	Lulin	3.98	18.9 ± 3.2	27.8 ± 5.3	X	X	1.47 ± 0.17
Oct 29	16:24–21:00	Lulin	3.99	21.8 ± 3.6	31.6 ± 5.4	X	X	1.45 ± 0.15
Nov 2	17:58–20:31	Lulin	4.17	20.3 ± 3.1	22.0 ± 3.2	X	X	1.07 ± 0.10
Dec 26	23:08–00:12	CA		7.54 ± 0.13	9.64 ± 1.6	0.29 ± 0.05	X	1.29 ± 1.23

Notes. Apertures are provided in log units of km. The unit in all gas production rates is 10^{24} molecules s^{-1}.

production rates of CN and C_2 as a function of heliocentric distance (r_h). The data points include those obtained by Lara et al. (2011a), Knight & Schleicher (2013), and the Lulin and CA results (this work) for pre-perihelion and post-perihelion observations during the 2010 apparition. We used linear fitting in log–log space to estimate the slope of the r_h dependence of the gas production rate, $Q \sim r_h^{-\alpha}$. The slopes (α) of CN and C_2 are 4.57 and 4.84 before perihelion and 3.21 and 3.42 after perihelion, respectively. These slopes are significantly steeper than the average value estimated for Jupiter-family comets, i.e., $Q(\text{gas}) \sim r_h^{-2.7}$ (A'Hearn et al. 1995). In addition, the average C_2-to-CN production rate ratio is 0.7–1.5, classifying 103P/Hartley 2 as typical in terms of cometary chemistry as defined by A'Hearn et al. (1995). Our measurement is consistent with results from spectroscopic observations (Lara et al. 2011a) and narrowband photometry observations (Knight & Schleicher 2013).

4. DUST COMA MORPHOLOGY AND PROPERTIES

4.1. *The Jet Feature in the Dust Coma*

We describe the morphology and evolution of the coma structures that can be treated with routine procedures, i.e., the Larson–Sekanina algorithm (Larson & Sekanina 1984). In case of doubt, we used additional techniques, such as azimuthal median profile division and the Adaptive Laplace filter (Böhnhardt & Birkle 1994), to clearly separate morphological features from artifacts. Figure 3 compares observations from October 11 of the jet structure and dust tail using three different image enhancement methods: (1) Larson–Sekanina filtering, (2) the azimuthal median profile, and (3) adaptive Laplace filtering. In spite of some differences in their appearances, the presence of two jets in the sunward quarter is common to all numerical treatments. It is therefore clear that the jet features are real and not artifacts associated with the image processing procedures.

Figure 4 is a summary of the *R*-band images enhanced by the Larson–Sekanina filtering method to bring out the inhomogeneous structures in the dust coma of 103P/Hartley 2. It can be seen that from 2010 April until July no clear sign of dust features could be found. However, beginning on August 1, a dust tail with a diffuse structure (labeled *T* in Figure 4) began to appear in the anti-sunward direction. On September 29, a short jet (indicated by arrows in Figure 4) in the sunward direction can be seen. Hereafter, this sunward jet feature can be detected in all our images obtained at Lulin and Calar Alto observatories. It is interesting to note that two distinct sunward dust structures

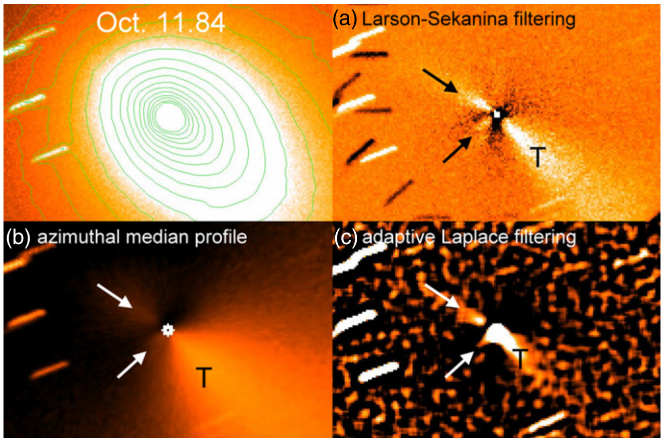

Figure 3. Image of comet 103P/Hartley 2 obtained on 2010 October 11 with the *R* broadband filter. In the top left corner, a contour plot of the original image is shown. In (a) we display the same image after Larson–Sekanina filtering, in (b) the image is divided by an azimuthal median profile, and in (c) the adaptive-Laplace technique has been applied. In all of these images, two jet features are visible. North is up, east is to the left. The field of view is $2'.92 \times 1'.94$, corresponding to 9200 × 6100 km at the comet distance. The images are centered on the nucleus, the arrows point out the jets, T labels the tail, and the streaks are trailed stars. The negatives of the star trails in panel A are the artifacts of the resulting image being subtracted using a combination of a 15° counterclockwise rotation and a 15° clockwise rotation. As the images are normalized, the brightness scales from 0.95 to 1.05.

(A color version of this figure is available in the online journal.)

are visible after October 29 lasting until November 2. Around the same time, from November 2 to November 4, Mueller et al. (2013) also reported seeing two separate continuum features in the sunward direction. Afterward, only a single jet could be seen in the sunward direction. This jet became fainter and fainter as Hartley 2's heliocentric and geocentric distances increased. The sunward jet features showed relatively little variation during a night but their shape and PA slightly changed from night to night until October 11 when two distinct jet features apparently emerged from the sunward direction (Figure 5). In order to examine the existence of this extremely faint jet feature and to distinguish it from the trail of a background star, we transformed the enhanced image into polar coordinates ρ–θ where ρ is the projected cometocentric distance from the nucleus and θ is the azimuth (PA). At several distances ρ from the nucleus, we analyzed the resulting azimuthal profile. In Figure 5 (right panel) we show the azimuthal profile at $\rho = 5000$ km. It can be seen that this faint jet (referred to as the main feature in the figure) appears on October 11.76 and persists until October 11.87, that is, ~0.7 hr later (bottom panel in Figure 5). It points toward the Sun and it does not display significant changes. On October 11.84, a new faint feature appears nearly perpendicularly to the Sun-comet line. It is interesting to note that the PA of the secondary jet is roughly the same as that of the CN jet features shown in Figure 1 (pointing to the eastsouth direction in the top middle panel). At first, one could think that icy grains mixed with the dust grains of this weaker jet could provide the partial fuel to the CN gas jet. However, the gas jets persist for most of a rotation period (Knight & Schleicher 2011; Samarasinha et al. 2011) and are clearly being released over an extended period of time as the nucleus rotates. Thus, the CN jets cannot mainly come from this faint jet feature if it is only active for a few hours as found here. That switching phenomenon may also be explained as a projection effect due to the comet nucleus rotation.

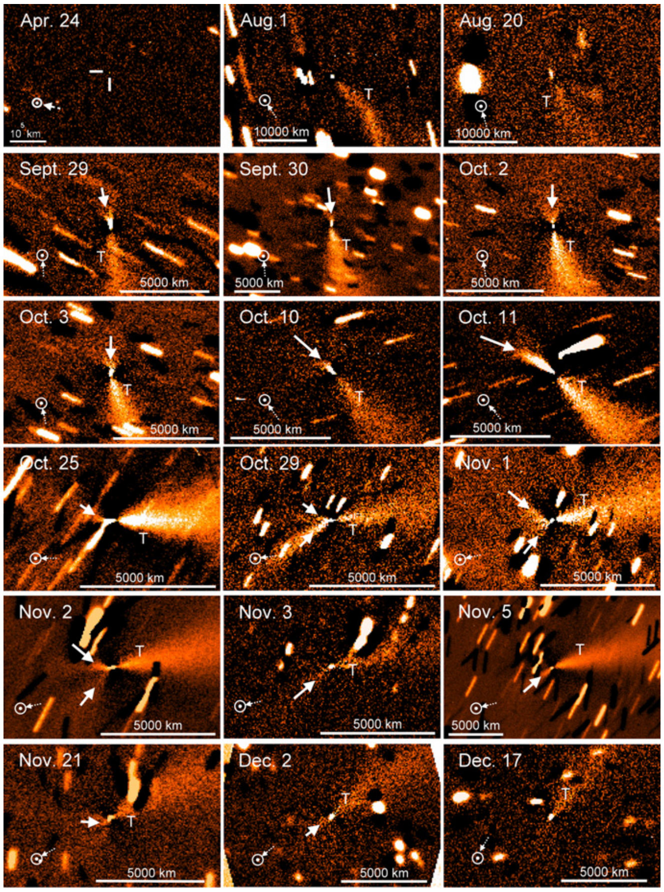

Figure 4. Images of comet 103P/Hartley 2 acquired with the *R*-band filter and enhanced by the Larson–Sekanina algorithm. The dust sunward jet feature sometimes appears as a straight jet but sometimes it shows multiple jet features during a night. The jet showed minimal change in shape, position angle, and extent from night to night. The Sun symbol and arrow indicate the projected direction toward the Sun. North is up, east is to the left. The field of view is $2'.92 \times 1'.94$ and the scale bar is shown in the bottom corner. All images are centered on the nucleus, arrows point out the jets, and T represents the tail.

(A color version of this figure is available in the online journal.)

On October 28 and 29, we obtained a series of images from Lulin and Calar Alto observatories that provide insight into how the sunward feature evolved throughout ~1.4 rotation cycles. Representative images from these nights are shown in Figure 6, with each panel enhanced by the Larson–Sekanina filtering method. Note that the PA of the Sun during these two days is near 97°. Setting the zero phase at 11:40 UT on October 10 and using a period of 18.11 hr (see Section 3), the rotational phase can be easily estimated in these three images (see the bottom right corner of the panels in Figure 6). A dust jet (labeled J and marked with an arrow in Figure 6) can be seen in the sunward direction; its shape slightly changes as the rotational phase changes from 0.22 (October 28.68 UT) to 0.82 (October 29.13 UT). Thirteen hours later (rotational phase of 0.57, October 29.70 UT) two dust jet features emanating in the sunward direction can be seen. One of them, labeled J_1, is close to the position of Sun ($\mathrm{PA} \sim 85°$) and the other, labeled J_2, lies at $\mathrm{PA} \sim 130°$. We consider the possibility that the J_1 feature might have the same source region as the jets in the previous two images (October 28.68 and October 29.13), since all the jets have similar PAs. Under this assumption, the J_2 feature is new. Another possibility is that the J_1 feature might be associated with the cometary rotational effect, i.e., local sunrise accompanied by a temperature increase

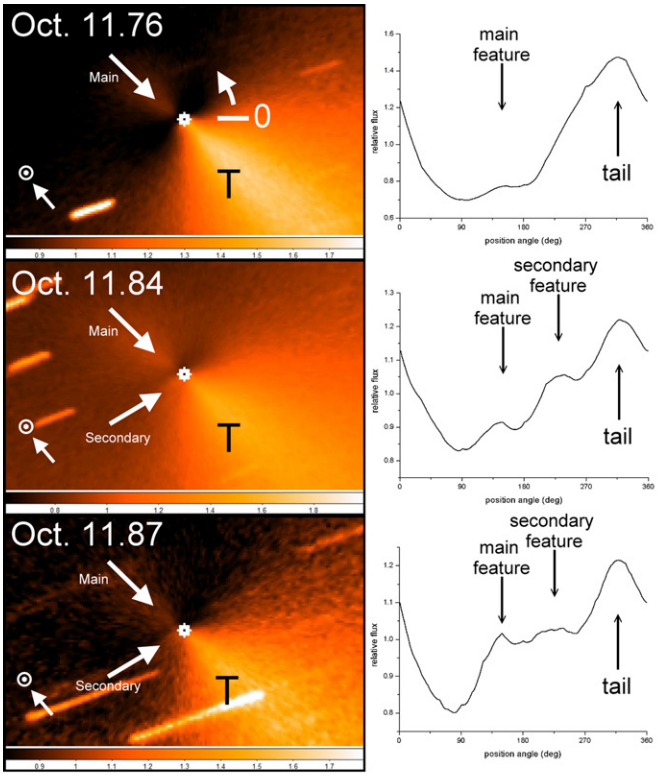

Figure 5. Dust jet features and tail enhanced by an azimuthal median profile (left panels) and the corresponding azimuthal profiles obtained at $\rho \sim 5000$ km (right panels). A sunward dust jet feature is revealed in the broadband R filter on October 11.76 UT (top panel). Two faint dust jet features are detected using both broadband R (middle panel) and narrowband red-continuum filters (bottom panel) on October 11.84 UT and 11.87 UT, respectively. The straight jet pointing toward the Sun (main feature) and the weaker one pointing nearly perpendicular to the Sun-nucleus direction (secondary feature) are marked in the graphs. Position angle is measured from north (up) in the counterclockwise direction (top left panel). In the left panels, all images are centered on the nucleus, with arrows indicating the jets and T indicating the dust tail. North is up, east is to the left. The field of view is $2'.92 \times 1'.94$, corresponding to 9200 × 6100 km at the comet distance; the Sun symbol and the corresponding arrow indicate the projected direction toward the Sun.

(A color version of this figure is available in the online journal.)

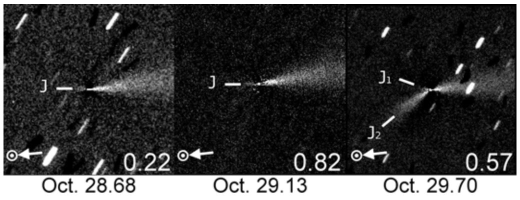

Figure 6. Time sequence of images of the comet 103P/Hartley 2 acquired from the Lulin (left and right) and CA (middle) observatories. Dust jet features are enhanced by Larson–Sekanina filtering. The rotational phase is given at the bottom right corner of each image. North is up, east is to the left. The field of view is $3'.8 \times 3'.8$ and all images are centered on the nucleus. J, J_1, and J_2 refer to the jets and the Sun symbol and arrow indicate the projected direction toward the Sun.

turns that jet on. This localized temperature difference in the regions of the waist and the Sun-lit end of the nucleus have been addressed by Belton et al. (2013). The J_2 feature, which has a collimated shape, is the persistent feature we detected on October 28.68 and October 29.13, although its PA and shape changed between those two dates. We note that the J_2 feature is brighter than the J_1 feature. This higher intensity could be related to dusty ice or to an outburst from the surface of the comet nucleus. To understand which of these processes is responsible for the differential brightening, our images need to be interpreted in the context of a larger image series that displays the time evolution of the jet structure over two or more rotational periods.

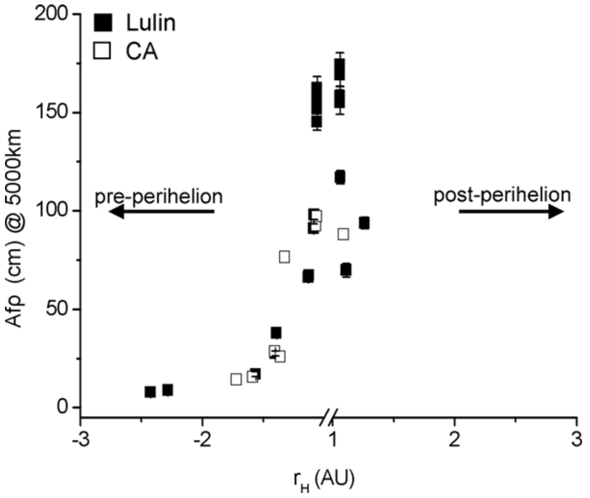

Figure 7. Afρ variation as a function of heliocentric distance both pre- and post-perihelion. Filled squares indicate the results obtained from the Lulin Observatory (LOT) and open squares pertain to the data from the Calar Alto Observatory. "//" refers to the break in heliocentric distance from −0.1 AU (pre-perihelion) to 0.99 AU (post-perihelion). The error bars are not clearly seen in this figure because they are smaller than 5%.

On the tailward side, only the dust tail was readily visible starting in 2010 August. The dust tail was found to point approximately in the antisolar direction. As expected, it appears to be curved slightly counterclockwise.

4.2. *The Properties of the Dust Coma*

We used Afρ (A'Hearn et al. 1984) to characterize the dust activity of the comet. The derived values acquired with the broadband R filter from 2010 April to November are presented in Figure 7. Except for the night of October 29, the average values estimated every photometric night were all measured within a projected distance of 5000 km. Note that Afρ shows a weak dependence on ρ, the projected cometocentric distance from the nucleus, from 5000 km to 20,000 km and that the variation was found to be less than approx. 5%–8%. The reason why we used 5000 km for the uniform radius was to reduce the influence of star trails in the FOV. The $Af\rho$ values steadily increased with decreasing heliocentric distance, although there was not a noticeable increase when the second jet appeared on October 11.64 UT or at perihelion. The $Af\rho$ value on October 29.77–29.85 UT increased from 155 cm to 174 cm in two hours, and at the same time the dust jet seen in Figure 6 (right panel) was more prominent on this night than on any of the other nights. A relatively weak secondary jet feature was also detected. Possible causes for this deviation might include changes in the physical properties of the grains as they traveled outward (i.e., loss of volatiles or fragmentation), the action of solar radiation pressure modifying the straight trajectories of small particles inside the FOV, or a long-lasting population of large particles (Schleicher et al. 1998). Furthermore, the power-law index of the r_h dependence for the dust, Afρ (5000 km), is -3.75 ± 0.45 before perihelion and -3.44 ± 1.20 post-perihelion. This result is completely consistent with the result of Knight & Schleicher (2013) when using A(θ)fρ.

The derived Afρ values for the narrowband filter can be used to estimate the color of the cometary dust (Jewitt & Meech 1987)

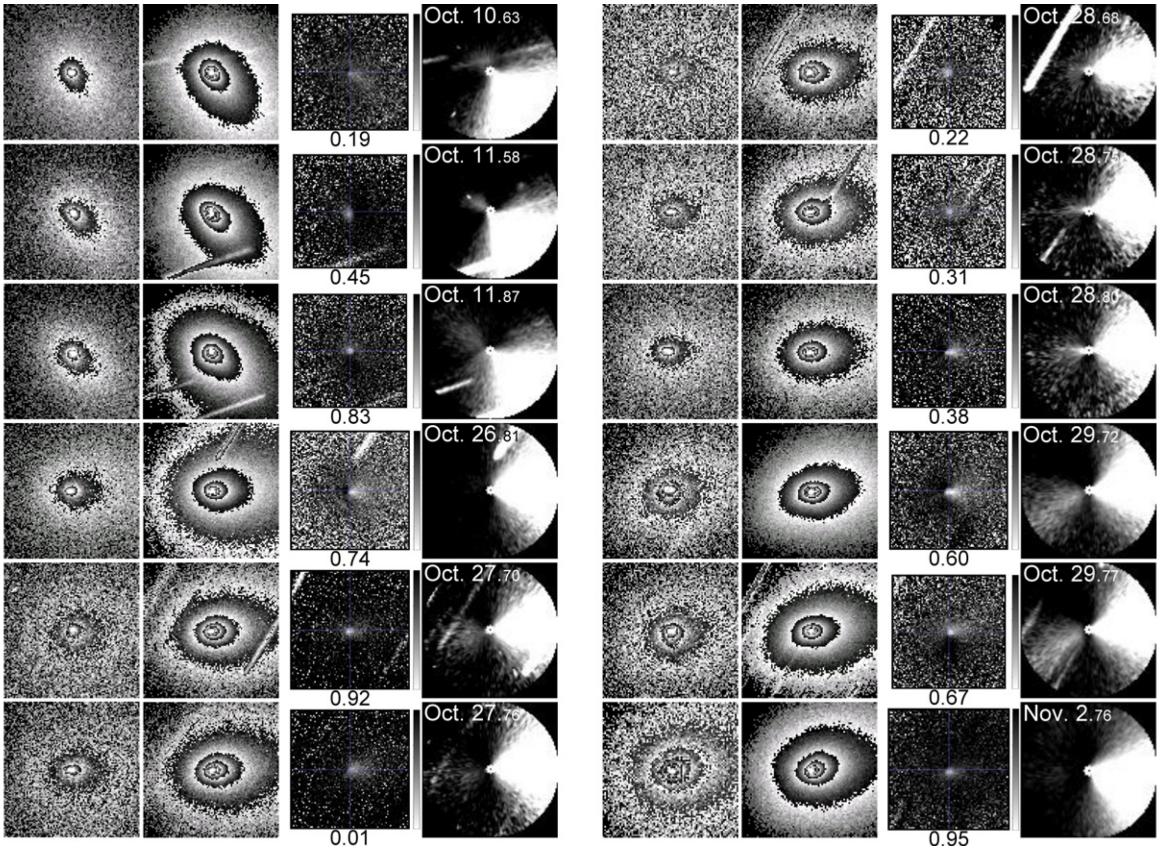

Figure 8. Jet activity and dust color of the coma of 103P/Hartley 2. The first two columns are images acquired with the blue continuum filter centered at 443 nm (BC) and with red continuum filter centered at 684 nm (RC), respectively. The third column shows the dust reddening computed with Equation (1). The color bar stretches from 0% (black) to 50% (white)/100 nm. The fourth column displays the ring-masking images obtained by subtracting the RC images from an image generated with the azimuthal average profile. North is up, east is to the left. The field of view is about 40″ × 40″, corresponding to 1800 km–2200 km at the comet distance depending on the different comet heliocentric distances.

Table 3
The Dust Color Averaged within the Innermost 5000 km of the Coma

Date	Color (%/100 nm)
Oct 10	9.40 ± 0.82
Oct 11	11.50 ± 0.934
Oct 25	5.06 ± 0.78
Oct 26	6.36 ± 0.82
Oct 27	6.43 ± 0.87
Oct 28	11.07 ± 0.83
Oct 29	10.01 ± 0.83
Nov 2	5.56 ± 0.88

as the normalized gradient of the Afρ product between the blue (BC, $\lambda_0 = 4430$ Å) and red (RC, $\lambda_0 = 6840$ Å) continuum filters. The dust color can be converted to a percentage of reddening per 1,000 Å and is defined by the following relation:

$$\text{color} = \frac{\text{RC}_{\text{Af}\rho} - \text{BC}_{\text{Af}\rho}}{6840 - 4430} \frac{2000}{\text{RC}_{\text{Af}\rho} + \text{BC}_{\text{Af}\rho}}. \quad (1)$$

The summarized results in Table 3 indicate that the average dust color within the innermost 5000 km of the coma did not appear to vary significantly with heliocentric distance. This behavior of the averaging dust color seems to indicate that the innermost coma does not introduce significant changes in the size distribution and/or overall properties of dust grains. As we found a jet feature that switches on and off from our images in Figures 4–6, we analyzed all the flux-calibrated images acquired with the BC and RC narrowband filters instead of integrating the whole flux in the innermost 5000 km. The resulting two-dimensional dust color map can be seen in Figure 8 (the third column). Figure 8 displays the dust coma of comet 103P/Hartley 2 from October 10 to November 2 imaged in the BC and RC narrowband filters (first two columns), the dust color map (the third column) and the azimuthal median profile subtracted RC filter images (the fourth column) displaying the jet activity in the dust coma. The data presented here pertaining to October and November indicate extreme dust reddening, with a normalized color ~30%–45% within a radius of ~50–100 km measured from the optocenter of the images. This red dust could be associated with strong jet activity. The sunward jet feature might give rise to higher dust abundances at closer cometocentric distances (i.e., nearer the optocenter). These dust grains are initially large with a reddening of ~30%–40%/1,000 Å; while traveling out, they split up and show less reddening at ~500 km with a dust reddening of ~10%–15%. In comparison with the tailward direction, the color variation is 5%–10%. The decrease in the dust reddening means that the optical properties of the dust grains change as the dust grains move outward. The decrease in the reddening could be also associated with an outburst (Bonev et al. 2002). A possible explanation for the color variation is that the larger dust grains mixed with the icy grains dominate the scattering behavior at close distance around the nucleus. When these larger dust grains move outward, they break up or sublimate into small submicron particles, resulting in a bluer continuum due to their smaller sizes (Lara et al. 2011a).

5. SUMMARY

We observed the comet Hartley 2 at the Lulin Observatory in Taiwan, the Calar Alto Observatory in Spain, and the Beijing Astronomical Observatory in China, from 2010 April to December using both broadband and narrowband filters, and long-slit spectrophotometry. The results are summarized below.

1. *CN morphology.* The processed CN images revealed two asymmetric jet features in the coma of comet Hartley 2. The CN jet features detected in the images presented here did not show the spiral-like structure seen by other authors at earlier dates due to a different observing geometry. One of these CN jet features always shows a higher intensity than the other, possibly because it is facing toward the Earth.
2. *Gas production rates.* Our Lulin, BAO, and CA results show that there is no significant variation of Q(CN) from mid-October to early November. The power-law slopes of the heliocentric distance of the gas production rate of CN and C_2 are −4.57 and −4.84 before perihelion and −3.21 and −3.42 after perihelion. The average C_2-to-CN production rate ratio is 0.7 $\sim$ 1.5, consistent with 103P/Hartley 2 being typical in terms of C_2 enrichment.
3. *Dust morphology.* The sunward jet feature was first detected in images acquired at the end of 2010 September. This sunward jet does not seem to be permanent. Instead, its morphology varies with time and two distinct jet features are found on October 11 and after October 29 until November 2.
4. *Afρ and dust color.* The power-law r_h dependence of the dust production rate, Afρ (5000 km), is -3.75 ± 0.45 before perihelion and -3.44 ± 1.20 during post-perihelion. The higher dust reddening found around the optocenter could be associated with a stronger jet activity. The dust color is getting bluer outward along the sunward jet, implying that the optical properties of the dust grains change with ρ. The average dust color did not appear to vary significantly when the heliocentric distance decreased to perihelion.

This work was based on observations obtained at Taiwan's Lulin Observatory. We thank the staff members and Yu-Chi Cheng for their assistance with the observations. We gratefully acknowledge valuable discussions with the referee. The research was supported by project AyA2009-08011 of the Ministerio de Ciencia e Innovacion. Z.Y.L. acknowledges a postdoctoral grant awarded by the Junta de Andalucia through project No. P07-TIC-274. This work was also supported by grant No. NSC 99-2923-M-008-002-MY3 for the Formosa Program (NSC-CSIC).

REFERENCES

A'Hearn, M. F., Belton, M. J. S., Delamere, W. A., et al. 2011, Sci, 332, 1396
A'Hearn, M. F., Millis, R. L., Schleicher, D. G., Osip, D. J., & Birch, P. V. 1995, Icar, 118, 223
A'Hearn, M. F., Schleicher, D. G., Millis, R. L., Feldman, P. D., & Thompson, D. T. 1984, AJ, 89, 579
Belton, M. J. S., Thomas, P., Li, J.-Y., et al. 2013, Icar, 222, 595
Böhnhardt, H., & Birkle, K. 1994, A&A, 107, 101
Bonev, T., Jockers, K., Petrova, E., et al. 2002, Icar, 160, 419
Drahus, M., Jewitt, D., Guilbert-Lepoutre, A., et al. 2011, ApJL, 734, L4
Fray, N., Bénilan, Y., Cottin, H., Gazeau, M.-C., & Crovisier, J. 2005, P&SS, 53, 1243
Harmon, J. K., Nolan, M. C., Howell, E. S., Giorgini, J. D., & Taylor, P. A. 2011, ApJL, 734, L2
Haser, L. 1957, BSRSL, 43, 740
Jewitt, D. C., & Meech, K. J. 1987, ApJ, 317, 992
Knight, M. M., & Schleicher, D. G. 2011, AJ, 141, 183
Knight, M. M., & Schleicher, D. G. 2013, Icar, 222, 691
Lara, L. M., Lin, Z.-Y., & Meech, K. 2011a, A&A, 532, 87L
Lara, L. M., Lin, Z.-Y., Rodrigo, R., & Ip, W.-H. 2011b, A&A, 525, 36L
Lara, L. M., Schulz, R., Stüwe, J. A., & Tozzi, G. P. 2001, Icar, 150, 124
Larson, S. M., & Sekanina, Z. 1984, AJ, 89, 571
Lin, Z.-Y., Chang, C.-P., & Ip, W.-H. 2007a, AJ, 133, 1861
Lin, Z.-Y., Lara, L. M., Vincent, J. B., & Ip, W.-H. 2012, A&A, 537, 101L
Lin, Z.-Y., Weiler, M., Rauer, H., & Ip, W.-H. 2007b, A&A, 469, 771
Meech, K. J., A'Hearn, M. F., Adams, J. A., et al. 2011, ApJL, 734, L1
Mueller, B. E. A., Samarasinha, H., Farnham, T. L., & A'Hearn, M. F. 2013, Icar, 222, 799
Mumma, M. J., Bonev, B. P., Villanueva, G. L., et al. 2011, ApJL, 734, L7
Samarasinha, N. H., Mueller, B. E. A., A'Hearn, M. F., Farnham, T. L., & Gersch, A. 2011, ApJL, 734, L3
Schleicher, D. G. 2010, AJ, 140, 973
Schleicher, D. G., Millis, R. L., & Birch, P. V. 1998, Icar, 132, 397
Waniak, W., Borisov, G., Drahus, M., & Bonev, T. 2012, A&A, 543, A32

The Astrophysical Journal, 775:123 (9pp), 2013 October 1
doi:10.1088/0004-637X/775/2/123

CHARACTERIZATION OF THE YOUNG OPEN CLUSTER G144.9 + 0.4 IN THE CAMELOPARDALIS OB1 ASSOCIATION

Chien-Cheng Lin (林建爭), W. P. Chen (陳文屏), and Neelam Panwar
Graduate Institute of Astronomy, National Central University, 300 Jhongda Rd., Jhongli 32001, Taiwan; cclin@astro.ncu.edu.tw

Received 2013 May 5; accepted 2013 August 2; published 2013 September 13

ABSTRACT

Our star-count analysis of the Two Micron All Sky Survey point sources resulted in an identification of the star cluster G144.9 + 0.4. The cluster was found, but not characterized, by Glushkova et al. We show that the cluster is physically associated with the Cam OB1 association at a distance of about 1 kpc and with an age of 1–2 Myr. Pre-main sequence stars are identified on the basis of photometric and proper motion data. A total of 91 additional OB star candidates was found in subgroups 1A and 1B, a significant increase from the currently known 43 OB stars. The OB members show an age spread that indicates a sustained star formation for at least the last 10–15 Myr. The young cluster G144.9 + 0.4 represents the latest episode of sequential star formation in this cloud complex.

Key words: infrared: stars – open clusters and associations: general – stars: early-type – stars: pre-main sequence – stars: variables: T Tauri, Herbig Ae/Be

Online-only material: color figures

1. INTRODUCTION

Hundreds of thousands of open clusters (OCs) should currently exist in the Milky Way galaxy based on the number of OCs present in the solar neighborhood (Piskunov et al. 2006). However, the databases of OCs (Dutra & Bica 2001; Dias et al. 2002; Bica et al. 2003; Dutra et al. 2003; Kronberger et al. 2006; Froebrich et al. 2007) contain only a few thousand entries that are limited to OCs within 1 kpc. This discrepancy is due partly to dust extinction in the Galactic plane, and partly to a lack of comprehensive all-sky searches for distant systems.

Star clusters are groupings of member stars in a six-dimensional phase space in position and motion. Kinematic studies of star clusters require special instrumentation and are often time-consuming. Initial identification of a star cluster via space grouping, i.e., by the "star-count" technique, is relatively straightforward and has been exploited efficiently on wide-field or all-sky surveys (Schmeja 2011). The Two Micron All Sky Survey point source catalog (2MASS; Cutri et al. 2003) provides a uniformly calibrated database of the entire sky in the near-infrared (NIR) wavebands, which allows us to recognize OCs even with moderate dust extinction, i.e., partially embedded, young star clusters. Earlier works by Bica et al. (2003), Dutra et al. (2003), and Froebrich et al. (2007) have indeed found hundreds of previously unknown infrared clusters using the 2MASS catalog.

We have developed a star-count technique to recognize star density enhancements and have applied it to the sky within $|b| < 50^\circ$ using the 2MASS data. Hundreds of density peaks were found. We then used the SIMBAD database to match these peaks with known sources within a radius of $5'$, resulting in 501 OCs, 89 globular clusters, 35 galaxies, 55 galaxy clusters, 11 H II regions, and 24 regions contaminated by neighboring bright stars. A total of five candidates remain unaccounted for. One such density peak is G144.9 + 0.4 (designated as G144) located at $\ell \approx 144\overset{\circ}{.}9$ and $b \approx 0\overset{\circ}{.}4$, or R.A. (J2000) $= 03^{\rm h}39^{\rm m}16\overset{\rm s}{.}7$, decl. (J2000) $= +55^\circ58'24''$, seen toward the Camelopardalis (Cam) OB1 association (Lin et al. 2012). This cluster candidate was recognized by Glushkova et al. (2010), who used a pipeline (Koposov et al. 2008) to search for star clusters with 2MASS data. However, the cluster candidate was not well characterized by their pipeline, apparently because of the nebulous contamination. The full results of our OC finding will be reported elsewhere. Here we present a characterization of this cluster using photometric and proper motion (PM) measurements, and discuss the context of the cluster amid the OB association and cloud complex.

2. PHOTOMETRIC, KINEMATIC, AND SPECTROSCOPIC DATA

Our data consist of the 2MASS and *WISE* infrared magnitudes, PPMXL PMs, and our own photometric and spectroscopic observations.

2MASS. The NIR magnitudes for point sources have been obtained from 2MASS to the 10σ limiting magnitudes of J $(1.25\,\mu{\rm m}) = 15.8$, $H\,(1.65\,\mu{\rm m}) = 15.1$, and $K\,(2.17\,\mu{\rm m}) = 14.3$, respectively. For our star count analysis, we included only stars with a photometric quality flag better than "CCC," which effectively gives a signal-to-noise ratio (S/N) $\geqslant 5$ and a photometric uncertainty of <0.2 mag in every band to ensure completeness. Subsequently, to characterize clusters, we constrained only stars with a photometric quality flag of "AAA," which corresponds to an S/N $\geqslant 10$ and a photometric uncertainty of <0.1 mag in every band for photometric accuracy.

WISE. The *Wide-field Infrared Survey Explorer* mapped the whole sky at 3.4, 4.6, 12, and 22 μm (designated as $W1$, $W2$, $W3$, and $W4$) with an angular resolution of $6\overset{\prime\prime}{.}1$, $6\overset{\prime\prime}{.}4$, $6\overset{\prime\prime}{.}5$, and $12\overset{\prime\prime}{.}0$, and a 5σ point-source sensitivity of 0.08, 0.11, 1 and 6 mJy, respectively, corresponding to Vega magnitudes of $W1 = 16.6$, $W2 = 15.6$, $W3 = 11.3$, and $W4 = 8.0$ (*WISE*; Wright et al. 2010). We exploited the identification scheme to search for potential young stellar objects (YSOs) used by Koenig et al. (2012). The *WISE* point sources within the cluster region are extracted from Vizier.[1] Only sources having 2MASS counterparts are included in the analysis.

PPMXL. In addition to photometric data, kinematic information is also employed to secure the membership in a star cluster.

---

[1] http://vizier.u-strasbg.fr/

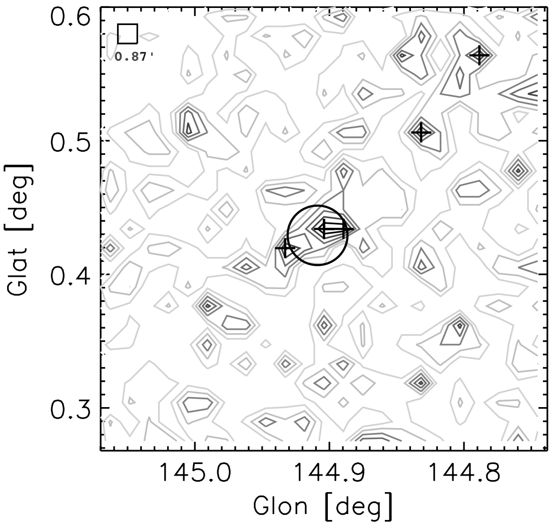

Figure 1. Stellar density map of G144. The pluses mark the grids 3σ above the average density. The circle shows the effective size, which is estimated from the three neighboring pluses.

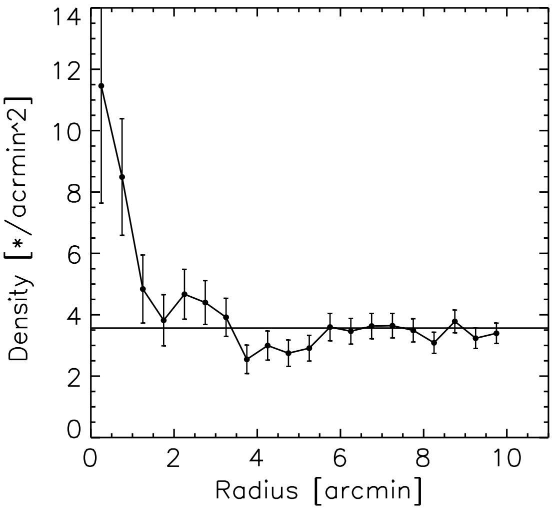

Figure 2. Radial density profile for G144. Filled dots are surface stellar density values with each error bar estimated by Poisson statistics. The horizontal line depicts the background density. The oscillation between the radius of 2′ and 4′ is due to the elongated shape of the cluster.

The PPMXL Catalog (Röser et al. 2010) contains stars down to about $V \approx 20$ mag and lists the USNO-B1.0 PMs (Monet et al. 2003) and 2MASS JHK magnitudes. The stars with PM uncertainties >5.0 mas yr^{-1} have not been used in our analysis.

Tenagra. Narrow-band imaging observations were carried out using the Tenagra II 0.81 meter $f/7$ telescope in Arizona on 2012 March 30. The CCD camera used an SITe chip with 1024×1024 pixels and a pixel size of $\sim 0\farcs8$, rendering a field of view of $\sim 15 \times 15$ arcmin^2 on the sky. The total exposure times were 540 s for the Hα and R bands, and 300 s for the I band. All images were reduced with standard routines, including dark and bias subtraction and flat-field normalization. SExtractor[2] was used for photometry. The stellar astrometric solution calibrated with the 2MASS coordinates was calculated with the astrometry package from Astrometry.net.[3] The Tenagra data reached about $R \sim 18$ mag. Supplementary Hα data for fainter stars were taken from the INT/WFC Photometric Hα Survey of the Northern Galactic Plane (IPHAS; Drew et al. 2005).

HCT and LOT. Follow-up spectroscopic observations were taken using the HFOSC on the Himalayan Chandra Telescope (HCT) with a slit width of $1\farcs15$ and Grism 8 (λ = 5800–8350 Å, dispersion = 1.45 Å pixel^{-1}) on 2012 July 26. Additional spectra were taken using the Hiyoyu spectrograph on the Lulin One-meter Telescope (LOT) with a slit width of $1\farcs5$ and grating of 300 mm^{-1} (λ = 3800–7600 Å) on the night of 2012 November 15. A one-dimensional spectrum was extracted from the dark, bias-subtracted and flat-field-corrected image in the standard manner using IRAF. The wavelength calibration was done using FeNe (HCT) or HeNeAr (LOT) lamp sources.

3. CHARACTERIZATION OF THE CLUSTER

G144 was first recognized by Glushkova et al. (2010) who used the pipeline developed by Koposov et al. (2008) to search for density peaks in a star catalog as star clusters. They found 153 previously unknown clusters within the Galactic latitude $|b| < 24°$, 23 of which were considered to be embedded star clusters and were not characterized by their pipeline. This candidate was also detected as a density peak by our pipeline. In this section, we present the properties of the cluster derived from our analysis.

3.1. Density Enhancements and Radial Density Profile

We selected the 2MASS point sources with S/N $\geqslant 5$ in J, H, K bands within 15′ of the apparent center of the cluster. Figure 1 shows the stellar density map for which the number of stars in a grid, whose scale was chosen to include an average of 10 stars, was counted. The resulting density map was then smoothed with a 3×3 grid width. For G144, a background density of ~ 3.1 stars arcmin^{-2} was estimated by 3σ clipping of the density outliers. A grid in the smoothed density map 3σ above the background would be considered a high-density region, and a grouping of more than three connected high-density regions would be identified as a density enhancement, i.e., a cluster candidate. The density map around G144 is shown in Figure 1.

We estimated the size of G144 based on the radial density profile, though the cluster appears slightly elongated in shape. As seen in Figure 2, the density starts to blend with the field at a radius of $\sim 3\farcm5$. We therefore adopted a radius of $3\farcm5$ for the cluster in subsequent analysis. Spatially, the cluster is seen near the Cam OB1 association and is likely physically related to it.

3.2. Proper Motion Members

Cluster members share the same age, metallicity, distance, PMs, etc. Accordingly, common PMs would be a necessary condition for cluster membership. The Cam OB1 association was first investigated by Morgan et al. (1953), who found eight early-type stars aggregated at a distance of ~900 pc. Several studies, e.g., Haug (1970), Humphreys (1978), and Lyder (2001), append the members of Cam OB1. However, the Cam OB1 members spread over an area on the sky of $\sim 20 \times 10$ deg^2 corresponding to a physical dimension of $\sim 320 \times 160$ pc^2, making a coeval formation of the Cam OB1 impossible (de Zeeuw et al. 1999). Straižys & Laugalys (2007a) divided the association into three subgroups—1A, 1B, and 1C—and found them all at nearly the same distance of ~1 kpc. G144 is located between 1A and 1B, which contain 30 and 13

---

[2] http://www.astromatic.net/software/sextractor

[3] http://astrometry.net/

Table 1
Three Subgroups of the Cam OB1 Association

Subgroup	ℓ, b (deg)	Angular Size (deg)	Distance (pc)	Age (Myr)	No. of Stars	$\mu_\alpha{}^{d}$ (mas yr^{-1})	$\mu_\delta{}^{d}$ (mas yr^{-1})
1A	140.0, +1.5	∼10 × 10	1010 ± 210	$\lesssim 10^{a}$	30^{a}	−1.1 ± 2.1	−1.9 ± 1.5
1B	148.0, −0.5	∼10 × 10	∼1000	$\lesssim 10^{a}$	13^{a}	−0.8 ± 0.6	−2.3 ± 1.0
1C	143.7, +7.7	0.1	1180 ± 160	$\sim 10^{c}$	76^{b}	−0.2 ± 1.5	0.4 ± 2.5

Notes.
[a] Straižys & Laugalys (2007a).
[b] Mostly NGC 1502 members (Weitenbeck 1997).
[c] Paunzen et al. (2005).
[d] Derived from PPMXL.

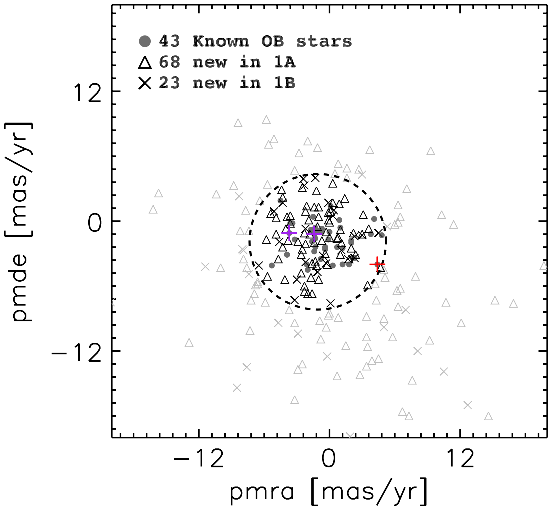

Figure 3. Newly identified OB stars in Cam OB1A and 1B. The filled circles mark known Cam OB1 members (Straižys & Laugalys 2007a), and the two purple and one red pluses are supergiants with $J-H$ larger than 0.5 mag (discussed in Section 3.4). The dashed circle is the 3σ range of the mean PMs of known OB stars in Cam OB1A and 1B. Triangles are OB star candidates in 1A and crosses are those in 1B. Symbols in black represent those with PMs consistent with being members.

(A color version of this figure is available in the online journal.)

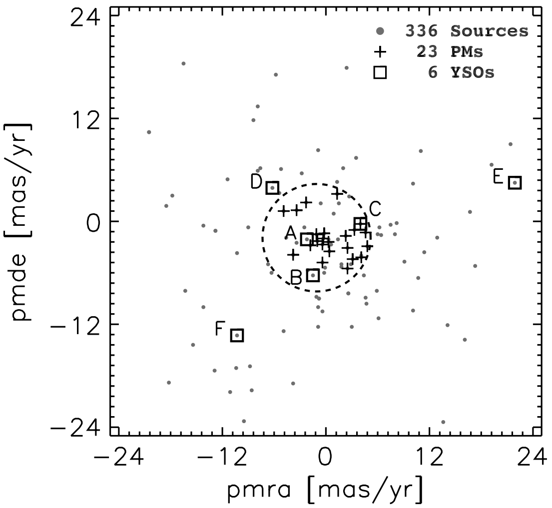

Figure 4. Stellar proper motions toward G144. Stars within a 3′.5 radius of the cluster are represented by gray dots. The dashed circle, as in Figure 3, shows the probable PM range for membership. Pluses mark PM candidates. Boxes, individually labeled, are stars with infrared excess or highly reddened colors (discussed in Section 3.3).

OB stars, respectively (Straižys & Laugalys 2007a). The other subgroup, 1C, has 76 known members mainly from NGC 1502 (Weitenbeck 1997).

To provide the criteria for selecting PM members in G144, we first extracted the PPMXL PMs of the known OB stars. The same data would also allow us to identify faint OB members that might have escaped recognition in previous works. The derived PPMXL PMs of each subgroup are $(\mu_\alpha, \mu_\delta) = (-1.1 \pm 2.1, -1.9 \pm 1.5)$ mas yr^{-1} for 1A, $(\mu_\alpha, \mu_\delta) = (-0.8 \pm 0.6, -2.3 \pm 1.0)$ mas yr^{-1} for 1B, and $(\mu_\alpha, \mu_\delta) = (-0.2 \pm 1.5, -0.4 \pm 2.5)$ mas yr^{-1} for 1C. Indeed the three subgroups share similar PMs, suggesting a physical association. The parameters for the three subgroups, including the PMs, are summarized in Table 1.

To identify previously unknown OB stars, we select stars within the same area ∼10 × 10 deg^2, as that of the known Cam OB1 association centered on Cam OB1A and 1B, respectively, which are (1) photometrically consistent with OB spectral types in the NIR color–magnitude diagram (CMD), and (2) kinematically consistent with the systemic PM of the 1A and 1B subgroups. The CMD criteria are 2MASS J brighter than 13.0 mag and $J - H < 0.2$ mag. Only stars with photometric uncertainties better than 0.02 mag in every 2MASS band were considered. The PM criteria include uncertainties less than 5 mas yr^{-1} and within the 3σ range of the mean PM of 1A and 1B, as shown in Figure 3. Table 2 lists the 68 and 23 newly found OB stars in 1A and 1B, respectively. The first column gives the numerical identification of the stars, in order of descending brightness, followed by subsequent columns listing the Galactic coordinates, 2MASS magnitudes, and PPMXL PMs of each star. The last column lists the data belonging in 1A or 1B. The photometric and color properties of these newly found OB stars will be discussed later together with the cluster members.

For cluster members, there are 23 stars that are spatially within the 3′.5 radius and kinematically within the 3σ range of the average PM of the known OB stars, as shown in Figure 4 and listed in Table 3. Again, only stars with PPMXL uncertainties less than 5 mas yr^{-1} were selected. The PM candidates need to be further winnowed by photometric selection as discussed in the next section.

3.3. *Young Stellar Objects*

Straižys & Laugalys (2007b) have used infrared photometric data extracted from 2MASS, *IRAS*, and *MSX* to identify 35 YSOs in a region 12 × 12 deg^2 toward the Cam OB1 association, none of which are located within G144. Nonetheless, nebulosity is clearly seen around G144, suggesting a young age. Generally, YSOs are identified by their infrared excess, Hα emission, or

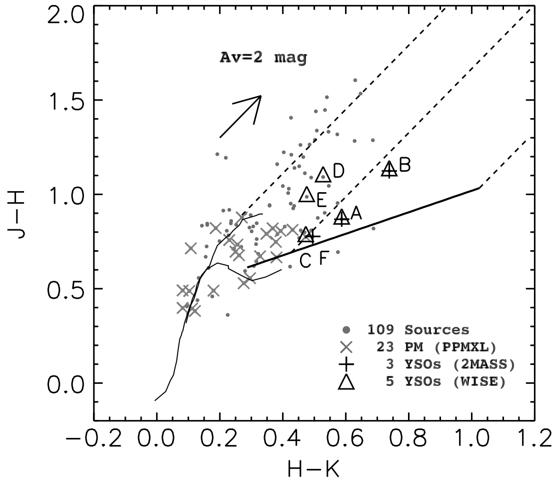

Figure 5. 2MASS color–color diagram in the cluster region. Pluses and triangles are CTTS candidates (pluses denote 2MASS sources and triangles denote *WISE* sources). Crosses represent proper motion members. Gray dots are none of the above. The thin curves show the giant and dwarf loci (Bessell & Brett 1988) converted to the 2MASS system. The thick line is the intrinsic CTTS locus (Meyer et al. 1997). The arrow represents the reddening direction (Rieke & Lebofsky 1985) for typical Galactic interstellar extinction ($R_V = 3.1$), and the dashed lines encompass the region of reddened giants and dwarfs. Stars to the right of this region have NIR excess and are possible YSOs.

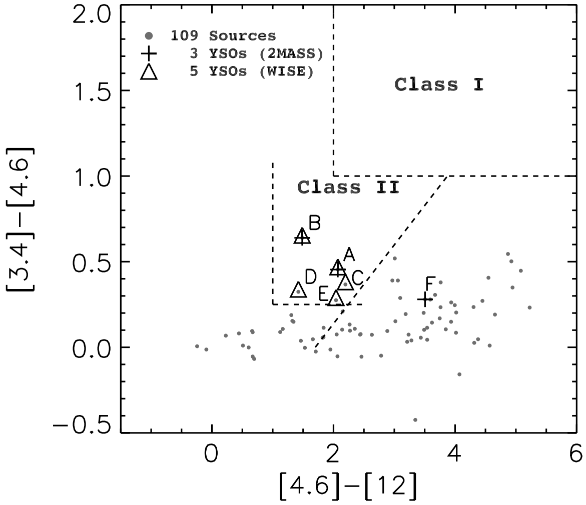

Figure 6. *WISE* [3.4] − [4.6] μm vs. [4.6] − [12] μm colors in the cluster region. The dashed lines defined by Koenig et al. (2012) are used to identify Class I and Class II young stellar objects. As in Figure 5, the 2MASS detections are in pluses and the *WISE* detections are in triangles.

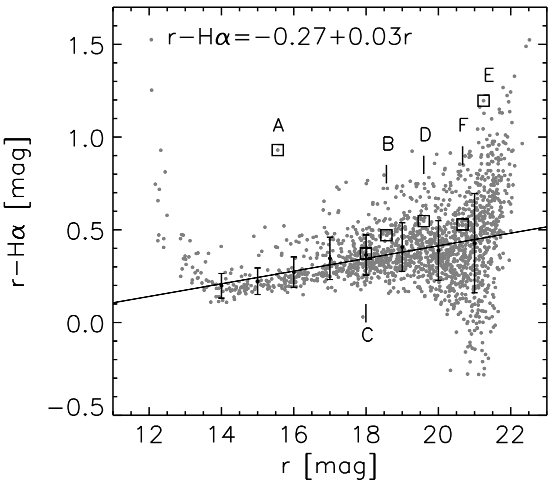

Figure 7. IPHAS magnitudes of $r - \mathrm{H}\alpha$ vs. r. Each YSO candidate is labeled and marked with a box. Bright stars ($r < 14$ mag) are saturated. The typical error, marked for each magnitude, has been estimated by Poisson statistics. The line shows the linear regression of $r - \mathrm{H}\alpha$ and r magnitudes of stars between $r \sim 14$–21 mag.

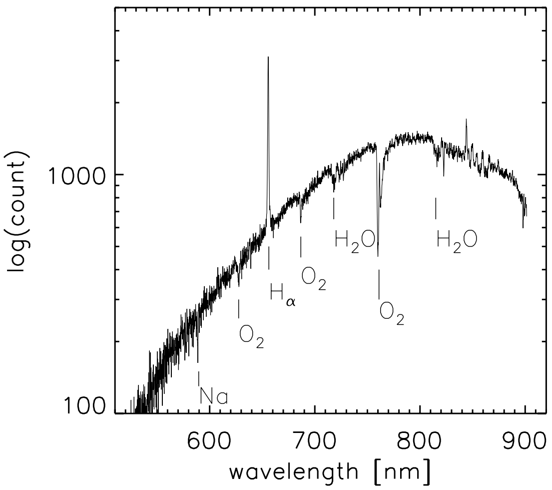

Figure 8. HCT spectrum of star A. A prominent Hα emission line is evident. Other spectral features are also marked.

X-ray emission. No X-ray data are available in the region, so we used 2MASS and *WISE* to identify possible YSOs or embedded stars in G144.

The NIR-excess sources were identified using the 2MASS ($J - H$) versus ($H - K$) and *WISE* [3.4] − [4.6] versus [4.6] − [12] color–color diagrams, shown in Figures 5 and 6. Three classical T Tauri (CTTS; class II objects) candidates were found in the empirical CTTS region (Meyer et al. 1997) in the 2MASS color–color diagram. On the other hand, using the criteria adopted by Koenig et al. (2012), five CTTS candidates were identified on the basis of the *WISE* colors, two of which coincide with the 2MASS sources. Therefore, a total of six CTTS candidates are selected, whose coordinates, 2MASS and *WISE* magnitudes, and PPMXL PMs are listed in Table 4. The first column gives the alphabetical identification of the star, in order of descending brightness, followed by subsequent columns of Galactic coordinates, 2MASS as well as *WISE* magnitudes, and PPMXL PM of each star. The last column lists the data used for the classification.

The IPHAS r and narrow-band Hα magnitudes are used to single out stars with possible Hα emission. Figure 7 shows the $r - \mathrm{H}\alpha$ versus r-band magnitude. Star A, the brightest among our CTTS candidates, is some ∼0.5 mag brighter in Hα than a “normal” star, defined as a star following the trend between the Hα- and r-band magnitudes for the majority of stars in the field. Subsequent HCT spectroscopic observations confirmed an emission spectrum for star A, as seen in Figure 8. On the basis of the NIR excess and the emission-line spectrum, we conclude that star A, located near the center of G144, should be a CTTS.

For other YSO candidates, star B, located near the nebulosity edge, has the most reddened NIR colors among our candidates, and is a CTTS candidate judging by both 2MASS and *WISE* colors. It may have weak Hα emission (see Figure 7), but, unfortunately, was too faint for our spectroscopic observations. Star B is likely a CTTS. Both stars C and D are marginal candidates in terms of their PMs and *WISE* colors. Their 2MASS

Table 2
New OB Candidates in Cam OB 1A and 1B

ID	ℓ, b (deg)	J (mag)	H (mag)	K (mag)	μ_α (mas yr^{-1})	μ_δ (mas yr^{-1})	Comments
1	136.423, −0.948	6.68	6.53	6.44	−0.1 ± 0.9	0.1 ± 0.7	1A
2	135.499, +0.833	7.31	7.14	7.02	−3.6 ± 1.1	−0.2 ± 0.8	1A
3	139.336, +2.513	8.31	8.31	8.26	−5.8 ± 1.0	−1.7 ± 0.9	1A
4	135.552, +2.559	8.73	8.65	8.57	−1.0 ± 1.8	−5.4 ± 1.8	1A
5	135.575, +1.579	8.89	8.82	8.76	−0.1 ± 1.4	0.8 ± 1.1	1A
6	139.909, +0.635	9.16	9.05	8.95	0.3 ± 1.8	1.7 ± 1.7	1A
7	142.940, −0.745	9.23	9.19	9.12	−1.3 ± 1.3	−3.7 ± 1.3	1A
8	139.404, +2.266	9.26	9.17	9.12	0.8 ± 1.6	−1.5 ± 1.6	1A
9	143.240, −1.364	9.29	9.19	9.10	−4.9 ± 1.8	0.3 ± 1.8	1A
10	144.540, +4.802	9.30	9.29	9.25	−4.3 ± 1.1	2.2 ± 1.0	1A
11	140.150, +2.163	9.39	9.37	9.32	−2.2 ± 1.6	0.9 ± 1.7	1A
12	142.818, +2.377	9.55	9.44	9.37	−1.1 ± 2.1	−0.5 ± 2.1	1A
13	135.773, +1.449	9.73	9.65	9.60	−3.9 ± 2.0	0.4 ± 2.0	1A
14	141.764, −2.567	9.79	9.63	9.53	−4.9 ± 2.9	−1.2 ± 2.9	1A
15	139.879, +4.601	9.83	9.75	9.69	−1.4 ± 1.9	1.3 ± 1.9	1A
16	144.565, +1.886	9.95	9.80	9.71	−4.4 ± 1.6	2.9 ± 1.6	1A
17	140.789, +2.781	9.95	9.78	9.68	0.3 ± 2.0	3.5 ± 2.0	1A
18	143.333, −0.103	9.96	9.82	9.76	−0.2 ± 2.1	−4.0 ± 2.1	1A
19	144.446, −1.431	10.04	9.86	9.76	−2.9 ± 2.1	−1.9 ± 2.1	1A
20	143.361, +3.974	10.06	9.95	9.87	−0.3 ± 1.7	−1.0 ± 1.7	1A
21	143.964, +3.254	10.25	10.17	10.12	1.1 ± 2.1	−2.0 ± 2.1	1A
22	144.320, +5.428	10.27	10.28	10.28	−4.3 ± 1.6	−2.4 ± 1.6	1A
23	137.583, +4.872	10.35	10.15	10.10	1.8 ± 2.0	−3.5 ± 2.0	1A
24	143.845, +5.805	10.37	10.22	10.17	−1.2 ± 1.9	2.8 ± 1.9	1A
25	136.891, +5.032	10.40	10.20	10.15	−1.0 ± 1.7	1.3 ± 1.7	1A
26	139.130, +1.675	10.41	10.22	10.14	−2.5 ± 1.7	−2.6 ± 1.7	1A
27	141.658, +1.215	10.46	10.35	10.27	−5.7 ± 2.3	−5.1 ± 2.3	1A
28	143.742, +1.059	10.46	10.32	10.24	−1.0 ± 2.2	0.4 ± 2.2	1A
29	143.141, +3.525	10.46	10.38	10.29	−1.9 ± 1.8	0.1 ± 1.8	1A
30	138.041, −0.551	10.49	10.40	10.31	−1.8 ± 2.1	−1.2 ± 2.1	1A
31	143.335, −0.101	10.50	10.37	10.27	−0.4 ± 2.2	−3.0 ± 2.2	1A
32	144.343, +4.769	10.51	10.35	10.28	−2.5 ± 1.7	3.1 ± 1.7	1A
33	143.773, +2.906	10.56	10.42	10.31	0.0 ± 1.8	−1.5 ± 1.8	1A
34	143.795, +3.308	10.56	10.42	10.35	0.7 ± 1.8	−1.6 ± 1.8	1A
35	139.743, +4.774	10.59	10.44	10.29	3.6 ± 2.7	−0.7 ± 2.7	1A
36	140.181, +2.158	10.63	10.52	10.48	−4.1 ± 2.0	−5.4 ± 2.0	1A
37	141.804, +2.273	10.66	10.55	10.48	3.5 ± 1.8	−5.9 ± 1.8	1A
38	144.248, +2.220	10.67	10.54	10.47	0.9 ± 1.8	1.6 ± 1.8	1A
39	142.569, +0.978	10.70	10.53	10.43	−1.4 ± 1.9	−2.0 ± 1.9	1A
40	143.314, −0.222	10.76	10.66	10.60	2.0 ± 1.6	−2.5 ± 1.6	1A
41	138.486, +3.456	10.77	10.59	10.54	2.4 ± 2.7	−3.1 ± 2.7	1A
42	135.654, +1.584	10.78	10.77	10.71	1.0 ± 2.0	−0.8 ± 2.0	1A
43	144.849, −2.906	10.82	10.67	10.48	−2.2 ± 4.1	−2.1 ± 4.1	1A
44	138.594, +2.357	10.85	10.66	10.53	2.2 ± 2.8	−1.1 ± 2.8	1A
45	144.165, +3.279	10.86	10.74	10.67	−2.1 ± 2.1	1.4 ± 2.1	1A
46	137.987, −0.541	10.88	10.69	10.58	−1.2 ± 1.8	−4.1 ± 1.8	1A
47	141.849, +2.190	10.95	10.80	10.73	3.0 ± 2.2	−1.2 ± 2.2	1A
48	143.304, −0.146	10.98	10.90	10.78	−2.6 ± 1.8	−4.8 ± 1.8	1A
49	138.642, +2.290	10.99	10.89	10.82	−3.6 ± 2.0	0.5 ± 2.0	1A
50	144.131, −2.173	11.01	10.89	10.82	0.1 ± 1.8	0.9 ± 1.8	1A
51	143.997, +3.374	11.02	10.84	10.74	−1.6 ± 2.1	−3.9 ± 2.1	1A
52	141.297, +2.745	11.04	10.91	10.83	−2.6 ± 2.1	−3.1 ± 2.1	1A
53	143.963, −1.950	11.07	10.93	10.87	−4.7 ± 2.3	−3.5 ± 2.3	1A
54	144.713, +2.623	11.09	10.90	10.80	−2.3 ± 2.2	−1.1 ± 2.2	1A
55	144.094, +2.151	11.10	11.01	10.91	−5.4 ± 1.8	0.7 ± 1.9	1A
56	143.235, +4.009	11.16	11.04	10.95	−2.3 ± 1.7	−6.0 ± 1.7	1A
57	143.371, −0.256	11.19	11.07	11.02	4.7 ± 1.7	−4.3 ± 1.7	1A
58	143.492, −1.700	11.22	11.06	10.96	−2.3 ± 2.3	−6.5 ± 2.3	1A
59	141.780, −2.387	11.24	11.04	10.95	0.0 ± 2.9	−0.1 ± 2.9	1A
60	137.154, +5.389	11.35	11.16	11.09	−1.6 ± 4.1	−6.7 ± 4.1	1A
61	137.392, +3.852	11.38	11.24	11.16	1.0 ± 1.7	−3.1 ± 1.6	1A
62	144.385, +2.014	11.42	11.24	11.13	3.1 ± 2.9	0.6 ± 2.9	1A
63	143.751, +3.354	11.45	11.26	11.19	−4.0 ± 1.8	−0.7 ± 1.8	1A
64	143.183, −1.119	11.49	11.32	11.21	1.4 ± 2.2	2.1 ± 2.2	1A

Table 2
(Continued)

ID	ℓ, b (deg)	J (mag)	H (mag)	K (mag)	μ_α (mas yr^{-1})	μ_δ (mas yr^{-1})	Comments
65	142.926, −0.749	11.53	11.43	11.33	−2.0 ± 2.2	−6.7 ± 2.2	1A
66	144.419, +3.040	11.53	11.39	11.34	−3.8 ± 1.7	−1.8 ± 1.7	1A
67	138.831, +6.303	11.59	11.46	11.37	−0.7 ± 4.0	−1.8 ± 4.0	1A
68	135.975, +1.828	11.88	11.73	11.63	−1.7 ± 2.7	−5.2 ± 2.7	1A
1	146.869, −5.801	6.04	5.89	5.83	0.4 ± 0.6	1.0 ± 0.7	1B
2	145.762, +3.327	9.32	9.20	9.10	−0.6 ± 1.8	−3.2 ± 1.8	1B
3	146.307, −5.275	9.50	9.43	9.36	−0.1 ± 1.4	1.7 ± 1.4	1B
4	146.855, −0.543	9.54	9.39	9.31	−4.6 ± 2.0	−1.9 ± 2.0	1B
5	146.016, +3.242	9.91	9.85	9.81	−2.4 ± 2.1	3.9 ± 2.1	1B
6	146.804, −0.548	9.94	9.83	9.73	−4.3 ± 2.7	1.7 ± 2.7	1B
7	145.503, −6.755	10.21	10.15	10.07	0.3 ± 1.7	0.5 ± 1.7	1B
8	146.309, −0.178	10.40	10.29	10.19	−1.3 ± 1.7	4.0 ± 1.7	1B
9	151.415, +3.612	10.42	10.31	10.22	−2.2 ± 2.0	−0.7 ± 2.0	1B
10	150.306, −6.250	10.44	10.37	10.28	0.1 ± 1.4	−7.6 ± 1.4	1B
11	151.443, +3.504	10.84	10.64	10.56	−6.5 ± 4.0	−4.1 ± 4.0	1B
12	146.497, +3.146	10.86	10.68	10.60	2.3 ± 1.8	−1.4 ± 1.8	1B
13	148.254, +2.582	10.87	10.75	10.70	−2.3 ± 1.8	3.3 ± 1.8	1B
14	148.387, +0.963	11.07	10.93	10.85	4.5 ± 1.7	−1.1 ± 1.7	1B
15	146.421, −5.025	11.14	10.97	10.84	−2.2 ± 4.1	−3.8 ± 4.1	1B
16	146.069, +3.633	11.52	11.47	11.39	−0.3 ± 1.8	−3.9 ± 1.8	1B
17	148.234, +2.526	11.52	11.39	11.30	−5.1 ± 2.2	0.9 ± 2.2	1B
18	146.432, −5.113	11.59	11.39	11.27	−3.0 ± 4.1	−5.4 ± 4.1	1B
19	151.412, +3.551	11.59	11.43	11.34	1.1 ± 4.0	−2.7 ± 4.0	1B
20	145.901, −4.777	11.72	11.58	11.49	−3.2 ± 4.1	−7.3 ± 4.1	1B
21	145.648, −4.026	11.86	11.67	11.56	3.0 ± 4.1	−1.3 ± 4.1	1B
22	156.362, −6.956	11.99	11.89	11.82	−1.1 ± 3.9	−4.7 ± 3.9	1B
23	145.908, −4.784	12.05	11.87	11.80	1.7 ± 4.1	−3.5 ± 4.1	1B

Table 3
Proper Motion Member Candidates

ID	ℓ, b (deg)	J (mag)	H (mag)	K (mag)	μ_α (mas yr^{-1})	μ_δ (mas yr^{-1})
1	144.911, +0.395	11.89	11.50	11.41	−0.4 ± 4.0	−4.8 ± 4.0
2	144.898, +0.437	11.93	11.25	10.99	−4.9 ± 4.0	1.2 ± 4.0
3	144.946, +0.409	12.28	11.53	11.15	−1.0 ± 4.0	−2.3 ± 4.0
4	144.913, +0.418	12.71	12.04	11.71	−0.3 ± 4.0	−2.0 ± 4.0
5	144.903, +0.437	12.96	12.15	11.76	1.3 ± 4.0	3.2 ± 4.0
6	144.891, +0.391	13.12	12.74	12.62	0.3 ± 4.0	−2.4 ± 4.0
7	144.918, +0.420	13.14	12.35	12.00	4.1 ± 4.0	−4.2 ± 4.0
8	144.909, +0.462	13.40	12.91	12.81	2.5 ± 4.0	−5.5 ± 4.0
9	144.940, +0.402	13.43	12.94	12.86	−3.4 ± 4.0	1.3 ± 4.0
10	144.858, +0.449	13.66	13.26	13.15	−0.2 ± 4.0	−1.4 ± 4.0
11	144.917, +0.465	13.69	13.20	13.02	3.1 ± 4.0	−4.4 ± 4.0
12	144.896, +0.430	13.94	13.16	12.69	4.0 ± 4.0	−0.3 ± 4.0
13	144.913, +0.468	14.58	13.91	13.53	−1.8 ± 4.0	−2.8 ± 4.0
14	144.955, +0.436	14.63	13.87	13.64	−3.8 ± 4.0	−3.9 ± 4.0
15	144.928, +0.430	14.67	13.97	13.72	−1.1 ± 4.0	−1.5 ± 4.0
16	144.942, +0.452	14.73	13.92	13.49	3.3 ± 4.0	−1.0 ± 4.0
17	144.862, +0.464	14.85	14.29	14.00	4.8 ± 4.0	−2.9 ± 4.0
18	144.877, +0.401	14.90	14.19	14.08	−0.4 ± 4.0	−2.7 ± 4.0
19	144.906, +0.455	14.92	14.10	13.91	2.5 ± 4.0	−3.1 ± 4.0
20	144.872, +0.473	14.92	14.39	14.11	4.6 ± 4.0	−1.3 ± 4.0
21	144.948, +0.453	15.13	14.31	13.94	0.4 ± 4.0	−3.5 ± 4.0
22	144.915, +0.456	15.43	14.69	14.44	2.3 ± 4.1	−1.7 ± 4.1
23	144.866, +0.404	15.91	15.04	14.77	−2.3 ± 4.1	2.2 ± 4.1

colors do not stand out, though star D, with possible Hα emission, is much more reddened than star C. Both stars E and F are very faint, so have large uncertainties in their PM measurements. They are marginal cases in either 2MASS or *WISE* colors, and seem to have motions inconsistent with membership. Hence, stars E and F should be classified as field stars.

3.4. Extinction, Distance, and Age

The average interstellar extinction to the cluster was estimated by tracing each of the 23 PM candidates back to the MS locus along the reddening vector in the 2MASS color–color diagram (see Figure 5). An average extinction of $A_J \sim 0.56$ mag was

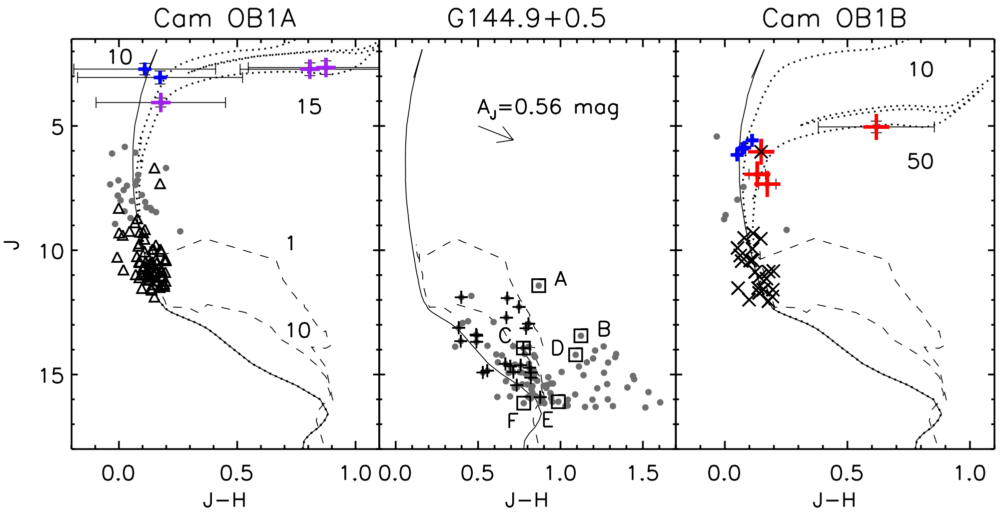

Figure 9. J vs. $J-H$ diagrams for Cam OB 1A (left), 1B (right), and G144 (middle). The solid line in each case delineates the ZAMS located at 1 kpc with an interstellar extinction of $A_V \sim 2.0$ mag. The dashed lines represent the pre-main-sequence isochrone for 1 and 10 Myr (Siess et al. 2000). The dotted lines represent the post-main-sequence isochrone for 10 and 15 Myr (left) and 10 and 50 Myr (right; Girardi et al. 2002). The gray dots in the left or right panels mark known 1A and 1B members, whereas those in the middle panel are stars in the cluster region. The newly found OB stars are represented by triangles (1A) and crosses (1B); purple, blue, and red pluses are supergiants (discussed in Section 3.4). In the cluster region, the pluses show the 23 PM candidates whereas the boxes represent YSO candidates (labeled).

(A color version of this figure is available in the online journal.)

Table 4
YSO Candidates in G144

ID	ℓ, b (deg)	J (mag)	H (mag)	K (mag)	$W1$ (mag)	$W2$ (mag)	$W3$ (mag)	$W4$ (mag)	μ_α (mas yr^{-1})	μ_δ (mas yr^{-1})	Comments
A	144.895, +0.439	11.4	10.6	10.0	9.4	9.0	6.9	2.9	-2.2 ± 5.0	-2.1 ± 5.0	*WISE*; 2MASS
B	144.881, +0.403	13.4	12.3	11.6	10.5	9.8	8.3	6.6	-1.5 ± 5.3	-6.3 ± 5.3	*WISE*; 2MASS
C	144.896, +0.430	13.9	13.2	12.7	12.1	11.7	9.5	5.3	4.0 ± 4.0	-0.3 ± 4.0	*WISE*
D	144.899, +0.426	14.2	13.1	12.6	11.9	11.6	10.2	6.1	-6.2 ± 5.4	3.9 ± 5.4	*WISE*
E	144.914, +0.412	16.1	15.1	14.6	14.5	14.2	12.1	8.7	21.9 ± 5.5	4.5 ± 5.5	*WISE*; non-member
F	144.853, +0.454	16.2	15.4	14.9	14.8	14.5	11.0	8.6	-10.3 ± 5.5	-13.3 ± 5.5	2MASS; non-member

derived. Figure 9 plots the J versus $J-H$ CMD for the Cam OB1 subgroups 1A and 1B, as well as for G144. In each case, a zero-age main-sequence (ZAMS) is shown with solar metallicity[4] at a distance of ∼1 kpc with corresponding extinction and reddening.

The 1C subgroup has a well constrained age (∼10 Myr) and distance (∼1 kpc) because of the cluster NGC 1502 (Tapia et al. 1991; Paunzen et al. 2005). A possible abnormal interstellar reddening has been suggested, as diagnosed by the total-to-selective extinction, $R_V = A_V/E(B-V)$ from 2.42 (Tapia et al. 1991) to 2.57 (Pandey et al. 2003), as compared to the average $R_V = 3.1$ in the diffuse interstellar medium. A reduced value of R_V is indicative of a smaller than typical average grain size, likely as the consequence of photoevaporation by OB stars in the region. The variation of R_V has little effect on our analysis of the properties of G144.

The cluster G144 therefore is at the same distance as the Cam OB1 association which makes it physically a part of that association. The newly found OB stars in 1A (Figure 9, left panel) and 1B (Figure 9, right panel) considerably augment the OB star inventory in the region. For G144 (Figure 9, middle panel), most PM candidates are distributed along the ZAMS. YSO candidates such as stars A, B, and D are located above the MS, i.e., at ages of $\lesssim$1 Myr and have NIR excess. The existence of CTTSs sets a stringent age limit for the cluster—no more than a couple of megayears.

Figure 10 illustrates the positional distribution of the young stellar population in Cam OB1. Subgroup 1B is associated with a molecular cloud ring (Straižys & Laugalys 2008). It is conceivably a remnant bubble created by a supernova, devoid of gas and dust, and the newly found OB stars in 1B, like the known sample, are distributed outside the ring. The OB stars in 1B are also collectively spread toward 1A. The cloud complex in 1A and 1B has a filamentary shape (see Figure 1 in Straižys & Laugalys 2008), along which the majority of the young stars are densely populated.

It has been proposed that Cam OB1 has sustained star formation for the last 100 Myr, with a stellar age progressively younger toward the northern part of the complex (Lyder 2001). A few evolved member candidates shed crucial light on the star formation history in the region. In Figure 9, one sees a handful of candidates in 1A along the 10–15 Myr post-MS isochrones. In particular, two very bright candidates, HD 22764 (spectral type of K4 Ib) and HD 17958 (spectral type of K3 Ib), could be as old as 15 Myr. Both are well within the spatial (see Figure 10) and PM (see Figure 3) groupings like other members. Thus the age spread in 1A should be secure.

In 1B, candidates are considerably older. One candidate suggests an age as old as 50 Myr. This star, HD 25056 (spectral type of G0 Ib), has a marginal PM (near the boundary circle in Figure 3) and is relatively isolated in location (see Figure 10);

---

[4] Available from the Padova isochrone database http://stev.oapd.inaf.it/cgi-bin/cmd.

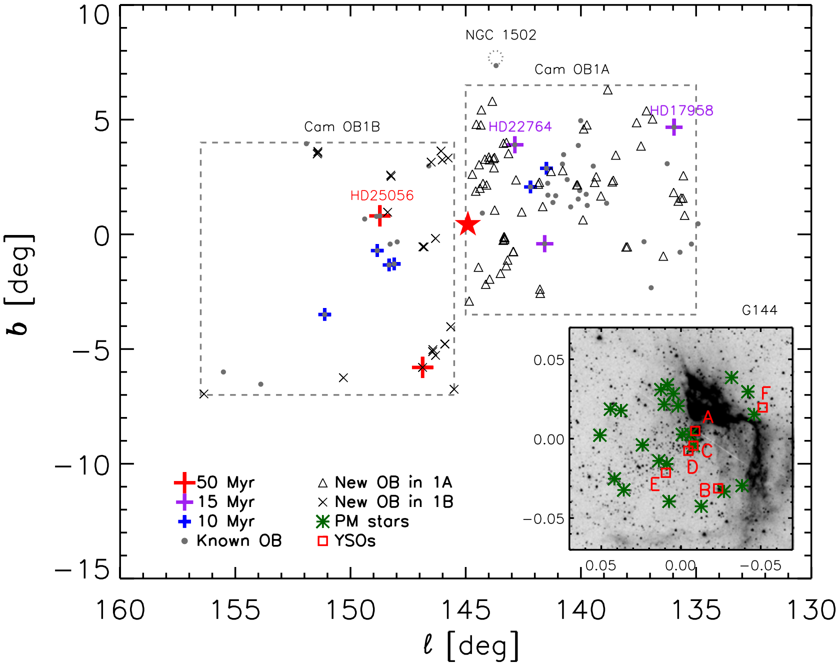

Figure 10. Atlas of the Cam OB1 complex and G144. Gray circles are known OB members. The dashed boxes mark the boundaries of Cam OB1A and 1B members. Black crosses and triangles mark newly found OB stars. The position of G144 is marked with a red star whose expanded view, centered around $\ell \approx 144^{\circ}\!.9$ and $b \approx 0^{\circ}\!.4$, is shown as the inset to the bottom right. Green asterisks are PM candidates and red boxes represent YSO candidates, which are labeled individually. Members following isochrones of ages 50, 15, or 10 Myr are represented with pluses.

(A color version of this figure is available in the online journal.)

its membership, and hence its isochrone age, is less secure. The subgroup 1B is at least up to 10–15 Myr old. It is also possible that, from the distribution of young stars, 1B formed as the consequence of the "collect-and-collapse" mechanism (Elmegreen & Lada 1977; Deharveng et al. 2005; Zavagno et al. 2006) with which massive stars sweep ambient material via photoionization pressure or supernova shocks so dense clumps are collected in a shell and collapse to form the next-generation stars. What we witness in G144 is the result of the most recent star birth in this cloud complex.

4. CONCLUSIONS

We used photometric, spectroscopic, and kinematic data to characterize the open cluster candidate G144 found in our OC search pipeline. The cluster is found to be a part of the Cam OB1 association. A total of 23 member candidates have been identified, some still in the pre-main-sequence stage, which are distributed within an angular diameter of $\sim 7'$ at a distance of 1 kpc, this corresponds to a linear scale of ~ 2 pc across. The cluster is no more than a couple of megayears old.

Moreover, we identified a total of 91 additional OB star candidates in subgroups 1A and 1B on the basis of the PMs of 43 known OB members. Cam OB1 is associated with a molecular cloud complex and is shown to have undergone sustained star formation in subgroups 1A and 1B (and also 1C which is not studied here) for at least the last 10–15 Myr. The open cluster G144 appears to highlight the latest episode of sequential star formation in the region.

We acknowledge financial support from Taiwan's National Science Council via grants NSC101-2628-M-008-002 and NSC101-2628-M-008-001 which made this study possible. We thank the HCT staff for their assistance with acquiring the spectral data reported here during the observing run. This publication makes use of data products from the Two Micron All Sky Survey and the *Wide-field Infrared Survey Explorer*, which is a joint project of the University of Massachusetts and the Infrared Processing and Analysis Center/California Institute of Technology, funded by the National Aeronautics and Space Administration and the National Science Foundation. This work is also based on observations made with the *Spitzer Space Telescope*, which is operated by the Jet Propulsion Laboratory, California Institute of Technology under a contract with NASA. We also acknowledge use of data obtained as part of IPHAS carried out at the Isaac Newton Telescope (INT). The INT is operated on the island of La Palma by the Isaac Newton Group in the Spanish Observatorio del Roque de los Muchachos of the Instituto de Astrofisica de Canarias. All IPHAS data are processed by the Cambridge Astronomical Survey Unit, at the Institute of Astronomy in Cambridge.

REFERENCES

Bessell, M. S., & Brett, J. M. 1988, PASP, 100, 1134
Bica, E., Dutra, C. M., Soares, J., & Barbuy, B. 2003, A&A, 404, 223
Cutri, R. M., Skrutskie, M. F., van Dyk, S., et al. 2003, yCat, 2246, 0
Deharveng, L., Zavagno, A., & Caplan, J. 2005, A&A, 433, 565
de Zeeuw, P. T., Hoogerwerf, R., de Bruijne, J. H. J., Brown, A. G. A., & Blaauw, A. 1999, AJ, 117, 354
Dias, W. S., Alessi, B. S., Moitinho, A., & Lépine, J. R. D. 2002, A&A, 389, 871
Drew, J. E., Greimel, R., Irwin, M. J., et al. 2005, MNRAS, 362, 753
Dutra, C. M., & Bica, E. 2001, A&A, 376, 434
Dutra, C. M., Bica, E., Soares, J., & Burbuy, B. 2003, A&A, 400, 533
Elmegreen, B. G., & Lada, C. J. 1977, ApJ, 214, 725
Froebrich, D., Scholz, A., & Raftery, C. L. 2007, MNRAS, 374, 399
Girardi, L., Bertelli, G., Bressan, A., et al. 2002, A&A, 391, 195
Glushkova, E. V., Koposov, S. E., Zolotukhin, I. Y., et al. 2010, AstL, 36, 75
Haug, U. 1970, A&AS, 1, 35
Humphreys, R. M. 1978, ApJS, 38, 309
Koenig, X. P., Leisawitz, D. T., Benford, D. J., et al. 2012, ApJ, 744, 130
Koposov, S., Belokurov, V., Evans, N. W., et al. 2008, ApJ, 686, 279

Kronberger, M., Teutsch, P., Alessi, B., et al. 2006, A&A, 447, 921
Lin, C. C., Chen, W. P., & Panwar, N. 2012, in AIP Conf. Proc. 1543, First International Conference on Chemical Evolution of Star Forming Region and Origin of Life: Astrochem2012, ed. S. K. Chakrabarti, K. Acharyya, & A. Das (Melville, NY: AIP), 120
Lyder, D. A. 2001, AJ, 122, 2634
Meyer, M. R., Calvet, N., & Hillenbrand, L. A. 1997, AJ, 114, 288
Monet, D. G., Levine, S. E., Canzian, B., et al. 2003, AJ, 125, 984
Morgan, W. W., Whitford, A. E., & Code, A. D. 1953, ApJ, 118, 318
Pandey, A. K., Upadhyay, K., Nakada, Y., & Ogura, K. 2003, A&A, 397, 191
Paunzen, E., Netopil, M., Iliev, I. K., et al. 2005, A&A, 443, 157
Piskunov, A. E., Kharchenko, N. V., Röser, S., Schilbach, E., & Scholz, R.-D. 2006, A&A, 445, 545
Rieke, G. H., & Lebofsky, M. J. 1985, ApJ, 288, 618
Röser, S., Demleitner, M., & Schilbach, E. 2010, AJ, 139, 2440
Schmeja, S. 2011, AN, 332, 172
Siess, L., Dufour, E., & Forestini, M. 2000, A&A, 358, 593
Straižys, V., & Laugalys, V. 2007a, BaltA, 16, 167
Straižys, V., & Laugalys, V. 2007b, BaltA, 16, 327
Straižys, V., & Laugalys, V. 2008, in Handbook of Star Forming Regions, Volume I, The Northern Sky, ed. B. Reipurth (San Francisco, CA: ASP), 294
Tapia, M., Costero, R., Echevarria, J., & Roth, M. 1991, MNRAS, 253, 649
Weitenbeck, A. J. 1997, AJ, 114, 222
Wright, E. L., Eisenhardt, P. R. M., Mainzer, A. K., et al. 2010, AJ, 140, 1868
Zavagno, A., Deharveng, L., Comerón, F., et al. 2006, A&A, 446, 171

フェルミの発見した珍種
—電波で暗いミリ秒パルサー—

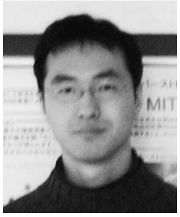

谷津

谷津陽一・河合誠之
〈東京工業大学大学院理工学研究科・基礎物理学専攻　〒152–8551 東京都目黒区大岡山2–12–1〉
e-mail: yatsu@hp.phys.titech.ac.jp; nkawai@phys.titech.ac.jp

片岡　淳・高橋洋輔
〈早稲田大学理工学術院総合研究所・先進理工学研究科　〒169–8555 東京都新宿区大久保3–4–1〉
e-mail: kataoka.jun@waseda.jp; s072803523@akane.waseda.jp

フェルミ衛星が発見した高銀緯の明るいガンマ線源，2FGL J2339.6−0532および2FGL J1311.7−3429が，これまで知られていなかった新しいタイプのパルサー，すなわち「電波で暗い」ガンマ線ミリ秒パルサーであることがわかりました．これまでの研究では，波長帯ごとにパルスの放射源・放射範囲が異なるという描像が確立されてきました．これは特定の波長帯でのみパルス放射が見られるようなパルサーが存在することを予言するものですが，いままで回転周期の短いミリ秒パルサーでは電波とガンマ線が両方見られる天体しか知られていませんでした．今回発見された電波で暗くかつガンマ線で明るいミリ秒パルサーの存在は，若い回転駆動型パルサーで議論されてきた放射モデルが，伴星からの質量降着期を経験してきたリサイクルド・パルサーにも適用できる普遍的な機構であることを示唆しています．今後，さらに同様の天体が見つかり，パルサーからの電磁放射現象の系統的な理解が進むと期待されます．

1. はじめに

2008年に打ち上げられたフェルミ（Fermi）衛星は，極めて高い感度で全天を観測し，これまでに知られていなかった数多くのガンマ線天体を発見しています．打ち上げから現在までに検出されたガンマ線源は1,800個を超え[1]，そのうち約3割はいまだに正体がわかっていません（図1）．その一方で，系内から発見されたガンマ線源のほとんど（検出された全ガンマ線源の10％以上）は，パルサーやパルサー星雲に関連していることもわかってきました[2]．パルサーという天体種族は，1967年にHewishらが発見してからすでに45

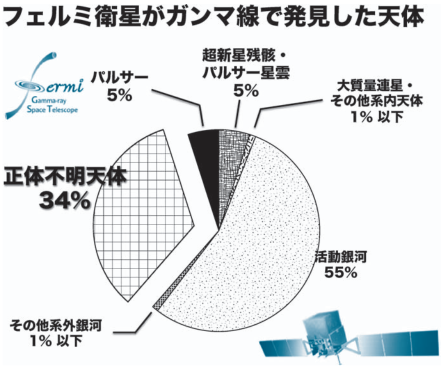

図1　フェルミが発見したガンマ線天体の内訳．発見された全ガンマ線源の1割，同時に系内のガンマ線源のほとんどはパルサーに関連している．

年が経ちました3)．回転する磁化した星という一見シンプルな物理系であるにもかかわらず，最も馴染み深く理解が進んでいると思われていたかに星雲が突然ガンマ線フレアを起こしてみたりと4)，その周辺における物理現象はいまだに謎に包まれています．

本稿では，昨年から今年にかけて立て続けに2例発見された「電波で暗い」ミリ秒パルサーと思われるガンマ線天体について紹介します5)–8)．これまで，なぜかスピン周期が30ミリ秒以下の「ミリ秒パルサー」では，電波で暗い天体が見つかっていませんでした．“当然あるべきなのになぜか見つからなかった”この種のパルサーの発見は，これまで積み上げられてきたパルス放射機構の理解が，本質的に間違っていないことを裏づけるたいへん貴重なサンプルです．また，これら二つの天体は，伴星を自身のパルサー風で蒸発させつつある珍種「ブラック・ウィドウ（Black widow）パルサー」でもあります．次章では，フェルミ衛星の登場によって大きく変化したパルサー観の変遷を簡単にまとめ，次にミリ秒パルサーの生い立ちとブラック・ウィドウについて紹介します．4章ではこれらの天体発見の経緯を解説し，5章ではわれわれの観測結果から得られる新しい示唆，そして今後の展望について議論したいと思います．

2.　フェルミ時代のパルサー観測

パルサーはよく「巨大な発電機」にたとえられます2)．その発見当初から，パルサー周辺の回転磁気圏が誘導電場を作り，その結果，荷電粒子が加速されてガンマ線が放射されるというシナリオができあがっていました．ところが，フェルミ衛星が打ち上げられるまでは，約2,000個ものパルサーが見つかっていたにもかかわらず，ギガ電子ボルト以上の高エネルギーガンマ線を放射するパルサーは，若くて活動的な六つしか知られていませんでした．この状況が，フェルミ衛星の打ち上げによって一変し，数多くのガンマ線パルサーが発見されました．この一連の発見により，パルサーは一躍，銀河系内における最もメジャーなガンマ線源として認知されるようになりました．

表1　これまでに見つかっているパルサーの内訳

周期	電波	ガンマ線	個数
30 ms以上	○	○	36
	×	○	35
	○	×	1658
30 ms以下（ミリ秒パルサー）	○	○	27[a]
	×	○	0
	○	×	189

注―○：パルスが検出されているもの．
×：パルスが未検出のもの（2012年3月の統計）．
[a] このうち5天体はガンマ線放射を伴うもののパルス検出には至っていない．

また，フェルミ衛星に搭載されたLarge Area Telescopeは広い視野と優れた検出感度をもち，ガンマ線の観測データだけを用いてパルスを探査する，いわゆる「ブラインド・サーチ」を可能にしました．この検出感度の飛躍的な向上により，打ち上げから1年でそれまで知られていなかった新しいパルサーを数多く発見しています11), 12)．特に興味深いのは，ガンマ線で見えているのに，電波では見えていないパルサーの存在です．それまで，ふたご座のガンマ線源ゲミンガ（Geminga）がその唯一の例として知られていましたが，フェルミ衛星の観測により，このようにガンマ線だけで光るパルサーがより一般的な存在になりました．表1に示すのは2012年3月までに見つかっているガンマ線パルサーの内訳です．フェルミで見つかっている周期30ミリ秒以上のパルサー（ほとんどは若く活動的な天体）の約半数は電波パルスが見られないのです．

これまで，パルサーからのガンマ線放射を統一的に説明するモデルとして，ポーラーキャップ（polar cap）起源説，スロットギャップ（slot gap）起源説，アウターギャップ（outer gap）起源説などが有力視されてきましたが，フェルミによって

得られたガンマ線のパルスプロファイルやスペクトルの形状により，現在ではアウターギャップが最有力視されています2)．このアウターギャップ起源説の予言するガンマ線放射は大きな立体角に広がっており，さまざまな方向から見ることができます．一方，電波パルスは（実はまだよく理解されてはいないのですが…），これまでの状況証拠から磁極の近くから細いビームで放射されていると推定され，中性子星の磁極がわれわれを向いたときにのみパルスが見えると考えられています．このように，「電波とガンマ線とでパルスの放射領域が異なる」という描像では，電波・ガンマ線のパルス放射の有無を磁極の構造とわれわれから見込む角度の組み合わせで説明できてしまいます*1．

そもそも，電波パルスは放射範囲が狭く実際には放射されていてもわれわれからは見えない確率が高いため，波長ごとに放射源・放射方向が異なる場合にはガンマ線でパルスが見えても電波パルスが同時に受かる必然性はありません．フェルミのブラインド・サーチで見つかったパルサーの統計結果はこの描像でよく説明され，多数のパルサーから電波放射が見られない事実は，むしろ妥当といえます（表1）．その一方で，パルス周期が30ミリ秒より短い「ミリ秒パルサー」では全く状況が異なり，ガンマ線だけでブラインド・サーチをすることが困難であったため，これまでに見つかっているサンプルでは，電波パルスが検出されているものに限られていました（表1）．

3.　ミリ秒パルサーの生い立ち

図2は既に知られているパルサーのパルス周期と周期変化率を示したP–$\dot{P}$ダイアグラムです．一般的な電波パルサー（図の中央付近に分布している一群）と比べて，ミリ秒パルサーの分布は図の左下側に寄っており，回転周期が極めて短く，周期変化率が小さいといった特徴をもっていることがわかります．また，ミリ秒パルサーの多くが連星系（図中にある黒四角）をなしていることが知られています．これらのスピン特性に加え，その多くが伴星を伴うこと，さらに低質量X線連星と同様に球状星団から多く見つかっていることなどから，ミリ秒パルサーは伴星のガスが星表面に降りつもることで少しずつ角運動量を得て，1秒間に数百回転するまでにスピンアップしてきたと考えられています15)．また，ミリ秒パルサーの多くが銀河面から離れた位置で見つかっていることも，これらの種族が極めて古い天体種であり，超新星爆発の反動で蹴り出され長い時間をかけて銀河面から離れつつあることを示唆しています．この様に，すでに年老いて冷えてしまった中性子星が，伴星からの質量降着により数億年の時を経て再度輝き出すことから，これらの天体はリサイクルド・パルサーとも呼ばれています．

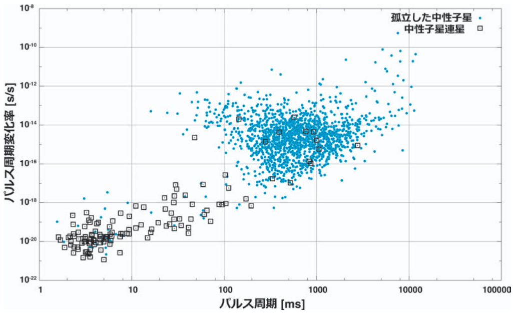

図2　P–$\dot{P}$ダイアグラム（パルス周期・周期変化率はThe ATNF Pulsar Catalogue13), 14) から抜粋）．青丸は伴星の見つかっていない孤立したパルサー，黒四角は連星系をなすパルサーを示す．

さらに時間が経つと，何らかの原因で降着が止まり，自身の回転エネルギーだけで光る回転駆動

---

*1 この描像では，電波で見えないパルサーも実際にはわれわれからは見えない方向に電波パルスを放射していることが示唆されます．また，電波ビームの縁，もしくはサイドローブがわれわれをかすめている可能性もあり，より高精度な電波観測が可能になれば，将来電波パルスが検出される可能性もあります．

型パルサーになります．なかでも，特にエネルギー放出が大きく，伴星との距離が近接している連星系の場合には，パルサーからの磁化したプラズマ（パルサー風）が伴星を加熱・蒸発させ，最終的には単独のミリ秒パルサーだけが残ると考えられています．近年発見されたパルサー（SDSS J102347.6＋003841）は，パルス周期が約1.7ミリ秒のミリ秒パルサー連星ですが，降着円盤がときおり消失するため，今まさに降着が止まろうとしていると考えられています16)．さらに進化の進んだ例としては，1988年に発見されたPSR B1957＋20が有名です．この天体ではすでに質量降着が終わっており，復活したパルサーからのパルサー風が伴星を加熱し，連星の軌道周期に従った可視光の激しい光度変化が観測されています．このように，長年養ってくれた伴星を蒸発させてしまうミリ秒パルサーは，交尾した後にオスを食べてしまうクロゴケグモ（黒後家蜘蛛）の生態になぞらえて，「ブラック・ウィドウ（black widow）」と呼ばれています．

実は，ミリ秒パルサーからガンマ線パルスが出ていることもフェルミ衛星が初めて発見しました17)．図3に示すのはフェルミが観測した比較的若い回転駆動パルサー（PSR J0007＋7303）とミリ秒パルサー（J0030＋0451）のガンマ線パルスプロファイルの比較です．P–$\dot{P}$ダイアグラム上でも明らかに異なるスピン特性をもっているにもかかわらず，ミリ秒パルサーからのガンマ線放射は若いパルサーと同様のダブルピーク構造をもち，スペクトルはべき関数型の高エネルギー側が切れ落ちた形をしているなど，周期を除けば全く同じ特徴をもっていました．このようなパルス波形やスペクトル形状の一致は，若いパルサーとミリ秒パルサーとでガンマ線放射機構が全く同じであることを示唆していると考えられます．

このような統一的パルス放射の描像を完成させる最後のピースとなるのが「電波で暗い」ミリ秒パルサーです．しかしながら，これらの天体をブラインド・サーチで見つけるには広い周波数空間を精査する必要があるため，同じガンマ線放射強度であっても通常の電波パルサーに比べるとその検出は格段に難しくなります．連星系にあることもドップラー効果による周期変動を引き起こすためパルス検出を妨げます．果たして電波で暗いミリ秒パルサーが見つからなかったのはこのような観測上の困難からでしょうか？　はたまた，リサイクルの過程や弱い表面磁場強度のために根本的に異なる電波放射機構をもつようになったのでしょうか？　このような中にあって，高い感度を有するフェルミ衛星こそが，その疑問に答えてくれると期待されていました．

4.　電波で暗いミリ秒パルサーの発見

私たちは，フェルミの発見した正体不明の未同

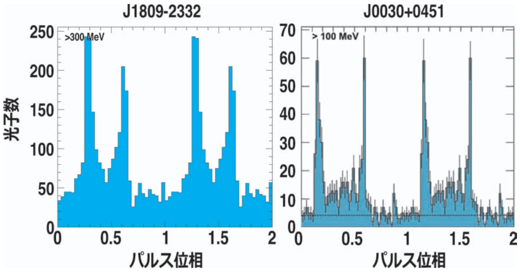

図3　フェルミ衛星の観測した若い回転駆動型パルサー J1809＋2332（P＝146.8 ms）12) と，ミリ秒パルサー J0030＋0451（P＝4.9 ms）17) のガンマ線パルスプロファイル．

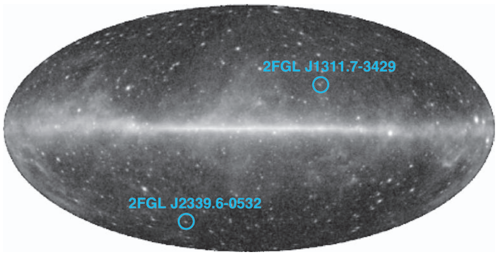

図4　フェルミ衛星が観測したガンマ線による全天画像．新たに見つかった電波で暗いミリ秒パルサーは天の川から遠く離れた天域で見つかった．

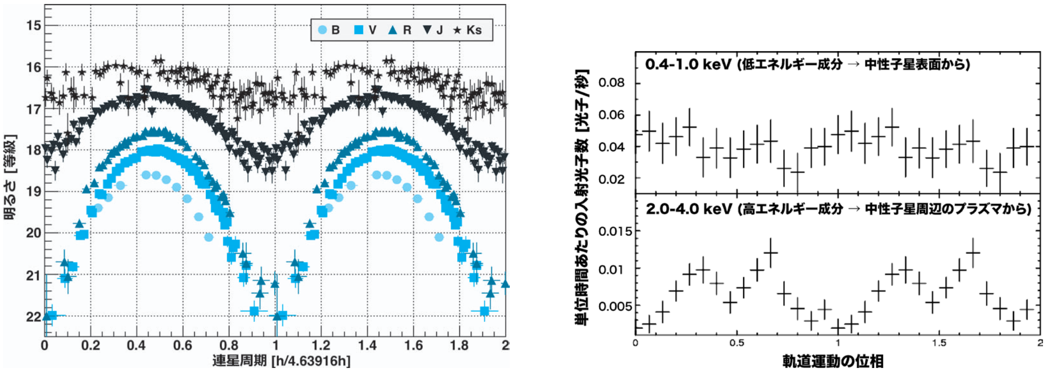

図5　(左)—軌道周期で畳み込んだ可視・近赤外線の光度曲線（光・近赤外線大学間連携による観測）．データ系列はそれぞれ，●: *B*-band, ■: *V*-band, ▲: *R*-band, ▼: *J*-band, ★: *Ks*-bandに対応．（右)—同じく「すざく」で観測したX線光度曲線．低エネルギー成分が強度一定なのに対して，高エネルギー成分はふた山の変動を示す．また，硬X線のダブルピークは可視光の増光に同期している．

定ガンマ線天体を日本のX線天文衛星「すざく」や可視光・近赤外線望遠鏡などを用いて追観測し，いままで知られていない新種の天体や高エネルギー現象の発見を目指しています．図4に示すのはフェルミが観測したガンマ線の全天画像であり，今回発見された二つの「電波で暗い」ミリ秒パルサーの位置は丸で示してあります．当時は特に銀河面から離れた高銀緯の未同定天体にターゲットを絞って観測を行っており，むしろ，パルサーや活動銀河核以外の奇妙な天体や，ダークマター起源のガンマ線が見つからないかと密かに期待していました[9), 10)]．

4.1　一例目：2FGL J2339.6−0532

第一のターゲットである2FGL J2339.6−0532は天の川からかなり離れた位置に見つかったガンマ線源であり，正体のわかっていない天体の中では最も明るいものの一つでした．このガンマ線源は1カ月オーダーの長期的な時間変動を見せていなかったことから，少なくとも活動銀河核（AGN）ではないと予想されていました．そのガンマ線スペクトルは〜5ギガ電子ボルト付近の折れ曲がりをもつ「パルサー的」な特徴を備えていましたが，電波での対応天体は見つかっていませんでした．その後，X線天文衛星チャンドラ（Chandra）によりX線対応天体が発見されたことを受けて，可視光・近赤外線・X線による追観測が行われました．

まずわれわれは，可視光対応天体の測光観測を行い，その明るさが激しく変動していること，さらにその変化が4.6時間の周期性をもっていることを発見しました．この結果は，ガンマ線源が連星系であることを示唆すると考えられます[5), 7)]．図5の(左）は昨年発足した光・近赤外線天文学大学間連携の望遠鏡ネットワークで観測した可視光対応天体の光度曲線です．可視光の*R*から*V*バンド付近で約4等級の最大振幅が見られ，軌道位相の変化に従い伴星表面の温度が3,000 Kから7,000 Kにまで周期的に変化していることを示唆しています．さらに，最大光度における分光エネルギー分布から推定される光源の半径は〜1.1×10^{10} cmであり，伴星がおよそ1/10太陽質量程度の矮星であることを示唆しています．一方，スタンフォード大学のRoger W. Romaniらも極小期の可視光分光を行っており，冷たい側からみた特徴はM型〜K型星であるという描像を得ています[7)]．

また，われわれは「すざく」を用いた100キロ秒の観測を実施しました．図5の(右）は「すざく」が取得したエネルギーごとのX線光度曲線です．1キロ電子ボルト以下の低エネルギー側ではほとんど明るさが変動していないのに対して，2

キロ電子ボルト以上の高エネルギー側では軌道位相に応じたふた山の光度変動が観測されました．これらエネルギーごとの振る舞いの違いは，X線の放射源がエネルギーバンドごとに異なることを示唆していると思われます．さらにこのデータを使ってスペクトル解析を行ったところ，べき関数と黒体輻射の足し合わせで観測結果をよく説明できることがわかりました．特に低エネルギー側で見つかった黒体輻射は，サイズR～1.6 km, 温度T～0.15 keVと小さく高温な放射源を示唆しており，主星が中性子星であることの決定的な証拠となりました18)．

本来であれば3,000 K程度しかないはずの矮星が異様な温度上昇を示していること，そしてX線で光るほど高温でコンパクトな主星の組み合わせは，過去に発見されたブラック・ウィドウパルサー（PSR B1957＋20）と酷似しています．これまでの電波～ガンマ線での観測では有意なパルスは検出されていませんが，伴星の加熱具合から推定されるシステムへのエネルギー供給は10^{34} erg s^{-1}に達すると推定され7)，これを説明する熱源は回転磁気圏の作るパルサー風以外には考えられません．これらを総合した結果，2FGL J2339.6－0532は「電波パルスのない」ミリ秒パルサーであるという結論に至りました．

4.2　二例目：2FGL J1311.7－3429

次にわれわれが注目したのは，2FGL J1311.7－3429という未同定天体です．この天体も高銀緯（銀緯28°）にあり，たいへん明るいガンマ線源として1990年代からすでに存在が知られていました．一方で，他の波長帯での対応が特定できずに，なんと20年もの間，孤高の未同定天体として君臨した難攻不落の天体です（図4）．われわれの当初の認識は“銀河系外の得体のしれない謎天体”という程度でしたが，2FGL J2339.6－0532の発見から，同様なパルサーがまだ潜んでいる可能性が示唆され，さらなるチャレンジへの意欲を与えてくれました．

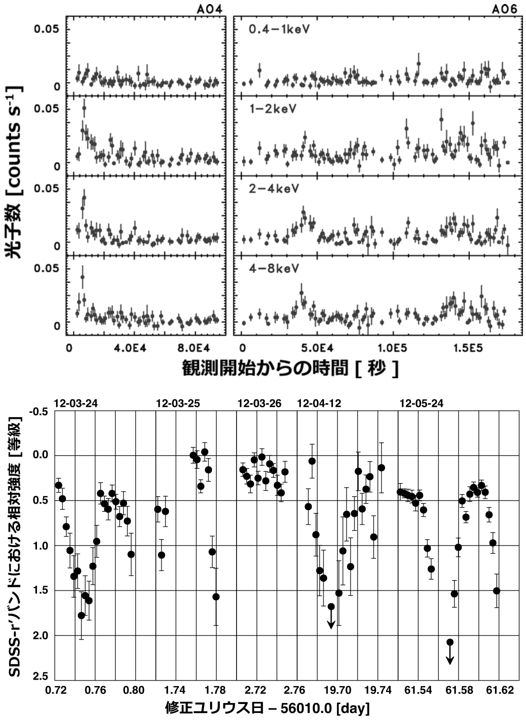

図6　（上）―「すざく」で観測した2FGL J1311.7－3429のX線光度曲線．2009年・2011年の観測ともに不規則なフレアが見られる6)．（下）―Lulin 1 m望遠鏡で観測した可視光光度曲線．

Swift衛星に搭載された紫外線・可視光望遠鏡（UVOT）による可視光対応天体の発見を受けて，われわれは「すざく」によるX線観測を2009年，2011年の2度にわたって実施しました．図6の（上）はエネルギーバンドごとのX線光度曲線です．2FGL J2339.6－0532からのX線放射は軌道周期に合わせた小さな変動しか見せなかったのに対して，こちらの天体は不規則で激しい時間変動を見せています．特徴的なのは，まるでブレーザー*2のような左右対称な形のフレアが散見されることです．各フレアのタイムスケールはおよそ数時間程度で，特に高エネルギー領域で顕著に

---

*2　活動銀河核の一種で，超巨大ブラックホールから放出される相対論的ジェット天体現象．電波からガンマ線にわたる広い波長域で変動する．

見えます．これまでにパルサーからのX線でこのような不規則なフレア現象が見られた例はなく，新天体発見の期待がますます募ります．一方，スペクトルはべき型で，光子指数は$\Gamma=1.3\sim1.7$と活動銀河核としても許容できるものでした．

不規則フレアの存在に惑わされていまいち正体がつかめないまま，次にわれわれは可視光観測を行いました．日本からだとかなり低空になるため，石垣島天文台・台湾Lulin天文台に協力を呼びかけて複数晩にわたって測光観測を行いました．図6の（下）はLulinでの5回の観測で得られたSDSS-r′バンド（中心波長＝6,222 Å）の光度曲線です．各晩の観測はおおよそ1–2時間程度ですが，最初の観測で急激な光度変動が見られました．「またしてもブラック・ウィドウ～」という想像が頭をよぎりますが，2晩目，3晩目の観測では期待したような周期変動が見られません．先に示した2FGL J2339.6−0532の光度曲線は，軌道周期で畳み込むまでもなく綺麗なサインカーブを描いていたのに対して，こちらは日によって変動が見えたり見えなかったり，見えてもピーク光度が変わってしまったりと，かなり不思議な振る舞いを見せています．不運にも，この時期の石垣地方は天候が優れず，最初の晩と同じ形の光度曲線が再度観測されたのは2カ月も後のことでした．

ちょうど同じ頃，Romaniも4 m級の望遠鏡を動員してより詳細な周期解析を行っており，2FGL J1311.7−3429が軌道周期～1.56時間の近接連星系であることを明らかにしました8)．X線のフレア・可視光の不規則な増光を除けばブラック・ウィドウに似ていること，電波の対応天体がないことなどから，この天体は2例目の電波で暗いミリ秒パルサーだと考えるに至りました8),6)．

5. 解釈と今後の展望

若いパルサーやミリ秒パルサーなどの「種族を超えた」パルス放射の描像を検証するという観点から，「電波で暗いミリ秒パルサー」の発見が期待されていました11)．これまでに紹介してきたとおり，フェルミ未同定天体の中から立て続けに二つの候補天体が見つかりました．ガンマ線のパルス放射については目下探査中ですが，伴星が加熱されているという間接的な証拠から，これらの天体がミリ秒パルサーであるという結論に至っています．これは連星系のパルサーが軒並み弱磁場であることや，伴星を蒸発させるほどの強いパルサー風を生成するためには高速で回転している必要があることなどから，もっともらしいと言えます．

さらに，パルサー本体からのガンマ線放射からもこの天体がパルサーらしいという証拠が見えてきています．図7に示したのはこれまでに見つかっているガンマ線源のスペクトル形状と時間変動の比較です．縦軸・横軸は，それぞれ月単位の

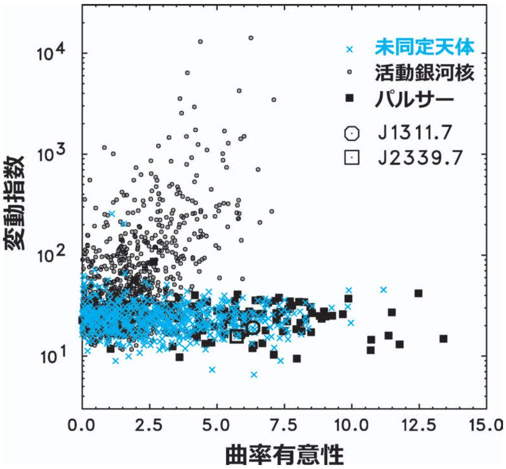

図7 フェルミで見つかったガンマ線源のスペクトル–光度変動の特徴．横軸はスペクトルの折れ曲がりの有意性（Curvature significance19)），縦軸は変動の有意性（Variability index19)）を示す．

ガンマ線光度変動の有意性（Variability index）[19]，スペクトルの折れ曲がりの有意性（Curvature significance）[19] を表しています．この空間上では，活動銀河核とパルサーが見事に異なる分布を見せており，活動銀河核が激しく変動して折れ曲がりのないスペクトルをもつのに対して，パルサーは放射強度が一定で，折れ曲がり（カットオフ）のあるスペクトルをもつらしいことが読み取れます．今回見つかった二つの候補天体も，このプロット上では典型的なパルサーの領域に納まっています．可視光やX線で激しい時間変動を示した2FGL J1311.7−3429も，ガンマ線ではほとんど変動していないことが伺え，フェルミの検出したガンマ線がパルサー起源であることを強く支持しています．今のところ，ガンマ線パルス検出の報告はありませんが，フェルミによる観測は日々続いており，近い将来，ガンマ線データの蓄積と，光学観測による連星軌道情報の改善によってパルスが発見されることが期待されます．

ところで，図7には活動銀河核やパルサーの他に，依然として正体のわかっていない天体も多数プロットしてあります（図中の×マーク）．そもそも，暗い天体の時間変動・スペクトルの形状は正確には決められないため，確度が低くなって図中では左下の領域に集中する傾向にあります．しかし，それらの暗い天体の寄与を差し引いても，ガンマ線パルサーはまだまだたくさん見つかりそうです．電波で暗いミリ秒パルサーは現時点ではたったの2例に過ぎませんが，今後これらの未同定天体の正体を一つ一つ明らかにしていくことで，より系統的な描像が得られると期待できます．

もう一つ，今回の観測で発見された極めて興味深い現象が2FGL J1311.7−3429の示すX線・可視光での不規則で激しいフレア現象です．これまでのところ，回転駆動型のミリ秒パルサーでこのようなフレアが見られた例はほかに知られていません．その特徴は，ライトカーブが左右対称な三角形であるという点で，活動銀河核（特にブレーザー）のものと酷似しています．活動銀河核のジェットでは，中心から断続的に撃ち出されるジェットが速度差をもって進行し，後から出てきた物質が先行する物質に追突することで内部衝撃波が発生すると考えられています．この衝撃波により電子が加速され増光が起こり，やがて冷えて暗くなるのですが，電子加速・放射冷却のタイムスケールに対して光源のサイズが大きく，光が放射源Rを横切るのにかかる時間（light crossing time）のほうが卓越するため，観測者から見ると増光も減光も一様にR/cのタイムスケールで鈍され，左右対称な光度曲線を描くと理解されています．

やや乱暴ですが，この解釈をそのまま今回のケースに適用すると，R/c〜10 ksとなり，光源のサイズは10^{14} cmと見積もることができます．一方で，1.56時間という公転周期からは2FGL J1311−3429連星間距離が〜5×10^{10} cm程度になると推定されるため，光源のほうが4桁も大きいことになってしまいます．これほどの大きさのものが瞬時に増光・減光するというのは考えにくいため，この天体では何か異なる機構が働いているものと考えられます．容易に思いつくところでは，伴星表面で激しいフレアが起こっているとか，パルサー風の放出そのものが数時間スケールでアウトバースト的に供給されているなどの可能性が考えられますが，現時点ではその原因はわかっておりません．また，一例目として紹介した2FGL J2339.7−3429（軌道半径〜10^{10} cm）ではこの不規則なフレアが見られていないというのも興味深い点であり，何がこの違いを生むのか，今後，すばる望遠鏡などの大型観測装置を使った詳細な分光観測を行うことで，長い連星進化の歴史やこれまで直接観測されることのなかったパルサー極近傍における粒子加速現象の解明が期待されます．

参考文献

1）Nolan P. L., et al., 2012, ApJ 199, 31
2）中森健之，河合誠之，金井義和，高橋弘充，2010, 天文月報 103, 324
3）Hewish A., et al., 1968, Nature 217, 709
4）Abdo A. A., et al., 2011, Science 331, 739
5）Kong A. K. H., et al., 2012, ApJ 747, 3
6）Kataoka J., et al., 2012, ApJ 757, 176
7）Romani R., Shaw M. S., 2011, ApJ 743, L26
8）Romani R., 2012, ApJ 743, L26
9）Maeda K., et al., 2011, ApJ 729, 103
10）Takahashi Y., et al., 2012, ApJ 747, 64
11）Halpern J. P., et al., 2009, Science 325, 821
12）Abdo A. A., et al., 2009, Science 325, 840
13）Manchester R. N., et al., 2005, AJ 129, 1993
14）http://www.atnf.csiro.au/people/pulsar/psrcat/
15）Alpar M. A., 1982, Nature 300, 728
16）Wang Z. et al., 2009, ApJ 703, 2017
17）Abdo A. A., et al., 2009, Science 325, 848
18）Kong A. K. H., et al., 2013, in preparation.
19）Ackermann M., et al., 2012 ApJ 753, 83

Radio-Quiet Millisecond Pulsars: Fermi Discovery of New Type Pulsars

Yoichi YATSU[1], Jun KATAOKA[2],
Yosuke TAKAHASHI[3] and Nobuyuki KAWAI[4]

[1, 4] *Department of Physics, Tokyo Institute of Technology, 2–12–1 Ookayama, Meguro-ku, Tokyo 152–8551, Japan*

[2, 3] *Research Institute of Science and Engineering, Waseda University, 3–4–1 Okubo, Shinjuku-ku, Tokyo 169–8555, Japan*

Abstract: Discovery of a new class of pulsars, "radio-quiet" millisecond pulsars, with the Fermi gamma-ray observatory is reported. Currently, a radio pulse and a gamma-ray pulse from a pulsar are believed to have different origins and to be beamed in different directions. Although this picture predicts the existence of pulsars that emit pulse radiation only in a single energy band, i.e., gamma-ray quiet radio pulsars or radio-quiet gamma-ray pulsars, all the known millisecond pulsar shows pulsations both in radio and gamma-ray energy bands. The discovery of the two radio-quiet gamma-ray millisecond pulsars, 2FGL 2339.6−0532 and 2FGL 1311.7−3429, proves that the standard model based on the young energetic pulsars can be applied to the recycled pulsars that have experienced very long accretion phase.

Available online at www.sciencedirect.com

SciVerse ScienceDirect

Advances in Space Research 51 (2013) 2207–2215

ADVANCES IN SPACE RESEARCH
(a COSPAR publication)

www.elsevier.com/locate/asr

Observation campaign dedicated to 1968-081E fragments identification

Masahiko Uetsuhara [a,*], Toshifumi Yanagisawa [b], Daisuke Kinoshita [c], Toshiya Hanada [a], Yukihito Kitazawa [d]

[a] *Kyushu University, 744 Motooka, Nishi-ku, Fukuoka 819-0395, Japan*
[b] *Japan Aerospace Exploration Agency, 7-44-1 Jindaiji Higashi-machi, Chofu, Tokyo 182-8522, Japan*
[c] *National Central University, 300 Jungda Rd, Jungli, Taoyuan 320-54, Taiwan*
[d] *IHI Corporation, 3-1-1 Toyosu, Koto-ku, Tokyo 135-8710, Japan*

Received 11 July 2012; received in revised form 5 February 2013; accepted 8 February 2013
Available online 20 February 2013

Abstract

This paper proposes a comprehensive approach to associate origins of space objects newly discovered during optical surveys in the geostationary region with spacecraft breakup events. A recent study has shown that twelve breakup events would be occurred in the geostationary region. The proposed approach utilizes orbital debris modeling techniques to effectively conduct prediction, detection, and classification of breakup fragments. Two techniques are applied to get probable results for origin identifications. First, we select an observation point where a high detection rate for one breakup event among others can be expected. Second, we associate detected tracklets, which denotes the signals associated with a physical object, with the prediction results according to their angular velocities. The second technique investigates which breakup event a tracklet would belong to, and its probability by using the *k*-nearest neighbor (*k*-NN) algorithm.

In this paper we conduct optical observations of breakup fragments to verify the proposed approach. We selected a well-known breakup event of the rocket body US Titan 3C Transtage (1968-081E) as the primary observation target, and then we conduct optical observations by campaign between two sensors in Taiwan and one sensor in Japan. While three nights observations, we detect 96 tracklets that are uncorrelated with the Space Surveillance Network catalogue at the observation epochs, and finally 50 tracklets among them are associated with the breakup event of 1968-081E.

Keywords: Orbital debris; Spacecraft breakup; Optical observation; Tracklet; Origin identification

1. Introduction

This research aims to define the current orbital debris (OD) environment and to conduct reliable risk assessments for future space explorations. This paper proposes an approach to associate origins of tracklets with spacecraft breakup events occurred in the geostationary region. The tracklet denotes a spatial-temporal series of signals associated with a space object. In typical OD observations of the geostationary region, one usually detects tracklets from optical images taken during observations. By analyzing a detected tracklet in the optical images, one can acquire parameters of a space object at each of the observation epochs such as position in the celestial sphere, angular velocity, and brightness. Origin identification of tracklets is another essential matter in the observations. When maintaining an orbital catalogue of space objects, one usually classifies origins of detected tracklets into the catalogued objects and the uncatalogued objects by associating the propagated states of a cataloged object with the measured states of a tracklet at the observation epoch. Once having found an origin of a tracklet, one can apply the results to such matters as orbit determination of the space object,

---

* Corresponding author. Address: Department of Aeronautics and Astronautics, Kyushu University, 744 Motooka, Nishi-ku, Fukuoka 819-0395, Japan. Tel.: +81 928023048.
E-mail address: ue2hara@aero.kyushu-u.ac.jp (M. Uetsuhara).

0273-1177/$36.00 © 2013 COSPAR. Published by Elsevier Ltd. All rights reserved.
http://dx.doi.org/10.1016/j.asr.2013.02.008

population analyses in surveyed regions, and OD environmental modeling. To contribute to the OD environmental modeling, however, the aforementioned classification is insufficient. If the uncatalogued objects are unlikely to associate with newly launched objects, operational debris, or intentionally uncatalogued objects, one should associate their origins with events that generated OD. When we think of the optical observations in the geostationary region, the majority of the observable OD, whose size is on the order of ten centimeters or larger, will be associated with spacecraft breakup events.

Here we review how many breakup events might have been occurred in the geostationary region. First of all, there are two confirmed breakup events in the geostationary region (e.g., summarized in (Johnson, 2001a)): the first one is a breakup of the Russian communication satellite Ekran 2 (the International Designator of 1977-092A) exploded on 23 June 1978, and the second one is a breakup of the US upper-stage rocket Titan 3C Transtage (the International Designator of 1968-081E) exploded on 21 February 1992. Along with the confirmed breakup events, there might have been a number of unconfirmed breakup events. Large number of uncatalogued space objects was detected during the optical survey of the geostationary region, as reported in Schildknecht et al. (2000). This result became the first definitive evidence that one has to consider the presence of unconfirmed breakup events in the geostationary region. Analyzing the optical survey results by iterative estimates, Krag (2002a,b) reported that fourteen breakup events in total might have been occurred in the geostationary region. Oswald (2008) further conducted the iterative estimates with more observation data and revised down the total event number from fourteen to twelve.

In the second section, we introduce the details of the proposed approach. In the third and fourth sections, we verify the proposed approach through demonstration of actual observations and evaluation of the observation results. In the verification sections, we utilize the breakup event list investigated by Oswald (2008) as will be mentioned in the third section (See Table 1).

2. The proposed approach

Fig. 1 schematically illustrates the framework of the proposed approach. The framework consists of the OD modeling, the predictions, the observation, the detection, and the two-step origin identifications. The main component of the framework is the two-step origin identification, so that we mention it first, and then the other components.

The first step of the origin identification adopts a common method: we propagate the orbits of catalogued space objects to the observation epochs of detected tracklets first, and then we associate each of the propagated space objects with a detected tracklet in terms of the angular position and angular velocity in the celestial sphere. If a space object matches a tracklet within defined thresholds, we can regard the tracklet as the space object. The threshold for the angular position should be the scale of the field-of-view (FOV) or smaller, whereas the threshold for the angular velocity should be in the order of arc-minute or smaller. By this step, we can classify the detected tracklets into the catalogued and the uncatalogued space objects. This method is only valid for space objects involving short-term orbit propagation (i.e., not months nor not years). The short-term propagation is capable of predicting appropriate angular positions, but the long-term propagation is not. Usually most of orbits of catalogued space objects are refreshed at days or weeks so that their angular positions at observation epochs will be predicted appropriately. Breakup fragments, however, require long-term propagation from their breakup epochs to an observation epoch so that their predicted angular positions at observation epochs become random anymore and therefore another origin identification step is required.

The second step of the origin identification applies an observable characteristic of breakup fragments: a group of fragments associated with a breakup event would have single and distinct distribution in the angular velocity plane when we observe them in an inertial point overnight, as verified in (Uetsuhara et al., 2012). This feature, thus, can associate tracklets with breakup events. To quantitatively associate the observations and the predictions, we adopt

Table 1
Breakup events in the geostationary region (Oswald, 2008).

ID	Name	Event epoch (yyddd.dddd)
1966-053J	TITAN 3C TRANSTAGE R/B	87276.6882
1967-066G	TITAN 3C TRANSTAGE R/B	94045.4161
1968-081E	TITAN 3C TRANSTAGE R/B	92053.3745
1973-040B	TITAN 3C TRANSTAGE R/B	81067.2007
1975-117A	SATCOM 1	99257.6799
1975-118C	TITAN 3C TRANSTAGE R/B	87072.6430
1977-092A	EKRAN 2	78174.0000
1979-053C	TITAN 3C TRANSTAGE R/B	82309.0000
1979-087A	EKRAN 4	82157.7550
1988-018B	TELECOM 1C	02263.0000
(AE-02)	–	98180.0000
(AE-03)	–	92280.0000

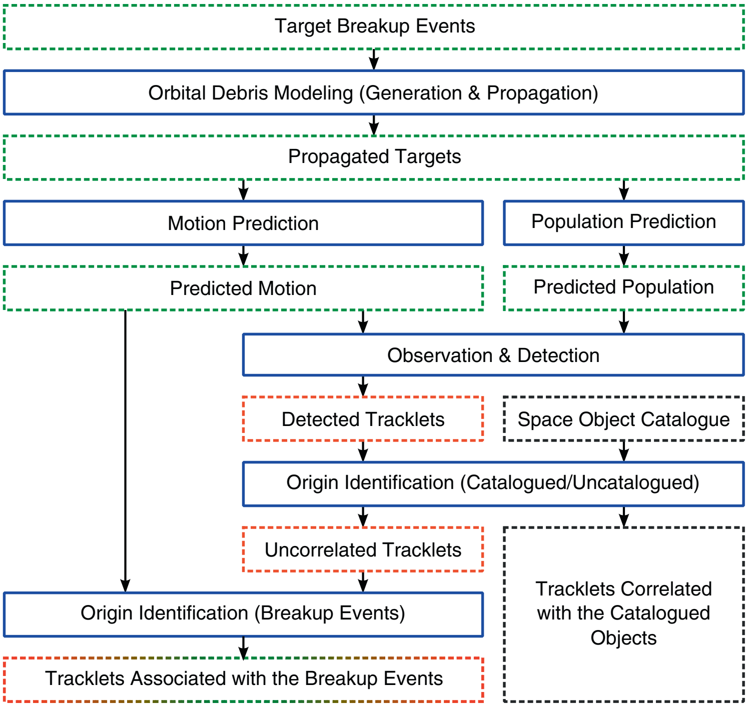

Fig. 1. The framework of the proposed approach.

the classification method widely used in pattern recognition researches: the *k*-nearest neighbor (*k*-NN) algorithm (e.g., Bishop, 2006). Fig. 2 illustrates the concept of the *k*-NN algorithm. The origin of an observation is determined by the majority voting by the *k*-predictions near to the observation in an observable space. The *k*-NN algorithm is superior to classification algorithms using histogram, because accuracy of the classification by the *k*-NN algorithm does not depend on the grid scale or origin. We have to be careful about selecting the number of the neighbors (*k*) to reduce error judgments. The advantage of this origin identification method is that we require orbital propagation for the objects generated by the OD modeling only so that we do not require orbit determination nor orbit propagation for detected tracklets. This approach makes us reduce uncertainty that may come from detected tracklets.

As shown in Fig. 1, we predict the states of breakup fragments at the observations epochs such as the distribution in the celestial sphere, hereinafter simply called population, and the angular velocity during one observation, hereinafter simply called motion. The population prediction and motion prediction require the orbital elements of the breakup fragments at the observation epoch, as will be evaluated by the OD modeling. We select an observation point where the detection rate for tracklets associated with a breakup event, which is defined as the primary target, will be high, so that we can determine the probable origins for the primary target. We also consider the predicted motion to optimize an exposure time for the primary target.

3. Observation planning

In this section, we demonstrate the proposed approach from the beginning to the population prediction and motion prediction. Final outcomes in this section include

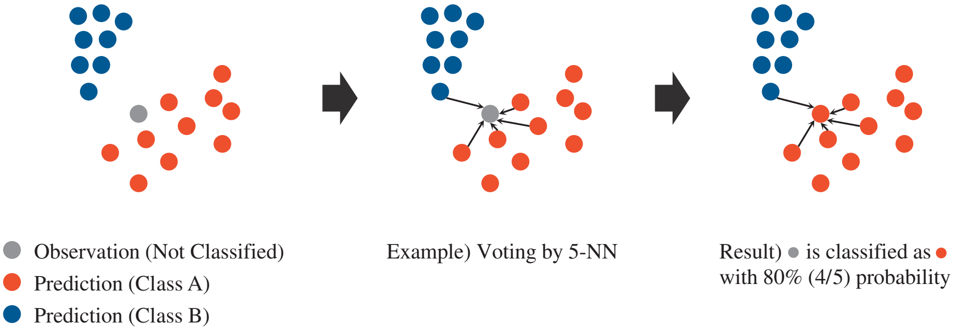

Fig. 2. Concept of the *k*-NN algorithm.

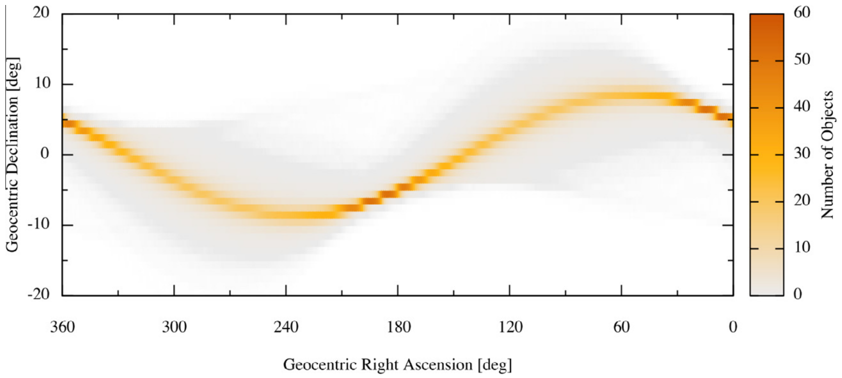

Fig. 3. Predicted population of 1968-081E fragments in time-integrated distribution during six hours. Bin size is 1° by 1°.

a single observation point where the high detection rate for a selected target will be expected, and an optimum exposure time for the selected target.

3.1. Target breakup events

To verify the proposed approach, we are going to observe breakup fragments by utilizing the breakup event list investigated by Oswald (2008), as summarized in Table 1. The list includes the breakup events of six Titan 3C Transtages, four satellites, and two artificial events (AE-02 and AE-03) that could not be associated with real space objects. In the list, each of the breakup events also include such as a probable parent object and its event epoch. The orbital elements at the event epochs are detailed in the reference (Oswald, 2008).

We select a primary target from the twelve breakup events to make the detection rate of the primary target become the majority among the other events. The most adequate target is the confirmed event of the Titan 3C Transtage (1968-081E) because large number of fragments has been spotted at near the breakup epoch, as reported in Pensa et al. (1996). The Maui GEODSS system accidentally observed 23 objects clustered within 0.5° of the nominal location of 1968-081E on 21 February 1992. They conducted intensive follow-up observations and analyses, and concluded that the clustered objects must be fragments of 1968-081E and the breakup epoch estimated was 09:31:12 UTC on 21 February 1992. A breakup cause of 1968-081E is inferred as tank explosion triggered by ignition on remnant fuel. The US Space Surveillance Network (SSN) now tracks 22 fragments associated with 1968-081E that are catalogued as of July 2012. It should be noted that, only eight fragments were catalogued when the observations for this research were conducted.

3.2. Observation conditions

We conduct an observation campaign for the breakup fragments from 20 October 2011 to 22 October 2011. To detect breakup fragments, whose individual presences, individual orbits, and temporal positions are not confirmed yet, one should observe a specific coordinate for long period. Change of weather condition and any operational troubles will suffer detectability at observation sites. Thus, the reason to take a campaign style observation is to gain a good detectability, i.e. to detect a sufficient number of

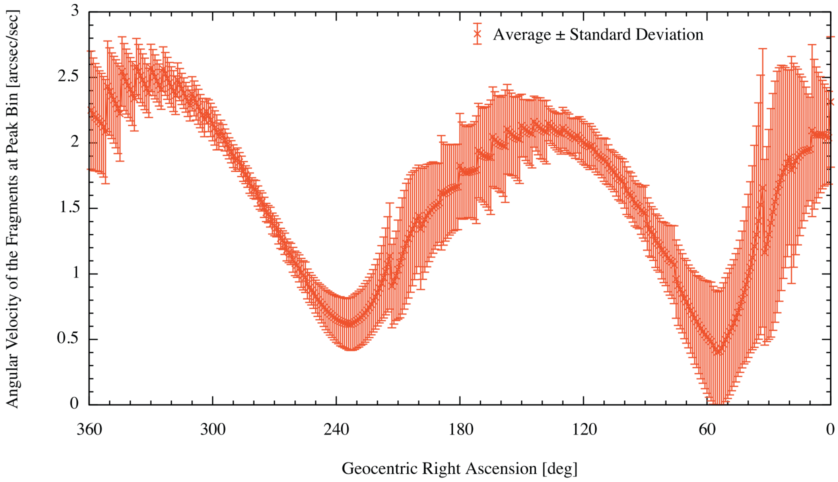

Fig. 4. Angular velocity of 1968-081E fragments at peak bins specified in Fig. 3. The observer is at the Lulin observatory in this case.

tracklets associated with 1968-081E to characterize the breakup event of 1968-081E.

Observation campaign is conducted between two sites: one is the National Central University (NCU) Lulin Observatory in Taiwan, located at 120°52′25″E, 23°28′07″N, and 2862-m altitude, and the other is the Japan Aerospace Exploration Agency (JAXA) Nyukasa Observatory in Japan, located at 138°10′18″E, 35°54′05″N, and 1870-m altitude. Two sensors at the NCU Lulin Observatory were used for the observation campaign, so that this paper distinguishes between them. One, called TAOS, consists of 50-cm aperture telescope and 2 k by 2 k cooled CCD, with a FOV of 1.74° by 1.78°. The other, called LOT, consists of 1-m aperture telescope and 4 k by 2 k cooled CCD, with a FOV of 26.4′ by 13.2′. On the other hand, this paper calls one sensor at the JAXA Nyukasa Observatory by JNO. JNO consists of 35-cm aperture telescope and 2 k by 2 k cooled CCD, with a FOV of 1.27° by 1.27°. TAOS and JNO will have a priority in survey observations because of their large format CCD, and LOT will be suited for follow-up observations by its fine sensor resolution. It should be noted that the following contents are focused on the results acquired from TAOS, because TAOS acquires a sufficient number of images that contribute to the verifications whereas JNO is affected by bad weather conditions and LOT is troubled by minor issues of sensor instruments.

3.3. Predictions and observation point selection

We adopt the NASA standard breakup model 2001 revision (Johnson et al., 2001b) to OD generation. In the OD generation, we have to configure the scaling factor that governs the number of fragments to be generated by a breakup event in the NASA model. The scaling factors for all the twelve breakup events are coordinated to 1.0 for initial guess. For the scaling factor of 1.0, the NASA model generates 238 fragments larger than 10 cm. Inclusion of variation of the area-to-mass ratio (*A*/*m*) may have a significant impact on results of long-term propagation and thus may significantly change predicted population and predicted motion of the targeted fragments. We surely adopt the *A*/*m* probability density functions in the NASA model to assign an *A*/*m* to each of the breakup fragments in this research. The orbital propagator adopts the general perturbation techniques including the J_2 effect, the lunisolar gravitational attraction effect, and the solar radiation pressure effect. One hundred Monte-Carlo runs are applied to the OD generation and propagation processes to represent mean and standard deviation of prediction results.

Table 2
Comparisons of predicted population and angular velocity of 1968-081E fragments at TAOS during six hours observation.

Sensor name	Predicted population [#]		Angular velocity [″/s]	
	Point A	Point B	Point A	Point B
TAOS	56.47 ± 1.09	39.95 ± 1.80	2.01 ± 0.55	0.87 ± 0.61

First, this paper overviews the predicted population of 1968-081E fragments. Fig. 3 represents the predicted population of 1968-081E fragments in terms of the time-integrated distribution during a given observation time. For initial guess, Fig. 3 assumes the observation time as the operational time of the sensor, which is six hours per night. In this case, the time-integrated distribution represents the number of fragments that will pass through a bin (1° by 1° for this case) at each night. If the observation time is defined as the sum of exposure time of a sensor at a night, then the time-integrated distribution represents the detection rate of the fragments at the bin. As described in the previous section, the predicted population of 1968–081E fragments clearly distinguishes a dense region from others at each geocentric right ascension column. Considering the Earth shadow and the visible and invisible region during the observation period, one should select the observation point from the dense regions in the right side of Fig. 3. Up to 51.6 fragments will pass through the densest bin at $(\alpha, \delta) = (6°, 5°)$ during six hours.

Fig. 4 represents the angular velocity of 1968-081E fragments at a peak bin in each geocentric right ascension

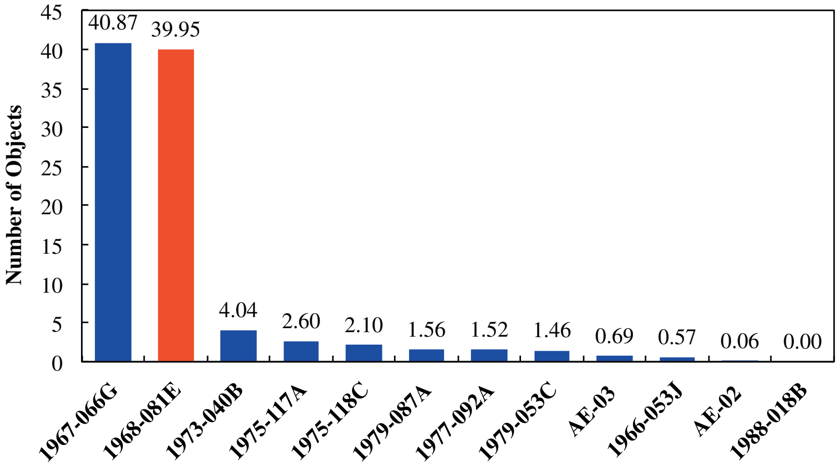

Fig. 5. Comparison of the detection rates between the twelve breakup events during six hours observation at the point B.

column that is specified in Fig. 3. As mentioned in the previous section, an observer measures a space object with non-sidereal mode (i.e. fixed in azimuth and elevation), so that TAOS becomes the observer to measure the angular velocity predicted in Fig. 4. The mean angular velocity has a maximum difference of approximately 2.0″/s. If one wants to keep the motion of center-of-light of the fragments within one pixel (e.g. 1 pixel = 3″ by 3″) per each shot, the maximum difference of the angular velocity will alternate the exposure time by 1.5 s. Such a difference in an exposure time results in a serious one in the total exposure time of a night.

Second, we determine the observation point by evaluating the predicted population and motion. Table 2 summarizes the predicted population scaled for the sensor size of TAOS, and the angular velocity in terms of average ± standard deviation. Two points (A and B) are compared as candidates. The point A is the bin of (6°, 5°) where the predicted population is the highest among whole bins, whereas the point B is the bin of (43°, 8°) where the traveling speed is almost half the point A but the predicted population is also half. For this observation campaign, we select the point B as the observation point because the detectability for individual fragments largely depends on the signal-to-noise ratio affected by the exposure time. The detectability resulting from the population is the second priority at this observation campaign. To maximize an exposure time with assumptions of keeping the motion of the fragment within one pixel or within the seeing size, we determine the exposure time as 5.9 s at the point B, whereas this values would decrease to 3.0 s at the point A.

As previously mentioned, we plan to get a high detection rate for 1968-081E fragments among the targeted twelve breakup events. Fig. 5 compares the detection rates of fragments from each of the targeted breakup events. In this evaluation, we assume the detection rate during six hours for TAOS. The result shows that the detection rates of 1968-081E fragments and 1967-066G fragments become the majority in the selected observation point. The detection rate of 1968-081E fragments spares 42% of the sum. Thus, even if we do not demonstrate the origin identification using the *k*-NN algorithm, we can say from the Bayesian estimation viewpoint that all of the tracklets uncorrelated with the catalogued space objects will be associated with 1968-081E fragments with 42% probability.

4. Origin identification

As a result of the observation campaign, TAOS acquires 189 sets of valid image sequences during three nights. In this section, we finally verify the proposed approach by conducting the origin identification of uncorrelated tracklets. We summarize tracklet detections at TAOS and their origin identifications using the SSN catalogue first,

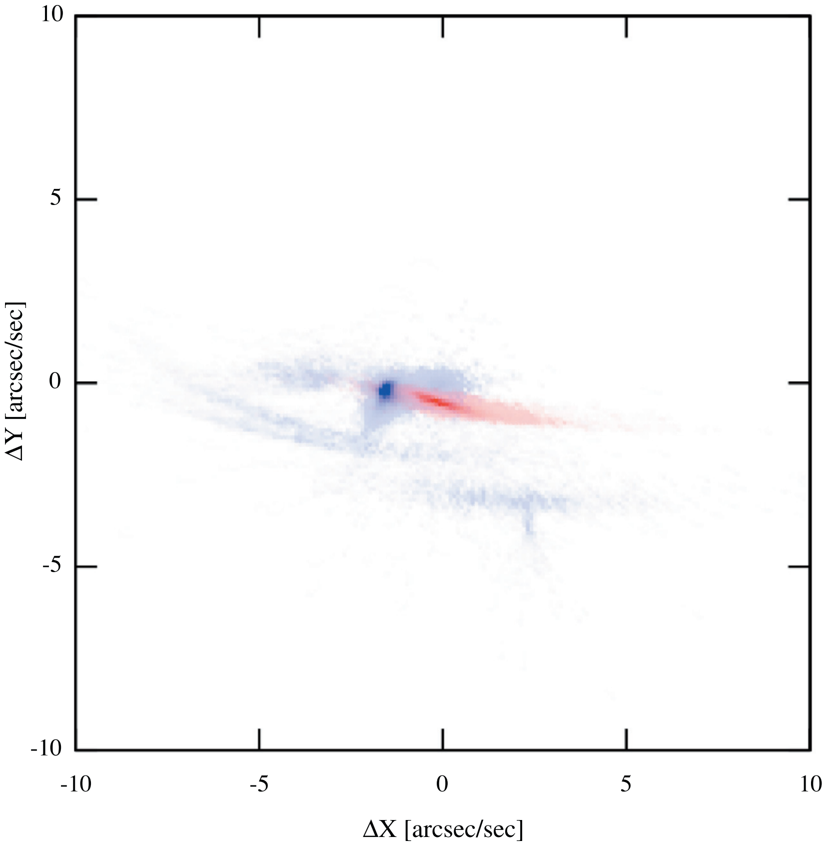

Fig. 6. Predicted motions of 1968-081E fragments in red gradation and the other fragments in blue gradation. (For interpretation of the references to color in this figure legend, the reader is referred to the web version of this article.)

and then devote to the demonstration of the origin identifications using the OD modeling results and the *k*-NN algorithm.

4.1. Tracklet detection and the SSN catalogue correlation

In this research we conduct tracklet detections from the 189 sets of images acquired at TAOS by applying the FPGA-based stacking method (Yanagisawa and Kurosaki, 2011). The FPGA-based stacking method is based on a so-called track-before-detect (TBD) algorithm, which assumes the motion vector of tracklets on a sensor frame first, and then stacks image sequences shifted along with the motion vector. The TBD algorithm can detect fainter signals by one or two apparent magnitude than conventional detection algorithms, which detect signals in an image first and then track the detected signals in image sequences to identify tracklets. TBD generally requires, though, very high computational performance because it has to try a lot of motion vectors to stack image sequences to detect tracklets. The FPGA-based stacking method resolves the problem by implementing the algorithms onto the field programmable gate array (FPGA). Thirty minutes are taken to process a set of image sequences with trials of 262,144 motion vectors (i.e. the motion vectors whose components are within the range of ±256 pixels per a image sequence).

In total, 147 tracklets are detected from the TAOS images by the FPGA-based stacking method. By applying the first step of the origin identification to the 147 tracklets, 51 tracklets are correlated with space objects in the SSN catalogue whose release date is near to the observation period, whereas the others (i.e., 96 tracklets) are judged as uncataloged ones. The faintest object detected is down to 19.0 apparent magnitude, which corresponds to approximately 16 cm in diameter assuming a Lambert sphere object whose albedo is 0.1.

4.2. Origin identification by the k-NN algorithm

This section addresses the origin identification of the 96 tracklets that are uncorrelated with the space objects in the SSN catalogue. To begin with this step, we evaluate the predicted motion of the fragments of the twelve breakup events. In Fig. 6, the predicted motion of 1968-081E fragments is visualized as red, and the others as blue. Transparent gradient is applied to both colors to distinguish the frequency of the presence of fragments in the motion plane grid. The gradient scale is same for both colors. This

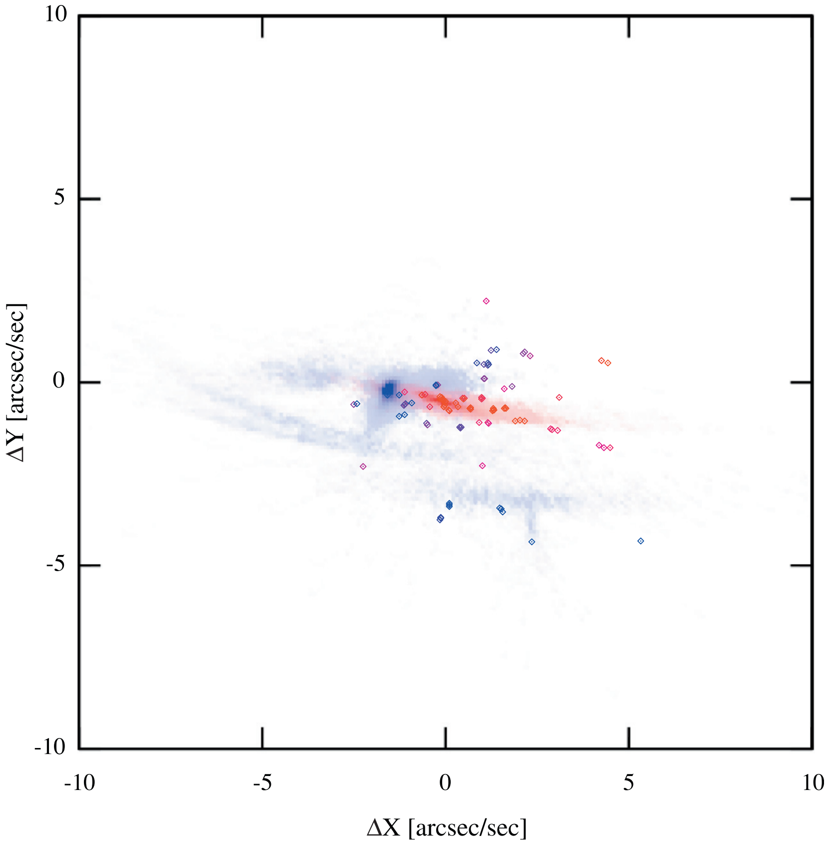

Fig. 7. Comparison between predicted motions of 1968-081E fragments and measured motions of the 96 tracklets uncorrelated with the SSN catalogue. The origin identification results for the tracklets are visualized by the gradation from blue to red. A red tracklet represents its probable origin is 1968-081E, and a blue tracklet represents its probable origin is one of the other breakup sources. (For interpretation of the references to color in this figure legend, the reader is referred to the web version of this article.)

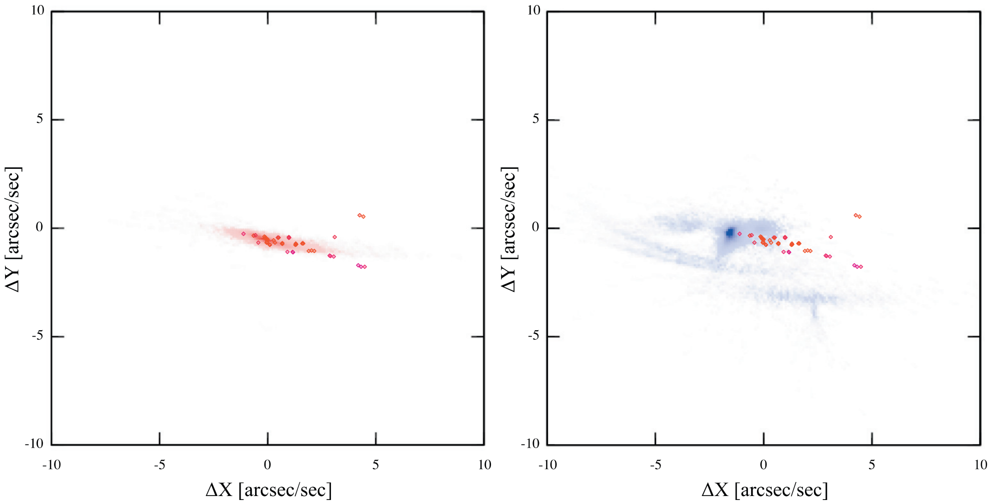

Fig. 8. Comparison between measured motions of the 50 tracklets associated with 1968-081E and predicted motions of 1968-081E fragments (in left) and the other fragments (in right).

two-dimensional distribution will give more probable decision viewpoint to the origin identification than the information in Fig. 5. It should be noted that, 1968-081E fragments near the dense red region are overlapped by the other breakup fragments. For example, 1967-066G fragments are appeared in the densest blue region. They may give some votes to a tracklet to be plotted in and near the overlapped region.

To apply the k-NN algorithm to the origin identification, we have to determine the adequate k for the observation point of TAOS because too small k or too large k will result in increasing misclassification for origins of tracklets. As a preliminary analysis we conduct the cross validation using the predicted motions of the entire breakup fragments. In the cross validation, we regard one of the predictions as a pseudo tracklet (i.e., an observation) and perform the k-NN algorithm for each of the pseudo tracklets. As a result of the cross validation, we find that 10-NN is adequate: the misclassification rate well converges with the minimum degree (the order of 8%) from $k = 10$. To prevent a misleading, it should be noted that $k = 10$ does not denote ten nearest “grids” in Fig. 6, but denotes ten nearest “tracklets” in the raw data of Fig. 6.

Fig. 7 visualizes the result of the origin identification of the 96 tracklets in comparison with the predicted motion. In the figure, a detected tracklet is represented as a point colored by the gradient from blue to red. The color gradient is linear to the ratio (P) of 1968-081E fragments in the 10-NN. For example, a tracklet of $P = 100\%$ is colored red, a tracklet of $P = 50\%$ is colored violet, and a tracklet of $P = 0\%$ is colored blue. The 10-NN clearly distinguishes the probable origins of tracklets between 1968-081E and the others. Following the classification concept using the k-NN algorithm, we classify the origin of a detected tracklet from the viewpoint that which breakup event among the twelve becomes the majority of the 10-NN for the detected tracklet. As a result, 50 tracklets are classified as 1968-081E fragments. Fig. 8 shows the distribution of the 50 tracklets in comparison with the predicted motion of 1968-081E fragments (in left) and the predicted motion of the other fragments (in right). The 50 tracklets are distributed in and around the predicted motion of 1968-081E fragments, and apart from the predicted motion of the other breakup fragments. Among the 50 tracklets, 29 tracklets have $P = 100\%$, 10 tracklets have $P = 80\%$, and 11 tracklets have $P = 60\%$. Some of the tracklets having lower P are distributed near the dense blue region, and the other lower P tracklets are distributed apart from the dense red region. Two tracklets plotted at $(\Delta X, \Delta Y) = (4.26, 0.60)$ and (4.43, 0.54) are unlikely to be associated with 1968-081E, but are voted by 1968-081E fragments because there are no other predicted fragments between the two tracklets and 1968-081E fragments. This case is a typical example of the misclassification by k-NN. One may need to revise hypotheses used in the predictions such as breakup conditions to reduce unlikely classification. It may be noted that there are 11 more tracklets voted by 1968-081E fragments but their votes are too small to take into consideration major revisions of the hypotheses.

5. Conclusions

This paper proposed a comprehensive approach to associate tracklets with the spacecraft breakup events in the geostationary region. We verified the proposed approach by conducting the predictive analyses, the actual observations, the tracklet detections, and the origin identifications. In this verification study, we adopted the breakup event list investigated by Oswald (2008) that can be regarded as the most probable sources at this time for the historical breakup events in the geostationary region. We selected the breakup event of 1968-081E from the event list as the primary target to effectively verify the proposed approach. The observation campaign for the primary target was conducted at the NCU Lulin Observatory and the JAXA Nyukasa Observatory. From three-nights survey observations, a significant number of tracklets was detected by the FPGA-based stacking method, and the two-step origin identification method finally associated 50 tracklets with the primary target 1968-081E.

The proposed approach was verified to be capable of investigating the probable origins of detected tracklets. It should be noted that the proposed approach may not be able to deterministically identify the origins of tracklets, but can evaluate a probability of relation between a breakup event and origin of a tracklet. Thus, applications of the proposed approach may include the probabilistic estimation of breakup event characteristics, and the development of an iterative search strategy that can improve the confidences of hypotheses on breakup events, resulting predictions, and origin identification.

Acknowledgements

The authors wish to acknowledge Mr. Hirohisa Kurosaki, Mr. Yoshitaka Nakaniwa, Mr. Osamu Hikawa, Mr. Takenori Ohtsuka, Mr. Taku Izumiyama, Mr. Andrew Wang, Mr. Dunkan Chen, Mr. Jason Wu, Dr. Shin-ichiro Okumura, Dr. Tsuyoshi Sakamoto, and the Japan Space Guard Association for their dedicated assistances to the observation campaign. The authors also wish to acknowledge Dr. Hitoshi Yamaoka, Dr. Tomoko Fujiwara, Dr. Tetsuharu Fuse, Mrs. Kozue Hashimoto, and Mr. Aritsune Kawabe for their contributions to the research.

A part of this research is supported by Grant-in-Aid for JSPS Fellows Grant Number 243000. IHI Corporation wishes to acknowledge US Air Force Office of Scientific Research (AFOSR) Asian Office of Aerospace Research and Development (AOARD) to support a part of this research under the grant No. FA2386-10-1-4136 (AOARD 104136).

References

Bishop, C.M. Pattern Recognition and Machine Learning. Springer, New York, pp. 122–127, 2006.

Johnson, N.L. Evidence for historical satellite fragmentations in and near the geosynchronous regime, in: Proceedings of the Third European Conference on Space Debris, Darmstadt, Germany, March 19–21, 2001 (ESA SP-473, October 2001). ESA Publications Divisions, ESTEC, Noordwijk, The Netherlands, pp. 355–359, 2001a.

Johnson, N.L., Krisko, P.H., Liou, J.-C., et al. NASA's new breakup model of evolve 4.0. Adv. Space Res. 28 (9), 1377–1384, 2001b.

Krag, H. Status of MASTER-2001 development, in: Minutes of the 20th Inter-Agency Space Debris Coordination Committee Meeting, Guildford, UK, April 8–12, 2002a.

Krag, H. PROOF-2001, in: Minutes of the 20th Inter-Agency Space Debris Coordination Committee Meeting, Guildford, UK, April 8–12, 2002b.

Oswald, M. New Contributions to Space Debris Environment Modeling. Shaker Verlag GmbH, Germany, 2008.

Pensa, A., Powell, G., Rork, E., et al. Debris in geosynchronous orbits. Space Forum 1 (1–4), 23–37, 1996.

Schildknecht, T., Hugentobler, U., Ploner, M. First GEO survey test observations with the ESA 1 m telescope in Tenerife, in: Proceedings of the 2000 Space Control Conference, pp. 73–79, 2000.

Uetsuhara, M., Hanada, T., Yamaoka, H., et al. Strategy to search fragments from breakups in GEO. Adv. Space Res. 49 (7), 1151–1159, 2012.

Yanagisawa, T., Kurosaki, H. Detection of faint GEO objects using JAXA's fast analysis methods, in: Paper 2011-r-02 presented at the 28th International Symposium on Space Technology and Science, Ginowan, Okinawa, June 5–12, 2011.

Icarus 224 (2013) 24–31

Contents lists available at SciVerse ScienceDirect

Icarus

journal homepage: www.elsevier.com/locate/icarus

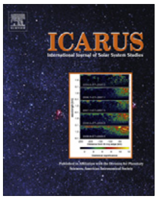

Rotational characterization of Hayabusa II target Asteroid (162173) 1999 JU3

Nicholas A. Moskovitz[a,b,*], Shinsuke Abe[c], Kang-Shian Pan[c], David J. Osip[d], Dimitra Pefkou[a], Mario D. Melita[e], Mauro Elias[e], Kohei Kitazato[f], Schelte J. Bus[g], Francesca E. DeMeo[a], Richard P. Binzel[a], Paul A. Abell[h]

[a] *Massachusetts Institute of Technology, Department of Earth, Atmospheric and Planetary Sciences, 77 Massachusetts Avenue, Cambridge, MA 02139, USA*
[b] *Carnegie Institution of Washington, Department of Terrestrial Magnetism, 5241 Broad Branch Road, Washington, DC 20008, USA*
[c] *National Central University, Institute of Astronomy, 300 Jhongda Road, Jhongli, Taoyuan 32001, Taiwan*
[d] *Carnegie Institution of Washington, Las Campanas Observatory, Colina El Pino, Casilla 601 La Serena, Chile*
[e] *Universidad de Buenos Aires, Instituto de Astronomica y Fisica del Espacio, Buenos Aires, Argentina*
[f] *The University of Aizu, Research Center for Advanced Information Science and Technology, Ikki-machi, Aizu-Wakamatsu, Fukushima 965-8580, Japan*
[g] *University of Hawaii, Institute for Astronomy, 640 N. A'ohoku Place, Hilo, HI 96720, USA*
[h] *NASA Johnson Space Center, Astromaterials Research and Exploration Science Directorate, Houston, TX 77058, USA*

ARTICLE INFO

Article history:
Received 20 December 2012
Revised 1 February 2013
Accepted 5 February 2013
Available online 27 February 2013

Keywords:
Asteroids
Asteroids, Rotation
Asteroids, Composition
Photometry
Spectroscopy

ABSTRACT

The Japanese Space Agency's Hayabusa II mission is scheduled to rendezvous with and return a sample from the near-Earth Asteroid (162173) 1999 JU3. Previous visible-wavelength spectra of this object show significant variability across multiple epochs which has been attributed to a compositionally heterogeneous surface. We present new visible and near-infrared spectra to demonstrate that thermally altered carbonaceous chondrites are plausible compositional analogs, however this is a tentative association due to a lack of prominent absorption features in our data. We have also conducted a series of high signal-to-noise visible-wavelength observations to investigate the reported surface heterogeneity. Our time series of visible spectra do not show variability at a precision level of a few percent. This result suggests two most likely possibilities. One, that the surface of 1999 JU3 is homogenous and that unaccounted for systematic effects are causing spectral variation across epochs. Or two, that the surface of 1999 JU3 is regionally heterogenous, in which case existing shape models suggest that any heterogeneity must be limited to terrains smaller than approximately 5% of the total surface area. These new observations represent the last opportunity before both the launch and return of the Hayabusa II spacecraft to perform ground-based characterization of this asteroid. Ultimately, these predictions for composition and surface properties will be tested upon completion of the mission.

1. Introduction

In June of 2010 the Japanese Space Agency's Hayabusa mission successfully completed the first ever sample return from an asteroid (Fujiwara et al., 2006; Abe et al., 2006; Nakamura et al., 2011, and references therein). The success of this mission has spawned a successor, Hayabusa II, which is scheduled to rendezvous with and return a sample from the Asteroid (162173) 1999 JU3. This object was discovered by the Lincoln Near-Earth Asteroid Research (LINEAR) survey on 1999 May 10. It is an Apollo-class near-Earth asteroid with one of the lowest values of Δv for any object with an absolute magnitude less than $H = 20$,[1] and thus is a highly favorable space mission target. The current Hayabusa II timeline proposes a launch in 2014 or 2015, rendezvous with the asteroid in 2018, and return of a sample to Earth in 2020. Like its predecessor this mission provides the opportunity to directly test the validity of ground-based analytical techniques with pre-encounter predictions for the physical and chemical properties of the asteroid (e.g. Binzel et al., 2001b).

Previous observations of 1999 JU3 were conducted following its discovery in 1999 and during its favorable apparition in 2007. Ground-based photometry determined a light curve period of about 7.63 h (Abe et al., 2008; Müller et al., 2011), which has since been confirmed with photometry from the 2012 apparition (Kim et al., 2013). A weighted average of space and ground-based observations in the mid-infrared suggest an effective diameter of 870 ± 30 m and an albedo of 6.954 ± 0.005% (Hasegawa et al., 2008; Campins et al., 2009; Müller et al., 2011). Prior to the present study, visible-wavelength spectra had been obtained in May 1999, July 2007, and September 2007 (Fig. 1, Table 1). These data display marked variability in spectral slope and in the presence of absorption

---

[*] Corresponding author at: Massachusetts Institute of Technology, Department of Earth, Atmospheric and Planetary Sciences, 77 Massachusetts Avenue, Cambridge, MA 02139, USA.
E-mail address: nmosko@mit.edu (N.A. Moskovitz).

[1] http://echo.jpl.nasa.gov/~lance/delta_v/delta_v.rendezvous.html.

0019-1035/$ - see front matter © 2013 Elsevier Inc. All rights reserved.
http://dx.doi.org/10.1016/j.icarus.2013.02.009

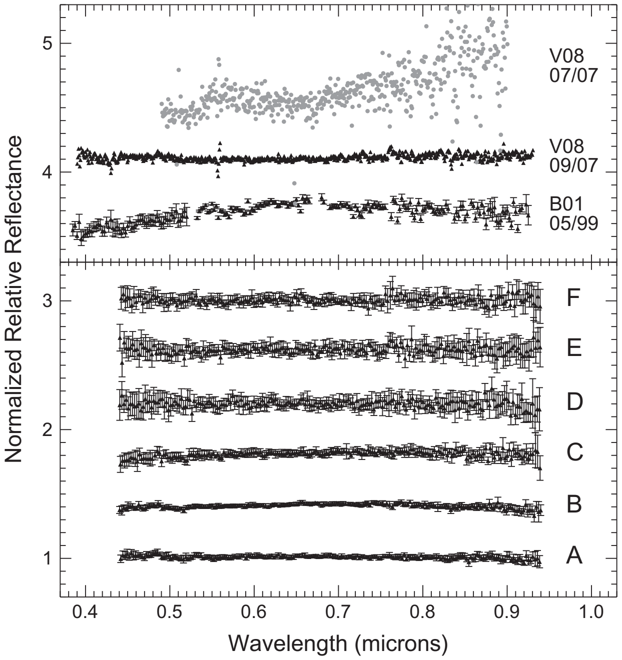

Fig. 1. Normalized visible-wavelength reflectance spectra of 1999 JU3. The data are vertically offset for clarity. The top panel shows the three previous visible spectra with the month/year of observation and respective references B01 = Binzel et al. (2001a) and V08 = Vilas (2008). The July 2007 data is shown in grey to distinguish it from the adjacent spectrum. Our spectra are in the bottom panel and are chronologically ordered from bottom to top with spectra A and B taken on June 1, C on June 2, and D–F taken on June 3. The midpoint times for each of these observations are given in Table 3. The progressive decrease in signal-to-noise in spectra A–F is due to the opposition effect, increasing geocentric and heliocentric distances, and increasing background from a waxing Moon.

features. The spectrum from 1999 shows UV absorption shortward of about 0.65 μm and a featureless neutral slope at longer wavelengths (Binzel et al., 2001a). The July 2007 data, which suffer from the lowest signal-to-noise, show an overall red slope with a pronounced absorption feature ~10% deep centered between 0.6 and 0.7 μm (Vilas, 2008). The September 2007 spectrum is a combination of data from two nights (Table 1) and is largely featureless with neutral slope (Vilas, 2008). Though these three spectra are broadly consistent with taxonomic classification in the C-complex, such pronounced variability, in this case at the level of ~10%, is highly unusual.

This spectral variability has been attributed to a compositionally heterogenous surface (Vilas, 2008). The absorption feature between 0.6 and 0.7 μm in the July 2007 spectrum was linked to $Fe^{2+} \rightarrow Fe^{3+}$ charge transfer transitions in iron-bearing phyllosilicates. The absence of this feature in the May 1999 and September 2007 spectra suggests a non-uniform distribution of these aqueous alteration byproducts. The possible existence of hydrated minerals on the surface of 1999 JU3 is of considerable interest for the purposes of mission planning and the potential sampling of primitive Solar System material. Such surface heterogeneity could be inherited from the asteroid's parent body or could be exogenous in origin, as may be the case for the "black boulder" seen by Hayabusa I on Itokawa (Fujiwara et al., 2006) and for the dark material imaged by the Dawn spacecraft on 4 Vesta (Reddy et al., 2012a).

We present observations of 1999 JU3 from the 2012 apparition, the last favorable observing window before both the scheduled launch and return of the Hayabusa II spacecraft. Visible and near-infrared spectra were obtained to constrain the composition of the asteroid and to investigate claims of a non-uniform surface. Other investigators obtained visible spectra during the 2012 observing window (Sugita et al., 2012; Vilas, 2012; Lazzaro et al., 2013). These other data are not directly addressed here, though we note that none of these works found evidence for a 0.7 μm absorption feature or any repeatable spectral variability through multiple rotation periods. We also present here new visible-wavelength photometry to constrain the rotational phases of the asteroid accessed by our 2012 spectroscopic observations. Our observations and reduction techniques are presented in Section 2. Analysis of these data are presented in Section 3. We summarize and discuss the results in Section 4.

2. Observations and data reduction

Data presented here were taken with seven different instruments at six telescopic facilities and include visible and near-infrared spectroscopy, and visible-wavelength photometry. With the exception of one near-infrared spectrum from 2007, all data were obtained between October of 2011 and July of 2012. Tables 1 and 2 summarize the observing circumstances.

2.1. Visible-wavelength spectroscopy: LDSS3

New visible wavelength spectra were obtained with LDSS3 at the Magellan Clay 6.5 m telescope on the nights of UT 2012 June 1–3, coinciding with the opposition of the asteroid at a phase angle of 0.2° on UT June 1 at 07:30. The instrument was operated with a 1.5″-wide and 4′-long slit and its VPH-All grism. These settings produced a single-order spectrum with a useful spectral range of 0.44–0.94 μm at an average resolution of about 430 and a dispersion of 1.89 Å/pixel. Each individual spectrum represents a set of 4 × 180 s exposures, split between two different nod positions approximately 20″ apart along the slit.

Table 1
Chronological summary of spectroscopic observations of 1999 JU3. The columns in this table are the UT date of observation, the instrument and facility that were used, the apparent V-band magnitude (from the Minor Planet Center), geocentric distance (Δ), heliocentric distance (R), the solar phase angle (α), the phase of the Moon (☾), the target–observer–Moon angle (T–O–M), and the solar analog stars used for calibration.

UT date	Instrument and facility	V	Δ (AU)	R (AU)	α (°)	☾	T–O–M (°)	Solar analogs
1999-05-17[a]	DSPEC Palomar 200″	17.7	0.305	1.314	6.1	5%	149	SA102-1081, 16 Cyg B
2007-07-11[b]	RCHAN MMT 6.5 m	20.3	0.569	1.381	40.3	12%	78	SA114-654
2007-09-10[b]	RCHAN MMT 6.5 m	17.9	0.273	1.254	22.5	2%	150	SA114-654
2007-09-11[b]	RCHAN MMT 6.5 m	17.9	0.271	1.251	22.8	0%	152	SA113-276, SA114-654
2007-09-18	SpeX IRTF	17.9	0.260	1.231	26.5	37%	90	SA112-1333, SA115-271, SA93-101, Hya64
2007-09-20	SpeX IRTF	17.9	0.258	1.226	27.9	56%	68	SA110-361, SA112-1333, SA115-271, SA93-101
2012-06-01	LDSS3 Magellan 6.5 m	17.7	0.353	1.367	0.2	85%	45	SA110-361, HD149182
2012-06-02	LDSS3 Magellan 6.5 m	17.8	0.354	1.368	1.0	92%	31	HD149182
2012-06-03	LDSS3 Magellan 6.5 m	17.9	0.356	1.370	2.0	98%	15	SA107-998
2012-06-05	FIRE Magellan 6.5 m	18.1	0.360	1.373	4.4	99%	15	SA107-998
2012-07-10	FIRE Magellan 6.5 m	19.9	0.518	1.410	33.1	60%	127	SA113-276

[a] From Binzel et al. (2001a).
[b] From Vilas (2008).

Table 2
Summary of 1999 JU3 photometric observations. The columns in this table are the same as in Table 1.

UT date	Instrument and facility	V	Δ (AU)	R (AU)	α (°)
2011-10-30	EEV 1 k CCD Lulin 1 m	20.1	0.438	1.002	76.1
2012-04-05	IMACS Magellan 6.5 m	19.8	0.461	1.237	49.4
2012-04-06	IMACS Magellan 6.5 m	19.8	0.457	1.240	48.9
2012-04-07	IMACS Magellan 6.5 m	19.8	0.454	1.243	48.5
2012-05-31	SITe1k Tenagra 0.8 m	17.7	0.352	1.366	0.7
2012-06-07	SITe1k Tenagra 0.8 m	18.2	0.366	1.377	7.1
2012-06-08	SITe1k Tenagra 0.8 m	18.3	0.368	1.378	8.2
2012-06-09	SITe1k Tenagra 0.8 m	18.4	0.371	1.380	9.2
2012-06-20	Tek1k Bosque Alegre 1.5 m	19.0	0.409	1.393	19.4
2012-06-21	Tek1k Bosque Alegre 1.5 m	19.0	0.413	1.394	20.3

Solar analog stars were observed several times throughout each night for calibration purposes (Table 1). With the exception of HD149182, the calibration stars were selected from a list of well-vetted analogs that were used extensively throughout the SMASS survey (Bus and Binzel, 2002). HD149182 was also included because of its close proximity (<10°) to the asteroid and was selected based on its photometric colors and G2V spectral classification. The high degree of consistency amongst our measured spectra (Section 3.2) confirms that HD149182 is a good solar analog.

Reduction of these spectra employed standard IDL and IRAF routines, including a set of IRAF tools developed specifically for LDSS3. Combined He, Ne and Ar arc lamp spectra were obtained at the beginning and end of each night to provide dispersion solutions. Exposures of a white screen illuminated by a quartz lamp were used for flat field calibration.

The extracted asteroid spectra were divided by each of the solar analogs (typically ~10 individual observations of solar analogs throughout the night). The best solar analog for a given asteroid spectrum was chosen based on minimization of residual telluric features long-wards of ~0.7 μm. After division by an analog, individual points in the spectra were then rejected based on a 0.25 μm boxcar sigma-clipping routine with a prescribed cutoff of 3 sigma. In all cases less than 10% of the data points were rejected and those that were removed were predominantly distributed at the extremes of the spectra outside the useful spectral range of 0.44–0.94 μm. Generally, less than 10 pixels were removed from within this final trimmed spectral range. After cleaning, the asteroid spectra were then re-binned by a factor of 13 pixels to produce a dispersion interval very close to 0.0025 μm per channel, similar to that of the 1999 spectrum (Binzel et al., 2001a) and a factor approximately 3 times larger than that of the 2007 data (Vilas, 2008). The error bar on each binned dispersion element was set to the standard deviation of the original 13 pixels. The data were finally normalized at 0.55 μm to produce relative reflectance spectra (Fig. 1).

The wavelength-averaged signal-to-noise ratio (S/N) of these spectra vary from ~60 on the first night (A and B in Fig. 1), to ~30 on the second night (C), to ~20 on the third night (D–F). Since exposure times were held constant, this drop in S/N is likely caused by several effects. First, spectra A and B were taken at solar phase angles less then 1° (Table 1) and thus may have captured an opposition surge in brightness. Second, the Moon was both waxing and increasingly close to the target throughout the run (Table 1), thus causing a progressive increase in background flux. Third, the target's geocentric and heliocentric distances were both increasing, causing a drop in brightness across the three nights.

2.2. Near-infrared spectroscopy: FIRE and SpeX

Near-infrared spectra were obtained in June and July of 2012 with FIRE at the Magellan Baade 6.5 m telescope and in September 2007 with SpeX (Rayner et al., 2003) at NASA's Infrared Telescope Facility (IRTF; Table 1). FIRE was operated in its high-throughput prism mode with a 0.8 × 50″ slit. These settings produced single-order spectra at a resolution of approximately 400 from 0.8 to 2.45 μm. Individual exposures were limited to 180 s to avoid saturation of telluric emission features and of thermal emission from the instrument and telescope at wavelengths longer than about 2.2 μm. Exposures were obtained in ABBA sequences with the object offset along the slit by 9″ for each nod position. On UT 2012 June 5 a total of 4 × 180 s exposures were obtained. On UT 2012 July 10, when the asteroid was nearly 2 magnitudes fainter, a total of 18 × 180 s exposures were obtained.

At the IRTF, SpeX was configured in its low resolution (R = 250) prism mode with a 0.8″ slit for wavelength coverage from 0.8 to 2.5 μm. All observations were made with the telescope operating in a standard ABBA nod pattern with individual exposures of 120 s. On UT 2007 September 18 a total of 40 individual exposures were obtained, on UT 2007 September 20 a total of 50 individual exposures were obtained.

For both near-infrared spectrographs the slit mask was oriented along the parallactic angle at the start of each observation to minimize the effects of atmospheric dispersion. As with the visible-wavelength spectra, solar analogs were observed to correct for telluric absorption and to remove the solar spectrum from the measured reflectance (Table 1). Reduction of the SpeX data followed Sunshine et al. (2004), reduction of the FIRE data employed an IDL package designed for the instrument and based on the Spextool pipeline (Cushing et al., 2004).

A composite visible/near-infrared spectrum of 1999 JU3 is shown in Fig. 2. The asteroid is a C-type in the DeMeo et al. (2009) taxonomic system. The visible portion is a weighted average of the six LDSS3 spectra in Fig. 1. The near-infrared portion is a weighted average of the SpeX and FIRE data, and thus represents a combination of data across multiple epochs. Other than some variability in slope, no significant differences were seen amongst the near-infrared spectra within the S/N of the data.

2.3. Visible-wavelength photometry: IMACS, Lulin, Tenagra II, and Bosque Alegre

Photometric observations (Table 2) were conducted with IMACS at the Magellan Baade 6.5 m telescope at Las Campanas Observatory in Chile, with a Princeton Instruments EEV 1 k CCD at the Lulin 1 m telescope in Taiwan, with a SITe 1 k CCD at the Tenagra II 0.81 m telescope in Arizona, and with a Tektronics 1 k CCD at the Bosque Alegre 1.5 m telescope in Argentina. These data were taken on ten separate nights between October 2011 and June 2012.

IMACS was operated using the *f*/2 camera, which has a 27.5′ field-of-view covered by a mosaic of eight 2 k × 4 k CCDs with plate scales of 0.2″/pixel. We employed only one of the eight chips with a subraster about 400 × 400″ in size. We used a Bessell R-band filter with exposure times of 60 s. These observations spanned approximately 3 h per night over three consecutive nights. The Princeton Instruments CCD at Lulin Observatory has a roughly 11′ field of view with a plate scale of 0.516″/pixel. These observations were conducted with a Johnson–Cousins R-band filter over the course of approximately 2 h on a single night. Exposure times were set to 300 s. The SITe 1 k CDD at the Tenegra II telescope has a 14.8′ field-of-view with a plate scale of 0.87″/pixel. A Johnson–Cousins R-band filter was used. These observations spanned approximately 4.5 h per night over 4 non-consecutive nights with individual exposure times set to 360 s. The Tektronics 1 k at the Bosque Alegre 1.5 m has a plate scale of 0.33″/pixel and a field-of-view of 5.7′. Observations were conducted with a Johnson R-band filter, spanning approximately 3.5 h on two consecutive nights. Exposure times were 240 s the first night and 200 s the second.

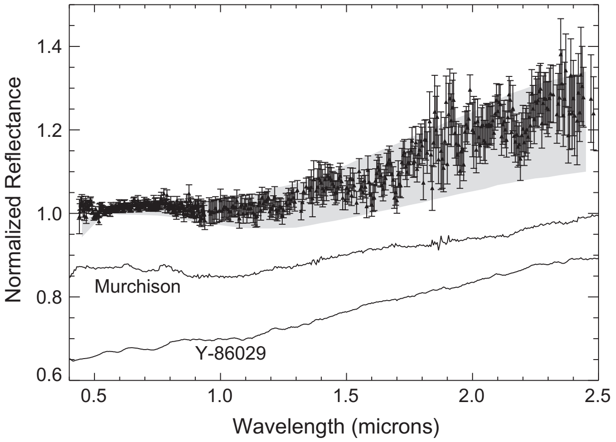

Fig. 2. Composite visible (LDSS3) and near-infrared (SpeX and FIRE) spectrum of 1999 JU3. The grey region in the background represents the envelope for C-type spectra in the DeMeo et al. (2009) taxonomic system. In spite of the low signal-to-noise in the near-infrared and the presence of residual telluric features around 1.4 and 1.9 μm, this spectrum shows no evidence for prominent absorption bands, though subtle features may be present around 0.9 μm and short-ward of 0.7 μm. The two best spectral matches from our χ^2 search through RELAB are a thermally altered sample of Murchison and the unusual CI chondrite Yamato 86029. These meteorite spectra have been normalized at 1 μm and then offset by −0.15 and −0.3 units respectively.

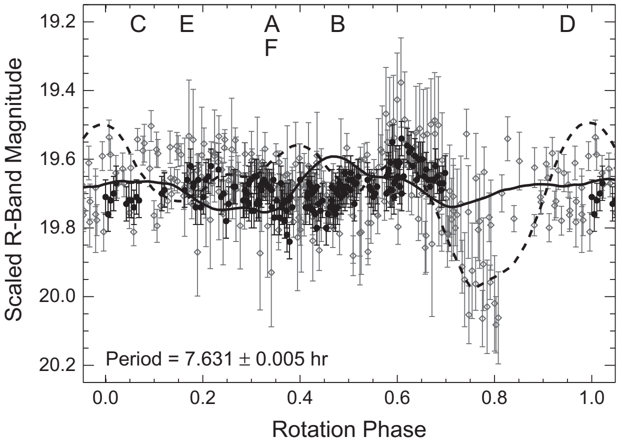

Fig. 3. Rotational light curve of 1999 JU3. Filled circles represent the IMACS Magellan data. Open diamonds represent our additional observations (Table 2) with magnitudes scaled to the IMACS data. The solid line represents the predicted light curve from the Müller et al. (2011) model, the dashed is the model prediction from Kawakami et al. (2010). The data have been phase folded to a synodic period of 7.631 h. A rotation phase of zero corresponds to the start of IMACS observations on UT 2012-04-05 at 06:40 (JD 2456022.778). The phases accessed by the visible-wavelength spectroscopic observations are indicated by the letters A-F. The total time for each spectrum (4 × 180 s plus readout and telescope offsets) is comparable to the width of the letters. Spectroscopic coverage was obtained over approximately 60% of rotation phases at a longitudinal resolution of ~45°.

Reduction of these data employed standard IRAF procedures. Aperture photometry was performed with aperture radii roughly 4 times the measured seeing and a background annulus equal to twice that separation. Some individual exposures were rejected based on contamination from nearby field stars. Photometric calibration was achieved for the IMACS data with observations of the RU 149 Landolt standard field (Landolt, 1992). All other photometry was performed differentially relative to at least one half dozen on-chip field stars and then scaled to match the calibrated IMACS data. A full table of the collected photometry is included in the Online supplementary Data.

3. Rotational and compositional analyses

Our visible-wavelength photometry is used to construct a phase-folded rotational light curve of 1999 JU3. This provides the means to constrain the specific rotational phases accessed by the spectroscopic observations and to quantitatively address the previously reported surface heterogeneity. The combined visible/near-IR spectrum is used to place preliminary constraints on composition.

3.1. Rotational light curve

Müller et al. (2011) find a rotation period for 1999 JU3 of 7.63 ± 0.01 h and Kim et al. (2013) find a period of 7.625 ± 0.003 h. We use these periods as a guide to phase-fold our broadband photometry (Fig. 3). The highest S/N data came from the three nights of observations at Magellan (Table 2). The magnitudes of all other observations are scaled to the mean value of the photometrically calibrated Magellan data. As with previous light curve measurements (Müller et al., 2011; Kim et al., 2013), our data suggest a small peak-to-peak amplitude of about 0.2 magnitudes. Attempts have been made to exclude data points contaminated by background field stars, however the low galactic latitude of the asteroid (<20° for all observations) certainly adds to the scatter in the measured photometry.

The light curve in Fig. 3 has been phase folded with a synodic period of 7.631 h relative to the first IMACS observation on UT 2012-04-05 at 06:40 (JD 2456022.778). Light time corrections have been applied relative to this first IMACS observation. This light curve is wrapped such that the first and last few points are repeated at phases <0 and >1. Robustly fitting a light curve period is difficult because the photometric errors are comparable to the amplitude of the light curve and our best quality photometry from IMACS does not span a full rotation period. A unique period is not found when employing the Fourier analysis of Polishook (2012). Thus we attempt to manually constrain the period based on three features in the IMACS data: a subtle peak at phase = 0.2, a minimum at phase = 0.4 and another peak around phase = 0.6. The period is adjusted in increments of 0.001 h until these three features are roughly aligned for all data. We find that these features are not aligned for periods within ±0.005 h of 7.631 h. This result is consistent with the range of periods suggested by Müller et al. (2011) and Kim et al. (2013), but is not meant to be a more accurate determination.

3.2. Non-detection of spectroscopic variability

The phase folded light curve is used to provide rotational context for each of the new spectroscopic observations (Fig. 3). This phase folding demonstrates that rotational coverage was obtained over approximately 60% of the asteroid's surface at a longitudinal sampling of ~45°. The spectroscopic observations from previous epochs (Binzel et al., 2001a; Vilas, 2008) are not included in Fig. 3 because current best estimates for the rotation period (e.g. Kim et al., 2013) still have an associated error that is large enough to preclude linking observations separated by several years.

We compute reflectance ratios to investigate the possibility of a heterogenous surface (Fig. 4). These ratios are computed by median combining spectra A through F and then dividing that median into each of the individual spectra. Any deviations from a flat line would indicate the presence of a heterogenous surface. Typical deviations are around 1%, with the largest (just under 4%) seen at the bluest wavelengths in spectrum C. However, all deviations fall within the S/N of the data and thus suggest that the regions on the surface accessed by our observations are homogenous to within a few percent.

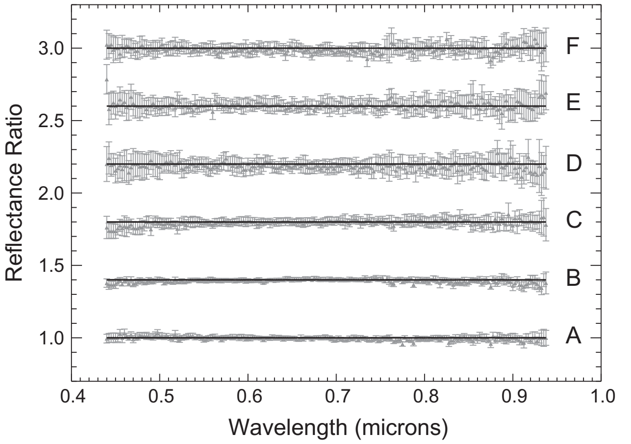

Fig. 4. Visible-wavelength reflectance ratios of 1993 JU3 relative to a median combination of all spectra. These reflectance ratios have been offset by multiples of 0.4 units. Deviations from a slope-zero line (black curves) would indicate spectroscopic heterogeneity. No variability is detected within the S/N of the data, though slight (<4%) deviations from a flat line are seen at the shortest wavelengths in spectra B and C.

Previously reported spectroscopic variability around 0.8 μm (Lazzaro et al., 2013) is not seen in our data set. This non-detection suggests the possibility raised by these authors, that it may be attributed to either instrumental optical fringing or residual effects from the telluric water absorption band centered near 0.8 μm.

The rotational context for these spectroscopic data provides a test of our observation and reduction techniques. Fig. 3 shows that spectra A and F were obtained at nearly identical rotation phases. The fact that these spectra are indistinguishable (Fig. 4), but taken on different nights and calibrated with different solar analogs (Table 1), is a nice validation of the consistency of our methodology.

3.3. Spectroscopic surface coverage

Shape models of 1999 JU3 based on photometry from 2007 have been independently developed by Kawakami et al. (2010) and Müller et al. (2011). In both cases, the small amplitude of the light curve produces nearly spherical shapes. These models are based upon different data sets, but because of issues of low S/N, do not offer a single unique solution. Unsurprisingly then, neither shape model produces light curves that match our data well (Fig. 3). Clearly the development of a new shape model that fits photometry from 2007 and 2012 is an important task for future work. Due to this ambiguity it is difficult to absolutely state the surface latitudes and longitudes accessed by the full ensemble of spectroscopic observations dating back to 1999. However we can compare model predictions for the spectroscopically accessed surface regions to illustrate the plausible spatial extent of any non-uniform surface features.

The spectra of 1999 JU3 from September 2007 are fully consistent with the new data presented here (Fig. 1). Any surface heterogeneity must then be restricted to regions accessed by the observations in May 1999, when the asteroid displayed UV absorption short-ward of about 0.65 μm (Binzel et al., 2001a) and in July 2007 when the asteroid showed a prominent absorption feature between 0.6 and 0.7 μm (Vilas, 2008). These regions would have to be limited in extent to avoid violating the lack of absorption features in the other spectra.

Table 3 presents the two sets of predicted sub-observer latitudes and longitudes for all visible-wavelength spectroscopic observations. Fig. 5 illustrates the sub-observer points predicted by the two shape models. Though these sub-observer points are not meant to be absolute and may change with future improvements to the shape model, their relative separations are informative. In particular, we are most interested in the distance that separates the sub-observer points for featureless spectra (September 2007, June 2012) from the sub-observer points for spectra that display absorption bands (May 1999, July 2007; B and V in Fig. 5). We can roughly calculate the physical distance between sub-observer points by assuming a spherical body with a diameter of 870 m, a reasonable approximation for this asteroid (Kawakami et al., 2010; Müller et al., 2011). The physical distance between sub-observer points is then just the distance along the great circle that connects these points.

According to the Kawakami et al. (2010) model, the observations from May 1999 were taken at a sub-observer point about

Table 3
Sub-observer points for all published visible-wavelength spectra of 1999 JU3. Columns in this table are the UT midpoint of observation, reference [B01 = Binzel et al. (2001a); V08 = Vilas (2008); letters A–F indicate the corresponding spectra in Fig. 1], the apparent V-band magnitude (from the Minor Planet Center), geocentric distance (Δ), heliocentric distance (R), solar phase angle (α), and the sub-observer longitude and latitude. These data are presented for both shape models of 1999 JU3.

UT midpoint	Reference	V	Δ (AU)	R (AU)	α (°)	Sub-observer long. and lat.
Müller et al. (2011) *Shape model*						
1999-05-17 07:49	B01	17.7	0.305	1.314	6.1	−169°, 19°
2007-07-11 10:05	V08	20.3	0.569	1.381	40.3	−40°, 8°
2007-09-10 07:00	V08	17.9	0.273	1.254	22.5	169°, 25°
2007-09-11 05:50	V08	17.9	0.271	1.251	22.8	172°, 25°
2012-06-01 07:07	A	17.7	0.353	1.367	0.2	158°, 27°
2012-06-01 08:09	B	17.7	0.353	1.367	0.2	109°, 28°
2012-06-02 03:54	C	17.8	0.354	1.368	1.0	−102°, 28°
2012-06-03 01:54	D	17.9	0.356	1.370	2.0	−59°, 28°
2012-06-03 03:34	E	17.9	0.356	1.370	2.1	−137°, 28°
2012-06-03 04:54	F	17.9	0.356	1.370	2.2	159°, 28°
Kawakami et al. (2010) *Shape model*						
1999-05-17 07:49	B01	17.7	0.305	1.314	6.1	−19°, 10°
2007-07-11 10:05	V08	20.3	0.569	1.381	40.3	25°, −71°
2007-09-10 07:00	V08	17.9	0.273	1.254	22.5	−61°, −77°
2007-09-11 05:50	V08	17.9	0.271	1.251	22.8	−57°, −78°
2012-06-01 07:07	A	17.7	0.353	1.367	0.2	−34°, −9°
2012-06-01 08:09	B	17.7	0.353	1.367	0.2	−83°, −9°
2012-06-02 03:54	C	17.8	0.354	1.368	1.0	65°, −9°
2012-06-03 01:54	D	17.9	0.356	1.370	2.0	107°, −8°
2012-06-03 03:34	E	17.9	0.356	1.370	2.1	29°, −8°
2012-06-03 04:54	F	17.9	0.356	1.370	2.2	−35°, −8°

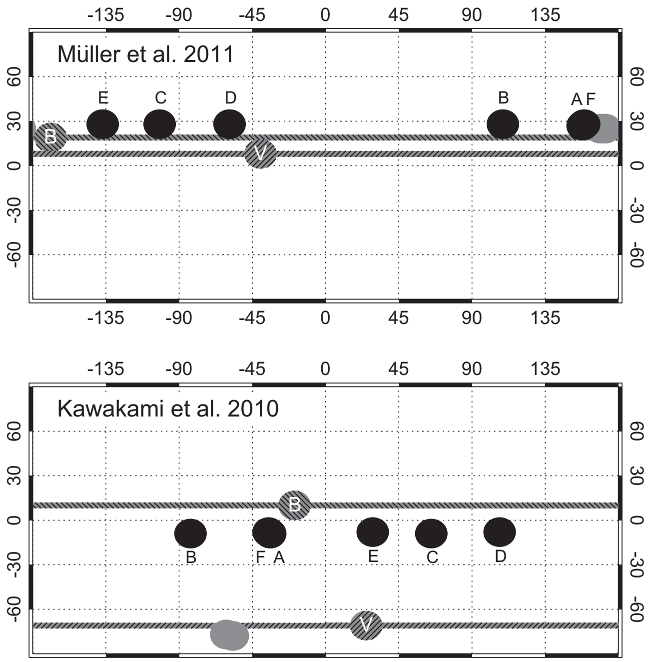

Fig. 5. Cylindrical projections of 1999 JU3's surface with circles indicating the sub-observer latitudes and longitudes from the two available shape models (Kawakami et al., 2010; Müller et al., 2011). The circles are not meant to indicate the physical extent of the surface accessed by the observations. Black circles represent sub-observer points from our new 2012 observations and are labeled A–F. Grey circles represent sub-observer points for the observations from 1999 and 2007. The two spectra that display absorption features are indicated with hatched regions and labeled B (Binzel et al., 2001a) and V (Vilas, 2008). Surface regions that produce absorption features must be limited in extent to avoid overlapping those corresponding to featureless spectra. The loss of rotational information across epochs (see text) suggests that the locations of these regions relative to the 2012 points could lie anywhere along the horizontal bands. This demands that any heterogeneity on the surface be confined to regions no more than a few hundred meters in extent.

180 m away from the next closest point which corresponds to spectrum F (June 2012). And the observations from July 2007 correspond to a sub-observer point about 160 m away from the September 2007 spectra. According to the Müller et al. (2011) model, the observations from May 1999 were taken about 140 m from the September 2007 points, and the observations from July 2007 correspond to a sub-observer point about 200 m away from spectrum D (June 2012). Taken as a whole, and independent of which shape model is employed, these calculations suggest that the reported spectroscopic variability would be a consequence of regional surface heterogeneity on spatial scales smaller than about 400 m in extent (200 m in radius). Regions of this size would occupy about 5% of the asteroid's total surface area.

The ambiguity in shape models emphasizes that rotational information is not correlated over multiple years. This is indicated by the horizontal bands in Fig. 5. The sub-observer points for those spectra with absorption features could lie anywhere along these bands. This provides some freedom for the spectrally anomalous regions to "hide" in the gaps between those sub-observer points corresponding to featureless spectra. However, the sub-observer points for both the Binzel et al. (2001a) and Vilas (2008) spectra would have to be shifted by very specific amounts to reconcile the full suite of visible spectra. This issue is further complicated upon consideration of the sub-observer hemispherical footprints of our spectroscopic observations (see online Supplementary Figure A). These footprints indicate that we accessed a significant majority of the surface, leaving very little surface area in which spectroscopically anomalous regions could exist.

3.4. Compositional analogs

With the full visible/near-infrared spectrum (Fig. 2) we can make preliminary statements about the composition of 1999 JU3. However, these statements must be interpreted with some skepticism due to the lack of prominent absorption features and issues of degenerate compositional interpretations when dealing with such featureless spectra (e.g. Vernazza et al., 2009; Reddy et al., 2012b,c). A preliminary attempt at compositional analysis is justified by the potential for predictions to be directly tested with a returned sample. We base this analysis solely on our new observations; see Vilas (2008) for an interpretation of previous visible-wavelength spectra.

Our visible and near-infrared spectra confirm a C-type taxonomic classification, but show no evidence for the previously detected 0.7 μm phyllosilicate band (Vilas, 2008) or a prominent UV drop-off short-wards of about 0.65 μm (Binzel et al., 2001a). The data may indicate weak bands around 0.9 μm and short-ward of 0.7 μm, but these features are near the limit of the S/N and are not robust detections. Without any strong features to directly analyze we employ spectral matching techniques to constrain plausible compositional analogs. Comparison spectra were obtained from a July 2012 release of Brown University's RELAB database (Pieters, 1983) containing reflectance spectra for just over 17,000 samples. Our search began by selecting only those samples with a spectral range overlapping that of the asteroid and only those samples with an albedo within 5% of that measured for 1999 JU3. This narrowed the list of comparison spectra to 8024 samples. For each of these, either the asteroid or the meteorite data were interpolated to match the wavelengths of the spectrum with the smallest dispersion interval. Both spectra were then normalized at the minimum asteroid wavelength (0.44 μm) before a reduced χ^2 difference was calculated.

The two meteorite spectra with the lowest χ^2 values are shown in Fig. 2. These meteorites are a thermally altered sample of the CM carbonaceous chondrite Murchison and the unusual CI chondrite Yamato 86029. The reduced χ^2 values for these meteorites were 2.89 and 3.25 respectively. These were clearly the best fits as the next lowest χ^2 was 6.75 for a sample of a mid-ocean ridge basalt (RELAB ID RB-CMP-023) that was ground to particle sizes 125–250 μm. This spectrum of oceanic basalt matched the general slope of 1999 JU3 but showed a subtle 1 μm absorption band and thus is unlikely to be a good analog.

The mean albedos of the two best-fit samples (6% for Murchison, 3% for Yamato) are by design of the search algorithm close to the ~7% measured for 1999 JU3 (Hasegawa et al., 2008; Campins et al., 2009; Müller et al., 2011). The two best-fit spectra both correspond to the smallest available particle size sorting, <63 μm for Murchison and <125 μm for Yamato. The Murchison spectrum represents one in series of heating experiments where the temperature of the sample was raised in increments of 100 °C from 300 to 1000 °C (Hiroi et al., 1996). At each temperature increment a reflectance spectrum was measured. Heating was shown to reduce spectral slope and decrease the depth of absorption bands. The Murchison spectrum corresponding to a temperature of 900 °C was the closest match to 1999 JU3. Yamato 86029 has unusual textural properties and a chemical composition indicative of a rare class of CI chondrites that experienced moderate thermal alteration at temperatures of 500–600 °C (Tonui et al., 2003). 1999 JU3 has been previously linked to carbonaceous chondrites (Vilas, 2008; Lazzaro et al., 2013), the analysis here expands upon these results by specifically identifying thermally altered samples as the best available spectral analogs.

4. Discussion

We have presented new observations of the Hayabusa II target asteroid 1999 JU3 taken during the favorable 2012 apparition, the last opportunity before both the launch and return of the spacecraft to perform ground-based characterization. Visible wavelength photometry was used to produce a rotational light curve. A period of 7.631 ± 0.005 h and a small amplitude of a few tenths of a magnitude are consistent with independent light curve measurements (Müller et al., 2011; Kim et al., 2013). Visible and near-infrared spectra were used to constrain taxonomy and composition. The asteroid is a C-type in the DeMeo et al. (2009) taxonomic system and the best spectral analogs are thermally altered carbonaceous chondrites. However, the lack of any prominent absorption features makes this compositional association tentative. High quality spectra that extend into the near-UV (0.3–0.4 μm) or the 3 μm region could provide further compositional clues if diagnostic absorption bands are detected (e.g. Hiroi et al., 1993; Rivkin et al., 2002) and may serve as a test of the collisional and thermal evolution of primitive asteroid types (Vilas and Sykes, 1996).

The putative link to carbonaceous chondrites and particularly those that are thermally altered is interesting and merits some preliminary speculation. CM and CI chondrites are primitive meteorites with appreciable quantities of organics and water of hydration (Cloutis et al., 2011a,b). The possible return of such samples would be relevant to issues of astrobiology and to understanding primordial chemistry in the solar nebula (e.g. Morbidelli et al., 2000). The suggested link to heated carbonaceous chondrites could imply that surface temperatures on 1999 JU3 were significantly higher at some point in its past. There is roughly a 50% probability that the chaotic orbital evolution of 1999 JU3 resulted in a perihelion inside of 0.5 AU (its current perihelion distance in 0.96 AU), which translates to surface temperatures of approximately 500 K (Marchi et al., 2009; Michel and Delbó, 2010). This is comparable to the in situ alteration temperatures experienced by Yamato 86029, but is less than the 900 °C experienced by the Murchison sample. Nevertheless, this highlights that thermally altered primitive meteorites could be relevant to understanding the composition of 1999 JU3. Ultimately, the results from Hayabusa II will provide the first-ever direct test of such compositional interpretations from largely featureless asteroid spectra.

We have also presented a time series of visible spectra to address previously reported spectroscopic variability (Vilas, 2008; Lazzaro et al., 2013). Our spectra show no variability at the level of a few percent. There are several possible explanations for this non-detection. First, the asteroid's surface may be spectroscopically and compositionally uniform, in which case some unaccounted for systematic effects would be the cause of spectral variation across epochs. The hemispherical footprints of our spectral observations cover nearly the entire surface of the asteroid (Supplementary Figure A), thus supporting this hypothesis. Variations in spectral slope are common with asteroid observations and can be attributed to observational issues such as weather, phase angle (Sanchez et al., 2012; Reddy et al., 2012d), or the use of imperfect solar analogs, but it is unclear how these issues would result in variable absorption features. Other than a moderately high airmass of ~1.9 for the Binzel et al. (2001a) spectrum, we find no obvious observational reasons why the two spectra with absorption features should be different.

Multi-epoch spectral variability could alternatively be linked to recent alteration events that induced global or near global changes in surface properties. Planetary encounters (Binzel et al., 2010) or impacts (Richardson et al., 2004) can alter reflectance properties, however these seem unlikely because two such events would be required in just 13 years to explain the observed spectroscopic variability from 1999 to 2007 to 2012.

A final explanation is that the surface of 1999 JU3 is in fact heterogenous. In this case spectral variability could result from the obscuration of surface regions by local topography as a consequence of changing viewing aspect. However, the orbital longitudes of both the Earth and the asteroid were very similar during the May 1999 and June 2012 observations. This would then require a highly irregular shape (i.e. large topographic relief) to result in significant obscuration and spectral variability. A highly irregular shape is inconsistent with current shape models (Kawakami et al., 2010; Müller et al., 2011). Therefore, spectral variability caused by a non-uniform surface would have to be attributed to rotational effects. The combination of rotational data and time resolved spectra provides a means to address this possibility. Existing shape models (Kawakami et al., 2010; Müller et al., 2011) suggest that the maximum physical separation of sub-observer points for the full ensemble of spectroscopic data is about 200 meters (assuming that the asteroid is 870 m in diameter; Fig. 5). Therefore any surface heterogeneity must be confined to regions no larger than about 400 m in extent, which corresponds to a size independent surface area fraction of around 5%. However, we note again that current shape models do not predict light curves consistent with photometry across multiple epochs. Therefore, the analysis here constrains the *plausible* spatial extent of non-uniform surface features, improved shape models will be required to refine the spectroscopically accessed terrains indicated in Fig. 5.

Few asteroids, particularly sub-km objects like 1999 JU3, have been so extensively observed across multiple epochs. However, non-uniform surfaces are generally believed to be rare. The longtime exception is asteroid 4 Vesta, one of very few objects where variability over multiple rotation periods has been confirmed with remote observations. Vesta displays regional and hemispherical color heterogeneity, in some cases well in excess of several 10's of percent (e.g. Bobrovnikoff, 1929; Gaffey, 1997; Reddy et al., 2012a). However, Vesta is much larger than 1999 JU3, is a different spectral class, and thus may not be the best object for comparison.

There have been reports of rotational spectroscopic heterogeneity amongst C-class asteroids. For instance, 10 Hygiea, 105 Artemis, 135 Hertha, and 776 Berbericia each show variability at levels less than about 5% in the depths of their 0.7 μm features (Rivkin et al., 2002; Vilas, 2008). Detecting such subtle variability is intrinsically difficult and as far as we are aware remains to be verified for any asteroid over multiple rotation periods. Asteroid 21 Lutetia, which was visited by the Rosetta spacecraft, shows variability in visible-wavelength spectral slope at the level of a few percent (Barucci et al., 2012). The S/N of our data for 1999 JU3 may be insufficient to detect such muted variability. But again, these examples of spectral variability occur on asteroids that are much larger than 1999 JU3.

The former target of the European Space Agency's Marco Polo mission (175706) 1996 FG3 and asteroid 25143 Itokawa, the target of the Hayabusa I mission, are examples of well-studied asteroids in a size regime closer to that of 1999 JU3. 1996 FG3 shows prominent (~10's of percent) spectral variability in the near-IR (de León et al., 2011). The origin of this variability remains a mystery. Itokawa displays up to 15% color variability on its surface (Saito et al., 2006; Abe et al., 2006). This non-uniformity is limited to regions on the order of 10's to 100 m in extent or at most a few percent of Itokawa's surface area. This extent is similar to the constraints we have placed on 1999 JU3's surface, though it remains unclear whether such small regions could significantly influence ground-based observations that only capture hemispherical averages. Ground-based observations of Itokawa prior to arrival of Hayabusa I did not exhibit any variability (Binzel et al., 2001b; Abell et al., 2007).

For now, the issue of heterogeneity on the surface of 1999 JU3 remains an open question that may find some resolution from updated shape models. The arrival of the Hayabusa II spacecraft will ultimately determine whether the full ensemble of visible spectra are truly indicative of a non-uniform surface. More generally, the possibility of multiple planetary missions to near-Earth asteroids in the coming decades will provide an opportunity to further investigate the extent of surface heterogeneity on sub-km asteroidal bodies, and thus provide clues about formational and evolutionary processes in the Solar System.

Acknowledgments

We are grateful to Vishnu Reddy and Faith Vilas for their insightful reviews. We thank David Polishook for his helpful input on the lightcurve analysis. This work includes data obtained at the Magellan 6.5 m telescopes located at Las Campanas Observatory in Chile and at NASA's IRTF located on Mauna Kea in Hawaii, which is operated by the University of Hawaii under Cooperative Agreement No. NNX-08AE38A with the National Aeronautics and Space Administration, Science Mission Directorate, Planetary Astronomy Program. Support for this project was provided to N.M. by the Carnegie Institution of Washington Department of Terrestrial Magnetism, the National Aeronautics and Space Administration through the NASA Astrobiology Institute (NAI) under Cooperative Agreement No. NNA04CC09A, and through the National Science Foundation Astronomy and Astrophysics Postdoctoral Fellowship.

Appendix A. Supplementary material

Supplementary data associated with this article can be found, in the online version, at http://dx.doi.org/10.1016/j.icarus.2013.02.009.

References

Abe, M. et al., 2006. Near-infrared spectral results of asteroid Itokawa from the Hayabusa spacecraft. Science 312, 1334–1338.

Abe, S. et al., 2006. Mass and local topography measurements of Itokawa by Hayabusa. Science 312, 1344–1347.

Abe, M. et al., 2008. Ground-based observational campaign for Asteroid 162173 1999 JU3. Lunar Planet. Sci. 39. Abstract 1594.

Abell, P.A., Vilas, F., Jarvis, K.S., Gaffey, M.J., Kelley, M.S., 2007. Mineralogical composition of (25143) Itokawa 1998 SF36 from visible and near-infrared reflectance spectroscopy: Evidence for partial melting. Meteorit. Planet. Sci. 42, 2165–2177.

Barucci, M.A. et al., 2012. Overview of Lutetia's surface composition. Planet. Space. Sci. 66, 23–30.

Binzel, R.P. et al., 2010. Earth encounters as the origin of fresh surfaces on near-Earth asteroids. Nature 463, 331–334.

Binzel, R.P., Harris, A.W., Bus, S.J., Burbine, T.H., 2001a. Spectral properties of near-Earth objects: Palomar and IRTF results for 48 objects including spacecraft targets (9969) Braille and (10302) 1989 ML. Icarus 151, 139–149.

Binzel, R.P., Rivkin, A.S., Bus, S.J., Sunshine, J.M., Burbine, T.H., 2001b. MUSES-C target Asteroid (25143) 1998 SF36: A reddended ordinary chondrite. Meteorit. Planet. Sci. 36, 1167–1172.

Bobrovnikoff, N.T., 1929. The spectra of minor planets. Lick Obs. Bull. 14 (407), 18–27.

Bus, S.J., Binzel, R.P., 2002. Phase II of the small main-belt asteroid spectroscopic survey: A feature-based taxonomy. Icarus 158, 146–177.

Campins, H. et al., 2009. Spitzer observations of spacecraft target 162173 (1999 JU3). Astron. Astrophys. 503, L17–L20.

Cloutis, E.A., Hiroi, T., Gaffey, M.J., Alexander, C.M., Mann, P., 2011a. Spectral reflectance properties of carbonaceous chondrites: 1. CI chondrites. Icarus 212, 180–209.

Cloutis, E.A., Hudon, P., Hiroi, T., Gaffey, M.J., Mann, P., 2011b. Spectral reflectance properties of carbonaceous chondrites: 1. CM chondrites. Icarus 216, 309–346.

Cushing, M.C., Vacca, W.D., Rayner, J.T., 2004. Spextool: A spectral extraction package for SpeX, a 0.85.5 micron cross-dispersed spectrograph. PASP 116, 363–376.

de León, J., Mothé-Diniz, T., Licandro, J., Pinilla-Alonso, N., Campins, H., 2011. New observations of Asteroid (175706) 1996 FG3, primary target of the ESA Marco Polo-R mission. Astron. Astrophys. 530 (L12), 1–4.

DeMeo, F.E., Binzel, R.P., Slivan, S.M., Bus, S.J., 2009. An extension of the Bus asteroid taxonomy into the near-infrared. Icarus 202, 160–180.

Fujiwara, A. et al., 2006. The rubble-pile asteroid Itokawa as observed by Hayabusa. Science 312, 1330–1334.

Gaffey, M.J., 1997. Surface lithologic heterogeneity of asteroid 4 Vesta. Icarus 127, 130–157.

Hasegawa, S. et al., 2008. Albedo, size, and surface characteristics of Hayabusa-2 sample-return target 162173 1999 JU3 from AKARI and Subaru observations. Publ. Astron. Soc. Japan 60, S399–S405.

Hiroi, T., Pieters, C.M., Zolensky, M.E., Lipschutz, M.E., 1993. Evidence of thermal metamorphism on the C, G, B, and F asteroids. Science 261, 1016–1018.

Hiroi, T., Zolensky, M.E., Pieters, C.M., Lipschutz, M.E., 1996. Thermal metamorphism of the C, G, B, and F asteroids seen from the 0.7 μm, 3 μm and UV absorption strengths in comparison with carbonaceous chondrites. Meteorit. Planet. Sci. 31, 321–327.

Kawakami, K., Abe, M., Hasegawa, S., Kasuga, T., 2010. Observation of the post Hayabusa mission target Asteroid (162173) 1999 JU3. Jpn. Soc. Planet. Sci. 19, 4–11.

Kim, M.-J. et al., 2013. Optical observations of NEA 162173 (1999 JU3) during the 2011–2012 apparition. Astron. Astrophys. 550 (L11), 1–4.

Landolt, A.U., 1992. UBVRI photometric standard stars in the magnitude range $11.5 < V < 16.0$ around the celestial equator. Astrophys. J. 104, 340–371.

Lazzaro, D., Barucci, M.A., Perna, D., Jasmim, F.L., Yoshikawa, M., Carvano, J.M.F., 2013. Rotational spectra of (162173) 1999 JU3, the target of the Hayabusa 2 mission. Astron. Astrophys. 549 (L2), 1–4.

Marchi, S., Delbó, M., Morbidelli, A., Paolicchi, P., Lazzarin, M., 2009. Heating of near-Earth objects and meteoroids due to close approaches to the Sun. Mon. Not. R. Astron. Soc. 400, 147–153.

Michel, P., Delbó, M., 2010. Orbital and thermal evolutions of four potential targets for a sample return space mission to a primitive near-Earth asteroid. Icarus 209, 520–534.

Morbidelli, A., Chambers, J., Lunine, J.I., Petit, J.M., Robert, F., Valsecchi, G.B., Cyr, K.E., 2000. Source regions and timescales for the delivery of water to the Earth. Meteorit. Planet. Sci. 35, 1309–1320.

Müller, T.G. et al., 2011. Thermo-physical properties of 162173 (1999 JU3), a potential flyby and rendezvous target for interplanetary missions. Astron. Astrophys. 525, 1–6. A145.

Nakamura, T. et al., 2011. Itokawa dust particles: A direct link between S-type asteroids and ordinary chondrites. Science 333, 1113–1116.

Pieters, C.M., 1983. Strength of mineral absorption featuresin the transmitted component of near-infrared reflected light: First results from RELAB. J. Geophys. Res. 88, 9534–9544.

Polishook, D. et al., 2012. Asteroid rotation periods from the Palomar Transient Factory survey. Mon. Not. R. Astron. Soc. 421, 2094–2108.

Rayner, J., Toomey, D.W., Onaka, P.M., Denault, A.J., Stahlberger, W.E., Vacca, W.D., Cushing, M.C., 2003. SpeX: A medium-resolution 0.85.5 micron spectrograph and imager for the NASA infrared telescope facility. PASP 115, 362–382.

Reddy, V. et al., 2012a. Color and albedo heterogeneity of Vesta from Dawn. Science 336, 700–704.

Reddy, V., Gaffey, M.J., Abell, P.A., Hardersen, P.S., 2012b. Constraining albedo, diameter and composition of near-Earth asteroids via near-IR spectroscopy. Icarus 219, 382–392.

Reddy, V., Le Corre, L., Hicks, M., Lawrence, K., Buratti, B., Abell, P., Gaffey, M.J., Hardersen, P.S., 2012c. Composition of near-Earth asteroid 2008 EV5: Potential target for robotic and human exploration. Icarus 221, 678–681.

Reddy, V. et al., 2012d. Photometric, spectral phase and temperature effects on Vesta and HED meteorites: Implications for Dawn mission. Icarus 217, 153–168.

Richardson, J.E., Melosh, H.J., Greenberg, R., 2004. Impact-induced seismic activity on Asteroid 433 Eros: A surface modification process. Science 306, 1526–1529.

Rivkin, A.S., Howell, E.S., Vilas, F., Lebofksy, L.A., 2002. Hydrated minerals on asteroids: The astronomical record. In: Bottke, W.F., Cellino, A., Paolicchi, P., Binzel, R.P. (Eds.), Asteroids III. Univ. Arizona Press, Tucson, pp. 235–253.

Saito, J. et al., 2006. Detailed images of Asteroid 25143 Itokawa from Hayabusa. Science 312, 1341–1344.

Sanchez, J.A., Reddy, V., Nathues, A., Cloutis, E.A., Mann, P., Hiesinger, H., 2012. Phase reddening on near-Earth asteroids: Implications for mineralogical analysis, space weathering and taxonomic classification. Icarus 220, 36–50.

Sugita, S. et al., 2012. Visible spectroscopic observation of Asteroid 162173 (1999 JU3) with the Gemini-S telescope. In: 44th DPS Meeting. American Astronomical Society (Abstract 102.02).

Sunshine, J.M., Bus, S.J., McCoy, T.J., Burbine, T.H., Corrigan, C.M., Binzel, R.P., 2004. High-calcium pyroxene as an indicator of igneous differentiation in asteroids and meteorites. Meteorit. Planet. Sci. 39, 1343–1357.

Tonui, E.K., Zolensky, M.E., Lipschutz, M.E., Wang, M.-S., Nakamura, T., 2003. Yamato 86029: Aqueously altered and thermally metamorphosed CI-like chondrite with unusual textures. Meteorit. Planet. Sci. 38, 269–292.

Vernazza, P., Brunetto, R., Binzel, R.P., Perron, C., Fulvio, D., Strazzulla, G., Fulchignoni, M., 2009. Plausible parent bodies for enstatite chondrites and mesosiderites: Implications for Lutetias fly-by. Icarus 202, 477–486.

Vilas, F., 2008. Spectral characteristics of Hayabusa 2 near-Earth asteroid targets 162173 1999 JU3 and 2001 QC34. Astrophys. J. 135, 1101–1105.

Vilas, F., 2012. New spectral reflectance observations of Hayabusa 2 near-Earth asteroid target 162173 1999 JU3. In: 44th DPS Meeting. American Astronomical Society (Abstract 102.03).

Vilas, F., Sykes, M., 1996. Are low-albedo asteroids thermally metamorphosed? Icarus 124, 483–489.

PUBLICATIONS OF THE ASTRONOMICAL SOCIETY OF THE PACIFIC, **125**:357–395, 2013 April

The Pan-STARRS Moving Object Processing System

LARRY DENNEAU,[1] ROBERT JEDICKE,[1] TOMMY GRAV,[2] MIKAEL GRANVIK,[3] JEREMY KUBICA,[4] ANDREA MILANI,[5]
PETER VEREŠ,[1] RICHARD WAINSCOAT,[1] DANIEL CHANG,[1] FRANCESCO PIERFEDERICI,[6] N. KAISER,[1] K. C. CHAMBERS,[1]
J. N. HEASLEY,[1] EUGENE A. MAGNIER,[1] P. A. PRICE,[7] JONATHAN MYERS,[8] JAN KLEYNA,[1] HENRY HSIEH,[1]
DAVIDE FARNOCCHIA,[5,9] CHRIS WATERS,[1] W. H. SWEENEY,[1] DENVER GREEN,[1] BRYCE BOLIN,[1] W. S. BURGETT,[1]
J. S. MORGAN,[1] JOHN L. TONRY,[1] K. W. HODAPP,[1] SERGE CHASTEL,[1] STEVE CHESLEY,[9] ALAN FITZSIMMONS,[10]
MATTHEW HOLMAN,[11] TIM SPAHR,[12] DAVID THOLEN,[1] GARETH V. WILLIAMS,[12] SHINSUKE ABE,[13]
J. D. ARMSTRONG,[1] TERRY H. BRESSI,[14] ROBERT HOLMES,[15] TIM LISTER,[16]
ROBERT S. MCMILLAN,[14] MARCO MICHELI,[1] EILEEN V. RYAN,[17]
WILLIAM H. RYAN,[17] AND JAMES V. SCOTTI[14]

Received 2012 November 28; accepted 2013 February 26; published 2013 March 25

ABSTRACT. We describe the Pan-STARRS Moving Object Processing System (MOPS), a modern software package that produces automatic asteroid discoveries and identifications from catalogs of transient detections from next-generation astronomical survey telescopes. MOPS achieves $>99.5\%$ efficiency in producing orbits from a synthetic but realistic population of asteroids whose measurements were simulated for a Pan-STARRS4-class telescope. Additionally, using a nonphysical grid population, we demonstrate that MOPS can detect populations of currently unknown objects such as interstellar asteroids. MOPS has been adapted successfully to the prototype Pan-STARRS1 telescope despite differences in expected false detection rates, fill-factor loss, and relatively sparse observing cadence compared to a hypothetical Pan-STARRS4 telescope and survey. MOPS remains highly efficient at detecting objects but drops to 80% efficiency at producing orbits. This loss is primarily due to configurable MOPS processing limits that are not yet tuned for the Pan-STARRS1 mission. The core MOPS software package is the product of more than 15 person-years of software development and incorporates countless additional years of effort in third-party software to perform lower-level functions such as spatial searching or orbit determination. We describe the high-level design of MOPS and essential subcomponents, the suitability of MOPS for other survey programs, and suggest a road map for future MOPS development.

1. INTRODUCTION

As with most scientific endeavors, the history of asteroid and comet studies depicts an exponential increase in the rate of discovery since the identification of Ceres by Piazzi more than 200 years ago. This work describes the next step in the evolution of asteroid surveys—an integrated, end-to-end moving object processing system (MOPS) for the Panoramic Survey Telescope and Rapid Response System (Pan-STARRS Kaiser et al. 2002; Kaiser 2004; Hodapp et al. 2004). The system's prototype telescope (PS-1) employs a 1.4 gigapixel camera able to detect asteroids and comets faster than ever before.

The first asteroids were discovered serendipitously and laboriously by eye until the dedicated photographic surveys of the 1950s and 1960s like the Yerkes–McDonald (Kuiper et al. 1958) and Palomar Leiden Surveys (van Houten et al. 1970). The photographic surveys required a major effort due to the need for human 'blinking' of the images to identify the moving objects. The realization in the early 1980s by Alvarez et al. (1980) that the extinction of the dinosaurs ~65 million years ago was precipitated by the impact of a large asteroid or comet with the Earth stimulated enhanced funding for wide field

---

[1] Institute for Astronomy, University of Hawai'i, 2680 Woodlawn Drive, Honolulu, HI 96822; denneau@ifa.hawaii.edu.

[2] Johns Hopkins University, Baltimore, MD.

[3] Department of Physics, P.O. Box 64, 00014 University of Helsinki, Finland.

[4] Google, Inc.

[5] University of Pisa, Pisa, Italy.

[6] Space Telescope Science Institute, 3700 San Martin Drive, Baltimore, MD 21218.

[7] Department of Astrophysical Sciences, Princeton University, Princeton, NJ 08544.

[8] University of Arizona, Tucson, AZ.

[9] Jet Propulsion Laboratory, Pasadena, CA.

[10] Astrophysics Research Centre, School of Mathematics and Physics, Queen's University Belfast, Belfast, BT7 1NN, UK.

[11] Harvard-Smithsonian Center for Astrophysics, 60 Garden Street, Cambridge, MA 02138.

[12] Smithsonian Astrophysical Observatory, Cambridge, MA.

[13] Institute of Astronomy, National Central University, Taiwan.

[14] Lunar and Planetary Laboratory, University of Arizona, Tucson, AZ.

[15] Astronomical Research Institute, 7644 NCR 1800E, Charleston, IL 61920.

[16] Las Cumbres Observatory Global Telescope Network, Inc., 6740 Cortona Drive, Suite 102, Santa Barbara, CA 93117.

[17] Magdalena Ridge Observatory, New Mexico Tech, 801 Leroy Place, Socorro, NM 87801.

asteroid surveys. While those surveys identified many asteroids and comets that may eventually strike the Earth, only one object has been discovered that actually hit the Earth—2008 TC_3 (e.g., Jenniskens et al. 2009).

The photographic searches leveraged decades of experience in wide field astronomical surveying but Spacewatch (Gehrels 1991; McMillan 2007) spearheaded the first use of CCDs in asteroid surveys. In the beginning, the small CCDs of the time limited the success of this search program, but the asteroid discovery rate improved dramatically when they obtained a high quantum efficiency 2 K × 2 K CCD with an ~30 arcmin field of view and adopted a 'drift scanning' survey technique that eliminated the need for long readout times. At the same time, Rabinowitz (1991) developed the first automated moving object detection program to identify asteroids and comets in Spacewatch's drift-scan images that launched the contemporary generation of wide field surveys such as NEAT (Helin et al. 1997), LONEOS (Bowell et al. 1995), LINEAR (Stokes et al. 2000), and CSS (Larson 2007).

These modern wide field asteroid surveys were prompted and subsequently funded by the NASA Spaceguard Program (Harris 2008) with the goal of identifying 90% of near-Earth objects[18] (NEOs) larger than 1 km diameter before the end of 2008. All the surveys broadly employ similar techniques for asteroid and comet identification. Their wide field cameras have large pixel scales (typically $\gtrsim 1''$) and image a field 3–5 times within about an hour. Their moving object detection software identifies 'sources' in each image, and then spatially correlates the detections between the images to identify and remove stationary objects. All the 'transient detections' are then searched for consistency with a single object moving linearly across the sky at a constant rate of motion between the exposures. The constant motion requirement allows the software to achieve per-detection signal-to-noise (S/N) levels of ~1.5 to 3σ. Sets of 3–5 linked detections (a 'tracklet') representing candidate real moving objects are reported to the Minor Planet Center (MPC), though some groups review the detections by eye before submission to reduce the false detection rate. Overall, these groups were wildly successful, identifying ~79% of the ≥1 km NEOs before 2008 June 10 (Harris 2008). Mainzer et al. (2011) report that the Spaceguard goal of discovering 90% of the ≥1 km diameter asteroids was actually met some time later, but before 2011.

The CCD surveys described above were designed to discover large, extremely hazardous NEOs, not to characterize the size–frequency distribution (SFD) of various solar system populations. While the process of searching for the NEOs, they discovered several objects interesting in their own right (e.g., Comet Shoemaker–Levy 9 [Shoemaker 1995]; very fast moving objects, typically very small and nearby asteroids [Rabinowitz et al. 1993]; the Centaur object (5445) Pholus; 2008 TC_3 [Jenniskens et al. 2009]); and post facto determinations of their surveying efficiency allowed new estimations of the SFD of many small body populations (e.g., objects with orbits entirely interior to Earth's orbit, or IEOs [Zavodny et al. 2008]; NEOs [Rabinowitz 1993]; main belt [Jedicke & Metcalfe 1998]; Centaurs [Jedicke & Herron 1997]; trans-Neptunian objects, or TNOs [Larsen et al. 2001]; and distant objects [Larsen et al. 2007]). Despite the success of these programs, there is room for improvement in surveying techniques, moving object detection software, and reporting and follow-up methods:

1. Survey Technique and/or depth

The surveys in operation in 2003 were not capable of meeting the Spaceguard goal due to their sky-plane coverage and/or limiting magnitude (Jedicke et al. 2003). These surveys concentrated on the region of sky near opposition because asteroids are generally brightest in that direction but objects on orbits that *will* impact the Earth are under-represented towards opposition. Their sky-plane density increases at relatively small ecliptic latitudes and solar elongations $\lesssim 90$ deg (e.g., Chesley & Spahr 2004; Vereš et al. 2009). However, asteroids in this region of the sky are notoriously difficult to observe because of the limited time that they are above the horizon, the high air mass when they are visible, their large phase angle (reduced illumination of the visible surface) and faintness. Furthermore, the 3–5 repeat visits/night to the same field is wasteful of survey time. More sky could be covered, or the same sky could be imaged to greater depth, if there were fewer visits to the same field each night.

2. Follow-up

To maximize survey coverage and their discovery rate most of the surveys visit a field on only one night per lunation to obtain a set of 3–5 linked detections. The detections provide the sky plane location and velocity vector for the object rather than an orbit. To identify NEOs, the surveys flag objects with unusual rates of motion (e.g., Rabinowitz 1991; Jedicke 1996) as NEO candidates and then reacquire the objects in special follow-up efforts that reduce the time available for discovery of new objects. Alternatively, they report the detections to the MPC, who then perform a more sophisticated probabilistic analysis to determine the likelihood that the object may be a NEO. If the object meets their likelihood cutoff, it is posted on their NEO confirmation webpage[19] and hopefully recovered by professional and amateur astronomers around the world. Given that telescope time is a valuable commodity and that the next generation of professional asteroid survey telescopes will discover more and even fainter objects, it is clear that the survey

---

[18] Near-Earth objects are asteroids or comets with perihelion distances of ≤1.3 AU. Most of these objects are in unstable orbits with dynamical lifetimes of <10 Myrs (e.g., Gladman et al. 2000) and will quickly be ejected from the Solar System or impact the Sun or Jupiter, but a small fraction will eventually strike Earth.

[19] See http://www.minorplanetcenter.net/iau/NEO/ToConfirm.html.

telescopes must provide their own target follow-up and it should be incorporated directly into their survey pattern.

3. Moving object detection and orbit determination software

With limited follow-up resources and inefficiency in the ability to determine if a candidate asteroid is likely a NEO based on its magnitude and apparent rate of motion (its ‘digest’ score), it would be useful for a survey’s moving object detection system to determine orbits from observations over multiple nights instead of merely reporting sets of detections (tracklets) to the MPC. This allows for improved discovery rates of NEOs that are ‘hidden in plain sight’, indistinguishable from main-belt asteroids by their brightness and velocity vectors alone, and therefore scoring too low using the MPC’s NEO digest scoring to warrant follow-up.

4. Reporting

The system of reporting sets of detections to the MPC has been very effective and the follow-up response of the international community of amateur and professional observers has been fantastic as amply demonstrated by the case of 2008 TC$_3$ (Jenniskens et al. 2009). Still, the process of submission by e-mail to the MPC, posting on the NEO confirmation page, downloading and acquisition by observers is unwieldy. Since there is little coordination between observers there is the potential for wasted time with multiple and unnecessary follow-up. A modernized, automated reporting system tuned specifically to the capabilities and interests of each follow-up observatory would be useful to coordinate the follow-up effort.

5. Measured system efficiency

Existing asteroid detection software packages do not monitor their own detection efficiency and accuracy. Instead, analysis of the survey data must be performed post facto. It would be convenient if the packages incorporated an intrinsic near real-time measure of both their efficiency and accuracy for the purpose of system monitoring and subsequent data reduction.

Some of the problems itemized above have been addressed by other surveys, in particular the well-characterized main belt program of Gladman et al. (2009) using software developed by Petit et al. (2004). They generate synthetic detections in the same images used to identify their TNO candidates to measure the detection efficiency and accuracy.

The future of wide field moving object processing systems is embodied in software such as the Panoramic Survey Telescope and Rapid Response System (Pan-STARRS; Kaiser et al. 2002; Kaiser 2004) Moving Object Processing System (MOPS), described in the remainder of this article. MOPS incorporates state-of-the-art spatial searching, orbit computation, and database management into a cohesive package. MOPS resolves many of the issues described above and the system is capable of very high efficiency and accuracy.

2. Pan-STARRS AND Pan-STARRS1

The University of Hawai‘i’s Pan-STARRS project was formed in 2002 to design and build a next-generation distributed-aperture survey system called Pan-STARRS4 (Kaiser et al. 2002). The Pan-STARRS4 design incorporates four distinct telescopes on a common mount on the summit of Mauna Kea. Shortly after inception, the project began development and construction of a single-telescope prototype system called Pan-STARRS1 (Hodapp et al. 2004; Morgan et al. 2006) on Haleakala, Maui, to validate essential components such as optics, camera and software pipelines. As of 2013, the Pan-STARRS project is constructing a second telescope called Pan-STARRS2, essentially identical to Pan-STARRS1, at the same site on Haleakala. The combination of Pan-STARRS1 and Pan-STARRS2 is called PS1+2, and it is expected that the two telescopes will be operated together as part of a single science mission.

The Pan-STARRS1 telescope on Haleakala, Maui, began surveying for asteroids in the spring of 2010. This 1.8 m diameter telescope has a $\sim 7\ \mathrm{deg}^2$ field of view and a ~ 1.4 gigapixel orthogonal transfer array (OTA) CCD camera (Tonry et al. 1997, 2004) with $0.26''$ pixels. Pan-STARRS1’s large aperture, field of view and $\lesssim 13$ s between exposures allows imaging of the entire night sky visible from Hawai‘i to $r \sim 21.2$ in about five or six nights. In practice, two to eight images of the same field are acquired each night, and consequently it takes longer to cover the entire night sky.

The Pan-STARRS1 telescope is operated by the Pan-STARRS1 Science Consortium (PS1SC; Chambers 2006, 2007) with a nominal mission of 3.5 surveying years. The PS1SC survey plan incorporates about a half dozen subsurveys, but only three are suitable for moving object discovery (all the surveys are suitable for moving object *detection* because they all obtain at least one pair of images of each field each night)—the 3π all-sky survey, the medium deep (MD) survey, and the solar system survey.

The Pan-STARRS1 detector system employs six passbands: g_{P1}, r_{P1}, i_{P1}, z_{P1}, y_{P1} and w_{P1}. Tonry et al. (2012) provide a detailed description of the Pan-STARRS1 photometric system—the first four passbands were designed to have similar characteristics to the SDSS (e.g., Karaali et al. 2005), y_{P1} was designed to take advantage of the good sensitivity of the Pan-STARRS1 camera near 1 μm and the $\mathcal{W}_{P1}$ has a wide bandpass with high- and low-wavelength cutoffs designed to optimize the S/N for S and C class asteroids. Transformations from each filter to the V band are provided in Table 1 for an object with solar colors and also for an object with an average S+C class spectrum. The difference between the solar and mean asteroid class transformations are significant since the Pan-STARRS1 photometric system currently provides better than 1% photometry (Schlafly et al. 2012) in at least the 3π survey’s filters.

The 3π survey images the entire sky north of -30° declination multiple times in three passbands (g_{P1}, r_{P1}, i_{P1}) in a single year. About half the sky within $\pm 30^\circ$ (2 hr) of opposition in R.A. is imaged in the different passbands each lunation. The solar system survey is performed in the wide filter ($\mathcal{W}_{\mathrm{P1}}$) and most

TABLE 1

MOPS PAN-STARRS1 FILTER TRANSFORMATIONS

Transform	Solar	Mean S+C	$t_{\rm exp}$ (s)[a]
V-g_{P1}	−0.217	−0.28	43
V-r_{P1}	0.183	0.23	40
V-i_{P1}	0.292	0.39	45
V-z_{P1}	0.311	0.37	30
V-y_{P1}	0.311	0.36	30
V-w_{P1}	0.114	0.16	45

NOTE.—Transformations from Johnson V to the six Pan-STARRS filters are provided for both a standard solar spectrum and asteroids with a mean S+C spectral type. These transformations have been implemented by the Minor Planet Center and AstDyS. From Tonry et al. (2012).

[a] Exposure times as of October 2012.

of that time is spent near the ecliptic and near opposition to maximize the NEO discovery rate. A small percentage of solar system survey time is used to image the 'sweet spots' for potentially hazardous asteroids[20] (PHAs) within about ±10° of the ecliptic and as close to the Sun as possible, subject to altitude, sky brightness constraints, etc. The MD survey obtains eight-exposure sequences at 10 different fixed footprints on the sky, with an integration time of 1920s per sequence. MD sequences are observed using either 8×240 s exposures in a single filter (i_{P1}, z_{P1}, y_{P1}), or back-to-back sequences of 8×120 s exposures in g_{P1} and r_{P1}.

Visits to the same footprint within a night are usually separated by about 15 minutes, a 'transient time interval' (TTI), suitable for asteroid detection. The Image Processing Pipeline (IPP; Magnier [2006]) produces a source list of transient detections, i.e., In new sources at some position in the image and/or those that change brightness but are otherwise not identifiable as false transients like cosmic rays or other image artifacts. The IPP then publishes the catalogs of transient detections to MOPS which searches for moving objects.

3. THE Pan-STARRS MOVING OBJECT PROCESSING SYSTEM (MOPS)

3.1. Overview

MOPS software development began in 2003 under management by the Pan-STARRS Project, with a mission to discover hazardous NEOs and other solar system objects while providing real-time characterization of its performance. Initial funds for Pan-STARRS construction and engineering were obtained by the University of Hawai'i via a grant from the United States Air Force Research Laboratory (AFRL). MOPS was the first and only science client to be funded by the Pan-STARRS Project—systems engineering, testing, performance tuning, and creation of the synthetic solar system model (S3M, § 3.10) were directly supported by project resources. Additional in-kind software contributions from external collaborators in the areas of orbit determination (Granvik et al. 2009; Milani & Gronchi 2010), spatial searching (Kubica et al. 2007) and algorithm design (Tyson & Angel 2001) were incorporated via memoranda of understanding (MOUs). In 2008, the NASA Near Earth Objects Observations (NEOO) Program Office began its support of continued MOPS development and Pan-STARRS1 operations.

MOPS is the first integrated detector system that processes data from per-exposure transient detection source lists through orbit determination, precovery, and attribution. We sought to create a system that could independently measure our system's end-to-end throughput and efficiency for the purpose of correcting for observational selection effects (Jedicke et al. 2002). Our philosophy was that it is more important to accurately know the system efficiency than to be place all our effort in optimization. Figure 1 provides a high-level view of data flow into, through and from MOPS. Each of the MOPS data processing substeps is described in the following subsections.

In the Pan-STARRS system design there is a functional separation between the image processing (IPP) and moving object processing (MOPS). Unlike the object detection algorithm of, e.g., Petit et al. (2004), the MOPS design mandates no integration with the image data. This was an intentional design decision based on the scale and organization of the Pan-STARRS project. The IPP is responsible for monitoring and reporting its detection efficiency and accuracy as is MOPS. In this way, each Pan-STARRS subsystem can be developed and characterized independently.

MOPS data processing consists of assembling groups of transient detections into progressively larger constructions until there are enough detections to produce a high-quality orbit believed to represent a real asteroid—a 'derived object'. Intranight (same night) detection groupings are called 'tracklets' and internight (multinight) groupings are called 'tracks'. All tracks created by MOPS are evaluated by an orbit computation module after which a track is either (1) deemed to represent a real asteroid, or (2) rejected and its constituent tracklets returned to the pool of unassociated tracklets. When a derived object is created MOPS uses the object's computed (derived) orbit to search for additional detections of the asteroid in MOPS data to further refine the orbit.

MOPS expects its incoming transient detection stream to be organized by exposure, or *field* in MOPS parlance. Each field within MOPS is defined by its metadata, e.g., (right ascension, declination [R.A., decl.]) boresight coordinates, exposure date and duration, filter. A MOPS detection by definition occurs in exactly one field and is defined by its position, e.g., (R.A., decl.) in the field, observed magnitude, signal-to-noise (S/N), and associated uncertainties.

---

[20] PHAs are NEOs with orbits that approach to within 0.05 AU of the Earth's orbit and have absolute magnitudes $H < 22$.

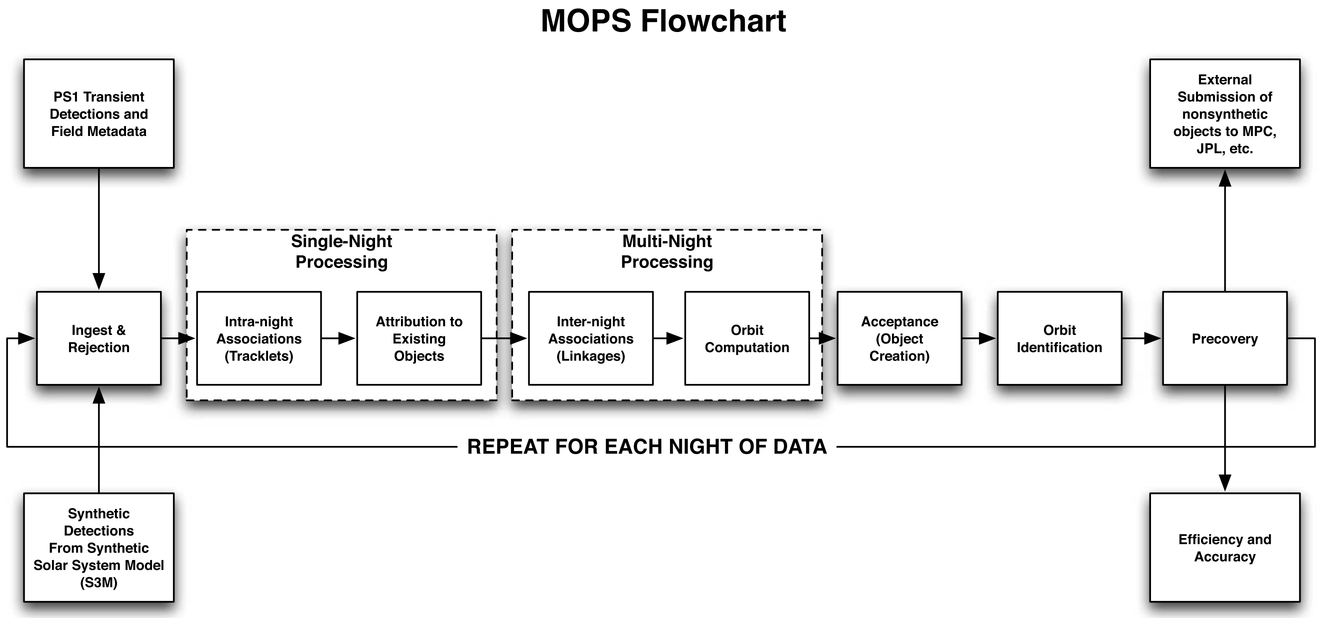

FIG. 1.—High-level flowchart for the Pan-STARRS1 Moving Object Processing System (MOPS). The data processing proceeds from left to right in the figure, then repeats for every additional night of data ingested by MOPS.

3.2. Pipeline Design

The MOPS pipeline operates by using a linear nightly processing model in which data are ingested and processed in the order they are observed. Nightly data are ingested from a live transient detection stream and discrete processing stages are executed until all processing is completed for the entire night. Many of the MOPS processing stages build upon data structures created from prior nights.

Out-of-order processing can be handled in a limited number of modes of operation as necessitated by the current Pan-STARRS1 system. Enhancements to the MOPS pipeline to perform full processing on out-of-order data while preserving essential MOPS efficiency computations is still under development. The fundamental difficulty in out-of-order processing lies with the amount of data that needs to be recomputed when new observations are inserted in the middle of the temporal data stream. The existing MOPS design prefers nights to be added incrementally; insertion into the middle of the existing dataset essentially forces all subsequent nights to be reprocessed.

Pipeline resource scheduling and management are handled by the Condor high-throughput-computing software (Thain et al. 2005). Condor provides effective, flexible management of hardware resources that need to run the MOPS production pipeline simultaneously with test simulations or experimental processing of MOPS data.

The MOPS pipeline is designed to be reliable in the event of cluster resource limitations and hardware failure (e.g., power outages, node failures). Working in tandem with Condor's process management infrastructure, the MOPS pipeline can be restarted easily at the proper point in the pipeline with all data structures intact. As an example, in 2011 the MOPS production MySQL database suffered a complete failure yet the MOPS pipeline was back online within hours after restoring the database from a backup.

The discussion of each element of the MOPS pipeline is deferred to § 5 where we follow the processing of detections from beginning to end of the pipeline and quantify the performance of each step using Pan-STARRS1 data.

3.3. Hardware

The Pan-STARRS1 MOPS runs on a modest cluster of standard Linux rack-mounted computers. MOPS makes no special demands on hardware so long as the cluster can keep up with incoming data. During early stages of MOPS design, we based hardware requirements on estimates for transient detections stored and orbits computed per night of observing for a Pan-STARRS4-like mission, and scaled down the storage for Pan-STARRS1 volumes. The current Pan-STARRS1 processing hardware is capable of keeping up with a Pan-STARRS4-like data stream, except for the storage of detections in the database. Table 2 lists the major hardware components employed by the Pan-STARRS1 MOPS production processing cluster, and Figure 2 shows the functional relationships between the MOPS hardware components.

To ensure against most of the types of disk failures we are likely to encounter, we use a multiple-parity redundant array of

TABLE 2

PAN-STARRS1 MOPS HARDWARE COMPONENTS (SEE FIG. 2)

Item	Purpose	Number	Total capacity
Disk	Database storage	2 × 10 TB	20 TB[a]
Disk	Administrative	2 × 2.7 TB	5.4 TB
CPU	Cluster processing	8 × 4 cores	32 cores (~100 GFLOPS)
CPU	Administrative[b]	2 × 4 cores	8 cores (~25 GFLOPS)
Network switch	Network	32 ports	1 Gbps/port

[a] All database storage employs RAID6 for data integrity.

[b] Administrative functions include a user console, pipeline and Condor workflow management, and the web interface.

independent drives (RAID6) for our database storage, meaning multiple parity bits for every byte stored on disk. This allows up to two drives to fail concurrently and still keep the disk array operational.

Condor's workflow management automatically detects host-level failures and redistributes jobs appropriately. An entire cluster computation node can fail during a processing step and the MOPS pipeline will adjust seamlessly.

MOPS pipeline administrative functions are handled by a 'fat' workstation-class computer that runs the main MOPS pipeline, Condor manager and MOPS web interface (described later). We distribute these functions between two identically configured hosts so that one can fail completely, its responsibilities then assumed by the other node at slightly degraded performance. During Pan-STARRS1 commissioning and operations we have experienced complete database host failures, accidental deletion of a production MOPS database by a MOPS administrator, and numerous compute node failures, without loss of data or significant interruption of MOPS processing.

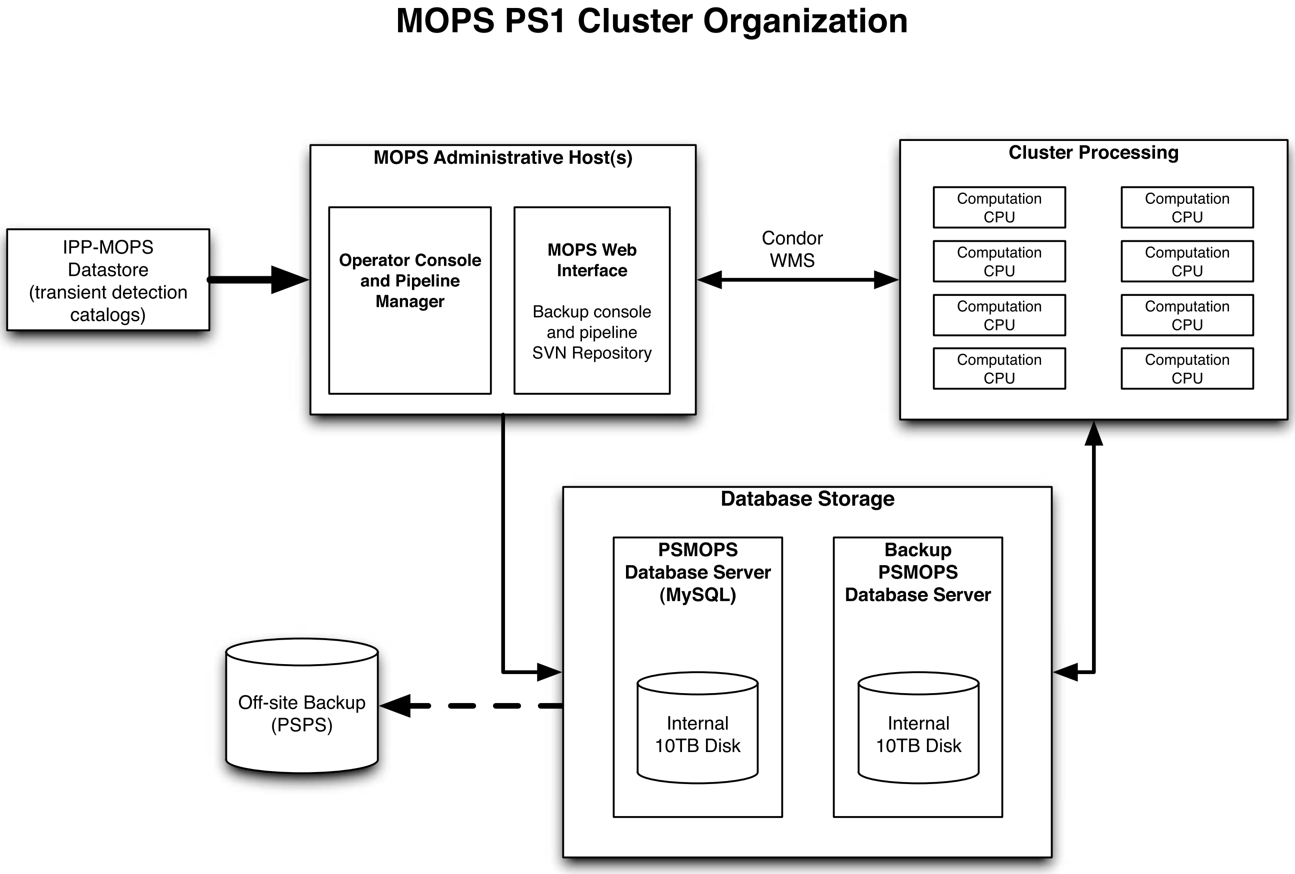

FIG. 2.—MOPS Pan-STARRS1 cluster configuration.

3.4. Database

Table 3 shows the storage required for MOPS database components under Pan-STARRS1 and estimates for Pan-STARRS4. The catalog of high-significance detections and derived data products are stored in an industry-standard relational database to maximize interoperability with external analysis software and provide data mining capability. Data are organized into multiple row–column tables in which rows of one table may be related to rows in another table (see Fig. 3). For example, the MOPS FIELDS table contains exposure metadata describing the telescope pointing, exposure time, filter, etc., for a single exposure. Each `FIELD` record is additionally assigned a unique identifier called `FIELD_ID`. A second table called `DETECTIONS` contains all transient detections ingested by MOPS and, to relate detections to a particular exposure, all detections from the exposure are assigned a `FIELD_ID` upon ingest that matches their exposure's `FIELD_ID`. Subsequent derived relations (e.g., groupings of detections into an asteroid 'identification' and computation of its derived orbit) are similarly maintained and are described in detail later.

A relational database allows MOPS data to be manipulated, analyzed and queried by any external software that supports structured query language (SQL). Requests for both a small amount of data (such as a detection) or a large amount of data (e.g., all derived objects with $q < 1.3$) are made through a SQL query and the results are returned in a tabular representation.

The MySQL relational database management system (RDBMS) was selected for MOPS because of its combination of performance and cost but other database vendors such as PostgreSQL and Oracle were considered and evaluated early in MOPS development. Any modern database system would work for MOPS as they all scale to billions of rows and have additional features that promote data integrity and system reliability.

3.5. Low-Significance Database

MOPS was designed to perform searches for recovery observations using a lower-significance data archive called the 'low-significance dataset' (LSD). In normal MOPS processing a nominal confidence level, typically 5σ, is used as a baseline for all processing. The Pan-STARRS4 camera and image processing are expected to deliver ~1500 5σ detections per exposure. Below this confidence level, the density of false associations becomes so great that it overwhelms the data processing. However, the search for recovery or precovery observations of an object with a known orbit may constrain the predicted position and velocity enough to make it possible to identify observations in the LSD.

Due to the much larger number of lower-significance sources in an astronomical image (there are 1000× more 3σ than 5σ detections) LSD detections are *not* stored in the MOPS relational database. Instead, they are stored in flat files on the local or network file system. The LSD archive is designed to be compact and efficiently searchable by exposure epoch, right ascension and declination. During only the attribution and precovery phases of MOPS processing, candidate 3σ recovery observations are extracted for analysis from this dataset based on predicted positions, and successful recoveries are than 'promoted' into the high-confidence database.

3.6. Data Exchange Standard

Significant work related to early MOPS development and simulations led to creation of the Data Exchange Standard (DES)

TABLE 3
MOPS DATABASE STORAGE REQUIREMENTS

Data component	PS4 estimated (GB)	PS1 estimated (GB)	PS1 actual[a] (GB)
Fields	0.2	0.06	0.02
3σ Detections	500,000	150,000	N/A[b]
5σ Detections	500	150	122
Derived object parameters	1,000	300	0.152[c]
Synthetic object parameters	1,100	330	2.43[d]
Tracklets	1,200	360	2.19[e]
Image postage stamps	N/A	N/A	1,800[f]

[a] As of October 2012, 2.5 years into the 3.5 year Pan-STARRS1 survey.

[b] Processing of transients below 3σ confidence is currently untenable for Pan-STARRS1 MOPS due to the systematic false tracklet rate.

[c] MOPS produces derived object parameters for only a small subset of Pan-STARRS1 data until the pipeline can be tuned for Pan-STARRS1 performance.

[d] Pan-STARRS1 operations uses a $1/10$ sampled synthetic solar system model (S3M). A final Pan-STARRS1 processing of its transient catalog will include a full S3M.

[e] Pan-STARRS1 single-exposure sensitivity reduces the actual tracklet count on top of the reduction from a shorter survey than Pan-STARRS4.

[f] Image postage stamps (200 × 200 pixels) are stored on a network file system, not in the MOPS database. They are locatable using database records.

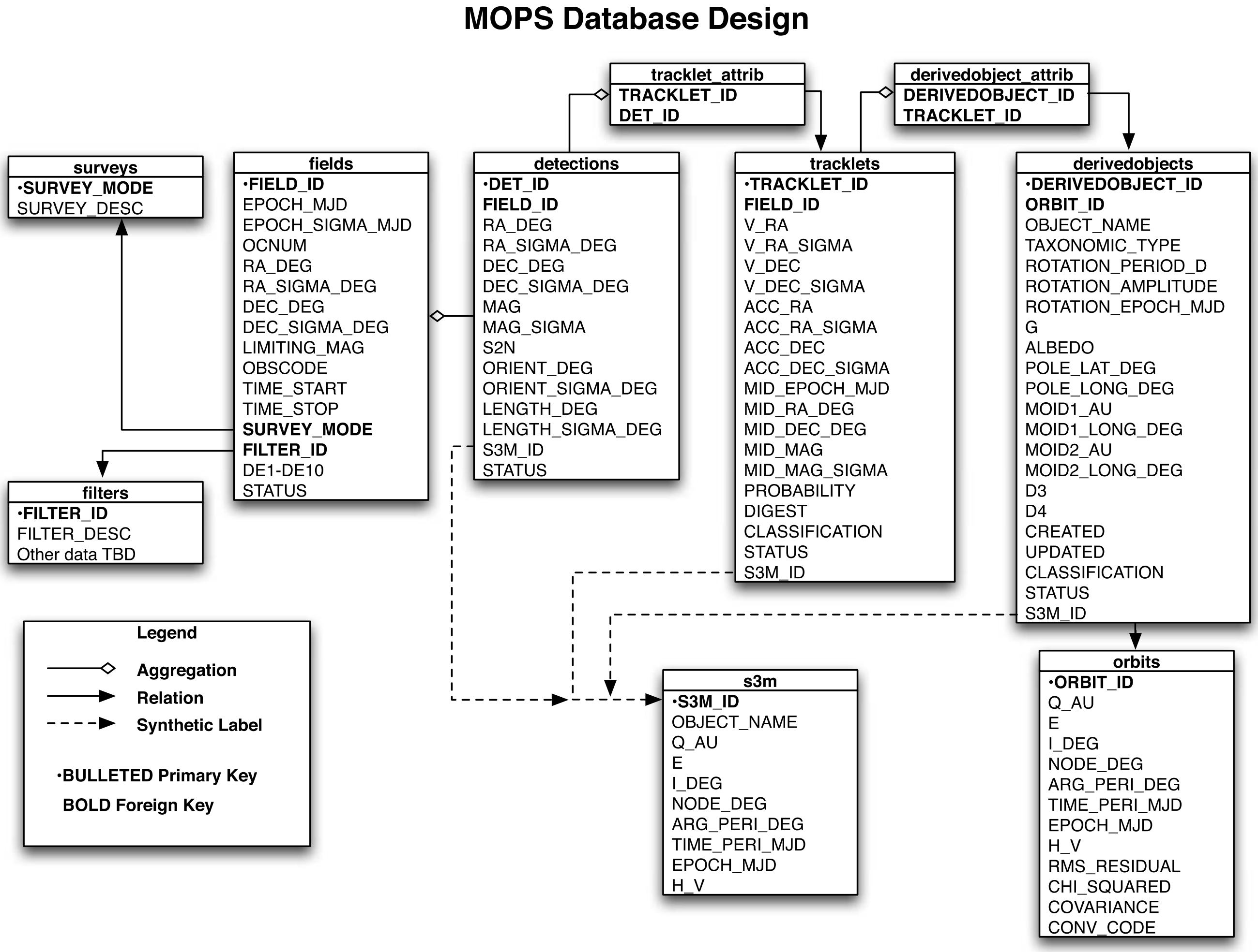

FIG. 3.—MOPS database schema. S3M columns indicate synthetic data for efficiency assessment.

for Solar System Object Detections and Orbits.[21] The DES describes a file format for dissemination of observations and orbits of solar system objects and is used within MOPS and between MOPS and add-on MOPS software developed by Milani and the OrbFit Consortium (Milani et al. 2008, 2012). It provides mechanisms for reproducing detection ⇔ tracklet and tracklet ⇔ derived object relations that exist in the MOPS database, and allows for specification of statistical uncertainties for observational measures. The DES includes provisions for propagating

1. orbit covariance and normal matrices,
2. detailed per-detection residuals,
3. ephemerides for real and synthetic asteroids,
4. detailed tracklet metrics beyond the scope of MOPS, and
5. radar and spacecraft observations.

3.7. Web Interface

Early in MOPS development we realized the utility of visual, Web-based interrogation of the MOPS database, leading to the creation of the MOPS *Web interface*. The MySQL RDBMS provides software 'hooks' into its internal code that allow Web-friendly scripting languages to perform queries so that web-based user interfaces and reporting tools can be developed rapidly.

The MOPS database user has ready visual representation of the MOPS processing stream, from a sky map of the nightly survey pattern, detection maps of each observed field indicating both synthetic and real detections, to the orbit distributions of derived objects, to the efficiency and accuracy of each of the processing steps. Pages for a single MOPS derived object show the object's linking history and the evolution of its orbit at each step. Figure 4 shows the nightly sky map of an active MOPS database.

3.8. Data Export

The primary consumer of MOPS exported data products is the IAU Minor Planet Center (MPC) that maintains the

---

[21] See Pan-STARRS document PSDC-530-004 by Milani et al., Data Exchange Standard (2.03) for solar system object detections and orbits: A tool for Input/Output definition and control.

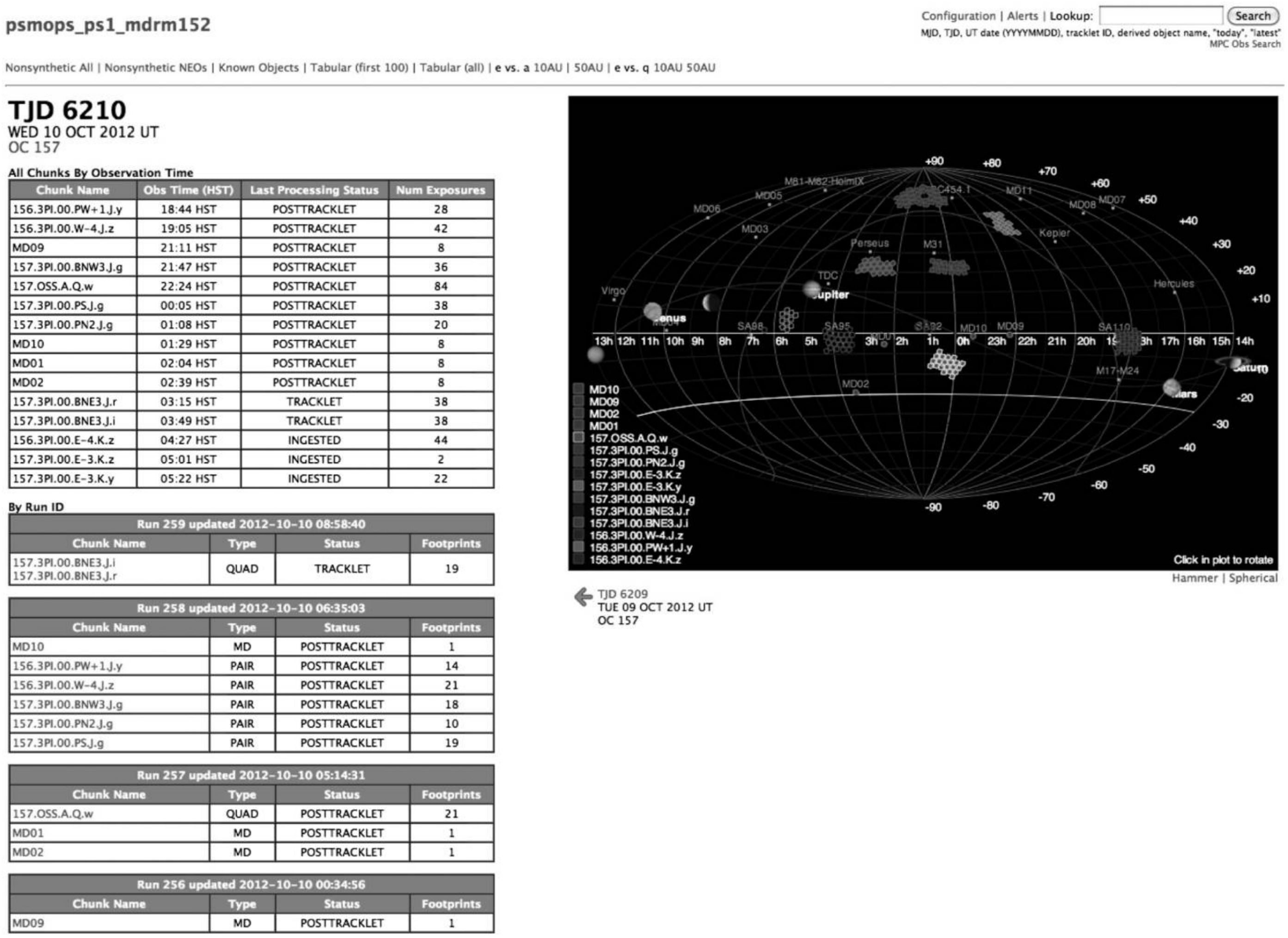

psmops_ps1_mdrm152

Configuration | Alerts | Lookup: Search
MJD, TJD, UT date (YYYYMMDD), tracklet ID, derived object name, "today", "latest"
MPC Obs Search

Nonsynthetic All | Nonsynthetic NEOs | Known Objects | Tabular (first 100) | Tabular (all) | e vs. a 10AU | 50AU | e vs. q 10AU 50AU

TJD 6210
WED 10 OCT 2012 UT
OC 157

All Chunks By Observation Time

Chunk Name	Obs Time (HST)	Last Processing Status	Num Exposures
156.3PI.00.PW+1.J.y	18:44 HST	POSTTRACKLET	28
156.3PI.00.W-4.J.z	19:05 HST	POSTTRACKLET	42
MD09	21:11 HST	POSTTRACKLET	8
157.3PI.00.BNW3.J.g	21:47 HST	POSTTRACKLET	36
157.OSS.A.Q.w	22:24 HST	POSTTRACKLET	84
157.3PI.00.PS.J.g	00:05 HST	POSTTRACKLET	38
157.3PI.00.PN2.J.g	01:08 HST	POSTTRACKLET	20
MD10	01:29 HST	POSTTRACKLET	8
MD01	02:04 HST	POSTTRACKLET	8
MD02	02:39 HST	POSTTRACKLET	8
157.3PI.00.BNE3.J.r	03:15 HST	TRACKLET	38
157.3PI.00.BNE3.J.i	03:49 HST	TRACKLET	38
156.3PI.00.E-4.K.z	04:27 HST	INGESTED	44
157.3PI.00.E-3.K.z	05:01 HST	INGESTED	2
157.3PI.00.E-3.K.y	05:22 HST	INGESTED	22

By Run ID

Run 259 updated 2012-10-10 08:58:40			
Chunk Name	**Type**	**Status**	**Footprints**
157.3PI.00.BNE3.J.i 157.3PI.00.BNE3.J.r	QUAD	TRACKLET	19

Run 258 updated 2012-10-10 06:35:03			
Chunk Name	**Type**	**Status**	**Footprints**
MD10	MD	POSTTRACKLET	1
156.3PI.00.PW+1.J.y	PAIR	POSTTRACKLET	14
156.3PI.00.W-4.J.z	PAIR	POSTTRACKLET	21
157.3PI.00.BNW3.J.g	PAIR	POSTTRACKLET	18
157.3PI.00.PN2.J.g	PAIR	POSTTRACKLET	10
157.3PI.00.PS.J.g	PAIR	POSTTRACKLET	19

Run 257 updated 2012-10-10 05:14:31			
Chunk Name	**Type**	**Status**	**Footprints**
157.OSS.A.Q.w	QUAD	POSTTRACKLET	21
MD01	MD	POSTTRACKLET	1
MD02	MD	POSTTRACKLET	1

Run 256 updated 2012-10-10 00:34:56			
Chunk Name	**Type**	**Status**	**Footprints**
MD09	MD	POSTTRACKLET	1

☐	MD10
☐	MD09
☐	MD02
☐	MD01
☐	157.OSS.A.Q.w
☐	157.3PI.00.PS.J.g
☐	157.3PI.00.PN2.J.g
☐	157.3PI.00.E-3.K.z
☐	157.3PI.00.E-3.K.y
☐	157.3PI.00.BNW3.J.g
☐	157.3PI.00.BNE3.J.r
☐	157.3PI.00.BNE3.J.i
☐	156.3PI.00.W-4.J.z
☐	156.3PI.00.PW+1.J.y
☐	156.3PI.00.E-4.K.z

← TJD 6209
TUE 09 OCT 2012 UT
OC 157

FIG. 4.—Pan-STARRS1 MOPS Web interface showing the sky map for the night of MJD 56210. On the left are lists of observing blocks executed by the telescope for the night.

authoritative catalog of observations and orbits for minor planets, comets and natural satellites. As of early 2013, the MPC prefers e-mail data submission because the Pan-STARRS1 survey is oriented toward reporting single-night tracklets, not multiple-night derived objects.

Under the Pan-STARRS4 processing model in which MOPS produces derived objects with secure orbits on a regular basis, MOPS is capable of exporting monthly DES catalogs of detections, tracklets, orbits and identification records for known and unknown derived objects. Pilot submissions to the MPC showed that this export and publication model works as long as the false derived object rate is suitably low (e.g., $<0.1\%$; Spahr, personal communication).

Early Pan-STARRS1 processing revealed a false derived object rate too high for automatic submission to the MPC and an unsatisfactory NEO discovery rate so, to improve the short-term science output and satisfy funding agency requirements, the PS1SC abandoned the derived object processing model in favor of the traditional tracklet reporting method employed by other asteroid surveys. Processing of derived objects will be restored for the final postsurvey MOPS processing, but the derived object throughput will be small due to the Pan-STARRS1 survey strategy being optimized for single-night NEO discovery.

Detections are distributed to the MPC via email after a human 'czar' visually verifies that candidates are real using the MOPS Web-based interface. (NEO candidates consume most of the czar's time because of the high rate of false tracklets at high rates of motion.) In this display, a page lists nightly probable real asteroid tracklets with highlighted NEO candidate tracklets (see Fig. 5). Tracklets that belong to known numbered and multi-opposition objects are identified by a MOPS add-on module called known_server (Milani et al. 2012) and automatically submitted to the MPC. A MOPS administrative e-mail account receives MPC confirmation email to verify the MOPS

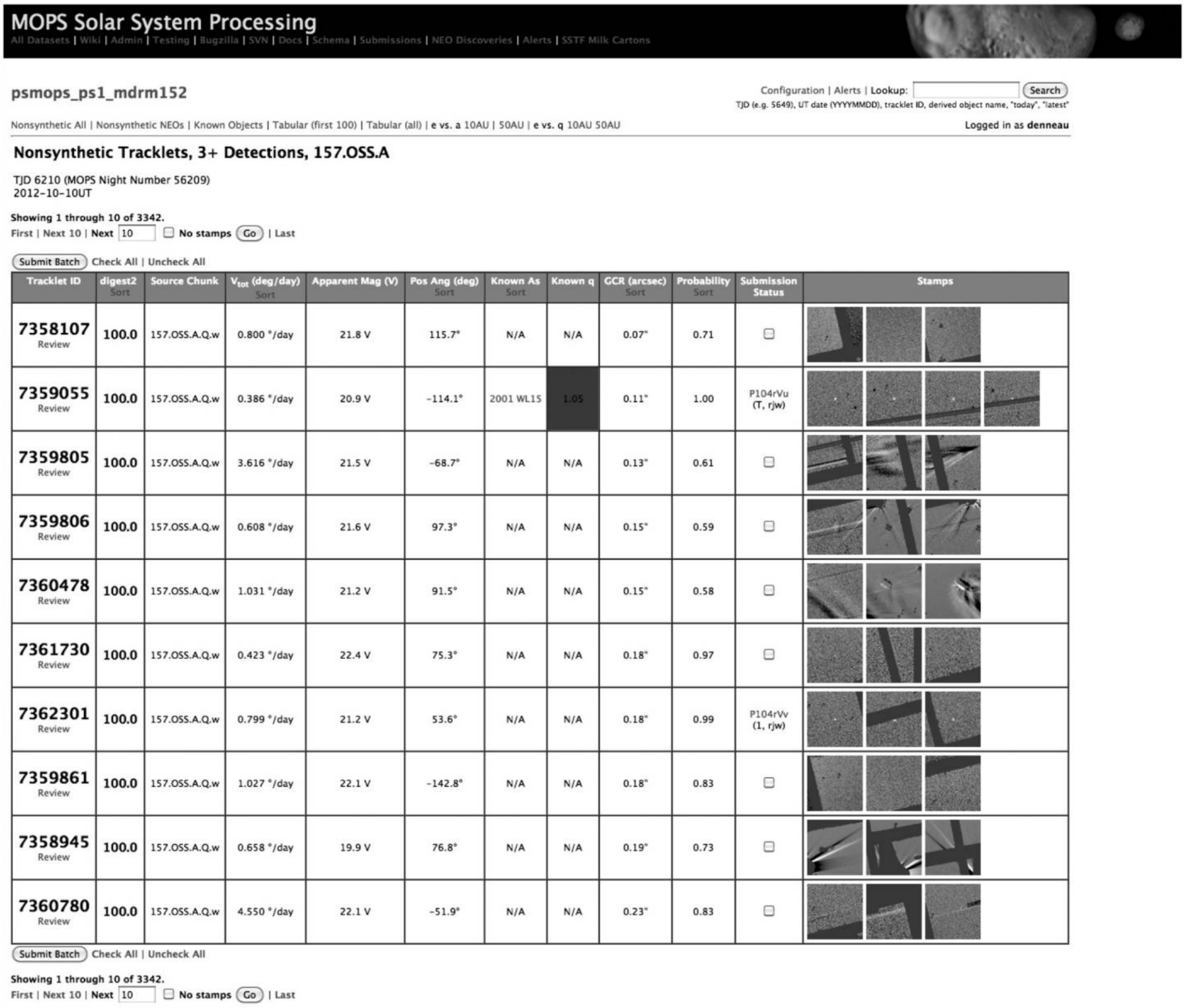

MOPS Solar System Processing

psmops_ps1_mdrm152

Nonsynthetic Tracklets, 3+ Detections, 157.OSS.A

TJD 6210 (MOPS Night Number 56209)
2012-10-10UT

Showing 1 through 10 of 3342.

Tracklet ID	digest2 Sort	Source Chunk	V_{tot} (deg/day) Sort	Apparent Mag (V)	Pos Ang (deg) Sort	Known As Sort	Known q	GCR (arcsec) Sort	Probability Sort	Submission Status	Stamps
7358107 Review	100.0	157.OSS.A.Q.w	0.800 °/day	21.8 V	115.7°	N/A	N/A	0.07"	0.71	☐	
7359055 Review	100.0	157.OSS.A.Q.w	0.386 °/day	20.9 V	-114.1°	2001 WL15	1.05	0.11"	1.00	P104rVu (T, rjw)	
7359805 Review	100.0	157.OSS.A.Q.w	3.616 °/day	21.5 V	-68.7°	N/A	N/A	0.13"	0.61	☐	
7359806 Review	100.0	157.OSS.A.Q.w	0.608 °/day	21.6 V	97.3°	N/A	N/A	0.15"	0.59	☐	
7360478 Review	100.0	157.OSS.A.Q.w	1.031 °/day	21.2 V	91.5°	N/A	N/A	0.15"	0.58	☐	
7361730 Review	100.0	157.OSS.A.Q.w	0.423 °/day	22.4 V	75.3°	N/A	N/A	0.18"	0.97	☐	
7362301 Review	100.0	157.OSS.A.Q.w	0.799 °/day	21.2 V	53.6°	N/A	N/A	0.18"	0.99	P104rVv (1, rjw)	
7359861 Review	100.0	157.OSS.A.Q.w	1.027 °/day	22.1 V	-142.8°	N/A	N/A	0.18"	0.83	☐	
7358945 Review	100.0	157.OSS.A.Q.w	0.658 °/day	19.9 V	76.8°	N/A	N/A	0.19"	0.73	☐	
7360780 Review	100.0	157.OSS.A.Q.w	4.550 °/day	22.1 V	-51.9°	N/A	N/A	0.23"	0.83	☐	

Showing 1 through 10 of 3342.

FIG. 5.—Pan-STARRS1 MOPS Web interface showing the NEO 'czar' page. From this page, NEO candidates can be submitted to the IAU Minor Planet Center. Rows 2 and 7 are 2001 WL_{15} and 2012 TN_{139} respectively.

submissions. MOPS maintains its own table of submitted tracklets to the MPC for easy reproduction of submitted detection details and to prevent multiple submissions of the same tracklets.

3.9. Alert System

The MOPS Alert System is a software agent that runs independently of standard MOPS processing and searches for events that require immediate notification or follow-up. The specific type of event is user-configurable using a small piece of Python code written by a MOPS scientist or engineer to query for interesting events. A typical example would be a fast-moving near-Earth object (NEO) candidate tracklet that is unlikely to be observed again by the survey telescope and/or needs immediate follow-up so that it is not lost. In this case, the alert system identifies the candidate tracklet by its sky-plane rate of motion and the fact that the tracklet's positions cannot be attributed to a known asteroid. Additional examples of alerts are tracklets of unknown objects with comet-like motion or extended morphology, or known objects with magnitude anomalies that indicate activity.

The alert system allows alerts to be triggered from either a MOPS derived object or an individual tracklet. The alert payload itself is an extensible markup language (XML) VOEvent (e.g., Seaman et al. 2011), a standardized data structure that can be consumed by automatic data-processing agents. The alert deployment infrastructure can be changed easily; the current MOPS implementation uses both a restricted internet email distribution list and a private Twitter feed to PS1 Science Consortium partners.

Alerts are organized using a publish-subscribe paradigm in which multiple alert definitions can be published to various 'channels' that may be subscribed to by multiple users. For example, a 'NEO channel' might publish alerts for near-Earth object alerts ($q < 1.3$ AU) and potentially hazardous objects (NEOs with $H < 22.5$ and minimum orbital intersection distance <0.05 AU). Such a channel could be subscribed to by NEO follow-up organizations. Alerts currently in use by the PS1SC include unusual lightcurves within a single night and detections of objects from asteroid families of interest (e.g., Hildas).

3.10. Synthetic Solar System Model

One major MOPS innovation is the incorporation of a synthetic solar system model (S3M; Grav et al. 2011) that allows us to monitor MOPS development and measure its performance in real-time operations as quantified by the metrics defined in § 3.1. It is important to introduce realistic detections of solar system objects into the processing system to ensure that it can handle real objects and to measure a realistic detection efficiency. The solar system model has been described in detail by Grav et al. (2011) and we only provide a brief overview here.

The S3M is a comprehensive flux-limited model of the major small body populations in the solar system that consists of objects ranging from those that orbit the Sun entirely interior to the Earth's orbit to those in the Oort cloud. It even includes interstellar objects passing through the solar system on hyperbolic orbits. The S3M contains a total of over 13 million synthetic objects from 11 distinct small body populations, with the only requirement being that they reach $V \leq 24.5$ during the time period from roughly 2005–2015 (the anticipated operational lifetime of the Pan-STARRS survey). The time period requirement only affects a subset of the populations in the distant solar system.

The S3M has proven invaluable for developing and testing MOPS but suffers from one major limitation—it only tests the software system for known types of objects. Since we cannot anticipate the properties of an unknown population, we supplemented the S3M with an artificial 575,000 object 'grid' population. Grid objects have a random and flat distribution in eccentricity ($0 \leq e < 1$), sin (inclination) ($0° \leq i < 180°$) and in the angular elements ($0° \leq \Omega, \omega, M < 360°$). The semimajor axes of the objects were generated using uniform random distributions over six different ranges as provided in Table 4. The ranges and number of objects were selected so that the sky-plane density of objects in each range is roughly equal and to provide denser coverage in the semi-major axis ranges that have large numbers of known objects. The absolute sky-plane density of the grid population is 50 per field, a factor of 20–30 less than the realistic S3M on the ecliptic and much higher than the S3M off the ecliptic.

TABLE 4

S3M GRID MODEL SEMIMAJOR AXIS NUMBER DISTRIBUTION (SEE FIG. 7)

Semimajor axis range (AU)	Number of objects
0.75–1.5	50,000
1.5–6.0	200,000
6.0–32	50,000
32–50	200,000
50–500	50,000
500–5000	25,000

NOTE.—The number of objects in each pseudo-logarithmic range and their absolute magnitudes were selected so that the sky-plane density of detected objects in the simulations will be similar.

The absolute magnitudes of the objects in the grid population were generated with uniform distributions in each semi-major axis range but with lower limits that decrease (i.e., the objects are made larger) according to the square of the semimajor axis so that the objects are visible from Earth.

A major benefit of testing MOPS with the grid population is that they can appear at the poles where the sky-plane density of real or S3M objects is small; § 4.3 discusses the results of simulations with the grid population.

3.11. MOPS Efficiency Concepts

During ~4 calendar years of MOPS development we continuously benchmarked its performance using 3 metrics for each MOPS subcomponent. The metrics count the correct and incorrect associations of synthetic sources available at each MOPS processing step. The metrics are:

1. Efficiency

The fraction of available associations that were correctly identified.

2. Accuracy

The fraction of associations that are correct, *e.g.* consisting of detections from the same synthetic object definition.

3. Quality

The fraction of correct associations that meet or exceed a predefined quality metric.

To provide the detailed accounting required to measure system efficiency and accuracy, data structures for each association created in a MOPS processing phase are decorated with a label describing their disposition after processing. These labels describe the detections incorporated in the resulting data structure:

4. `AVAILABLE`—the data structure should have been created in the processing phase and is available to be assigned.

5. `CLEAN`—the data structure contains only synthetic detections or tracklets that belong to the same synthetic object, i.e., is a 'correct' data structure. This label might describe a tracklet that is created from two detections of the same synthetic object, or a derived object consisting of three tracklets that are each `CLEAN` and belong to the same synthetic object.

6. `MIXED`—the data structure contains only synthetic objects but the detections or tracklets are from different synthetic objects.

7. `BAD`—the data structure contains both synthetic and nonsynthetic detections. For tracklets this is a common and normal occurrence since we expect that synthetic detections will occasionally fall near real detections.

8. `UNFOUND`—an expected data structure for a synthetic object was not created. `UNFOUND` data structures are 'dummy' structures that represent an operation that *should have* happened. For example, if two sequential fields at the same boresight contain two detections of the same asteroid but a tracklet is not created, a dummy tracklet containing tracklet metadata is created so that the event can be counted and characterized.

9. `NONSYNTHETIC`—the data structure contains 'real' detections from actual telescope data. `NONSYNTHETIC` data consists of true detections of asteroids and false detections from image artifacts.

The pipeline must 'peek' at the input and output data structures before and after a MOPS processing step to assign synthetic labels but this is the only time that the pipeline knows that a data structure is synthetic—the labels are never examined during any MOPS computation or algorithm. Data structures that are 'contaminated'—contain mixtures of real and synthetic detections or different synthetic objects—continue to be propagated through the pipeline. The only exception is for `UNFOUND` objects for which dummy structures are created and decorated with the `UNFOUND` label so that these occurrences can be counted by analysis tools.

MOPS uses the labels to calculate the incremental efficiency after each processing stage. For a derived object, the state at each processing stage is preserved so that a 'paper trail' exists for each modification. This allows a complete step-by-step reconstruction of a derived object's history from its tracklets including the ability to identify the exact processing step where an object was lost or incorrectly modified by MOPS.

3.12. Simulations

The MOPS pipeline is exercised through the creation and execution of a 'simulation'. Each simulation begins with a collection of telescope pointings called 'fields' and a population of synthetic solar system objects whose positions and magnitudes are computed for every field. Objects that 'appear' in fields are converted into detections and stored in the MOPS database as though they were reported from an actual telescope. Detections can be 'fuzzed' astrometrically and photometrically using parameters that model the telescope performance; these include sky background, detector noise, and the point-spread function (PSF). The full fuzzing model incorporates a baseline astrometric uncertainty from the plate solutions added in quadrature with a flux-dependent positional uncertainty. Poisson-distributed (in S/N) false detections may be inserted in the fields to simulate noise from a real detector. After the injection of synthetic detections for a night the MOPS pipeline is invoked as though operating on real data.

MOPS simulations are used both to verify correct operation of the pipeline and to interrogate performance of a hypothetical survey. A simple verification test consists of creating a small main belt object (MBO) simulation with several nights of synthetic fields spanning two lunations, executing the pipeline, and verifying that all expected MBOs were 'discovered' through creation of a derived object and 'recovered' via attribution or recovery where possible. In this fashion all essential elements of the pipeline are exercised and verified after software modifications.

For comprehensive testing, a larger, more realistic synthetic population of objects is inserted into the simulation, the MOPS pipeline is executed, and the output provides a quantitative assessment of the system's efficiency and accuracy. The pipeline is designed to be essentially 100% efficient at creating tracklets and derived objects for MBOs with the designed Pan-STARRS performance.

When evaluating survey performance we configure MOPS to more precisely mimic the astrometric and photometric characteristics using filter- and field-dependent limiting magnitudes and FWHMs. Given the calculated V-band apparent magnitude for a synthetic asteroid, we calculate its expected signal-to-noise (S/N) using per-field detection efficiency parameters, and then generate a fuzzed magnitude and S/N. From the fuzzed S/N and the field's FWHM we compute the asteroid's fuzzed right ascension and declination. If there is variation in sensitivity due to sky brightness or airmass, these effects can be modeled by supplying appropriate values for photometric zeropoint or sky noise in the field's detection efficiency parameters.

During MOPS development we ran thousands of small-to medium-scale simulations for software unit testing and verification. More importantly, we ran several large simulations with synthetic solar system models containing millions of asteroids spanning several years of synthetic PS1 observations. These simulations were run on our modest PS1 MOPS production cluster and took many weeks or months to simulate the multiyear Pan-STARRS mission. For instance, our `full_S1b` simulation used the full S3M population in a 2 yr simulation and required ~180 calendar days (see § 4.1) while our 4 year NEO-only simulation (`neo_4yr`) required 88 calendar days (see § 4.2). At various times during the pipeline processing the cluster was offline for maintenance or power outages but MOPS is designed to be interrupted and restarted.

The upstream image processing subsystem (e.g., the Pan-STARRS IPP) can improve MOPS fidelity by providing a live pixel server (LPS) that reports whether a pixel at or near a specific (R.A., decl.) in an image falls on 'live' camera pixels. This service improves MOPS simulations in two ways: (1) by generating synthetic moving object data with behavior that simulates real observations (e.g., to account for the loss of field due to the camera fill factor), and (2) accounting for missing detections when attempting to recover known asteroids that are in the field of view. In a single Pan-STARRS1 exposure there are many reasons an area of the detector can be inactive besides simple chip gaps, such as saturation from a bright object in the field of view, or a cell used for guide star tracking. Thus the LPS tells MOPS what areas of the detector are active for any given exposure. If a LPS is not available from the upstream image processing subsystem, MOPS has provisions for allowing static specification of a detector mask that defines areas on a detector where detections cannot occur (see Fig. 6). Synthetic detections that land on a dead part of the detector (as determined by the LPS) are marked with a special 'unfound' decorator so that they can be accounted for but otherwise omitted from all subsequent processing.

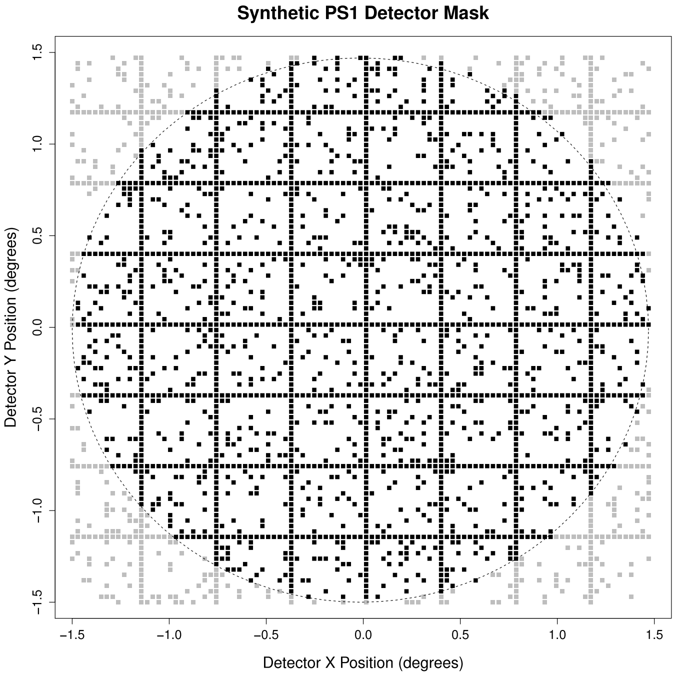

FIG. 6.—Synthetic 7.0 deg^2 field-of-view static focal plane mask for Pan-STARRS1 MOPS simulations that simulates losses due to chip gaps and other masked area. The horizontal and vertical bands simulate the chip gaps while the remaining squares represent losses due to bad cells or those used for guide stars. The squares do not correspond to actual masked area on the real Pan-STARRS1 detector; they exist simply to simulate additional area loss. The actual distribution of masked area on the real Pan-STARRS1 detector is very different—there is more power on small scales than shown here. The overall simulated camera fill factor is fixed at 75% in agreement with the measured values shown in Figure 23.

For increased simulation fidelity MOPS can accept a per-field detection efficiency for point sources and trailed detections as a function of S/N and rate of motion so that MOPS can generate more realistic synthetic photometry.

4. MOPS VERIFICATION

During MOPS development we undertook several large-scale simulations to probe the performance limits of the MOPS design and implementation and understand where further attention was needed in software development. These simulations consisted of a complete S3M or large S3M subpopulation, a multiyear set of telescope pointings, and detector performance that simulated a Pan-STARRS4 system. Our motivation was to investigate MOPS performance for the Pan-STARRS4 system as specified in its design requirements, not the reduced, changing performance of the single Pan-STARRS1 prototype telescope undergoing development and commissioning.

4.1. Two-Year S3M Simulation (`full_S1b`)

The MOPS 2 yr S3M simulation consists of the full S3M and 100,424 fields spanning 245 distinct nights over nearly 2 years (2007 Dec 29 through 2009 Oct 22). The simulation took ∼3 months to execute including various interruptions for cluster downtime and maintenance. It assumes a nominal positional measurement uncertainty of $0.01''$, a FWHM of $0.7''$, a fill factor of 100%, and a constant limiting magnitude of $R = 22.7$, representing a single idealized Pan-STARRS1 telescope. Poisson-distributed false detections were added to each field at a density of $\sim 200/\mathrm{deg}^2$. The simulated field pointings were generated by the TAO survey scheduler[22] configured to produce a Pan-STARRS-like survey covering $\sim 3,600$ deg^2 near opposition and ~ 600 deg^2 near each of the morning and evening sweetspots. Each area is visited three times per lunation, with some nights lost due to simulated poor weather. MOPS achieved an overall 99.99997% tracklet efficiency and 99.26% derived object efficiency. Tables 5 and 6 detail the tracklet and derived object efficiencies per S3M subpopulation.

For classes other than NEOs, Jupiter-family comets (JFCs) and long-period comets (LPCs), MOPS has an efficiency better than 99% for converting three or more tracklets to a differentially corrected orbit when observed within a 14 day window. For NEOs, our performance is not as good, but as stated elsewhere in this work, we have been more concerned with quantifying MOPS performance for various populations than in optimization. MOPS contains many runtime configuration parameters that allow performance of individual modules to be tuned, often at the cost of greater false results. Pan-STARRS1

---

[22] © 1999–2006 Paulo Holvorcem; http://sites.mpc.com.br/holvorcem/tao/readme.html.

TABLE 5

Tracklet (Intranight) Efficiency and Accuracy in the 2 Year Pan-STARRS4 MOPS Full-Density Simulation

Avail.	Clean	%	Unfound	%	Mixed	%	Bad	%	Non-syn.
24056199	24056191	100.0	8	0.0	417774	1.7	553475	2.3	1854648

Note.—This simulation used a realistic solar system model (S3M) and "next-generation" (0.01″) astrometric uncertainty (about 10 times better than delivered by the best contemporary surveys like Pan-STARRS1). The tracklet terminology in the headings is described in detail in § 3.11. See § 3.1 and 3.11 for definitions of efficiency and accuracy.

operations have led the project to a different mode of NEO discovery than originally envisioned, so we have not focused on improving NEO derived object performance. Similarly for LPCs, we can again improve efficiency by tuning MOPS orbit determination modules to reject fewer parabolic or hyperbolic orbits.

Our differential correction performance (§ 5.5) is probably overstated because the OrbFit initial orbit determination (IOD) software (Milani et al. 2005; Milani & Gronchi 2010) employed by MOPS can perform its own differential correction after IOD, and we elect to use it in this mode. Therefore orbits handed to the JPL differential correction module are almost always close to a minimum in the solution space where convergence will occur. MOPS supports other packages besides OrbFit to perform IOD, and in early evaluation of these packages we saw outstanding performance from the JPL differential corrector.

4.2. Four-Year NEO Simulation (`neo_4yr`)

We ran the `neo_4yr` simulation to calculate upper limits on the NEO detection and discovery rates with a Pan-STARRS1-like system. This system differed from the `full_S1b` simulation by using a 0.1″ baseline astrometric uncertainty and by containing almost 4 years of TAO simulated opposition and sweetspot observations over the expected Pan-STARRS1 mission from March 2009 through January 2013. The simulation only used the 268,896 NEO subset of the S3M. We were not able to simulate the Pan-STARRS1 focal plane fill factor, as the code had not been incorporated into MOPS yet, but we felt it would be reasonable to use a 100% fill factor and scale down our results based on true Pan-STARRS1 detector performance. False detections were not added to this simulation to speed up execution time, but the `full_S1b` results showed that this would not impact our results.

The `neo_4yr` simulation found over 9405 derived objects of which nearly half had orbital arc lengths greater than 30 days. As with the 2 yr `full_S1b` simulation, the tracklet efficiency is essentially 100%, with 10 out of 105,439 tracklets lost. MOPS linking performance is similar to `full_S1b` (See Table 7) but we find that orbit determination performs less well, at 81.7%, purely due to greater RMS residuals across the orbit from the larger astrometric uncertainty. Again, this acceptance threshold can be relaxed to improve efficiency (fraction of

TABLE 6

Derived Object Efficiency for Eight Different Classes of Synthetic Solar System Objects in the 2 Year Pan-STARRS4 MOPS Full-Density Simulation

Object class[a]	Avail.[b]	Clean[b] (Linked)	%	Pass IOD[c]	%	Pass diff.[d]	%
NEO	5203	4994	96.0	4924	94.6	4924	94.6
MBO	2043584	2032676	99.5	2029618	99.3	2029618	99.3
TRO	56214	56061	99.7	55923	99.5	55923	99.5
CEN	557	556	99.8	556	99.8	556	99.8
JFC	551	546	99.1	541	98.2	541	98.2
LPC	1714	1713	99.9	1584	92.4	1584	92.4
SDO	2289	2286	99.9	2281	99.7	2281	99.7
TNO	12719	12710	99.9	12686	99.7	12686	99.7

Note.—This simulation used a realistic solar system model (S3M) and "next-generation" (0.01″) astrometric uncertainty (about 10 times better than delivered by the best contemporary surveys like Pan-STARRS1). The tracklet terminology in the headings is described in detail in § 3.11. The impactor and hyperbolic models are omitted because they did not exist in the S3M at the time of this simulation.

[a] NEO—Near Earth Objects; MBO—Main Belt Objects; TRO—Trojans; JFC—Jupiter Family Comets; LPC—Long Period Comets; CEN—Centaurs; SDO—Scattered Disk Objects; TNO—Trans-Neptunian Objects.

[b] See § 3.1 and 3.11 for definitions of efficiency and accuracy.

[c] The number (and percentage) for which initial orbit determination was successful.

[d] The number (and percentage) for which a differentially corrected orbit was successfully computed.

TABLE 7

Derived Object Efficiency for the 4 Year Pan-STARRS1 MOPS NEO-Only Simulation

Object class[a]	Avail.[b]	Clean[b] (Linked)	%	Pass IOD[a]	%	Pass diff.[c]	%
NEO ………	11515	11025	95.7	9404	81.7	9404	81.7

Note.—This simulation used a realistic population of ~$250,000$ NEOs with Pan-STARRS1-like astrometric uncertainty (0.1″) simulation and a 100% fill-factor detector. This simulation was run during commissioning of the Pan-STARRS1 telescope before the actual Pan-STARRS1 survey was implemented

[a] The number (and percentage) for which initial orbit determination was successful.

[b] See § 3.1 and 3.11 for definitions of efficiency and accuracy.

[c] The number (and percentage) for which a differentially corrected orbit was successfully computed.

correct linkages surviving orbit determination) at a cost of an increase in false linkages.

4.3. Grid Simulations

We have run several grid simulations to ensure that we were not tailoring the efficiency to localized regions in (a, e, i) phase space. However, we do not inject the grid population into the detection pipeline during normal MOPS operations as this would needlessly increase the tracklet linking combinatorics in an artificial and unrepresentative manner.

To illustrate MOPS operations over the entire phase space we ran the real Pan-STARRS1 survey (i.e., actual pointings and cadence) for two consecutive lunations with the grid population and a realistic (0.1″) astrometric error model. Figures 7 through 9 show that MOPS is ~100% efficient for semimajor axes in the range from 0.75 AU to 5,000 AU, eccentricities in the range [0,1] and all possible inclinations. Fifteen fast-moving objects were rejected (out of 190,973) by the rate limit of $5.0\ \mathrm{deg\ day}^{-1}$ in the current Pan-STARRS1 production configuration to reduce false tracklets.

Figures 10 through 12 show that the derived object efficiency is consistently high for all synthetic grid objects on orbits ranging from those with semi-major axes well within the Earth's orbit to beyond 100 AU, over all inclinations with no deterioration in the efficiency for retrograde orbits, and for nearly circular orbits to those with $e \lesssim 1$. There is a degradation in the efficiency for $e \sim 1$ due to the orbit determination failing at the highest eccentricities.

One important feature of the grid population is that it includes objects that can appear near the poles where the sky-plane density of real solar system objects is negligible, *i.e.* it allows us to check that MOPS works correctly even for objects at high declinations as shown in Figures 13 and 14. While tracklet creation efficiency is nearly 100% for all declinations $\lesssim$88°, within 2° of the pole the grid simulation revealed that slightly conservative tracklet acceptance parameters rejected several fast-moving objects. The derived object efficiency is typically $\gtrsim 95\%$ for declinations ranging from $-30°$ to the north celestial pole indicating that the tracklet linking algorithm works across the entire sky. The drops in efficiency to ~90% are largely due to an inability to compute an initial orbit (see § 5.6) which is in turn usually due to a sparse observation cadence for the track.

5. MOPS VALIDATION AND REAL DATA

Processing of data from the current generation of surveys has been addressed by software pipelines already employed by Spacewatch (e.g., Rabinowitz 1991; Larsen et al. 2001), the Catalina Sky Survey, LINEAR, etc. We did not want to reproduce their work. MOPS was designed for use with a high-quality transient detection stream delivered by a next-generation Pan-STARRS4 or LSST-class survey system with nearly 100% fill-factor and a relatively modest number of systematic false detections. In many respects, despite the much higher data volumes expected from these telescopes, moving object algorithm design is simpler due to the high quality astrometry and photometry of the input data. MOPS performs less effectively with real Pan-STARRS1 data because it is the *prototype* for the next-generation Pan-STARRS4 survey—not a next-generation survey itself.

That said, the Pan-STARRS1 telescope represents a significant step forward in wide field survey astronomy, and has become a major contributor in NEO detection and discovery and the largest single-telescope source of asteroid observations while satisfying multiple, disparate survey programs. We have adapted MOPS to Pan-STARRS1 to maximize asteroid detection and NEO discovery from the Pan-STARRS1 data stream through the creation of tools to reject false detections and tracklets and allow for human review of data before they are submitted to the Minor Planet Center. Additionally, due to a realized survey cadence that is inefficient at producing enough repeat observations to compute reliable orbits, we have de-emphasized MOPS's derived object functionality in normal Pan-STARRS1 processing. In practice, the MOPS pipeline is executed through the tracklet-creation stage, with some "add-on" tools that are described below. MOPS is still used to its full capability as a simulation and research tool.

In this section we describe in detail all the Pan-STARRS1 MOPS processing steps and quantify its performance on the transients provided by the prototype telescope.

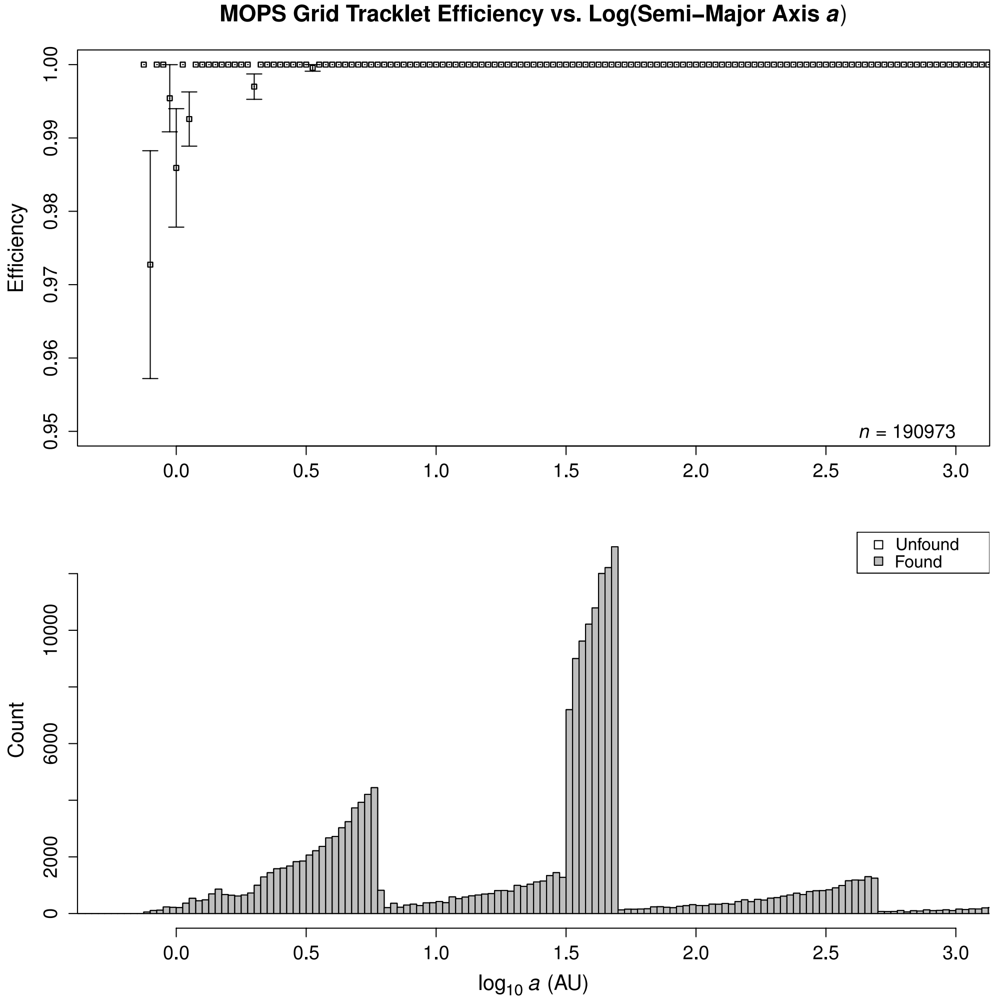

FIG. 7.—Tracklet creation efficiency as a function of semimajor axis for a one lunation MOPS simulation using S3M grid objects. Note the truncated Y-axis range of 0.95–1.0. Fifteen fast-moving objects with sky-plane rates that exceed the configured limits for the production Pan-STARRS1 MOPS account for the reduced efficiency at small semimajor axis. These limits will be tuned upon reprocessing the full Pan-STARRS1 survey.

5.1. Pan-STARRS1 Surveying

The Pan-STARRS1 ‘effective’ camera fill factor (f) as measured by MOPS is ~75%. The loss of image plane coverage results from gaps between the OTAs, dead cells, and gaps on the CCDs themselves, problematic pixels (e.g., anomalous dark current or non-linearity), and the allocation of subsections on the OTAs (known as cells) to high-speed acquisition of bright guide stars. The original MOPS design assumed $f \sim 100\%$ (Pan-STARRS4) and three two-detection tracklets per lunation for new object discovery, so that with $f < 100\%$ the maximum achievable system efficiency ($\epsilon_{\max}$) for moving objects must be somewhere in the range of $f^6 \leq \epsilon_{\max} \leq f^1$, depending on the object’s rate of motion, the distribution of ‘dead’ image plane pixels unit area and the telescope pointing repeatability. This implies that the maximum Pan-STARRS1 MOPS end-to-end derived object efficiency for objects in the field of view must lie in the range 26–75% even for objects that would be imaged at high S/N.

In part to compensate for the fill-factor, in October 2010 the Pan-STARRS1 survey was modified to obtain a four-exposure ‘quad’ in a manner similar to other NEO surveys instead of a single pair of exposures. The four images of a quad are typically acquired at the same boresight and rotator angle with a transient time interval (TTI) of about 15 minutes between sequential detections. Thus, a tracklet containing four detections would have a typical arc length of about 45 minutes. We then search for tracklets with three or four detections in the quad. The false tracklet rate decreases as the number of detections in the tracklet increases, but even with four detections per tracklet there are still false tracklets. To cope with the false tracklet rate we implemented a NEO ‘czaring’ procedure and an associated infrastructure for extracting ‘postage stamp’ 100 × 100 pixel images centered on every detection incorporated into a tracklet.

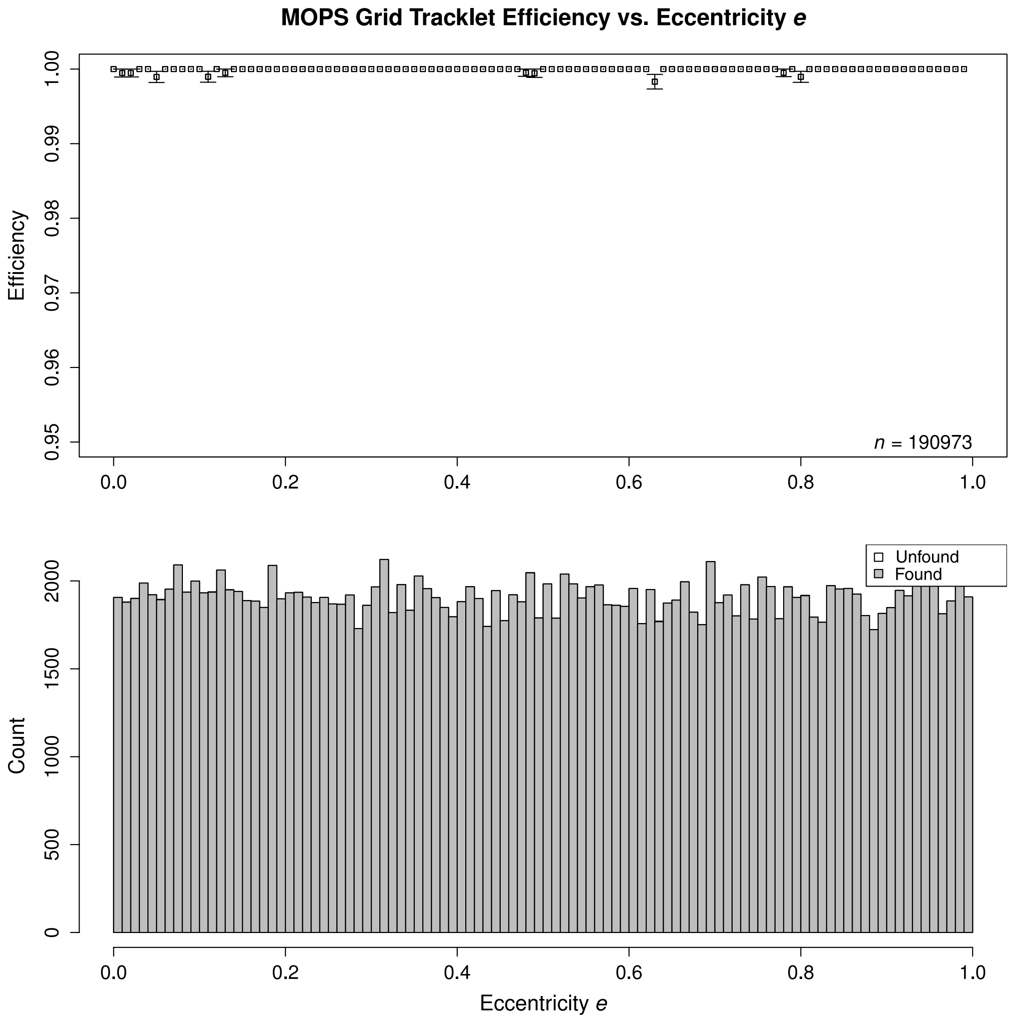

FIG. 8.—Tracklet creation efficiency as a function of eccentricity for a one lunation MOPS simulation using S3M grid objects. Note the truncated *Y*-axis range of 0.95–1.0.

A human observer, the 'czar', vets every tracklet before submission to the MPC.

The tracklet processing for pair observations by other Pan-STARRS1 surveys is specifically directed towards NEO detection and is divided into two rate-of-motion regimes—slow and fast, corresponding to 0.3° to 0.7° day^{-1} and 1.2° to 5° day^{-1}, respectively—i.e., tracklets containing just two detections are not detected if they have rates of motion between 0.7° and 1.2° day^{-1}. The reason for the two-regime processing is that the confusion limit from false detections becomes unmanageable around 0.7° deg day^{-1}, but beyond ~1.2° day^{-1} we can use trailing information to reduce the false tracklet count. The slow regime's lower limit corresponds roughly to a rate of motion that easily distinguishes between NEOs and main belt asteroid motions at opposition. The upper limit in the slow regime is set empirically at the rate at which the confusion limit becomes too high for the czar. The gap between 0.7° day^{-1} and 1.2° day^{-1} leaves a 'donut hole' in the velocity space where pairwise tracklets will not be found. Recent improvements in our ability to screen false detections will allow this hole to be removed when Pan-STARRS1 is observing away from the Galactic plane.

In the fast pairwise tracklet regime MOPS makes use of morphological information (e.g., moments) provided by the IPP as a proxy for trailing information. Quality cuts require similar morphology between the two detections and that the position angles (PA) calculated from the detection moments be aligned with the PA of the tracklet.

5.2. Detections

The false detection rate delivered by the Pan-STARRS1 IPP to MOPS is shown in Figure 15. The rate is dominated by systematic image artifacts rather than statistical noise. At high Galactic latitudes the transient detection rate is about the expected value from statistical fluctuations in the background but

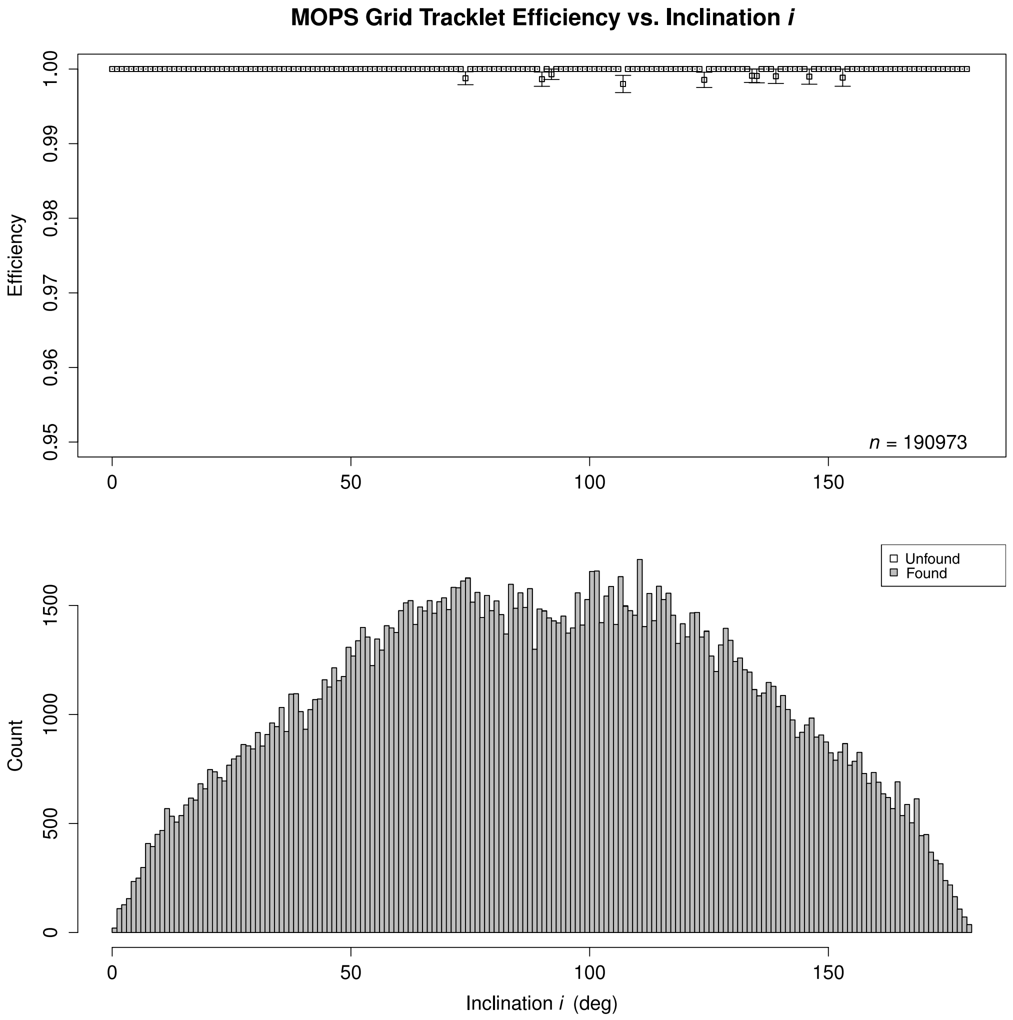

FIG. 9.—Tracklet creation efficiency as a function of inclination for a one lunation MOPS simulation using S3M grid objects. Note the truncated *Y*-axis range of 0.95–1.0.

the rate increases dramatically as the field center approaches the galactic plane where the false detection rate is 10–50 ×higher than expected. The increase in false detections with proximity to the galactic plane is due to image subtraction issues in regions with high stellar sky plane density and residual charge in the CCDs from bright stars. The transient rate in the $\mathcal{W}_{P1}$ filter does not have data for galactic latitudes $\lesssim 30$ deg because this filter was solely used for solar system surveying and detection of moving objects. The solar system team does not survey into the galactic plane because we learned early-on that the false detection and tracklet rates are too high to efficiently detect solar system objects.

Overall, the rate of transient detections at $\geq 5\sigma$ is $\sim 8200/\mathrm{deg}^2$—orders of magnitude higher than expected with Poisson statistics and with far more systematic structure, e.g., from internal reflections and other artifacts. This structure is especially problematic because, unlike Poisson-distributed false sources that are evenly distributed across the detector, systematic false sources tend to be clumped spatially and form many false tracklets that can clog and contaminate subsequent data processing. A large number of reported false detections for which the S/N is much lower than expected at a given magnitude could easily be removed with a field-dependent cut on S/N versus magnitude (see Fig. 16).

Figure 17 shows a representative sample of the types of false detections provided to MOPS by the IPP. Accurate machine classification of these artifacts using methods such as those described by (Donalek et al. 2008) can greatly reduce contamination and is under exploration by the PS1SC. We use imaginative monikers like ‘arrowheads’, ‘chocolate chip cookies’, ‘feathers’, ‘frisbees’, ‘pianos’ and ‘UFOs’ to classify them when iterating with the IPP on improving the detection stream. Many of the false detections are easily explained as internal reflections, ghosts, or other well-understood image artifacts, but some are as

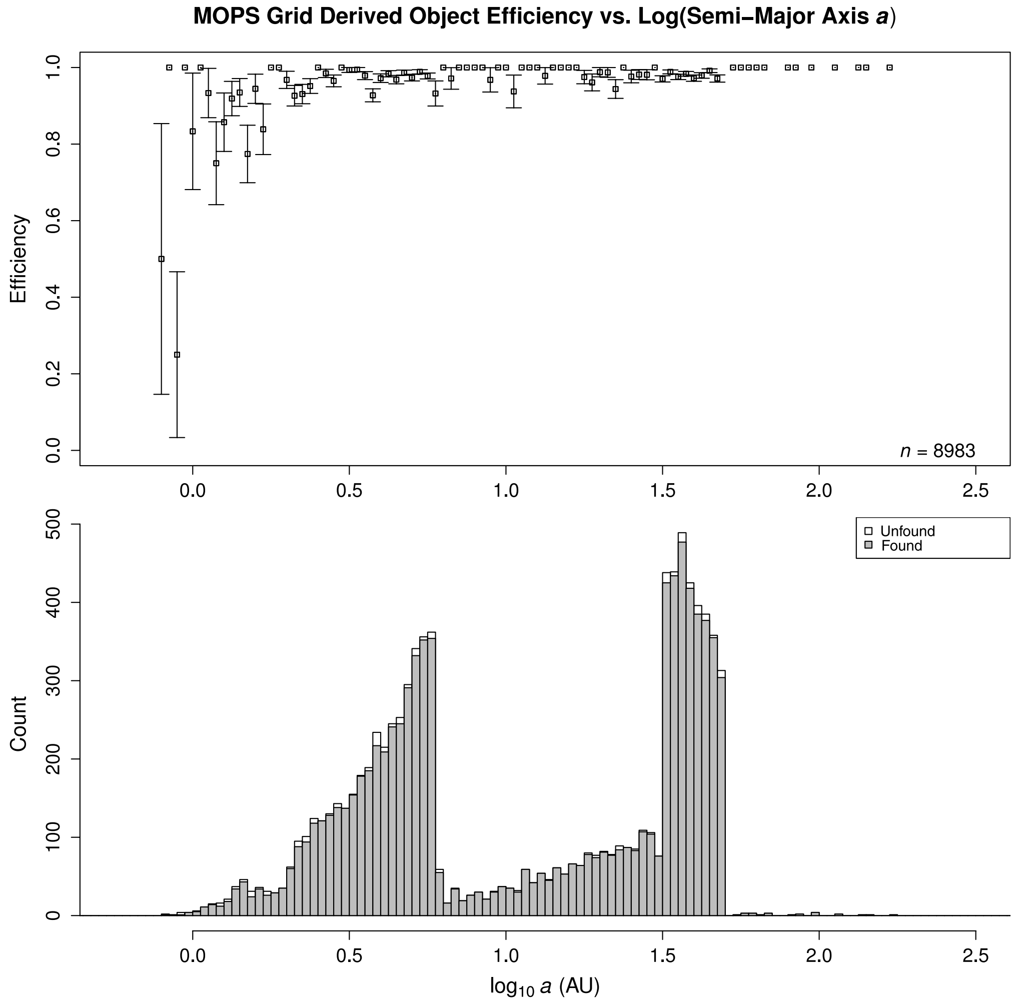

FIG. 10.—Derived object creation efficiency as a function of semi-major axis for a one lunation MOPS simulation using S3M grid objects. The total efficiency is 97.5%. Losses at small semi-major axis are due to conservative acceptance limits in the current Pan-STARRS1 production MOPS that reject objects with large sky-plane accelerations and/or large RMS residuals. These limits will be tuned upon reprocessing the full Pan-STARRS1 survey.

yet unexplained. MOPS screens false detections using their morphological parameters but many survive the cuts into tracklet formation because they must be conservative so that diffuse comet detections are not removed.

Finally, when the density of false detections spikes to rates that are difficult to manage, e.g., near a very bright star, we invoke a last-ditch spatial density filter to reduce the local sky-plane density to no more than 10,000 detections per square degree in a circle of 0.01° radius. The filter eliminates false detections by discarding those with the highest PSF-weighted masked fraction until the detection density is manageable.

Even real detections are often not well formed PSFs, as illustrated in Figure 18. Trailed detections often intersect with cell and chip gaps (Fig. 18*a*), PSF-like detections of slower moving objects have overlapping PSFs (2012 PF_{12}), or sit on the boundary of a masked region (e.g., Fig. 18*e*). Whenever a detection is poorly formed, it creates difficulties in astrometry and photometry and therefore in linking the detections into tracklets and tracks.

Despite these problems, Pan-STARRS1 astrometry and photometry reported to the MPC for slow-moving objects is currently excellent by contemporary standards. The average RMS astrometric uncertainty is about 0.13″ (Milani et al. 2012). The intrinsic photometric uncertainty in the calibrated[23] Pan-STARRS1 data is <10 mmag in the g_{P1}, r_{P1}, and i_{P1} filters and ~10 mmag in the z_{P1} and y_{P1} filters (Schlafly et al. 2012). The asteroid photometry is not yet as good as in the five primary Pan-STARRS1 filters because (1) much of the data is in the still to be fully calibrated w_{P1} filter, and (2) the detections are often trailed enough to cause problems with the photometric fit. We expect to solve these problems soon and begin reporting

---

[23] Pan-STARRS1 began reporting calibrated magnitudes in May 2012.

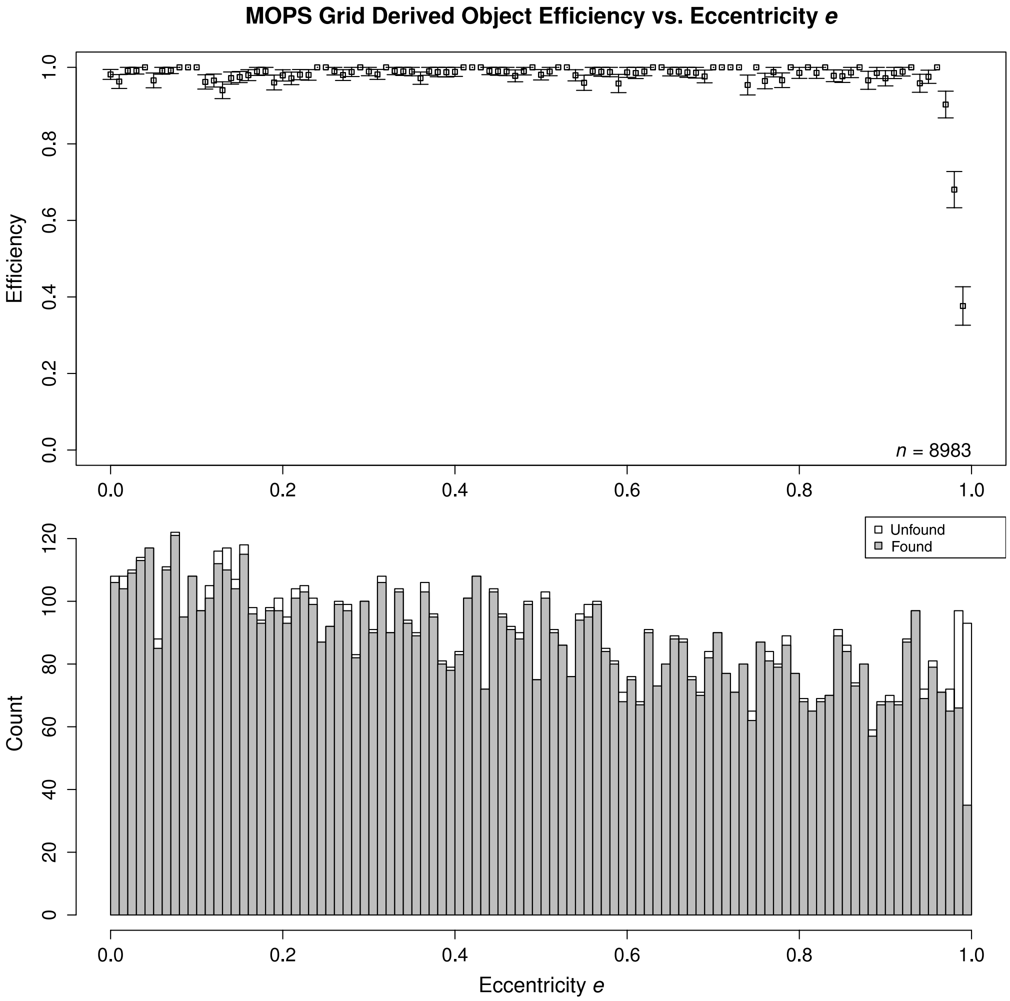

FIG. 11.—Derived object creation efficiency as a function of eccentricity for a one lunation MOPS simulation using S3M grid objects. The failures at high eccentricity ($e > 0.99$) occur in initial orbit determination (IOD) for grid objects with semi-major axis $a \lesssim 5$. These failures can be corrected by modifying IOD acceptance parameters.

$\mathcal{W}_{P1}$ band photometry for moving objects with a calibration accuracy of a few tens of mmag.

5.3. Tracklets

Kubica et al. (2007) provide detailed information on our algorithms and their performance for linking detections of moving objects on a single night into 'tracklets' or linking tracklets between nights into 'tracks'. Their techniques rely on the use of 'kd-tree' structures to provide fast and scalable performance.

Their Table 1 shows that the algorithms yield nearly 100% tracklet creation efficiency for the S3M in the presence of the expected but random false detection rate of 250 $\deg^{-2}$. About 10–15% of the generated tracklets are `MIXED` or `BAD` but this tracklet accuracy is perfectly acceptable because false tracklets should not link together across nights to form a set of detections with a good orbit. The mixed tracklets cause no loss of objects because the tracklet creation is non-exclusive *i.e.* the same detection can appear in the correct `CLEAN` tracklet and in multiple other tracklets. Kubica et al. (2007) note that the technique still worked with high efficiency even without using the detections' orientations and lengths but at the expense of a much higher false tracklet rate. Furthermore, they showed that the system maintains its integrity even at $>10\times$ higher random false detection rates.

The algorithm for linking tracklets between nights uses a kd-tree to quickly identify candidate tracks. Each track is then fit to a quadratic in RA and Dec with respect to time to eliminate tracks based on their fit residuals. The number of candidate tracks increases exponentially with the number of detections as shown in Table 3 in Kubica et al. (2007)—while 98.4% of the correct tracks are properly identified only 0.3% of the tracks that pass all the cuts are real. The false tracks are eliminated in the next step through initial orbit determination (IOD) described in the following sub-section.

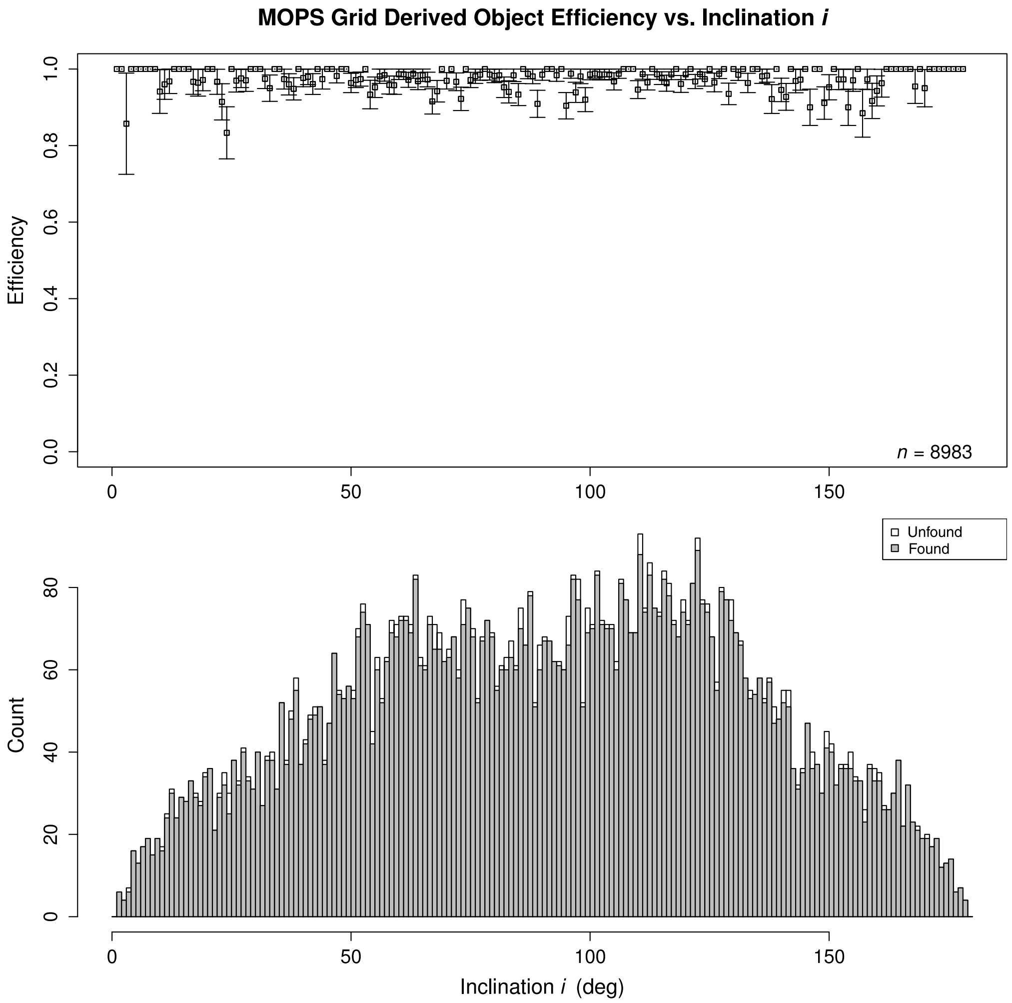

FIG. 12.—Derived object creation efficiency as a function of inclination for a one lunation MOPS simulation using only grid objects.

As discussed in the previous section, tracklet formation must take place in the presence of false detections due to statistical fluctuations on the sky background but also the usually much more numerous and problematic systematic false detections. We note that Kubica et al. (2007) performed their tests using two-detection tracklets and with assumptions on the astrometric and photometric performance expected for the cosmetically clean images of an idealized Pan-STARRS 4 survey. Their simulations are thus not directly applicable to the real Pan-STARRS1 system that includes more noise and degraded astrometry. The Pan-STARRS1 false detection rate is 10–50 × greater than expected at $\geq 5\sigma$ and almost all of them are systematic. They pose problems for MOPS in that the detections "line up" well enough to pass the tracklet formation cuts and the tracklets represent objects with asteroid-like rates of motion. The high false tracklet rate significantly slows down derived object processing because of the resulting tremendous false track rate.

The realized tracklet creation efficiency and accuracy was measured with synthetic detections injected into the real Pan-STARRS1 data. In this data stream typically four images are acquired at the same boresight with roughly a TTI separating each image in the sequence. We form tracklets of two, three, or four detections with some limits on the effective rate of motion depending on the number of detections in the tracklet. Table 8 shows that the tracklet creation efficiency is 99.98%—the algorithm correctly identifies almost every possible set of detections in a tracklet even in the presence of real detections and noise.

The algorithm returns additional `MIXED` and `BAD` tracklets though at a small fraction of the `CLEAN` rate (see § 3.1 and 3.11 for definitions). Tracklets are also identified for the nonsynthetic detections, i.e., detections of real objects or false detections. For the purpose of the efficiency and accuracy calculation both types of nonsynthetic detections are 'noise' as viewed from the perspective of the synthetic solar system objects. Thus, nonsynthetic tracklets may be sets of detections of real solar system objects—but the numbers in Table 8 indicate that there is a problem. There are roughly seven times more nonsynthetic detections than synthetic but, if our simulation and

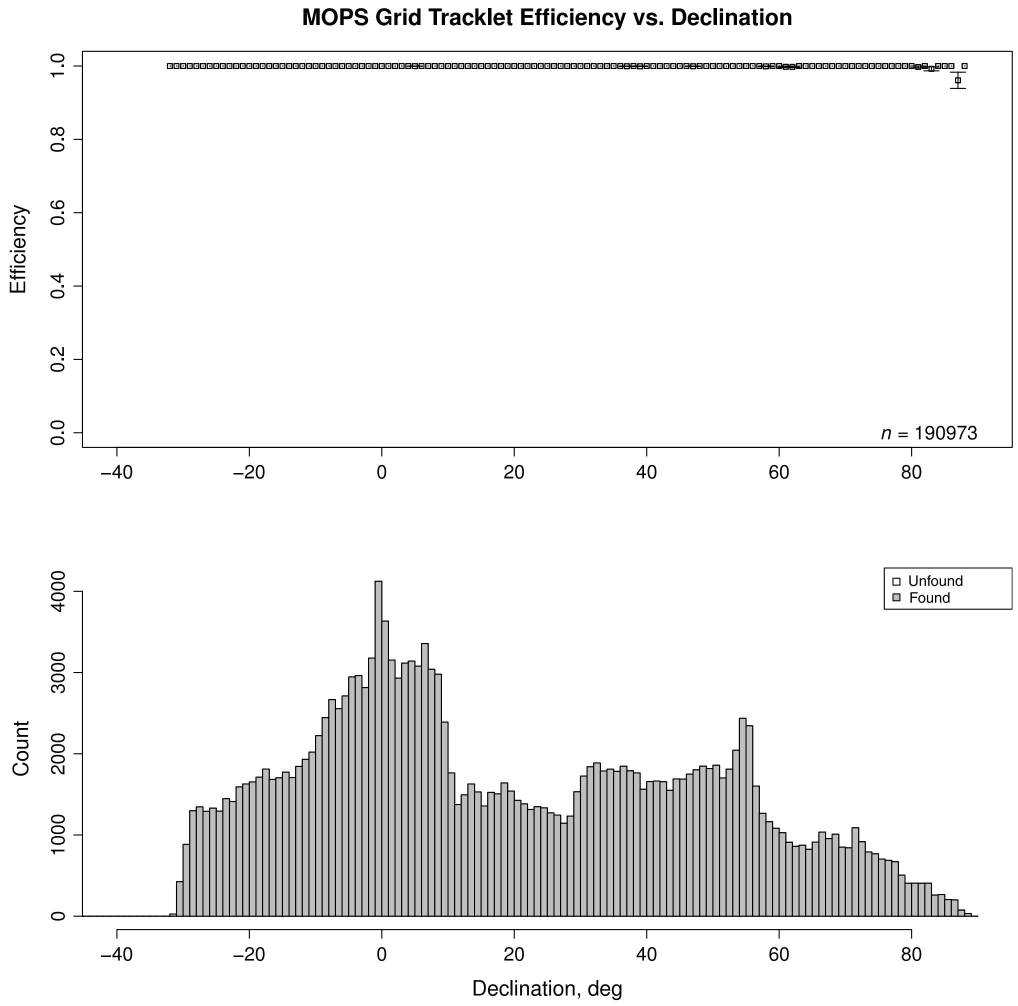

FIG. 13.—Tracklet creation efficiency as a function of declination for a one lunation MOPS simulation using PS1 telescope pointings and S3M grid objects with Pan-STARRS1 realistic (0.1″) astrometric uncertainty. The uneven declination coverage is due to uneven coverage of the Pan-STARRS1 survey during the lunation (2011 Aug 14 through 2011 Sep 12). Several fast-moving objects in the declination $= 89°$ bin were lost due to overly conservative tracklet acceptance parameters.

synthetic population are an accurate representation of reality, and all the nonsynthetic detections are real, the two values should be roughly the same.

Tracklets can only be formed from detections in images acquired within a reasonably short time frame with sequential detections of the same object separated by about a TTI. Linking detections into tracklets across longer time intervals creates a combinatoric explosion that can not be addressed by the current linking algorithms. On the other hand, it often happens that multiple tracklets for the same object are created on the same night separated by time intervals large compared to a TTI. The most common cause is overlap between adjacent fields acquired at times separated $\gg$TTI. Even more problematic are ‘deep-drilling’ situations where $\gg 4$ images are acquired at the same boresight in rapid succession. In this situation a real object moving between the images is not necessarily detected in every image due to, e.g., chip and cell gaps, passing over a star, masking, photometric fluctuations, etc., and detections from the same object may appear in different tracklets. Furthermore, the detections within the tracklets may overlap in time due to astrometric fluctuations. (e.g., detections from images 1, 3, and 6 appear in tracklet A and detections from images 2, 5, and 8 appear in tracklet B with no detections in images 4 and 7.) Thus, when there are >4 exposures in a sequence at the same boresight we post-process the tracklet list with `collapseTracklets`.

`collapseTracklets` merges colinear tracklets within a single night or data set using a method similar to a Hough transform. The approximate sky plane location of each tracklet is determined at the midtime of all tracklets in the set assuming that their motion is linear in R.A. and decl. during the time frame ($\dot{\alpha}$ and $\dot{\delta}$, respectively). Colinear tracklets corresponding to the same object should have similar positions and motion

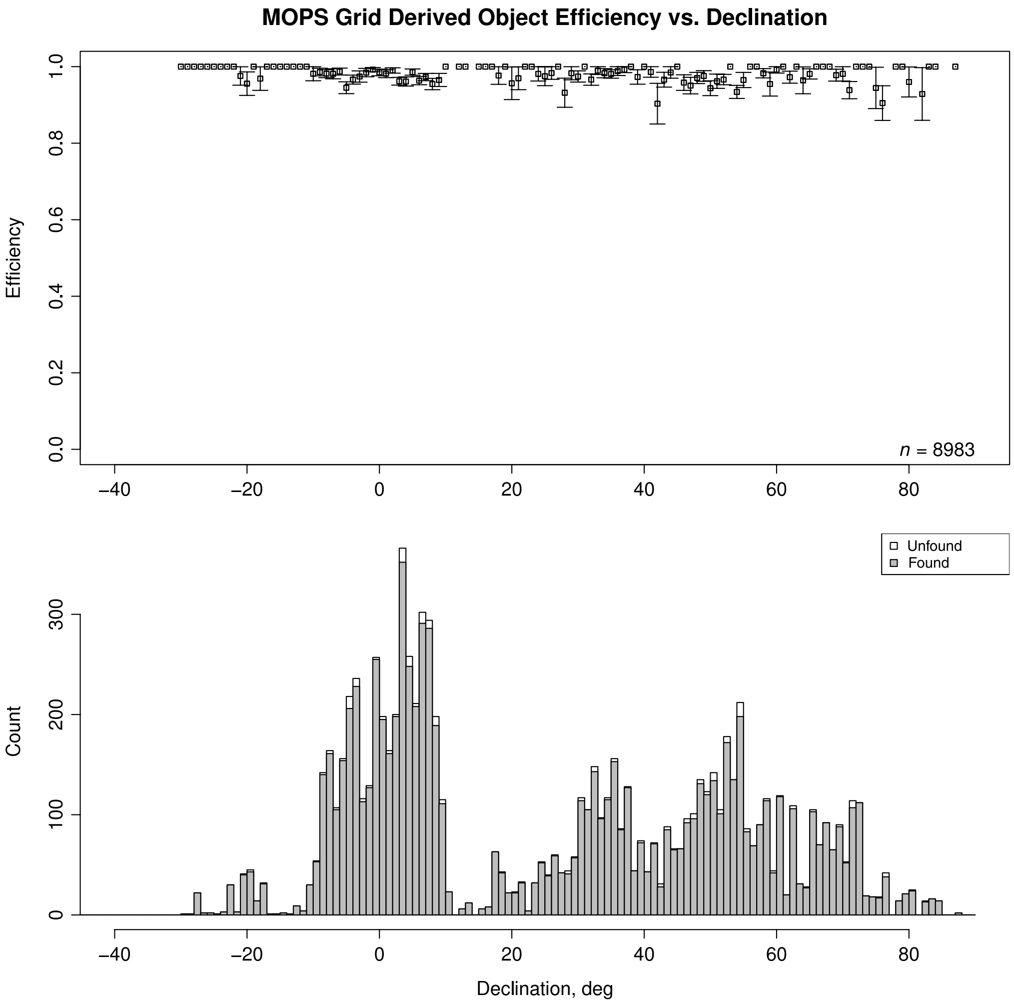
MOPS Grid Derived Object Efficiency vs. Declination

FIG. 14.—Derived object creation efficiency as a function of declination for a one lunation MOPS simulation using S3M grid objects with Pan-STARRS1 realistic (0.1″) astrometric uncertainty. The uneven declination coverage is due to uneven multi-night coverage of the Pan-STARRS1 survey during this particular lunation (2011 Aug 14 through 2011 Sep 12). While the total grid derived object efficiency is 97.5%, we believe this number can be improved further by tuning of MOPS linking parameters.

vectors making them straightforward to identify as ‘clumps’ in $(\alpha, \delta, \dot{\alpha}, \dot{\delta})$-space using a series of range searches implemented with a four-dimensional kd-tree. Given candidate groupings of tracklets in the transform space, `collapseTracklets` attemps to merge them using straight forward rms residual acceptance criteria, where there is a basic tradeoff between creating false merges versus allowing too many duplicates. The cost of duplicate tracklets in the deep-drilling sequences is that if there are duplicate tracklets for the same object, a potential derived object will rightly use the distinct tracklets to create two distinct derived objects for the same object, and derived object discordance rejection (see § 5.5) will disallow the derived objects on the grounds that multiple tracklets for an object cannot exist in the same set of fields.

We adopted `collapseTracklets` essentially unmodified upon delivery from the development team at LSST, and beyond simple tests that verify basic capability, we have not attempted to maximize its efficiency with Pan-STARRS1 deep-drilling cadences or data quality. Informal evaluations against the Pan-STARRS1 eight-exposure medium deep (MD) sequences show a duplicate ratio of ~25% with essentially zero lost tracklets.

In the time span from February 2011 through May 2012, MOPS created $1,513 \times 10^3$ tracklets of which 534×10^3 were real (35%) and 345×10^3 were automatically attributed to numbered or multiopposition objects (see § 5.9). The situation is much worse for tracklets containing just two detections: $11,691 \times 10^3$ created with just 780×10^3 attributed (6.7%). Assuming that the attributed:real ratio is the same as for the three- and four-detection tracklets it implies that only ~10% of two detection tracklets are real.

In theory, the Pan-STARRS1 +MOPS system is capable of detecting the highest proper motion stars within a single lunation. Consider the unusual case of Barnard’s star with an annual

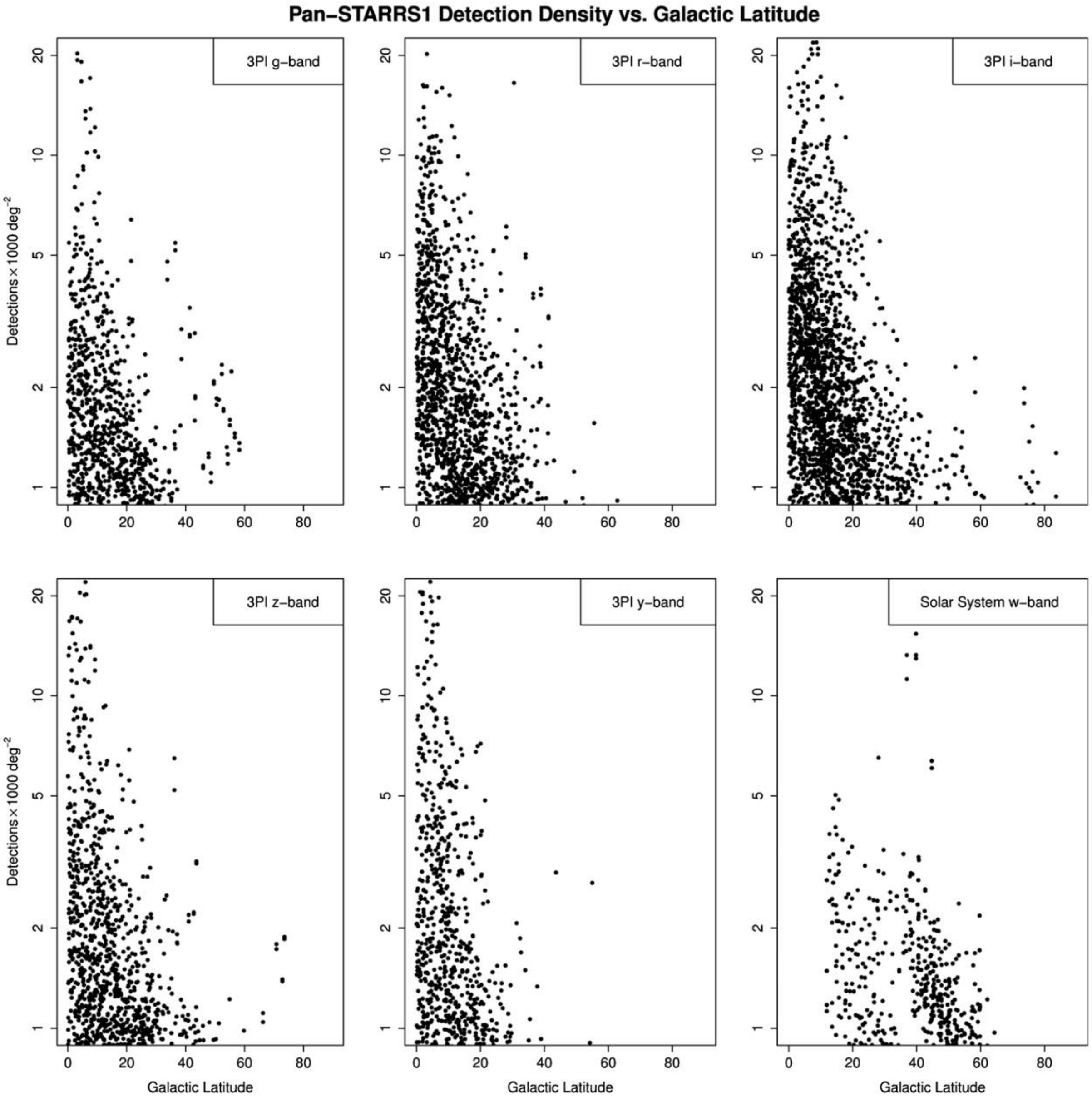

FIG. 15.—Number of transient detections reported to the MOPS by the IPP as a function of galactic latitude in all six Pan-STARRS1 filters. Almost all the transient detections are false.

proper motion[24] of $\sim 10.3''$ year^{-1} or about day^{-1}. Pan-STARRS1's average RMS astrometric uncertainty is about $0.13''$ (Milani et al. 2012) so that Barnard's star shows noticeable astrometric motion in about 5 days. Barnard's star would be provided as a transient detection to MOPS if the Pan-STARRS1 IPP created difference images using a static sky created from earlier images (Magnier et al. 2008). On each night MOPS would create a 'stationary' transient and if the survey provided more detections 5 and 10 days later MOPS would link the tracklets together. Thus, even in normal operations it is theoretically possible that MOPS could provide detections of high proper motion stars light years from the Sun. It takes little imagination to realize that MOPS could process 'stationary' tracklets identified in three successive *months* to discover proper motion stars to even larger distances. The false detection rates for image differencing using a static sky should be no worse than pairwise image differences at the same S/N.

---

[24] See http://simbad.u-strasbg.fr/simbad/sim-id?Ident=V*+V2500+Oph.

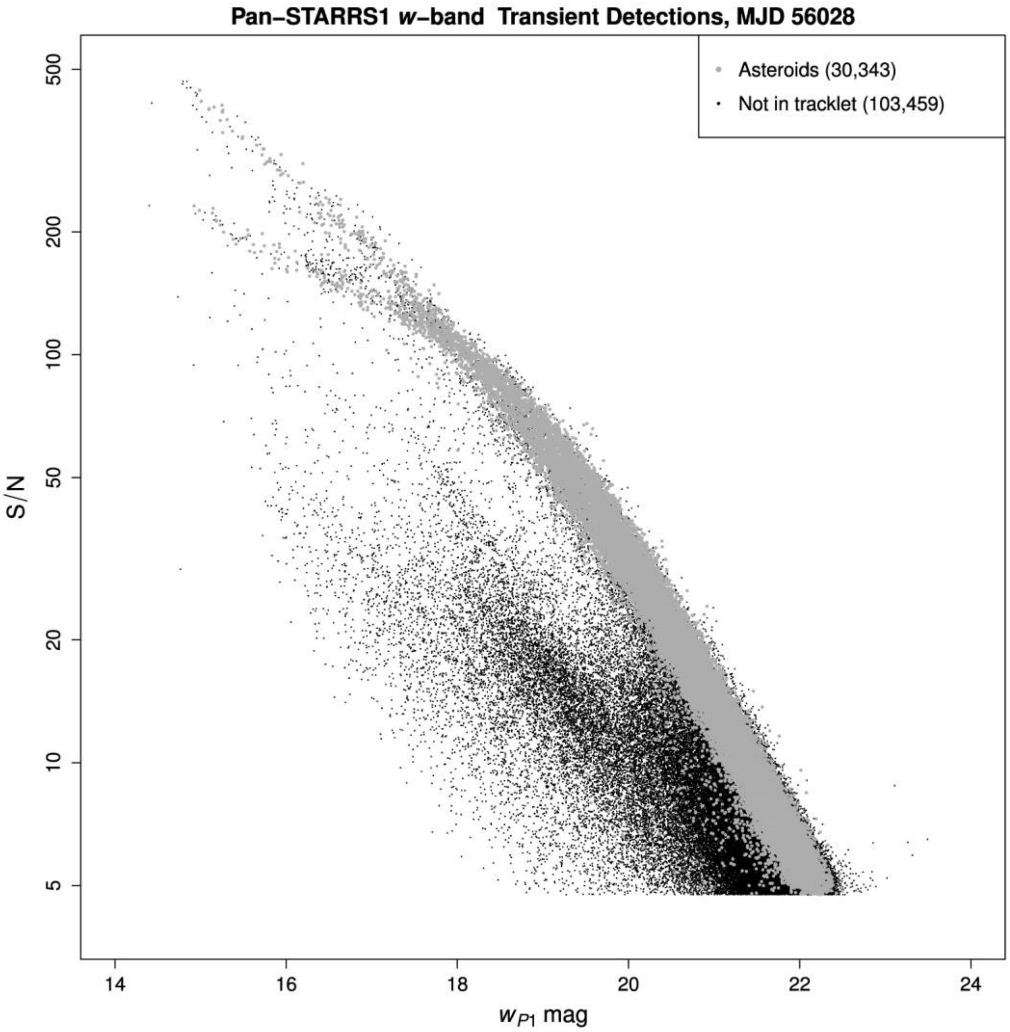

FIG. 16.—Pan-STARRS1 transient detections reported to MOPS by the IPP as a function of S/N and $\mathcal{W}_{P1}$ magnitude on MJD 56028. *Grey dots* are detections in tracklets that are real asteroids. *Black dots* are all other detections. The 'fork' in the distribution at $\mathcal{W}_{P1} \sim 18$ is due to a change in observing conditions that caused distortion of PSFs for bright objects.

5.4. Tracks

Tracklets are linked into 'tracks' across previous nights over a time window of typically 7–14 days using another kd-tree implementation called `linkTracklets` (Kubica et al. 2007). The MOPS runtime configuration specifies how many days prior to the current night to search and how many tracklets are required to form a linkage. The tracklets search locates combinations of tracklets that collectively fit quadratic sky-plane motion to within some configured error. Of course actual asteroid motions are not truly quadratic, but within the time interval of track creation this approximation holds for most objects.

Column 4 in Table 9 shows that the tracklet linking efficiency is ~80% for most classes of solar system objects ranging from the inner solar system to beyond Neptune. The linking efficiency is reduced from our grid simulations for several reasons: (1) linkages are contaminated with false tracklets and fail orbit determination; (2) medium deep sequences generate multiple tracklets for the same object, causing rejections in the discordance checks (see § 5.5); and (3) we simply have not yet tuned `linkTracklets`' operational parameters to Pan-STARRS1 's current survey mode and astrometric performance. Early MOPS tests with synthetic and real data obtained from Spacewatch (e.g., Larsen et al. 2001) showed that the derived object efficiency can be increased to nearly 100% with a suitable survey strategy, false detection rate, and set of `linkTracklets` configuration parameters

Table 9 does not show `linkTracklets's` accuracy but it is similar to the $\ll 1\%$ accuracy reported by Kubica et al. (2007), i.e. $\gtrsim 99\%$ of all the tracks are *not* real. However, very few of the tracks survive the subsequent motion, acceleration, astrometric and photometric residual cuts, etc. Those that do pass all the

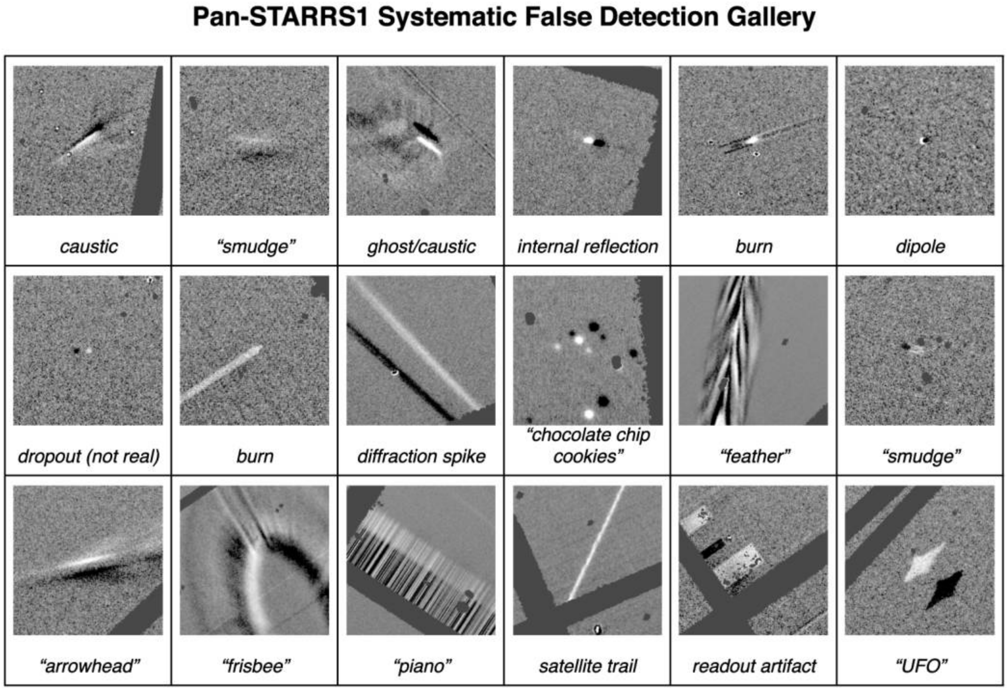

FIG. 17.—A sample of false source detections delivered to MOPS. The cause of the detection is provided under the image when known. The source detections are in the positive image (*white pixels*). Each image is a 200 × 200 pixel difference image with the original source detection in the center, i.e., the difference between two successive images acquired at the same boresight. *Solid dark grey* regions represent gaps between CCDs or cells or masked regions.

cuts are subject to initial and differential orbit determination to eliminate essentially all the bad tracks as described in the following two subsections.

5.5. Orbit Determination

MOPS identifies tracks that represent a real or synthetic asteroid through 'orbit determination'. A six-parameter orbit is calculated for each track and only those that do not exceed a rms residual requirement are accepted and passed on to the next processing phase. Orbit determination is a two-stage process within MOPS beginning with initial orbit determination (IOD) and followed by a least-squares differentially corrected orbit determination. Tracks that do not satisfy the residual requirement are discarded and their tracklets made available for use in other linkages.

Occasionally there may be cases where a tracklet is included in multiple distinct linkages whose fitted orbits produce rms residuals that meet MOPS acceptance thresholds. When this occurs the tracklet cannot logically be included in both derived objects, so MOPS includes code 'discordance identification' software that identifies this situation and either

1. chooses one linkage as 'correct' if its rms residual is significantly smaller than all others, or
2. rejects all linkages as bad since no correct linkage can be determined.

Similarly, two distinct tracklets may share a common detection and be included in otherwise separate linkages with acceptable rms residuals. In this case it is logically impossible for the detection to belong to two different objects, so the discordance identification routines select one linkage as described above or rejects them all if none stands out as correct. Tracklets in rejected linkages can be recovered later in processing through precovery (see § 5.10).

5.6. Initial Orbit Determination (IOD)

Orbit determination using a small number of observations over a short time interval has been studied for centuries, since Kepler first described the laws of planetary motion. Many techniques have been devised, each with its own advantages, and modern computers allow many different methods to be evaluated for a set of input detections.

For MOPS's purposes, IOD is a module that produces six-parameter orbits given a set of detections. We implemented the 'OrbFit' package developed by the OrbFit Consortium (Milani and Gronchi 2010). Our selection criteria for an orbit determination package were (1) efficiency at producing an orbit given a 'true' linkage; (2) orbit accuracy for observations using Pan-STARRS cadences and astrometric uncertainties; (3) speed of computation; and (4) availability and support. We tested the orbit determination software against millions of synthetic tracks to measure performance. As with other MOPS software, while we

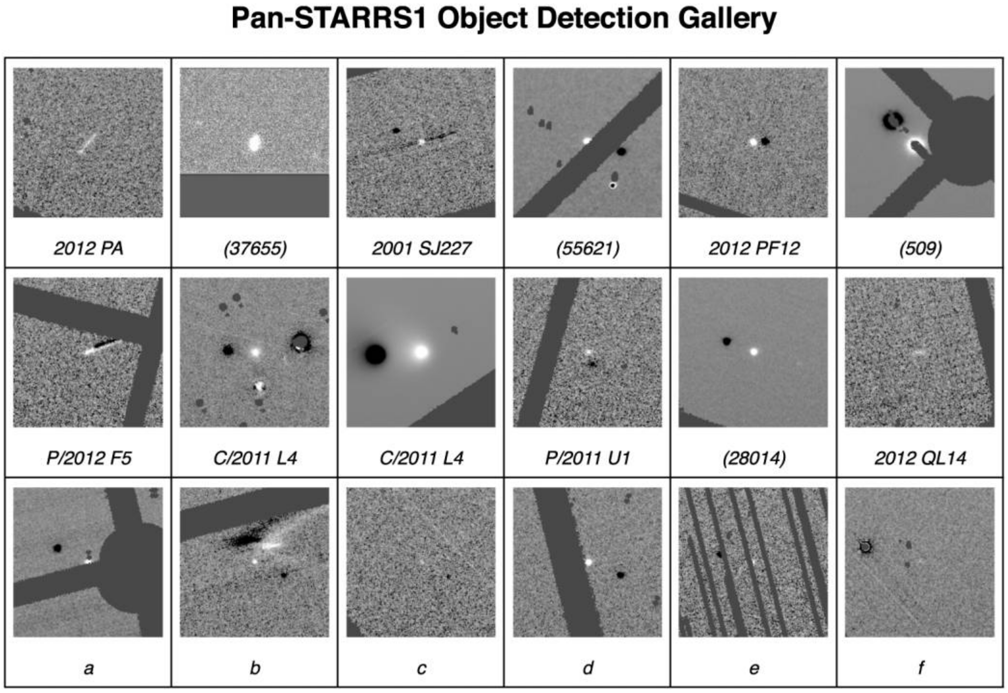

FIG. 18.—A sample of real object detections delivered to MOPS via difference imaging. Each image is a 200 × 200 pixel difference image with the positive source detection in the center. Many detections lie near artifacts or in heavily masked regions or are difficult to distinguish from systematic false detections. Objects (*a*) through (*f*) are unknown asteroids. *Solid dark grey* regions represent gaps between CCDs or cells or masked regions.

wanted high efficiency and accuracy in our orbit determination software, it was equally important to precisely measure the orbit determination efficiency.

Table 9 shows that the IOD efficiency is essentially 100% for all classes of solar system objects. i.e., OrbFit successfully provides an orbit when provided a correctly linked set of tracklets (a track).

5.7. Differential Correction

MOPS attempts to improve the IOD by navigating the parameter space of orbit solutions to minimize the least-square rms residual of the fitted detections. As with initial orbit determination, differential correction is a long-studied problem, spanning many decades of research, made routine by today's computer hardware. Modern differential correction techniques use precise models for the motion of the Earth and other large solar system bodies and are able to predict positions on the sky to within hundreths of an arcsecond many years into the future given enough input observations.

Through a memorandum of understanding (MOU) with the Jet Propulsion Laboratory (JPL) Pan-STARRS obtained permission to use a subset of JPL's Solar System Dynamics (SSD) software to compute asteroid ephemerides and differentially corrected orbits. SSD is a workhorse of solar system analysis, used for guiding spacecraft missions to their asteroid and comet destinations and for assessing impact probabilities for high profile NEOs.

Table 9 shows that the differential correction efficiency for objects that have passed IOD is essentially 100% for all classes of solar system objects.

Despite the overall effectiveness of the OrbFit IOD+JPL differential corrector combination, certain geometric configurations can lead to convergence to an incorrect orbit—the motion

TABLE 8

TRACKLET EFFICIENCY AND ACCURACY IN PAN-STARRS1 OBSERVING CYCLE 143 (2011 AUG 13 THROUGH 2011 SEP 10)

Avail.	Clean	%	Unfound	%	Mixed	%	Bad	%	Non-syn.
246596	246558	100.0	38	0.0	1969	0.8	8884	3.6	1429073

NOTE.—Measured performance for a single observing cycle of real Pan-STARRS1 telescope pointings using realistic astrometric uncertainty (0.1″) and a simplistic 75% fill-factor model. See § 3.1 and 3.11 for definitions of efficiency and accuracy. Fields within 15° of the Galactic plane excluded.

TABLE 9

CUMULATIVE DERIVED OBJECT EFFICIENCY FOR 10 DIFFERENT CLASSES OF SYNTHETIC SOLAR SYSTEM OBJECTS IN PAN-STARRS1 OBSERVING CYCLE 143 (2011 AUG 13 THROUGH 2011 SEP 10)

Object class[a]	Avail.[b]	Clean[b] (Linked)	%	Pass IOD[c]	%	Pass diff.[d]	%	Dup.[e]	%
IMP	88	68	77.3	67	76.1	67	76.1	0	0.0
NEO	24	18	75.0	18	75.0	18	75.0	0	0.0
MBO	18301	14608	79.8	14551	79.5	14461	79.0	6	0.0
TRO	662	538	81.3	538	81.3	522	78.9	0	0.0
CEN[f]	0	0	0.0	0	0.0	0	0.0	0	0.0
JFC	22	18	81.8	18	81.8	18	81.8	0	0.0
LPC	50	39	78.0	36	72.0	36	72.0	0	0.0
SDO	7	1	14.3	1	14.3	1	14.3	0	0.0
TNO	17	15	88.2	15	88.2	15	88.2	0	0.0
HYP	32	27	84.4	19	59.4	19	59.4	0	0.0

NOTE.—Measured performance for a single observing cycle of real Pan-STARRS1 telescope pointings using realistic astrometric uncertainty (0.1″) and a simplistic 75% fill-factor model. Fields within 15° of the Galactic equator excluded.

[a] IMP—Earth Impactor; NEO—Near Earth Objects; MBO—Main Belt Objects; TRO—Trojans; JFC—Jupiter Family Comets; LPC—Long Period Comets; CEN—Centaurs; SDO—Scattered Disk Objects; TNO—Trans-Neptunian Objects; HYP—Hyperbolic (Interstellar) Objects.

[b] See § 3.1 and 3.11 for definitions of efficiency and accuracy.

[c] The number (and percentage) for which initial orbit determination was successful.

[d] The number (and percentage) for which a differentially corrected orbit was successfully computed.

[e] The number (and percentage) of duplicate derivations. The duplicates contain non-identical but intersecting sets of detections of the same object.

[f] Centaurs were inadvertently omitted from the S3M for this study.

of objects in the small-solar-elongation sweetspots leads to dual solutions for orbits computed with short arcs. For short windows around the orbit computation, typically up to 30 days, the ephemeris uncertainty using the 'wrong' orbit is small enough that an attribution or precovery tracklet can still be found. With the additional arc length from the attribution or precovery the new orbit will collapse to a single solution.

5.8. Derived Objects

The tracklets and orbital parameters of tracks that survive the rms residual cuts for orbit determination are stored in the MOPS database as a 'derived object'. A derived object represents a moving object 'discovered' by MOPS; in other words, the detections are believed to belong to the same body with an orbit that allows the body's motion to be predicted well enough to recover the body in an adjacent lunation to the discovery lunation.

The derived object efficiency and accuracy is provided in Table 9. The realized efficiency for the Pan-STARRS1 survey is currently in the 70–90% range for most classes of solar system objects. Due to the high false detection rates the survey has concentrated on identifying candidate NEO tracklets by their anomalous rates of motion (e.g., Rabinowitz 1991; Jedicke 1996) and has temporarily abandoned the idea of creating derived objects. Despite a survey pattern, cadence and unoptimized MOPS configuration that are not particularly well-suited to creating derived objects, the system still achieves 70–90% efficiency for objects that appear in multiple tracklets within a lunation.

5.9. Attribution of Known Objects

MOPS was designed to operate agnostically on all tracklets regardless of whether they correspond to known or unknown objects, i.e., no a priori information about known objects is used when creating MOPS tracklets, tracks or derived objects. The motivation was to create a final set of 'derived objects' from Pan-STARRS1-only data with good controls on observational selection effects.

On the other hand, for the purpose of extracting more science from the data, and as an alternate means of measuring the system's detection efficiency and accuracy, we also attribute tracklets to known numbered and multiopposition asteroids using the `known_server` module from Milani et al. (2012). They show that it has essentially 100% efficiency and 100% accuracy using Pan-STARRS1 data for those classes of objects and § 5.13 discusses the realized Pan-STARRS1 +MOPS detection efficiency characteristics using the known objects.

As of October 2012, we have reported detections for approximately 240,000 numbered and 84,000 multiopposition objects identified by `known_server` to the MPC. These detections represent about 73% of the total 3.4 million detections, the remainder being mostly previously unknown asteroids. The fraction of known objects decreases with increasing V-magnitude such that 50% of the reported objects are unknown for $V > 21.6$ (see Fig. 19).

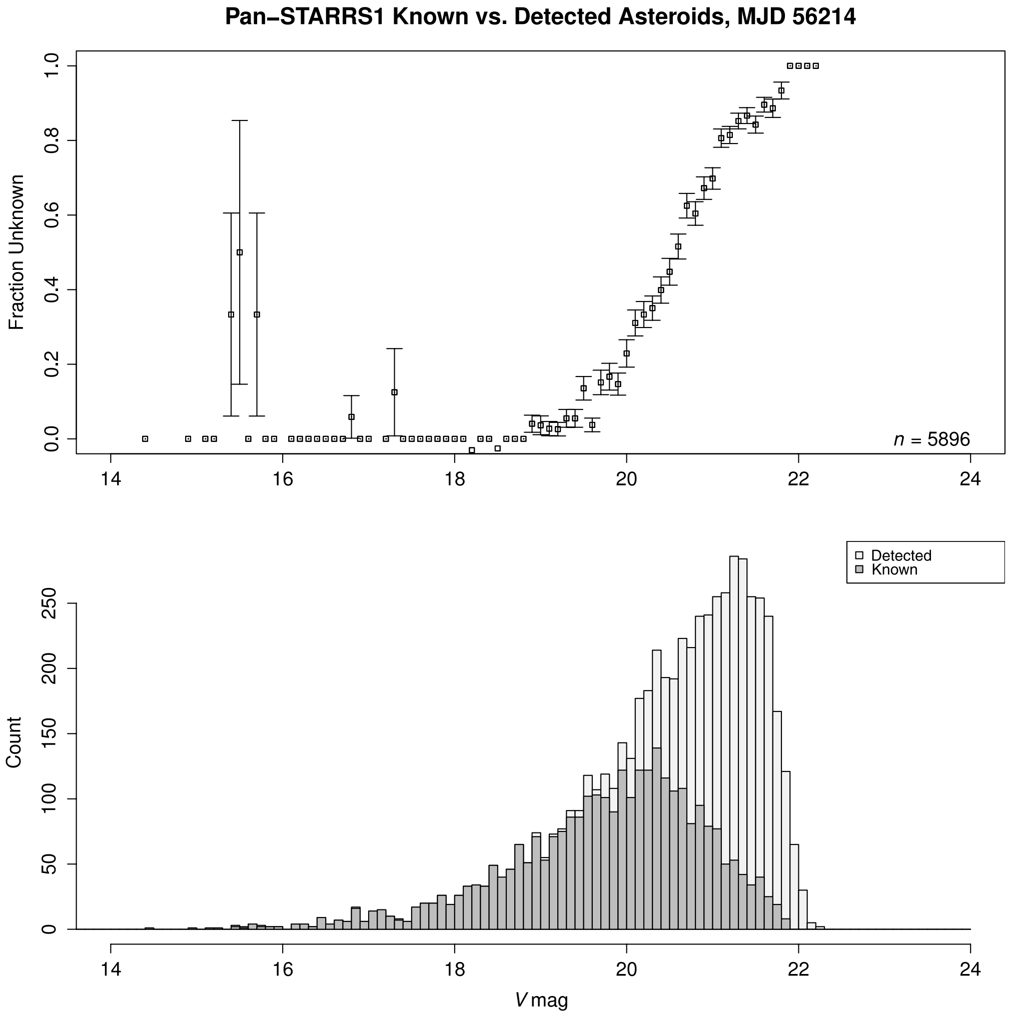

FIG. 19.—Overlapping detected and known asteroid distributions for a single night of Pan-STARRS1 solar system observing.

5.10. Precovery and Attribution ('PANDA') of Derived Objects

In keeping with the principle of MOPS agnosticism with respect to previously known objects we implemented the capability within MOPS to 'attribute' new tracklets each night to MOPS's derived objects. Recall that the time window for creating a MOPS derived object is typically 7–14 days, but we want to associate individual tracklets from new data with existing derived objects if possible (attribution), and search the MOPS database for individual tracklets observed previously that did not form a derived object because not enough tracklets were observed at the time (precovery). Early Pan-STARRS work showed that with sufficiently high-quality astrometry, an orbit with arc length of typically 10–14 days would have a prediction uncertainty small enough to locate the object in an adjacent lunation. Then, after a successful precovery or attribution extends the arc to beyond 30 days, the orbit is secure.

The PANDA algorithm is a simplified version of that described by Milani et al. (2012)—in essence we integrate every derived object's motion to the time of observation of each image and compare the predicted location and velocity to all nearby tracklets to see if there is a match. If there is a match, we attempt a differential orbit computation and if the resultant fit and residuals are within acceptable bounds we attribute the tracklet to the derived object. In practice, we predetermine the locations and velocities of all derived objects at the beginning, middle and end of the night and then use `fieldProximity` (Kubica et al. 2005) which interpolates their locations and velocities to each image time and uses a kd-tree implementation to make candidate associations between derived objects and tracklets.

Table 10 shows that the attribution efficiency is ~93% but it is important to keep two points in mind: (1) this is the cumulative efficiency for *all* possible attributions on that night and (2) the statistics are dominated by the main belt asteroids. In regard to the first point, our efficiency determination software

TABLE 10

ATTRIBUTION EFFICIENCY AND ACCURACY IN PAN-STARRS1 OBSERVING CYCLE 143 (2011 AUG 13 THROUGH 2011 SEP 10)

Avail.	Clean	%	Mixed	%	Bad	%	Non-syn.
9684	8971	92.6	5	0.1	26	0.3	3625

NOTE.—Measured performance for a single observing cycle of real Pan-STARRS1 telescope pointings using realistic astrometric uncertainty (0.1″) and a simplistic 75% fill-factor model. See § 3.1 and 3.11 for definitions of efficiency and accuracy. Fields within 15° of the Galactic plane excluded.

knows when a new synthetic tracklet is detected for an existing synthetic derived object but it does not account for the accuracy of the derived orbit's ephemerides at the time of observation, e.g., the derived object's arc-length. It may be that the available attribution was for a derived object detected on each of the last three nights or it may be a derived object whose last observation was 3 years beforehand. Thus, we expect that attribution efficiency will decrease as a function of time. Even though the results in Table 10 are dominated by the main belt the attribution efficiency mostly increases with the semimajor axis of the object—it is relatively easy to attribute distant, slow moving objects because their sky plane density is low and their motion is mostly along a great circle, and it is difficult to attribute nearby objects for the opposite reasons.

The mixed and bad attributions in Table 10 are of particular concern (see § 3.11 for definitions of the terms). In these types of attributions *unassociated* detections are added to the derived object, i.e., the derived object is being contaminated by noise or detections of other objects. Since the synthetic MOPS objects are intended to mimic the behavior of the real objects we assume that the real objects suffer the same 'contamination' levels (from real and synthetic detections and from false detections). Some level of contamination is always unavoidable but it will degrade the quality of the derived orbits so that future attributions are less likely to be real.

There are several ways to mitigate the contamination including (1) tighter controls on the residuals of candidate detections added to derived objects or (2) post facto 'scrubbing' of all derived orbits to identify outlying detections associated with derived objects. We never implemented these techniques and have essentially abandoned improvement of the attribution algorithm because it was designed for a survey pattern that would provide ≥3 tracklets for most observed asteroids in each lunation.

The complement to attribution is 'precovery' in which historical unattributed tracklets are linked to new derived objects. Our precovery algorithm is essentially identical to attribution but applied backwards in time. The only enhancement is that when a successful precovery enhances the derived orbital element accuracy with a consequent reduction in the ephemeris errors we iterate on the precovery attempts until all possible precoverable tracklets are associated with the new derived object.[25] We also allow for the precovery of tracklets intermediate in time between existing tracklets in the derived object.

When the observed arc length of a derived object exceeds a configurable time span such that the prediction uncertainty over the entire survey is below some threshold, the object has reached a stage where the orbit solution is stable, all possible detections have already been associated with the object, and it no longer needs to be precovered. This optimization reduces the processing time required for precovery (see Fig. 20) because over a long enough survey many objects will be 'retired' out of precovery when their orbits become sufficiently accurate. For synthetic objects, MOPS records all successful and failed precoveries so the pipeline can produce statistics on objects that have reached orbit stability but still have recoverable tracklets (see Table 11).

Figure 21 illustrates the sequence of events within MOPS for a hypothetical asteroid that is observed over three successive lunations. For synthetic objects, the 'paper trail' allows us to interrogate derived object performance and understand how and what kinds of objects get lost in the system. For each derived object 'event' (derivation, attribution, or precovery), the object's orbit is modified (hopefully improved) and recorded, allowing easy inspection of the orbit history for the derived object within MOPS.

5.11. Orbit Identification

When a new derived object (A') is created it is automatically checked for possible precoveries as described above. If the arc length is still short even after precovery it is possible that much earlier detections of the object A' appear in the database that can not be precovered because the ephemeris uncertainty becomes too large when the current derived orbit is integrated backwards in time. On the other hand, those much earlier detections may also have been incorporated into a derived object (A) that similarly can not be attributed to the current detections because integrating derived object A forward in time generates too large an ephemeris uncertainty. Thus, the same object may exist in two separate derived orbits that are unlinkable by our precovery and attribution techniques.

Rigorous techniques exist for 'orbit identification'—associating short arcs of detections within an apparition to the same object observed with a short arc in another apparition (e.g., Granvik and Muinonen 2008; Milani et al. 2005)—but given the high astrometric quality we could assume for Pan-STARRS4, we adopted a simplified strategy that searches for neighboring orbits in orbit parameter space.

---

[25] The precovery algorithm is invoked any time any orbit changes. *i.e.* the attribution of a new tracklet to an existing derived objects also triggers the precovery algorithm.

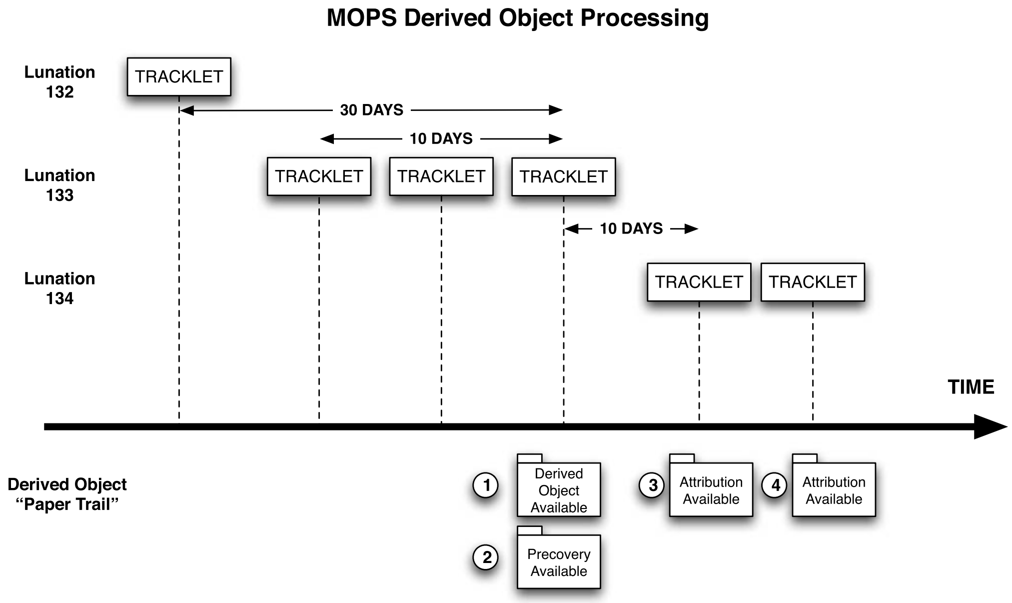

FIG. 20.—Processing times for different MOPS pipeline stages over one simulated year of a 2-year simulation using Pan-STARRS4 data volumes. Some data prior to MJD 54850 was discarded because MOPS pipeline software was not separating processing times for synthetic and tracklet stages.

If each of the two derived orbits are themselves reasonably accurate and precise then it is possible to identify the two derived objects as being identical simply by checking that the derived orbit elements are similar. Given that we expected to find $>10^7$ objects with Pan-STARRS and thousands of new derived objects each night we implemented the search for similar derived orbits in a kd-tree (`orbitProximity`). For any new derived object A' `orbitProximity` identifies a set of candidate derived orbits ($X = \{A, B, C, D\}$) for which all six orbit elements match A' to within the tolerances shown in Table 12. Then we attempt a differential correction (§ 5.7) to an orbit including all detections from pairwise combinations of A' with each of the candidate orbits, e.g., $\{A, A'\}$, $\{B, A'\}$. If the differentially corrected orbit meets our rms residual requirements then the two derived objects are merged into one derived object (e.g., A and A').

Our MOPS simulations for a Pan-STARRS4 system showed that the orbit identification efficiency and accuracy were close to 100% using the tolerances in Table 12. The realized orbit identification efficiency for Pan-STARRS1 is ~26% as show in Table 13. The reduced efficiency is because the Pan-STARRS1 cadence and astrometry yields orbits with uncertainties larger than our configured orbit identification tolerances.

TABLE 11

MOPS PRECOVERY EFFICIENCY AND ACCURACY IN PAN-STARRS1 OBSERVING CYCLE 143 (2011 AUG 13 THROUGH 2011 SEP 10)

Avail.	Clean	%	Mixed	%	Bad	%	Non-syn.
8557	6635	77.5	14	0.2	23	0.3	1966

NOTE.—Measured performance for a single observing cycle of real Pan-STARRS1 telescope pointings using realistic astrometric uncertainty (0.1″) and a simplistic 75% fill-factor model. See § 3.1 and 3.11 for definitions of efficiency and accuracy. Fields within 15° of the Galactic equator excluded.

5.12. Data Rates and MOPS Timing

Figure 20 shows execution times for various MOPS processing stages over 1 year of a 2-year MOPS simulation with the S3M. Processing times for per-night stages within the pipeline (generation of synthetics and tracklets) are generally constant, while stages that operate on the simulation's internal catalog of derived objects grows linearly or worse, depending on gross algorithmic considerations. Naively, the precovery stage exhibits quadratic growth, as the number of derived objects seen by MOPS and the number of precovery images to search both grow linearly as a function of simulation time, but optimizations in the precovery algorithm that limit the search windows reduces this growth below quadratic [$\sim O(n \cdot \log n)$].

The bimodality of timing results in Figure 20 is due to the survey containing nights with either sweetspots (168 exposures) or opposition regions (660 exposures) or both. The slow growth of the synthetic generation stage is due to the increased integration time required to produce a position for an asteroid at the observation epoch from the survey start date. Recent MOPS versions eliminate this overhead by periodically propagating the epoch of S3M orbits to the current end-of-survey. Internight linking and orbit determination computation time grow slowly as the size of the MOPS database increases.

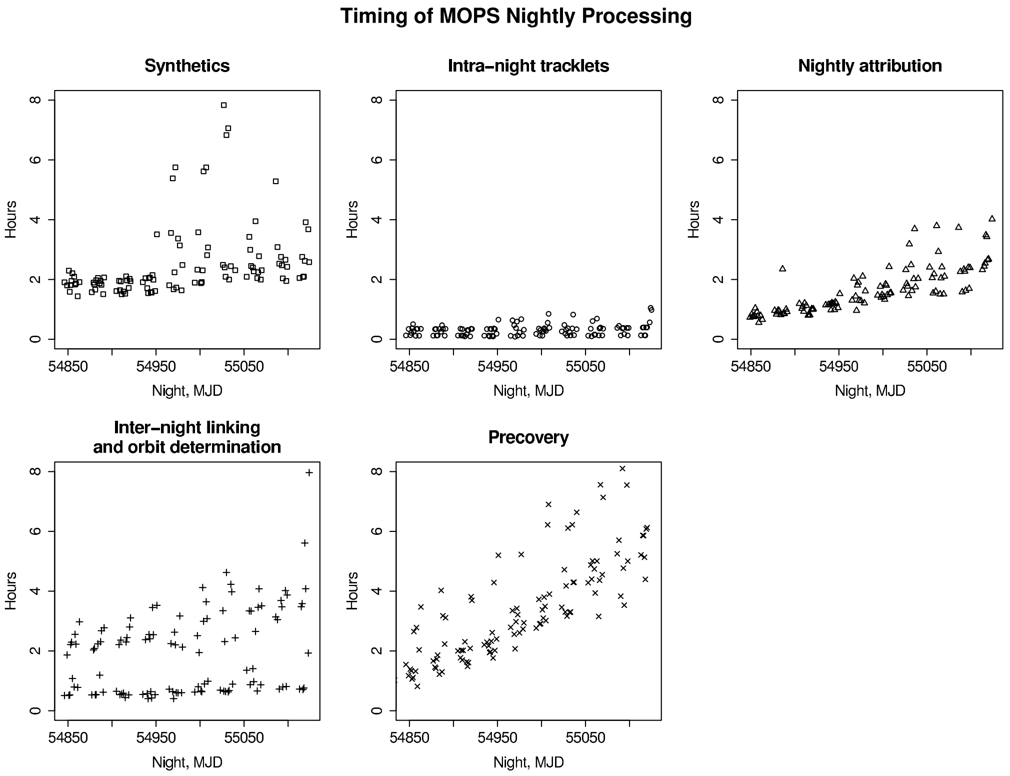

FIG. 21.—MOPS derived object processing overview for a single hypothetical asteroid, showing observed tracklets and the created derived object. In lunation 132, no derivation is available because there is only a single tracklet observed. In lunation 133, three tracklets are observed in a 10 day window, so a derived object is created and the precovery in lunation 132 becomes available. In lunation 134, two attributions are available using predictions from the object's derived orbit. Numbers in *circles* show the sequence of 'paper trail' records inserted into the MOPS database.

5.13. Detection Efficiency

Figure 22 illustrates the realized tracklet detection efficiency of the combined Pan-STARRS1 +MOPS systems as measured using asteroids attributed (or not) by `known_server` (see § 5.9). The data in each filter were fit to the function $\epsilon = \epsilon_0[1+\exp([V-L]/w)]^{-1}$ where ϵ_0 represents the maximum efficiency for bright but unsaturated detections, V and L are the apparent and limiting V-band magnitudes respectively, and $\mathcal{W}$ is the 'width' of the transition from maximum to zero efficiency. The limiting magnitude L is the magnitude at which the efficiency is 50% of the maximum value. The magnitudes in all bands were converted to V using a mean C+S class asteroid type as shown in Table 1. The function is a good representation of the efficiency near the limiting magnitudes and the scatter at bright values is simply due to low statistics.

The maximum efficiency in all four filters in Figure 22 is ~78% which is almost entirely driven by the effective Pan-STARRS1 camera fill factor of ~80%. This implies that when a asteroid is imaged on a live and unmasked camera pixel it is

TABLE 12

ORBIT IDENTIFICATION MATCHING TOLERANCES

Orbit element[a]	Tolerance
Perihelion	0.1 AU
Eccentricity	0.05
Inclination	0.1°
Ascending node	1°
Arg. of perihelion	1°
Time of perihelion[b]	0.1

NOTE.—The maximum difference between two derived object's orbits before they are tested for consistency with being the same object.

[a] Cometary form.

[b] In terms of fractional orbit period.

TABLE 13

MOPS ORBIT IDENTIFICATION EFFICIENCY AND ACCURACY IN PAN-STARRS1 OBSERVING CYCLES 143 AND 144 (2011 AUG 13 THROUGH 2011 OCT 10)

Avail.	Found	%	Mixed	%	Bad	%	Non-syn.
40	7	17.5	1	2.5	2	5.0	22

NOTE.—Measured performance for a single observing cycle of real Pan-STARRS1 telescope pointings using realistic astrometric uncertainty (0.1″) and a simplistic 75% fill-factor model. See § 3.1 and 3.11 for definitions of efficiency and accuracy. Fields within 15° of the Galactic equator excluded.

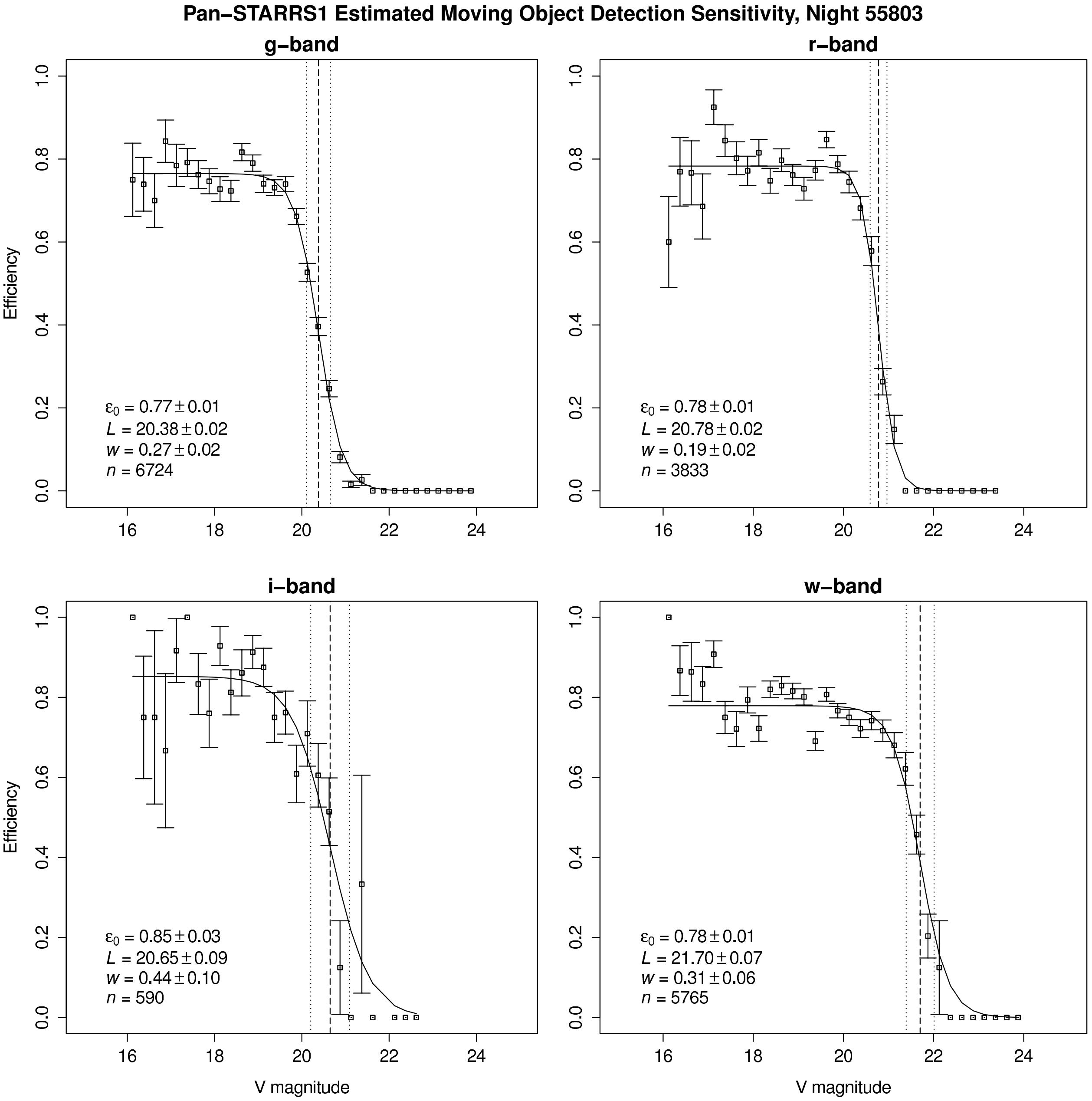

FIG. 22.—Pan-STARRS1 moving object detection efficiency on a single night (MJD 55803) for detections of known numbered and multi-opposition asteroids in each filter as a function of V magnitude. The data in each filter were fit to the function $\epsilon = \epsilon_0[1 + \exp([V - L]/\mathcal{W})]^{-1}$ as described in § 5.13. The *vertical dashed line* is at the V magnitude where the efficiency drops to 50% of the maximum (L). The *vertical dotted lines* provide the range $[L - \mathcal{W},\ L + \mathcal{W}]$ over which the efficiency drops quickly.

detected with ~97$\%$ efficiency. The limiting magnitudes in g_{P1}, r_{P1}, and i_{P1} are roughly equal at $V \sim 20.5$ and any difference between the bands is due to unbalanced exposure times. The wide-band filter $\mathcal{W}_{P1}$ goes ~1 V-mag deeper through a combination of the 45 second exposure time and its ~3 ×higher bandwidth.

Figures 23 and 24 show that Pan-STARRS1 +MOPS performance was roughly constant over the first year of operations. The dip in efficiency in the range $55,700 \lesssim$ MJD $\lesssim 55,800$ is due to overly aggressive filtering of false detections during that time period. The fit to the limiting magnitude in each passband as a function of time is consistent with there being no change in any filter.

In Figure 25, we compare the predicted number of tracklets using the S3M to Pan-STARRS1 tracklets reported to the MPC during the period 2011 Aug 13 through 2011 Oct 11. For bright

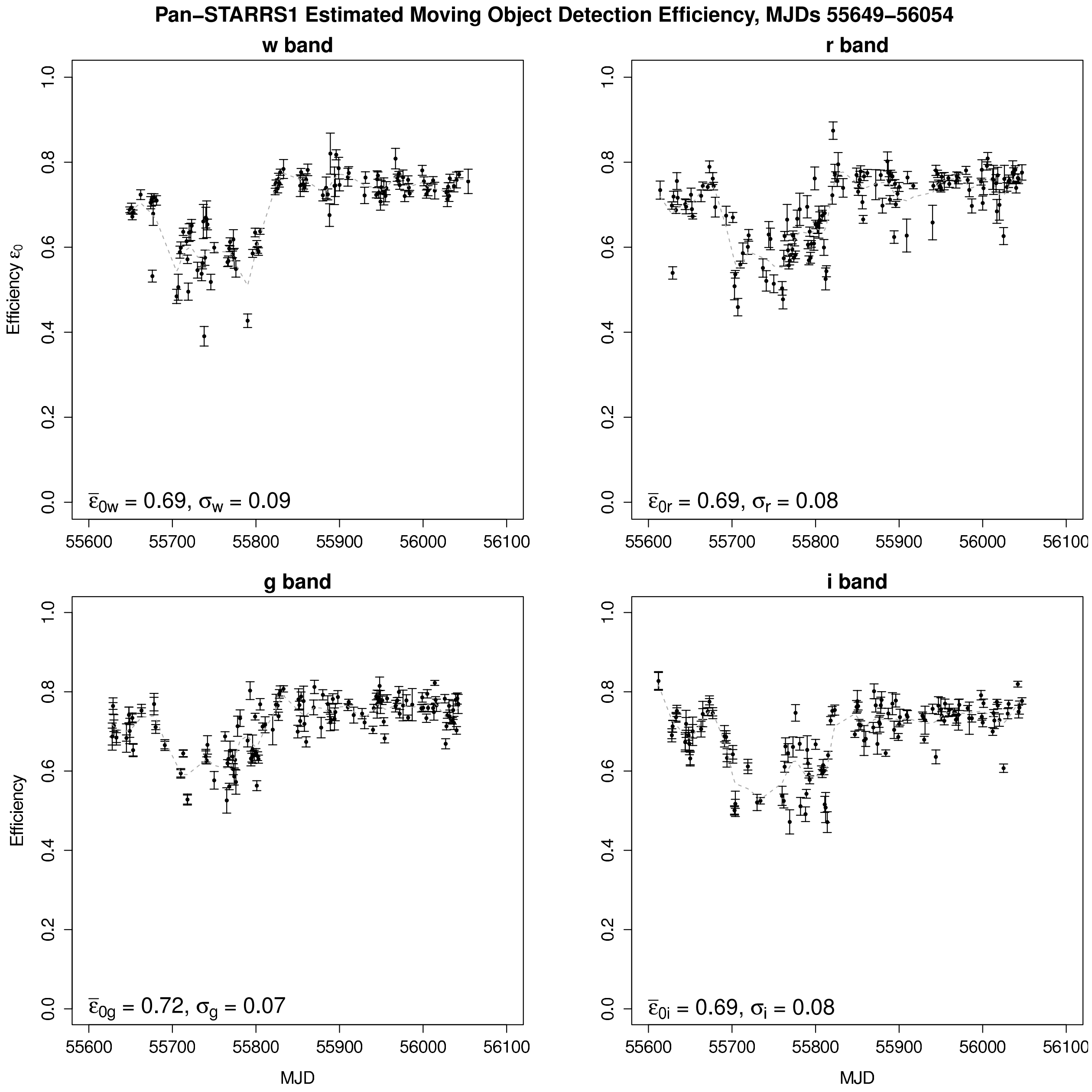

FIG. 23.—Pan-STARRS1 moving object detection efficiency for bright non-saturated detections as a function of MJD corresponding to the time period from approximately Feb 2011 through Jun 2012. Around MJD 55820, MOPS began employing less-aggressive false detection filtering of IPP transient detections, boosting per-exposure detection efficiency to 75% consistently. The *dashed line* is a spline-fit to the data.

main-belt asteroids with $\mathcal{W}_{P1} < 19$, Pan-STARRS1 reported about 1/3 the predicted number. Fainter than $\mathcal{W}_{P1} = 19$ the reported rate drops further until the sensitivity limit is reached. Many factors account for the discrepancy between the predicted and realized rates:

1. objects can be lost (primarily MBOs) in image differencing when observing away from opposition because of stationary points (i.e., the differencing subtracts all or part of the detection)
2. tracklets submitted to the MPC might not yet be assigned a designation (a ‘one night stand’ tracklet)
3. per-exposure live detector fraction may fall below the nominal 75% due to *e.g.* aggressive masking in regions with high stellar sky-plane density
4. true night-to-night sensitivity in $\mathcal{W}_{P1}$ is poorer than the constant model used for synthetics
5. the synthetic S/N model overestimates faint-end performance

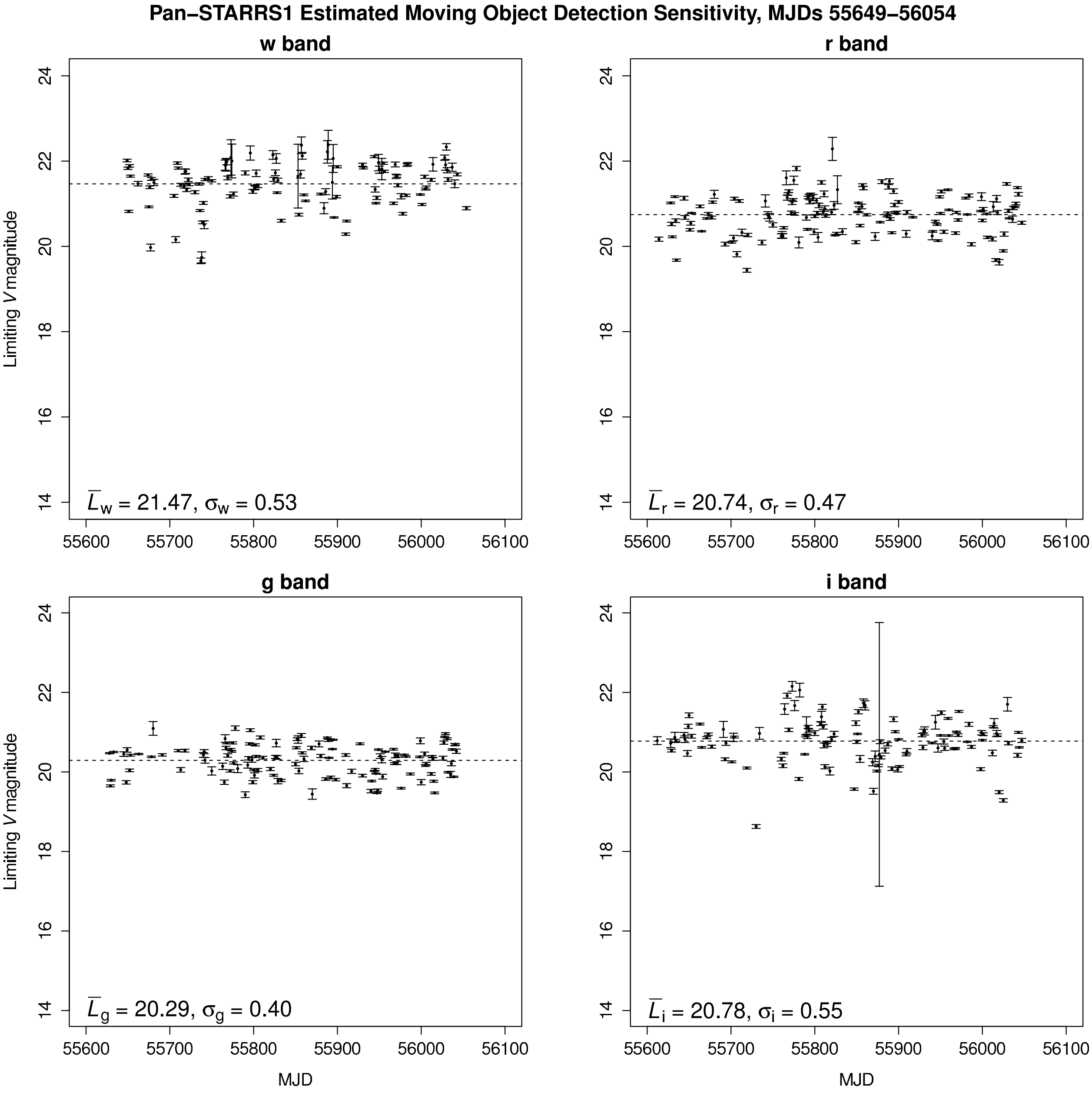

FIG. 24.—Pan-STARRS1 nightly limiting magnitude in each of the four main filters used to detect moving objects as a function of MJD corresponding to the time period from approximately Feb 2011 through Jun 2012. The *dashed lines* represent fits to the passband data as a function of time.

6. the S3M may overstate the number of objects in some sub-populations.

The situation is better for the NEOs that show better agreement between the model and Pan-STARRS1 down to the sensitivity limit. The effect of (1) almost disappears because NEOs will rarely have stationary sky-plane motion, and (2) is reduced because of the NEO confirmation process for one-night tracklets coordinated by the MPC.

6. CURRENT Pan-STARRS1 PERFORMANCE

As of late 2012, great strides have been made image processing and telescope scheduling to increase the yield of asteroids from the Pan-STARRS1 survey. Better measurement and modeling of detector readout noise has resulted in greater detection sensitivity in image processing. Finer characterization of detection morphology by the IPP allows MOPS to reject many classes of false detections upon ingest so that they do

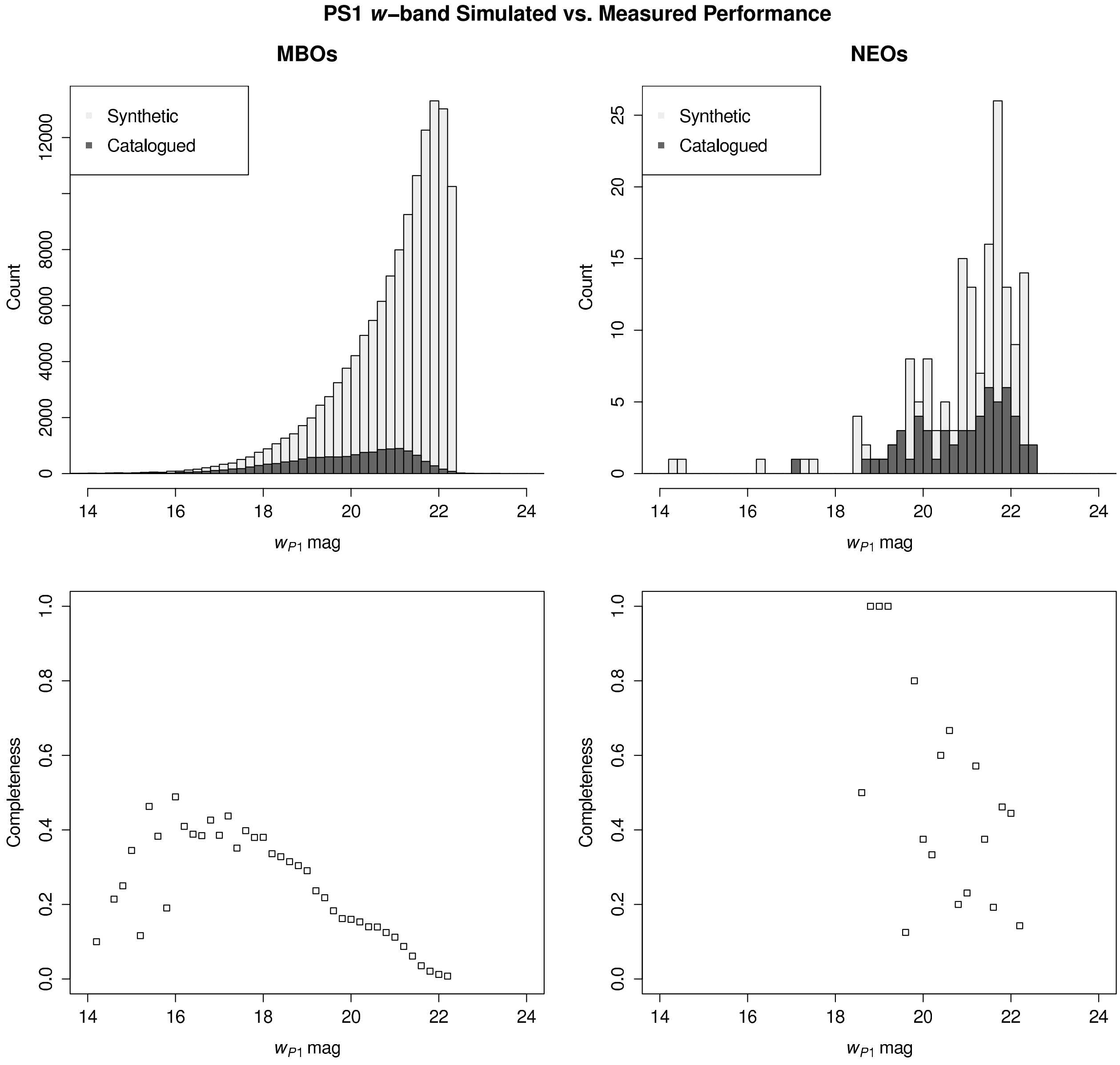

FIG. 25.—Comparison of MOPS synthetic tracklet counts to Pan-STARRS1 submitted tracklets during the period 2011 Aug 13 through 2011 Oct 11 for (*left*) main belt objects and (*right*) near-Earth objects.

not contaminate the NEO tracklet review process. The Pan-STARRS1 Modified Design Reference Mission survey (Chambers 2012) has increased the fraction of 3π survey time spent observing in quads. With the recent completion of the 3π static sky processing, there will be additional improvement in the system limiting magnitude of at least 0.4 mag as IPP moves from pairwise difference imaging to static sky differencing.

Figure 26 shows NEO discovery and submitted object totals for Pan-STARRS1 and other NEO surveys. Although monthly totals can vary with weather losses, since late 2010 the Pan-STARRS1 NEO discovery rate has been increasing. Using IPP's morphological characterization and a MOPS comet candidate review procedure similar to that for NEOs, Pan-STARRS1 has become a capable comet finder, discovering 30 to date and 8 in October 2012 alone.

7. AVAILABILITY AND ONGOING DEVELOPMENT

The MOPS software is available under the GNU General Public License Version 2, and can be retrieved by sending a query to the PS1 Science Consortium.[26] MOPS has become a large and somewhat unwieldly package, employing (too many)

---

[26] See http://www.ps1sc.org.

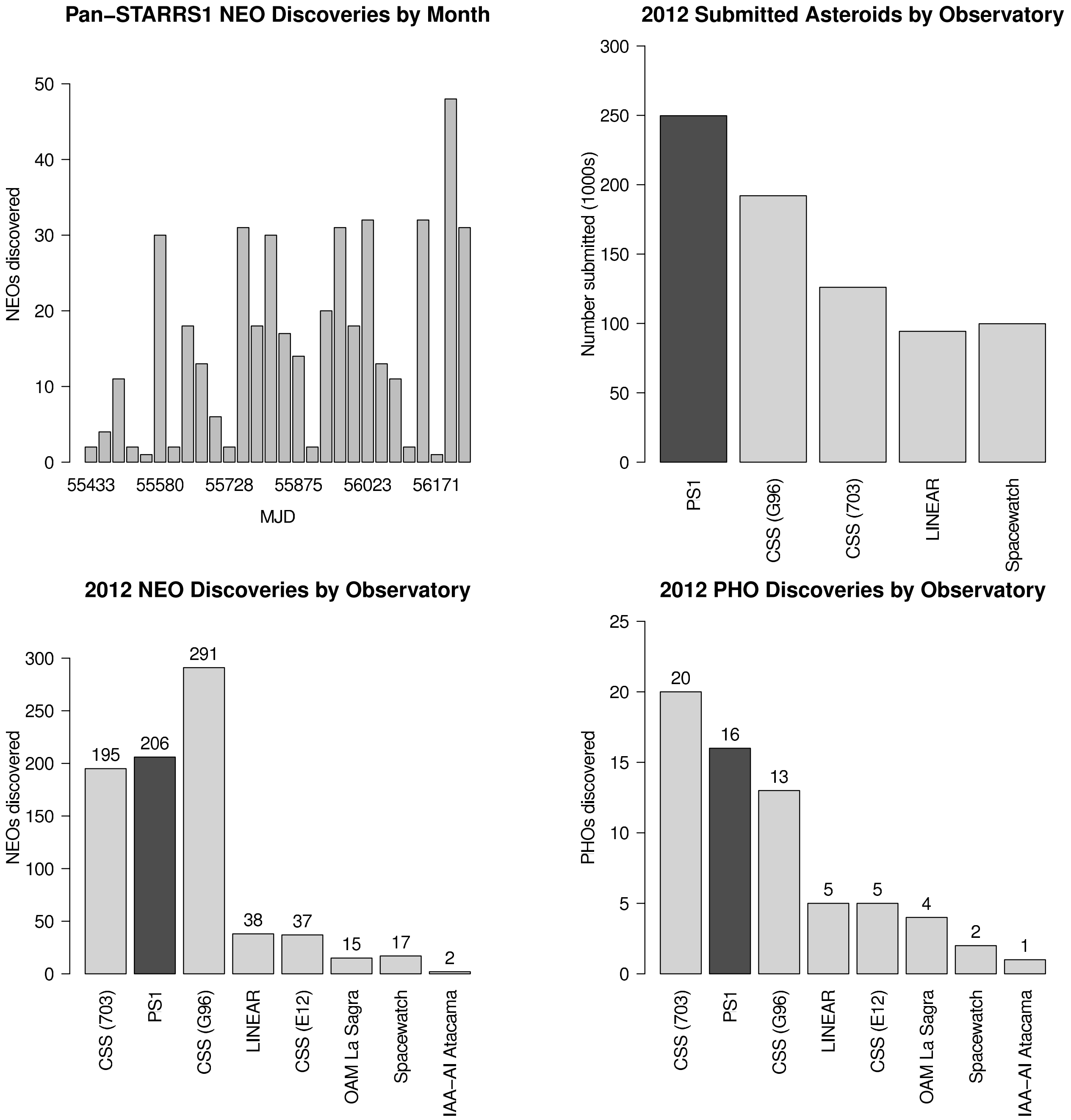

FIG. 26.—Pan-STARRS1 discovery statistics as of November 2012 (from the Minor Planet Center).

different programming languages preferred by third-party software (not all available directly from the PS1SC), and containing many installation dependencies for Perl and Python modules. Fortunately, documentation and development notes are available via the PS1SC web site.

Not all MOPS subcomponents are freely available and some are not integrated into the MOPS software distribution. In particular, the JPL Solar System Dynamics package that performs MOPS differential correction must be obtained directly from JPL. Other packages such as OrbFit and the SLALIB positional astronomy library must be downloaded separately.

Approximately 15–20 full-time equivalent (FTE) years have gone into the development of MOPS and the S3M, and development continues in support of Pan-STARRS1's ongoing NEO survey and upcoming NEO surveys such as ATLAS (Tonry et al. 2012). Prior to handling live Pan-STARRS1 data, MOPS processed testing data from Spacewatch (e.g., Gehrels 1991; Gehrels and Jedicke 1996) and raw data in support of the

Thousand Asteroid Light Curve Survey (TALCS; Masiero et al. 2009). MOPS has additionally been instrumental in providing simulation results for Pan-STARRS, LSST and ATLAS, and as a research tool for many graduate students and postdocs.

8. FUTURE IMPROVEMENTS

The future of MOPS likely falls in several areas:

1. Optimizing execution speed for next-generation Pan-STARRS4-like data volumes through reduction of database I/O and greater in-memory processing.
2. Improved MOPS installation and configuration for non-Pan-STARRS surveys.
3. Modeling of photometric artifacts, e.g., partially masked PSFs and trails.
4. The linear processing model employed by MOPS is appropriate for a mature survey but can be inadequate when evaluating production parameters. It is difficult to merge separate MOPS databases created under different runtime configurations into a single coherent database. Future versions of MOPS should be more agile in its ability to perform non-linear processing and merge datasets.
5. Increased fidelity of synthetics. For example, although our simulations coarsely avoid the moon they do not incorporate the effects of varying sky sensitivity or effects due to the presence of bright objects in the field of view. In one sense, however, these effects are really an aspect of detector sensitivity and not MOPS itself, and they can be integrated via per-field detection efficiency parameters if they are measured by IPP.
6. Fill-factor modeling. There is experimental code to use the mask of Figure 6 as a crude live-pixel server (LPS, § 3.12) to simulate detections lost on dead areas of the detector.
7. Simplified processing for large-scale simulations, *e.g.* two-body ephemerides instead of a perturbed dynamical model.

9. SUMMARY

MOPS has proven to be a capable tool for detecting moving objects in the Pan-STARRS1 transient detection stream. Despite the differences between the targeted Pan-STARRS4 capability and current Pan-STARRS1 performance, we have deployed MOPS effectively in our search for NEOs and comets and in characterizing the main belt. Importantly, we have estimates of our efficiency of object detection so that we can provide a foundation for large-scale population studies.

Additionally, we have made progress toward our design goal of creating a system that can detect objects and compute their orbits with $>99\%$ efficiency for most solar system populations when provided next-generation survey astrometry and data quality. Our experience with Pan-STARRS1 shows that the desired performance is challenging to achieve with real telescope data.

With nearly 1 year remaining in the Pan-STARRS1 survey, we expect further broad improvements in astrometry, photometry, difference imaging and sensitivity in the final Pan-STARRS1 data release. The Pan-STARRS2 telescope (Burgett 2012) is under construction adjacent to the Pan-STARRS1 facility and will have a raw detector sensitivity and optical performance exceeding that of Pan-STARRS1. Operating modes currently under consideration for the two telescopes have them working in tandem, increasing performance even further. Combined with optimization and tuning of the Pan-STARRS1 MOPS pipeline, we look forward to applying the full capability of MOPS to this data and to the subsequent riches that will lie in this catalog of moving objects.

The Pan-STARRS1 Survey has been made possible through contributions of the Institute for Astronomy, the University of Hawai‘i, the Pan-STARRS Project Office, the Max-Planck Society and its participating institutes, the Max Planck Institute for Astronomy, Heidelberg and the Max Planck Institute for Extraterrestrial Physics, Garching, The Johns Hopkins University, Durham University, the University of Edinburgh, Queen's University Belfast, the Harvard-Smithsonian Center for Astrophysics, and the Las Cumbres Observatory Global Telescope Network, Incorporated, the National Central University of Taiwan, and the National Aeronautics and Space Administration under Grant No. NNX08AR22G issued through the Planetary Science Division of the NASA Science Mission Directorate.

The design and construction of the Panoramic Survey Telescope and Rapid Response System by the University of Hawaii Institute for Astronomy was funded by the United States Air Force Research Laboratory (AFRL, Albuquerque, NM) through grant number F29601-02-1-0268.

We thank the Jet Propulsion Laboratory, an operating division of the California Institute of Technology, for providing an executable version of their Rapid Comet and Asteroid Orbit Determination Process software (NTR-41180) to the Institute for Astronomy at the University of Hawai‘i for use in MOPS.

We acknowledge the financial and technical contributions to this work made by the Large Synoptic Survey Telescope (LSST) Corporation team, in particular Tim Axelrod, Lynne Jones and Jeff Kantor. In addition, we acknowledge the support by Pan-STARRS and LSST management to enable and facilitate this productive collaborative effort between the two projects.

Don Yeomans (JPL) and Ted Bowell (Lowell Observatory) provided expert feedback as external reviewers for the MOPS system in the early years of its development.

Many colleagues provided helpful feedback on the MOPS system operation and usability as well as supporting MOPS development. We would in particular like to thank Wen-Ping Chen and Rex Chang from the Institute of Astronomy, National Central University, Taiwan.

This research has made use of the SIMBAD database, operated at CDS, Strasbourg, France.

REFERENCES

Alvarez, L. W., Alvarez, W., Asaro, F., & Michel, H. V. 1980, Science, 208, 1095

Bowell, E., Koehn, B. W., Howell, S. B., Hoffman, M., & Muinonen, K. 1995, BAAS, 27, 1057

Burgett, W. S. 2012, Proc. SPIE, 8449, 84490T

Chambers, K. 2006, in The Advanced Maui Optical and Space Surveillance Technologies Conference (New York: Curran Associates)

Chambers, K. C. 2007, BAAS, 39, 142.06

———. 2012, in American Astronomical Society Meeting Abstracts, 220, 107.04

Chesley, S. R., & Spahr, T. B. 2004, in Mitigation of Hazardous Comets and Asteroids, ed. M. J. S. Belton, T. H. Morgan, N. H. Samarasinha, & D. K. Yeomans (Cambridge: Cambridge University Press), 22

Donalek, C., Mahabal, A., Djorgovski, S. G., Marney, S., Drake, A., Glikman, E., Graham, M. J., & Williams, R. 2008, in AIP Conf. Proc. 1082, Classification and Discovery in Large Astronomical Surveys, ed. C. A. L. Bailer-Jones, (New York: AIP), 256

Gehrels, T. 1991, Space Sci. Rev., 58, 347

Gehrels, T., & Jedicke, R. 1996, Earth Moon Planets, 72, 233

Gladman, B., Michel, P., & Froeschlé, C. 2000, Icarus, 146, 176

Gladman, B. J., et al. 2009, Icarus, 202, 104

Granvik, M., & Muinonen, K. 2008, Icarus, 198, 130

Granvik, M., Virtanen, J., Oszkiewicz, D., & Muinonen, K. 2009, Meteoritics Planet. Sci., 44, 1853

Grav, T., Jedicke, R., Denneau, L., Chesley, S., Holman, M. J., & Spahr, T. B. 2011, PASP, 123, 423

Harris, A. 2008, Nature, 453, 1178

Helin, E. F., Pravdo, S. H., Rabinowitz, D. L., & Lawrence, K. J. 1997, Ann. N. Y. Acad. Sci., 822, 6

Hodapp, K. W., et al. 2004, Astron. Nachr., 325, 636

Jedicke, R. 1996, AJ, 111, 970

Jedicke, R., & Herron, J. D. 1997, Icarus, 127, 494

Jedicke, R., Larsen, J., & Spahr, T. 2002, Asteroids III, 71

Jedicke, R., & Metcalfe, T. S. 1998, Icarus, 131, 245

Jedicke, R., Morbidelli, A., Spahr, T., Petit, J. M., & Bottke, W. F. 2003, Icarus, 161, 17

Jenniskens, P., et al. 2009, Nature, 458, 485

Kaiser, N. 2004, Proc. SPIE, 5489, 11

Kaiser, N., et al. 2002, Proc. SPIE, 4836, 154

Karaali, S., Bilir, S., & Tunçel, S. 2005, PASA, 22, 24

Kubica, J., Moore, A., Connolly, A., & Jedicke, R. 2005, Proc. SPIE, 5913, 242

Kubica, J., et al. 2007, Icarus, 189, 151

Kuiper, G. P., Fujita, Y., Gehrels, T., Groenveld, I., Kent, J., van Biesbroeck, G., & van Houten, C. J. 1958, ApJS, 3, 289

Larsen, J. A., et al. 2001, AJ, 121, 562

———. 2007, AJ, 133, 1247

Larson, S. 2007, in IAU Symp. 236, Near Earth Objects, our Celestial Neighbors: Opportunity and Risk, ed. G. B. Valsecchi, & D. Vokrouhlický, (Cambridge: Cambridge University Press), 323

Magnier, E. 2006, in The Advanced Maui Optical and Space Surveillance Technologies Conference (New York: Curran Associates), 30

Magnier, E. A., Liu, M., Monet, D. G., & Chambers, K. C. 2008, in IAU Symp., 248, A Giant Step: From Milli- to Micro-Arcsecond Astrometry, ed. W. J. Jin, I. Platais, & M. A. C. Perryman (Cambridge: Cambridge University Press), 553

Mainzer, A., et al. 2011, ApJ, 743, 156

Masiero, J., Jedicke, R., Ďurech, J., Gwyn, S., Denneau, L., & Larsen, J. 2009, Icarus, 204, 145

McMillan, R. S. 2007, in IAU Symp. 236, Near Earth Objects, our Celestial Neighbors: Opportunity and Risk, ed. G. B. Valsecchi, D. Vokrouhlický, & A. Milani, (Cambridge: Cambridge University Press), 329

Milani, A., & Gronchi, G. F. 2010, Theory of Orbital Determination (Cambridge: Cambridge University Press)

Milani, A., Gronchi, G. F., Farnocchia, D., Knežević, Z., Jedicke, R., Denneau, L., & Pierfederici, F. 2008, Icarus, 195, 474

Milani, A., Gronchi, G. F., Knežević, Z., Sansaturio, M. E., & Arratia, O. 2005, Icarus, 179, 350

Milani, A., et al. 2012, Icarus, 220, 114

Morgan, J., Siegmund, W., & Hude, C. 2006, in The Advanced Maui Optical and Space Surveillance Technologies Conference (New York: Curran Associates), 28–29

Petit, J., Holman, M., Scholl, H., Kavelaars, J., & Gladman, B. 2004, MNRAS, 347, 471

Rabinowitz, D. L. 1991, AJ, 101, 1518

———. 1993, ApJ, 407, 412

Rabinowitz, D. L., et al. 1993, Nature, 363, 704

Schlafly, E. F., et al. 2012, ApJ, 756, 158

Seaman, R., et al. 2011, Proc. Int. Astron. Union, 7, 221

Shoemaker, E. M. 1995, Geophys. Res. Lett., 22, 1555

Stokes, G. H., Evans, J. B., Viggh, H. E. M., Shelly, F. C., & Pearce, E. C. 2000, Icarus, 148, 21

Thain, D., Tannenbaum, T., & Livny, M. 2005, Concurrency—Practice and Experience, 17, 323

Tonry, J., Burke, B. E., & Schechter, P. L. 1997, PASP, 109, 1154

Tonry, J. L., Luppino, G., Kaiser, N., Burke, B. E., & Jacoby, G. H. 2004, in Astrophysics and Space Science Library, 300, Scientific Detectors for Astronomy, The Beginning of a New Era, ed. P. Amico, J. W. Beletic, & J. E. Belectic (Dordrecht: Springer), 395

Tonry, J. L., et al. 2012, ApJ, 750, 99

Tyson, A., & Angel, R. 2001, in ASP Conf. Ser. 232, The New Era of Wide Field Astronomy, ed. R. Clowes, A. Adamson, & G. Bromage (San Francisco: ASP), 347

van Houten, C. J., van Houten-Groeneveld, I., Herget, P., & Gehrels, T. 1970, A&AS, 2, 339

Vereš, P., Jedicke, R., Wainscoat, R., Granvik, M., Chesley, S., Abe, S., Denneau, L., & Grav, T. 2009, Icarus, 203, 472

Zavodny, M., Jedicke, R., Beshore, E. C., Bernardi, F., & Larson, S. 2008, Icarus, 198, 284

（別紙様式２）

論文要旨

区分	[✓ 甲]・乙	氏名	上津原正彦

論文題名　○○○○　----------------------　○○○○
Search strategy applicable for breakup fragments in the geostationary region
(静止軌道領域における破砕由来スペースデブリの効率的な探索方法に関する研究)

論文内容の要旨

This dissertation proposes an effective search strategy applicable for fragmentation debris generated by energetic breakups of large space objects, e.g., satellites and rocket upper-stages, in the geostationary region. There are two definitive breakups in the geostationary region whose occurrences were occasionally confirmed by observations soon after the breakups. Past observation campaigns for the geostationary region have been found thousands of uncatalogued space objects, which may be associated with breakups. Moreover, it is confirmed that some of large space objects in the geostationary region have experienced unintended orbital change, i.e., orbital anomaly, that might be associated with breakup. Thus, search for the fragmentation debris will directly contribute to verify relations between uncatalogued space objects, breakups, and suspected orbital anomalies for the better understandings of current situations in the geostationary region.

The search strategy to be proposed in this dissertation utilizes orbital debris modeling techniques that describe debris generation and orbit propagation. The orbital debris modeling can predict behaviors of individual and group of fragmentation debris at breakups and also at observations. The search strategy, thus, enables effective observation planning, sensitive detection, straightforward origin identification, and breakup event characterization.

This dissertation introduces five principal roles required for the search strategy and verifies the roles in each chapter. The second chapter formulates the search strategy based on orbital debris modeling techniques. The third chapter addresses the deterministic origin identification of fragmentation debris, which enables simultaneous search for multiple breakup events and identification of unconfirmed breakups. The fourth chapter addresses the probabilistic origin identification of fragmentation debris, which enables characterization of breakup scale and improvement of orbital debris

modeling in the search strategy. The fifth chapter formulates breakup event characterization methodologies including fragmentation profile assessment and breakup scale assessment. The breakup scale assessment is demonstrated by applying a Bayesian approach combined with the probabilistic origin identification technique. The sixth chapter addresses unconfirmed breakup identification by evaluating uncertainties of unconfirmed breakups, and by applying the deterministic origin identification technique.

Along with theoretical confirmations of the search strategy to be addressed in each chapter, this dissertation also conducts empirical confirmations of the search strategy. The empirical confirmations utilize ground-based optical measurement techniques, which is a common approach for the geostationary objects observation. Optical sensor to be used consists of a small aperture telescope (≤1m) equipped with a charge coupled devise camera. Through the theoretical and empirical confirmations from the second chapter to the sixth chapter, this dissertation will finally establish the effective search strategy that contributes to define current situation in the geostationary region.

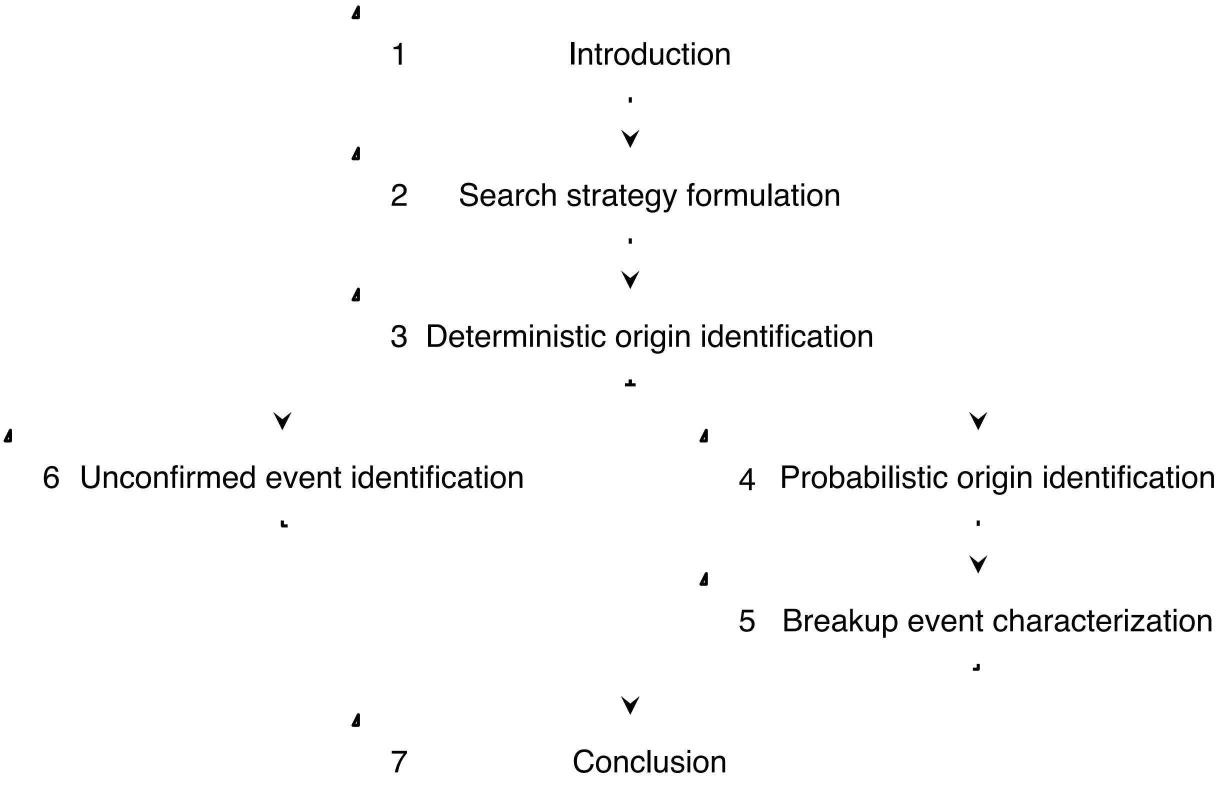

Figure 1. The structure of the dissertation.

工作報告

2013A LOT Time Allocation Report

This is a report for the time allocation of the Lulin 1m telescope (LOT) for the 2013A semester. There were 27 proposals including 4 educational programs and 3 ToO proposals. February and March was the most competitive observing time window. Several proposals were arrived after the deadline of the proposal submission. These were simply rejected. The proposal evaluations were performed following criteria,

- Ranking of external reviewers
- Publications using LOT and/or achievements if the proposal is continuous programs
- Thesis programs with specific "Planned date of the defense"
- Clear publication (thesis, refereed journal etc) plans with well planned sciences

To keep competitive and effective scientific outputs of LOT (thesis and refereed journal), TAC invited experts who have huge experiences both on science and instrumentations with small to 8m class telescopes. They kindly made constructive suggestions and comments that were very helpful to improve our scientific operation and effective outputs. These experts made ranking for our proposal based on scientific merits with LOT and instruments. They also encouraged proposals with the TRIPOL instrument.

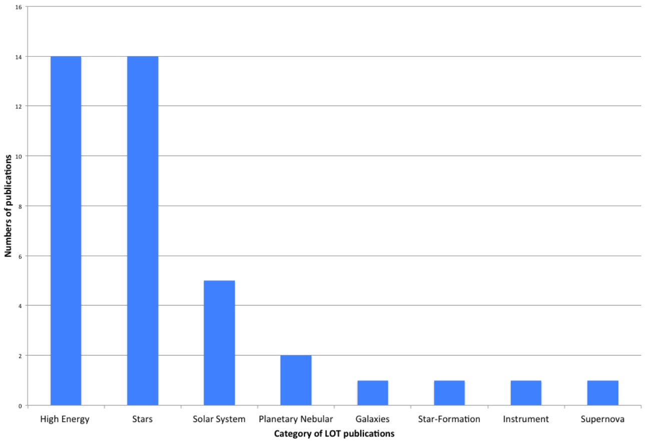

We have also checked scientific outputs based on PI's publications with LOT (right figure). The most efficient scientific categories are high-energy and stars. Because qualities of proposals and the ranking also showed this trend, the publication status was used simply as reference. Generally, the worst situation on telescope operations is no scientific outputs with significant amount of actual observations. To avoid these situations, TAC also evaluated the external collaborations (e.g. campaign observations) and additional resources (e.g. multi-wavelength observations and/or analysis skills). In addition, to avoid halfway jobs, TAC allocated significant numbers of observing time for highly ranked programs.

About thesis programs (student PI programs), general quality of proposals was insufficient to allocate time. Main problems were no obvious scientific objectives and unclear planned research. Reviewers strongly encourage consulting with supervisors. The planning is one of the most important parts to conduct observational sciences. To help these programs, TAC inflated their scores. Two ToO programs (GRB with any instruments and CV with LCI) will run during the 2013A semester. GRB ToO has higher priority if the triggering occurs on the same night.

ID		Title	Note
2	C. C. Ngeow	LOT Experience for Summer Undergraduate Students	Edu
3	WenPing Chen	Whole-Earth Telescope Campaign of WD J1518+0658	
4	WenPing Chen	Searching for Transiting Young Exoplanets in Galactic Open Clusters	
5	Chien De Lee	Simultaneous Observations of Be Stars with Strong Near Infrared Excess	
6	Shih-Ping Lai	Observation Experience for High School Teachers	Edu
7	WenPing Chen	Magnetic Field Structure in Molecular Cloud Probed by Optical Polarization	
8	Ishioka Ryoko	Positive and negative superhumps in extremely active dwarf nova, RZ LMi	
9	Jia Wei Wang	Reveal the magnetic structure in the filamentary cloud Aquila rift	
10	Yu-Mei Lin	Student Training for TFG's Astronomy Curriculum with E-learning	Edu
11	Tzu-Ching Yen	The nature of Fermi-identified black widow pulsar candidates	
12	ZhongYi Lin	Monitoring the brightest comet C/2011 L4 (PANSTARRS) of the decade	
13	Hilding Neilson	Polarization of Mira Variable Stars: Constraints on stellar structure	
14	Hilding Neilson	What drives a Cepheid wind – Constraints from polarization observations	
15	Jingshown Wu	Measurement of the Speed of Light from Extraterrestrial Sources	
16	Yuji Urata	Gamma-Ray Burst Afterglows	ToO(A)
17	Yuji Urata	Core-collapse Supernova and Optical Transients	
18	Anli Tsai	Optical Identification of the Unidentified Fermi Objects	
19	ZhongYi Lin	Polarimetric Observations on Hot Jupiters and comet 29P/S-W 1	
21	Shih-Chao Lin	Students Training for Dali Senior High School's	Edu
23	Ting-Chang Yang	Fast Photometry on Outbursting Cataclysmic Variables	ToO(B)
25	Kang-Shian Pan	Polarimetric Observations of Themis Asteroid Family	
27	I Ling Lin	Follow-Up Observation of Galactic Cepheids Identified from PS1 3π Data	

2013B LOT Time Allocation Report

This is a report for the time allocation of the Lulin 1m telescope (LOT) for the 2013B semester. There were 26 proposals including 7 educational programs and 2 ToO proposals. Two programs were also requested to director time for testing of AO and NCUCam. As usual, the evaluation of proposals was performed following criteria,

- **Ranking of external reviewers**
- **Publications using LOT and/or achievements if the proposal is continuous programs**
- **Thesis programs with specific "Planned date of the defense"**
- **Clear publication (thesis, refereed journal) plans with well planned sciences**

To keep competitive and effective scientific outputs (thesis and refereed journal), TAC invited experts who have huge experiences both on science and instrumentations with small to 8m class telescopes. They kindly made constructive suggestions and comments that were very helpful to improve our scientific operation and effective outputs. These experts made ranking for our proposal based on scientific merits with LOT and instruments.

We have also checked scientific outputs based on PI's publications with LOT (right figure). The most efficient scientific categories are high-energy and stars. The qualities of proposals and the ranking also showed this trend. Generally, the worst situation on telescope operations is no scientific outputs with significant amount of actual observations. To avoid these situations, TAC also evaluated the external collaborations (e.g. campaign) and additional resources (e.g. multi-wavelength coordination, skills). In addition, to avoid halfway jobs, TAC allocated significant numbers of observing time for highly ranked programs. Due to difficulties of scheduling for some of monitoring program with the ranking, the cadences/durations may be insufficient.

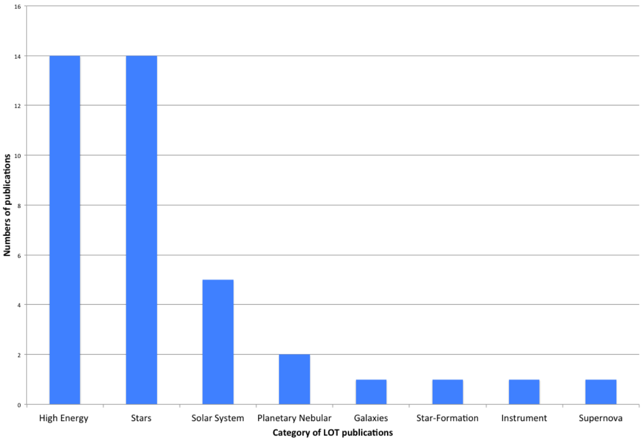

About thesis programs (student PI programs), general quality of proposals was insufficient to allocate time. Main problems were no obvious scientific objectives and unclear planned research. Reviewers strongly encourage consulting with supervisors. The planning is one of the most important parts to conduct observational sciences. To help these programs, TAC inflated their scores. Two ToO programs (GRB and SLSN/ULSN) will run during the 2013B semester. GRB ToO has higher priority if the triggering occurs on the same night.

ID		Title	Note
1	Lupin Chun-Che Lin	Teaching Excellence Project of CMU	Edu
2	Ngeow Chow-Choong	LOT Observation Training for NCU's Observational Astronomy Course	Edu
3	W. P. Chen	Searching for Transiting Young Exoplanets in Galactic Open Clusters	
4	Shengbang QIAN	Searching for Transiting Young Exoplanets in Galactic Open Clusters	
5	Wu Jingshown	An Optical System of Comparing the Speeds of Light from Moving Stars	
6	Lai Shih-Ping	Student Training for NTHU's "Fundamentals of Observational Astronomy" Course	Edu
7	Hilding Neilson	Polarization of Mira Variable Stars: Constraints on stellar structure (Part II)	
8	Hilding Neilson	What drives a Cepheid wind – Constraints from polarization observations (Part II)	
9	Ip, Wing-Huen	Multicolor observations of Near-Earth Asteroids	
10	Lin I Ling	Follow-Up Observation of Galactic Cepheids Identified from PS1 3π Data II	
11	Lin Shih-chao	Students Training for Dali Senior High School's	Edu
12	Li-Ching Huang	G-type flare stars observation	
13	Jia Wei Wang	Reveal the magnetic structure in the filamentary cloud, NGC1333	
14	Shen Pei Min	Optical Spectroscopy on the Rotation of Classical Be Stars with Infrared Excess	
15	Chen, I-Chenn	Probing Variability of non-HBLR Type 2 AGNs	
16	Yu-Mei Lin	Student Training for TFG's Earth Science Club	Edu
17	Lin, ZhongYi	What will happen to the sungrazing comet C/2012 S1 (ISON)	
18	Yuji Urata	Gamma-Ray Brust Afterglows	ToO
19	Yuji Urata	Core-collapse Supernova and Optical Transients	ToO
21	Shih-Ping Lai	Observation Experience for Students Participating in ACE Project	Edu
22	Cheng Yu Chi	Follow-up Observation on Selected Jovian Trojans from Pan-STARRS Survey	
23	Pan, Kang-Shian	Polarimetric Observations of Themis Asteroid Family	
24	Bing-Xun Wu	Workshop of astronomical astronomy in LOT	Edu
25	Lee Chien De	Simultaneous Observations of Be Stars with Strong Near Infrared Excess	
26	Abe, Shinsuke	Polarimetric Observations of Main-belt Origin of 1999 JU3 Target of HAYABUSA2	

DOGIOYA 儀器進度報告

CHEN Tse-Chuan, KINOSHITA Daisuke
December 2013

Abstract

DOGIOYA 為鄒族語「蝴蝶」的意思，借由蝴蝶四隻彩色的翅膀象徵「可見光四色同步成像儀」用來觀測四個不同顏色波段的天文相機之儀器總成。此儀器完成後，將運往夏威夷大學位於 Mouna Kea Summit 的 UH88 望遠鏡安裝，做為本所與夏威夷大學天文所為期四年合作計畫的觀測儀器。DOGIOYA 為本所儀器室團隊歷經數年開發完成，隸屬於「泛星後續追蹤觀測計畫－ 鹿林兩米天文望遠鏡儀器研製」項下，本計畫已於 2013 年 5 月底結案，歷年來累積許多珍貴的天文儀器開發經驗與技術，為本所奠定儀器開發的重要里程碑。以下我將簡單報告：新修正鏡組的採購緣由、交貨與驗收紀要、由舊修正鏡組到新修正鏡組的安裝方法；DOGIOYA 整體儀器安裝步驟、儀器安裝過程的機構建設計與修改、以及為了儀器安裝便利性和安全性考量所重新設計的電路板組等議題。

1. DOGIOYA 儀器介紹

DOGIOYA 儀器主要分為上下兩層，圖 1 為其儀器配置示意圖。下層為「Optics Layer」，包含新修正鏡組、分光器、三台 SI1100 相機、NCUcam-1 相機、電路板組以及轉接環等；上層為「Power & Control system Layer」，包含 UCAM 控制器電源、UCAM 控制器、快門驅動器、做為溫度記錄的類比/數位轉換器、做為真空值記錄的真空計、電路板組電源及延長線座。圖 2 則為 DOGIOYA 外觀照片。

2. 新修正鏡組

原來的「可見光四色同步成像儀」(即 DOGIOYA 的前身)是設計來安裝在鹿林兩米望遠鏡上的主要觀測儀器，其與望遠鏡連接之光學系統，原是考量兩米望遠鏡的規格所設計，而今若要與其他望遠鏡搭配使用，其光學系統中的修正鏡組必需重新設計方能與之安裝。因此，我們於 2012 年 8 月啟動新修正鏡組的採購，同樣委由日本 Photocoding 公司設計與製作，並於 2013 年 5 月底完成交貨及驗收。修正鏡組與望遠鏡、儀器之關係如圖 3 所示。

新修正鏡組交貨的同時，日本原廠的設計者 YUJI Ikeda 博士也隨同前來台灣參與驗收過程和儀器教育訓練，全程指導我們如何拆除舊修正鏡組、將光學系統移至另一儀器架、而後再安裝新修正鏡組；模擬夏威夷 UH88 現場，如何將 DOGIOYA 安裝至望遠鏡上；保養方法及注意事項說明。

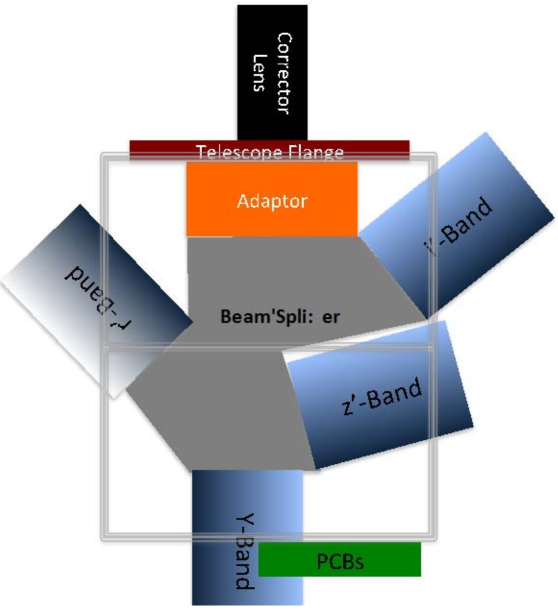

(a) Optics Layer

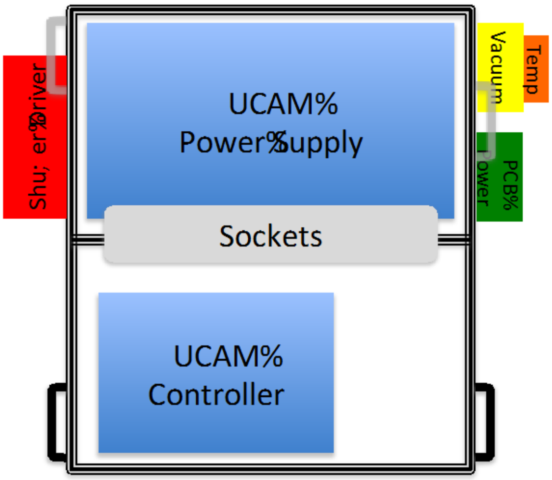

(b) Power & Control system Layer

圖 1 DOGIOYA 儀器配置示意圖。(a)為下層的 Optics Layer，(b)為上層的 Power & Control system Layer。

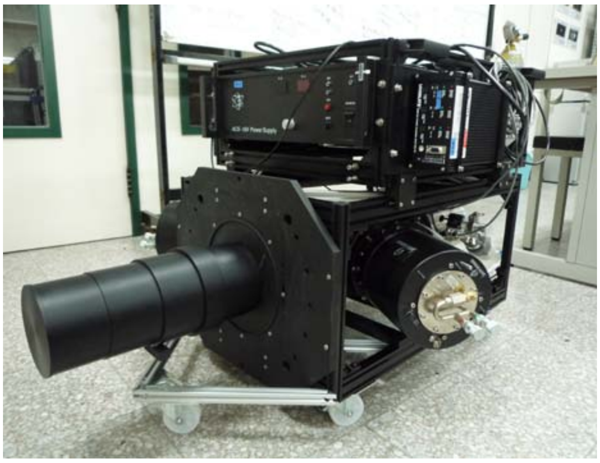

圖 2 DOGIOYA 外觀照片。

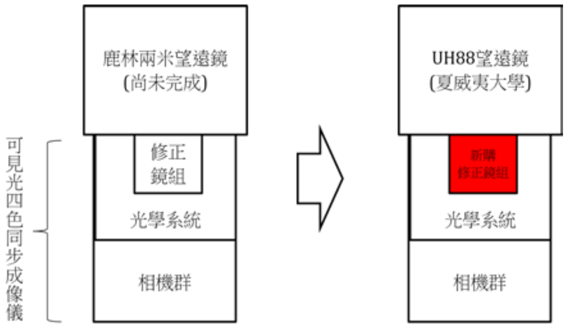

圖 3 修正鏡組與望遠鏡、儀器關係示意圖。

圖 4 為新修正鏡組的外觀照片，圖 5 將由六張照片依序說明舊、新修正鏡組轉換的過程。

圖 4 新修正鏡組外觀：長約 50cm、重約 5.5kg。

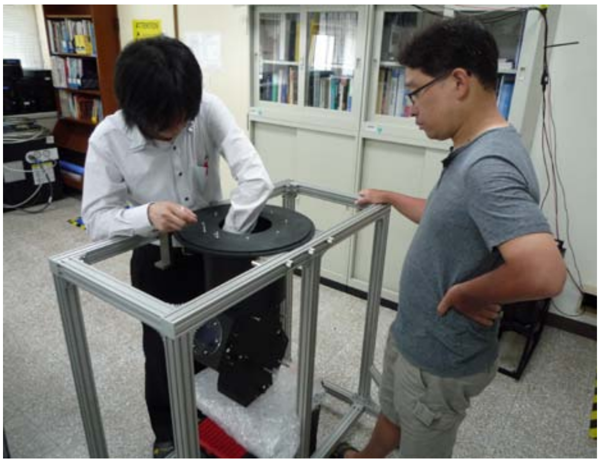

(a) 將原本安裝在「四波段同步光學系統」上的光學系統拆下

(b) 拆下的光學系統包含分光器和舊修正鏡組兩部份

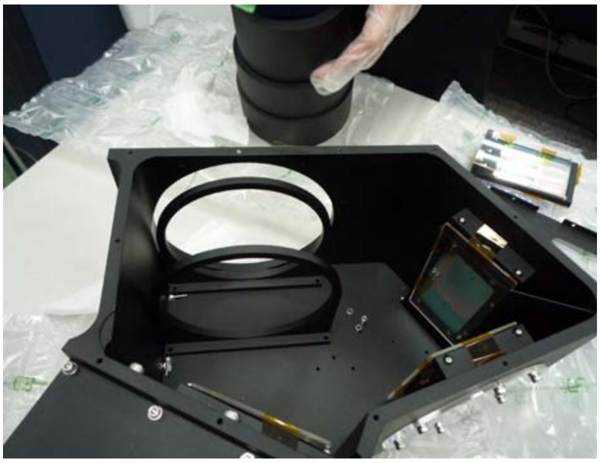

(c) 將舊修正鏡組自分光器中分離出來

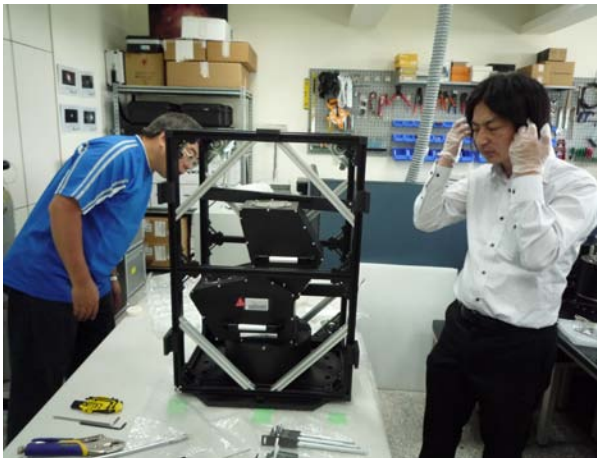

(d) 將分光器安裝至新的儀器架上

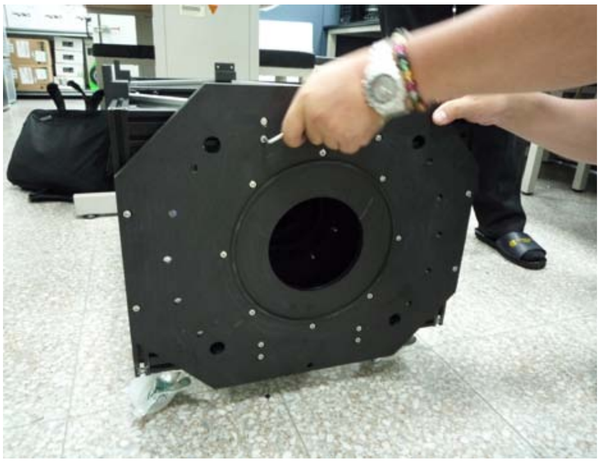

(e) 裝上儀器架與 UH88 望遠鏡連接的介面板

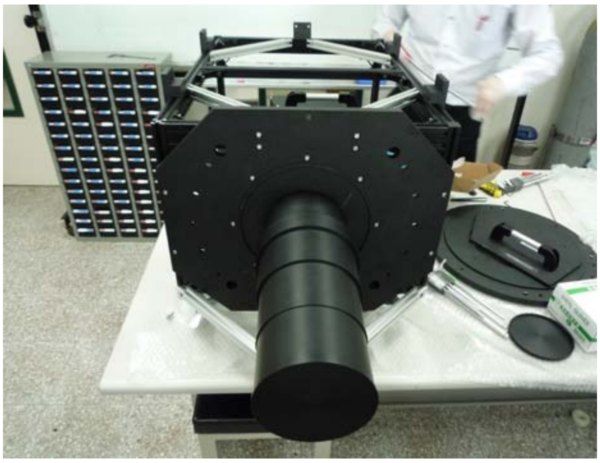

(f) 插入新修正鏡組至分光器內並旋緊

圖 5 (a)-(f)依序概述從舊修正鏡組換至新修正鏡組的完整過程。

3. 電路板組的設計與改良

NCUcam-1 相機在 DOGIOYA 四台相機中負責 Y 波段的觀測，此相機的電路部份由以離職的吳景煌所設計，採類比電路的方式，不管在相機腔內溫度的量測與控制、CCD 指令傳送與信號讀取、類比/數位信號的輸出、視窗加熱器及電路板電源管理等方面的功能，基本上已可進行正常觀測工作。但基於下列理由，我們在相同的功能架構下將單一的電路板改成電路板組的型式：

a. 原電路直接已連接器接於相機本體旁，使得插拔不易，且外露的 pin 腳在安裝上具有一定危險性；

b. 將溫度及讀取功能分開，有助於電路板的維護，即使其中一部份功能損壞，也可以單獨維修而不會相互影響；

c. 改善原電路跳線、割線及外焊零件之情況。

由圖 6 可以清楚比較電路板修改前後在設計概念上的差異。

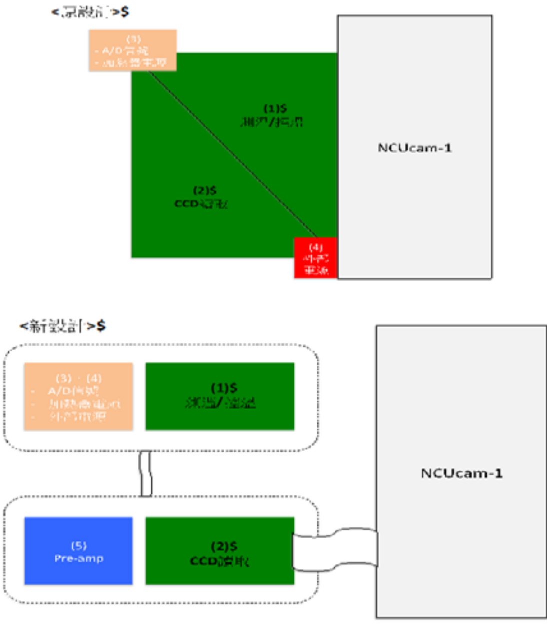

圖 6 NCUcam-1 電路板新舊設計比較圖。原設計中，將四種功能全部集中在一塊電路板上；新設計則把各個功能獨立出來。

為了降低信號傳送的雜訊，從相機端至 UCAM 控制器的信號線長度必需越短越好，因此我們把修改後的電路板組固定在 DOGIOYA 儀器架上靠近 NCUcam-1 相機處，以螺絲固定，並加上保護蓋防止外部撞擊。圖 7 即為電路板組所在位置的照片。

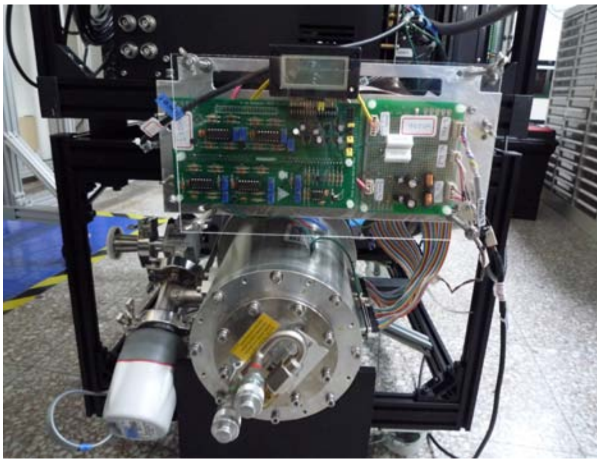

圖 7 電路板組照片。我們把修改後的電路板組移至 DOGIOYA 儀器架上靠近 NCUcam-1 相機處。

4. 四色同步控制軟體介紹

DOGIOYA 所使用的四色相機涵蓋了二種作業系統，分別是 SI1100 的 Windows 系統和 NCUcam-1 的 Linux 系統。而為了方便觀測，我們希望將其統一成單一操作平台，觀測者只需在主電腦上下達指令，即可同步控制四台相機，在此我們選擇了 TCP/IP 作為中間的溝通協定。軟體架構圖如圖 8 所示。

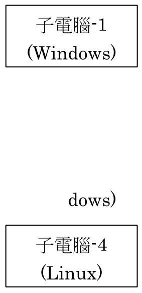

圖 8 四色同步控制軟體架構圖

我們於 101 年 8 月已公開招邊方式委請永光儀器公司設計此軟體，並於同年 12 完成測試和驗收，確認廠商的設計完全符合我們的觀測需求。

5. 結論

整個 DOGIOYA 計畫目前尚在跟夏威夷大學方面討論備忘錄的簽訂細節，待完成後即可進行後續儀器的運送等相關事宜。

由於 DOGIOYA 即將在夏威夷 UH88 望遠鏡進行為期至少四年的觀測任務，儀器團隊除了需負責初期的儀器導入及相關教育訓練外，更需建立完整的使用者手冊，包括儀器安裝、軟體操作、資料分析和故障排除等說明文件，以教導駐地的技術人員能夠獨立完成絕大部份的操作和維護工作，使觀測者不因軟硬體等外在因素而影響既定的觀測計畫。

國立中央大學天文研究所

NCUcam-1 相機安裝至 LOT 操作手冊

編輯：陳澤銓

日期：2013/5/1

一、 輔助工具介紹

1. 下儀器架（簡稱“下架”）: 用以支撐 Filter wheel、NCUcam-1 相機和週邊配件，只在安裝時會使用，安裝完成後會拆下來。

2. 上儀器架（簡稱“上架”）: 用以固定 UCAM 電源、Filter wheel 控制器、快門驅動器和真空顯示計，安裝於 LOT 主鏡室北側。

二、 儀器安裝步驟

1. 將 Filter wheel 裝入下架。

① 將下架上端的方框取出

② 放入 Filter wheel

③ 裝回方框

2. 將上架倒置，平放於桌面或平台上。

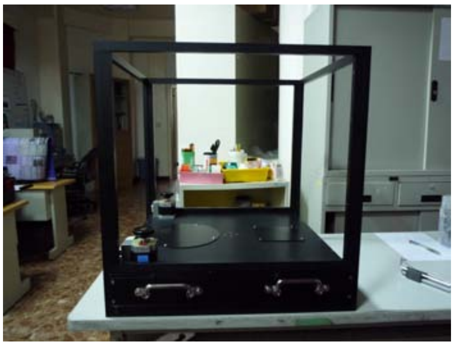

3. 打開 Filter wheel 圓蓋，準備裝入 Filter。

4. 裝入 Filter。

① 小心取出 Filter，並以吹球清潔之

② 旋開 Filter holder 四顆螺絲、裝入 Filter 至對應位置、旋緊螺絲

※ 注意：Filter 鏡面（即反射率較高者）需面向望遠鏡上方

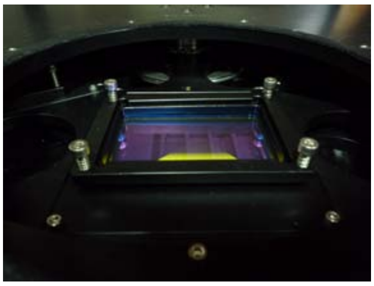

③ Filter 安裝完畢後，蓋回圓蓋

5. 打開 NCUcam-1 保護蓋。

6. 將“相機環”裝上 NCUcam-1。

① 箭頭凹槽處對準快門線

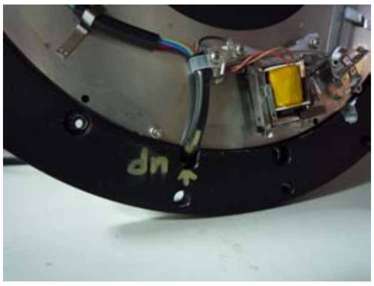

② 鎖緊八顆 M4 螺絲

7. 將 NCUcam-1 裝上 Filter wheel。

① 先手動將 Filter wheel 轉至沒有 Filter 的位置，以免安裝過程傷及 Filter

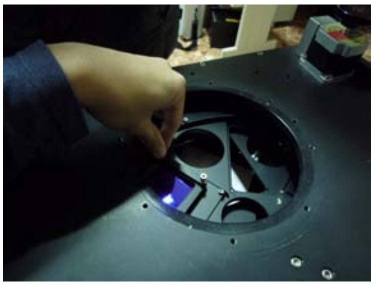

② 小心將 NCUcam-1 由上至下緩慢套入 Filter wheel 圓孔中

③ 在“相機環”和 Filter wheel 躋身上有標示 N 和 S，請依此方向性安裝

④ 鎖緊八顆 M5 螺絲

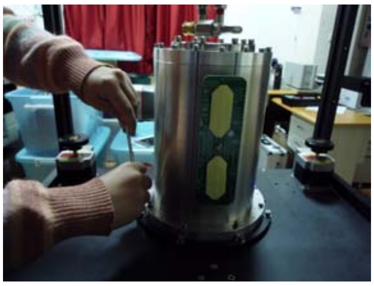

⑤ 確認方向性為：真空閥朝向 Filter wheel 兩個步進馬達方向

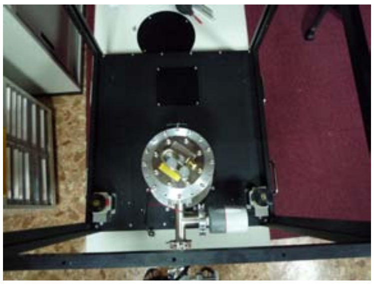

8. 裝上 UCAM 控制器。

① 將“a 板”裝入 NCUcam-1 近 Filter wheel 端，以四顆 M4 螺絲固定

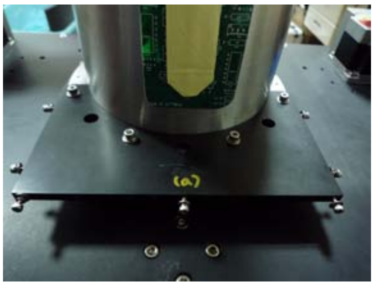

② 將“b 板”裝入 NCUcam-1 尾端，以四顆 M4 螺絲固定

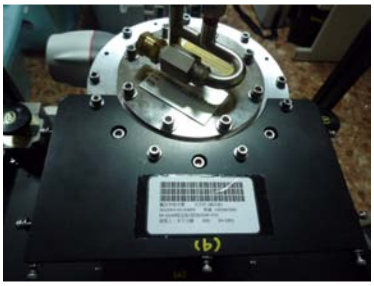

③ 鬆開 NCUcam-1 側邊的電路板保護套螺絲，小心取出保護套

※ 注意：過程中人體不得碰觸連接器的 pin 腳，以免靜電導入而破壞 CCD

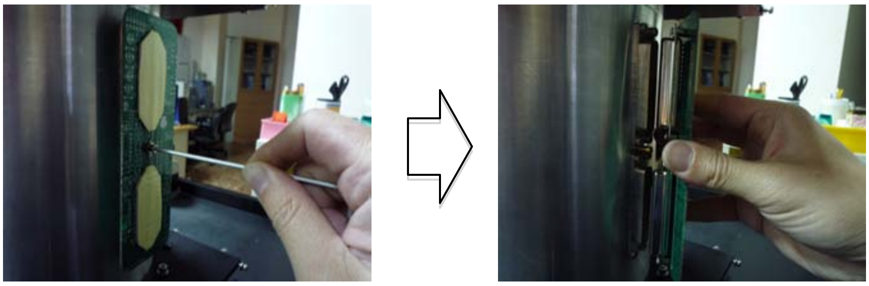

④ 以平行且施力平均的按壓方式，裝入“I/F board“

※ 注意：過程中人體不得碰觸泡綿以外的 pin 腳處，以免靜電導入而破壞 CCD

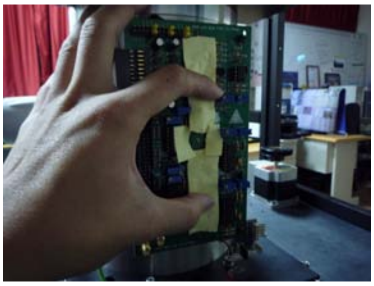

⑤ 找出 UCAM 排線

⑥ 將步驟⑤排線的綠色接地線，與“I/F board“上的綠色接地線，以 M4 螺絲固定於“I/F board“正中央的螺孔（也就是與 NCUcam-1 的機殼接地）

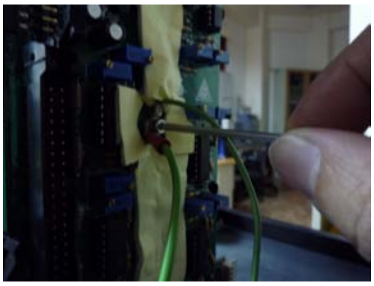

⑦ 將溫度顯示錶頭插入“I/F board“對應連接器

⑧ 將“Pre-amp“依下圖所示之方向固定於“c 板“上的箭頭處

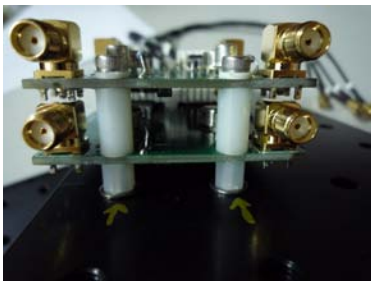

⑨ 將四條黑色信號線，依所標示的號碼分別接至“Pre-amp“靠白色連接器端

⑩ 將四條彩色信號線，依所標示的號碼分別接至“Pre-amp“另一端

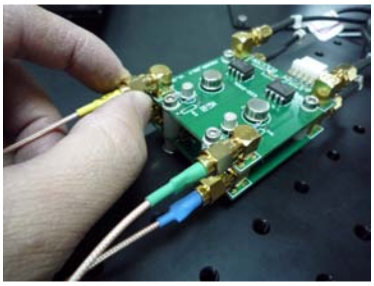

⑪ 將四條彩色信號線的另一頭，依照標示分別接至“I/F board“上

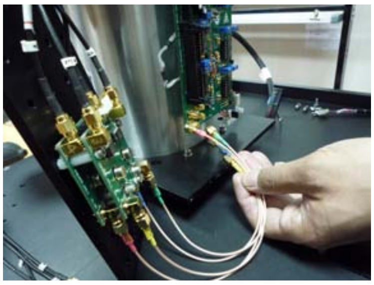

⑫ 依下圖所示，蓋上“c 板“，並以四顆 M3 螺絲固定

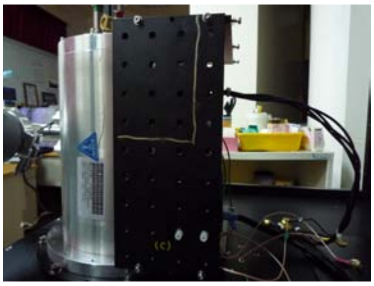

⑬ 連接 NCUcam-1 鏡頭端有一條 2 pin 視窗加熱器電源線，將其插入“I/F board“對應連接器

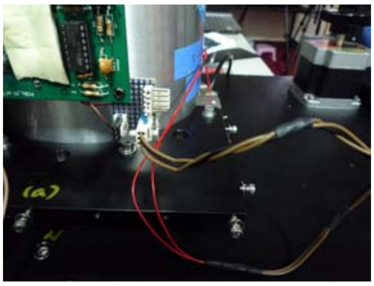

⑭將 3 pin 的電源線接上“Pre-amp“上的白色連接器

⇨

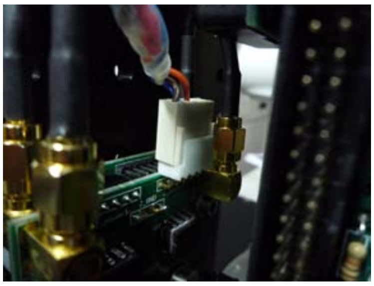

⑮ 將供應“I/F board“電源的 3 pin 電源線插上“I/F board“對應連接器

⇨

⑯ 將“A/D converter“的 5 pin 信號線插上“I/F board“對應連接器

※ *注意：“I/F board“電源線與“A/D converter“信號線外觀極為相似，請勿接反！！*

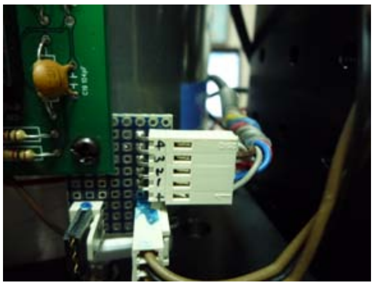

⑰ 依下圖所示，蓋上“d 板“，並以四顆 M3 螺絲固定

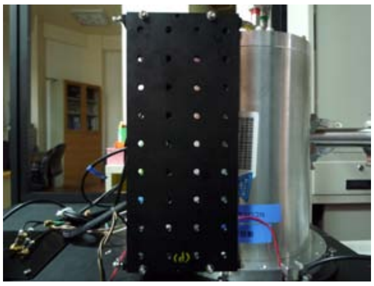

⑱ 插上步驟⑤排線的“I/F board“端至對應連接器

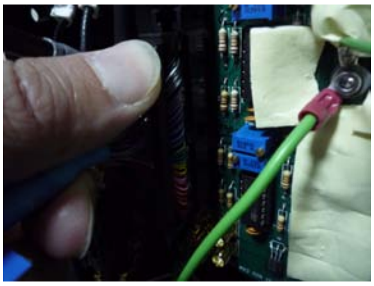

⑲ 依下圖所示將“e 板“蓋上，然後將相關排線自“e 板“下方的長方孔穿出，下圖中由左至右依序為：Pre-amp 電源線、Pre-amp 信號線（四條）、UCAM 排線

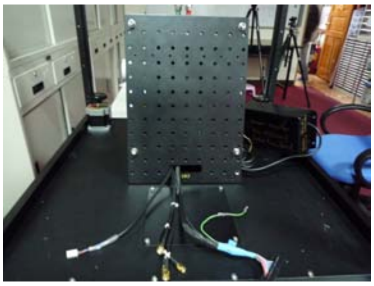

⑳ 鎖上六顆 M4 羅斯以固定“e 板“

㉑ 將“A/D converter”以束線帶固定於“c 板“上

㉒ 將“I/F board“的電源黑盒以束線帶固定於”d 板“

㉓ 將 UCAM 控制器拿至靠近“e 板“位置，照號碼標示依序將步驟⑲的四條 Pre-amp 信號線接上 UCAM 控制器端

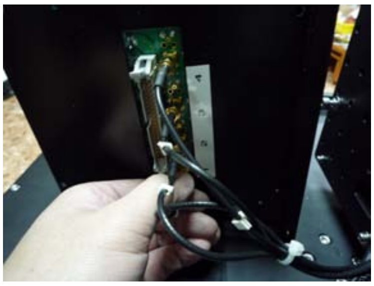

㉔ 將步驟⑲的 Pre-amp 電源線接上 UCAM 控制器端

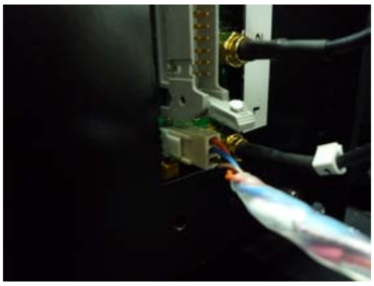

㉕ 將步驟⑲的 UCAM 排線接上 UCAM 控制器端

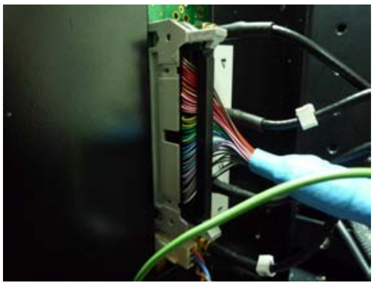

㉖ 將 UCAM 排線的綠色接地線以 M3 螺絲鎖在 UCAM 控制器上（如下圖所示位置）

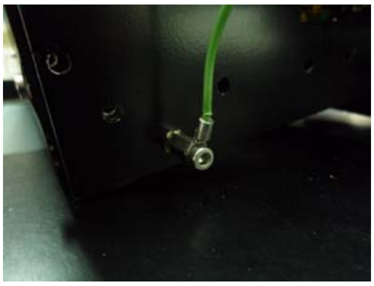

㉗ 將 UCAM 控制器底板緊貼“e 板“固定，並鎖緊四個角落的 M5 螺絲

9. “下架”完成，請以兩人合力將其翻轉 180 度，並放回地面上。

10. 安裝儀器與 LOT 連接的相關連接環。

① 打開 Filter wheel 上方圓形防塵蓋

② 取出“24 mm 環“，並套入 O-ring 於此環的下方（靠 Filter wheel 側）

③ 鎖緊八顆 M6 螺絲，以固定“24 mm 環“於 Filter wheel 上

④ 再套入 O-ring 於“24 mm 環“上方

⑤ 取出“LOT 環“，將其置於”24 mm 環“上，並鎖緊八顆 M6 螺絲，將此二環連接

⑥ 以兩根細扳手插入圓形防塵蓋之螺絲孔，小心將防塵蓋自“LOT 環“開口放入，到底為止（此舉為避免後續安裝過程中，有異物掉入而傷及 Filter 或相機）

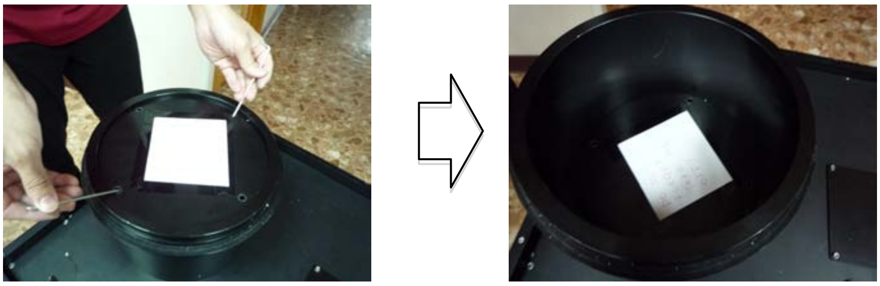

11. 依下圖之配置，依序將 UCAM 電源、Filter wheel 控制器、快門驅動器和真空顯示計，固定於“上架”。

12. 安裝所有儀器至 LOT。

① 以油壓車將上架儀器撐至 LOT 主鏡室北側之適當高度

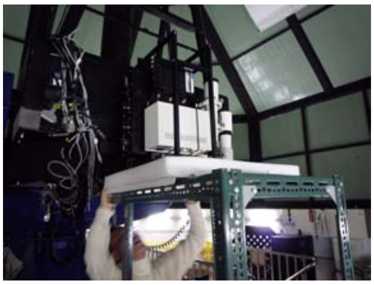

② 緩慢將上架儀器往 LOT 靠近，確認對準螺絲孔位後，依序鎖緊“上架”的上端和下端各二顆英制 1/8”螺絲

③ 降下油壓車，上架儀器即安裝完成

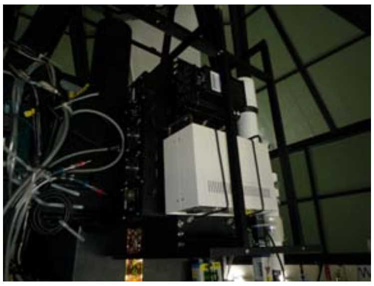

④ 將 LOT 調至水平位置

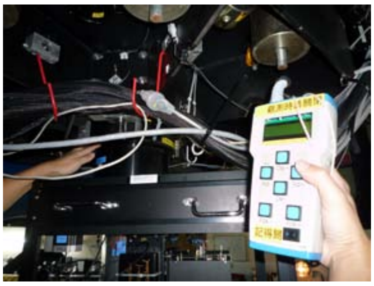

⑤ 取出步驟 10-⑥之防塵蓋

⑥ 以油壓車承載下架儀器，推入至 LOT 下方位置

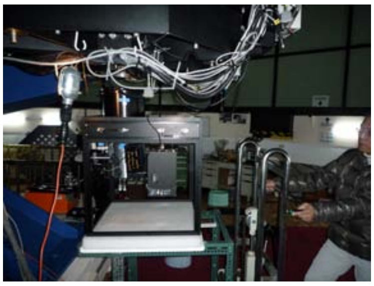

⑦ 緩慢升起油壓車，使“LOT 環“套入 LOT 鏡筒內，並頂緊

⑧ 用力鎖緊位於 LOT 鏡筒之三顆 M8 螺絲，以連接此二部份

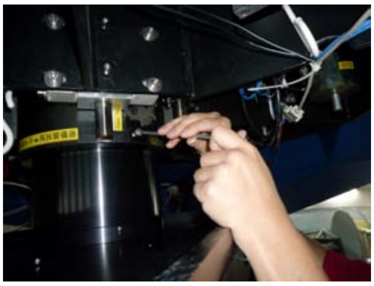

⑨ 將“下架”拆出

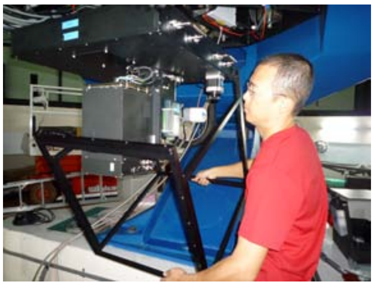

⑩ 下架儀器安裝完成

13. 配重。

① LOT 上方：在現有配置下，再依下圖所示增加配重塊

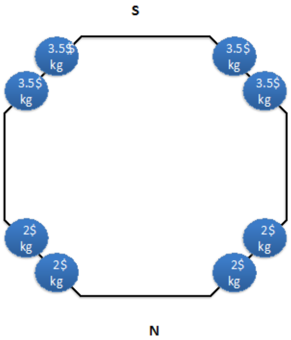

② LOT 主鏡室南側：請依下圖所示掛載配重塊

14. 管線配置。

① 依“SUPPLY”和“RETURN”標示，連接二條冷卻管至 NCUcam-1 下方

② 接上各儀器電源線和相關連接線

15. NCUcam-1 抽真空及冷卻。

① 依下圖所示，將 Turbo pump 接至 NCUcam-1 的真空連接管

② 開啟 Turbo pump 電源，並將下圖之真空閥門扳至“OPEN”位置

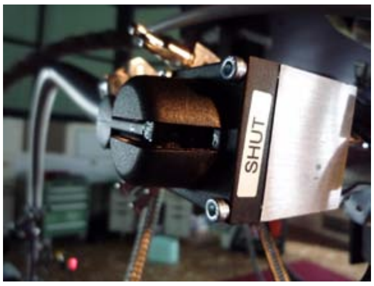

③ 開始抽真空後，觀察上架儀器的真空顯示計，當其顯示 XX^{-2} 時，即可開啓位於控制室旁的冷卻機開始冷卻

④ 直至真空顯示計穩定顯示 XX^{-6} 時，即可關閉 Turbo pump 電源，準備進行觀測

NCUcam-1 相機性能的改良

CHEN Tse-Chuan, KINOSHITA Daisuke

December 2013

摘要

NCUcam-1 雖已於 2011 年夏天開發完成，並利用 LOT 取得了 First light，使用至今也沒有太大的問題發生。但隨著多年來的經驗累積，以及我們對天文相機相關知識的理解漸深，同時也思考著屆時儀器在夏威夷當地觀測時，如何能讓技術人員更簡單、更有效率地使用儀器，因此儀器團隊希望能夠在現有條件適當地改良 NCUcam-1 性能。我們針對了機構設計、電路和接線、溫度偵測和傳導、真空維持、腔體內真空材料的選用、安裝方式和順序、零件清潔…等多方面，進行細部的修改，希望藉此提升 NCUcam-1 的性能和使用上的效率。在這份報告裡，我們將一一說明各項修改的理由和做法。

1. 溫度 sensor 的型式和套管選用

相機內有三個溫度 sensor，分別是 TP1～3，由 1N914 二極體和 1uF 積層電容並聯組成，外部套上一白色矽耐熱套管保護並防止短路。由於矽耐熱套管在低溫環境下容易脆化而有碎屑剝落，若剝落的碎屑在相機翻轉過程中不幸掉落至 CCD 表面，除了影響影像品質外，也會汙染 CCD 晶片本身，因此我們嘗試找出可用在低溫環境下而不劣化的材料做為溫度 sensor 的套管。以下是幾種我們試驗過的方法：

1-1. 鐵氟龍(Teflon)套管

工作溫度範圍-70～250℃，但溫度傳導的效果不理想。

1-2. 熱縮套管

溫度傳導效果不理想。

1-3. 裸露二極體，以熱縮套管包覆零件腳

溫度傳導效果仍不理想。

1-4. 矽耐熱套管

經由 1-1～1-3 的實驗我們發現到，利用 1N914 二極體做為溫度 sensor，其用來感測溫度的部份為零件腳，因此我們必需增加零件腳與銅網的接觸面積。所以，我們回到最初的設計，即 1N914 二極體和 1uF 積層電容並聯，外部套上一白色矽耐熱套管，但矽耐熱套管在尺寸的選擇和裁切上必需特別注意，兩端切口處不得留有碎裂的棉絮以避免掉落後污染腔體。實際做法如圖 1 所示。

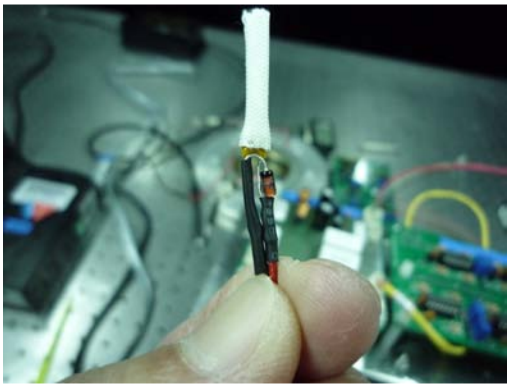

圖 1 溫度 sensor 由二極體和積層電容並聯而成，上方的白色矽耐熱套管略具彈性，可將溫度 sensor 緊緊包覆住，但套管的切口處不得留有過多棉絮，以免掉落腔體內部造成污染。

2. 溫度 sensor 的固定位置

三個溫度 sensor 分別用來偵測相機腔體內壁溫度(TP1)、冷卻機 Cold-end 處的溫度(TP2)及 CCD 晶片附近的溫度(TP3)。

在原來的設計中，已確定 TP2 位於下層 Cold-plate 的正中央處、TP3 置於上層 Cold-plate 的一邊，但 TP1 則無固定的位置而任其散落在艙體內靠近腔壁處。因此，我們同樣以銅網的方式將 TP1 固定在腔壁靠近上層 Cold-plate 的位置。TP1～3 的固定位置如圖 2 所示。

圖 2 三個溫度 sensor 固定的位置，由左至右依序為 TP1、TP2 及 TP3。

3. 相機腔體內導線的選用

在最低可達-130℃低溫的相機腔體內，若使用不耐低溫的材料，很容易使該材料碎裂，而碎裂的物質將會污染潔淨的真空腔體，甚至最重要的 CCD 晶片。

相機內有幾組導線，主要做為三個溫度 sensor 的接線、溫控功能的接線、以及電機體和加熱電阻間的接線。在原來的設計裡，採用的是強調耐高溫特性卻未標明低溫性能的一般塑膠外皮導線，這將不利於低溫環境下的使用。

於是我們改採工作溫度範圍在-70～250℃之間的鐵氟龍導線取代之，可解決此疑慮。圖 3 為使用在相機腔體內鐵氟龍導線的照片。

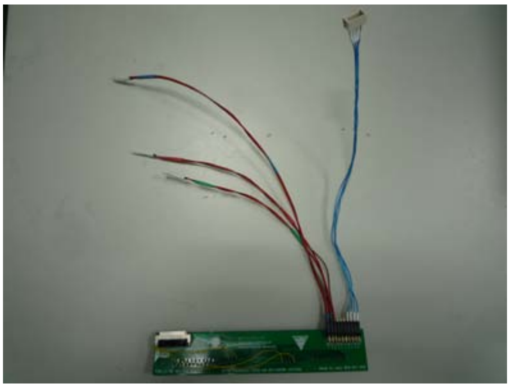

圖 3 相機腔體內使用的鐵氟龍導線及電路板，中間三組紅線為溫度 sensor 接線，右邊藍線則為溫控功能接線。

4. 連接器的導入

由於相機腔體空間狹小、內部接線長度有所限制，在安裝各部份組件時，會有一定之困難度，甚至為了其中一個環節的疏忽而必需全部拆除才能夠重新安裝。

因此，我們將藍色的溫控線從單一導線改成兩段式連接器的安裝方式，如圖 4 所示。如此一來，只要先安裝好各部位組件，最後再接上連接器即可，既省時又便於安裝。

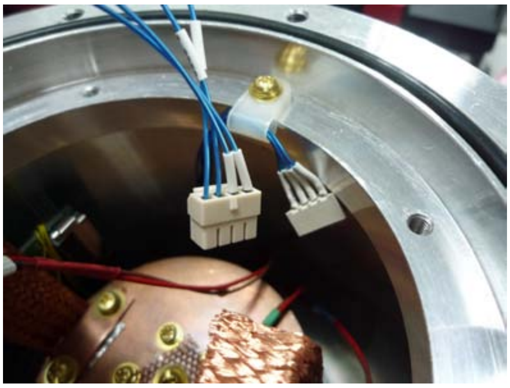

圖 4 將藍色溫控線從單一導線改成兩段式連接器方式，可使安裝步驟更有效率。

5. Cold-path 固定方式修改

連接上下層 Cold-plate 的細緻銅網線我們稱之 Cold-path，其作用是將下層較低的溫度傳導至上層，配合溫控功能，將 CCD 晶片溫度控制在-100℃左右。

如圖 5 所示，左邊舊的設計是將 Cold-path 與電晶體擠在一塊，再以小鋁片壓住鎖緊，此做法會造成小鋁片隆起變形，使 Cold-path 無法緊密與 Cold-plate 接觸而影響溫度傳導；右邊則為新的設計，我們將電晶體移至上層 Cold-plate 的底端，僅留 Cold-path 在頂端並以小銅片將其壓住鎖緊，以達到更佳的溫度傳導效果。

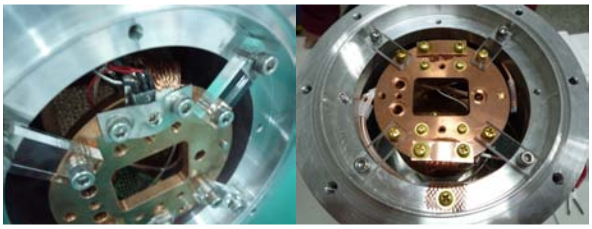

圖 5 新舊 Cold-path 固定方式比較。左圖為舊設計，溫度傳導性不佳；有圖則為新設計，Cold-path 與 Cola-plate 有更緊密的接觸，進而提升溫度的傳導性能。

6. 電晶體與加熱電阻位置和固定方式修改

溫度控制的功能主要以二組電晶體與加熱電阻所組成，當上層 Cold-plate 的溫度低於 -100℃時，加熱電阻將被通以電流而發熱，並透過回授電路調整其發熱功率以達到溫控功能。

在第 5 項修改中有提到，因為將 Cold-path 單獨固定在 Cold-plate 的頂端，因此原先置於頂端的電晶體就被移到底端和加熱電阻位處同一側了。而位於電晶體背面的絕緣片，我們也將原先使用較易受低溫而脆化的塑膠片改成尺寸為 20x15x2 (mm)，較適合低溫環境使用的 PC (Poly carbonate)片取代之。圖 6 即為電晶體與加熱電阻固定方式的照片。

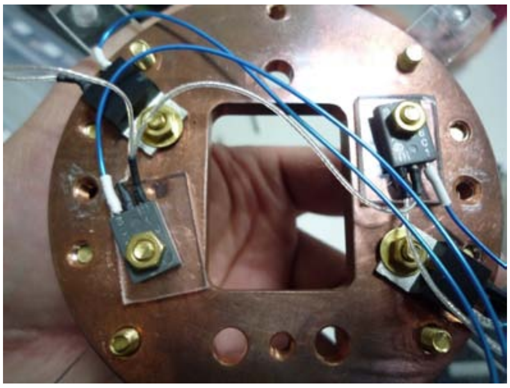

圖 6 位於上層 Cold-plate 底端的電晶體/加熱電阻組。左下與右上是電晶體，置於其下方的是 PC 片；右下與左上則是加熱電阻，其熱能會經由散熱片傳導至 Cold-plate。

7. 黃銅螺絲的導入

整個相機腔體內的螺絲在原來的設計中全數使用俗稱的白鐵螺絲，然而白鐵螺絲與 Cold-plate 的銅材質的溫度係數有所不同，在低溫的環境下有可能造成機構與機構之間無法有效且緊密地密合。因此，我們將所有白鐵螺絲改成溫度係數與銅相近的黃銅螺絲，藉此讓機構與機構的連接更為密合，如圖 7 照片所示。

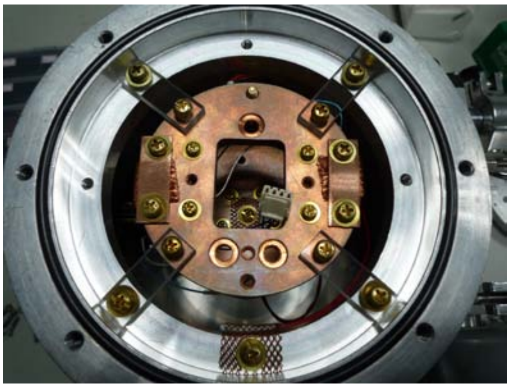

圖 7 照片中金色的即為黃銅螺絲，其溫度係數與銅相近，在低溫的環境中，會使機構與機構的連接更為密和與穩固。此外，位於四個對角的透明塊是 Poly carbonate。

8. 腔體與 Cold-plate 改以 PC 塊連接

相機腔體與上層 Cold-plate 原先是用四個壓

克力塊連接之，但壓克力材質有相對於 PC (Poly carbonate)較佳的溫度傳導係數，如此一來，會將腔壁上將近 0℃的相對高溫傳導至 Cold-plate 上，而造成 CCD 晶片降溫不易之情況。因此，我們改以 PC 取代之，圖 7 中四個對角的透明塊即是 Poly carbonate。

9. CCD 晶片固定方式的修改

整個 NCUcam-1 組裝的過程中，CCD 晶片的安裝可說是最重要、也具有一定危險性的環節，必需特別注意和謹慎。

圖 8 左邊照片是舊的設計，CCD 晶片必需待所有組件都安裝完成，最後才放至上層 Cold-plate 中央處，而且需利用二個小鋁片將晶片的長邊頂住才能夾緊，這個過程很可能會傷害到晶片本體，而使造價極為高昂的 CCD 晶片毀損，同時，繁瑣及緩慢的安裝程序，將會使得分子篩(Molecular sieves)吸入過多水氣而影響其效能。因此，如何快速、安全、又有效率地安裝 CCD 晶片，是我們必需思考的重要課題。

上層 Cold-plate 的設計原本就預留三個孔洞供 CCD 晶片的定位腳使用，因此我們決定直接使用此三個孔洞來固定 CCD 晶片。此做法的優點是，我們可以把 CCD 晶片先固定在上層 Cold-plate 上，帶相機的其他部份都安裝好後，最後再將上層 Cold-plate 連同 CCD 晶片一起裝入即可，既省時又安全。圖 8 右邊照片即是新的安裝方式。

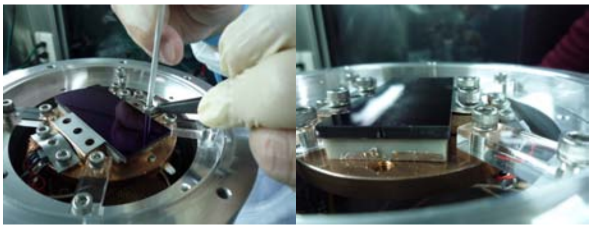

圖 8 新舊 CCD 晶片固定方式比較圖。左邊為舊的方式，是利用二個小鋁片從 CCD 晶片的長邊將其夾緊和固定，安裝時間長、過程繁瑣且不安全；右邊為新的方式，直接利用 CCD 晶片的三支定位腳來固定，省時又安全。

10. 分子篩(Molecular sieves)安裝方式修改

分子篩安裝在相機腔體內，可吸附腔體內殘餘的水汽，在中空泵浦關閉的情況下，可維持腔體內的真空度。我們的做法是利用一個銅網做成的小盒子來裝填分子篩，然後固定在相機腔體內的適當位置。

圖 9 左邊是舊的方式，利用一個大約 70x60x10 (mm)大小的銅網盒裝填分子篩，然後固定在下層 Cold-plate 上，其下方還夾了 TP2 溫度 sensor，佔用了腔體內一部份的空間，造成其他如排線、導線和零件等安裝空間受到限制，增加安裝的困難度。

圖 9 右邊則是新的方式，我們將裝填分子篩的銅網盒移至下層 Cold-plate 的下方，也就是 PT-30 冷卻頭的附近，銅網由原先的一個增加至二個，尺寸分別為 50x30x20 及 50x25x20 (mm)，因此除了上下層 Cold-plate 之間的空間變寬敞了，分子篩的容量也較原來增加約 30%。

圖 9 新舊分子篩銅網盒安裝方式比較圖。左邊為舊的方式，利用一個銅網盒安裝在下層 Cold-plate 上方，有佔用空間及安裝不易的缺點；右邊為新的方式，將二個銅網盒安裝在下層 Cold-plate 下方的兩端，優點是不佔用空間、且分子篩裝填的容量增加了，可提高水汽吸附的能力。

11. 溫度切換開關的製作

由於 LCD 錶頭只有一個，而相機腔體內欲監測的溫度點有三個，在一次僅能讀到一個溫度值的情況下，舊的設計是要重覆插拔電路板上的 jumper (如圖 10 左邊照片黃色的小物)，切換過程不甚方便；因此我們在電路板外加裝了一個五段式指撥開關(使用其中的三段)，切換時直接指撥開關的 ON/OFF 即可分別監測三個不同溫度點之溫度值。未來將考慮將此功能納入電路板組中，增加操作的便利性。

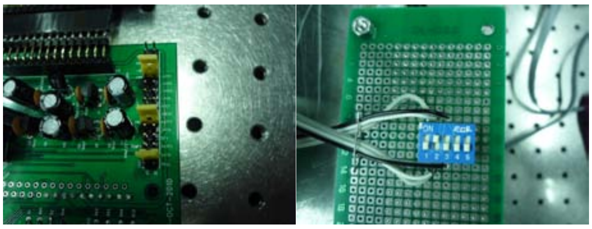

圖 10 新舊溫度監測切換開關照片。左邊為利用 jumper 插拔來做切換，操作不便；右邊為利用指撥開關作切換，便於操作。

12. CCD 晶片及視窗玻璃保護治具的設計

在整個 NCUcam-1 組裝的過程中，最重要也最具危險性的無非是 CCD 晶片的安裝，因為在有限的空間內施作，很容易因為碰撞而傷及 CCD 晶片的本體，或是不慎誤碰讓靜電導入使得 CCD 晶片報銷，因此，適當的保護措施是必要的。

我們利用實驗室剩餘的壓克力板及小零件，製做出一個比 CCD 晶片略大的長方形保護蓋(如圖 11 右邊所示)，可在組裝時使用，避免不慎的人為碰撞或接觸。

除了 CCD 晶片需要被保護外，在最後一道組裝程序—相機上蓋的安裝時，為了保護位於中央的視窗玻璃，避免組裝過程中螺絲或工具不慎掉落鏡面而造成刮傷甚至破裂等情況，我們也利用剩餘的壓克力半圓球及廢棄鋁片製做了一個保護罩(如圖 11 左邊所示)，可有效罩住視窗玻璃達到保護作用。

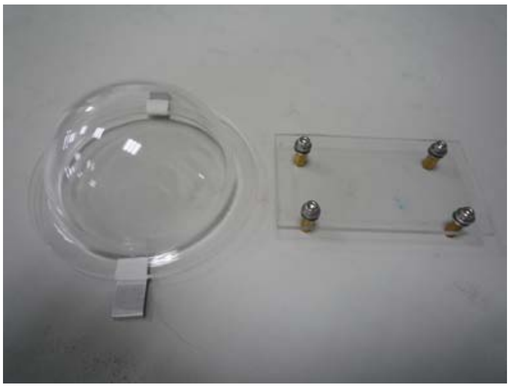

圖 11 CCD 晶片及視窗玻璃保護治具。右邊是長方形的 CCD 晶片保護蓋，由壓克力片和螺絲等零件製成；左邊是半圓球狀的視窗玻璃保護罩，由壓克力半圓球二端黏上小鋁片製成。

13. 視窗加熱片的固定

為了防止因相機腔體內外劇烈的溫度差異而產生結露的現象，我們在視窗玻璃上貼了一片電熱片，藉由對視窗玻璃加熱來消除結露的疑慮。

但是電熱片為浮貼的方式，無法有效將其固定在一定的位置，若安裝的位置有所偏移，很可能會使視窗玻璃收熱不均，或是遮住 CCD 的感光面。因此，我們在固定電熱片

時，利用小片的防焊膠帶先將電熱片粘牢在我們想要的位置，然後再裝上 O-ring 和固定環以固定之，如此一來便可以簡單且有效解決電熱片位移的問題。

這裡之所以使用防焊膠帶，主要因為它具有耐高溫(電熱片通電時會產生數十度的高溫)及不殘膠(撕除時不會有殘膠留在鏡片上)的特性。

14. 真空腔體內零件的清潔

為了維持相機腔體的潔淨度和真空度，所有在相機腔體內的大小零件，包括腔體本身、上下 Cold-plate、Cold-path、所有螺絲(含墊片及滑司)…等，在組裝前都需經過清洗。清洗的方式，我們在超音波清洗槽內注入適當容量的甲醇(Methyl alcohol)，分批放入欲清洗的零件，然後開啓電源清洗一段時間，待油污或雜質被分解出來後，將其取出並放至無塵台內直到組裝時，以確保零件不受二次污染。

15. O-ring 的更新

NCUcam-1 相機所使用到的 O-ring 一共有四處，分別是：視窗玻璃和相機上蓋的連接、相機上蓋和腔體的連接、相機下蓋和腔體的連接、以及 Cold-end 和相機下蓋的連接。由於這些 O-ring 已經使用一段時間，難免會有受汙染或劣化的情況，因此我們添購一批新的 O-ring，材質為普遍應用於真空設備中，耐熱性和耐油性俱佳的 Viton 橡膠。

16. 溫度 sensor 的校正方法介紹

如本文一開始所提到，相機內有三個溫度 sensor (TP1～3)，由 1N914 二極體和 1uF 積層電容並聯組成。為了精確的量測各點的溫度值，在使用前此溫度 sensor 必需經過一校正的程序，使用材料及工具可參考圖 12，有冰塊/水(做 0℃的校正)、液態氮(做-196℃的校正)、溫度計及探棒、小一字起子。

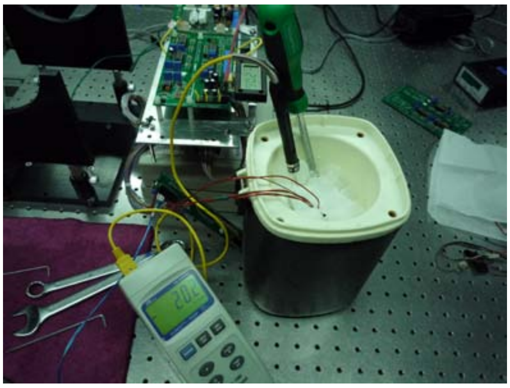

圖 12 溫度 sensor 之溫度校正。將 TP1-3 連同溫度探棒一起放入冰桶內(或液態氮桶)，依序將三個溫度 sensor 的溫度值調成與溫度計的讀值一致即可。

溫度校正的步驟說明如下：

a. 將 TP1-3 連同溫度探棒一起放入冰塊＋水的容器內並靜置數分鐘，此時溫度計所顯示的溫度應該在 0℃左右；

b. 用小一字起子依轉動設定”Zero”的可變電阻旋鈕(TP1=VR2, TP2=VR4, TP3=VR6)，至 LCD 表頭的讀值顯示 0℃為止，即完成三個溫度 sensor 的 0℃校正；

c. 將 TP1-3 連同溫度探棒一起放入裝有液態氮的容器內並靜置數分鐘，此時溫度計所顯示的溫度應該在-196℃左右；

d. 用小一字起子依轉動設定”Spam”的可變電阻旋鈕(TP1=VR1, TP2=VR3, TP3=VR5)，至 LCD 表頭的讀值顯示-196℃為止，即完成三個溫度 sensor 的-196℃校正，同時也完成整個溫度校正程序。

在此需特別注意，三個溫度 sensor 外需用黑色膠帶以片狀方式封住，以免水滲入而造成短路，同樣溫度碳棒也要如此。

Development of Visible 4-color Simultaneous Imager "Dogioya" for Medium-sized Telescopes

Dogioya Development Team
KINOSHITA Daisuke, CHEN Tse-Chuan, CHEN Wen-Ping,
CHOU Yi, HUANG Kuei-Yu, HUANG Ru-Huei, HSUEH Yi-Ting,
HWANG Chorng-Yuan, IP Wing-Huen, KO Chung-Ming,
NGEOW Chow-Choong, SHEN I-Cheng, SHEN Pei-Hsien,
WANG Bo-Jhou, WU Ching-Huang, and YANG Hui-Hsin

August 2013

Abstract

In order to carry out immediate follow-up observations for new discoveries by large scale astronomical surveys, a visible 4-color simultaneous imager "Dogioya" has been developed. Three dichroic mirrors are used to split the beam from the telescope, and images at four different pass bands are recorded simultaneously by four CCD cameras. The main scope of this instrument is to conduct efficient and reliable color measurements of moving and transient celestial objects, such as asteroids and supernovae, even under relatively poor condition nights. Optical multi-band color information of an astronomical object right after its discovery is a clue for understanding the origin, physical properties, and chemical composition of the body. Visible 4-color simultaneous imager also improves the observing efficiency due to the fact that we are able to obtain the imaging data at different pass bands at the same time. We have successfully developed key components of the instrument, including a fully depleted CCD imager "NCUcam-1", and assembled the system in the laboratory. Four unit cameras, including "NCUcam-1" has been tested using existing 1-m telescope at Lulin observatory, and unit cameras have been characterized using the data both from the observatory and laboratory. The whole system of "Dogioya" is now ready to be tested with a telescope, and the shipping to Hawaii is planed at the end of 2013 for the test observation using 2.2-m telescope at the summit of Mauna Kea under the collaboration with University of Hawaii. We report the scientific objectives, design, development strategy, current status of the instrument, status of the instrumentation laboratory, testing and characterization of the instrument, and near-future plan for the first-light observation of the whole Dogioya system.

Key Words: Methods: observational – Instrumentation – Techniques: photometric

1 Introduction

Panoramic Survey Telescope and Rapid Response System (hereafter, Pan-STARRS) is an innovative and unique cyclical wide-field astronomical survey project (Kaiser 2004). A prototype telescope, PS1, is installed and being operated at the summit of Haleakala on the Maui island of Hawaii (Fig. 1). It is a telescope with the aperture of 1.8-m. With three sets of corrector lenses, a wide field-of-view of three degrees in diameter is achieved. A dedicated imaging instrument, named Giga Pixel Camera (hereafter, GPC) is attached to the telescope (Fig. 2). GPC is an wide-field imager with 1.4 giga pixels which covers the entire area of the focal plane of PS1 telescope. CCD chips used for this instrument are orthogonal transfer CCDs. Orthogonal transfer CCDs are capable of moving electrical charges to neighbouring pixels in both vertical and horizontal directions during the exposure, and hence offer on-chip guiding to improve the image quality. PS1 system is one of the most powerful observing facilities in the world to perform astronomical wide-field surveys. The official surveys of PS1 has started in May 2011, and this telescope is now being used to carry out a sky survey for 75%

of the sky which is observable from Hawaii. It is the first trial to image such a wide area of the sky repeatedly in a sysmatic way. PS1 provides unique data sets for time-domain astronomy, and it opens new opportunities for knowing variable universe. Intensive studies on moving objects in the solar system, such as asteroids and trans-Neptunian objects, and transient objects, such as supernovae and gamma-ray bursts, are expected.

Figure 1: The dome of the PS1 telescope at the summit of Haleakala on the Maui island of Hawaii. PS1 is a unique and innovative observing facility for time-domain astronomy. The telescope and related facilities are operated by PS1 Science Consortium. The photo was taken by Kinoshita Daisuke in November 2007.

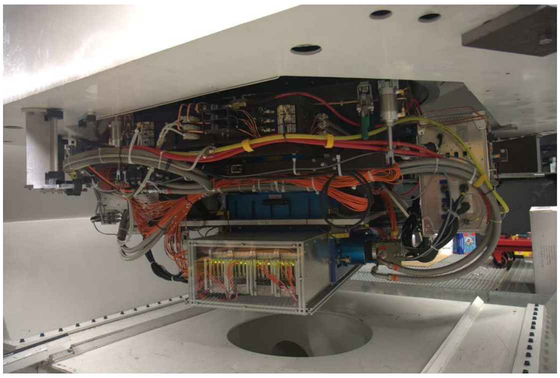

Figure 2: Giga Pixel Camera installed at PS1 telescope. GPC is still one of the biggest format astronomical CCD camera in the world. It covers three degrees field-of-view on the sky. The CCD chips used for this instrument are orthogonal transfer CCD which can carry out on-chip guiding by moving electrical charges both in horizontal and vertical directions during the exposure. This photo was taken by Kinoshita Daisuke in November 2007.

In order to maximize scientific outputs of PS1 sky surveys, quick follow-up observations are essential to investigate physical properties, chemical compositions, and origin of newly discovered objects and mechanisms of observed phenomena. Note that PS1 keeps observing wide area of the sky, and cannot focus on small number of celestial objects to monitor. Telescopes exclusively used for follow-up observations are highly needed. In our case, a 2-m telescope is being constructed at Lulin observatory in Taiwan. The primary mirror has an effective aperture of 2.0-m, chosen to make it possible to observe majority of PS1 discovered objects in imaging mode. The mirrors are made of low thermal expansion glass of Astro-Sitall, and a protective layer of SiO is coated on the surface after the aluminizing of the mirrors. The optical system is a Ritchey-Chrétien, and the focal length of the system is 16.0-m for Cassegrain focus. This results in F/8, and it allows us to share some instruments with existing 1-m telescope at the same site. The mount of the telescope is alt-az mount. The expected image quality is 0.35 arcsec, and it is reasonably good considering a typical seeing condition of $\sim$ 1.5 arcsec at Lulin observatory. The pointing accuracy of 2 arcsec in RMS and tracking accuracy of 0.3 arcsec per 10 min are expected. The telescope is designed to have a maximum slew speed of 4 deg per second to enable efficient observations and quick response of sudden change of the observing plan. The telescope sometimes needs to do quick pointings right after the triggers of transient alert.

We have decided to build a visible 4-color simultaneous imager "Dogioya" for the 2-m telescope to carry out follow-up observations for PS1 sky surveys. This report describes the scientific objectives, design, development strategy, current status of the instrument, status of the instrumentation laboratory, testing and characterization of the instrument, and the near-future plan for the first-light observation of the whole Dogioya system.

2 Visible 4-Color Simultaneous Imager "Dogioya"

An optical 4-color simultaneous imager "Dogioya" was selected to be the first generation instrument for the 2-m telescope. There are two reasons for this decision. First, the most important task of the 2-m telescope is to perform follow-up observations for celestial objects discovered by PS1 sky surveys. Then, majority of targets are (1) moving objects, such as asteroids, comets, and trans-Neptunian objects, and (2) transient objects, such as variable stars, supernovae, and gamma-ray bursts. Moving objects in the solar system are irregularly shaped and are spinning in general. This fact suggests that these bodies change their cross-section and exhibit brightness variation. Color change may also be attributed to the heterogeneity on the surface. As transient objects change the brightness and/or colors, we need to complete the brightness measurements at two or more pass bands for accurate color determination before those objects change their brightness in order to avoid false colors. Simultaneous measurements of brightness at two or more pass bands dramatically improve the quality of color measurements of variable targets. Second, Lulin observatory is not the world's best observing site, like Mauna Kea in Hawaii or the high altitude desert in northern Chile. The sky condition at Lulin is often unstable and variable within a night. We see occasional cloud passing, and only have limited number of photometric nights. The utilization of poor condition nights has to be well considered, otherwise significant fraction of observing time may be wasted. Again, simultaneous imaging at multiple pass bands provides us the data taken under exactly the same atmospheric transparency, and make the photometric calibration easier. To summarize, we need to measure colors accurately for targets which change their brightness with time even under unstable sky condition.

Reliable and efficient color measurements of celestial objects are achieved by simultaneous imaging using a set of dichroic mirrors. The beam from the telescope is split into two or more paths, and images at different wavelength regions are recorded at the same time. In this way, derived colors are less affected by intrinsic variability of the target and change of atmospheric conditions. It also makes the calibration and data analysis easier under the assumption that the transmittance of the cirrus is neutral over the wavelength coverage of the instrument, and the use of the simultaneous imager increases the number of observable nights. Furthermore, the simultaneous imaging improves the observing efficiency of the telescope. In conventional method of multi-color photometry by exchanging filters, the total amount of observing time needed T_c is given by

$$T_c = (t_{exp} + t_{ro}) \times N_{band}, \tag{1}$$

where t_{exp} is the integration time necessary for each band, t_{ro} is the readout time, and N_{band} is the number of filters used. On the other hand, the total amount of observing time needed for simultaneous imaging T_s is shown by

$$T_s = \frac{t_{exp}}{E_{throughput}} + t_{ro}, \tag{2}$$

where $E_{throughput}$ is the throughput of the additional optics in the instrument. Substituting values of $t_{exp} = 60$ sec, $t_{ro} = 8$ sec, $N_{band} = 4$, then we obtain $T_c/T_s \sim 3.3$, and the simultaneous imaging is suggested to be about three times more efficient than the conventional observations. These advantages are critically important for the operation and scientific productivity of Lulin observatory.

2.1 Scientific Objectives

In astronomy, color measurements are often used to obtain the first look of the physical conditions and chemical composition of celestial objects. An example of scientific objectives of this instrument is the color measurements of asteroids. Some asteroids are known to be rocky composition and classfied as S-type asteroids. Some other asteroids are known to be carbonaceous composition and classified as C-type asteroids. The reflectance spectra for different types of asteroids differ due to the compositional differences of the surface (Fig. 3). Color measurements are a technique to do the taxonomic classification. It gives us a clue to understand the chemical composition, origin, and evolution of the body. It is essential to know the taxonomic type of the object to infer the origin and nature, when an asteroid with peculiar orbital properties is discovered. In addition, dozens of pairs and clusters of asteroids with extremely similar orbits have been identified recently. Color determination of pairs / clusters asteroids is useful to support (or deny) the common origin hypothesis (Kinoshita et al. 2007). Color measurements and successive classification are equally important for other classes of astronomical objects.

2.2 Conceptual Design

In a conventional method of color measurements, we image the target using a filter, then later reimage the same object using another filter. In this way, there is a time lag between two measurements at different wavelength. Our targets, transient objects and moving objects, change their brightness with time, and the conventional color measurements may produce false colors due to the time lag between exposures.

A different and new approach is proposed here. That is, accurate measurements can be achieved by observing the target at two or more different wavelength regions simultaneously. This is realized by beam splitting using dichroic mirrors. The dichroic mirror is an optical device that reflects the light shorter than the characteristic wavelength and transmits the light longer than the characteristic wavelength (Fig. 4). By using three dichroic mirrors and four bandpass filters and detectors, one is able to measure the target flux at four different wavelength regions at the same time.

The conceptual design of the visible 4-color simultaneous imager is shown in Fig. 5. Three

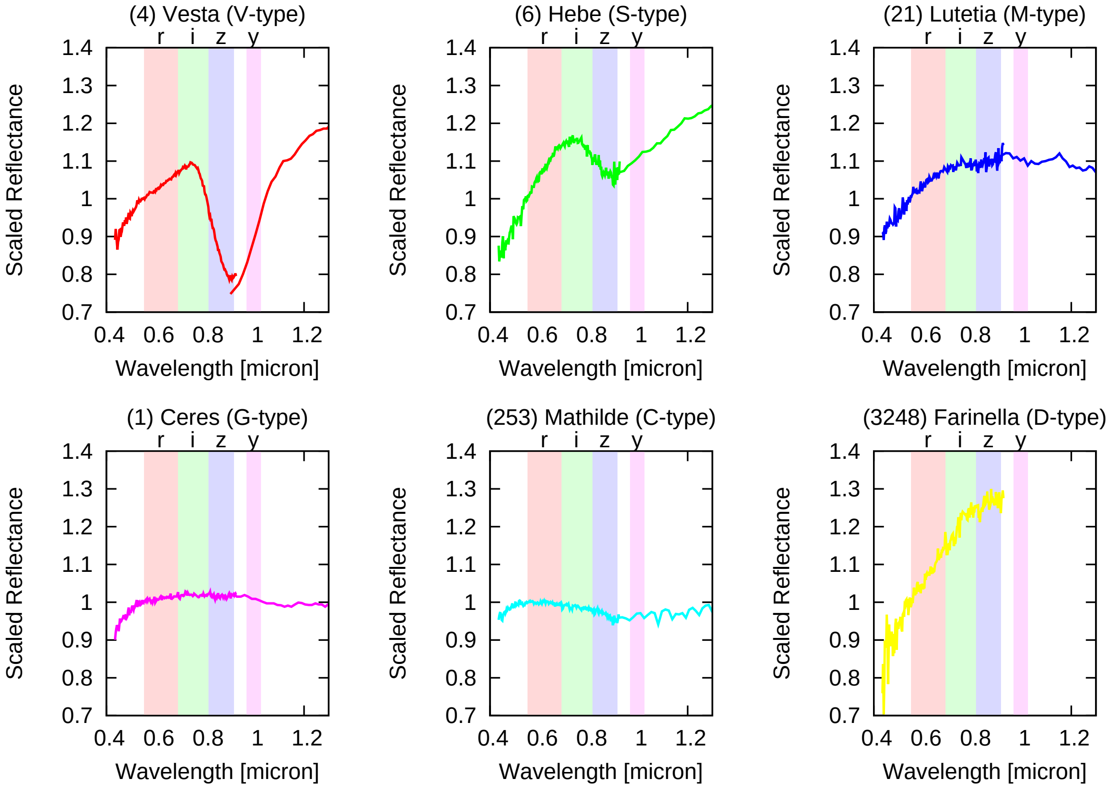

Figure 3: Typical spectra of major subclasses of asteroids. Rocky igneous asteroids exhibit deep absorption band around 0.9-1.0 micron, while more primordial carbonanceous asteroids show rather flat reflectance spectra.

dichroic mirrors on the optical path split the light from the telescope into four components. These four beams pass through the bandpass filters (PS1 r', i', z', and y filters), and the signals are received by four detectors at the same time. In order to combine data both from PS1 in Hawaii and the 2-m telescope in Taiwan, the filter system of our visible 4-color simultaneous imager "Dogioya" is designed to be compatible with those of PS1 filter system. The transmittance properties of PS1 r', i', z', and y filters are shown in Fig. 6. Four unit CCD cameras are used as detectors. Each camera is equipped with 4096 × 2048 pixels CCD chip. The pixel size is 15 μm, and resultant pixel scale with the 2-m telescope is 0.19 arcsec per pixel. 2 × 2 binning is planned for usual operation. These unit cameras provide a field-of-view of 13.2 arcmin × 6.6 arcmin. In order to reduce the noise, the CCD chips are cooled down to -100°C.

2.3 Development Strategy

When we discussed the development strategy, we have focused on following two aspects. First, it is important to deliver the instrument in timely fashion. If the project has a delay and the instrument is delivered after the PS1 mission, then there will be less scientific impact and we have less scientific outputs from this instrument. Also, early scientific results are very appealing to the scientific community. Significant delay of the project may affect to successive projects. Second, it is equally important to do in-house developments of some key components and accumulate experiences. If one uses commercially available products only for the research activities, then the uniqueless of the data is not easily emphasized. With the data obtained commercially available instruments, the competition with other facilities is tough. Meanwhile, in-house development may add unique functions to the instrument and/or achieve advantages in sensitivity / data quality, and one may be able to obtain a set of data that nobody else has. Unique and high quality data sets produce publications more easily.

CCD cameras are key components of our instrument, and we have reached to following conclusion for the development strategy. We have decided to purchase three commercially available CCD cameras to secure the delivery of the instrument by the telescope first-light, while fourth camera is developed by ourselves to let us accumulate experiences from the development processes. This strategy fulfills both two aspects mentioned above.

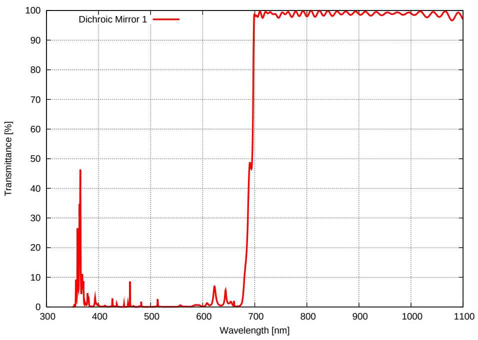

Figure 4: An example of transmittance curve of dichroic mirror. For this case, the light bluer than 700 nm is reflected on the surface of the dichroic mirror, and the light redder than 700 nm is transmitted. Hence, the beam from the telescope can be split into two components, and it allows us to have images of bluer band and redder band are recorded at the same time.

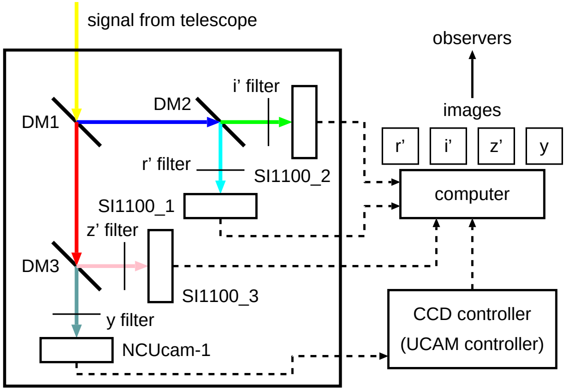

Figure 5: The conceptual design of the visible four-color simultaneous imager. Three dichroic mirrors, shown as DM1, DM2, and DM3, split the signal from the telescope into four, and four detectors acquire images at different wavelength regions at the same time.

Even in the situation of the delay of fourth camera, the instrument is able to start the early-science observations as 3-color simultaneous imager, and it will not be a fatal problem for the project. Three CCD cameras imaging in r', i', and z' bands, we have purchased SI1100 series cameras of Spectral Instruments, Inc. in USA. A reason that we have chosen this product is that the manufacturer allows us to select a CCD chip to install in the camera. The CCD chips we selected are CCD 44-82-1-D23 of E2V, Inc. It is a scientific grade (grade 1) CCD chip with 4K × 2K format. The pixel size of this CCD is 15 μm. The fringe suppression process is given to the chip, so that significant degradation of photometric accuracy due to the fringing on the image in z'-band is significantly reduced. There are two amplifiers and A/D convertors for this CCD chip, and the readout time is shortened by a factor of two using both two readout ports. Fourth camera, namely "NCUcam-1", is developed by ourselves. NCUcam-1 will be used for imaging at y-band ($\lambda \sim 1\,\mu m$). We have decided to utilize a recently developed fully depleted CCD chip (Kamata et al. 2008). Majority of CCD chips used for astronomical observation at this moment are thinned back-illuminated CCDs. Because of thin depletion layer compared to the absorption depth of silicon, the sensitivity of thinned back-illuminated CCDs are very low at longer wavelength. Typical quantum efficiency of thinned back-illuminated CCDs at $\lambda \sim 1\,\mu m$ is about 10% or less. The low sensitivity of CCD at this wavelength region is critical problem for small aperture telescopes, and in fact we had difficulty to carry out observations at z and Y bands using small aperture telescopes due to poor sensitivity.

To overcome the difficulty, we have decided to use a fully depleted CCD for NCUcam-1. The quantum efficiency of fully depleted CCD with 200 μm thickness reaches 40% at $\lambda \sim 1\,\mu m$, and it dramatically improves the sensitivity of y-band imaging (Fig. 7).

2.4 Development

2.4.1 Instrumentation Laboratory

We first established a laboratory for the instrumentation at the Institute of Astronomy, National Central University. The Institute provided the room 1001 of the Science Building 4 for the laboratory space. We have arranged dark room with an optical table, clean room, and mechanical assembly and testing area in the laboratory space. The dark room is used for the tests and experiments of unit cameras. The clean room is used for the installation of a CCD chip into the camera body of NCUcam-1 and assembly of the camera system. The mechanical assembly and testing area is used for the soldering, development of electric boards, assembly and testing of mechanical parts, and software development. The power supply with UPS (Uninterruptible Power Supply) was arranged, and the wired and wireless network was settled in the laboratory. A set of tools was purchased. We also pay attention to the operation and maintenance of the laboratory, and regularly check the availability and condition of tools and equipments in the laboratory. We have been developing the instrument in this laboratory since 2008 (Fig. 8).

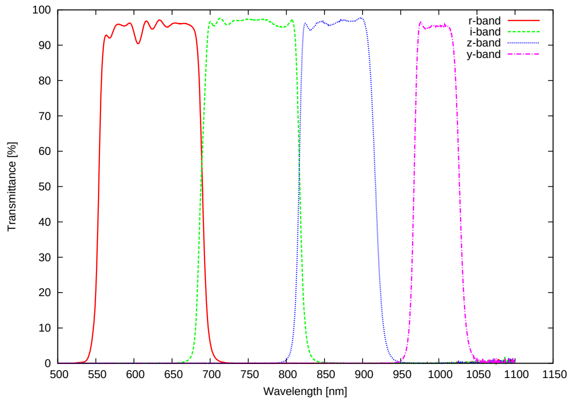

Figure 6: The measured transmittance properties of PS1 r', i', z', and y-band filters for our instrument. The filter system of visible four-color simultaneous imager will be compatible with those of PS1 filter system. These filters were manufactured by Asahi Spectra, Inc., and the transmittance data was obtained using Cary 60 spectrometer at NCU main campus.

2.4.2 SI-1100 Series Cameras

As described in previous section, we purchased three SI-1100 series CCD cameras from Spectral Instruments, Inc. in Arizona, USA, as three unit cameras for our instrument. For the CCD chip inside the camera, we specified CCD 44-82-1-D23 manufactured by E2V, Inc. of UK/France. This is 2K × 4K CCD chip with the pixel size of 15 μm. It gives 13.2 arcmin × 6.6 arcmin field-of-view when attached to the 2-m telescope of F/8. This field-of-view is reasonably large for our observations even for relatively fast moving objects. In order to reduce the dark current, we have chosen a model with the cryocooler. The CCD can be cooled down to -100°C. Under the operation temperature of -100°C, we do not need to take dark exposures, and it simplify the observations. The CCD controller allows us to have overscan region along with the imaging data, and the overscan region can be used to estimate the bias level. Three SI-1100 series cameras were delivered to us in summer 2010. We have developed a filter wheel for test observations of SI-1100 series cameras, and those cameras were tested using 1-m telescope at Lulin observatory. The first-light of SI-1100 series cameras was achieved in July 2010 (Fig. 9). Through the experiences of test observations at Lulin, we learned a lot on the installation and operation of the instrument. For CCD camera which is cooled by a cryocooler, a good consideration for the arrangement of the cryocooler lines and compressor is needed. An attention to the cable lengths for various signal cables, such as RS-232C, USB, and fibre optic cables, is always required.

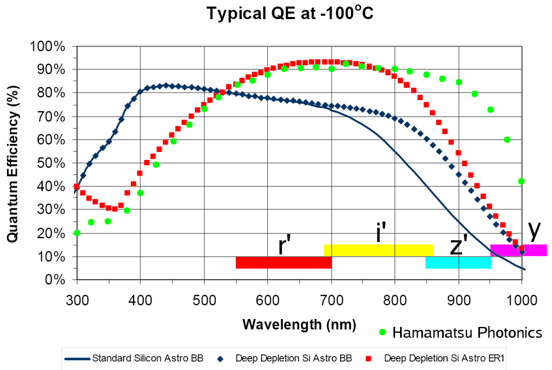

Figure 7: The comparison of quantum efficiencies of conventional thinned back-illuminated CCD and fully depleted CCD. The data shown by red squares are quantum efficiency of 44-82-1-D23 chip manufactured by E2V, and the data shown by green circles are quantum efficiency of fully depleted CCD manufactured by Hamamatsu Photonics. Thicker depletion layer for fully depleted CCD dramatically increases the sensitivity at Y-band.

2.4.3 NCUcam-1

Fourth unit camera "NCUcam-1" has been designed, developed, and being tested by ourselves at Institute of Astronomy, National Central University. Fig. 10 shows the schematic design of NCUcam-1. The main body of the camera head is a vacuum dewar made of aluminum. The vacuum environment is required to keep stable low temperature of the CCD chip. The vacuum pump is connected to the camera dewar, and the vacuum level of $\sim 10^{-6}$ torr is achieved before the observation. During night time observation, the vacuum pump is disconnected from the camera head to prevent the vibration.

At the top of the vacuum dewar, a glass window made of fused silica is attached. The fused silica has excellent transparent properties at visible wavelength, which is suitable for optical astronomical observations. Properties of fused silica are summarized in Table 1. The size of the CCD is 30.7-mm × 61.4-mm, and we decided to have ϕ = 90-mm fused silica window for our camera. We have estimated the required thickness for the fused silica window. A set of equations for the calculation is given by

$$\sigma_{max} = \frac{3P(3+\nu)}{32}\left(\frac{D}{t}\right)^2 < \frac{F_a}{S} \quad (3)$$

$$l = \frac{3P(1-\nu)(5+\nu)}{256E}\frac{D^4}{t^3} \quad (4)$$

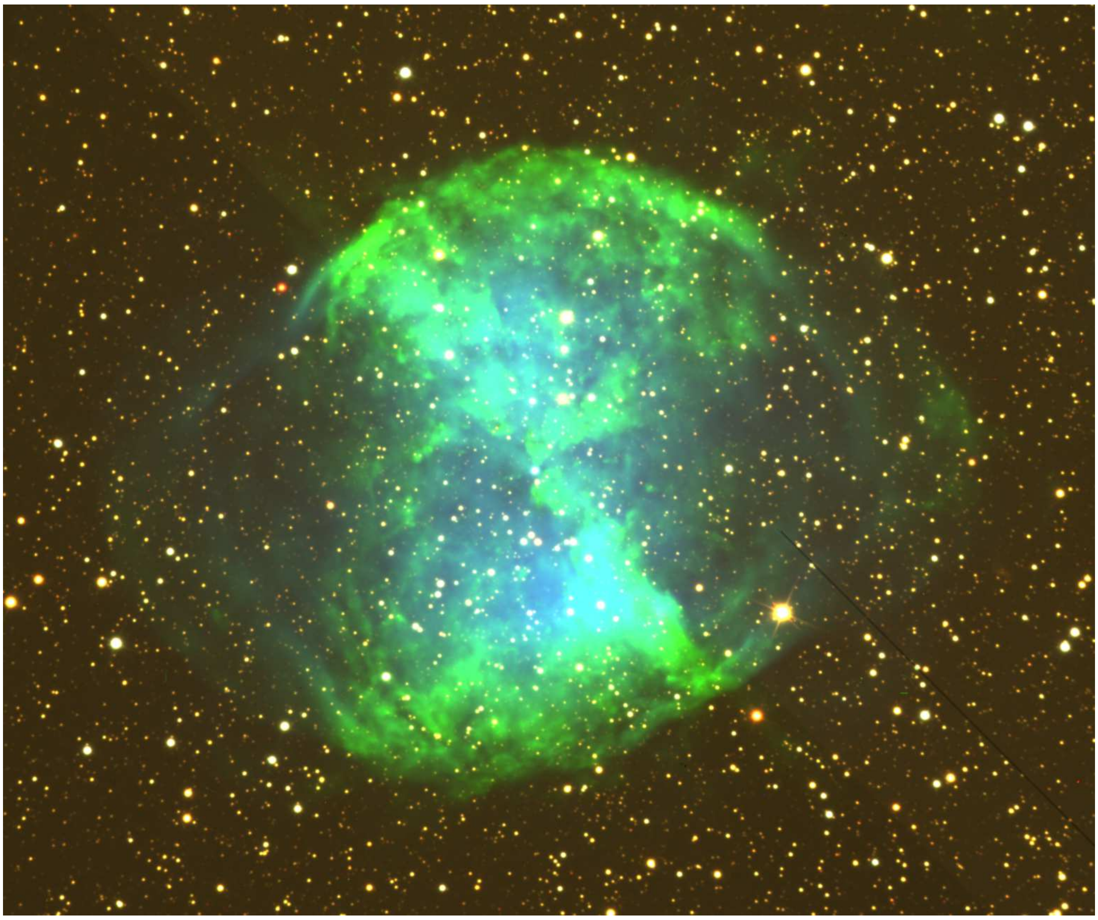

Figure 9: The first light image by the CCD camera SI1100-156. M27 was imaged using the 1-m telescope at Lulin observatory at 17:10-17:54 on 20 July 2010. SDSS g', r', and i' filters were used. The integration time was 10 min for each band. The image shown here has the field-of-view of 10.0 arcmin × 8.3 arcmin.

$$R = \frac{l^2 + \left(\frac{D}{2}\right)^2}{2l} \quad (5)$$

Here, D is the diameter of the circular window, t is the thickness of the window, σ_{max} is the stress to the window surface at the window center, P is the pressure difference between the inside and outside of the dewar, ν is the Poisson ratio, F_a is the breaking strength, S is the safety factor, l is the displacement of the window surface at the window center, E is the Young's modulus, and R is the curvature radius of the deformed window. According to Okamura et al. (1996) and Miyazaki et al. (2002), it is recommended to have safety factor of 4 or larger. Under the condition of the safety factor of 3 or smaller a small impact may break the window. The window thickness, window displacement at the center, and curvature radius of the deformed window are calculated for $S = 3, 4, 5, 6, 7, 8, 9$, and summarized in Table 2. The thickness of the window for the safety factor of 4 is calculated as 4.5-mm. We conclude to use a 5-mm thickness fused silica for the dewar window. The fused silica window must be anti-reflection coated before the installation. The broad-band anti-reflection coating was designed by our partner, Photocoding Inc., and our fused silica windows were coated when a set of corrector lenses was AR coated. The reflectance property of AR coating on fused silica is shown in Fig. 11.

Breaking strength	$F_a = 4.892 \times 10^7$ Pa
Young's modulus	$E = 6.966 \times 10^{10}$ Pa
Poisson ratio	$\nu = 0.17$

Table 1: The properties of fused silica. The data are from Okamura et al. (1996) and Miyazaki et al. (2002).

Cryocooler is used to achieve the CCD operation temperature of -100°C. For the choice of the cryocooler, we have carried out the calculations for the thermal design of the dewar. The nominal CCD operation temperature is set to -100°C

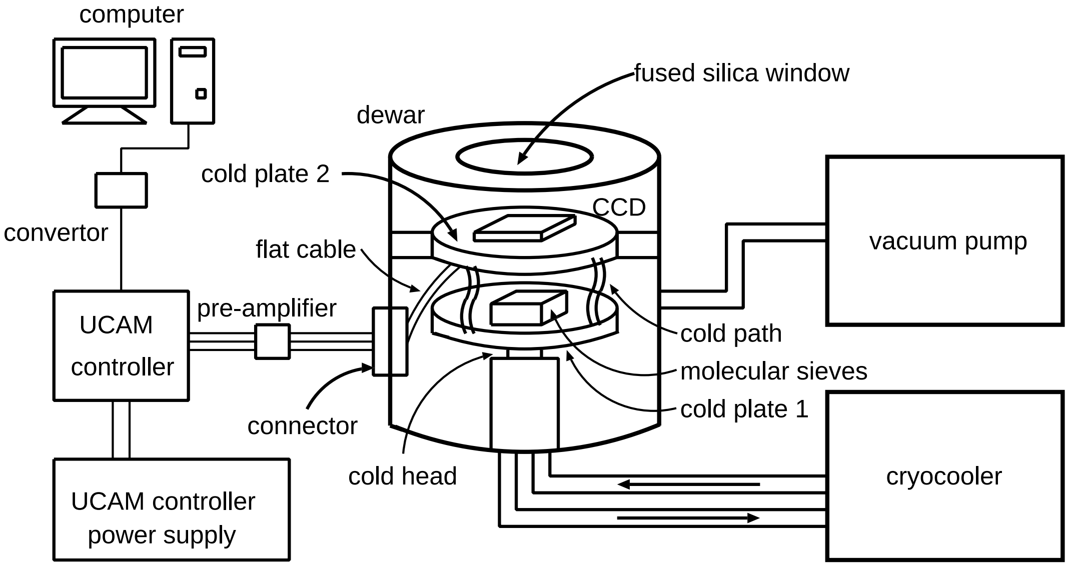

Figure 10: The schematic drawing of NCUcam-1. The CCD chip is installed in the dewar, and a vacuum pump and a cryocooler are connected to the dewar. The temperature control electronics and heaters are used to make the CCD temperature stable. UCAM CCD controller is used to acquire images.

S	t [mm]	l [μm]	R [m]
3	3.9	83	12.2
4	4.5	53	18.8
5	5.0	38	26.2
6	5.5	29	34.5
7	5.9	23	43.4
8	6.3	19	53.1
9	6.7	15	63.3

Table 2: Calculated window thickness, window displacement at the center, and curvature radius of the deformed window for given $S = 3, 4, 5, 6, 7, 8, 9$.

mainly because dark current is negligible at this temperature. In order to estimate the required cooling power of the cryocooler, the calculations of inflow heat flux into the dewar are needed. Here, we assume a cylindrical shaped dewar with the diameter of 150-mm and the height of 100-mm. The size of a circular window of the dewar is set to be $\phi = 90$-mm. The total inflow heat flux into the dewar was calculated as follows. Four heat sources were considered. Those are the radiation from the dewar window, the radiation from the dewar wall, the conduction through the supporting structure of the CCD chip, and the conduction through signal lines. The incoming heat flux by the thermal transfer due to the radiation from the dewar window is expressed as

$$\begin{aligned}\dot{Q}_{win} &= \sigma\left(T^4_{ambient} - T^4_{CCD}\right) A_{win} \\ &\quad \times \frac{\epsilon_{win}\epsilon_{CCD}}{\epsilon_{win} + \epsilon_{CCD} - \epsilon_{win}\epsilon_{CCD}}. \qquad (6)\end{aligned}$$

Here, $\dot{Q}_{win}$ is the inflow heat flux by the radiation from the window, σ is the Stephan-Boltzmann constant ($\sigma = 5.67 \times 10^{-8}$ Wm^{-2}K^{-4}), A_{win} is the area of the dewar window, $T_{ambient}$ is the ambient temperature near the dewar window, T_{CCD} is the CCD operation temperature, ϵ_{win} is the emissivity of the fused silica window, ϵ_{CCD} is the emissivity of the CCD. The area of the dewar window is $A_{win} = \pi\left(\frac{D_{win}}{2}\right)^2 = 6.36 \times 10^{-3}\,\mathrm{m}^2$. The ambient temperature near the window and CCD temperature are chosen to be $T_{amb} = 283$ K and $T_{CCD} = 173$ K, respectively. The emissivities of the window and CCD are assumed as $\epsilon_{win} = 1.0$ and $\epsilon_{CCD} = 0.5$, respectively. Then, the heat inflow by the radiation from the dewar window is estimated as $\dot{Q}_{win} = 1.0$ W. The incoming heat flux by the thermal transfer due to the radiation from the dewar wall is expressed as

$$\begin{aligned}\dot{Q}_{wall} &= \sigma\left(T^4_{ambient} - T^4_{CCD}\right) A_{wall} \\ &\quad \times \frac{\epsilon_{Al}\epsilon_{CCD}}{\epsilon_{Al} + \epsilon_{CCD} - \epsilon_{Al}\epsilon_{CCD}}. \qquad (7)\end{aligned}$$

Here, $\dot{Q}_{wall}$ is the inflow heat flux by the radiation from the wall, A_{wall} is the area of the dewar wall, ϵ_{Al} is the emissivity of the dewar wall which is made of the aluminum. The area of the dewar wall is $A_{wall} = \pi\left(\frac{D_{win}}{2}\right)^2 = 5.84 \times 10^{-2}\,\mathrm{m}^2$. The emissivity of the aluminum are assumed as $\epsilon_{Al} = 0.06$. Then, the heat inflow by the radiation from the dewar wall is estimated as $\dot{Q}_{wall} = 1.0$ W. The incoming heat flux by the thermal transfer due to the conduction through the supporting structure

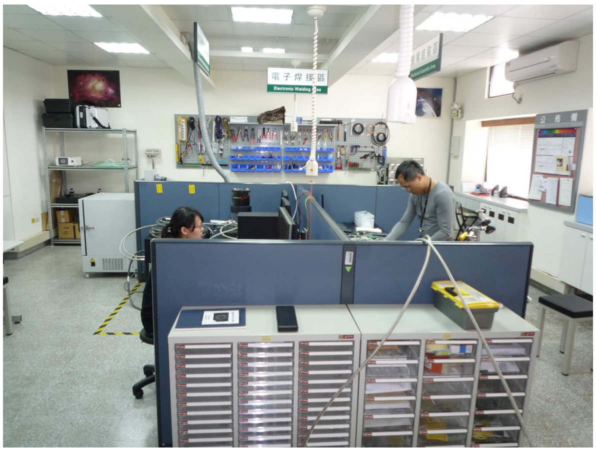

Figure 8: The astronomical instrumentation laboratory at 10th floor of Science Building No. 4 at the main campus of National Central University. We have divided the laboratory space into three regions, and those are the clean room, the dark room, and the mechanical assembly area. This photo shows the mechanical assembly area. The photo was taken by T.-C. Chen.

of the CCD chip is expressed as

$$\begin{aligned}\dot{Q}_{post} &= \frac{A_{post}}{L_{post}}\int_{T_{amb}}^{T_{CCD}}\kappa_{post}(T)dT \\ &\sim \frac{A_{post}}{L_{post}}\bar{\kappa}_{post}\left(T_{amb}-T_{CCD}\right). \qquad (8)\end{aligned}$$

Here, $\dot{Q}_{post}$ is the inflow heat flux by the conduction through a polycarbonate post, A_{post} is the cross-section of the polycarbonate post, L_{post} is the length of the polycarbonate post, κ_{post} is the thermal conductivity of the polycarbonate post, $\bar{\kappa}_{post}$ is the mean thermal conductivity of the polycarbonate post. The cross-section and length of the polycarbonate post are assumed to be $A_{post} = 20\times20\,\mathrm{mm}^2$ and $L_{post} = 40$ mm, respectively. The mean thermal conductivity of the polycarbonate is assumed as $\bar{\kappa}_{post} = 0.2$ W m^{-1} K^{-1}. The number of polycarbonate posts is 4. Then, the heat inflow by the conduction through the polycarbonate posts is estimated as $\dot{Q}_{posts} = 0.9$ W. The incoming heat flux by the thermal transfer due to the conduction through the copper line is expressed as

$$\begin{aligned}\dot{Q}_{line} &= \frac{A_{line}}{L_{line}}\int_{T_{amb}}^{T_{CCD}}\kappa_{Cu}(T)dT \\ &\sim \frac{A_{line}}{L_{line}}\bar{\kappa}_{Cu}\left(T_{amb}-T_{CCD}\right). \qquad (9)\end{aligned}$$

Here, $\dot{Q}_{line}$ is the inflow heat flux by the conduction through a copper line, A_{line} is the cross-section of a copper line, L_{line} is the length of a copper line, $\bar{\kappa}_{Cu}$ is the mean thermal conductivity of the copper. The cross-section and length of the copper line are assumed to be $A_{line} = 75\times18$ μm^2 and $L_{line} = 150$ mm, respectively. The mean thermal conductivity of the copper is assumed as $\bar{\kappa}_{post} = 420$ W m^{-1} K^{-1}. The number of copper lines is 50. Then, the heat inflow by the conduction through the copper lines is extimated as $\dot{Q}_{lines} = 0.02$ W. Therefore, the total inflow heat flux is estimated to be $\sim$ 3W under the ideal situation. The cryocooler PT-30 manufactured by Polycold, Inc., has the cooling power of 22W at 173K, and it is confirmed to be powerful enough for our camera. The cold-end of the cryocooler is installed in the camera head. The cold-end and the CCD chip is connected using copper lines, and the heater is placed in between to achieve stable temperature. The analog feedback circuit developed by us starts heating when the CCD needs to be warmed up, and stops heating CCD temperature is higher than the setting temperature. Near the cold-end, molecular sieves are installed to absorb remaining gas particles. This is critically important to keep vacuum level because the vacuum pump is switched off and disconnected during the observation. Remaining gas particles are sticked on the surface of molecular sieves under low temperature, and hence good vacuum environment is kept in the dewar as long as the cryocooler is working.

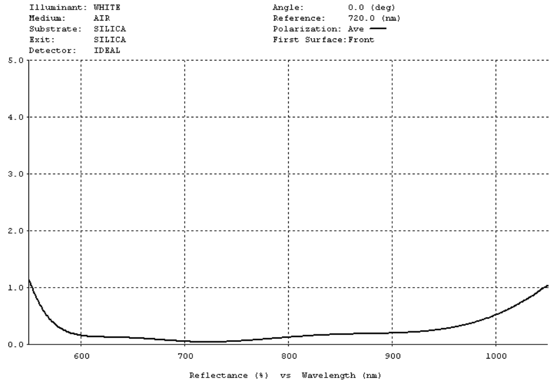

Figure 11: The design of broad-band anti-reflection coating on fused silica. It was designed by our partner, Photocoding, Inc.

The military-grade hermetic connector is used to have signals from the CCD while keeping the vacuum condition. The pins on the back-side of the CCD package and the hermetic connector is connected via flat cable. Lines from the temperature sensors are also connected to the hermetic connector. Signals from the CCD are transfered to the CCD controller through the hermetic connector.

Outside the dewar, the electric circuit board is attached to the hermetic connector. This circuit board has functions to communicate with the CCD chip to acquire the data and control the heaters in the dewar to stabilize the cooling temperature. The temperature measurement is achieved by a Zener diode. We utilize nearly linear temperature dependence of the output voltage of Zener diode. This choice is based on the fact that an extremely accurate measurements of absolute temperature is not required, but the measurements of relative temperature changes are enough for our purpose. The voltage from the Zener diode placed in the dewar is converted into the temperature using operational amplifiers and adjustable resistors. The Zener diode is calibrated by the measurements at -196°C (liquid nitrogen temperature) and 0°C. The design of this analog circuit for the temperature measurements is shown in Fig. 12, and the developed circuit board is shown in Fig. 13. The signal lines from the circuit board are feeded into the pre-amplifiers, and amplified signals are sent to the CCD controller. The CCD controller we use is Universal Camera Controller (hereafter, UCAM) developed by AET (Astronomical Electronics Technology), Inc. One of the most notable features of CCD imaging is the charge transfer. Signals in each pixel of the CCD are moved to the low-noise analog-to-digital converter for the examination of the amount of electrical charges received. The charge transfer is realized by changing potential wells in pixels. The schematic drawing of the charge transfer in a CCD is shown in Fig. 14. The CCD controller is responsible to generate a set of clock patterns for the charge transfer. UCAM CCD controller has been set up to create clock patterns which fulfill the specifications of the fully depleted CCD manufactured by Hamamatsu Photonics, including timing of the voltage changes and values of high and low voltages. We have confirmed the compatibility of clock patterns generated by UCAM by measuring the voltages using an oscilloscope. The result is shown in Fig. 15. UCAM is operated by a Linux PC.

An engineering grade CCD chip was installed in the camera dewar (Fig. 16), Assembly of NCUcam-1 was done with an engineering grade CCD chip in autumn 2010. Fig. 17 shows the assembled NCUcam-1 in the laboratory. Initially, we found a problem for keeping reasonably good vacuum level, and the aluminum surface near the hermetic connector was polished again and the problem was fixed. In December 2010, NCUcam-1 was drived successfully using UCAM and the bias frame was acquired (Fig. 18). Later on, scientific grade CCD chip was installed in the camera dewar, and the first data from the scientific grade chip were read from the camera in May 2011. Fig. 19 is the dark frame with the exposure time of 3600 sec. Due to thicker depletion layer, cosmic rays do not appear as points, but trailed patterns are seen. The dark current generation rate was measured to be ~ 4 e$^-$ under the cooling temperature of -100°C, and it fulfills the specifications. The readout noise was also estimated, and it was ~ 4 e$^-$ per read when the sampling speed of 125 kHz was selected. This is good enough for most of our application, because the sky background noise dominates for exposures of 20-30 sec or longer.

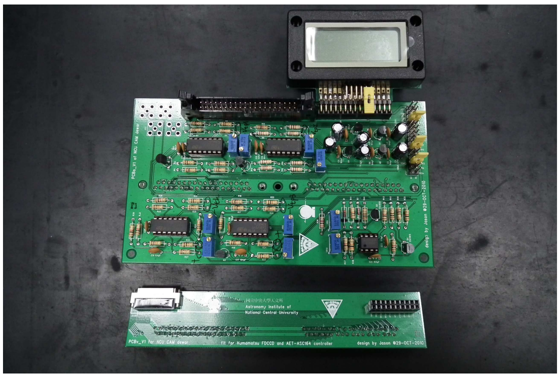

Figure 13: The electronic circuit board developed by us. This board mainly has two functions. One is the communication to/from CCD chip, and the other is the measurements and control of CCD cooling temperature.

After the tests and ajustments in the laboratory, we brought the whole system of NCUcam-1 to Lulin observatory, and NCUcam-1 was tested using existing 1-m telescope there as a stand-alone CCD imager. Although we have struggled with the setting and adjustment of UCAM controller, shutter controller, and control software for a while, NCUcam-1 successfully received the star light from the sky and acquired astronomical images for the first time in July 2011 (Fig. 20). We believed it was a big achievement for our project and also for our institute that our “hand-made” CCD imager finally worked out. Before NCUcam-1, only commercially available CCD cameras were used at Lulin observatory. With those cameras, it is not easy to obtain unique data sets for our research. We often need to accumulate data for longer time span to complete with other researchers. Now, our institute has an ability to design, develop, test, and characterize astronomical instruments. NCUcam-1 exhibits superb sensitivity even around wavelength of 1 micron, and there are only a few such CCD imager in the world at this moment. This is a great advantage for our institute. It is also worth to note that NCUcam-1 is the first CCD imager cooled by cryocooler at Lulin observatory and it achieves the cooling temperature of -100°C. Previous CCD cameras at Lulin were all cooled

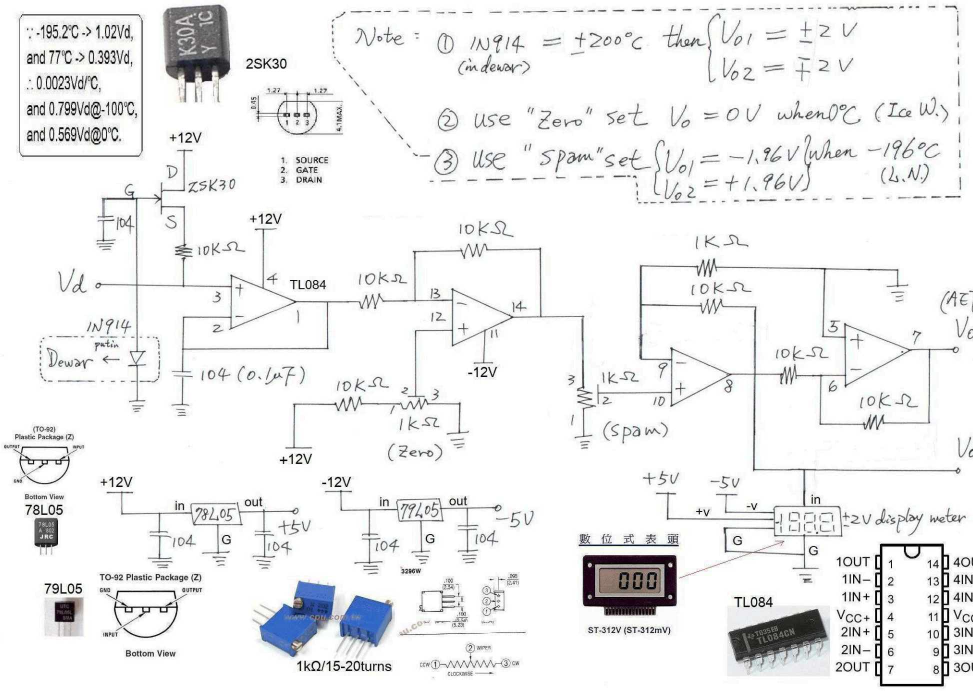

∵ -195.2℃ -> 1.02Vd,
and 77℃ -> 0.393Vd,
∴ 0.0023Vd/℃,
and 0.799Vd@-100℃,
and 0.569Vd@0℃.

Note: ① 1N914 (in dewar) = ±200°C then $V_{o1} = \pm 2$ V, $V_{o2} = \mp 2$ V
② use "Zero" set $V_o = 0$ V when 0°C (Ice W.)
③ use "spam" set $V_{o1} = -1.96$ V, $V_{o2} = +1.96$ V when -196°C (L.N.)

Figure 12: The design of the analog circuit to measure the temperature in the dewar. The temperature is estimated by measurements of output voltage from Zener diode. The voltage from Zener diode is converted into the temperature by using a set of operational amplifiers and adjustable resistors. The measured temperature is read by the control PC using A/D convertor. The temperature is also displayed on a digital panel meter on the circuit board. The design was given by a former member of this project, C.-H. Wu.

by thermoelectric cooler and we had to take dark frames and deal with dark current subtraction. We measured the vacuum condition and temperature at CCD chip and cold-end of the cryocooler during the observing run. The vacuum level was around 10^{-5} torr even after we stopped the vacuum pump, and the CCD temperature was stable at -100°C during the whole observing run (Fig. 21).

The detection limits of NCUcam-1 with Lulin 1-m telescope were estimated. Here, the definition of the detection limit is given by the magnitude of an astronomical object detected with signal-to-noise ratio of 10 for specified integration time. The aperture radius is set to be 1.5 times of FWHM of stellar point-spread function. We took two consecutive images of standard star fields for PS1-compatible r', i', z', and Y filters. These data sets provide two independent photometric measurements of field stars under the same instrumental and atmospheric conditions. By comparing two measurements, and statistical analysis of errors enables us to estimate detection limits. Note that there are not information for calibrated magnitudes for field stars, but photometric standard star can be used to calibrate field stars. The data were taken on 11 December 2012 using NCUcam-1 and Lulin 1-m telescope. The standard field of Ru149 was selected, and photometric standard star Ru149F was used for the analysis of r', i', and z' band images, while Ru149 on UKIRT IR bright standard catalog was used for the analysis of Y band images. The integration time of each exposure is set to 90 sec. The airmass of Ru149 field at the time of the observation was ∼ 1.1-1.2. We used astronomical image analysis software package IRAF (Image Reduction and Analysis Facility), developed by NOAO (National Optical Astronomy Observatory) of USA, for our data processing. The flow chart of the analysis is shown in Fig. 22. For the estimation of the detection limit, we divided field stars into 0.1 mag bins according to their brightness. Fig. 23 shows the magnitude differences of photometric measurements from 1st and 2nd images of r'-band. The data shows wider scattering toward fainter sources. Fig. 24 is a figure of RMS error vs. magnitude. Roughly speaking, signal-to-noise ratio of 10 corresponds to RMS error of 0.1 mag. According to our definition, magnitude which corresponds to 0.1 mag RMS error is the detection limit. The results of the anaysis is summarized in Table 3. The detection limit of single 90-sec integration is 20.0 mag for r'-band while it is 17.1 mag for Y-band.

Currently, a series of experiments with NCUcam-

Figure 20: The first-light image by NCUcam-1 with the Lulin 1-m telescope. Lagoon Nebula M8 was imaged using PS1 r', i', and z' filters on 6 July 2011. The exposure times for r', i', and z' bands are 60 sec × 8, 60 sec × 8, 90 sec × 8, respectively. The field-of-view of this image is 26.4 arcmin × 13.2 arcmin.

	r'	i'	z'	Y
Lim. Mag.	20.0	19.5	19.0	17.1
PSF	1.5"	1.4"	1.4"	1.3"

Table 3: The estimated detection limit of NCUcam-1.

1 in the laboratory in NCU main campus are being carried out. These experiments utilize an integrating sphere, and the goals of the experiments are the measurements of (1) full well capacity, (2) linearity of the response, (3) gain and readout noise. The ingrating sphere was developed by ourselves. Two half-sphere foamed styrol were used to make a main body of the integrating sphere, and the interior of the sphere was painted and eight LED were installed. We also developed a circuit board using current regulative diode (CRD) to provide stable electric current. Note that the brightness of LED depends on the current provide. We measured the stability of the brightness of inner wall of integrating sphere. Fig. 25. The standard deviation of the brightness variation in the integration sphere is found to be 0.16% of the mean brightness over 1.5 hours. This is good enough for our purpose. We plan to compete the experiments by the end of April 2013.

2.4.4 Beam Splitter and Corrector Lens

The optics part of visible 4-color simultaneous imager "Dogioya", including dichroic beam splitters, corrector lenses, and their housing, has been outsourced to Photocoding, Inc. in Japan. This is mainly because we needed to concentrate on the development of NCUcam-1 considering the amount of available human resources. The optics part is composed of the beam splitter to separate the beam from the telescope into four components, and corrector lens system to improve the image quality over the entire field-of-view of the instrument. The optical layout of the beam splitter and corrector lens is shown in Fig. 26. Three dichroic mirrors are placed on the optical path, and the light from the telescope are divided into four components which correspond to r', i', z', and Y band images. The beam splitter "BS A" split the beam into (r'+i') and (z'+Y). The transmittance property of "BS A" is shown in Fig. 27. All the three beam splitters are confirmed to satisfy the specifications. We did not find any problem on the anti-reflection coating on the corrector lenses and surface irregularity on the surface of beam splitters and band-pass filters. To examine the expected image quality, diameters of 80% encircled energy were checked. The results are shown in Table 4. Optics part of the instrument was delivered to us in summer 2011. We have assembled the optics and four unit cameras in our laboratory, and the system was successfully integrated.

2.4.5 Software

The basic commands to acquire the image from NCUcam-1 was written by ourselves. A set of command-line interface tools offers a way to conduct observations. Spectral Instruments provided

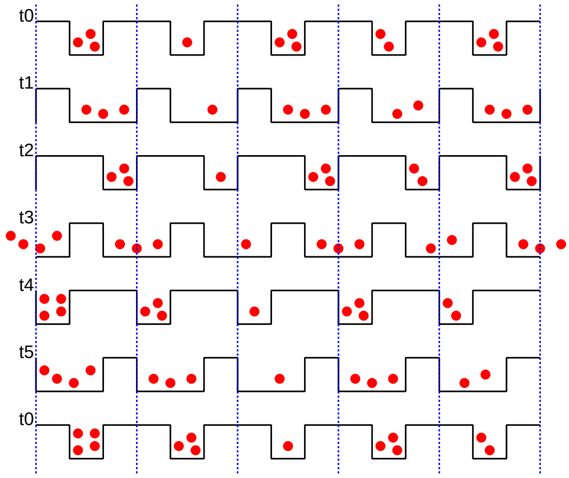

Figure 14: The schematic drawing for the CCD charge transfer. This figure shows how charges in each pixel move to a neighbouring pixel without mixing for 3-phase clocking. A pixel is divided into three regions and the voltages applied on those three regions are independently controlled. By changing voltages in timely fashion, charges are smoothly moved to adjacent pixels.

	r'	i'	z'	Y
80EE Dia. (arcsec)	0.14	0.29	0.22	0.19

Table 4: The diameter of 80% encircled energy for r', i', z', and Y bands are summarized. The specifications is 0.60 arcsec, and we have satisfactory results for all the four bands.

a CCD camera control software and SDK (Software Development Kit) for SI-1100 series camera. In order to achieve the simultaneous imaging by all the four unit cameras, we have decided to develop a server / client model software. The main control PC sends commands to camera control PCs, and then four camera control PCs start exposures. After the completion of the data acquisition, camera control PCs send the data back to the main control PC. Nick Enterprise, Inc. in Taipei supported us to develop TCP/IP server / client software platform for our instrument. The system now works fine, and is able to control four cameras and acquire four images by typing a single command on the main control PC.

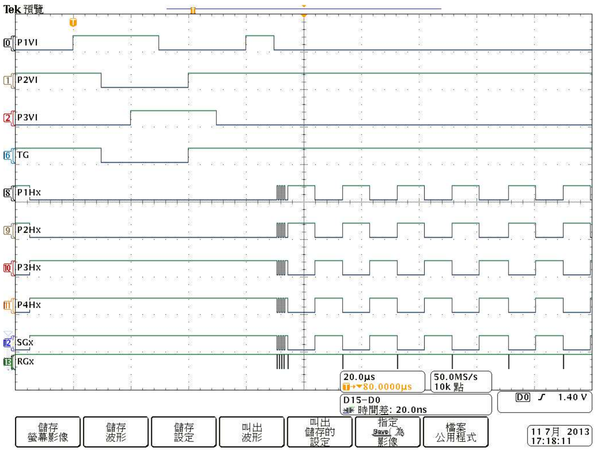

Figure 15: The clock patterns for the CCD charge transfer generated by UCAM CCD controller. Upper four clocks, including ones that labelled as P1VI, P2VI, P3VI, and TG, are used for parallel transfer of charges which shift charges in pixels by one line towards the serial register.Lower six clocks, including P1Hx, P2Hx, P3Hx, P4Hx, SGx, and RGx, are for serial transfer on the serial register to move charges into the readout ports which consists of reset and output MOSFETs. The fully depleted CCD manufactured by Hamamatsu Photonics utilizes 3-phase clocking for parallel transfer and 2-phase clocking for serial transfer. The clocks were measured by voltages using an oscilloscope manufactured by Tektronix, Inc.

2.5 Current Status

We had worked on the development of visible 4-color simultaneous imager "Dogioya" for years, and now all the components, including unit cameras, optics, electronics, mechanics, and control software, are ready. Unfortunately, Lulin 2-m telescope is not yet installed at Lulin observatory due to the delay caused by the environmental assessment study. Dogioya is tightly linked with large-scale astronomical surveys, such as Pan-STARRS and PTF (Palomar Transient Factory), and immediate start of the operation is highly expected. To start the operation of Dogioya together with a 2-m class telescope, we have established a collaboration with Institute for Astronomy, University of Hawaii. University of Hawaii (UH) provides 2.2-m telescope at the summit of Mauna Kea (Fig. 28), and NCU provides Dogioya. UH will have a right to use Dogioya with 2.2-m telescope, while NCU will have an access to the telescope time of 2.2-m telescope. It gives mutual benefits to both sides of the collaboration. Note that both NCU and UH joins Pan-STARRS project. Both sides of the collaboration agree to operate the instrument for four years in Hawaii. The memorandum of understanding (MoU) for this collaboration is about to be signed by both parties. The draft version of MoU is shown in Fig **??** and **??**. A new corrector lens system for UH 2.2-m telescope is required for the operation of the instrument in Hawaii. The design and manufacturing of the cor-

Figure 16: The engineering grade CCD chip installed in the dewar. The chip is supported by the copper plate. The window in front of the CCD is anti-reflection coated fused silica.

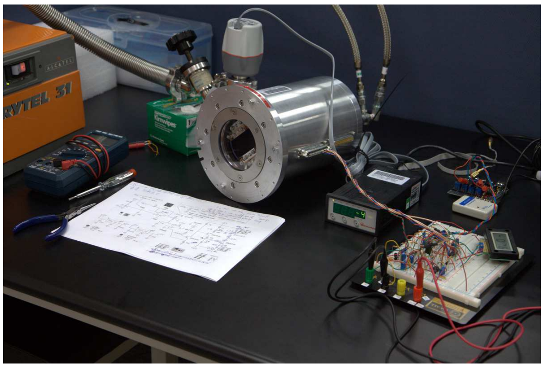

Figure 17: Assembled NCUcam-1 under testing in the laboratory. NCUcam-1 consists of the camera head, vacuum pump, cryocooler, temperature control electronics, and CCD readout electronics.

rector lens were completed in spring 2013, and a set of new corrector lens and telescope adapter was delivered. The assembly tests were carried out and the integration of the whole Dogioya system for UH 2.2-m telescope was successfully done (Fig. 29). We were planning to send all the components of the instrument to Hawaii in April 2013. However, the telescope and dome of UH 2.2-m telescope was damaged at the beginning of February 2013, and UH-side now requests us to postpone the instrument test using the telescope by half a year. With our current plan, we will ship our instrument to Hawaii in autumn this year, and will assemble all the components in Hawaii, and attach Dogioya to bent-Cassegrain focus of 2.2-m telescope. We expect to have a first-light of Dogioya using UH 2.2-m telescope by the end of this year.

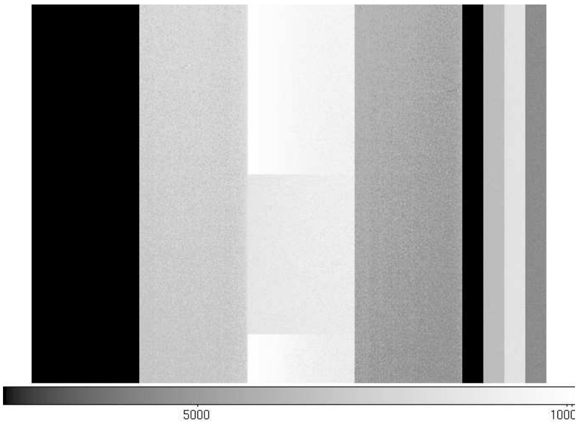

Figure 18: The bias frame obtained by NCUcam-1 with an engineering grade chip of the fully depleted CCD manufactured by Hamamatsu Photonics. The CCD was drived by UCAM controller. The CCD has four readout ports, and the mean levels of the bias for each region are slightly different. The most left side of the CCD was not working properly. Four narrow stripes on the right hand side are overscan regions.

3 Project Members

This project has been supported by faculties, postdocs, project asssitants, and graduate students of our institute. Wu Ching-Huang contributed to the project for four years since 2008. He is an expert of analog electronics, and a successful CCD drive could not be achieved without his work. Yang Hui-Hsin worked hard on administrative issues for more than three years since 2009. Chen Tse-Chuan was responsible for keeping the laboratory in good condition since 2009. Kinoshita Daisuke gave a conceptual and overall design of the instrument at

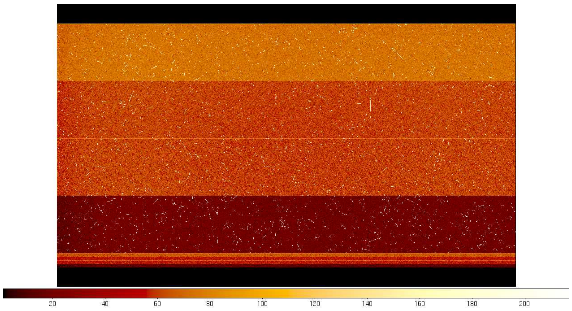

Figure 19: 3600 sec dark exposure of NCUcam-1. Four regions on the CCD image is recognized, and this is because the CCD chip is equipped with four amplifiers. Four narrow stripes are also found at the bottom of the image, and those are overscan regions for each amplifier.

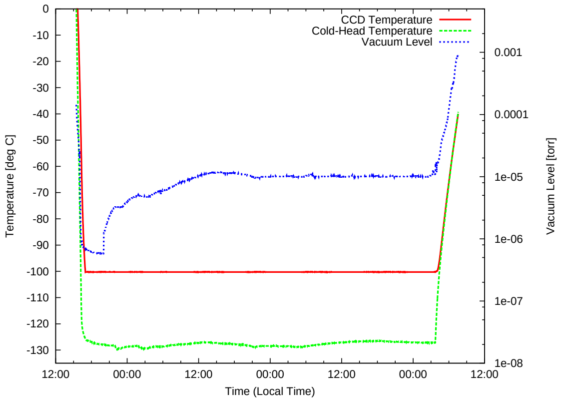

Figure 21: The vacuum level in the dewar and temperature at CCD chip and cold-end of the cryocooler. The measurements started around 15:00 in the afternoon on 5 July 2011, and ended around 09:00 in the morning on 8 July 2011. The vacuum level was good enough for 3 nights, and the CCD cooling temperature was stable at -100°C for the whole period of the observing run.

the beginning of the project, and has coordinated the project for the whole project period. A complete list of the project members is given in Table 5.

4 Summary

For quick and efficient follow-up observations for large-scale astronomical surveys, visible 4-color simultaneous imager "Dogioya" is proposed. We have designed and developed Dogioya, and the instrument is ready to be used. We have established a collaboration with University of Hawaii, and Dogioya will be shipped to Hawaii later this year. Dogioya will be operated using UH 2.2-m telescope for four years. The advantages of Dogioya includes, but not limited to, (1) reliable color measurements by simlutaneous imaging, (2) high sensitivity of fully depleted CCD imager "NCUcam-1" which has been developed by ourselves, and (3) PS1-compatible band-pass filters which allow us to combine the data from Pan-STARRS and Dogioya in a easier way. More importantly, we have gained experiences through the development of astronomical instrument. The astronomical instrumentation project requires wide range of knowledge and experiences, such as mechanics, electronics, optics, software, and project management. Those are usually new to astronomers. At NCU, our project of developing the Dogioya, was the very first trial to design and develop an instrument. We believe that the trial was successful, and we have a working instrument and have accumulated experiences. The instrumentation is a key activity in astronomical research, and it is a way to produce unique, useful, and valuable scientific data.

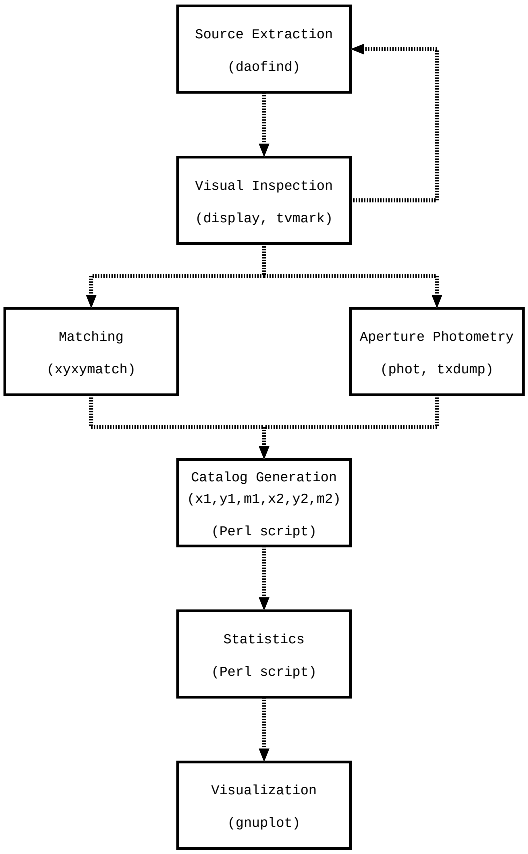

Figure 22: The flow chart of detection limit analysis. First, all the sources in the image are identified and extracted. After the visual inspection of the result of source extraction, the source lists of 1st and 2nd images are compared and matching is tried. At the same time, precise aperture photometry is applied to each source in the image. Then, a complete catalogue with object ID and photometric measurements is generated. After the statistical analysis, the detection limit is calculated.

Acknowledgements

We are grateful to Prof. Wei Ming-Zhi at UCO / Lick Observatory. He has developed UCAM CCD controller that we use, and kindly visited us twice to help us to drive the CCD chip. Dr. Wang Shiang-Yu at Institute of Astronomy and Astrophysics at Academia Sinica provided valuable information on for the mechanical structure and CCD readout. Dr. Ikeda Yuji at Kyoto Sangyo University supported optical and mechanical design of the instrument. Comments from Prof. Sato

Table 5: A list of members who have contributed to the Dogioya project. Names are listed in alphabetical order.

Name	Period	Contribution
Chen Tse-Chuan	2009-2013	mechanics, administration
Chen Wen-Ping	2007-2013	supervising
Chou Yi	2007-2013	PI of the project (2010-2011)
Huang Kuei-Yu	2012-2013	administration
Huang Ru-Huei	2008-2012	CCD camera characterization
Hsueh Yi-Ting	2012-2013	CCD camera characterization
Hwang Chorng-Yuan	2007-2013	PI of the project (2007-2010)
Ip Wing-Huen	2007-2013	supervising
Kinoshita Daisuke	2007-2013	overall design and coordination, PI of the project (2011-2013)
Ko Chung-Ming	2007-2013	supervising
Ngeow Chow-Choong	2009-2013	supervising
Shen I-Cheng	2009-2010	software
Shen Pei-Hsien	2010-2011	software
Wang Bo-Jhou	2013-2013	electronics
Wu Ching-Huang	2008-2012	electronics, mechanics
Yang Hui-Hsin	2009-2012	administration

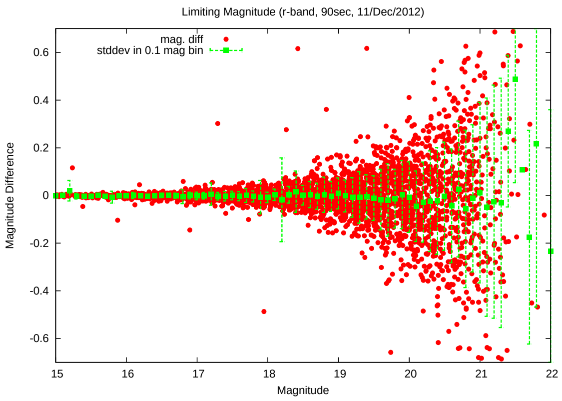

Figure 23: The magnitude differences of 1st and 2nd images vs. field star magnitude for r'-band. The data are binned for each 0.1 mag, and standard deviation is calculated for distribution of data points in each bin.

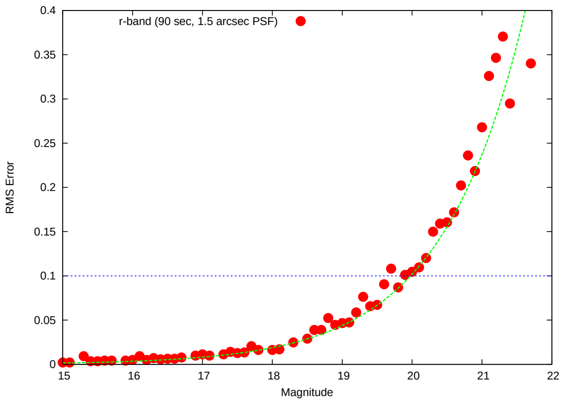

Figure 24: RMS error vs. magnitude for r'-band. The magnitude which corredsponds to RMS error of 0.1 mag is the detection limit.

Shuji at Nagoya University were always helpful to our project. We thank Mr. Kawai Toshihide at Nagoya University for his comments on the selection of material for mechanical design. We appreciate many suggestions on cryocooling and vacuum technology by Dr. Chen Yu-Jung at Physics Department of National Central University.

References

[1] Jia, L., Wei, M., Zou, S., Luo, Y., "The UCAM CCD system of LAMOST", 2010, Proceedings of the SPIE, Volume 7733, pp. 77335E-77335E-11.

[2] Kaiser, N., "Pan-STARRS: a wide-field optical survey telescope array", 2004, Proceedings of the SPIE, vol. 5489, pp. 11-22.

[3] Kamata, Y., Miyazaki, S., Nakaya, H., Tsuru, T. G., Tsunemi, H., Miyata, E., Muramatsu, M., Suzuki, H., Miyaguchi, K., "Evaluation of the fully-depleted back-illuminated CCD for Subaru Suprime-Cam", 2008, Proceedings of the SPIE, vol. 7021, pp. 70211S-70211S-9.

[4] Kinoshita, D., Ohtsuka, K., Sekiguchi, T., Watanabe, J., Ito, T., Arakida, H., Kasuga, T., Miyasaka, S., Nakamura, R., Lin, H.-C., "Surface heterogeneity of 2005 UD from photometric observations", 2007, A&A, 466, 1153-1158.

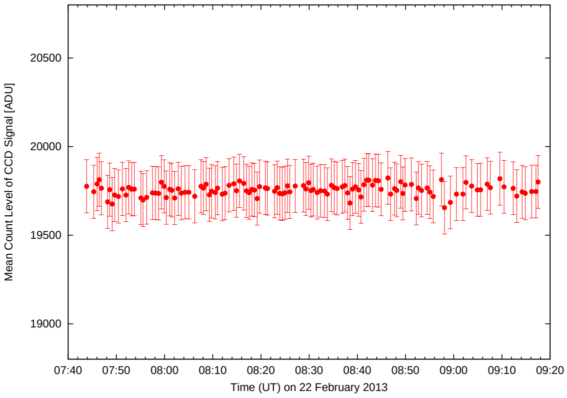

Figure 25: The stability of brightness in the integrating sphere. The brightness of LEDs is controlled by current regulative diode. The standard deviation of the brightness variation is 0.16% of mean signal level.

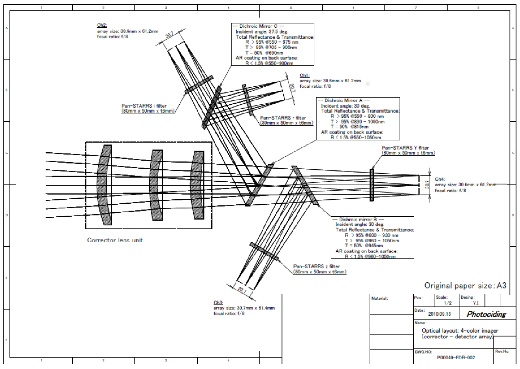

Figure 26: The optical layout of the beam splitter and corrector lens. The corrector lens improves the image quality, and the beam splitter split the beam from the telescope and feed them to CCD imagers.

[5] Miyazaki et al., 2002, PASJ, 54, 833-853.

[6] Okamura et al., 1996, "Suprime-Cam Final Design Review".

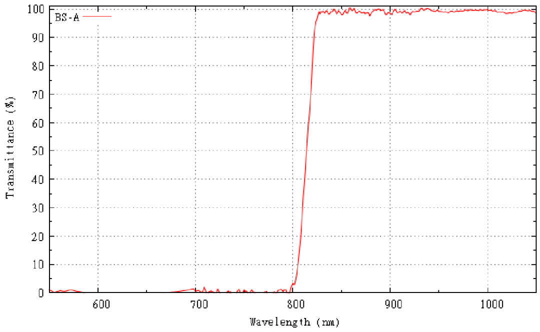

Figure 27: The transmittance property of the beam splitter "BS A". This dichroic mirror splits the beam from the telescope. The light of wavelength shorter than 815 nm is reflected on the surface and the light of wavelength longer than 815 nm is transmitted.

Figure 28: The dome of University of Hawaii 2.2-m telescope at the summit of Mauna Kea. The telescope is located at one of the best sites for ground-based astronomical observations in the world. The altitude of the observatory is 4,200-m above sea level.

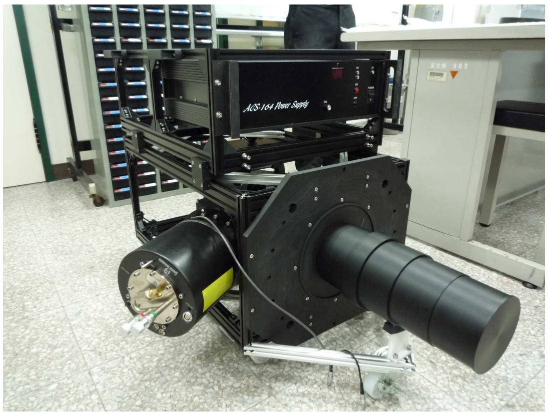

Figure 29: Sucessfully integrated Dogioya system. The existing beam splitter part was assembled with a new corrector lens system and telescope adapter for UH 2.2-m telescope. The photo was taken by T.-C. Chen.

Appendix: Memorandum of understanding with the University of Hawaii

Following is the draft of the memorandum of understanding for Dogioya collaboration with the Institute for Astronomy, the University of Hawaii. The Institute of Astronomy, the National Central University provides 4-channel simlutaneous imager Dogioya, and the Institute for Astronomy, the University of Hawaii provides the 2.2-m telescope at the summit of Mauna Kea.

Memorandum of Understanding

April 29, 2013

Introduction

This is a Memorandum of Understanding (MOU) between the Institute of Astronomy (IoA), National Central University of Taiwan (NCU) and the Institute for Astronomy (IfA), University of Hawai'i (UH). This MOU defines the agreement between NCU and IfA for use of the NCU Four-Channel Imager (FCI) on the University of Hawai'i 2.2 meter telescope located on Mauna Kea, HI.

Participants

Dr. Colin Aspin is the IfA Principal Investigator (PI). Dr. Günther Hasinger is the IfA Director.

Dr. Wen-Ping Chen is the NCU Principal Investigator. Dr. Chung-Ming Ko is the NCU IoA Director.

Definition of the FCI

The FCI is a four-channel optical imager that has been designed, funded, and fabricated by NCU. It consists of four separate optical light paths defined by dichroic mirrors and astronomical filters, each of which feeds a temperature-controlled CCD camera capable of direct sky imaging. The astronomical filters provided with the FCI will be r’,i’,z, y. In addition to the optical components and CCD cameras, the FCI includes cryogenic units and computer systems for readout and storage of images acquired in each of the four channels.

Statement of Work

The FCI will be loaned to the IfA for use on the UH 2.2 meter telescope for an initial period of four years starting when the FCI is considered to be in an operational state by a joint agreement between the IfA and NCU PIs.

Compensation

In compensation for the development of the FCI and the loan to the IfA, NCU will be allocated ten nights of observations per semester using FCI on the UH 2.2 meter telescope. There are two semesters per year covering the periods February 1st to July 31st (semester A) and August 1st to January 31st (semester B). NCU agrees to allow UH/IfA astronomers to use FCI on the UH 2.2 meter telescope at any other time during the loan period.

Lost Nights

Nights on the UH 2.2 meter telescope lost to (i) bad weather, (ii) an inoperable science instrument (the FCI), or (iii) telescope and ancillary equipment failure, shall not qualify for compensatory nights in future semesters.

IfA Effort - Extent and Requirements

IfA staff effort will be allocated by the IfA PI. This effort is required to perform the following tasks, to (i) mount the FCI on the north bent Cassegrain focus mount of the UH 2.2 meter telescope, (ii) mount the associated FCI electronics on the telescope, (iii) provide the required closed-cycle cooler (CCC) lines from the telescope CCC room to the instrument, (iv) provide electrical power to the FCI and computer network connections from the FCI to the IfA computer network, and (v) provide space for the FCI operations computers in the UH 2.2 meter telescope control room and/or the computer room. In addition, the IfA staff will provide technical assistance as required and if available, to aid in solving operational problems with the FCI.

NCU Effort - Extent and Requirements

NCU staff will provide the FCI in an operational state. NCU effort will be provided to commission the FCI on the UH 2.2 meter telescope during the commissioning nights allocated by the IfA Director. The FCI will be considered “commissioned” when the instrument is fully functional at a level of performance acceptable for astronomical use. This level of functionality will be defined by both NCU and IfA staff and be in terms of such parameters as, but not limited to, detector readout noise, astronomical image quality, and interface to the UH 2.2 meter telescope sub-systems and computer network. NCU staff will provide the IfA with a set of documentation for FCI aimed at on-going support of the instrument. This documentation should also include complete operating instructions for FCI. It is expected that NCU technical staff will provide on-going assistance with FCI in case of future technical problems/issues and improvements.

Data Access Rights

NCU will retain exclusive data access rights to all scientific data acquired using FCI during the dedicated NCU observing nights on the UH 2.2 meter telescope. Data access rights to data acquired with FCI during any other observing nights e.g. by IfA astronomers and students, will remain with UH and the IfA.

Signed: Dr. Günther Hasinger (IfA Director) Dr. Chung-Ming Ko (NCU IoA Director)

Signed: Dr. Colin Aspin (IfA PI) Dr. Wen-Ping Chen (NCU PI)

鹿林天文台十年(2002-2012)回顧與展望

Graduate Institute of Astronomy, NCU
國立中央大學天文研究所

林宏欽及鹿林天文台團隊

摘要

鹿林天文台位於中臺灣玉山國家公園塔塔加的鹿林前山，海拔2,862公尺，是臺灣最重要的光學天文基地。平均視相為1.39角秒。此台址的天空背景相當暗，每年可觀測時數約1500小時，較好的觀測季是每年的秋季到初冬。主要的研究設施有 1 米、0.4米、0.35米望遠鏡以及四座中美掩星計畫(TAOS) 0.5米自動望遠鏡。目前正在籌建台灣最大的 2 米望遠鏡。本文回顧了鹿林天文台近10年(2002~2012)的發展以及未來展望。

2002

- 中大天文所成立10週年
- 鹿林天文台控制中心落成
- 鹿林 1 米望遠鏡(LOT)開光
- 發現台灣首顆小行星

2003

- 鹿林 1 米望遠鏡(LOT)時間開放申請
- 首次觀測到伽瑪射線爆(GRB)光學餘暉觀測
- LOT參與WET及WEBT兩大全球望遠鏡聯測網

2004

- 臺灣超新星巡天計劃(TSS)發現首顆超新星，至2007年止共發現15顆超新星

2005

- 中美掩星計畫(TAOS)望遠鏡開始運轉
- 參與全球物理年點燈活動，台灣亮燈全球第一
- SLT 0.4米望遠鏡開光

2006

- LOT光譜儀上線
- 開始鹿林巡天計畫(LUSS) ，以SLT 0.4米望遠鏡進行小天體巡天
- 2 米望遠鏡計畫啟動

2007

- IAU通過「中大」與「鹿林」兩顆小行星永久命名
- 發現台灣首顆彗星—鹿林彗星(C/2007 N3)
- 發現台灣首顆近地小行星(2007 NL1)
- 參與「泛星計畫」（Pan-STARRS）

2008

- TAOS第一個科學結果: 太陽系的古柏帶天體數量遠低於預期

2009

- 鹿林彗星到達最大亮度，全球都在看
- LUSS至2009年止共發現了約800顆小行星

2010

- TAOS六年觀測結果對太陽系中直徑大於500公尺的古柏帶天體數量設下了非常嚴格的上限
- IAU通過「慈濟」與「雲門」兩顆小行星永久命名

2011

- 鹿林小行星發現數排名全球前50大
- LOT三色同步偏振成像儀(TRIPOL)開光
- 自製近紅外相機NCUCAM1開光

2012

- 中大天文所成立20週年
- 中大命名的22顆小行星回娘家
- 0.35米望遠鏡(L35)啟用

未來展望

- 鹿林最後一塊拼圖— 2 米望遠鏡
- 前進最後一塊天文淨土—西藏

致　謝

鹿林天文台能有今日要特別感謝許多人的無私奉獻，並對教育部、國科會及中研院天文所的長期支持致敬。


中大天文所成立10週年(2002)


鹿林天文台

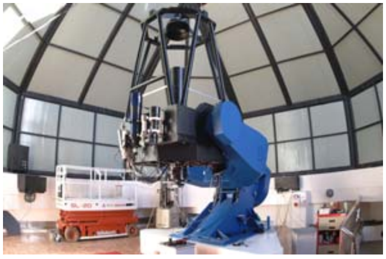
鹿林1米望遠鏡(LOT)


中美掩星計畫(TAOS)

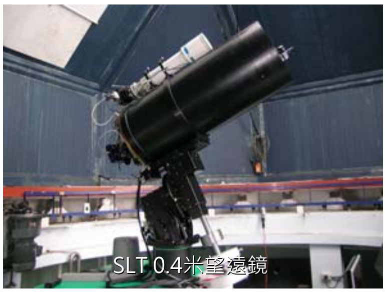
SLT 0.4米望遠鏡


0.35米望遠鏡(L35)


2米望遠鏡

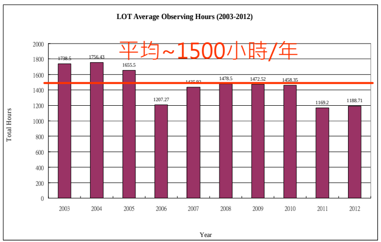

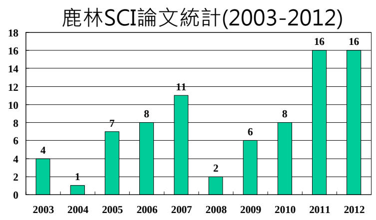


玉山群峰伴鹿林天文台

鹿林天文台使用單位及人數統計(2013)

林宏欽、林啟生、蕭翔耀、張明新

2013 年鹿林天文台使用單位及人數統計如下，總計有 20 個使用單位，共 1538 人次。使用目的主要為研究、教學及媒體採訪。其中前三大使用者為環保署鹿林背景測站、中大天文所及台大，共佔了 74%。

單位	人次	目的
環保署鹿林背景測站	421	研究
中大天文所	401	研究、教學
台大	326	研究
北一女	82	教學
中研院	54	研究
大里高中	54	教學
清大	51	研究、教學
大愛電視台	32	媒體採訪
中國醫大	32	教學
儀科中心	23	研究
中大太空所	14	研究
深圳氣象局	12	研究、教學
成大	9	研究、教學
攝輯手(國科會)	8	媒體採訪
台北天文館	5	研究、教學
東森電視台	4	媒體採訪
台視熱線追蹤	3	媒體採訪
中視	3	媒體採訪
大均傳播(國科會)	2	媒體採訪
蘋果日報	2	媒體採訪
總計	1538	

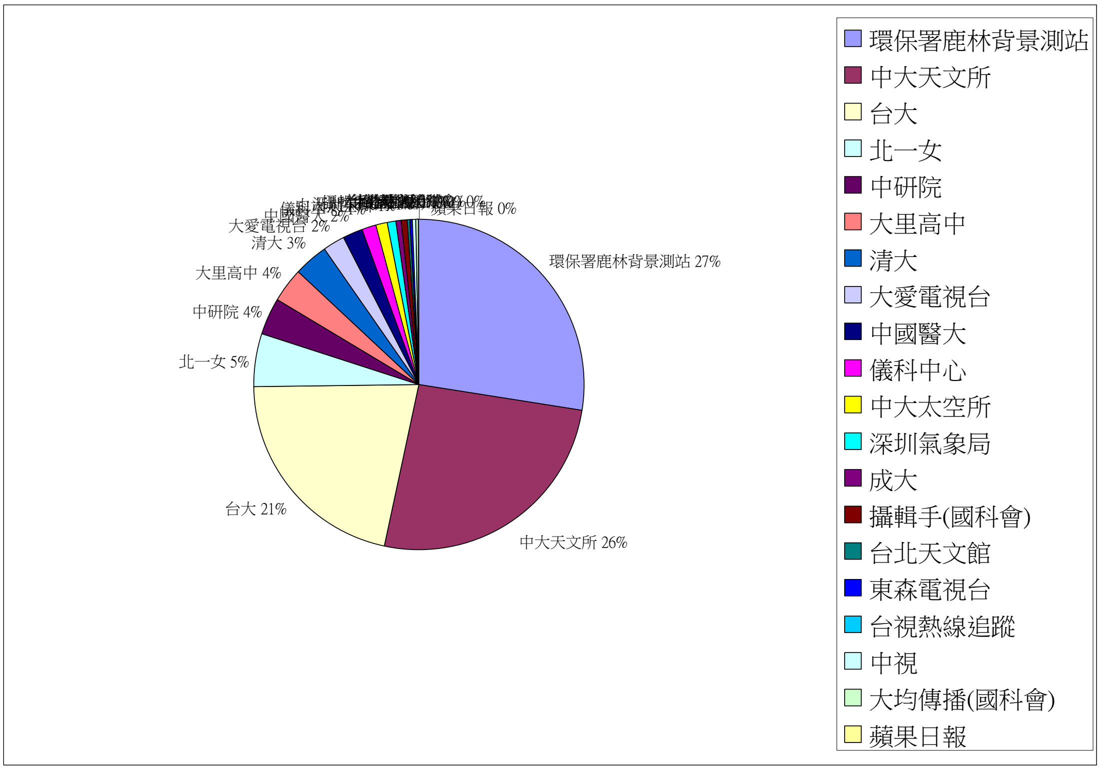
環保署鹿林背景測站 27%
中大天文所 26%
台大 21%
北一女 5%
中研院 4%
大里高中 4%
清大 3%
大愛電視台 2%
中國醫大 2%
蘋果日報 0%
環保署鹿林背景測站
中大天文所
台大
北一女
中研院
大里高中
清大
大愛電視台
中國醫大
儀科中心
中大太空所
深圳氣象局
成大
攝輯手(國科會)
台北天文館
東森電視台
台視熱線追蹤
中視
大均傳播(國科會)
蘋果日報

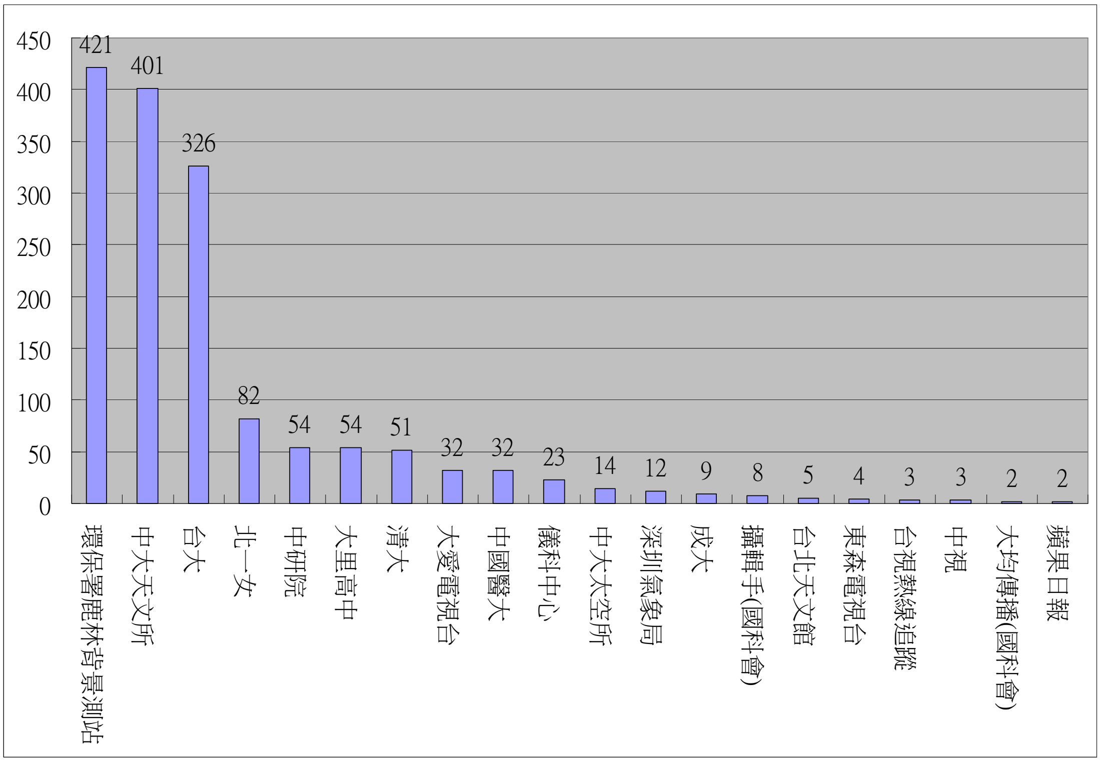
450
400
350
300
250
200
150
100
50
0
421
401
326
82
54
54
51
32
32
23
14
12
9
8
5
4
3
3
2
2
環保署鹿林背景測站
中大天文所
台大
北一女
中研院
大里高中
清大
大愛電視台
中國醫大
儀科中心
中大太空所
深圳氣象局
成大
攝輯手(國科會)
台北天文館
東森電視台
台視熱線追蹤
中視
大均傳播(國科會)
蘋果日報

鹿林天文台參訪團體統計(2013)

日期	單位	人數
1 月 1 日	香港保良局陳守仁小學/星河科研社	26
1 月 19 日	海鷗直升機大隊	9
2 月 4 日	清華大學天文社	20
2 月 6 日	成功高中天文社	24
2 月 16 日	交大天文社	12
3 月 09 日	黃裕仁	4
4 月 21 日	攝輯手	8
4 月 21 日	經濟部標準檢驗局	27
4 月 23 日	台視熱線追蹤	3
4 月 26 日	北回歸線太陽館	26
6 月 16 日	台灣中油	5
6 月 22 日	大愛電視台	5
7 月 5 日	雄女天文社	23
7 月 6 日	親子觀星會	33
7 月 26 日	行政院中部聯合服務中心	15
7 月 27 日	中大太空所呂凌霄老師	6
8 月 2-6 日	大愛電視台採訪	6
9 月 14 日	是方電訊	5
10 月 26 日	台南市天文協會	40
11 月 26 日	雲南天文台 吳光節	2
12 月 2 日	蘋果日報採訪鹿林	2
12 月 5 日	東森新聞主播王淑麗鹿林連線	5
12 月 6 日	教育部長視察暨文教記者會	27
12 月 7 日	彰化高中天文社	16
12 月 9 日	塔塔加警察隊	28
12 月 14 日	玉管處	20
12 月 21 日	中央大學理學院	8
12 月 30 日	大均傳播	2
	總計	381

鹿林天文台觀測時數統計(2003-2013)

林宏欽、蕭翔耀、林啟生

鹿林天文台自 2002 年 9 月開始有人員常駐，2003 年 LOT 一米望遠鏡上線，始有正式觀測時數紀錄，可供瞭解鹿林長期的觀測條件。依 11 年來(2003-2013)的統計結果，鹿林天文台年平均觀測時數約為 1440 小時。一年大略分為四個觀測季，

- 最佳觀測季：10-12 月。
- 次佳觀測季：1-3 月。
- 最差觀測季：4-6 月。4 月開始進入雨季，5-6 月受梅雨影響，天氣最差。
- 次差觀測季：7-9 月。主要受颱風及夏季午後對流雲系影響，天氣變化很大。此外夏季晝長夜短，每晚可觀測時間原本就比冬季少許多。

詳細統計資料及統計圖如下，

表 1 每月觀測時數統計 (2003-2013)

Month	2003	2004	2005	2006	2007	2008	2009	2010	2011	2012	2013	Average**
1	78.75	125	163.25	129	127.32	179	234.52	206.9	90.8	113.42	153.58	143.14
2	142.5	145.98	94.75	149	128.55	118.25	165.7	100.6	123.8	64.88	183.63	129.90
3	147.5	163	143	126.05	116.4	138.5	146.75	181.3	75.9	168.23	134.26	142.63
4	126.5	110.5	144.75	86.8	53.75	85.25	71.8	75.8	151.45	32.75	55.83	90.11
5	129.75	106.25	136.25	59.5	106.6	98.25	167.4	86.05	56.6	74.3	41.02	94.84
6	24	133	45	39.3	54	37	81.75	26.5	61.5	35.15	80.14	51.15
7	222.5	48	167.75	91.57	128.88	88.4	76.6	99.85	81.75	106.4	88.05	103.25
8	137.75	142	76	111.65	56.6	118.95	6.8*	98.3	97.9	35.7	72.2	89.45
9	142	116	129.25	60.05	69.55	59.8	0*	109.95	90.1	117.35	107.84	95.54
10	149.25	219.75	210.25	150.6	172.63	191.38	175.6	139.8	136.95	214.51	200.57	178.29
11	166.5	214.5	216.25	71.75	160.55	152.55	175.8	163.65	87.2	93.81	136.1	150.07
12	271.5	232.45	129	132	261.09	211.17	169.8	169.65	115.25	132.21	86	172.51
Total	1738.5	1756.43	1655.5	1207.27	1435.92	1478.5	1472.52*	1458.35	1169.2	1188.71	1339.22	**1441.61**

* 2009 年因受 88 風災影響，自八月八日起至十月初約 2 個月期間，受停電影響以至於無法觀測。所以 2009 之八、九月時數不準。

**Average=扣除最高及最低值後取平均。

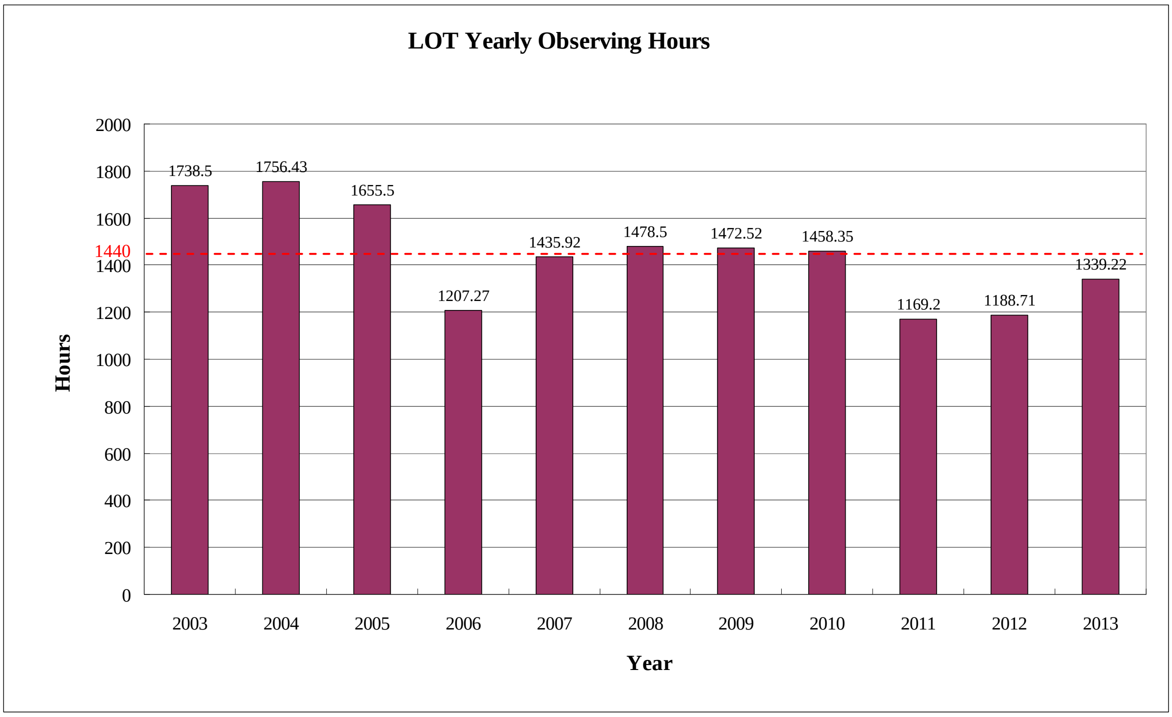

圖 1　鹿林天文台年平均觀測時數統計圖(2003-2013)

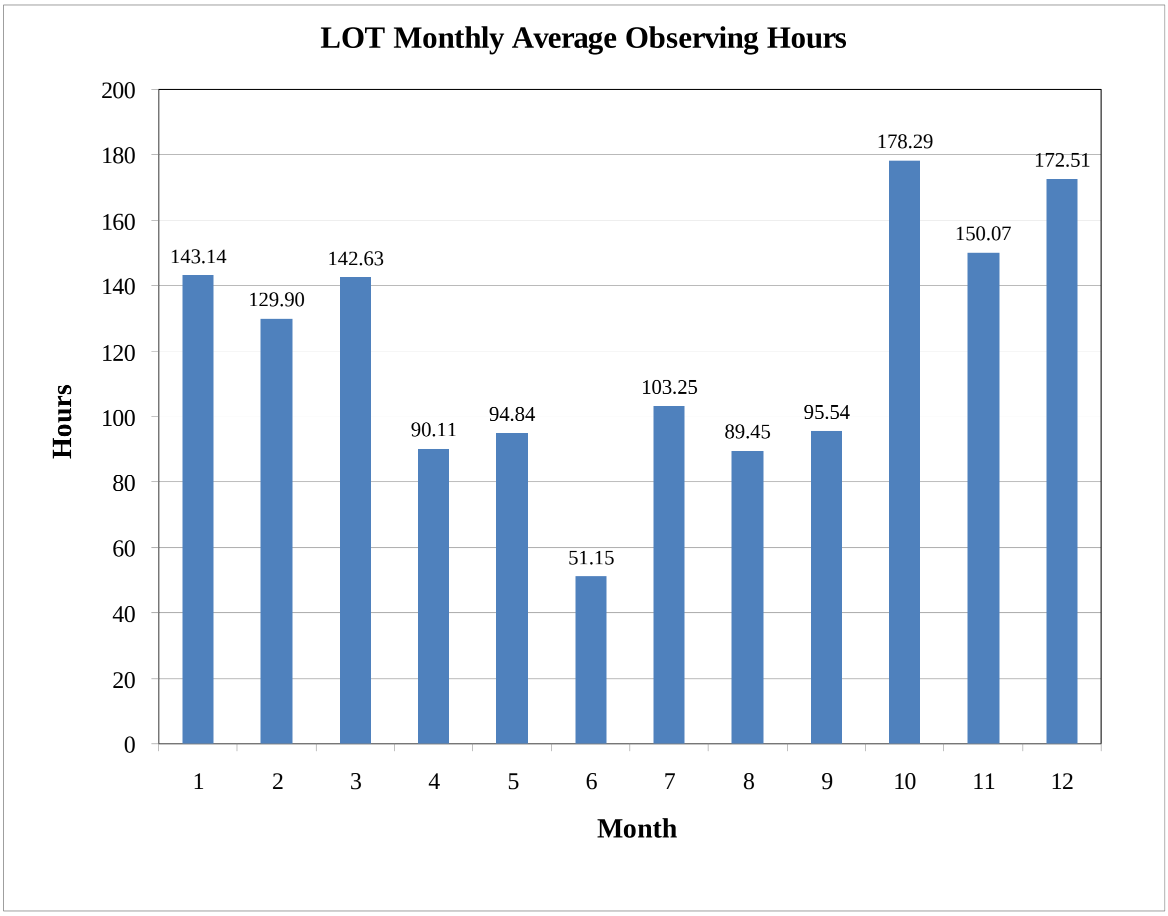

圖 2　鹿林天文台月平均觀測時數統計圖 (2003-2013)

全球第一 北一女拍到超新星SN 2013ej爆發

2013-10-13 02:00　中國時報　【石文南、湯雅雯／台北報導】

↑北一女師生團隊在鹿林天文台前合照。（台北市教育局提供）

北一女中由國科會補助的特色課程「星雲行動」，今年7月前往鹿林天文台觀星，師生團隊意外率先拍攝到超新星SN 2013ej爆發。經比對發現是全球第1個拿到SN 2013ej爆發光度資料的團隊。

北一女地球科學教師林郁梅表示，此次鹿林天文台觀星拍攝M74星系。M74星系距地球3200萬光年，位於雙魚座附近。

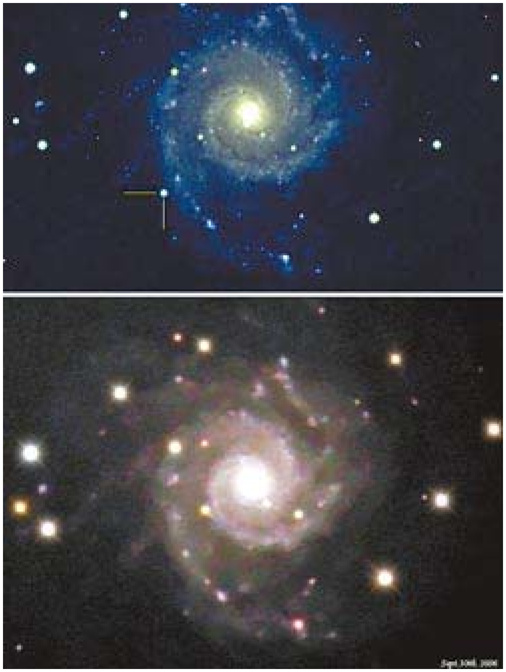

↑北一女學生7月24日晚上7點多拍攝的M74星系，圖左下角出現一顆亮度極高的就是超新星SN 2013ej（上圖，北一女提供），下圖為超新星SN 2013ej未爆發前的M74星系（摘自Astronomy Magazine網站）。

師生在世界標準時間2013年7月24日19點18分（台灣時間7月25日3點18分），於中央大學鹿林天文台拍攝到SN 2013ej超新星，並提供第1個經過校對的亮度數據。15個小時後，美國李克文天文台的超新星搜尋團隊（Lick Observatory Supernova Search）於世界標準時2013年7月25日10點18分確認為超新星。

教師林郁梅表示，研究團隊整理資料照片比對發現，學生拍攝的M74星系圖的左下角，出現一顆亮度極高的，就是超新星SN 2013ej。恆星爆炸後形成超新星，像煙火般亮度瞬間爆亮，一段時間後轉暗，全世界的天文學家都在緊盯它，以窺知這顆超新星的前身。北一學生許苡蕾表示，在拍攝M74星系圖，剛好碰上恆星爆炸很亮，當時並不知道是超新星的形成。

清大天文所教授江國興表示，天文學家推斷SN 2013ej超新星的前身，應是顆超級巨大的紅色巨星，稱為「紅超巨星」，質量大約為太陽的8-10倍，半徑為太陽的400到600倍。北一女師生拍到光度正上升的超新星爆發，有一定的科學研究價值。

台北市立天文館研究員葛必揚表示，拍到超新星很難得，因為它「可遇不可求」，不像日月蝕規律變化或什麼季節看到什麼星座，可

以事先預測，未來可作為恆星演變或天文物理上的學術研究。

至於是否為全世界最早拍攝到？葛必揚指出，這要送到美國哈佛史密斯松天文台進一步判定，若確認無誤，「真的要給這群厲害的學生拍拍手鼓勵一下」。

至於是否為全台第一例？氣象局天文中心表示，中央大學團隊或高雄天文學會個人，都曾拍到超新星；但可以說是台灣第一個高中學生團體，首次發現超新星。

↑北一女學生7月24日晚上7點多拍攝的M74星系，圖左下角出現一顆亮度極高的就是超新星SN 2013ej（上圖，北一女提供），下圖為超新星SN 2013ej未爆發前的M74星系（摘自Astronomy Magazine網站）。

Outside
GCN
IAUCs

Other
ATel on Twitter and Facebook
ATELstream
ATel Community Site
MacOS: Dashboard Widget

The Astronomer's Telegram

Post a New Telegram | Search | Information
Telegram Index
Obtain Credential To Post | RSS Feeds | Email Settings

Present Time: 9 Apr 2014; 07:52 UT

[Previous | Next | ADS]

Early Photometry of the Type IIP supernova SN 2013ej

ATel #5466; *M. Lee (Taipei First Girls' High School), K. L. Li, J.-W. Wang, A. K.H. Kong (National Tsing Hua U.), H. B. Liu (ASIAA), H.-J. Huang (National Taiwan U. & ASIAA), Y.-H. Huang (U. of Chicago), Y.-M. Lin, K.-C. Yang (TFGHS), on behalf of the Taipei First Girls' High School High Scope Program*
on ***13 Oct 2013; 07:22 UT***
Credential Certification: Albert Kong (akong@phys.nthu.edu.tw)

Subjects: Optical, Supernovae

Tweet 7 Recommend 21

We report an early photometric observation of the Type IIP supernova SN 2013ej taken 15 hours before the official discovery (CBET #3606). We observed the field of M74 on 2013 July 24.80 - 24.83 UT using the 1m telescope at the Lulin Observatory in Taiwan. The supernova 2013ej was clearly detected in our multi-color observations. By comparing with the USNO and GSC2.3 catalogs, we derived the following optical (B, V, and R) photometry: B=13.8, V=14.0, and R=14.3.

The observations were taken under unstable weather condition and we estimated the uncertainties as ~0.2 mag. We note that SN 2013ej was also seen (but without photometry) in a pre-discovery image taken by C. Feliciano on 2013 July 24.125 (Bright Supernovae web site). The supernova was not seen by the All Sky Automated Survey for SuperNovae (ASAS-SN) on 2013 July 23.54 with a detection limit of V > 16.7 (ATel #5237).

The observation is part of an observing training program at Taipei First Girls' High School. This project is funded by the National Science Council of Taiwan as part of the High Scope Program through grants NSC 101-2514-S-007-002 and NSC 101-2514-S-577-001.

Pre-discovery image of SN 2013ej

Related
5466 Early Photometry of the Type IIP supernova SN 2013ej
5275 SN 2013ej is a Highly Polarized Type II-Plateau Supernova
5264 Medicina-Noto VLBI observation of SN2013ej
5243 Swift XRT and UVOT detection of SN2013ej
5237 Pre-explosion ASAS-SN V-Band Upper-Limits on SN 2013ej (PSN J01364816+1545310)
5230 Possible Spitzer Counterpart of PSN J01364816+1545310
5229 The Probable Progenitor of PSN J01364816+1545310 in M74
5228 Spectroscopic classification for PSN J01364816+1545310 in M74 with FLOYDS at Faulkes Telescope South
4033 Early-Time Polarization of the Type II-Plateau Supernova SN 2012aw

[Telegram Index]

因著國科會第二期高瞻計畫的資助、清華大學賴詩萍等諸位教授的輔導、以及中央大學與鹿林天文臺的協助，於2013年7月底，北一女中高瞻計畫團隊師生進行了鹿林天文臺的初次拜訪。從行前的觀測計畫擬定、實地進行觀測操作、以及最後的影像處理，一連串的訓練過程帶領喜愛星空的師生初探了天文研究的大門，更徘徊流連於玉山夜空的美。三天兩夜的過程，意外訪客SN 2013ej的現蹤更是驚奇的收穫。架構在此次的初訪經驗，於2013年10月中旬，北一女中地科社邀請建中天文社共同進行聯合觀測活動、再次拜訪了鹿林天文臺。

兩次的觀測行，同學們將觀測經驗分享與傳承，從規劃到執行，除了想分享感動、更想穩固一同追逐星夢的夥伴情誼。以下文章為同學們造訪鹿林天文臺的觀測心得與省思，期能分享給有志一同的天文愛好者們，也將我們的經驗提供給各友校師生作為參閱。　～林郁梅老師


2013年7月份北一女中高瞻計畫團隊師生鹿林天文臺觀測行。

那一夜，
鹿林的星空
我們的心空

文/ 陳心平、廖乙馨、許苡蕾、蔡欣儒、許雅婷、王蕾婷、沈庭、陳麒瑞


2013年10月份北一女中與建國中學師生鹿林天文臺觀測行。

啟程

都市的影子逐漸遠去，橫越新中橫的崎嶇山路，我們沿著臺二十一線前行，遠處的山峰在和我們捉迷藏。從臺北出發，五個多小時的車程、一個小時的漫長跋涉，對於習慣以車代步的都市小孩而言，這是一場體力與毅力的長跑戰。好不容易，我們來到了雲霧上頭的世界，海拔兩千八百六十二公尺的高度，我們前腳在嘉義、後腳在南投，左手邊的太陽一溜煙的躲到了山後，右手邊的玉山依然挺拔，看見白色矮房在鬱鬱蔥蔥的樹林綻放，那正是此趟旅程的目的地——鹿林天文臺。

等待

夜幕低垂之時，總算要是履行這次行程的主要目的——星體觀測，只可惜起初雲霧沒有散去的意思，一次又一次的落空，無可奈何也只能耐心等待。到了午夜時分，天空終於揭開神秘的面紗，我們像個小小的冒險者來到天臺，探索著鹿林的夜景。我們觀賞著一頭的月明，與另一頭的星漢，曝曬一段月光浴，讓光芒照耀我們心空。以前的星空對我們而言，僅是一幅美麗的插畫，而這次的邂逅才使我們和星空逐漸有了共通的語言……仙后與北極星的微妙連結；夏季大三角勾勒夏季的清爽俐落；秋四邊的皇族宮廷盛狀；獵戶座陽剛的姿態傲視群雄；木星與天狼星在空中閃爍最明亮的色彩……突然間，這樣生澀的我們也變得專業了！而專業的是心情，不是智慧，也開始有了如同身為天文臺的家人一般的認同感，體會到一位天文學家在黑夜靜待時機成熟之際的殷勤盼望。

慌亂

鹿林是我們與大型望遠鏡的第一次接觸，有些陌生。在天未開時，我們依循著操作流程，一步步進行，調焦距、確認目標、試拍秒數、調整曝光時間等，一一完成。等待天氣狀況穩定後，終得以開啓天文臺圓頂正式進行拍攝，聽著望遠鏡轉動的嗡嗡聲，坐在螢幕前，按按鍵盤，影像出爐，觀看示範時一切似乎如此容易，自己上陣又如登天難，忘了按某個鍵、無法攝出理想影像、甚至因天候曝光時間須重算等。我們體悟到，身為初學者，要帶著謙卑的心，多練習、多問、多嘗試，才能成長，機會是留給準備好的人！雲朵遮蔽了我們上半夜的觀測計畫，此時備案才顯得特別重要，我們開始聽星體呢喃、訴說它們的故事、存下一張張影像、寫下一行行觀測紀錄。

天未開前，於鹿林天文臺觀測室內進行模擬觀測操作。

夜半天開後，忙碌地進行計算與操控望遠鏡進行觀測。

在實際拍攝星雲時，常有“流血”(過度曝光)的現象，是因在選擇觀測星體時，忽略了其內部的亮星，因此亮星已過曝而雲氣尚未露臉；亦或是理論所估算之曝光時間與實際情況的差距，而這就需要經驗的指點了。在數次拍攝、修正以及觀測員陪伴的指導下，終於漸入佳境。由於夜半才開始觀測，鹿林駐站人員更替我們多開了一臺口徑35公分的望遠鏡，操作方式與鹿林望遠

鏡1公尺相同，但換了望遠鏡一切數據需重來規劃計算。幸好上山前擬定觀測計劃時的練習，我們能不遲疑、迅速切換尋找新目標。來到清晨時分，我們開始捕捉ISON彗星那燦爛優雅卻短暫的身影，輸入事前預備的數據試拍，多次嘗試後總算測出適用數值卻已過最佳拍攝時間，此時才體悟須在出發前即做好一切資料查詢，以免錯過良時，這些事在在告訴我們萬全的準備是重要的。

反　思

觀測計畫

拜訪鹿林山之前，為了善用夜晚的時光，把握老天給我們開天的機會，觀測計畫的重要性是不容小覷的，深深攸關到此趟行程的最終目的的成功與否。在安排計畫前，也必須清楚如何去選取觀測的目標物，因此，行前的集訓課程是不可或缺的，大約一至兩堂課的時間，需解說(1)關於展源星等的計算方式，並藉此由觀測星體估算最佳的所需拍攝時間；(2)目標物與月亮的距離及仰角必須大於30度，以確保在可觀測高度之上，並且不會被明亮的月光蓋過；(3)目標物大小是否符合望遠鏡視野範圍，初估可能的成像畫面……等多項因素。讓同學們有一定的先備知識，並對於拍攝星體的流程具有熟悉度，會使觀測活動更有目標與成就感。

2013年10月中旬聯合觀測行前課程，學生們互相教學如何規劃觀測計畫。

食、衣

除了學術方面，上山前的準備事項也得注意。隨著海拔高度的變化，氣溫驟降，即使在夏季溫暖的七月，天文臺的溫度就如同冬季的臺北，更可與寒流來襲相作比擬。更遑論受到溼潤季風的吹拂，上山時車子便在霧裡鑽入鑽出，而此時眺望層巒群峰，更是雲霧繚繞，若隱若現。當高山的溼度創造了美景，卻也使原本微涼的氣溫因含了許多水氣而越發令人覺得冷冽了。而若在十月中旬、正值深秋之際的時刻前往，山上的氣溫在夜裡下降後總徘徊於5度左右，山風更是颼颼吹個不停，這時保暖的衣著便是十分重要。

建議的事前準備有：

(1)行前數天可查詢當地的最高溫及最低溫才不會錯估衣物的準備。

(2)溫差大的山頂上適合多件衣物的洋蔥式穿著。

(3)需注意臉部、手部的保暖，外衣應以防風防潮的羽絨外套為佳，而下半身的穿著儘量避免

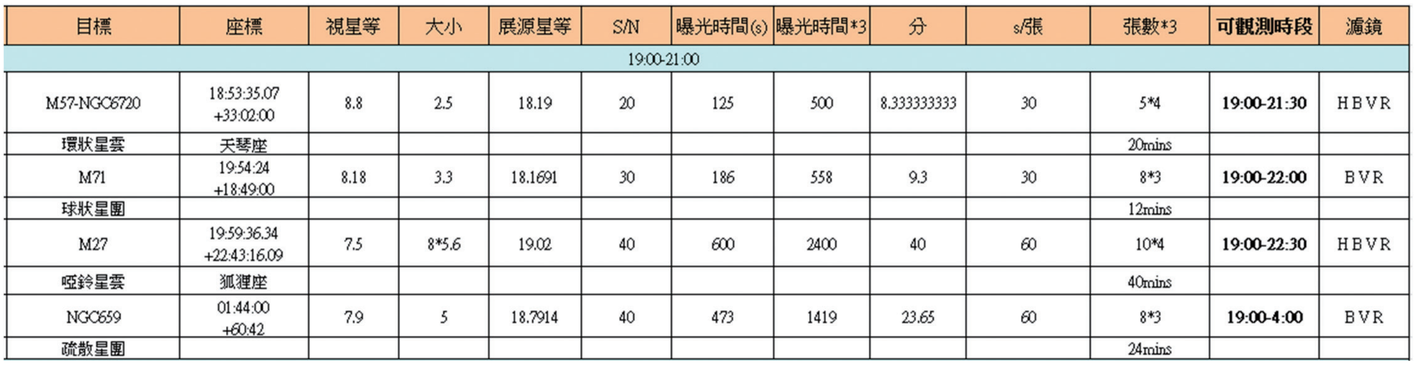

目標	座標	視星等	大小	展源星等	S/N	曝光時間(s)	曝光時間*3	分	s/張	張數*3	**可觀測時段**	濾鏡
19:00-21:00												
M57-NGC6720	18:53:35.07 +33:02:00	8.8	2.5	18.19	20	125	500	8.333333333	30	5*4	**19:00-21:30**	H B V R
環狀星雲	天琴座									20mins		
M71	19:54:24 +18:49:00	8.18	3.3	18.1691	30	186	558	9.3	30	8*3	**19:00-22:00**	B V R
球狀星團										12mins		
M27	19:59:36.34 +22:43:16.09	7.5	8*5.6	19.02	40	600	2400	40	60	10*4	**19:00-22:30**	H B V R
啞鈴星雲	狐狸座									40mins		
NGC659	01:44:00 +60:42	7.9	5	18.7914	40	473	1419	23.65	60	8*3	**19:00-4:00**	B V R
疏散星團										24mins		

行前的觀測計畫擬定。

2013年10月中旬的聯合觀測後，電腦處理後獲得的三色合成影像。NGC2261/北一女中邱楚玉同學。(左圖)

M78/北一女中楊曉晴同學。(右圖)

牛仔褲，才不會因褲子吸水造成不舒服的感覺，必要時再加件衛生褲更能保持溫暖。此外，沒有登山經驗的同學容易忽略山上的低溫，準備的衣物不夠而感冒，甚至加重高山症症狀。

(4)而溼寒的天氣裡徹夜未眠讓人不知不覺就想補充熱量、進食，糧食方面需注意的是，充氣式包裝的食品可能會因為高山的低壓而出現膨脹甚至是爆破的情況，使這些食品不易存放，建議攜帶沖泡式的熱飲與泡麵會是為最佳的選擇。

住、行

上山時結伴同行，是避免落單且安全登山的好方法之一。進行戶外活動必須三人以上才可成行，以讓小組成員足以互相照應。另外，由於空氣稀薄再加上低氣溫，每個人會因體質異同或多或少有些不適的症狀，諸如頭痛、胸痛等，一有不適應需立即反應，以免耽誤自身生命安全。所以，行前身體的保養也十分重要，睡眠充足、飲食正常、衣著保暖，特別是調整好上山前一周的生理作息，讓自己有一副強健的身體以避免高山症乘虛而入，也別忘攜帶健保卡等重要證件。抱持健康愉快的心情和身體，即是觀測活動不可缺少的動力之一！

省思

而身為入山者的我們，是來到這座山的客人，應懷有對大自然的敬意；對天文臺、對當地應有的禮節；對老師長輩的尊重。隨手的簡易小事如整理垃圾和回收物、走路輕聲避免驚擾休息的人、不浪費各種得來不易的資源、懂得讓位而不霸據一方，離去前把環境回歸適當。高山大地之美是大家共同維護的，讓鹿林永遠是逐星最美好的聖地。

夜未眠

雲雨擾亂，始終沒澆熄我們對於開天的一絲希望，一夜的觀測，雖然等待的時間稍顯漫長，但天文觀測偶爾必然掌握於運氣之間的。在這身處高山的夜晚之後，帶著熬了一晚的倦意，我們靜盼著曙光亮起的時刻、早晨的歸來。

莫約七點出頭，屋外的景致已換上不同的光彩，陽光散去微薄空氣中的寒意，灑落在一片山巒之中，山稜線因光影而勻稱，那遠在一方的玉山主峰格外撼動人心。站在天臺上，凝視雲海的遼闊，雲海之後的地平線上湛橙的金星帶交疊於暗藍地影之上，此時身在一片綠意中的鹿林顯得意外小巧。雖然待在這兒的時間短暫，但仍然很是高興能夠有如此難能可貴的機會來訪鹿林天文臺，擁有那全臺最接近天空的望遠鏡，在絕佳的視野靜觀天文景象。

超新星

照片裡的一個亮點，同世間成萬上億顆星靜止於此瞬間，安靜到我們沒有察覺，靜到星系的美將之覆蓋，我們起初歎為觀止的對象不是它，

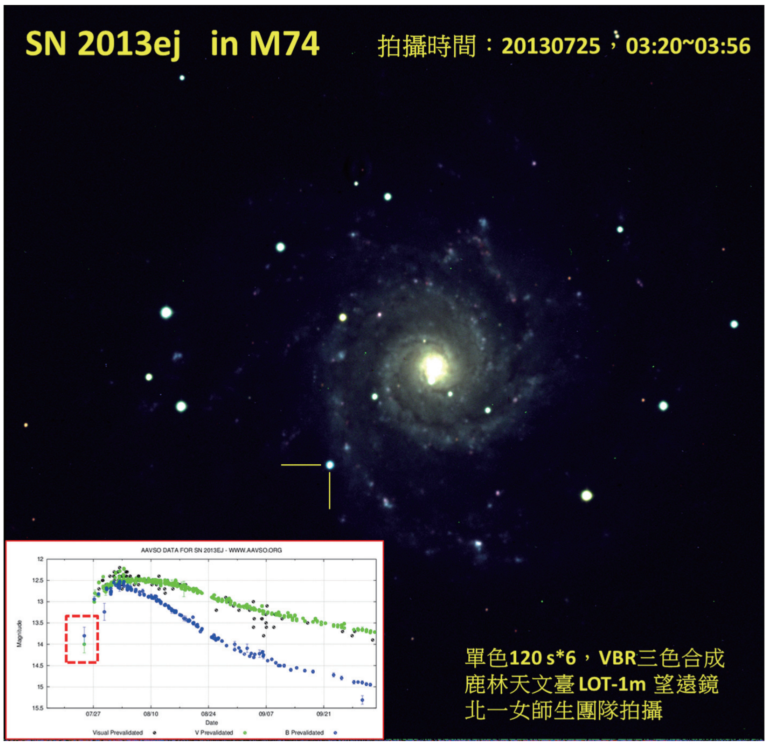

→ 北一女中高瞻計畫師生團隊七月底於鹿林天文臺所拍攝的SN 2013ej影像。左下圖爲該超新星的光度變化曲線，紅框處即爲本團隊的貢獻成果。

超新星爆發 北一女率先捕捉

【許敏溶／台北報導】台北市北一女中師生團隊今年7月利用中央大學鹿林天文台的望遠鏡，拍攝到超新星SN 2013ej爆發前的照片，上月確認是全球拍到該顆超新星爆發前最早的照片，有助於天文界進一步探索超新星的爆發機制。參與觀測的北一女學生昨說：「很意外、興奮」。

在國科會補助下，北一女10多名師生7月下旬到鹿林天文台操作望遠鏡並觀測星空，7月24日晚上7時多拍到超新星SN 2013ej亮度上升前的照片，經整理資料比對，上月才確認領先全球拍到其爆發前最早的照片。

意外拍到很難得

該團隊指導教授之一、清華大學天文所教授張祥光昨說，超新星是大質量恆星在生命最末期劇烈爆發的現象，全球天文界1年中可看到上千顆新星爆發，但多數只拍到超新星爆發變亮時的片，每年僅約近百張拍接近爆發前的照片，北女師生雖是意外拍到，十分難得，有助天文學研究超新星爆發機制。

北一女2年級學生苡蕾說，參加活動的3天夜裡都過著日夜顛倒的活，能獲得成果很興奮星空神秘又美麗，未來投入天文物理領域。

▲北一女師生在鹿林天文台和望遠鏡合影。　台北市教育局提供

▶圖中央偏左下方的亮點就是北一女師生拍到的超新星SN2013ej在爆發前的照片。台北市教育局提供

↘2013年7月使用鹿林天文臺1公尺望遠鏡拍攝到SN 2013ej超新星身影的報紙新聞與媒體採訪。

直到其身份被發掘：那宇宙中最激烈的爆炸——邁向死亡的星。幾張照片將數萬年前的光芒限縮於幾個pixel，照片後的它並不如其貌優雅，是更加瘋狂、特殊，無意間我們留存下這份光線。無意間，只是循著觀測計劃的安排，我們抓到渺小的機會，是運氣，讓我們對鹿林與星空牽上更深一層的羈絆。

不如其名超新星並非新的星，而是一直存在於比它光彩的世界當中隱沒。然而星等銳減，亮度暴增，竭盡所能的閃耀，或許是最後掙扎但它做到了，讓世人看見，在資料庫上畫下深刻的一筆，這好像我們一樣，原本安靜的生活被打破，突然間接到來自各報記者的電話詢問、採訪，瞬時一躍上報，成了歷史紀錄其中的小小版面，發光發熱一時，連著激發周圍環境物質，儘管如今已黯淡，還是有殘骸、有遺跡，溫度並未褪去。餘溫尚存，因超新星而沸騰的心情伴著我們，繼續探索無際的天外，想要遇見更多可能性，益加堅定這條通往天文的未來之路。

懷　恩

回憶隨著流逝的時間被逐漸拉長，切割成細碎的片段，形成一種短暫卻深刻的駐留，記得那躍過天際的流星、獵戶排列的腰帶、如本壘板一樣稜角分明的御夫……。鹿林天文臺帶給我們的感動很多，但感謝，更多。更要謝謝隨行的師長，以及天文臺全體的人員。當我們沉浸在星空之美時，他們在一旁默默的照看，不厭其煩的講解、不時提供協助，讓我們在觀測時能快速就上手。每個人都很熱情、都很有耐心，沒有因為我們只是一介年少輕狂的高中生，而有差別待遇。

我們都會記得，那天山上很是寒冷，但鹿林天文臺的氛圍是溫暖人心的。

林郁梅：臺北市立第一女子高級中學 地科老師
陳心平、廖乙馨、許苡蕾、 蔡欣儒、許雅婷、王蕾婷、沈庭：就讀於臺北市立第一女子高級中學
陳麒瑞：就讀於臺北市立建國高級中學

鄧雨賢影音展開幕暨鄧雨賢小行星頒贈

2013年07月22日

列印　字級：小中大　RSS

中央大學校長周景揚（左2）頒贈小行星與鄧仁侃（左1）邱鏡淳（右2）。（記者彭瑞蘭／攝影）

【記者彭瑞蘭／新竹報導】台灣歌謠之父鄧雨賢，孕育出「四・月・望・雨」創作曲，今年由客委會補助、奇美文化基金會董事長許文龍贊助及國立中央大學頒贈鄧雨賢小行星模型，20日在竹北市新瓦屋客家文化保存區、建置「鄧雨賢影音展」呈現，許文龍帶領自家樂團蒞臨，爲「鄧雨賢影音館」擴建揭序。

縣長邱鏡淳表示：感謝許董事長贊助，捐贈17世紀「街頭風琴」演奏台灣歌謠。親手雕塑鄧雨賢銅像，分別放置於芎林鄉鄧雨賢音樂紀念公園，新瓦屋客家文化保存區。

許文龍賀「鄧雨賢影音展」開幕，以曼陀鈴與小提琴演奏「四、月、望、雨」（四季紅、月夜愁、望春風、雨夜花）。他說：小小的村莊裡，有一位年輕人留下了不起的創作，鄧雨賢爲文化有貢獻，讓人永遠懷念著。人生有限要做有意義的事，讓鄧雨賢歌謠繼續傳唱是有意義的事。

鄧仁侃說：「您雕塑了我的父親，

奇美創辦人許文龍雕塑鄧雨賢銅像。（記者彭瑞蘭／攝影）

我很謝謝您，我很想抱抱您」。許董立刻趨前擁抱他，現場爆出掌聲很溫馨。

鄧雨賢小行星的發現，源自中央大學鹿林巡天計畫（Lulin Sky Survey，簡稱 LUSS）。由中央大學天文所觀測員林啓生和廣州中山大學葉泉志於鹿林天文台所共同發現。國立中央大學爲感念鄧雨賢對台灣民謠發展之貢獻，特將2006年10月15日所發現的編號 255989小行星，經國際天文學聯合會(IAU/CSBN)通過，正式命名爲「鄧雨賢 Dengyushian」，作曲家在歌詞意境中，尋求靈感與創作，賦予歌曲豐富的生命力，一如天文學家致力追尋新的天文知識，探尋宇宙萬物的起源一般，充滿創造力和想像力。而小行星的命名，正是連結天地之間的重要橋樑，代表天人合一，宇宙永恆的追思和紀念。 **(170)**

蘋果日報南投報導

感念助建天文台　中大將小行星名為布農

http://www.appledaily.com.tw/realtimenews/article/new/20131204/303379/

2013 年 12 月 04 日 14:29

【高堂堯／南投報導】中央大學天文觀測員楊庭彰、葉泉志於 7 年前，在玉山鹿林天文台發現一顆小行星，中大特以鄰近的原住民族「布農」命名，經過國際天文學聯合會多年審查認證，今年正式命名為「Bunun 布農」，國際永久編號編號 268669；玉管處和中大天文所今天上午在玉管處水里遊客中心，舉辦「布農小行星」發表會。

鹿林天文台站長林宏欽表示，小行星位於火星和木星間，體積約 1 座 2000 米高山、公轉太陽一周超過 5 年，中大為了感念布農族人當年鼎力協助興建天文台的恩情，因此命名為「布農」；位在塔塔加地區的鹿林天文台，擁有目前全國最大口徑(1 米)的天文望遠鏡，從 2006 至 2009 年間執行「鹿林巡天計畫」時發現近 800 顆小行星，除了布農小行星，還包括同年發現的鄒族小行星、6 年前發現的「玉山小行星」，成果豐碩。

玉管處表示，小行星以「Bunun 布農」命名，具有歷史意義與地緣關係，今天也邀請信義鄉久美國小、人和國小布農學童演出踢踏舞和話劇，表示對布農小行星的歡迎和感謝。

【更多新聞請看《蘋果跑跳碰》粉絲團】

布農族學童載歌載舞，歡迎與自己同名的小行星。高堂堯攝

左圖：布農族學童製作「布農小行星」道具，演出話劇。高堂堯攝
右圖：長周景揚(右)致贈布農小行星紀念牌給玉管處處長游登良。高堂堯攝


Graduate Institute of Astronomy, NCU
國立中央大學天文研究所

國立中央大學

布農族小行星
268669 Bunun

Epoch = 2456400.5 (2013-Apr-18.0)
e = 0.1849307 i = 10.51931 deg peri = 356.10170 deg
node = 179.08851 deg M = 128.36875 deg n = 0.18761026 deg/d
q = 2.4631613 AU a = 3.0220269 AU Q = 3.5808925 AU
period = 5.25 yr TP = 2011-Jun-03.76903100 (2455716.2690310 JED)

(268669) Bunun = 2006 FA
Discovered 2006 Mar. 18 by T.-C. Yang and Q.-z. Ye at Lulin.
The Bunun tribe is a native tribe of Taiwan. Its 50000 members are distributed mainly in Namasia Township of Kaohsiung County, Haiduang Township of Taitung County, and Nantou County. (M.P.C. 83584)

左圖：布農小行星紀念牌。高堂堯攝

右圖：鹿林天文台站長林宏欽手捧小行星紀念牌，向布農族人致謝。高堂堯攝

布農學童與參與來賓一起慶祝布農小行星誕生。高堂堯攝

台灣中央大學拍攝到嫦娥三號火箭脫落

http://www.CRNTT.com 2013-12-03 00:47:49

長征三乙火箭搭載嫦娥三號探測器，發射升空後，火箭推進器墜落台灣東部，被台灣中央大學拍攝到火光亮點。(照片:台灣中央大學天文所專任助理張永欣提供)

中評社桃園12月3日電(記者 黃文杰)“嫦娥三號”探測器在西昌衛星發射中心於12月2日凌晨1時30分由長征三乙火箭搭載發射升空，台灣方面也高度密切注意後續發展，台灣中央大學天文所2日凌晨，也同步成功拍攝到火箭推進器，墜落台灣東部外海瞬間畫面。

拍攝到火箭推推進器墜落瞬間火光，是台灣中央大學天文所專任助理張永欣，他特別留意大陸這次發射“嫦娥三號”相關報道，算準時間與方位，在桃園中壢雙連坡附近，單純利用廣角數位相機，成功捕捉瞬間畫面。

從張永欣提供的動態照片，可以看到拍攝時間是在12月2日凌晨01點39分59秒到01點40分59秒，火箭推進器墜落地表，瞬間高溫引燃火花爆開。

為了怕漏失畫面，張永欣也透過汽車行車紀錄器，選定時間，算準方位，也拍攝瞬間火花，不過畫質比較不清晰，只有一點亮點，不像數位相機局部放大，可以看到爆開的火花。

張永欣說，他並非整夜沒睡覺，徹夜守候拍火箭推進器墜海，只是透過定時器，讓數位相機每隔幾秒連拍數張，隔天再仔細檢查拍攝畫面，成功拍到大陸長征三乙火箭墜海，也覺得很高興。

他解釋，當初“嫦娥二號”發射後，火箭推進器也墜落在台灣東部外海，當時瞬間引爆火花，令好多人驚訝，這次站在台灣西部，往東邊拍攝還能拍到亮點，主要還是夜晚冷度夠，空氣沒有汙染，視線佳。

【 第1頁 第2頁 第3頁 第4頁 第5頁 第6頁 】 下一頁 >>

分享到

【CNML格式】【大 中 小】【打 印】

相關新聞：

- 日媒：嫦娥三號彰顯中國向宇宙大國邁步 (2013-12-02 15:59:55)
- 長三乙火箭托舉嫦娥三號穿越中國史上最窄窗口 (2013-12-02 11:58:49)
- 評論：開啟中國航天新征程 (2013-12-02 10:13:16)
- 66米大口徑“順風耳”助力中國“嫦娥”探月 (2013-12-02 09:58:26)
- 嫦娥三號飛天　海外媒體“亮眼”解讀 (2013-12-02 09:20:15)
- 嫦娥三號攜“玉兔”發射升空（組圖） (2013-12-02 09:02:57)
- 氣象條件適合“嫦娥三號”如期發射 (2013-12-01 15:53:50)
- “嫦娥三號”發射進入最後準備階 (2013-12-01 15:27:12)
- 嫦娥三號的新使命、新挑戰、新看點 (2013-12-01 12:20:13)
- 總設計師解讀“嫦娥三號”探測器十大特點 (2013-11-30 15:11:56)

劃過天際的台灣彗星

文／圖 鹿林天文台台長林宏欽、觀測員林啓生

彗星，古稱掃帚星，向來是以發現者命名，而台灣天文界百年來發現的第一顆彗星，名叫「鹿林」。

位於桃園縣中壢市的鹿林天文台，與玉山主峰遙望，傳說是群鹿如林的地方，不僅是台灣最高的天文台，也是國內天文學術的研究重鎮。這個國際上少數「沒有路」的天文台，規模設備雖小，卻有全世界最好的觀測優勢。

2007年7月12日，經過國際天文學聯合會的小行星中心確認後，首次由台灣本土發現、編號C/2007 N3的「鹿林彗星」正式誕生。根據軌道計算，這顆台灣彗星位置在木星與土星之間，距離地球約8.25億公里，將在2009年2月24日最接近地球，由於它不像哈雷慧星具週期性的軌道，錯過至少要等200年以後。我們也發現台灣首顆「阿波羅型近地小行星」，編號2007NL1。自從2002年發現第一顆小行星起，迄今累計近400顆，成爲亞洲發現小行星最活躍的地方；其中有6顆已正式取得編號並擁有命名權，兩顆已命名爲「中大」與「鹿林」。

天文觀測員常常得前往海拔2,800多公尺的天文台工作，爲了發現新天體，日夜顛倒更是家常便飯，所以稱我們是「夜貓族」，一點也不爲過；由於彗星是屬於動態的行星，必須在不同時間、不同座標加以觀測，詳加比對觀測圖上的差異，所以從事「追星」不但像是大海撈針，還要跟全世界競爭，因此發現彗星的機率更是萬中選一。

2010年，鹿林天文台將完成二米望遠鏡的設置，晉升全球中大型望遠鏡之列，加上與夏威夷大學策略結盟所推動的下一世代巡天—泛星計畫（Pan-SATRRS），全面取代現今所有的巡天系統。期望有了精良的設備後，能看得更多、更遠，培養出更多的本土天文學者，在全球的天文學術研究上，讓台灣發光，開創台灣未來的天文研究新領域。

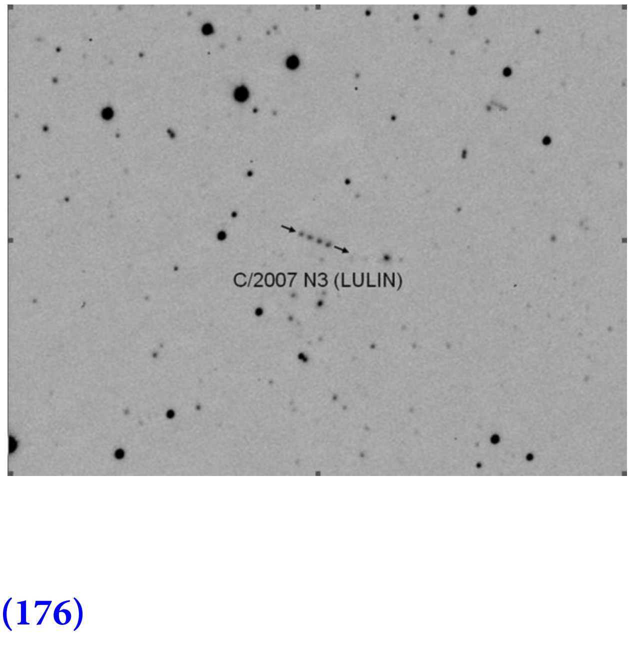

台灣首次以本土望遠鏡所發現的第一顆彗星，編號C/2007 N3的「鹿林彗星」。圖爲2007年7月18日所拍攝彗星於30分鐘內在星空中移動的軌道情形。（陳婷琬攝）▶

◀現設置於鹿林天文台的1公尺望遠鏡，爲台灣目前最大的天文望遠鏡，簡稱LOT。口徑1公尺，焦距8公尺，目前裝置的CCD相機所能觀測的視野是月亮的3分之1。

鹿林天文台的工作人員在自家門口就能看到台灣第一高峰—玉山，可以說是台灣最幸福的一群人。圖爲玉山冬季時節景象。▶

◀位於台灣地勢最高的鹿林天文台，不僅是國內天文學術的研究重鎭，更是全世界少數極佳的觀測地點。

發現台灣「鹿林彗星」的最大功臣—40公分望遠鏡。口徑40公分，集光力比肉眼強上3000多倍，加上搭配的高感度CCD相機，曝光後是肉眼看到星星的百萬分之一暗。▶

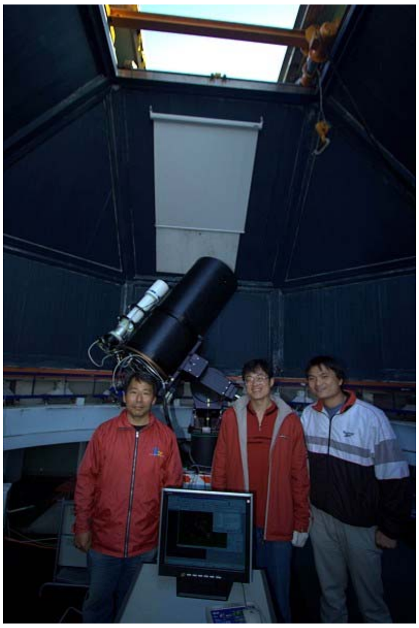

◀台灣慧星的發現者—林啓生先生（左邊），與台灣天文界重要推手鹿林天文台台長林宏欽先生（中間者）。

阿扁推薦：

鹿林天文台從無到有，在有限的資源及條件下，創下發現首顆台灣彗星及近地小行星的成就，充分發揮了「以小搏大」的驚人毅力，不僅帶領著台灣的天文學術領域向前跨進一大步，寫下台灣天文界的「歷史新頁」，也讓世界見證了「台灣天文觀測的實力」！

尚青指數：青青青青青

本單元長期徵稿，歡迎讀者來稿分享最特別、最感動、也可以是最Kuso的生活故事與體驗，來稿請附上照片，並寄至president@oop.gov.tw，獲刊作品將可獲得精美小禮物！

▲ TOP

發行單位：總統府公共事務室
地　　址：10048 台北市中正區重慶南路一段122號
總　　機：(02)2311-3731
傳　　真：(02)2381-8062
如欲取消訂閱或變更收件郵址，請至訂戶專區

新聞報導

以管窺天探蒼穹　鹿林天文台　寫下里程碑

◎專題報導/記者羅智華

這陣子引發眾多天文迷關注的大事就是中國大陸發射的嫦娥三號探測器，在日前成功登月，不但是繼美、俄之後，第三個實現登月大夢的國家，亦寫下探索月球歷史新頁的里程碑。

事實上，探索宇宙並非現代人的專利，早在千百年前，我們的老祖宗就已經對浩瀚的滿天星斗展現高度好奇心，不但中國許多朝代都曾經對彗星或日、月食等奇特天象具有文字記載，知名詩人屈原更曾在《天問》中寫下「天何所遝？十二焉分？日月安屬？列星安陳？…」等文句，希望一探蒼穹的奧妙。

到了西元 1609 年，義大利科學家伽利略藉由自製的望遠鏡來探索星空，揭開人類利用望遠鏡「以管窺天」的歷史序幕，而伽利略也在這次的天文觀測初體驗中，看見了他以前從未見過的月球表面坑洞與浩瀚銀河，不但令他驚奇不已，亦帶動日後的天文科學發展。

而說到天文觀測，就不能不提到望遠鏡與天文台，回顧望遠鏡的發展史，最早可回溯到西元 1608 年，當時是由荷籍商人立普塞發明全球首架折射式望遠鏡。1668 年，知名科學家牛頓更進一步發明世界上首支反射式面鏡望遠鏡，推動天文觀測品質更往前一步。時至今日，拜日新月異的科技之賜，更讓觀測設備推陳出新，我們不但比前人看得更遠更廣，許多先進國家更積極投入天文台的興建，像是在智利海拔達 5000 公尺的高原沙漠中，就正在興建一座目前全球最大的阿塔卡馬陣列天文台（Atacama LargeMillimeter-submillimeter Array）。

當然，台灣也沒有在這段天文發展史中缺席，早在 1990 年代，中央大學就已在鹿林山開始籌設搭建一米望遠鏡的天文台，為國內的天文研究邁出一大步。中央大學天文所所長高仲明表示，中大天文所是國內最早成立的天文研究與教學單位，在天文台落成後的 2003 至 2013 這十年間，可說是鹿林天文台的「黃金十年」，不但陸續發表 80 篇的 SCI 科學論文，更發現了大約 800 顆的小行星，名列全球前 50 大，2007 年時亦寫下台灣首次發現彗星的新紀錄，像是「鹿林彗星」就是台灣首度發現的彗星，因此天文台特別以鹿林兩字來命名，以彰顯其意義。

不過這些研究成果並非憑空而來，而是一連串的心血結晶集結而成。鹿林天文台台長林宏欽表示，當初光是選擇天文台位置就費了好一番功夫，從 1989 年開始啟動選址，花了三年時間四處尋覓，在團隊長思深考下，最後決定落腳於鹿林山上，選在海拔高達 2862 公尺的地方搭建天文台，過程中甚至得用流籠方式運送建材上高山，才得以完成天文台的一磚一瓦，而這也是東北亞目前海拔最高的天文台。

推動天文教育　引領學童觀測初體驗

看到這裡，讀者可能會納悶為何要把天文台蓋在這麼高的位置呢？林宏欽解釋，觀測星空最怕的就是看不清楚，高海拔除可避開低層大氣的擾動外，還可隔絕空氣汙染與霾害，因此全世界天文台大都是蓋在高山上。

除了高度是首要條件外，氣候也是影響天文研究的重要因子，晴天率必須要夠高才適合觀測，林宏欽說，以台灣氣候來說，北部容易受到冬天東北季風影響，南部則是夏天的西南氣流，因此天文台特別選在靠近中部的鹿林山，降低氣候的影響，像鹿林天文台一年中就有一百八十個適合夜晚進行觀測的良好晴天。

林宏欽表示，鹿林天文台的望遠鏡直徑達一米，多年來除了發現數量眾多的小行星外，亦與歐美等國攜手合作，投入泛星計畫、中美掩星計畫等跨國研究，藉此發揮團結力量大成效。明年起還將進一步打造直徑達兩米的大型天文望遠鏡，其觀測效率為一米望遠鏡的四倍，預計於 2018 年完工並開光，屆時將可推動台灣的天文研究更上層樓。

而不只投入天文觀測，鹿林天文台近年也積極推動天文教育，經常與鄰近的原住民中小學進行戶外教學，許多學生更把參觀鹿林天文台視為畢業旅行的夢想地點。

對此，教育部長蔣偉寧也樂見其成。他表示，隨著十二年國教明年上路，如何發展與培養學生多元興趣與能力亦是教育目標之一，以天文教育來說，就是很重要的科普教育，他自己也很鼓勵家長和校方有機會應該多讓孩子走出教室，親近國內的天文館或科教館等科普場域，讓學童可以透過親身體驗與親眼觀察來開啟天文觀測初體驗的第一步，從中培養出對天文科學研究的興趣與熱情。

(原文來源網址：http://www.merit-times.com/NewsPage.aspx?unid=330917)

原文轉載自【2013-12-20/人間福報/13 版/遇見科學】

鹿林天文台 6 年前新小行星　命名「布農」

【No/戈論/巴浩】

繼鄒族小行星之後，又有一顆以布農族為名的小行星在宇宙的眾多天體中運行，人和國小校長伍福義也代表布農族人來感謝中央大學以及玉管處等單位，願意將他們發現到的小行星，命名為「布農」，這對布農族來說確是意義非凡。

2006 年中央大學以及鹿林天文台的巡天計畫，發現了將近八百粒的小行星，其中包括已經發表過的鄒族小行星以及玉山小行星，後來為了感謝布農族人過去熱情協助興建天文台的功勞，決定將其中編號 268669 號星，正式命名為「布農小行星」。為了要共同慶祝「布農小行星」被的發表的喜悅，人和國小的學生們也特別表演行動劇來歡迎布農小行星。

原文轉載自【2013-12-05/原視新聞網】

台灣/鹿林天文台　鄰近學校畢旅首選

http://www.cdnews.com.tw　2013-12-06 16:06:50

宋其佳/整理

位於嘉義、南投交界的中央大學鹿林天文台，近年積極和周邊中小學合作，引進學習資源，天文台並成為學生畢業旅行的首選。

根據中央社 6 日報導指出，鹿林天文台位於嘉義縣阿里山鄉和南投縣信義鄉的交界處，海拔 2862 公尺，主要由中央大學天文所管理。天文台目前設有 1 公尺及 40 公分口徑望遠鏡，2 公尺的望遠鏡則預計於明年開始興建。

除了科學研究，鹿林天文台近年來積極「敦親睦鄰」，和周遭的原住民部落中小學互動密切。中央大學協助自北部引進音樂師資，到山美國小、阿里山國中、達邦國小教學鋼琴，彌補偏鄉教學資源不足。

參與這些計畫的音樂老師許家馨表示，平時居住在平地，很難體會山上生活的艱難，一下雨就可能山崩路斷。不過看到孩子逐漸對音樂產生興趣，再辛苦也都值得。

除此之外，鹿林天文台也協助周邊中小學進行天文教學，近年也成為畢業旅行的首選地點。天文台指出，興建天文台至今，當地原住民的協助功不可沒，現在必須加緊回饋。【中央網路報】

原文轉載自【2013-12-06/中央日報網路報-走遍台灣】

鹿林黃金 10 年　2 米望遠鏡明年開工

時間：2013/12/6 19:08　撰稿‧編輯：江昭倫　　新聞引據：　採訪

教育部長蔣偉寧今天(6 日)前往中央大學鹿林天文台視察，聽取央大天文研究所未來發展計畫。央大表示，明年 2 米望遠鏡可望取得建照開工，未來啟用後，對於台灣本土的光學天文觀測、拓展國際合作能力、天文儀器軟體開發，以及專業人才的養成，將有莫大助益。

中央大學天文研究所是台灣最早成立的天文研究與教學單位，鹿林天文台的建置更象徵台灣天文研究邁開大步伐。自 2003 啟用至今，可說是「鹿林黃金 10 年」，共發表約 80 篇 SCI 科學論文，小行星發現數約 800 顆，擠入全球排名 50 大，2007 年更創造台灣首度發現彗星紀錄，成果豐碩。

央大天文所所長高仲明指出，目前鹿林台建置有 7 個望遠鏡，直徑最多的是 1 米望遠鏡；至於建置中的 2 米望遠鏡，可望明年取得建照開工，光是儀器與房舍總經 費就將近新台幣 3 億。2018 年正式啟用後，對於台灣天文研究將是一

個新的里程碑，有助提升台灣本土光學天文觀測能力，對於台灣天文人才培養也有很大的幫 助。高仲明說：『(原音)這個是 2 米望遠鏡的計畫，大概可以主要是提升我們台灣可見光部份的觀測能力；我們這個站在東亞區也算數一數二的高啦。』

教育部長蔣偉寧表示，天文教育是很重要的基礎教育，鼓勵家長和學校應該多帶孩子親近天文館與科博館，他也會指示教育部所屬館所單位盡量開放，幫助小朋友從小培養對天文科學的興趣。

此則報導的來源網址：http://news.rti.org.tw/index_newsContent.aspx?nid=469443
原文轉載自【2013-12-06/中央廣播電臺新聞頻道】

鹿林天文台　鄰近學校畢旅首選

中央社 － 2013 年 12 月 6 日 下午 3:28（中央社記者陳至中嘉義 6 日電）位於嘉義、南投交界的中央大學鹿林天文台，近年積極和周邊中小學合作，引進學習資源，天文台並成為學生畢業旅行的首選。

鹿林天文台位於嘉義縣阿里山鄉和南投縣信義鄉的交界處，海拔 2862 公尺，主要由中央大學天文所管理。天文台目前設有 1 公尺及 40 公分口徑望遠鏡，2 公尺的望遠鏡則預計於明年開始興建。

除了科學研究，鹿林天文台近年來積極「敦親睦鄰」，和周遭的原住民部落中小學互動密切。中央大學協助自北部引進音樂師資，到山美國小、阿里山國中、達邦國小教學鋼琴，彌補偏鄉教學資源不足。

參與這些計畫的音樂老師許家馨表示，平時居住在平地，很難體會山上生活的艱難，一下雨就可能山崩路斷。不過看到孩子逐漸對音樂產生興趣，再辛苦也都值得。

除此之外，鹿林天文台也協助周邊中小學進行天文教學，近年也成為畢業旅行的首選地點。天文台指出，興建天文台至今，當地原住民的協助功不可沒，現在必須加緊回饋。1021206

原文轉載自【2013-12-06/中央社】

鹿林天文台全台最高　冬季適看獵戶座

東森新聞-2013 年 12 月 06 日 下午 14:06
位於玉山塔塔加的鹿林天文台，擁有全台最高最大的天文望遠鏡，更因為這裡鮮少光害，能觀測到美麗的星海，東森氣象主播王淑麗這次就帶大家去那趴趴 go，欣賞夜晚的星軌，白天也要帶大家來看看，這宛如人間仙境的塔塔加美景。
原文轉載自【2013-12-06/東森新聞首頁 ＞ 影音 ＞ 東森新聞 ＞ 生活】

鹿林天文台 2 米望遠鏡　明年開工

【記者王志誠／南投報導】

教育部蔣偉寧部長昨（六）日來到鹿林山天文台的建置，象徵台灣天文研究邁開大步伐，從民國九十二年迄今，積蓄十年的能量，發表了約八十篇 SCI 科學論文， 小行星發現數約八〇〇顆，排名全球前五〇大，更於民國九十六年創造台灣首度發現彗星的紀錄，明年兩米望遠鏡也有機會取得建照開工，繼續開拓天文研究領域的 新頁。

目前中央大學天文研究所是台灣最早成立之天文研究與教學單位，天文教育與研究工作並重，並與美、德、英等國家研究機構共同參與泛星計畫，極受國際學界矚目，近期還榮登國際頂尖期刊《自然（Nature）》。

關於備受矚目的兩米望遠鏡，所長高仲明提及，預計於明年取得兩米望遠鏡天文台的建照與開工，兩米望遠鏡計畫為中央大學「發展國際一流大學及頂尖研究中心計畫」的重點項目，也將成東亞最大天文望遠鏡之一。

這座成立近十年的鹿林天文台，因為海拔高、緯度低、接近赤道，可以觀測到較寬廣的範圍，尤其沿著夏威夷的大天文台，向西到台灣，中間沒有任何觀測站，因此，鹿林天文台成為國際上重要的觀測點。

鹿林天文台在鹿林前山，橫跨南投縣和嘉義縣，海拔二八六二公尺，位於逆溫層之上，光害和塵害少，中央大學強調，這是目前台灣最高的天文台，由於接近赤道， 可以觀測到日本、韓國等國家，觀測不到的南半球天體，中央大學天文所所長黃崇源說，靠著鹿林天文台的觀測系統，去年首次由台灣本土的望遠鏡發現第一顆彗星 「鹿林彗星」，並從二〇〇二年起到現在，已發現將近四〇〇顆小行星，其中有七顆取得正式編號，擁有命名權，當中已命名的三顆小行星分別叫「鹿林」、「中 大」、「嘉義」。

原文轉載自【2013-12-07/台灣新生報/6 版/綜合新聞】

鹿林山天文台　兩米望遠鏡明年開工

鹿林山天文台為台灣天文研究的重要據點，明年即將取得兩米望遠鏡的建照開工，成為東亞最大天文望遠鏡之一，對於臺灣本土的光學天文觀測能力及專業天文人才的養成等，產生極大效益。

中央大學天文研究所是臺灣最早成立的天文研究與教學單位，天文教育與研究工作並重，與美、德、英等國家研究機構共同參與泛星計畫，極受國際學界矚目，

近期還榮登國際頂尖期刊《自然（Nature）》。

國立中央大學天文所所長高仲明表示，從民國 92 年到現在，鹿林山天文台共發表了約 80 篇 SCI 科學論文，小行星發現數約 800 顆，排名全球前 50 大，更在民國 96 年創造臺灣首度發現鹿林彗星的紀錄。

關於備受矚目的兩米望遠鏡，高仲明所長表示，預計在明年取得兩米望遠鏡天文台的建照與開工，兩米望遠鏡計畫為中央大學「發展國際一流大學及頂尖研究中心計畫」的重點項目，將成為東亞最大的天文望遠鏡之一。

高仲明所長也表示，希望未來能推動鹿林成為國家級的研究中心，促進臺灣未來天文研究的發展。
(2013-12-06 19:11:00 周菊芳)

原文轉載自【2013-12-06/國立教育廣播電台 】

「布農小行星」發表及頒贈會　天上又多了一顆小行星

NOWnews － 2013 年 12 月 4 日 下午 8:46

記者吳素珍／南投報導

玉山國家公園管理處與中央大學天文所，於 4 日在水里遊客中心一樓視聽室，共同辦理「布農小行星」發表及頒贈會活動，久美國小學童的布農歌、舞表演，為活動揭開序幕，來自各界貴賓參與盛會。

玉山國家公園管理處處長游登良，感謝參與「布農小行星」發表及頒贈會活動的所有貴賓之盛情，他表示，很驚喜天上又多了一顆「布農小行星」。也感謝中央大學 校長周景揚選在玉管處辦理這項活動，讓園區周邊的小朋友有更多的機會接觸。玉山國家公園區周邊布農族部落久美國小及人和國小為此次活動表演踢踏舞及話劇演 出，展現原住民部落學童多才多藝的表演，期望藉由參予此次活動表演也認識、學習天文知識，以達到推廣天文教育之目的。

中央大學校長周景 揚、南投縣代理縣長陳志清、台灣聯合大學校長、人和國小校長等貴賓一一致意。玉管處指出，中央大學天文所是國內少數幾所大學擁有天文系所的學校，在塔塔加 地區的鹿林天文台擁有目前全台最大口徑之望遠鏡，設立以來除主要從事天文觀測等研究外，也極力推廣相關天文環境教育活動並參與不少國際間的合作計畫，對於 學術研究上也有很大的貢獻。

96 年中央大學天文所發現 185546 號小行星，首顆以台灣高山命名的小行星-玉山，正式發表命名。而在 2006 年 3 月 1 日由楊庭彰與葉泉志兩位學者於鹿林

天文台發現，編號 268669 號小行星，特別以塔塔加地區鄰近的原住民族「布農」來命名，並經國際天文 學聯合會多年的審查認證，於 2013 年 4 月 25 日正式通過命名為「Bunun 布農」，具有其歷史意義與地緣關係。

中央大學天文所為布農小 行星做介紹時指出，布農族 Bunun，台灣原住民的一個族群，人口約有 5 萬餘人，分佈於中央山脈海拔一千至二千公尺的山區，廣及高雄市那瑪夏區、台東縣海 端鄉和南投縣境。布農族祭儀中所唱的「祈禱小米豐收歌」，以「八部合音」聞名於世，為世界音樂之瑰寶。

玉管處成立 28 年，在生態保育上， 不僅與相關學術單位合作，致力推動相關保育與環境教育；中央大學天文所在推廣天文教育上也是不遺餘力，不僅結合學校，合作推廣天文與科學教育，也配合舉辦 各種天文、生態性展覽，讓台灣的天文及生態性教育向下紮根。該處期望雙方在相關的領域上能互相協助與支援，並在寓教於樂的氛圍下，能達到國家公園以保育、 研究、育樂的目標。

原文轉載自【2013-12-04/NOWnews】

布農小行星發表　推廣天文教育

作者：吳素珍 轉貼自：本站原創 更新時間：2013/12/5 文章錄入：commons

布農小行星發表 推廣天文教育

【本報記者吳素珍水里報導】玉山國家公園管理處與中央大學天文所，於 4 日在水里遊客中心一樓視聽室，共同辦理「布農小行星」發表及頒贈會活動，久美國小學童的布農歌、舞表演，為活動揭開序幕，來自各界貴賓參與盛會。

玉山國家公園管理處處長游登良，感謝參與「布農小行星」發表及頒贈會活動的所有貴賓之盛情，他表示，很驚喜天上又多了一顆「布農小行星」。也感謝中央大學 校長周景揚選在玉管處辦理這項活動，讓園區周邊的小朋友有更多的機會接觸。玉山國家公園區周邊布農族部落久美國小及人和國小為此次活動表演踢踏舞及話劇演 出，展現原住民部落學童多才多藝的表演，期望藉由參予此次活動表演也認識、學習天文知識，以達到推廣天文教育之目的。

中央大學校長周景 揚、南投縣代理縣長陳志清、台灣聯合大學校長、人和國小校長等貴賓一一致意。玉管處指出，中央大學天文所是國內少數幾所大學擁有天文系所的學校，在塔塔加 地區的鹿林天文台擁有目前全台最大口徑之望遠鏡，設立以來除主要從事天文觀測等研究外，也極力推廣相關天文環境教育活動並參與不少國際間的合作計畫，對學 術研究上也有很大的貢獻。

96 年中央大學天文所發現 185546 號小行星，首顆以台灣高山命名的小行星-玉山，正式發表命名。而在 2006 年 3 月 1 日由楊庭彰與葉泉志兩位學者於鹿林

天文台發現，編號 268669 號小行星，特別以塔塔加地區鄰近的原住民族「布農」來命名，並經國際天文學聯合會多年的審查認證，於 2013 年 4 月 25 日正式通過命名為「Bunun 布農」，具有其歷史意義與地緣關係。

中央大學天文所為布農小行星做介紹時指出，布農族 Bunun，台灣原住民的一個族群，人口約有 5 萬餘人，分佈於中央山脈海拔一千至二千公尺的山區，廣及高雄市那瑪夏區、台東縣海端鄉和南投縣境。布農族祭儀中所唱的「祈禱小米豐收歌」，以「八部合音」聞名於世，為世界音樂之瑰寶。

玉管處成立 28 年，在生態保育上，不僅與相關學術單位合作，致力推動相關保育與環境教育；中央大學天文所在推廣天文教育上也是不遺餘力，不僅結合學校，合作推廣天文與科學教育，也配合舉辦各種天文、生態性展覽，讓台灣的天文及生態性教育向下紮根。該處期望雙方在相關的領域上能互相協助與支援，並在寓教於樂的氛圍下，能達到國家公園以保育、研究、育樂的目標。

原文轉載自【2013-12-05/民眾日報全球資訊網 報導 大台中新聞 南投新聞】

「布農（Bunun）族小行星」躍上天際

【大紀元 2013 年 12 月 04 日訊】(大紀元記者徐乃義台灣桃園報導)《看見台灣》紀錄片中，布農族小朋友在玉山高唱，天籟美聲讓世界「聽見台灣」，布農族是最能適應山地生活的高山子民，中央大學為感念布農族在鹿林天文台草創時期對基礎建設之貢獻，特將 2006 年 3 月 18 日發現的 268669 號小行星，經國際天文學聯合會(IAU/CSBN)通過，正式命名為 Bunun （布農），象徵天人合一、宇宙永恆！ 「布農族小行星」是 2006 年 3 月 18 日由中央大學天文所楊庭彰與廣州中山大學葉泉志同學於鹿林天文台所共同發現，國際永久編號 268669，位於火星和木星之間的小行星帶。

慶祝布農族小行星的發現與命名，玉山國家公園管理處與國立中央大學共同舉辦布農族小行星頒贈儀式。南投縣久美國小以「踢出希望、踏上未來」作開場表演，天真無邪的孩童身著傳統服飾，傳唱著布農族的天籟美聲，以及精彩的踢踏舞表演扣人心弦；人和國小則以話劇演出，訴說一個布農婦女被敵人擄走的傳說，地上做的樹枝記號被土石流沖走，最後靠著天上星星的指引，才順利找到回家的路。

中央大學校長周景揚強調，玉山國家公園為台灣天文研究發展的搖籃，其海拔高、緯度低、接近赤道，空氣清新無污染，非常適合天文觀測。中央大學經過長期間選址，於民國 78 年開始籌設鹿林天文台，海拔 2,862 公尺的鹿林前山，沒水、沒電更沒有路，多虧布農族勇士一步一腳印將鐵皮、建材等揹上山，打下重要的建設基礎，如今成為亞洲最重要的天文觀測據點。因此將發現的小行星

命名為 Bunun （布農），以表達飲水思源，感念之意。

中央大學天文所所長高仲明表示，鹿林天文台的觀測工作，主要應用小型望遠鏡和台灣觀測條件的優勢。最近《看見台灣》獲得廣大回響，布農族孩童在玉山高歌，讓世界不僅看見台灣，更聽見台灣，如今布農族小行星能躍上天際，永垂不朽，更加相得益彰。

（責任編輯：呂美琪）

原文轉載自【2013-12-04/大紀元時報首頁 > 新聞 > 台灣地方新聞 > 國內要聞 > 正文 】

第一個原民命名　布農小行星正式發表

【大紀元2013年12月04日訊】（大紀元記者林萌騫台灣南投報導）民國95年於玉山國家公園鹿林天文台發現的編號268669號小行星，經過國際天文學聯合會多年的審查認證後，正式命名為「Bunun 布農」，4日由玉管處和中央大學共同舉行「布農小行星」發表會；布農族久美和人和國小學童也在玉管處以歌舞歡慶。

「布農小行星」是鹿林尋天計畫3年中所發現的800多顆小行星之一，大小相當於一座2千公尺的高山，繞行太陽一周約5年，2006年發現之後經過這幾年的確認軌道，才在4日正式發表命名；鹿林天文台長林宏欽認為小行星本身沒有生命，是「布農」的名字賦予了他的生命。

玉管處處長游登良表示，中央大學天文所在塔塔加的鹿林天文台，擁有全國最大的天文望遠鏡，由楊庭彰和葉泉志利用該台設備所發現編號268669號的小行星，是位於火星跟木星之間，特別以「Bunun 布農」命名，具有歷史意義與地緣關係。

塔塔加是全台最適合觀星及天文研究的地區，鹿林天文台更是國內天文研究的搖籃，中央大學校長周景揚指出，校方正在建構更大的2米口徑天文望遠鏡，希望未來能藉由觀星將科普往下紮根，啟發孩子對科學教育的熱情和認知。

「布農小行星」是第一個以原住民族命名的行星，具有非凡的意義，南投縣代理縣長陳志清認為，和布農族喜歡分享的意義非常契合，希望藉由中央大學天文團隊發現的這顆小行星與大家共享，讓大家看到布農族的好客和熱情。

（責任編輯：羅令尹）

原文轉載自【2013-12-04/大紀元時報首頁 ＞ 新聞 ＞ 台灣地方新聞 ＞ 文教工商 ＞ 正文 】

感念原民 小行星命名「布農」

【高堂堯／南投報導】中央大學鹿林天文台人員七年前發現一顆小行星，為感念布農族人協助興建天文台、搭救工作人員的恩情，特命名為「Bunun（布農小行星）」，今年獲國際天文學聯合會審查認證，成為第二顆以台灣原住民族為名的太陽系星體。

小行星位於火星和木星間，距地球約二點二億公里，體積約一座二千公尺高山、公轉太陽一周需時五點二五年。這是繼「鄒族小行星」後，第二顆以台灣原住民族為名的小行星。

「布農小行星」發表會，邀請信義鄉久美國小、人和國小布農學童演出踢踏舞和話劇。

族人助建天文台

鹿林天文台站長林宏欽指出，天文台十四年前興建時沒水、沒電、沒路，全賴當地布農族勇士扛建材上山，一步一腳印打下建設基礎，成為亞洲重要天文觀測據點；「我自己也被布農族救過一命。」林宏欽笑說，多年前在站內工作時，脊椎受傷無法站立，布農族朋友連夜揹他下山就醫，他一直感念在心。

鹿林天文台小檔案

◆歷史：14 年，1999 年落成啟用

◆地點：南投縣信義鄉和嘉義縣阿里山鄉交界處的鹿林前山，海拔 2862 公尺

◆興建經費：1 億元

◆設備：擁有全國最大口徑 1 米天文望遠鏡，另有 40 公分口徑望遠鏡

◆觀測成果：「鹿林巡天計畫」2006 年至 2009 年間發現近 800 顆小行星，其中 20 顆已獲國際正式編號和命名

資料來源：中央大學

原文轉載自【2013-12-05/蘋果日報/A14 版/地方新聞】

看見布農 小行星以它為名

【廖志晃／南投報導】

國立中央大學鹿林山天文台 95 年發現編號 268669 小行星，特別以原住民「Bunun 布農」命名；經過國際天文學聯合會多年審查認證確定，4 日正式發表，此後，在宇宙間，不僅看見台灣，還看得見布農！

布農小行星發表會，昨天在玉山國家管理處舉行，中央大學校長周景陽、中央大學天文所長高仲明、玉管處長游登良，及代理縣長陳志清、縣議員史清水都到場祝賀。

布農族久美國小學童，以傳統歌舞，結合西方的踢踏舞蹈；人和國小則演出《星星帶我回家》短劇，展現布農族與世界結合、以及擁有布農之星的榮耀。

周景陽指出，鹿林天文台擁有全國最大口徑的天文望遠鏡，從事天文觀測、研究，並參與國際合作計畫；而由學者楊庭彰、葉泉志發現的小行星，以活躍在玉山群峰間的原民族「布農」命名，希望以後出現布農族天文學家。

陳志清表示，「布農」是第一顆以原住民族命名的行星，讓大家看到南投、看到布農，非常難得，也歡迎大家到部落旅遊，體驗布農族人好客熱情。

游登良表示，玉管處與學術單位合作推動環境教育，而中央大學推廣天文與科學教育不遺餘力，希望雙方相互支援，讓天文與生態教育向下扎根。

原文轉載自【2013-12-05/中國時報/A10 版/綜合新聞】

布農小行星　發表會飄原味

95 年間，楊庭彰與葉泉志 2 名學者由中央大學設在塔塔加地區的鹿林天文台，觀測發現編號 268669 號的小行星，經國際天文學聯合會多年審查，確定將以南 投縣信義鄉布農族聚落的地緣關係，命名為「Bunun 布農」小行星，昨日玉管處、南投縣府及中央大學等相關單位在玉管處水里遊客中心舉辦發表會，開心迎接 「布農」小行星的誕生。

中央大學校長周景揚將小行星認證交由玉管處保管後指出，塔塔加地區是全台最適合觀星與星座天文研究的地區，目前他們正在建置 2 米口徑的天文望遠鏡，希望未來能藉由觀星活動，讓學童認識、學習更多的天文科學知識。

（文：記者謝介裕）

原文轉載自【2013-12-05/自由時報/A12 版/生活新聞】

玉山發現小行星命名「布農」

玉山鹿林天文台發現一顆小行星，特別以鄰近的原住民族「布農」命名，玉管處與中央大學天文所 4 日在玉管處水里遊客中心舉辦「布農小行星」發表會。玉管處表示，中央大學天文所在塔塔加地區的鹿林天文台，擁有目前全國最大口徑的天文望遠鏡；楊庭彰與葉泉志兩名學者 95 年在鹿林天文台發現編號 268669 號的小行星，特別以塔塔加地區鄰近的原住民族「布農」來命名，經過國際天文學聯合會多年的審查認證，正式命名為「Bunun 布農」。

中央大學校長周景揚表示，塔塔加地區是全台最適合觀星及座天文研究的地區，鹿林天文台更是國內天文研究的搖籃，目前他們正在建置 2 米口徑的天文望遠鏡，希望未來能藉由觀星活動，將科普往下紮根，讓學童認識、學習天文知識，進而啟發孩子對科學教育的熱情和認知。
(2013-12-04 15:45:28 劉文珍)

原文轉載自【2013-12-04/國立教育廣播電台 】

投布農小行星　發表

記者蔡榮宗/投縣報導

布農小行星發表會昨(四)日上午於水里玉山國家公園管理處遊客中心舉辦，玉管處長游登良主持，中央大學校長周景揚與玉，代理縣長陳志清、縣議員史清水都到場祝賀。

這顆於二〇〇六年由楊庭彰與葉泉志兩名學者在鹿林天文台發現編號二六八六六九號的小行星，以原住民族「布農」命名，經過國際天文學聯合會多年的審查認證，正式定名為「Bunun 布農」。

原文轉載自【2013-12-05/台灣新生報/6 版/綜合新聞】

玉管處舉辦新行星布農命名發表會

【記者林玉芬南投報導】玉山國家管理處遊客中心 4 日舉辦布農小行星發表會，

這顆於2006年由楊庭彰與葉泉志兩名學者於鹿林天文台發現編號268669號的小行星，以原住民族「布農」來命名，經過國際天文學聯合會多年的審查認證，正式命名為「Bunun 布農」。

活動開始由布農部落久美國小學童以原民傳統歌曲吟唱及舞步，結合現代踢踏舞蹈，展現出原民文化傳統與創新融合的精采表演，並邀請到人和國小全校學生合力演 出，以布農族原住民因為布農小行星的協助而返回部落的故事話劇，結合歌曲舞蹈及原民文化等元素，充分展現出原住民學童多才多藝的一面。

代理縣長陳志清表示，很高興能有新的行星在鹿林天文台被發現，並且是第一個以原住民族布農族作為行星命名，能以此與大家共有並分享一顆行星，讓大家看到南投，是相當難得，也期望以布農族人好客熱情的心情，來歡迎更多朋友來原民部落參訪旅遊。

玉管處處長游登良表示，中央大學天文所在塔塔加地區的鹿林天文台，擁有目前全國最大口徑的天文望遠鏡，設立以來除從事天文觀測等研究，也極力推廣天文環境 教育活動，並參與不少國際間的合作計畫，此次編號268669號的小行星，是位於火星跟木星之間，特別以「Bunun 布農」命名，相當具有歷史意義與地緣 關係。

中央大學校長周景揚表示，塔塔加地區是全台最適合觀星及座天文研究的地區，鹿林天文台更是國內天文研究的搖籃，目前他們正在建置2米口徑的天文望遠鏡，希望未來能藉由觀星活動，將科普往下紮根，讓學童認識、學習天文知識，進而啟發孩子對科學教育的熱情和認知。

原文轉載自【2013-12-04/自立晚報 】

台灣/布農小行星發表　原民學童分享

許人元/整理

以台灣原住民布農族命名的一顆小行星「Bunun 布農」，4日在玉山國家公園管理處舉行發表會，邀請布農族學童共同見證分享。

中央社4日報導，這顆於2006年由楊庭彰與葉泉志兩名學者在玉山塔塔加地區鹿林天文台發現、編號268669號的小行星，特別以鄰近的原住民族「布農」命名，經過國際天文學聯合會多年的審查認證，正式定名為「Bunun 布農」。

發表會於玉管處水里遊客中心舉行，由中央大學校長周景揚與玉管處長游登良共同主持，南投縣代理縣長陳志清等人到場祝賀。

活動中安排鄰近布農族部落久美國小學童表演原住民歌舞、人和國小學童演出

話劇，融合傳統與創新，同時讓原住民學童了解這項命名的意義，並共同見證歷史的一刻。

游登良說，中央大學天文所設立鹿林天文台以來，除從事天文觀測等研究，也極力推廣天文環境教育活動，並參與不少國際間的合作計畫，這次小行星以「布農」命名，具有人文意義與地緣關係。

周景揚表示，塔塔加地區是全台最適合觀星及進行天文研究的地區，鹿林天文台更是國內天文研究的搖籃，目前正在建置2米口徑的天文望遠鏡，希望未來能藉由觀星活動，將科普往下扎根，讓學童認識、學習天文知識，進而啟發孩子對科學教育的熱情和認知。

陳志清致詞說，很高興有新的小行星在鹿林天文台被發現，並且是第一個以原住民族布農族作為命名，這個分享活動讓大家看到南投，也期望以布農族人好客熱情的心情，歡迎更多朋友到原住民部落參訪旅遊。

中央大學天文所於2007年也發現一顆編號185546號小行星，並首次以台灣高山為名，正式以「玉山」命名發表。 【中央網路報】

原文轉載自【2013-12-04/中央日報網路報-教育藝文】

玉管處中央大學共同發表「布農小行星」

學者多年前在玉山鹿林天文台發現一顆小行星，特別以鄰近的原住民族「布農」命名，並且經過國際天文學聯合會多年的審查認證，正式命名為「Bunun 布農」，玉管處跟中央大學天文所今天在玉管處水里遊客中心，舉辦「布農小行星」發表會，讓民眾認識這顆小行星。

（張文祿報導）

玉山國家公園管理處指出，中央大學天文所是國內少數擁有天文系所的學校，在塔塔加地區的鹿林天文台則擁有目前全台最大口徑的望遠鏡，設立以來了除主要從事天文觀測等研究外，也極力推廣相關天文環境教育活動並參與不少國際間的合作計畫。

中央大學校長周景揚說，在95年由楊庭彰與葉泉志兩位學者在鹿林天文台發現編號268669號小行星，這顆小行星位於火星跟木星之間，特別以塔塔加地區鄰近的原住民族「布農」來命名，並經國際天文學聯合會多年的審查認證，正式命名為「Bunun 布農」。

活動中，邀請信義鄉布農族部落久美國小及人和國小演出踢踏舞及話劇，展現原住民學童多才多藝的一面，也期望藉由活動，讓學童認識、學習天文知識，達到推廣天文教育的目的。

民國 96 年，中央大學天文所發現 185546 號小行星，這顆小行星當時以台灣高山「玉山」命名發表。

原文轉載自【2013-12-04/中廣新聞網 】

「布農小行星」發表及頒贈會　各界貴賓玉管處參與

台灣好新聞-2013 年 12 月 04 日 下午 17:07

記者吳素珍／南投報導

玉山國家公園管理處與中央大學天文所，於 4 日在水里遊客中心一樓視聽室，共同辦理「布農小行星」發表及頒贈會活動，久美國小學童的布農歌、舞表演，為活動揭開序幕，來自各界貴賓參與盛會。

玉山國家公園管理處處長游登良，感謝參與「布農小行星」發表及頒贈會活動的所有貴賓之盛情，他表示，很驚喜天上又多了一顆「布農小行星」。也感謝中央大學 校長周景揚選在玉管處辦理這項活動，讓園區周邊的小朋友有更多的機會接觸。玉山國家公園區周邊布農族部落久美國小及人和國小為此次活動表演踢踏舞及話劇演 出，展現原住民部落學童多才多藝的表演，期望藉由參予此次活動表演也認識、學習天文知識，以達到推廣天文教育之目的。

中央大學校長周景 揚、南投縣代理縣長陳志清、台灣聯合大學校長、人和國小校長等貴賓一一致意。玉管處指出，中央大學天文所是國內少數幾所大學擁有天文系所的學校，在塔塔加 地區的鹿林天文台擁有目前全台最大口徑之望遠鏡，設立以來除主要從事天文觀測等研究外，也極力推廣相關天文環境教育活動並參與不少國際間的合作計畫，對於 學術研究上也有很大的貢獻。

96 年中央大學天文所發現 185546 號小行星，首顆以台灣高山命名的小行星-玉山，正式發表命名。而在 2006 年 3 月 1 日由楊庭彰與葉泉志兩位學者於鹿林天文台發現，編號 268669 號小行星，特別以塔塔加地區鄰近的原住民族「布農」來命名，並經國際天文 學聯合會多年的審查認證，於 2013 年 4 月 25 日正式通過命名為「Bunun 布農」，具有其歷史意義與地緣關係。

中央大學天文所為布農 小行星做介紹時指出，布農族 Bunun，台灣原住民的一個族群，人口約有 5 萬餘人，分佈於中央山脈海拔一千至二千公尺的山區，廣及高雄市那瑪夏區、台東縣 海端鄉和南投縣境。布農族祭儀中所唱的「祈禱小米豐收歌」，以「八部合音」聞名於世，為世界音樂之瑰寶。

玉管處成立 28 年，在生態保育 上，不僅與相關學術單位合作，致力推動相關保育與環境教育；中央大學天文所在推廣天文教育上也是不遺餘力，不僅結合學校，合作推廣天文與科學教育，也配合 舉辦各種天文、生態性展覽，讓台灣的天文及生態性教育向下紮根。該處期望雙方在相關的領域上能互相協助與支援，並在寓教於樂的氛圍下，能達到國家公園以保 育、研究、育樂的目標。

更多：台灣好新聞：http://yam.taiwanhot.net
原文轉載自【2013-12-04/台灣好新聞 】

玉管處與中大發表布農小行星

記者謝新鈕／南投報導

玉山國家公園管理處與中央大學天文所，昨日在玉管處視聽室，共同辦理「布農小行星」發表及頒贈會活動。玉管處長游登良興奮地說，天上又多了一顆「布農小行 星」，實應感謝中央大學協助，而能讓園區周邊的小朋友有更多的機會接觸；再者，園區周邊布農族部落久美國小及人和國小為此次活動表演踢踏舞及話劇演出，展 現原住民部落學童多才多藝的表演，期望藉由參與此次活動表演也認識、學習天文知識，以達到推廣天文教育之目的。

玉管處指出，中大天文所是國內少數幾所大學擁有天文系所的學校，在塔塔加地區的鹿林天文台擁有目前全台最大口徑之望遠鏡，設立以來除主要從事天文觀測等研究外，也極力推廣相關天文環境教育活動並參與不少國際間的合作計畫，對學術研究上貢獻良多。

天文所為布農小行星做介紹時指出，布農族 Bunun，臺灣原住民的一個族群，人口約有 5 萬餘人，分布於中央山脈海拔 1 千至 2 千公尺的山區，廣及高雄市那瑪夏區、東縣海端鄉和南投縣境。布農族祭儀中所唱的「祈禱小米豐收歌」，以「八部合音」聞名於世，為世界音樂之瑰寶。
原文轉載自【2013-12-05/青年日報首頁 > 地方 】

玉管處今舉辦「布農小行星」發表會

【聯合報／記者賴香珊／即時報導】 2013.12.04 01:54 pm

以臺灣原住民布農族命名的小行星—「布農小行星」，4 日上午由玉山國家管理處與中央大學天文所共同發表，發表會在玉管處水里遊客中心一樓視聽室舉行，鄰近布農族部落的人和國小及久美國小分別表演話劇及踢踏舞，生動活潑演出凸顯這項命名活動的教育意義。

【2013/12/04 聯合報】@ http://udn.com/
原文轉載自【2013-12-04/聯合新聞網 生活 即時新聞 】

感念助建天文台 中大將小行星名為布農

2013年12月04日 14:29

【高 堂堯／南投報導】中央大學天文觀測員楊庭彰、葉泉志於7年前，在玉山鹿林天文台發現一顆小行星，中大特以鄰近的原住民族「布農」命名，經過國際天文學聯合 會多年審查認證，今年正式命名為「Bunun 布農」，國際永久編號編號268669；玉管處和中大天文所今天上午在玉管處水里遊客中心，舉辦「布農小行 星」發表會。

鹿林天文台站長林宏欽表示，小行星位於火星和木星間，體積約1座2000米高山、公轉太陽一周超過5年，中大為了感念布農 族人當年鼎力協助興建天文台的恩情，因此命名為「布農」；位在塔塔加地區的鹿林天文台，擁有目前全國最大口徑(1米)的天文望遠鏡，從2006至2009 年間執行「鹿林巡天計畫」時發現近800顆小行星，除了布農小行星，還包括同年發現的鄒族小行星、6年前發現的「玉山小行星」，成果豐碩。

玉管處表示，小行星以「Bunun 布農」命名，具有歷史意義與地緣關係，今天也邀請信義鄉久美國小、人和國小布農學童演出踢踏舞和話劇，表示對布農小行星的歡迎和感謝。

原文轉載自【2013-12-04/蘋果日報 即時新聞 】

布農小行星發表 原民學童分享

最新更新時間：18:19:05

（中央社記者林恆立南投縣4日電）以台灣原住民布農族命名的一顆小行星「Bunun 布農」，今天在玉山國家公園管理處舉行發表會，邀請布農族學童共同見證分享。

這顆於2006年由楊庭彰與葉泉志兩名學者在玉山塔塔加地區鹿林天文台發現、編號268669號的小行星，特別以鄰近的原住民族「布農」命名，經過國際天文學聯合會多年的審查認證，正式定名為「Bunun 布農」。

發表會於玉管處水里遊客中心舉行，由中央大學校長周景揚與玉管處長游登良共同主持，南投縣代理縣長陳志清等人到場祝賀。

活動中安排鄰近布農族部落久美國小學童表演原住民歌舞、人和國小學童演出話劇，融合傳統與創新，同時讓原住民學童了解這項命名的意義，並共同見證歷史的一刻。

游登良說，中央大學天文所設立鹿林天文台以來，除從事天文觀測等研究，也極力推廣天文環境教育活動，並參與不少國際間的合作計畫，這次小行星以「布農」命名，具有人文意義與地緣關係。

周景揚表示，塔塔加地區是全台最適合觀星及進行天文研究的地區，鹿林天文台更是國內天文研究的搖籃，目前正在建置 2 米口徑的天文望遠鏡，希望未來能藉由觀星活動，將科普往下扎根，讓學童認識、學習天文知識，進而啟發孩子對科學教育的熱情和認知。

陳志清致詞說，很高興有新的小行星在鹿林天文台被發現，並且是第一個以原住民族布農族作為命名，這個分享活動讓大家看到南投，也期望以布農族人好客熱情的心情，歡迎更多朋友到原住民部落參訪旅遊。

中央大學天文所於 2007 年也發現一顆編號 185546 號小行星，並首次以台灣高山為名，正式以「玉山」命名發表。1021204

原文轉載自【2013-12-04/中央社首頁 > 生活醫藥 】

布農小行星命名　原民部落登上太空

【本報南投訊】布農小行星宇宙現身！台灣原民部落再登太空。玉山國家公園管理處與中央大學天文所昨天舉行「布農小行星」命名發表會。在玉山國家公園內的 鹿林天文台發現編號第 268669 號小行星，因地緣關係，以塔塔加地區鄰近的原住民族「布農」命名，而布農族的神話傳說也有星星存在，使命名活動更具歷史 意義。268669 不是電話號碼，也不是這期彩券的中獎券號，它是民國九十五年由中央大學楊庭彰和廣州大學葉泉志兩位學者在鹿林天文台共同發現的小行星編 號。經過國際天文聯合會長達五年的資料庫比對、確認軌道，昨天終於以原住民族「布農（Bunun）」命名，永遠閃耀在銀河系裡。

布農族的八部合音舉世聞名，本次活動也邀請久美國小及人和國小布農族學童， 用優美的歌聲搭配踢踏舞和話劇，為「布農小行星」的現身獻上祝福。人和國小校長伍福義說，以「布農」命名行星使他很感動，也期許布農孩子肯定自己的族群， 永續傳承布農文化，就如同布農小行星永遠在宇宙閃耀。

鹿林天文台站長林宏欽表示：「行星沒有生命，是『布農』之名讓第 268669 號小行 星新生。」布農小行星繞太陽公轉，需五年才繞完一圈，但一年會有一次最接近地球。鹿林天文台的巡天計畫從二〇〇六到二〇〇九年共發現八百多顆小行星，已有 五百顆獲得行星編號，其中五十多顆已完成命名。

中央大學校長贈頒布農小行星銘版給玉管處時提到，為了天文科普教育，中央

大學與鹿林天文台將推動「追星築夢鹿林兩米望遠鏡計畫」，期望藉由設備－的提升讓天文教育更加普及。

原文轉載自【2013-12-05/人間福報/綜合／社區 】

台學者葉永烜：大陸發展航天後生可畏

http://www.CRNTT.com 2013-12-04 00:29:03

中評社桃園12月4日電(記者 黃文杰專訪)台灣聯合大學系統系統副校長、台灣中央大學天文研究所與太空科學研究所教授葉永烜接受中評社訪問表示，大陸 發射“嫦娥三號”探測器到月球著陸，連台灣的科學家都會高興拍手叫好，樂見科學貢獻，因為月球發展或是太空殖民計劃已經可行，這也是繼“美國夢”、“中國 夢”之後，下一個“月球夢”，可以促成國際合作、和平發展。

葉永烜，知名德國籍華人天文學家，原籍廣東梅縣的客家人，出生於南京，在澳門成長，曾任台灣中央大學副校長，研究專長是彗星、行星大氣與地球高層大氣、太陽系與行星形成、電漿物理。

他認為，中國發展月球計劃過程，可以想見的是，根本得不到其他國家奧援，一切只有自立自強，但中國按步驟累積實力，令人刮目相看。國外有人開玩笑形容，俄國航天人員年紀60歲，美國航天人員50歲，中國航天人員30、40歲，足以證明中國發展航天“後生可畏”。

1982年時葉永烜和法國科學家丹尼爾・高迪耶（Daniel Gautier）、美國科學家托比・歐文（Toby Owen）向NASA與ESA提出探測土星系統的計劃。

該計劃就是現在的卡西尼-惠更斯號。NASA在2009年授予他特殊公共服務榮譽勳章，表彰他對卡西尼-惠更斯號計劃的貢獻。

除了卡西尼計劃以外，葉永烜還曾參加喬托號、深度撞擊號、羅塞塔號等太空探測任務。

媒體報道“嫦娥三號”，是中國發射的第一個地外軟著陸探測器和巡視器，也是美國阿波羅計劃結束後全球重返月球的第一個軟著陸探測器。

葉永烜說，事實上，中國大陸積極發展航天與月球計劃，不同於印度發射火星探測，是屬於長期計劃，或者應該說三部曲，依序分別是“繞”、“落”、“回”。

先前“嫦娥二號”等發射升空，著重在月球軌道繞行，這次“嫦娥三號”著陸如果順利成功，代表進入到“落”，接下來，就要看看中國大陸是否繼續推動太空特測器返回地球。

太空探測器如果可以從月球返回地球，不是單純月球表面資料收集，這意味著，未來搭載太空人登陸月球計劃更成熟。

葉永烜回憶，十多年前剛開始聽說，中國要發展月球計劃，當時很多科學家都覺得不可思議，認為這很複雜、又沒有辦法得到外援技術。

如今短短時間，從繞行軌道進入探測器著陸，相信科學家都覺得很高興，對科學發展很有大貢獻。

(原文來源網址：
http://hk.crntt.com/doc/1029/0/0/3/102900379.html?coluid=93&kindid=8110&docid=102900379&mdate=1204002904)

台學者葉永烜：大陸發展航天後生可畏

http://www.CRNTT.com 2013-12-04 00:29:03

中評社記者好奇，印度都發展火星計劃，中國大陸發展月球計劃，兩者是否可比相比？為何美國蘇聯都不再發展太空人登陸月球，日本航天技術也很驚人，是否亞洲國家進入太空競賽？

葉永烜認為，火星計劃單純是科學研究，月球計劃被視為可執行的目標。

他引述統計數字，月球表面的面積，大約是美國三倍這麼大，當初歐洲人前往美洲發現新大陸，不論基於淘金夢或是其他資源利益爭取，至少替人類史編織所謂的“美國夢”。

“美國夢”代表是一種驅力，靠新大陸的開發，帶動進步，不久將來，相信世界各國會高喊“月球夢”，它的象徵意義在於“這是可行”，也就是建立太空殖民計劃。

葉永烜簡單舉例，中國大陸也以月球興建房屋為例，如果沒有水應該如何克服，這個道理，也有助於地球資源日益貧乏。

如果殖民到月球，惡劣環境如何克服？應該採取哪種替代方案？以前沒有注意過的事，會有一股新的驅動力，帶領人類不斷往前邁進。

“勇敢往不熟悉領域勇敢挑戰，這就是人類偉大！”葉永烜說。

是否需要太空人登陸月球？這牽扯到各國發展太空計劃的重心不同。

現在太空計劃偏重在小行星研究，發展月球計劃的配套方案，類似抓小行星放在月球軌道繞行，變成衛星，可以放許多資源在上頭，有助於太空站使用。

他說，當初美俄冷戰期間，美國大力發展太空計劃，不斷修正缺失，馬上又發射升空，最後把阿姆斯壯送上月球登陸，主要是著眼兩大國競爭，生死存活。

現在是太平盛世，加上機械人可以克服外太空惡劣環境，連飛機都有無人飛機，可以替代發展航天的風險，屆時地球到月球，就類似搭快速升降機到太空站，接著像搭高鐵繞行軌道進入。

至於中美日等國都在發展航天事業，中國這幾年進步，確實可以用“後生可畏”來形容。

(原文來源網址：
http://hk.crntt.com/doc/1029/0/0/3/102900379_2.html?coluid=93&kindid=8110&docid=102900379&mdate=1204002847)

原文轉載自【2013-12-04/中國評論新聞】

中國評論新聞：台灣中央大學拍攝到嫦娥三號火箭脫落

台灣中央大學拍攝到嫦娥三號火箭脫落 http://www.CRNTT.com 2013-12-03 00:47:49

中評社桃園 12 月 3 日電(記者　黃文杰)“嫦娥三號”探測器在西昌衛星發射中心於 12 月 2 日凌晨 1 時 30 分由長征三乙火箭搭載發射升空，台灣方面也高度密切注意後續發展，台灣中央大學天文所 2 日凌晨，也同步成功拍攝到火箭推進器，墜落台灣東部外海瞬間畫面。

拍攝到火箭推推進器墜落瞬間火光，是台灣中央大學天文所專任助理張永欣，他特別留意大陸這次發射“嫦娥三號”相關報道，算準時間與方位，在桃園中壢雙連坡附近，單純利用廣角數位相機，成功捕捉瞬間畫面。

從張永欣提供的動態照片，可以看到拍攝時間是在 12 月 2 日凌晨 01 點 39 分 59 秒到 01 點 40 分 59 秒，火箭推進器墜落地表，瞬間高溫引燃火花爆開。

為了怕漏失畫面，張永欣也透過汽車行車紀錄器，選定時間，算準方位，也拍攝瞬間火花，不過畫質比較不清晰，只有一點亮點，不像數位相機局部放大，可以看到爆開的火花。

張永欣說，他並非整夜沒睡覺，徹夜守候拍火箭推進器墜海，只是透過定時器，讓數位相機每隔幾秒連拍數張，隔天再仔細檢查拍攝畫面，成功拍到大陸長征三乙火箭墜海，也覺得很高興。

他解釋，當初“嫦娥二號”發射後，火箭推進器也墜落在台灣東部外海，當時瞬間引爆火花，令好多人驚訝，這次站在台灣西部，往東邊拍攝還能拍到亮點，主要還是夜晚冷度夠，空氣沒有汙染，視線佳。

原文轉載自【2013-12-03/中國評論新聞】

小行星發表　原住民族布農為名

時間：2013/11/29 19:39　撰稿·編輯：曾美惠　　新聞引據：中央社

學者於多年前在玉山鹿林天文台發現一顆小行星，特別以鄰近的原住民族「布農」命名，12 月 4 日將於玉管處舉辦發表會。

玉山國家公園管理處今天(29 日)表示，中央大學天文所在塔塔加地區的鹿林天文台，擁有目前全國最大口徑的天文望遠鏡，設立以來除從事天文觀測等研

究，也極力推廣天文環境教育活動，並參與不少國際間的合作計畫。

玉管處指出，中央大學天文所於2007年發現的185546號小行星，是首顆以台灣高山命名的小行星，正式以「玉山」為名發表。

而在2006年由楊庭彰與葉泉志兩名學者於鹿林天文台發現編號268669號的小行星，也特別以塔塔加地區鄰近的原住民族「布農」來命名，經過國際天文學聯合會多年的審查認證，正式命名為「Bunun布農」。

玉管處表示，這顆小行星以「Bunun布農」命名，具有歷史意義與地緣關係，玉管處與中央大學天文所預定於12月4日上午在玉管處水里遊客中心共同舉辦 「布農小行星」發表會，將邀請鄰近機關、學校與布農團體共襄盛舉，期望藉由活動，讓學童認識、學習天文知識，達到推廣天文教育的目的。

此則報導的來源網址：http://news.rti.org.tw/index_newsContent.aspx?nid=467819

原文轉載自【2013-11-29/中央廣播電臺新聞頻道】

鹿林天文台發現小行星　命名布農

（中央社南投縣二十九日電）

學者多年前在玉山鹿林天文台發現一顆小行星，特別以鄰近的原住民族「布農」命名，十二月四日將在玉管處舉辦發表會。

玉山國家公園管理處二十九日表示，中央大學天文所在塔塔加地區的鹿林天文台，擁有目前全國最大口徑的天文望遠鏡，設立以來除從事天文觀測等研究，也極力推廣天文環境教育活動，並參與不少國際間的合作計畫。

九十五年由楊庭彰、葉泉志兩名學者在鹿林天文台發現編號268669號的小行星，也特別以塔塔加地區鄰近的原住民族「布農」來命名，經過國際天文學聯合會多年的審查認證，正式命名為「Bunun布農」。

原文轉載自【2013-11-30/青年日報/6版/新視界】

小行星發表　原住民族布農為名

中央社 – 2013年11月29日 下午7:27（中央社記者林恆立南投縣29日電）學者於多年前在玉山鹿林天文台發現一顆小行星，特別以鄰近的原住民族「布農」命名，12月4日將於玉管處舉辦發表會。

玉山國家公園管理處今天表示，中央大學天文所在塔塔加地區的鹿林天文台，擁有目前全國最大口徑的天文望遠鏡，設立以來除從事天文觀測等研究，也極力推廣天文環境教育活動，並參與不少國際間的合作計畫。

玉管處指出，中央大學天文所於民國 96 年發現的 185546 號小行星，是首顆以台灣高山命名的小行星，正式以「玉山」為名發表。

而在 95 年由楊庭彰與葉泉志兩名學者於鹿林天文台發現編號 268669 號的小行星，也特別以塔塔加地區鄰近的原住民族「布農」來命名，經過國際天文學聯合會多年的審查認證，正式命名為「Bunun 布農」。

玉管處表示，這顆小行星以「Bunun 布農」命名，具有歷史意義與地緣關係，玉管處與中央大學天文所預定於 12 月 4 日上午在玉管處水里遊客中心共同舉辦「布農小行星」發表會，將邀請鄰近機關、學校與布農團體共襄盛舉。

活動中將邀請玉山園區周邊布農族部落久美國小及人和國小演出踢踏舞及話劇，展現原住民部落學童多才多藝的一面，也期望藉由活動，讓學童認識、學習天文知識，達到推廣天文教育的目的。1021129

原文轉載自【2013-11-29/中央社】

台灣/小行星發表　原住民族布農為名

http://www.cdnews.com.tw　2013-11-29 23:17:51

李漢揚/整理

學者於多年前在玉山鹿林天文台發現一顆小行星，特別以鄰近的原住民族「布農」命名，12 月 4 日將於玉管處舉辦發表會。

中央社 29 日報導，玉山國家公園管理處今天表示，中央大學天文所在塔塔加地區的鹿林天文台，擁有目前全國最大口徑的天文望遠鏡，設立以來除從事天文觀測等研究，也極力推廣天文環境教育活動，並參與不少國際間的合作計畫。

玉管處指出，中央大學天文所於民國 96 年發現的 185546 號小行星，是首顆以台灣高山命名的小行星，正式以「玉山」為名發表。

而在 95 年由楊庭彰與葉泉志兩名學者於鹿林天文台發現編號 268669 號的小行星，也特別以塔塔加地區鄰近的原住民族「布農」來命名，經過國際天文學聯合會多年的審查認證，正式命名為「Bunun 布農」。

玉管處表示，這顆小行星以「Bunun 布農」命名，具有歷史意義與地緣關係，玉管處與中央大學天文所預定於 12 月 4 日上午在玉管處水里遊客中心共同舉辦「布農小行星」發表會，將邀請鄰近機關、學校與布農團體共襄盛舉。

活動中將邀請玉山園區周邊布農族部落久美國小及人和國小演出踢踏舞及話劇，展現原住民部落學童多才多藝的一面，也期望藉由活動，讓學童認識、學習天文知識，達到推廣天文教育的目的。

【中央網路報】

原文轉載自【2013-11-29/中央日報網路報-教育藝文】

注意！天文界大事件
艾森彗星　3 天後上演脫逃秀

28 日繞過太陽時它會融化、遭碎屍或成功脫逃？若是夠幸運的話明年 1 月它會靠近地球打招呼！

【本報記者陳皓嬿】

千呼萬喚始出來，艾森（ISON）彗星終於要接近太陽了，2012 年被發現後，曾被天文學家視為「會讓月亮也相形失色」的超亮世紀大彗星，雖然後來隨其越接近太陽，科學家發現它並不如預期那麼活躍和耀眼，不過仍不減其魅力。

因為艾森彗星是一顆「掠日彗星」，屆時將會距離太陽非常近，當它 11 月 28 日繞過太陽時，究竟會被融化殆盡、碎屍萬段，或是成功脫逃，仍是天文學家無法預測的謎。

艾森彗星是 2012 年 9 月 21 日時，由俄羅斯的國際科學可見光觀測網（International Scientific Optical Network, ISON）兩位天文學家維塔利・涅夫斯基和阿爾喬姆・諾微切諾克發現的，「艾森」就是該組織的名稱縮寫。

艾森彗星的正式名稱是 C/2012 S1 彗星，C 代表「沒有週期、或是週期超過兩百年」的彗星，2012 是發現的年份，S1 則代表九月下半月的第一顆發現的新彗星（國際天文學聯合會將一個月分成上下半月，因此一月上半月為 A，一月下半月為 B，以此類推）。

根據觀測，美國太空總署（NASA）預估艾森彗星的直徑約有 4.8 公里，大概像一座小山那麼大，重量介於 32 億噸到 3.2 兆噸之間。

就像大部分的彗星，艾森彗星也是顆「髒兮兮的雪球」，由塵埃、結凍的水、氨、甲烷和二氧化碳組成。

根據 2013 年 6 月擷取到的影像顯示，這些物質被太陽風吹出的「彗尾」，有 30 萬公里長，約等於 86 個月球相連的長度。

剛發現艾森彗星時，天文學家預測它接近太陽時的亮度，從地球上觀測可達-14

等，比滿月時月亮的-12.47 等，還要亮三倍（星等越小，星體越亮），但隨著觀測到的資訊越來越多，艾森彗星的亮度表現卻不如預期，十一月中一路下修到-2.5 等，和水星最亮的時候差不多。

不過 11 月 14 日時，天文學家發現艾森彗星亮度卻突然減兩等，從 8 等變 6 等，也就是先前的 6.3 倍亮，又讓一度對這顆「世紀大彗星」失望的天文迷再度熱血沸騰。

一直關注艾森彗星的氣象局天文站技士鄭振豐說，不到月底，還真不知道艾森會如何發展，如果亮度足夠的話，11 月 28 日前後，在台灣從凌晨三點到日出前，都有機會看到艾森彗星。

艾森彗星不像著名的哈雷彗星，走封閉的橢圓形軌道，已經和地球打過好幾次招呼，其軌道是開放的雙曲線，這意味十一月底艾森彗星繞過太陽之後，就會和太陽系漸行漸遠，最後一去不回頭。

不過，這只是在艾森彗星經過太陽仍「劫後餘生」的情況，艾森彗星是顆「掠日彗星」－即近日點離太陽中心 136 萬公里內的彗星，在最接近太陽時，艾森彗星距離太陽表面只有 110 萬公里遠。

到時候，不只會有太陽「攝氏 2760 度的高溫燒烤」洗禮，還會受到太陽強大的重力拉扯，艾森彗星很可能當場就被五馬分屍，碎成片片。

有科學家認為，這樣的「悲劇」通常容易發生在小型的掠日彗星上，以艾森彗星的大小來說，也許有機會逃過一劫，待艾森彗星成功繞過太陽，便可在 2014 年 1 月接近地球軌道上方；夠幸運的話，從十一月到明年一月，地球人都可以用肉眼觀測艾森彗星的英姿。

原文轉載自【2013-11-25/聯合報/AA3 版/新聞中的科學】

科學家提假說
古柏帶、歐特雲　慧星的老家

彗星分中短周期和長周期兩種短周期住古柏帶　長周期住歐特雲

【本報記者陳皓嬿】

為什麼有些彗星像梁祝，幾千幾萬年來不斷和太陽系中心十八相送，有些彗星卻像刺秦王的荊軻，壯士一去不復返？要解開這個問題，得從彗星從何而來談起。

一般而言，彗星分成中短周期和長周期兩種。以 200 年為分界，周期在 200 年以下為中短週期彗星，周期在 200 年以上則是長周期彗星；一去不回的彗星周期可視為無限大，因此也在長周期一族中。

彗星是太陽形成太陽系和行星、衛星之後的殘餘物質，如果把彗星想像成建築垃圾的話，理論上中短周期彗星的故鄉，是海王星外圍類似甜甜圈的盤狀垃圾場－「古柏帶」。

而長周期彗星的故鄉則包覆整個太陽系，它是距離太陽相當遙遠的球狀垃圾場－「歐特雲」。

古柏帶是以此假說的提出人之一，荷蘭天文學家傑拉德．古柏的名字命名。古柏帶距離太陽系中心約 30AU 到 55AU 遠（1AU 為 1 天文單位，約為地球到太陽 的平均距離），大致平行黃道面（可大略類比為各行星的軌道面）；之前被踢出九大行星行列的冥王星，就是古柏帶的成員，而中短周期彗星大多從此來。

另一位荷蘭天文學家楊．亨德理克．歐特則提出歐特雲的概念。他認為歐特雲是一坨距離太陽系中心 5 到 10 萬 AU，遠遠包圍著太陽系的球殼；當中含有幾千億甚至幾兆顆的冰凍碎塊，受到太陽引力擾動，碎塊被拉入太陽系，變成長周期彗星。

中央大學天文所教授說，從古柏帶來的中短周期彗星，大抵來說相當規矩，和黃道面的夾角約在 40 度上下，公轉的方向也大多和眾行星相同，鳥瞰太陽系時為逆時針轉，軌道則是橢圓形。

台北市立天文館的助理研究員洪景川舉例，周期為 76 年的哈雷彗星、造成獅子座流星雨且周期為 33.22 年的坦波．塔特彗星，都是中短周期的彗星，皆可能從古柏帶誕生。
另一族群長周期彗星可不那麼安分。
從歐特雲來的它們方向混亂，有的從下往上穿過太陽系中心，角度和黃道面幾乎垂直，有的公轉方向和眾行星們相反，更不用說一堆軌道呈拋物線或雙曲線，和太陽只有一面之緣的非周期「荊軻彗星」，或是軌道是極狹長的橢圓，讓太陽苦等百年、千年的長周期「薛平貴彗星」了。

陳文屏說，這些長周期彗星可能是太陽系形成時，被甩出去的碎片，因為逃跑得不夠快，又被太陽抓回來，繞個圈再甩出去。

他說，今年底的「準世紀大彗星」艾森、上個世紀末曾造成信徒集體自殺的海爾－波普彗星都屬此類。

比較特別的是，也有安分規矩但只來一次非周期彗星，那就是台灣鹿林天文台於 2007 年發現、第一顆由台灣命名的鹿林彗星。

鹿林彗星的軌道，和黃道面大致平行。不過，其運行方向和其他行星相反，仍讓它「裝乖破了功」。

原文轉載自【2013-11-25/聯合報/AA3 版/新聞中的科學】

彗星…髒兮兮
分解掃把星… 灰塵　甲烷　冰渣

【本報記者陳皓嬿】

如果把太陽系想像成「模型組合包」，那行星、衛星系統就是太陽幾億年來組合好的模型完成體，小行星和彗星則是組裝完後剩下的碎片和垃圾，離太陽較近的（通常存在於火星和木星之間）稱為小行星，被太陽和「幫凶」大型行星如木星，拋到九霄雲外的則是彗星。

彗星和小行星最大的不同是，小行星由岩石和金屬組成，彗星是一團混合灰塵、水、甲烷等物質所組成的冰渣「彗核」，加上受到太陽輻射影響，冰渣昇華而環繞在彗核周遭的氣體雲狀物「彗髮」，和接近太陽時，噴出的長尾巴「彗尾」（彗星最重要的特徵之一）。

彗尾細看有兩條，一條是「離子尾」，一條是「塵埃尾」，離子尾是彗髮被太陽風「吹拂」而向後推出來、由離子等顆粒較小的電漿物質組成，是條藍色尾巴，長得又直又細長，可長達幾千萬、甚至一億公里。

塵埃尾則是由彗髮中顆粒較大的灰塵組成，受到太陽輻射壓力影響，塵埃尾如扇子般散開在彗星背對太陽的地方，由於塵埃顆粒也會受太陽重力影響，因此塵埃尾會略為彎向太陽，反射陽光後呈白色。

歷史上幾個經典的彗星，最著名的要屬哈雷彗星，哈雷彗星是人類第一顆確認其周期的彗星，也是唯一可以用肉眼觀察的短周期彗星（即周期在 200 年內的彗星），許多古文明都有記載哈雷彗星出現的紀錄，可是世人並不知道這顆彗星會一再出現。

一直到 1703 年英國天文學家愛德蒙・哈雷（Edmond Halley）發現這顆彗星會每 76 年造訪地球一次，世人才知道哈雷彗星有周期地繞行太陽；哈雷彗星最近一次回歸是 1986 年，下一次回歸則是 2061 年。

1965 年由日本業餘天文學家池谷薰和關勉發現的池谷－關彗星，則是近千年地球上所見最亮的彗星之一，該年 10 月 21 日它接近近日點時，其視星等有-17 等，比滿月還要亮 60 倍，連白天在太陽旁邊都可以看得到它。

池谷－關彗星也是一顆長周期的掠日彗星，不過即使人類活得再久，也無法再次見到它，因為池谷－關彗星在經過近日點前 30 分鐘，就碎成三塊碎片，其中一塊不見蹤影，只剩其中兩塊繼續前進，科學家認為就算下次池谷－關彗星「回歸」，可能只是一堆迷你軍團，而非當年的大彗星了。

原文轉載自【2013-11-25/聯合報/AA3 版/新聞中的科學】

研究：解開極亮超新星超閃之謎

2013 年 11 月 23 日

【大紀元訊】數量極少的「極亮超新星」肇因成謎，台灣中央大學參與的跨國研究計畫發現，極亮超新星不僅源於超重質量，且與高磁場、高轉速的中子星相關。

這項發現並登上近期出刊的國際期刊《自然》（Nature）。

據中央社報導，台灣中央大學表示，大質量恆星以超新星爆法結束一生，其中「極亮超新星」的亮度更勝百倍，其爆發時產生的能量，相當於 90 個太陽一生中所釋放的能量總和。

由於數量極少，探索「極亮超新星」的來源和成因，成為許多國際團隊研究重點。不過，超新星爆發無法事先預測，必須長期監測星系，以拍長期紀錄片方式，才得以追蹤觀測。

中央大學天文所助理教授浦田裕次與英國教授司馬特帶領的團隊共同合作，透過位於夏威夷的泛星計畫（Pan-STARRS）望遠鏡，不斷掃描天空及後續觀測，研究 PTF12dam、PS1-11ap 兩個極亮超新星，連續追蹤觀測超過 1 年，總算得以一窺極亮超新星的神祕面紗。

浦田裕次表示，第一個被發現的極亮超新星 SN2007gi，證實這些極亮超新星可能源自於 100 倍太陽質量的超級重恆星死亡時，產生的爆發。

然而，這次研究的兩顆極亮超新星，不僅理論模型無法合理解釋，連這兩個極亮超新星的晚期演化也與 SN2007gi 不相同，意味超重恆星死亡並不是極亮超新星的唯一解釋。

司馬特的博士班學生尼科爾（Nicholl）將觀測資料應用於理論模型發現，這兩

個超新星「極亮」的原因，為超新星爆發後留下的高磁場、高轉速中子星，自轉減速時所造成的能量加持。◇

原文轉載自【2013-11-23/大紀元時報首頁> 生活> 教育科普 】

觀星象　台師大 9 日開放天文台

（中央社記者許秩維台北 6 日電）台師大今天表示，9 日將開放老圓頂天文台，現場備有口徑 40 公分的電腦遙控望遠鏡，供民眾一睹金星、木星、艾桑彗星等星象。

台灣師範大學地球科學系舉辦的「老圓頂開放日」今年已邁入第 15 年。台師大表示，今年主題是「太陽系夜未眠」，現場備有口徑 40 公分的電腦遙控望遠鏡，以及多台小型天文望遠鏡，並有專人在旁負責解說，帶領民眾認識滿天星斗。

除了觀測星象外，台師大表示，現場也將使用星象儀引領大家辨認滿天繁星，同時將介紹四季星空，以及詩意又浪漫的星座神話故事，另外中央大學教授葉永烜將講演「彗星任務與生命起源的探索」，內容深入淺出，幽默詼諧，帶領大小朋友以不一樣的角度進入天文世界。

台師大表示，9 日晚間 7 時將開放老圓頂天文台，民眾有機會看到黃昏時的金星和月亮風采，月落時，可仰望太陽系明亮的木星，還有地球的近鄰火星，接近凌晨時，還有機會看到有可能成為「世紀大彗星」的艾桑彗星，歡迎民眾一起體驗觀星樂趣。1021106

原文轉載自【2013-11-06/中央社】

中央大學參與泛星計畫　登《自然》期刊

2013 年 10 月 17 日 18:26 【許敏溶／台北報導】中央大學天文所助理教授浦田裕次參與國際團隊，進行「泛星計畫」研究發現，極亮超新星不僅源於超重質量恆星，且與高磁場、高轉速的中子星相關，該成果榮登最新一期出刊的國際頂尖期刊《自然》（Nature）。

浦田裕次的太太黃麗錦說，所謂超新星，指的是質量比太陽大 8 倍以上恆星在生命最末期劇烈爆發的現象，爆發後產生中子星，而「極亮超新星」，顧名思義就是爆發時亮度比超新星亮上百倍，但數量極少，目前學者預測極亮超新星可能源自於比太陽質量 100 倍大的超級重恆星死亡時產生的爆發，這次研究成果則提供另一個可能性。

原文轉載自【2013-10-17/蘋果日報 即時新聞】

北一女團隊照見超新星爆發　獨步全球

〔記 者陳慰慈／台北報導〕在位於 M74 星系的超新星 SN 2013ej 正式被確認的十五個小時前，北一女師生組成的高瞻團隊，已在玉山國家公園鹿林前山的「鹿林天文台」，搶先拍攝到 SN 2013ej 爆發，成為全世界第一個拿到 SN 2013ej 光度資料的團隊。高瞻團隊指導教授、清大天文所江國興表示：「根據星等的判斷，我們拍到了光度正在上升的超新星爆發，對於超新星的研究有一定 的科學價值。」

首次帶學生上鹿林天文台

SN 2013ej 最早是由 Lick 天文台的超新星搜尋團隊，在今年七月二十五日上午十點確認為超新星，但北一女師生團隊七月二十四日晚上七點，就率先拍攝到該顆超新星。

江國興教授表示：「天文學家推斷這顆超新星的前身，應是顆巨大的紅色巨星，質量大約為太陽的八到十倍，半徑則為太陽的四百到六百倍。」

意外拍到 師生直呼幸運

北一女中的化學科老師楊國珠表示，一開始選定觀測目標時，不知道會拍到什麼，回來後整理數據、比對照片，才發現多了一顆 SN 2013ej，「第一次帶學生上鹿林天文台進行專業的天文拍攝，就拍到超新星爆發，真是湊巧又幸運。」

可提供全球天文學家參考

北一女中地球科學老師林郁梅則說，團隊拍到的是這顆超新星剛開始變亮及亮度變化過程，可提供給全世界的天文學家參考。

北一女中的物理科李美英老師形容：「好像目睹了一場華麗的死亡，對我們來說，是最近距離炫目的接觸，畢生難忘經驗，也是另一段旅程最華麗的開始。」

北一女中學生盧宥璇及許苡蕾也說，能夠在高中階段就跟經驗豐富的專家學習，且使用大型的望遠鏡進行觀測，十分興奮，從中得到許多的啟發與激勵。

原文轉載自【2013-10-13/自由時報/A14 版/生活新聞】

台灣/研究：解開極亮超新星超閃之謎

http://www.cdnews.com.tw 2013-10-17 21:51:08

李漢揚/整理

數量極少的「極亮超新星」肇因成謎，中央大學參與的跨國研究計畫發現，極亮超新星不僅源於超重質量，且與高磁場、高轉速的中子星相關。

中央社 17 日報導，這項發現並登上今天出刊的國際期刊「自然（Nature）」。

中央大學表示，大質量恆星以超新星爆發結束一生，其中「極亮超新星」的亮度更勝百倍，其爆發時產生的能量，相當於 90 個太陽一生中所釋放的能量總和。

由於數量極少，探索「極亮超新星」的來源和成因，成為許多國際團隊研究重點。不過，超新星爆發無法事先預測，必須長期監測星系，以拍長期紀錄片方式，才得以追蹤觀測。

中央大學天文所助理教授浦田裕次與英國教授司馬特帶領的團隊共同合作，透過位於夏威夷的泛星計畫(Pan-STARRS) 望遠鏡不斷掃瞄天空及後續觀測，研究 PTF12dam、PS1-11ap 兩個極亮超新星，連續追蹤觀測超過一年，總算得以一窺極亮超新星的神秘面紗。

浦田裕次表示，第一個被發現的極亮超新星 SN2007gi，證實，這些極亮超新星可能源自於 100 倍太陽質量的超級重恆星死亡時，產生的爆發。

他說，然而，這次研究的兩顆極亮超新星，不僅理論模型無法合理解釋，連這兩個極亮超新星的晚期演化也與 SN2007gi 不相同，意味超重恆星死亡並不是極亮超新星的唯一解釋。

司馬特的博士班學生尼科爾（Nicholl）將觀測資料應用於理論模型發現，這兩個超新星「極亮」的原因，為超新星爆發後留下的高磁場、高轉速中子星，自轉減速時所造成能量加持。

【中央網路報】

原文轉載自【2013-10-17/中央日報網路報-即時新聞】

研究：解開極亮超新星超閃之謎

（中央社記者林孟汝台北 17 日電）數量極少的「極亮超新星」肇因成謎，中央大學參與的跨國研究計畫發現，極亮超新星不僅源於超重質量，且與高磁場、高轉速的中子星相關。

這項發現並登上今天出刊的國際期刊「自然（Nature）」。

中央大學表示，大質量恆星以超新星爆發結束一生，其中「極亮超新星」的亮度更勝百倍，其爆發時產生的能量，相當於 90 個太陽一生中所釋放的能量總和。

由於數量極少，探索「極亮超新星」的來源和成因，成為許多國際團隊研究重點。不過，超新星爆發無法事先預測，必須長期監測星系，以拍長期紀錄片方式，才得以追蹤觀測。

中央大學天文所助理教授浦田裕次與英國教授司馬特帶領的團隊共同合作，透過位於夏威夷的泛星計畫(Pan-STARRS) 望遠鏡不斷掃瞄天空及後續觀測，研究 PTF12dam、PS1-11ap 兩個極亮超新星，連續追蹤觀測超過一年，總算得以一窺極亮超新星的神秘面紗。

浦田裕次表示，第一個被發現的極亮超新星 SN2007gi，證實，這些極亮超新星可能源自於 100 倍太陽質量的超級重恆星死亡時，產生的爆發。

他說，然而，這次研究的兩顆極亮超新星，不僅理論模型無法合理解釋，連這兩個極亮超新星的晚期演化也與 SN2007gi 不相同，意味超重恆星死亡並不是極亮超新星的唯一解釋。

司馬特的博士班學生尼科爾（Nicholl）將觀測資料應用於理論模型發現，這兩個超新星「極亮」的原因，為超新星爆發後留下的高磁場、高轉速中子星，自轉減速時所造成能量加持。1021017

原文轉載自【2013-10-17/中央社首頁 > 財經新聞 】

全球第一　北一女拍到超新星爆發

記者姜伯誠／台北報導

北市教育局表昨日表示，北一女高瞻計畫團隊七月間透過鹿林天文台意外拍到超新星 SN 2013ej 爆發，是全球第一個拿到該光度資料的團隊，成果相當令人振奮。

SN 2013ej 最早是由 Lick 天文台的超新星搜尋團隊，在世界時間今年七月二十五日十時十八分確認為超新星，北一女師生早一步在世界時間七月二十四日晚間七時十八分（台灣時間 七月二十五日三時十八分），即已於中央大學位於鹿林的天文台拍到，並且提供第一個經過校對的亮度數據。

北一女中團隊是在進行「星雲行動」課程的天文觀測時，意外捕捉到 SN 2013ej 超新星爆發。這個課程是由國科會高瞻計畫補助，由清大天文所教授指導，並為該校的特色課程之一。

團隊指導教授、清大天文所教授江國興表示，根據目前最新的觀測結果，天文學家推斷這顆超新星的前身，應該是一顆超級巨大的紅色巨星，稱為「紅超巨星」，其質量大約為太陽的八至十倍，半徑則為太陽的四百到六百倍。

他說：「根據星等的判斷，我們拍到了光度正在上升的超新星爆發，對於超新星的研究有一定的科學價值。」

由於北一女觀測到的日期很早，尚未達到該顆超新星的最大亮度，因此也提供研究超新星爆發早期的重要資訊。

江國興強調，他們的數據是全球第一個用不同濾鏡得到的，因此全球第一個最有意義的光度資料，是由他們貢獻。

另一位指導教授清大天文所教授張祥光說，根據觀測結果，可以推論 SN 2013ej 應該是屬於第二型超新星。

原文轉載自【2013-10-13/中華日報/A1 版/全國焦點】

全球第一　北一女拍到超新星 SN 2013ej 爆發

【石文南、湯雅雯／台北報導】

北一女中由國科會補助的特色課程「星雲行動」，今年 7 月前往鹿林天文台觀星，師生團隊意外率先拍攝到超新星 SN 2013ej 爆發。經比對發現是全球第 1 個拿到 SN 2013ej 爆發光度資料的團隊。

北一女地球科學教師林郁梅表示，此次鹿林天文台觀星拍攝 M74 星系。M74 星系距地球 3200 萬光年，位於雙魚座附近。

師生在世界標準時間 2013 年 7 月 24 日 19 點 18 分（台灣時間 7 月 25 日 3 點 18 分），於中央大學鹿林天文台拍攝到 SN 2013ej 超新星，並提供第 1 個經過校對的亮度數據。15 個小時後，美國李克文天文台的超新星搜尋團隊（Lick Observatory Supernova Search）於世界標準時 2013 年 7 月 25 日 10 點 18 分確認為超新星。

教師林郁梅表示，研究團隊整理 資料照片比對發現，學生拍攝的 M 74 星系圖的左下角，出現一顆亮度極高的，就是超新星 SN 2013ej。恆星爆炸後形成超新星，像煙火般亮度瞬間爆亮，一段時間後轉暗，全世界的天文學家都在緊盯它，以窺知這顆超新星的前身。北一學生許苡蕾表 示，在拍攝 M74 星系圖，剛好碰上恆星爆炸很亮，當時並不知道是超新星的形成。

清大天文所教授江國興表示，天文學家推斷 SN 2013ej 超新星的前身，應是顆超級巨大的紅色巨星，稱為「紅超巨星」，質量大約為太陽的 8-10 倍，半徑為太陽的 400 到 600 倍。北一女師生拍到光度正上升的超新星爆發，有一定的科學研究價值。

台北市立天文館研究員葛必揚表示，拍到超新星很難得，因為它「可遇不可求」，不像日月蝕規律變化或什麼季節看到什麼星座，可以事先預測，未來可作為恆星演變或天文物理上的學術研究。

至於是否為全世界最早拍攝到？葛必揚指出，這要送到美國哈佛史密斯松天文台進一步判定，若確認無誤，「真的要給這群厲害的學生拍拍手鼓勵一下」。

至於是否為全台第一例？氣象局天文中心表示，中央大學團隊或高雄天文學會個人，都曾拍到超新星；但可以說是台灣第一個高中學生團體，首次發現超新星。

原文轉載自【2013-10-13/中國時報/ A1 版/要聞】

北一女學生觀星　拍到超新星

【聯合報／記者廖珮妤／即時報導】 2013.10.12 02:39 pm

北一女中和清大、中央大學合作，成立「高瞻團隊」，暑假期間帶學生到鹿林天文台觀星，讓 13 名學生學習操作專業儀器，拍攝距離地球 3200 萬光年的 M74 星系圖片。學生也罕見地拍到恆星爆炸，演變成超新星的過程。

地球科學教師林郁梅說，目前天文學家對於超新星的研究不多，學生運氣很好，拍攝到超新星 SN 2013ej 初形成的樣貌，可做為未來專家研究 M74 星系的數據資料之一。

【中央社／台北 12 日電】

台北市教育局今天表示，北一女師生團隊率先拍攝到超新星 SN 2013ej 爆發，是全球首個拿到該光度資料的團隊。

北一女中物理老師李美英形容，這次觀測經驗就像目睹一場華麗的死亡，對於熱愛天文的師生而言，這場近距離炫目的接觸是畢生難忘的經驗，無疑是最大的鼓勵。

台北市政府教育局指出，北一女師生團隊於世界標準時間 7 月 24 日晚上 7 時許就在鹿林天文台拍攝到超新星 SN 2013ej，並搶先提供相關亮度數據。過了 15 個小時後，這顆超新星由李克天文台(Lick Observatory)確認為超新星。

團隊指導教授、清華大學天文所教授江國興表示，根據星等來判斷，北一女師生團隊拍到了光度正在上升的超新星爆發，對於超新星的研究，有一定的科學價值，團隊率先貢獻相關光度資料，極具意義。

依據台北市教育局現有資料，北一女師生團隊是全球首個拿到這顆超新星光度資料的團隊。北一女師生從事前準備尋找觀測目標，到真正上山操作，到事後將觀測資料處理成照片 ，整個過程費時費力。

北一女中學生盧宥璇表示，能夠跟經驗豐富的專家學習，並使用大型的望遠鏡進行觀測，真的十分興奮，並且得到許多啟發。

【2013/10/12 聯合報】@ http://udn.com/

原文轉載自【2013-10-12/聯合新聞網 生活 即時新聞 】

發現超新星　北一女觀星領先全球

記者黃進福／臺北報導

在位於 M74 星系的超新星 SN 2013ej 正式被確認前十五小時，北一女師生團隊已率先拍攝到超新星 SN 2013ej 爆發，成為全世界第一個拿到光度資料的團隊，這次觀測經驗對熱愛天文的師生而言，就像目睹一場華麗的死亡，這場近距離眩目的接觸是畢生難忘的 經驗，相關資料將可做為未來專家研究 M74 星系的數據之一。

北一女中與清大、中央大學合作成立「高瞻團隊」，暑假期間帶領學生到鹿林天文台觀星，讓十三名學生學習操作專業儀器，拍攝距離地球三千二百萬光年的 M74 星系圖片，在世界標準時間七月二十四日晚間七時許，學生罕見地拍到恆星爆炸，演變成超新星的過程。

團隊指導、清華大學天文所教授江國興表示，天文學家推斷這顆超新星的前身，應該是一顆超級巨大的紅色巨星，稱為「紅超巨星」，這顆紅超巨星質量大約為太陽 的八至十倍，半徑則為太陽的四百到六百倍。而根據星等來判斷，北一女師生團隊拍到光度正在上升的超新星爆發，對超新星的研究，有一定的科學價值，團隊率先 貢獻相關光度資料，極具意義。

清大天文所教授張祥光進一步說明，根據觀測結果，可推論 SN 2013ej 應該是屬於第二型超新星，這類超新星由一個質量大於八倍太陽質量的恆星演化而成，在這種大質量恆星生命的末期，內部已經核融合到鐵，此時產生 能量開始抵抗不了重力往內縮的力量，會開始往內塌縮，當塌縮到內部密度很高的地方時，則會產生一個很強的震波往外傳，使得恆星的外層往外飛散爆炸。

計畫主持人清大天文所教授賴詩萍指出，這次意外捕捉到超新星現身身影，由北一女中高瞻計畫團隊於中央大學鹿林天文台進行「星雲行動」課程的天文觀測時發 現，這個課程由國科會高瞻計畫補助，以及在清大天文所教授指導下研發而成，成為北一女中的特色課程之一，這次發現充分展現學術界與高中教育的結合，可以產 生的火花令人振奮。

參與學生盧宥璇及許苡蕾均表示，能夠在高中階段就跟經驗豐富的專家學習，並使用大型的望遠鏡進行觀測，真的十分興奮，且得到許多啟發與激勵。

依據臺北市教育局資料，北一女師生團隊在世界標準時間七月二十四日晚上七時許，在鹿林天文台拍攝到超新星 SN 2013ej，並搶先提供相關亮度數據，經過十五個小時後，這顆超新星由李克天文台確認為超新星；北一女師生團隊是全球首個拿到這顆超新星光度資料的團隊。

原文轉載自【2013-10-13/青年日報/1 版/今日頭條】

高中生・追星夢　拍到超新星　「像中樂透」

【記者廖珮妤／台北報導】

北一女中與清華大學、中央大學合作成立「高瞻團隊」，暑假期間帶學生到鹿林天文台，學習操作專業天文攝影儀器，拍攝 M74 星系圖片。研究團隊最近整理照片，發現學生罕見地拍到超新星 SN 2013ej 初形成的樣貌，師生都說「運氣太好了，簡直像中樂透」。

配合十二年國教特色課程，北一女開設「星雲行動」選修課。暑假期間由清大天文所教授江國興、賴詩萍等人，帶 13 名高一生上山觀星。

M74 星系距地球 3200 萬光年，北一女地球科學教師林郁梅說，這個星系位於雙魚座附近，適合夏天觀察，且星星亮度高，對學生來說較容易上手。

學生利用 2 天晚上，學習透過電腦操作天文望遠鏡、攝影機及各項器材，並實際拍攝 M74 星系照片。學生許苡蕾說，同學初次看到 1 公尺天文望遠鏡，及各式專業天文器材，都很興奮。

事隔 2 個多月，研究團隊最近整理照片，經過多方比對、確認資料，發現學生拍攝的 M74 星系圖片左下角，有一顆非常亮的「超新星 SN 2013ej」。

林郁梅說，恆星爆炸後會形成超新星，就像煙火一樣，亮度瞬間變大，然後漸漸黯淡。

她表示，美國利客天文台超新星搜尋團隊於世界時 2013 年 7 月 25 日 10 時 18 分確認 SN 2013ej 為超新星，而高瞻團隊在世界時 7 月 24 日 19 時 18 分（台灣時間為 7 月 25 日 3 時 18 分）就拍到它初形成時的樣貌，整整早了 15 個小時，運氣非常好。

原文轉載自【2013-10-13/聯合報/B2 版/北市綜合新聞】

超新星爆發　北一女率先捕捉

【許敏溶／台北報導】台北市北一女中師生團隊今年 7 月利用中央大學鹿林天文台的望遠鏡，拍攝到超新星 SN 2013ej 爆發前的照片，上月確認是全球拍到該顆超新星爆發前最早的照片，有助於天文界進一步探索超新星的爆發機制。參與觀測的北一女學生昨說：「很意外、興奮」。

在國科會補助下，北一女 10 多名師生 7 月下旬到鹿林天文台操作望遠鏡並觀測星空，7 月 24 日晚上 7 時多拍到超新星 SN 2013ej 亮度上升前的照片，經整理

資料比對，上月才確認領先全球拍到其爆發前最早的照片。

意外拍到很難得

該團隊指導教授之一、清華大學天文所教授張祥光昨說，超新星是大質量恆星在生命最末期劇烈爆發的現象，全球天文界 1 年中可看到上千顆超新星爆發，但多數只拍攝到超新星爆發變亮時的照片，每年僅約近百張拍到接近爆發前的照片，北一女師生雖是意外拍到，仍十分難得，有助天文學界研究超新星爆發機制。

北一女 2 年級學生許苡蕾說，參加活動的 3 天 2 夜裡都過著日夜顛倒的生活，能獲得成果很興奮，星空神秘又美麗，未來想投入天文物理領域。

原文轉載自【2013-10-13/蘋果日報/A11 版/生活】

32 年歷史望遠鏡修復　中大推天文教育

【羅安達　桃園中壢】

為了讓天文科學教育深根，桃園中壢中央大學天文台，日前修復了有 32 年歷史的科一館天文台望遠鏡後，開始讓桃、竹、苗偏鄉小學，前來參加天文體驗教育，中大天文所希望讓修復的望遠鏡，以嶄新的面貌，發揮教育與推廣之功能，培養學生認識並接近天文科學，讓這些孩子，有機會成為未來台灣天文研究與教育的種子。

拿著圖片，跟小朋友說明月球目前狀況，然後再搭配上修復完成的望遠鏡，讓這些從沒有真正接觸過天文科學的偏鄉小學孩子，可以親自操作，增加他們對於天文科學的想像力。

新屋鄉蚵間國小學生　楊宜祥：「就會想要跟他們(老師)一樣，去當科學家。」

新屋鄉蚵間國小行政組長　李鳳怡祥：「然後我就覺得，像這樣的刺激，然後讓他們覺得，就是這些東西不是遙不可及的，他們以後有機會，會實現他們的夢想。」

國立中央大學，日前修復了一台 60 公分口徑的望遠鏡，為了嘉惠偏鄉學子，日後將不定時開放天文台，負責指導孩子的天文台技士說，從小培養學生們，在書本之外的天文興趣，或許這些孩子，未來就是台灣的天文專業人才。

中央大學天文所技士　張光祥：「來到中央大學看到這望遠鏡，啟發他們對天文的興趣，將來可以做一個科學家。」

中央大學說，希望這裡的天文台，未來能成為國內天文推廣教育的重要基地，搭配上天文所的師資，用更簡單易懂的方式，指導孩子喜歡這門科學知識，未來可以去發現太空更多的奧祕。 (2013-09-24)

原文轉載自【2013-09-24/客家電視台　CH 17】

不怕雲來亂　守到月露臉　百人尖叫

中原大學天文台開放賞月 唉！雲層太厚等半天 不見月娘來 哇！等到快走才看到 驚呼「值得」

【記者劉愛生／中壢報導】

中原大學在中秋夜開放科學館 9 樓頂端天文台，想讓民眾以高倍率望遠鏡觀測月球，惜入夜後天空雲層太厚，遲遲無法看見月娘，當民眾失望地準備離去，突然豁然開朗、撥雲見月，民眾驚呼「真值得」。

而中央大學因入夜後的雲層太厚，臨時決定取消昨晚開放的天文台觀月活動，師生與民眾只好用肉眼仰望天空厚雲，希望從雲縫中看到今年中秋的月亮，結果徒留嘆息、早早散去。

中原大學為讓國人了解宇宙天文，昨晚特別舉辦「中秋賞月在中原」活動，開放科學館天文台望遠鏡及影片欣賞，要讓民眾近距離欣賞中秋明月，希望為傳統的中秋 節妝點天文的謎樣色彩，吸引 100 多人到場，惜入夜後雲層太厚，在場人士一直等不到中秋明月，失望地準備離去時，晚上八點左右，天空突然豁然開朗，民眾高 聲尖叫「月亮露臉了」，大家排隊等候見月娘。

中原大學天文社長呂芊曄表示，中壢的天空傍晚雲層一直很厚，天色灰暗，烏雲掩蓋，不但無法看到天上的明月，連天上的星星也沒看到，還好稍晚撥雲見月，讓民眾沒白等。

啟英高中學生范姜瑧表示，「為了看中秋明月，專程到中原大學科學館，剛開始沒月亮，從原先的失望到興奮，心情起伏很大，希望明年還可以如願觀月」。

中原大學天文社指導老師物理系教授徐芝姍表示，觀測設備包括與台北市立天文科學教育館相同的 6 米圓頂、口徑 30 公分的蓋賽格林式天文望遠鏡、3 片螢石折射式天文望遠鏡，還有較小口徑天文望遠鏡、雙筒望遠鏡等，可以清楚看到月球表面，解析度相當高，明年還會為鄉親服務。

原文轉載自【2013-09-20/聯合報/B2 版/桃園綜合新聞】

中原、中央天文台　賞月好所在

【楊宗灝／桃園報導】

中秋賞月何處去？國內大專院校最具歷史的中原大學天文社，中秋節當天將開放科學館天文台，邀請民眾透過「蓋賽格林」30 公分口徑望遠鏡直擊月球表面。

除了中原大學外，中央大學天文台也將於秋節當晚 7 至 10 點開放，校方表

示，本次用來賞月的是科學 1 館 60 公分口徑望遠鏡，當晚若天候狀況許可，也將在無光害的戶外草坪架設 8 公分及 20 公分小望遠鏡，方便民眾追月。

有 43 年歷史的中原大學天文社，今年中秋將開放與台北市立天文館同級的巨砲望遠鏡，指導老師物理系副教授徐芝珊說，中原創天文社，受阿姆斯壯登月球影響很大，每年賞月成社團傳統。

徐芝珊說，中原天文社配備的「蓋賽格林」式天文望遠鏡，與台北市立天文館同等級，除了口徑達 30 公分外，放大倍率更可達到 300 倍，鏡身部分還搭載自動導星晶片與電荷耦合影像偵測器，不但能一窺月球表面盈虧地形，也能配合修正觀測光學角度。

天文社同學指出，今年是「彗星年」，例如 10 月底的獵戶座流星雨、11 月的 ISON 彗星等，屆時都將配合開放，歡迎有興趣的民眾一同加入追星行列。

原文轉載自【2013-09-17/中國時報 /B1 版/桃竹苗焦點・運動】

秋節訪嫦娥　中原、中大開放天文台

〔記者李容萍／中壢報導〕中原、中央兩大學中秋節當晚分別開放科學館天文台，讓民眾透過不同口徑的天文望遠鏡，高倍率觀測月球。若遇風雨，觀測活動取消。

中原天文台設於科學館九樓，備配與台北市立天文科學教育館相同的六米電動圓頂，可以三百六十度旋轉，調整最適當觀測角度。

今年開放三組天文望遠鏡供民眾觀測，其中「大砲級」蓋賽格林式天文望遠鏡是重頭戲，口徑約卅公分，放大倍率可達三百倍，月球表面的坑坑洞洞都能一覽無遺。

另兩組口徑較小的反射式望遠鏡與折射式望遠鏡，可輕鬆一窺月球全貌，還展示多款較小口徑天文望遠鏡及雙筒望遠鏡。

天文社表示，當天晚上七點卅分到九點卅分，因今年是彗星年，中原天文台將配合開放民眾追星，像獵戶座流星雨在十月底是極大期，十一月 ISON 彗星也是觀賞重點，肉眼就可以觀測。

中央大學隨著天文台完成重建，十九日晚上七點至十點開放科學一館六十公分

口徑望遠鏡，並於戶外草坪架設八公分和廿公分的小型望遠鏡供民眾賞月。

原文轉載自【2013-09-17/自由時報/A14 版/桃園焦點】

中大天文台　與月娘有約

2013-09-15 16:13:01
【大紀元 2013 年 09 月 15 日訊】(大紀元記者徐乃義台灣桃園報導)嫦娥奔月？月球自古以來有許多美麗的傳說與想像，隨著科技的進步，人類登陸月球，帶回標本，但依然不減那來自神話的神秘美感。中秋節到來，中央大學將於 19 日晚間開放科學一館 60 公分口徑望遠鏡，並於戶外草坪架設 8 公分和 20 公分的小型望遠鏡供民眾賞月。

台灣的天文教育與研究，肇始於中央大學，民國 66 年成立物理與天文研究所時，即開始籌建科一館天文台，並配備當時全國最大的 60 公分口徑之光學望遠鏡，於民國 70 年啟用，成為我國在當時天文研究之重要基地。當時利用科一館天文台做研究的學生，如今都成為我國天文研究與教育之中堅份子。

中壢市區急遽發展，光害污染日趨嚴重，因此自民國八十年代中期起，中央大學的天文研究重心慢慢轉移至海拔 2,862 公尺的鹿林天文台，不但成為亞洲發現小行星最活躍的地方，並發現台灣第一顆鹿林彗星，並有許多卓越科學成果。

中央大學科一館天文台在我國天文發展上佔重要地位，歡迎有興趣的民眾，在中秋一同與天文所「以管窺月」，探索宇宙科學之美。洽詢電話：中央大學天文所（03）427-8445。
（責任編輯：呂美琪）

原文轉載自【2013-09-15/大紀元台灣網】

中秋賞月來中大…看月娘洞洞臉

科一館天文台晚間 7 點到 10 點開放 提供 60 公分口徑光學望遠鏡 連阿波羅登月隕石坑都看得到 若下雨活動取消

【記者賴佑維、楊孟立／中壢報導】

只用肉眼看月亮不滿足嗎？中央大學科一館天文台預計 9 月 19 日晚間 7 點到 10 點開放，提供 60 公分口徑光學望遠鏡讓民眾使用，戶外也準備 20 公分及 8 公分的小型望遠鏡。

中央大學天文研究所長高仲明說：「歡迎民眾用專業的光學望遠鏡把月亮看個仔細。」

「甚至可以看到阿波羅登月的隕石坑。」高仲明表示，預計開放給民眾使用的60公分口徑光學望遠鏡是全台第三大的光學望遠鏡，因此可以清楚的看到月球上密密麻麻的隕石坑。

中央大學在民國66年成立物理與天文研究所，當時就籌建科一館天文台，60公分口徑光學望遠鏡甚至是當時全國最大，後來中央大學鹿林等天文台陸續成立後才退居第三。

高仲明表示，最要感激的是台達電創辦人鄭崇華。位於中壢的天文台，因光害越來越嚴重，使用率逐年降低，導致機器疏於使用損壞。台達電創辦人鄭崇華等企業家獲悉後出資重建，天文台才能恢復以往的面貌。

「如果下雨活動就會取消。」高仲明特別提醒，請民眾注意天候，以免大老遠跑到天文台卻撲空。

目前科一館天文台平日也開放給桃竹苗等地學生參訪使用。高仲明說：「歡迎學校師生多加利用，天文台會安排專業人員解說，也會讓學生實地使用，窺探宇宙奧秘。」
原文轉載自【2013-09-16/聯合報/B2版/桃園綜合新聞】

中秋賞月　中央大學開放天文台

〔記者李容萍／中壢報導〕迎接中秋節到來，中央大學將於十九日中秋當晚七點至十點開放科學一館的六十公分口徑望遠鏡，另於戶外草坪架設八公分及廿公分的小型望遠鏡，供民眾賞月，但若遇雨將取消活動。

此次天文台的開放，中大特別感謝企業家台達公司創辦人暨榮譽董事長鄭崇華等人慷慨捐助，讓已有卅二年歷史的科一館天文台得以重建。

為扎根台灣的天文教育與研究，中大於民國六十六年成立物理與天文研究所時，即籌建科一館天文台，並配備當時全國最大的六十公分口徑光學望遠鏡，天文館於民 國七十年啟用，為我國使用現代觀測工具及尖端技術研究天文的開端，當時利用科一館天文台做研究的學生，如今都成為我國天文研究與教育的中堅份子。

中大天文館後來因中壢市區急遽發展，光害日趨嚴重，自民國八十年代中期起，中大的天文研究重心慢慢轉移至海拔二八六二公尺的鹿林天文台，成為亞洲發現小行星最活躍的地方，並發現台灣第一顆鹿林彗星，另有許多卓越科學成果。

想在中秋一同與天文所「以管窺月」，探索宇宙科學之美的民眾，可洽中大天文所，電話：427-8445。

原文轉載自【2013-09-16/自由時報/A13 版/桃園焦點】

中央大學科一館天文台　中秋開放賞月

2013/09/16
【桃園訊】月球，地球的衛星，自古以來有許多美麗的傳說與想像，隨著科技的進步，人類登陸月球，帶回標本，但依然不減那來自神話的神秘美感。迎接中秋節的到來，中央大學將於 9 月 19 日晚間開放科學一館 60 公分口徑望遠鏡，並於戶外草坪架設 8 公分和 20 公分的小型望遠鏡供民眾賞月。

此次天文台的開放，中央大學要特別感謝企業家台達創辦人暨榮譽董事長鄭崇華等的慷慨捐助，讓已有 32 年歷史的科一館天文台得以重建，以嶄新的面貌與大家見面，再次發揮教育與推廣之功能，嘉惠廣大民眾。

台灣的天文教育與研究，肇始於中央大學，民國 66 年成立物理與天文研究所時，即開始籌建科一館天文台，並配備當時全國最大的 60 公分口徑之光學望遠鏡，於民國 70 年啟用，成為我國在當時天文研究之重要基地。當時利用科一館天文台做研究的學生，如今都成為我國天文研究與教育之中堅份子。

後因中壢市區急遽發展，光害污染日趨嚴重，因此自民國八十年代中期起，中央大學的天文研究重心慢慢轉移至海拔 2,862 公尺的鹿林天文台，不但成為亞洲發現小行星最活躍的地方，並發現台灣第一顆鹿林彗星，並有許多卓越科學成果。

中央大學科一館天文台在我國天文發展上佔重要地位，為我國使用現代觀測工具及尖端技術研究天文的開端，未來將肩負天文教育和推廣的光榮使命，歡迎有興趣的民眾，在中秋一同與天文所「以管窺月」，探索宇宙科學之美。本活動，若遇雨則暫停或取消。

中央大學天文所電話（03）427-8445。（曹松清）

原文轉載自【2013-09-16/經濟日報 Economic Daily News】

中大天文台開放　以管窺月

記者成志平／桃園報導

迎接中秋節來臨，中央大學 19 日中秋夜晚間，開放校園科學一館 60 公分口徑

望遠鏡，並於戶外草坪架設 8 公分和 20 公分的小型望遠鏡供民眾賞月，歡迎有興趣的民眾參加，洽詢電話：中央大學天文所（03）427-8445。

原文轉載自【2013-09-15/青年日報/13 版/地方通訊 桃竹苗】

中秋夜　以管窺月

（圖：中央大學提供）

為迎接中秋節到來，讓大家欣賞到美麗的圓月，中央大學 19 日晚上 7 時起開放科學一館 60 公分口徑望遠鏡，並於戶外草坪架設 8 公分和 20 公分的小型望遠鏡供民眾賞月，歡迎有興趣的民眾，在中秋一同與天文所「以管窺月」，探索宇宙科學之美。（文：記者黃進福）

原文轉載自【2013-09-15/青年日報/11 版/教育藝文】

與月娘有約　中大開放天文台賞月

【聯合晚報／記者游婉琪／即時報導】 2013.09.14 12:39 pm

迎接中秋節的到來，中央大學將於 9 月 19 日晚間開放科學一館 60 公分口徑望遠鏡，並於戶外草坪架設 8 公分和 20 公分的小型望遠鏡供民眾賞月。中央大學表 示，這次天文台的開放，特別感謝台達電子創辦人暨榮譽董事長鄭崇華慷慨捐助，讓已有 32 年歷史的科一館天文台得以重建，以嶄新的面貌與民眾見面，再次發揮 教育與推廣功能。

【2013/09/14 聯合晚報】@ http://udn.com/

原文轉載自【2013-09-14/聯合新聞網 生活 即時新聞 】

世紀大彗星-艾松彗星　首次在台灣曙光中現身

生活中心／生活中心

世紀大彗星－艾松彗星(C/2012 S1 (ISON，亦作艾桑彗星)，8 月 26 日清晨在台灣曙光中現身！中央大學天文所鹿林天文台利用 40 公分望遠鏡清晰地觀測到影像，預估今年 11 月接近太陽時，肉眼清晰可見，對於久違彗星的北半球觀測者而言，將是一大天文饗宴。

中央大學天文所指出，這顆艾松彗星影像（疊加四幅 180 秒，視場大小 2.7 角分）是由中央大學鹿林天文台觀測助理林啟生於 8 月 26 清晨不到 15 度的仰角中 拍攝到，當時它正從距太陽 2.26 天文單位與距地球 3.10 天文單位地方飛過。1 天文單位為地球與太陽平均距離，約 1 億 5000 萬公里。

艾松彗星在去年 2012 年 9 月由「國際科學光學網路」（ISON）的巡天資料中首先偵測到，之後由經驗算式推得此彗星即將成為一顆世紀大彗星，或將成為人類能見到最壯觀的天體之一。尤其對北半球觀測者而言，在著名的海爾－包伯彗星（C/1995 O1 Hale-Bopp）後，就沒有再讓北半球的追星者掀起觀測潮。

專門研究彗星的中央大學天文所助理教授林忠義指出，艾松彗星目前測得的亮度約在 14~15 等，尚無法經由肉眼或雙筒望遠鏡觀測到，需藉由大型望遠鏡才能找到它的蹤跡，但隨著艾松彗星漸漸靠近太陽，它的亮度就會漸漸增亮。

天文所表示，艾松彗星發現後曾估計其在近日點（今年 11 月 28 日，距離太陽表面大約 110 萬公里）的亮度可能超過月亮，經由長時間監測，最大亮度已經下修到與織女星相同（約是 0 等星），但無論如何，艾松彗星仍將是下半年天文迷所引頸期待的天文景象。

原文網址: 世紀大彗星-艾松彗星　首次在台灣曙光中現身 | ETtoday 新奇新聞 |

自然力量　從動物　植物　大地　到星空

大成報 (2013-09-04 15:21)

【大成報記者吉雄世／高雄報導】由中鋼集團教育基金會主辦的「中鋼市民講座」，將於 9 月 7 日下午 4~6 點在捷運巨蛋站旁的三民家商演講廳舉辦，邀請自然科學博物館館 長孫維新 博士帶來「自然力量-從動物.植物.大地.到星空」演講。

孫維新館長，1987 年獲得美國加州大學洛杉磯分校天 文學 博士。後於美國國家航空暨太空總署戈達德太空飛行中心擔 任 博士後研究員(NASA)。返台任教於國立中央大學物理系，並曾出任中華民國天文學會理事長、國立中央大學科學教育中心主任。2007 年轉任國立台灣大學 物理系研究所，2011 年至國立自然科學博物館擔任館長。

孫維新在台灣以天文學普及教育聞名。他在 1993 年主持的公共電視節目《航向宇宙深處》系列獲得 1994 年金帶獎。並以該節目獲得 2000 年第 35 屆金鐘獎「教科文節目主持人獎」。

今年高雄市文化局舉辦的春天藝術節草地音樂會「NASA 星世界天文探索音樂會」，邀請孫館長蒞臨解說，以深入淺出方式介紹天文知識給市民朋友，此次演

講再將透過科學大師之眼，帶您遨遊翰浩星空，領略古往今來的自然奧妙，絕不能錯過，歡迎市民朋友踴躍搭捷運前往聽講。
原文轉載自【2013-09-04/大成報 】

天文科展導覽　東女多元學習

自由時報首頁 ＞ 南部新聞 2013-9-7
天文科展導覽　東女多元學習
〔記者王秀亭／台東報導〕台東科學展覽少之又少，台東大學地球系統科學實驗室與台東縣天文協會合辦「行星科學與太空科技海報展覽」，台東女中學生昨天把握難得機會參觀，在東大副教授楊義清的生動解說下，聽得興致高昂，直說科學好有趣，學到一些沒在課本裡的新知識。

台東縣各類型的展覽資訊不如其他都會區豐富，尤其在科學發展上，更因專業人員、設備不足，成為科學展覽的沙漠之地，此次獲國家科學委員會科普計劃補助，即日起至十九日在台東市寶桑國小活動中心推出展覽活動，提供預約導覽。

在台東推動天文活動不遺餘力的台東大學應用科學系副教授楊義清表示，在各種物理知識中，天文最引人入勝，也是讓小朋友對科學產生興趣的最快入門項目，有助學生埋下科學興趣的種子，在台東卻少人推動，於是成立天文協會，更積極辦展。

展覽位在寶桑國小活動中心二樓，有美國在台協會（AIT）在台灣僅兩套的海報，及中央大學電離層電波科學實驗室合作推廣的數位地球儀系統，透過投影機將地球或行星的影像投影到球型的螢幕上。

台東女中學生林立心表示，此行收穫多，還聽到如無線電能傳輸電力等許多意想不到的科學發展，盼未來有機會對物理科學有更進一步的認識。

台東女中生物老師李心如表示，縣內少有如高雄的科學工藝博物館、台北的台灣科學教育館、台中的自然科學博物館等與科學相關的大型展館就近學習，沒有實地體驗動手做的機會，不少學生對自然科學都感到害怕，東大及台東天文協會的展出是難得機會。

李心如說，此次展覽雖是海報展，但透過台東大學老師的解說，可看到國際間的科技發展，不是課本上感覺遙不可及的知識，也不是電動玩具上看到的那樣簡單，而是真實存在的，對資訊偏遠地區的學生而言是個多元學習的難得機會。

原文轉載自【2013-09-07/自由時報首頁 ＞ 南部新聞】

天文推手，沙漠播種　廟外架望遠鏡　校內展太空海報

【記者李蕙君／台東報導】

台東縣天文協會向美國在台協會爭取到全台僅有兩套的太空科技海報，昨天起在寶桑國小活動中心展出，結合與中央大學電離層電波科學實驗室合作推廣的數位地球儀系統，動態展現衛星圖，台東女中學生昨天率先參展，驚呼「好玩、好酷」。

台東天文推手、天文協會的楊義清本身是台東大學應數系副教授，身為台東子弟的他，期待「科學沙漠」的故鄉能增加常態調查研究及展覽，每個月的第 2、第 4 個 周日晚上，在台東天后宮架設高倍速望遠鏡，供民眾欣賞行星風采，每月也舉辦 1 次觀星活動，逗趣解說，希望灑下天文科學種子。

楊義清說，要 讓孩子對自然科學產生興趣，天文觀察是最快速的入門法，能引發孩子的好奇心及想像力，持續探索。日前他因緣際會得知美國在台協會有兩套太空科技海報，已在 都會區巡迴展示結束，搶得先機，向該協會爭取到一套海報永久保存台東，昨天起至 19 日在寶桑國小活動中心舉辦「行星科學與太空科技海報展」。

儘管場地或設備不比大都會區，與中央大學電離層電波科學實驗室合作推廣的數位地球儀系統，甚至「陽春」地放置在大垃圾桶上，取代一般的放置基柱，但在專人專業及有趣的解說下，昨天首度參訪的台東女中學生興致勃勃。

「很有趣的科學展，對太空科技不僅有更進一步的認識，也想像得到未來發展，登火星都不是問題。」學生顏妤庭興奮地說，台東很難得有類似的展覽，即使只是簡單的海報或設備，卻令人印象深刻。

東女教師李心如表示，台東不似都會區有常態科學館展出，孩子只要有機會學習，都當珍惜。該展覽平常上班日開展，團體預約參展可寄電子郵件至 icyang@nttu.edu.tw。

原文轉載自【2013-09-07/聯合報/B2 版/高屏東綜合新聞】

世紀彗星艾松　台灣看見了

〔記 者陳炳宏／台北報導〕天文迷引頸期待的世紀大彗星—艾松彗星（C/2012 S1 ISON），八月二十六日清晨首度在台灣曙光中現身，中央大學天文所鹿林天文台觀測助理林生，利用四十公分望遠鏡，清晰觀測到影像，預估今年十一月艾松彗 星接近太陽時，用肉眼亦清晰可見，對北半球天文迷而言，是一大天文饗宴。

艾松彗星在去年九月由「國際科學光學網路」（ISON）的巡天資 料中首先偵測到，再由經驗算式推得此彗星即將成為一顆世紀大彗星。中央大學天文所助理教授林忠義指出，艾松彗星目前測得亮度約在十四到十五等，隨著漸漸靠 近太陽，亮度會漸漸增亮，十一月二十八日近日點時，距離太陽表面約一百一十萬公里，估計最大亮度會與織女星相同。

林忠義說，由於彗星物理結構尚不清楚，所以屆時亮度可能變化，十月中旬後，民眾只要在無光害的東海岸或高山，天亮前朝東方水平線上觀看，就可清楚看到

彗星蹤跡。由於艾松彗星將極度貼近太陽表面，有可能會被燒毀，在結束生命前，民眾可以好好欣賞難得一見的世紀彗星。

原文轉載自【2013-08-30/自由時報/A10 版/生活新聞】

世紀大彗星艾松　首次在台灣曙光中現身

中評社桃園 8 月 30 日電(記者 黃文杰)全球天文迷引頸期待的世紀大彗星－艾松彗星 (C/2012 S1 (ISON) ，本月 26 日清晨在台灣曙光中現身。

台灣中央大學天文所鹿林天文台，利用 40 公分望遠鏡，清晰地觀測到影像，預估今年 11 月接近太陽時，肉眼將清晰可見，對於久違彗星的北半球觀測者而言，是一大天文饗宴。

台灣中央大學 29 日新聞稿指出，這顆艾松彗星影像（疊加四幅 180 秒，視場大小 2.7 角分）是由中大鹿林天文台觀測助理林啟生，在本月 8 月 26 日清晨不到 15 度的仰角中拍攝到，當時它正從距太陽 2.26 天文單位，與距地球 3.10 天文單位地方飛過。

艾松彗星在去年（2012 年）9 月由“國際科學光學網路”（ISON）的巡天資料中首先偵測到。

之後由經驗算式推得此彗星即將成為一顆世紀大彗星，或將成為人類能見到最壯觀的天體之一。

尤其對北半球觀測者而言，在著名的海爾－包伯彗星 (C/1995 O1 Hale-Bopp) 後，就沒有再讓北半球的追星者掀起觀測潮。

專門研究彗星的台灣中大天文所助理教授林忠義指出，艾松彗星目前測得的亮度約在 14-15 等，尚無法經由肉眼或雙筒望遠鏡觀測到，需藉由大型望遠鏡才能找到它的蹤跡。

(原文來源網址：
http://www.chinareviewnews.com/doc/1027/0/6/8/102706821.html?coluid=0&kindid=0&docid=102706821&mdate=0830010249)

世紀大彗星艾松　首次在台灣曙光中現身

但隨著艾松彗星漸漸靠近太陽，它的亮度就會漸漸增亮，艾松彗星發現後曾估計其在近日點（今年 11 月 28 日，距離太陽表面大約 110 萬公里）的亮度可能超過月亮。

然而經由長時間監測，最大亮度已經下修到與織女星相同（約是 0 等星），但無論如何，艾松彗星仍將是下半年天文迷所引頸期待的天文景象。

台灣中央大學天文所鹿林天文台，於 1999 年設立，是台灣最重要的光學天文基地。

台灣中大指出，鹿林天文台位於台灣玉山國家公園塔塔加地區的鹿林前山，海拔 2,862 公尺。

台址位於台灣中部，較不受東北季風、西南氣流以及颱風的影響；加上地處高山，透明度及天空條件較佳。

鹿林台天文台研究工作，始於 1990 年，於鹿林前山設置一個臨時觀測站進行選址研究及天文教學。

花了將近 3 年的視相研究，得到台址的平均視相為 1.39 角秒。

此台址的天空背景極暗，幾無光害，可觀測天數約 180 天，較好的觀測季節是每年的秋季與初冬。

1997 年獲得台灣“國科會”太空計劃室（今“國家太空中心”）補助，正式開工興建第一座天文台建築，1999 年完工，安裝測試自行設計製造的 76 公分超輕型望遠鏡，2001 年完成水電建設。2002 年安裝台灣首座突破 1 公尺口徑的鹿林一米望遠鏡。

(原文來源網址：http://www.chinareviewnews.com/doc/1027/0/6/8/102706821_2.html?coluid=93&kindid=8110&docid=102706821&mdate=0830005815)

原文轉載自【2013-08-30/中國評論新聞】

艾松大彗星現蹤　中大 26 日首次發現

〔記者陳炳宏／台北報導〕天文迷引頸期待的世紀大彗星－艾松彗星(C/2012 S1 (ISON)，八月二十六日清晨首度在台灣曙光中現身，中央大學天文所鹿林天文台觀測助理林啟生，利用 40 公分望遠鏡，清晰地觀測到影像，預估今年十一月接近太陽時，肉眼將清晰可見，對久違彗星的北半球而言，是一大天文饗宴。

艾松彗星在去年九月由「國際科學光學網路」（ISON）的巡天資料中首先偵測到，之後由經驗算式推得此彗星即將成為一顆世紀大彗星。中央大學天文所助理教授林忠義指出，艾松彗星目前測得的亮度約在十四到十五等，隨著漸漸靠近太陽，它的亮度就會漸漸增亮，十一月二十八日近日點時，距離太陽表面大約一百一十萬公里，不到太陽直徑距離，估計最大亮度會與織女星相同（約是 0 等星）。

林忠義說，由於彗星物理結構尚不清楚，所以屆時亮度也有可能變化，十月中以後，民眾只要在無光害的東海岸或高山，天亮前朝東方水平線上觀看，就可清楚看到彗星蹤跡。

林忠義表示，由於艾松彗星將極度貼近太陽表面，所以有可能會被燒毀，不過在結束生命前，民眾可以好好欣賞難得一件的世紀彗星。

原文轉載自【2013-08-29/自由電子報 即時新聞】

網路現場直播　看流星雨畫過台東夜空

2013 年 08 月 12 日 19:47 【陳嘉恩／台北報導】明天是七夕情人節，今晚還有年度三大流星群之一的英仙座流星雨報到。中央氣象局天文站指出，今晚 9 時 15 分到明天上午 9 時 45 分是英 仙座流星雨的極大期，民眾在光害少、視野廣的地方，有機會看到流星在夜空中出現，以下半夜流星出現機率較高，幸運的話能在 1 小時內看到 30 到 50 顆流星。

由台東大學、中央大學、東華大學及台中科博館等多名學者和國高中教師組織而成的「台灣流星與高空閃電觀測網」（https://www.facebook.com/TaiWEET）已開始提供流星雨網路轉播，由台東大學地球系統科學實驗室把研究中所拍攝的畫面提供給民眾欣賞，民眾可上網觀賞流星雨畫過東部的星空，但目前雲層較厚，觀測狀況不佳。因流星雨會持續 3 到 5 天，該觀測網明天晚上仍會持續提供轉播服務。轉播網址：http://www.ustream.tv/channel/scipopular

原文轉載自【2013-08-12/蘋果日報 即時新聞 】

英仙座流星雨今晚登場　網路有轉播

2013 年 08 月 12 日 09:20 【陳嘉恩／台北報導】年度三大流星群之一的英仙座流星雨今晚將進入極大期。中央氣象局天文站指出，從台北時間今晚 9 時 15 分到明天上午 9 時 45 分是英仙座 流星雨的極大期，民眾在光害少、視野廣的地方，有機會看到流星在夜空中出現，以下半夜流星出現機率較高，幸運的話能在 1 小時內看到 30 到 50 顆流星。北市 天文館指出，觀察流星雨不需特殊設備，用雙眼欣賞整個天空即可，因流星出現的時間和位置並不固定也無法預測，觀看時切勿只盯著天空某個固定的地方，以免錯 失流星。

由台東大學、中央大學、東華大學及台中科博館等多名學者和國高中教師組織而成的「台灣流星與高空閃電觀測網」（https://www.facebook.com/pages/%E8%87%BA%E7%81%A3%E6%B5%81%E6%98%9F%E8%88%87%E9%AB%98%E7%A9%BA%E9%96%83%E9%9B%BB%E8%A7%80%E6%B8%AC%E7%B6%B2-TWEET/255543191253962）今晚 8 時起將提供流星雨網路轉播，由台東大學地球系統科學實驗室把研究中所拍攝的畫面提供給民眾欣賞。轉播網址：http://www.ustream.tv/channel/scipopular
原文轉載自【2013-08-12/蘋果日報 即時新聞 】

鄧雨賢影音展開幕暨鄧雨賢小行星頒贈

【記 者彭瑞蘭／新竹報導】台灣歌謠之父鄧雨賢，孕育出「四・月・望・雨」創作曲，今年由客委會補助、奇美文化基金會董事長許文龍贊助及國立中央大學頒贈鄧雨賢 小行星模型，20 日在竹北市新瓦屋客家文化保存區、建置「鄧雨賢

影音展」呈現，許文龍帶領自家樂團蒞臨，為「鄧雨賢影音館」擴建揭序。

縣長邱鏡淳表示：感謝許董事長贊助，捐贈 17 世紀「街頭風琴」演奏台灣歌謠。親手雕塑鄧雨賢銅像，分別放置於芎林鄉鄧雨賢音樂紀念公園，新瓦屋客家文化保存區。

許文龍賀「鄧雨賢影音展」開幕，以曼陀鈴與小提琴演奏「四、月、望、雨」（四季紅、月夜愁、望春風、雨夜花）。他說：小小的村莊裡，有一位年輕人留下了不起的創作，鄧雨賢為文化有貢獻，讓人永遠懷念著。人生有限要做有意義的事，讓鄧雨賢歌謠繼續傳唱是有意義的事。

鄧仁侃說：「您雕塑了我的父親，我很謝謝您，我很想抱抱您」。許董立刻趨前擁抱他，現場爆出掌聲很溫馨。

鄧雨賢小行星的發現，源自中央大學鹿林巡天計畫（Lulin Sky Survey，簡稱 LUSS）。由中央大學天文所觀測員林啟生和廣州中山大學葉泉志於鹿林天文台所共同發現。國立中央大學為感念鄧雨賢對台灣民謠發展之貢獻，特將 2006 年 10 月 15 日所發現的編號 255989 小行星，經國際天文學聯合會(IAU/CSBN)通過，正式命名為「鄧雨賢 Dengyushian」，作曲家在歌詞意境中，尋求靈感與創作，賦予歌曲豐富的生命力，一如天文學家致力追尋新的天文知識，探尋宇宙萬物的起源一般，充滿創造力和想像力。而小行星的命名，正是連結天地之間的重要橋樑，代表天人合一，宇宙永恆的追思和紀念。

原文轉載自【2013-07-22/台灣大紀元首頁> 地方> 社會生活】

鄧雨賢影音館 許文龍親手塑雕像

民視 (2013-07-20 16:55)

提到知名的台灣民謠四季紅、望春風、雨夜花這些歌曲，民眾一定都耳熟能詳，為了紀念台灣歌謠之父鄧雨賢，奇美董事長許文龍，不僅大手筆出錢，協助興建鄧雨賢影音館，還親手雕出了鄧雨賢的銅像，除此之外，中央大學也特地把最新發現的小行星，取名叫做鄧雨賢，讓台灣人永遠記得鄧雨賢。

熱愛藝術表演的奇美董事長許文龍，在眾人面前，用小提琴拉起了台灣民謠雨夜花，率領著自家交響樂團的成員，用音樂，紀念一代台灣音樂才子，鄧雨賢，不只拉小提琴， 許文龍還親自，花了三個月的時間，跟鄧雨賢的家人要來了照片，自己親手慢慢的雕刻出鄧雨賢銅像，雖然不是專業的雕刻師傅，但為了這銅

像，許文龍可是改了又 改，而且雕著雕著，連鄧雨賢的孫子看了，都直呼好像。

新竹市政府為了紀念新竹芎林在地的作曲家鄧雨賢，不僅找來許文龍大手筆贊助，希望 能成立鄧雨賢影音館，紀錄下鄧雨賢創作的好聲音，更是與中央大學合作，直接把小行星，命名作，鄧雨賢，鄧雨賢的子孫相當感謝各界的幫忙，讓一代音樂才子， 可以永遠永遠的，伴隨著後代子子孫孫。

原文轉載自【2013-07-20/民視 】

鄧雨賢影音展 許文龍演奏經典

【陳育賢／竹縣報導】

台灣歌謠之父鄧雨賢影音展，廿日在新竹縣竹北市新瓦屋客家文化保存區開幕。此次特別贈送兩座鄧雨賢銅像的奇美文化基金會董事長許文龍，在現場以小提琴演奏鄧雨賢的經典歌曲（見圖，陳育賢攝），為系列音樂祭揭開序幕。

新竹縣長邱鏡淳表示，許文龍贈送的兩尊鄧雨賢銅像，一尊放在芎林鄉鄧雨賢音樂紀念公園；一尊放在新瓦屋客家文化保存區，以教育下一代，有這麼一位偉大的音樂家為台灣這塊土地默默付出。

許文龍以曼陀鈴與小提琴，彈奏鄧雨賢的「四、月、望、雨」，即〈四季紅〉、〈月夜愁〉、〈望春風〉、〈雨夜花〉四首台灣經典歌謠。他說，人生沒有多長，有限的時間，就是要來做有意義的事，「讓鄧雨賢歌謠繼續傳唱，就是最有意義的事。」

文化局表示，鄧雨賢影音展以人文與自然融合為概念出發；音樂為主軸；新瓦屋客家建築為體，佐以深入淺出的樂曲導讀，同時結合中央大學天文所發現、命名的鄧雨賢小行星，希望讓民眾在悠揚的音樂中，領會自然之美，創造音樂、人文、環保的新生活美學體驗。

鄧雨賢小行星源自中央大學鹿林巡天計畫，中央大學為感念鄧雨賢對台灣民謠貢獻，特將二〇〇六年十月十五日發現的編號二五五九八九小行星，命名為「鄧雨賢 Dengyushian」。

原文轉載自【2013-07-21/中國時報/A16 版/文化新聞】

影音館開幕 望春風響起…許文龍演奏 向鄧雨賢致敬

【記者羅緗綸／竹北報導】

新竹縣在竹北新瓦屋客家文化保存區設置「鄧雨賢影音館」昨天開幕，支持音樂、藝文的奇美文化基金會董事長許文龍到場演奏，大夥高歌望春風等，向鄧雨賢致敬。

許文龍說，他喜愛四季紅、望春風等樂曲，當他獲悉是鄧雨賢創作時，打從心底敬佩，他說，鄧雨賢當年創作時，用了曼陀林、小提琴等樂器，他昨連續以這2種樂器演奏。

「感謝客委會、奇美和國立中央大學…」新竹縣長邱鏡淳連聲道謝，指奇美董事長許文龍除提供經費贊助，還為鄧雨賢塑了兩尊銅像，一尊放置芎林鄧雨賢音樂紀念公園，一尊放在新瓦屋，昨天還帶來樂器和樂團表演。

中央大學則贈送「鄧雨賢小行星」模型，這是中央大學天文所觀測員林啟生和廣州中山大學葉泉志共同發現，為感念鄧雨賢對台灣民謠的貢獻，2006年10月 15日將編號255989小行星送經國際天文學聯合會通過，命名「鄧雨賢Dengyushian」，彰顯他創作充滿創造力和想像力。

許文龍昨天和樂團演奏四季紅、月夜愁、望春風、雨夜花等鄧雨賢的成名曲，他表示，人生有限，就是要做有意義的事，讓鄧雨賢歌謠繼續傳唱，是最有意義的事。

新竹縣文化局表示，未來鄧雨賢影音館以音樂為主軸，提供深入淺出的樂曲導讀，和由奇美文化基金會捐贈17世紀街頭風琴所演奏的台灣經典歌謠，也會安排鄧雨賢相關資料與樂曲展演。

原文轉載自【2013-07-21/聯合報/B1版/新竹．運動】

紀念鄧雨賢　許文龍親手捏雕像

〔記者黃美珠／竹北報導〕新竹縣政府昨天舉辦一年一度「鄧雨賢影音展」，紀念這位本土音樂家。奇美文化基金會董事長許文龍不僅致贈兩座出自他雙手的鄧雨賢雕像，還當場表演曼陀鈴和小提琴，向鄧雨賢致敬。

許文龍說，這兩座雕像是他親手所捏，在「望春風的」樂音中，他曾修改過三次才成功。

新竹縣長邱鏡淳除了感謝許文龍為台灣歌謠付出這麼多心力，也說明，未來這兩尊雕像，一尊將放在芎林鄉的鄧雨賢音樂紀念公園，另一尊則將留在新瓦屋客家文化保存區。

許文龍稍後還為祝賀「鄧雨賢影音展」開幕，以曼陀鈴與小提琴彈奏鄧雨賢的

經典台灣歌謠「四、月、望、雨」(四季紅、月夜愁、望春風、雨夜花)，博得滿堂彩。

此外，國立中央大學天文所觀測員林啟生和廣州中山大學葉泉志，在鹿林天文台一起發現編號「二五五九八九」號小行星。該校感念鄧雨賢對台灣民謠發展的貢獻， 特別以鄧雨賢替這個小行星命名，經國際天文學聯合會（IAU/CSBN）通過，正式稱為「鄧雨賢 Dengyushian」。

昨天這顆「鄧雨賢小行星」的模型，也一併在新瓦屋客家文化保存區的「鄧雨賢影音展」上亮相。

原文轉載自【2013-07-21/自由時報首頁 > 北部新聞】

以故鄉命名　小行星名叫台南

【動新聞／台南報導】出現台南小行星！天文迷林啟生六年前發現一顆小行星，送往美國鑑定獲永久編號及命名權，有別於常以偶像明星或父母命名，他感念家鄉栽培，特別取名為「台南」，昨日公開發表，市長賴清德開心笑說「台南不僅是日不落城市，衝到外太空去了！」

南瀛天文教育園區昨日舉辦「台南小行星」發表會，台南市天文協會為此打造台南小行星模型給台南市政府，市長賴清德代表接受，回贈感謝狀。該模型將展示於天文園區隕石區供民眾參觀，也是繼桃園、台中、嘉義、南投、高雄之後，台灣第六個以縣市名命名的小行星。

發現者林啟生是中央大學天文研究所鹿林天文台的研究人員。他說，這顆小行星 2006 年 10 月在玉山國家公園研究時所發現的，經送往美國國際小行星中心鑑定，透過電腦分析比對確定為新星，獲永久編號為 187514 號。不過他當初為命名傷透腦筋，一想就是好幾年，「台南養我生我育我，且有豐富歷史與文化，所以最後以故鄉命名」。

賴清德表示，過去參訪許多國家都可以遇到熱情的台南市民，所以台南具有「日不落」城市的特質，如今連外太空都有「台南」，希望往後若再發現新小行星能以台南三十七個行政區為名，把台南行銷到國際。

原文轉載自【2013-06-21/蘋果日報】

台南　登外太空　觀星解鄉愁！

發現者思鄉　將小行星命名「台南」 南瀛天文教育園區辦發表會 搭橘線公車遊園 憑票根享門票優惠

【記者謝進盛／大內報導】

「台南」地名躍上外太空！南瀛天文教育園區昨天舉辦「台南小行星」發表會，天文工作者林啟生將所發現的小行星命名為「台南」，由市長賴清德代表接受，賴也為將開幕的南瀛天文教育園區宣傳，未來遊客搭乘橘幹線公車，憑票根可享門票優惠。

林啟生投入天文工作多年，曾任台南市天文協會理事長，目前服務於中央大學鹿林天文館，民國95年10月15日在該天文台發現一顆小行星，由於發現者有命名 權，老家在歸仁區的林啟生為表達思念家鄉之情，決定命名為「台南」，天文協會打造了「台南小行星」模型送台南市府，由賴清德代表接受，將放在南瀛天文館供 遊客參觀。

「以後還有大內、新營等大台南各區名字，都有可能在天文界出現。」賴清德除頒發感謝狀給台南市天文協會外，也不忘為本月29日開幕的南瀛天文教育園區宣傳，尤其北玄宮無償提供用地，讓台南學子有超棒學習環境。

為因應園區開幕，橘幹線公車免費搭乘期限將延長至7月7日，晝憑橘幹線票根，享門票優惠。

天文館館長何秋蓮說，29日當天開幕不收門票，將邀請樹谷生活科學館、嘉義市天文協會等團體與會，中華郵政提供郵戳紀念章，以及歷年活動照片展示；29日 園區天文觀測館、星象館都延長開放至晚上9點，30日起將收費，天文展示館全票50元，星象館100元起，可洽詢館方，電話（06）5761076。
原文轉載自【2013-06-21/聯合報/B2版/大台南綜合新聞】

台南小行星發表會　南瀛天文教育園區可窺天文奧妙

2013年6月20日 21:24
記者李文生／台南報導
宇宙中也有一顆行星叫「台南」。南瀛天文教育園區20日舉行「台南小行星」發表會，由台南市天文協會贈送小行星模型給台南市府，由台南市長賴清德代表受贈。
台南小行星是由台南市天文協會前理事長林啟生於2006年10月15日發現，由於發現者具有命名權，為表達感念家鄉之情，林啟生將其命名為「台南」，模

型將展示於園區天文展示館隕石區供民眾參觀，為感謝其貢獻，市府亦頒發感謝狀表達謝意。

賴市長表示，南瀛天文教育園區將於 6 月 29 日開幕，為推展天文教育普及，啟發民眾對天文知識的興趣，園區於 6 月 29 日及 6 月 30 日舉辦體驗活動，歡迎全國朋友前來共襄盛舉。為了因應園區開幕活動，大台南公車橘線的免費搭乘期限，也會延長至 7 月 7 日。

台南市天文協會理事長周銀王表示，南瀛天文館還未成立前，協會就已舉辦過天文觀測活動，現今座落於大內的天文館設備完善，且資料已足夠讓一般民眾了解基本的天文知識，這是南部人的福氣。

原文網址: 台南小行星發表會 南瀛天文教育園區可窺天文奧妙 | 台灣好 | NOWnews 今日新聞網

http://www.nownews.com/2013/06/20/11689-2953520.htm#ixzz2WzyIfBdL

原文轉載自【2013-06-20 /今日新聞網 台灣好 NOWnews】

小行星命名 台灣素人「閃」宇宙

【李宗祐／台北報導】

台灣素人宇宙耀星光！國際天文聯合會審查通過中央大學鹿林天文台在二〇〇六年發現的兩顆小行星，分別命名為「呂其潤」和「陶蕃麟」，創下我國發現小行星以來，首度以素人命名的先例，表彰兩人長期在基層推廣天文科普教育。

國內知名天文社群網站「星星工廠」最近兩天流傳有個「轟動武林、驚動萬教」的消息，即將在七十二小時內曝光，引發天文迷熱烈討論，答案終於在昨日揭曉，原來是跟國際天文聯合會在官方網站公布編號 236484 號小行星命名為「Luchijen」和編號 231346 號小行星命名為「Taofanlin」有關。

呂其潤陶蕃麟 熱中天文

本報記者根據網站公布的小行星發現者英文姓名，求證於鹿林天文台長林宏欽，證實這兩顆小行星確實是他在二〇〇六年三月觀測發現，並取得命名權。林宏欽半年前向國際天文聯合會申請，以台中市富春國小電腦教師呂其潤和台北市立天文科學教育館前展示組長陶蕃麟作為兩顆小行星命名。

相對於國內過去慣以「吳大猷（中研院已故院長）」、「沈君山（清華大學前校長）」或「周杰倫」等名人，或「鹿林」、「嘉義」等地名作為小行星命名，林宏欽指出，他只是很單純的想用這個方式，肯定呂其潤和陶蕃麟長期執著於基層教育推廣。「他們在業餘天文教育這麼多年，從沒得過大獎，也沒有什麼實質回饋，希望透過小行星命名給他們象徵性的肯定。」

辦觀測活動 桃李滿天下

「呂其潤很早就投入國內大型天文活動推廣，他在一九九六年創辦的星空饗宴，每年定期在合歡山翠峰舉辦觀測活動，已經成為國內最大型的天文活動，現在每年都吸引上千人上山開趴。」國立自然科學博物館副研究員林志隆驚訝地說，大家都認為用呂其潤的名字命名小行星是遲早的事，只是不曉得什麼時候而已！

陶蕃麟則是國內很多業餘天文迷，甚至是年輕天文學者在童年或青少年時期開始喜愛天文觀測的啟蒙者。

林宏欽笑說，自己在念高中時期，就經常在周六到當時的圓山天文館，跟著陶蕃麟學習如何利用天文望遠鏡觀星。

林志隆透露，也在成功大學念物理系時，國內天文科學還不普及，有個住台北的學弟每次回家，「經常去找陶老師，帶很多訊息回來給我們！」

原文轉載自【2013-05-14/中國時報/A8 版/社會綜合】

江山萬里行之何處是人間—葉永烜油畫創作個展

大成報-2013 年 04 月 17 日 下午 15:42

【大成報記者劉鳳瑩/苗栗報導】當理性的天文學家遇到感性的藝術會激盪出怎樣的火花？天文學家眼中的油畫世界又是如何呢？雪霸國家公園將於 102 年 4 月 19 日起在汶水遊客中心 2 樓特展室舉辦知名天文學家葉永烜的油畫創作展。透過其手中感性的畫筆，帶領大家遨遊科學家眼中特有的雪霸風華及臺灣景緻的奇特光影變化。

現任臺灣聯合大學系統（中央、清華、交通、陽明等大學）副校長葉永烜教授為國際知名天文學家，1974 年在美國加州大學取得博士學位，於 1978 年前往德國工作。1998 年回臺受聘為中央大學天文所教授，行蹤遍及全球。其研究專長為彗星、行星大氣與行星環、太陽系與行星形成以及電漿物理等，是推動探測土星的「卡西尼計畫」（Cassini）三位原始推動者之一，1982 年促成美國國家航空暨太空總署探測土星任務，因此獲頒 2009 年 NASA 特殊公共服務榮譽勳章。

葉永烜教授因從事科學研究之故，常在世界各地旅遊。早先以鏡頭記錄各地風光，後轉以油畫方式進行創作。 由於長年從事太空科學和天文研究，覺得太空裡大部分是單調的黑，只有少數色彩呈現在星雲和少量的星球，因此葉永烜教授藉著繪畫，在自我意念中追求色彩的揮灑。其作品多半呈現印象派畫風，內容包括風景、人物和花卉靜物為主，創作量高達百餘幅。

葉永烜教授常驚嘆臺灣風景的秀麗與豪雄氣勢，因而此次展出的作品即以環

繞臺灣風景為軸線，以宜蘭龜山島的日出帶出旅程的開始，由北往南、由西往東的呈現臺灣寶島特有風情，其中亦有多幅作品呈現雪霸國家 公園特有的山勢及壯麗的聖稜線，並將觸角延伸至花蓮及台東，最後以臺灣海峽的日落做為旅程的結尾。畫作從光影和色彩的千變萬化之中，呈現只在臺灣這塊寶島 特有的時空之旅。

「江山萬里行之何處是人間─葉永烜油畫創作個展」展期自102年4月19日至6月16日止，並於4月22日上午 10:30舉行開展茶會，有興趣的民眾千萬別錯過此次理性與感性交織的油畫創作個展。活動洽詢專線037-996100轉850
（圖：雪霸國家公園提供。 大成報記者/劉鳳瑩翻攝）

原文轉載自【2013-04-17/大成報】

超新星爆炸亮度不定 動搖諾貝爾物理獎發現

新頭殼newtalk 2013.04.09 鄭凱榕/編譯報導

恆星終其一生最後引起的的大爆炸中，到目前為止其中一種名為「Ia型超新星爆炸」的亮度，一般都認為是平穩一定的，但是宮崎大學等研究團隊8日發表不一樣的結果。根據日本X射線天文衛星「朱雀」(Suzaku)的觀察結果，發現Ia型超新星爆炸的亮度可能是分散不均的。

根據日本共同通信社8日報導，2011年諾貝爾物理學獎的得獎研究，是基於Ia型超新星(Supernova)爆炸的明亮度一定的前提架構下，從觀察到的亮度差來證明宇宙膨脹速度正在加速中。

宮崎大學研究團隊表示，這次朱雀衛星觀察到的結果，「是否有可能動搖影響到諾貝爾獎得獎研究呢？」仍有待進一步的研究。

根據我國行政院國家科學委員會官方網站所公布的科普知識文章〈2011年諾貝爾物理獎─千年的追尋〉(中央大學天文所黃崇源，2012/4/5)中的說 明，「......20世紀末，天文學家沙爾・伯爾穆特(Saul Perlmutter)、布萊恩・施密特(Brian P. Schmidt)、亞當・黎斯(Adam Guy Riess)等人卻發現宇宙的膨脹速度正在加快，意即實際上宇宙並非如預期般因受到重力吸引而減速膨脹。這也意味著宇宙中確實存在著某種排斥力，如同第五 元素或宇宙常數般能克服物質的萬有引力。這個發現實在太驚人了，沙爾・伯爾穆特等人因此共同獲頒2011年諾貝爾物理獎。但是沙爾・伯爾穆特等人是如何量 出宇宙的加速膨脹呢？實際上他們是透過觀測遙遠的Ia型超新星才得以發現這項事實。」

2011 年諾貝爾物理獎的研究，關鍵方法就在超新星的恆定性。根據《科學人雜誌》〈醞釀黑暗力量的宇宙學家〉(David Appell，2008 年第 76 期 6 月號)文中介紹，特別是那些歸類為 Ia 型的，它們有著驚人的恆定性：Ia 型超新星爆炸有一定的亮度，而且亮度隨時間減弱的情形是可預測的，因此天文學家可以將它們當做「標準燭光」，並且能測量它們與地球的距離。

因此，如果本次日本宮崎大學團隊的觀察發表確認為真，意即超新星亮度不定，將根本動搖了 2011 年諾貝爾物理獎研究的前提假設與研究基礎，那麼宇宙加速膨脹的研究結果也將必須重新加以檢驗。

圖片說明：日本 X 射線天文衛星「朱雀」觀察到的「克卜勒超新星」(SN1604)爆炸殘骸的 X 射線圖，從圖中顏色的差異可以看出明亮度的強弱。克卜勒超新星是銀河系內最後一顆被觀測到的超新星，距地球僅約 13,000 光年。圖片來源：宮崎大學森浩二(MORI, Koji)副教授提供。

大霹靂清晰殘跡　宇宙嬰兒照現身

斷定宇宙高齡 138 億多歲　找到星系、地球、人類的出現原因

【本報記者張錦弘、劉盈慧】

宇宙在「大霹靂」之後誕生，爆炸後第 38 萬年產生的光，隨著宇宙不斷擴張，慢慢降溫到約攝氏零下 270 度，變成看不見的「宇宙微波背景」，在宇宙流浪了 138 億多年後，如今被歐洲太空中心的普朗克衛星（Planck）拍下歷來最清晰的畫面，形同宇宙混沌初始的嬰兒照片，更能印證「大霹靂」的宇宙學模型。

普朗克升空 3 年之後，歐洲太空中心 3 月 23 日在巴黎首次發表其研究成果，台大「梁次震宇宙學與粒子天文物理學中心」美籍研究員高提耶參與研究計畫，台大當天特別連線轉播巴黎舉行的記者會，向國人介紹「宇宙微波背景」（cosmic microwave background，CMB）的奧秘。

梁次震宇宙學中心主任陳丕燊指出，1929 年，美國天文學家哈伯首次發現，遠方的星系正離地球加速遠去，推測宇宙仍不斷在膨脹，為大霹靂的理論奠下基礎。後續天文物理學家發展出更完整的學說，認為宇宙最初只是一個小小的點，經過一場「大霹靂」才誕生。

陳丕燊說，宇宙誕生的一剎那，瞬間「暴脹」到 10 的 32 次方倍，打個比方，相當於在 10 的負 35 次方秒內，101 大樓由 0.5 公分大小的模型，膨脹到實體建築那麼大。

初始的宇宙，像一個高溫高熱的爐子，充滿了活躍的質子、電子，和光交換

能量。隨著宇宙不斷膨脹、降溫，到了宇宙誕生後的第 38 萬年，質子和電子結合成氫原 子，能量減弱的光，不足以拆散質子、電子，就在宇宙各處流浪，持續減能、降溫、波長也越來越長，變成肉眼看不到的「宇宙微波背景」。

陳丕燊指出，1964 年，美國貝爾實驗室的工程師阿諾・彭齊亞斯和羅伯特・威爾遜架用天線接收人造衛星微波信號時，發現一種無法消除的雜訊，進而確認這就是宇宙微波背景，為大霹靂理論，提供有力證據，兩人因此獲諾貝爾物理獎。

美國太空總署 1989 年發射人造衛星「COBE」，首次拍到 CMB 的畫面，更加鞏固大霹靂理論。學者馬瑟和史穆斯在 1992 年發現 CMB 從各個不同方向測量，溫度有 10 萬分之一的些微差異，因為這種溫度的不平均，星系、地球、人類才得以出現。兩人在 2006 年獲諾貝爾物理獎。

陳丕燊解釋，因為溫度、能量高的地方，重力較強，會吸引其他能量，集結成星球、星系；而能量低者，弱者越弱，最後化為一無所有的太空。

2009 年 5 月，歐洲太空中心發射觀測 CMB 的第三代人造衛星普朗克，溫度精確 10 倍，拍到更精確的 CMＢ影像。陳丕燊說，透過 3 月 23 日發表的相關數據 分析，可斷定宇宙的年紀約 138 億 8200 萬年；也可推估，組成所有星球及星系的常態物質，僅占宇宙的 5%，「暗質」約占 25%，被視為加速宇宙膨脹的神 秘力量「暗能」，則占 70%。

原文轉載自【2013-04-08/聯合報/AA3 版/新聞中的科學】

和宇宙一樣會發熱 人體也有電磁波

【劉盈慧】

中央大學天文研究所教授陳文屏表示，人眼只能看得到可見光，但除可見光外，大自然還有 X 光、紅外線、紫外線、伽馬射線等眼睛看不到、必須用特殊的儀器才能照出的電磁波。

他解釋，物質散發熱度時會發出電磁波，溫度越高會發出越高能量。

「人體會發熱，就會放出電磁波」，陳文屏說，只是因人體不會發出可見光，所以大家不容易查覺到，但只要透過特殊儀器，電磁波一樣無所遁形。例如消防隊員或警察要救人或攻堅時，會用紅外線透視鏡，查看有無發出熱能的物體存在，用來判斷敵人或受困者所在的位置。

看得更遠一點，我們存在的宇宙會發熱，也有電磁波，這要從「宇宙大爆炸 」說起。

陳文屏表示，根據大爆炸理論，宇宙一開始是個密度極高、溫度極熱的「點」，約 138 億 8200 萬年前大爆炸後，散發出很高能量的光和熱，且宇宙體積還持續

不斷地膨脹。

不過，因宇宙的能量是固定的，當宇宙不斷膨脹的過程，溫度就會降下來。從大爆炸初期，無法以數字描述的高溫，到後來慢慢降溫，現在已減弱到 3 度絕對溫度。而 3 度絕對溫度散發出的電磁波，就屬於微波的波長。

宇宙輻射是一種熱輻射，也是大爆炸留下的痕跡，這份殘存在宇宙間的能量，以微波的型式存在著。

歐洲太空總署的普朗克人造衛星上，也有能感應微波的裝備，「兩方就這樣對上線」，普朗克的儀器具有極高的靈敏度及解析度，才能把收集到的宇宙微波，繪製成宇宙大爆炸 38 萬年後的「宇宙嬰兒照」。
原文轉載自【2013-04-08/聯合報/AA3 版/新聞中的科學】

全球最大天文計畫　台灣有分

【劉盈慧】

台灣在國際天文研究領域中逐漸嶄露頭角，參與的大型的國際合作觀測計畫有 7 個。其中包括目前全球最大的天文計畫—阿塔卡瑪大型毫米及次毫米波陣列（Atacama Large Millimeter/sub-millimeter Array, ALMA）。

林凱揚指出，宇宙太大了，天文研究無法一個國家悶著頭自己做，要與全球各國合作才行；並且要做最新的天文研究，觀測儀器也要盡可能自己蓋，才能掌握一定的研究權，不會凡事都需要別人幫忙。

林凱揚說，ALMA 計畫在智利北部設置了 66 座天線，其中 54 座的直徑達 12 公尺寬，「非常巨大」；科學家能透過這些天線，把宇宙的訊號截取下來，再把訊號拿給超級電腦運算，一張張觀測星雲的圖就能顯像出來。

林凱揚表示，有 17 國參與 ALMA 計畫，美國、日本、歐盟國家都是成員，台灣的經費貢獻約占總計畫 5%，但在科學觀測及科研結果上，卻能拿到 7%的研究，可見台灣的天文研究越來越受肯定。

原文轉載自【2013-04-08/聯合報/AA3 版/新聞中的科學】

天文學家：整個製作真是世界水準之上

【大紀元2013年03月30日訊】（大紀元李芳如台灣桃園報導）2013年3月29日晚間，擔任過美國泛星計畫共同主持人，天文學家、現任中央大學天文研究所教授陳文屏，偕同太太及孩子全家一起觀賞神韻巡迴藝術團在桃園第四場演出，陳文屏看完演出後，對神韻出神入化的舞蹈以及氣勢磅礡的現場交響樂團伴奏甚感震撼，他表示：「整個製作真是世界水準之上！」

陳文屏表示：「動態天幕搭配舞蹈及現場音樂伴奏，整體給人感覺相當棒。」他特別欣賞神韻的中國古典舞演出，「神韻的舞蹈最能展現中國各民族特色，以中國的民族舞蹈，如果要擺在台面上、要放在世界上，神韻的演出堪稱世界頂級。」

喜愛神韻舞蹈演出的陳文屏，對神韻舞蹈演員的傑出表現讚賞不已，並大感驚奇，走出劇院時，他腦海裡頻頻自問：「這些演員他們究竟是怎樣培養出來的？」

「神韻演員非常專業，這些舞蹈演員的藝術造詣非常高，我們（陳文屏一家）還在討論他們到底是怎麼培養出來的？他們來自哪裏？真是令人好奇。」陳文屏說。

此外，神韻交響樂團中西樂器合璧的現場音樂伴奏也讓陳文屏感到相當震撼，並讚不絕口地說：「怎麼可以有這麼高水準的表演？真的非常棒，令人震撼！」他強調，「很棒！非常的棒！現場音樂伴奏給人感覺很棒，時而感到音樂優雅、時而令人震撼、時而感動，真的很棒！非常棒！」

陳文屏認為，神韻交響樂團的伴奏水準非常高，高到令他感到不可思議，神韻藝術家的來歷可能並非一般：「我覺得她們很不簡單，這些藝術家不是一般的藝術家。」

另外，神韻獨特華美的原創服飾，也讓陳文屏印象深刻，「我們也看過很多不同的表演，但神韻的服裝更是非常漂亮、非常非常華麗！」

神韻的高科技動態天幕也讓陳文屏頻頻讚歎並深感好奇，「那個（天幕）我是第一次看到，雖看似簡單，但效果卻非常好，我沒有看過這種從天而降，從天幕跳出來，又能飛回去，很令人好奇。所以感覺上很巧妙，這樣的構思非常好。」

所有節目中最令陳文屏印象深刻的是《大漢風》。他說：「主持人有介紹說漢代本來就是文武雙全，我覺得他們（舞蹈演員）有那種漢朝文武雙全的那種氣勢，舞蹈演員把漢朝文武雙全的氣勢展現得淋漓盡致，真的很棒！」

陳文屏是台灣的天文學家，他的研究主要是觀測天文學和恆星形成，並且積極推動天文教育。他曾任天文研究所所長和中華民國天文學會理事長，也曾經是美國泛星計畫台灣團隊的其中一位共同主持人。

原文轉載自【2013-03-30/大紀元時報】

全球最大望遠鏡　探宇宙奧祕

編譯中心綜合 13 日電 March 14, 2013 06:00 AM

由北美、歐洲及亞洲聯手研發的全球最大型太空望遠鏡「阿塔卡馬大型毫米及次毫米波陣列」（ALMA，靈魂）13 日在智利沙漠啟用。它將透過無線電波接收影像，清晰度是哈伯太空望遠鏡 10 倍，能窺見宇宙中最黑最遠之地，猶如時光機，能探索 120 億年前的事物。

科學家希望透過「靈魂」，得以一窺宇宙大爆炸之後的星系，也可以觀察個別的恆星與行星組成，了解太陽系起源。

英國每日郵報報導，ALMA 耗資 9.5 億英鎊(約 14 億美元)興建，設有 66 台直徑介乎 7 至 12 公尺的大型天線。各天線獨自運作，會把接收到的資訊透過超級電腦整合，形式如人類利用雙耳接收聲音。

研發團隊有來自北美、歐洲與亞洲等 20 國的多個機構聯合參與，包括台灣也做出貢獻，參與該計畫的團隊包括中央研究院、台灣大學、中央大學、清華大學、成功大學與中山科學研究院等。

ALMA 負責人表示，ALMA 能穿透星塵，直達本體，讓研究員了解星體及行星如何形成，有別於其他望遠鏡，是天文研究史上毫米及次毫米技術的一大革命。不過，ALMA 目前只有少於一成的部分運作，要待一年後才能達致最強力量。

ALMA 位處智利接壤玻利維亞邊境海拔 5000 公尺的高原沙漠，相當於 747 噴射機飛行高度的一半，氣候極乾旱。科學家解釋，選址此處是因為上空無雲，ALMA 能在毫無遮擋下觀測宇宙。

原文轉載自【2013-03-14/世界新聞網 北美華文新聞、華商資訊】

隕石來襲！威震千里

【本報記者劉盈慧】

俄羅斯中部的的烏拉爾地區，上個月 15 日發生隕石雨，直徑 17 公尺、7 千噸重的隕石，以每秒 5 點 4 萬公里的速度衝進大氣層，在地表 30 到 50 公里高空處爆裂，碎裂成千片小碎片砸中建築物，其中 1 塊墜入了切巴爾庫利湖，還砸出直徑 8 公尺的大洞。

科學家預估，爆炸釋放出的能量約是 50 萬噸黃色炸藥，差不多是廣島原爆的 30 倍威力。

隕石爆炸時引發的震波，震破了 5 千多棟建築物的玻璃窗，然而有的房子玻璃沒破，但屋內的玻璃罐、盤子卻都破了。短短幾秒間，隕石自我爆炸，建築物的反應也不盡相同，科學家開始用「摩擦燃燒」與「次聲波」等方式來解釋這些現象。

中央大學天文研究所教授陳文屏表示，當隕石掉進大氣後，會先與空氣產生劇烈摩擦，離地表越遠，大氣越稀薄；離地表越近，摩擦力越重，摩擦生熱後就開始燃燒，最後瞬間爆裂，在高空中像散彈槍一樣散射開。

爆炸後產生的震波震破了當地建築物的玻璃，有的連屋頂也被掀開。陳文屏指出，因震動的力量而產生的波都可統稱為震波，如果要具體舉例，那就有點像「掌風」；我們用手揮動空氣來熄滅蠟燭，就是用手擠壓空氣，空氣再產生一股力量把火熄滅。

萬一這股空氣來得很快，相對的壓力就很強；隕石爆裂時會推動氣體，以超音速的速度流動，四周會產生一股壓縮現象，這就是能量非常強的震波。

「爆炸時我們看得到光，聽得到聲響，而人耳聽不到的次聲波也很有威力」，陳文屏說，人耳能聽到的聲波頻率範圍是 20 赫茲至 2 萬赫茲，其中頻率低於 20 赫茲的稱為次聲波（ｉｎｆｒａｓｏｕｎｄ）、高於 2 萬赫茲的稱為超音波（ｕｌｔｒａｓｏｕｎｄ）。

陳文屏指出，次聲波的頻率越低、波長越長，穿透力也越大；像是頻率低於 1 赫茲的次聲波，能傳到幾千以或上萬公里以外的地方，不像一般的聲波，被牆壁等障礙物擋到就穿透不了。

因此，當地有些房子的玻璃窗沒破，空氣進不去，震波還沒辦法破壞到的地方，次聲波卻能穿透牆壁、玻璃，把屋內的玻璃罐、盤子等較脆弱的物品給震破，只不過人耳聽不見，容意忽略到次聲波的存在罷了。

並且，每個物體都有屬於它固定的頻率，像敲碗的聲響跟敲鐘的聲響就不一樣，當頻率相近，物體會互相共振，甚至震破；隕石墜落所發出的次聲波，也會與被震破的玻璃產生共振效應。

原文轉載自【2013-03-18/聯合報/AA3 版/新聞中的科學】

次聲波　常發生　低頻人耳聽不到

【本報記者劉盈慧】

隕石墜落跟原子彈爆炸都會發出次聲波，日前俄羅斯隕石墜落，位於全球 60 處的核爆監測網，有 17 個監測站都測到了次聲波反應。

中央大學天文研究所教授陳文屏表示，低頻的次聲波雖然人耳聽不到，但在自然界卻很常出現，像地震、火山爆發、隕星墜落及強烈的海浪，都會產生次聲波；而原子彈爆炸時的聲響也會產生次聲波，威力強大，還會傳播數千里遠。

陳文屏說，全面禁止核試驗組織（Comprehensive Nuclear Test Ban Treaty Organization, CTBTO）為了預防核武國家自行試爆原子彈，就利用原子彈爆炸會產生次聲波的原理，在格陵蘭島、南極洲、俄羅斯堪察加半島等地設置了 60 個監測站，並於 2001 年啟用了監測網，讓任何在大氣層內人為試爆的原子彈都不會被忽略。

陳文屏還說，上次監測到的大規模爆炸是在 2009 年，印尼蘇拉威西島上的超火星流。

原文轉載自【2013-03-18/聯合報/AA3 版/新聞中的科學】

隕石，墜落地表　流星，空中燒盡

【本報記者劉盈慧】

俄羅斯隕石碎片中傷千人，但也有隕石碎片愛好者，正忙著上網登廣告購買隕石碎片，還有民眾願意付 30 萬盧布（約台幣 29 萬元）購買，引發「淘隕石潮」。清華大學天文研究所教授張祥光說，「其實每天都有 1 百萬公噸的外太空物質，被地心引力吸引，掉進地球。」且隕石的主要成分多是矽與鐵，都是地球上看得到的元素。

張祥光表示，俄羅斯科學家分析這些隕石碎片，發現這些石塊的成分含橄欖石、亞硫酸鹽，約有 10%是鐵。他還說，掉落在地球上的隕石大概分成兩類，不是矽酸鹽礦物組成的石隕石，就是鐵與鎳組成的鐵隕石，「這些元素地球都有，頂多就是元素分布的比例不一樣。」

張祥光說，這些來自外太空的物質，大部分的在進入到地表前，就跟大氣起作用，還來不及掉到地面，就在天空中燃燒殆盡，放射出光線，拉出長長的尾巴，這類稱為「流星」；而這次掉進俄羅斯的隕石，雖然它在墜落的途中有跟大氣起作用、爆炸燃燒，但最後它沒有被燒光，還碎成上千個石頭，掉到地表上，這種則稱為「隕石」。

另外，張祥光還說，像「極光」也是外太空物質進入地球後的一種自然現象。

他解釋，極光是地球周圍一種大規模放電的過程，來自外太空的帶電粒子在到達地球附近後，會受到地球磁場的吸引，順著地球的磁力線往南、北極跑。當這些粒子進入極地的高層大氣時，會與大氣中的原子、分子碰撞，產生光芒，形成極光。

原文轉載自【2013-03-18/聯合報/AA3 版/新聞中的科學】

高緯度容易中彈？「掉哪是隨機」

【本報記者劉盈慧】

1908 年 6 月 30 日俄羅斯通古斯加河附近的上空也發生過隕石爆炸事件，當時還焚毀了 8 千萬顆樹。這次俄羅斯烏拉爾地區又發生隕石墜落，不少人懷疑是否高緯度地區較容易「中彈」，對此清大天文研究所教授張祥光說，「地球有三分之二都是海洋，俄羅斯的國土又占陸地的八分之一，隕石掉到哪都是隨機。」

張祥光指出，直徑達十多公尺大的隕石墜落事件很少發生，發生頻率約是每一百年一次，最近兩次巨型的隕石墜落雖然都發生在俄羅斯，但並非是緯度比較高才比較容易「中彈」。

張祥光解釋，地球有三分之二是海洋，大部分掉落在海洋的隕石「我們較難察覺」，而且俄羅斯又占了全球陸地面積的八分之一，隕石墜落在那的運氣也比較高，並且隕石也很常掉在美國，都是因為占地較廣的關係。另外，隕石也曾墜落在低緯度的古巴。

原文轉載自【2013-03-18/聯合報/AA3 版/新聞中的科學】

台灣有貢獻／全球最大望遠鏡　擺陣探天機

探索太陽系起源

〔國 際新聞中心／綜合報導〕由 66 座巨型天線組成、占地約一個足球場大小的地表最大天文望遠鏡陣列「阿塔卡馬大型毫米波／次毫米波陣列 」（ALMA），13 日在智利寸草不生的阿塔卡馬（Atacama ）沙漠中正式啟動。它看來像是科幻小說才有的東西，但這個「時光機」可以一窺宇宙最深處，告訴我們太陽系從何而來。

台大等校參與團隊

ALMA 斥資 15 億美元（約 446 億台幣），有來自北美、歐洲與亞洲等 20 國的多個機構聯合參與，包括台灣也做出貢獻，參與該計畫的團隊包括中央研究院、台灣大學、中央大學、清華大學、成功大學與中山科學研究院等。

影像比哈伯好 10 倍

目前 ALMA 電波望遠鏡陣列只啟動其中 50 座天線，等到 66 個直徑 7 公尺到 11.9 公尺不等的接收碟傾全力運作，就能提供相當於哈伯太空望遠鏡 10 倍清晰的影像。接收碟先各自擷取天文訊號，再由超級電腦整合分析，由於 ALMA 蒐集的是電波，可以穿透太空中厚厚的塵雲，科學家得以一窺宇宙大爆炸之後的星系， 也可以觀察個別的恆星與行星組成，了解太陽系起源。

位於智利高原 收訊佳

ALMA（西班牙語意為靈魂）位於智利與玻利維亞 邊境的查南托高原（Llano Chajnantor），這裡海拔近 5000 公尺，相當於 747 噴射機飛行高度的一半，更特別的是，這裡濕度超低，是地球最乾燥的地方之一，天體或星系發 散的光線都可以不受干擾的來到這裡。由於濕氣會吸收電波，這裡濕度幾乎零的特性，不會干擾接收碟取得資訊，ALMA 電波望遠鏡陣列因此得以取得超清晰的電 波。

ALMA 負責人德格拉夫說：「科學界希望利用 ALMA 研究恆星組成、行星起源，不只是觀察我們太陽系裡正在發生的狀況，也想研究宇宙大爆炸之後 ，整個太陽系是如何創造的。」

原文轉載自【2013-03-14/自由時報/A9 版/國際萬象】

小行星掠地球 鹿林全都錄

2013/2/18 下午 04:24:16

／編輯／李碧華

在俄羅斯發生隕石爆炸墜落事件的同時，2012DA14 近地小行星也在十六日凌晨以超近距離飛掠地球，再度引發近地小行星可能撞擊地球，引發毀滅性災難的 重視。我國「中美掩星計畫」研究團隊成功利用位於玉山國家公園的鹿林天文台，全程觀測追蹤 2012DA14 最接近地球擦身而過的影像。

中 央大學天文研究所教授陳文屏指出，近地小行星 2012DA14 是到目前為止，以最近距離飛掠地球的小行星，十六日凌晨最接近時，距離地球表面不到三萬公 里，跟地球直徑一萬三千公里比較，「這是非常近的距離，比很多人造衛星

都還接近地球。」但因歐美正值白天無法觀測，我國研究團隊佔地利之便，由中央研究院 天文及天文物理研究所研究助技師汪仁鴻在十六日凌晨成功拍攝到 2012DA14 飛掠地球的影像。

陳文屏表示，「中美掩星計畫」利用鹿林天 文台四座五十公分口徑的天文望遠鏡，配備最先進的電子相機，快速偵測太陽系靠外區域的小型天體遮掩恆星（掩星）造成的亮度變化，藉此研究這些接近地球小天 體跟地球的距離、最接近的時間，及可能造成的威脅。由於小行星運動速度極快，望遠鏡必須指向預定地點「守株待兔」，即使曝光不到一秒鐘，小行星不再是點 狀，而呈現長條狀。

原文轉載自【2013-02-18/中國網路電子報】

天文台電子相機最先進　小行星掠地球　鹿林全都錄

【李宗祐／台北報導】

在俄羅斯發生隕石爆炸墜落事件的同時，2012DA14 近地小行星也在十六日凌晨以超近距離飛掠地球，再度引發近地小行星可能撞擊地球，引發毀滅性災難 的重視。我國「中美掩星計畫」研究團隊成功利用位於玉山國家公園的鹿林天文台（上圖，摘自中美掩星計畫研究網頁），全程觀測追蹤 2012DA14 最接近地 球擦身而過的影像。

中央大學天文研究所教授陳文屏指出，近地小行星 2012DA14 是到目前為止，以最近距離飛掠地球的小行星，十 六日凌晨最接近時，距離地球表面不到三萬公里，跟地球直徑一萬三千公里比較，「這是非常近的距離，比很多人造衛星都還接近地球。」但因歐美正值白天無法觀 測，我國研究團隊佔地利之便，由中央研究院天文及天文物理研究所研究助技師汪仁鴻在十六日凌晨成功拍攝到 2012DA14 飛掠地球的影像。

陳文屏表示，「中美掩星計畫」利用鹿林天文台四座五十公分口徑的天文望遠鏡，配備最先進的電子相機，快速偵測太陽系靠外區域的小型天體遮掩恆星（掩星） 造成的亮度變化，藉此研究這些接近地球小天體跟地球的距離、最接近的時間，及可能造成的威脅。由於小行星運動速度極快，望遠鏡必須指向預定地點「守株待 兔」，即使曝光不到一秒鐘，小行星不再是點狀，而呈現長條狀。

原文轉載自【2013-02-18/中國時報/A5 版/焦點新聞】

「狼真的來了」 地球小心！

【李宗祐／台北報導】

「這次隕石掉到俄羅斯，打傷一千多人，雖然很糟糕，但也很幸運地沒有造成更大傷亡！」中央大學天文研究所教授葉永烜指出，過去大家都認為彗星或小行星撞 地球是「狼來了」，但這次狼真的來了，雖然是隻小狼，但也提醒大家要認真面對外太空小型天體可能撞擊地球的毀滅性威脅。

葉永烜指出，其實過去就有很多小型天體撞向地球，但大都在穿越大氣層時，燃燒變成流星、最後化成灰燼；或墜落海洋等人煙稀少之處。總有一天，地球會跟直徑達幾公里的天體發生碰撞危機。

國立自然科學博物館長孫維新說，外太空每天都有六十到一百噸的小型天體碎片掉到地球，中國古籍曾記載，明朝時期在一四九〇年，陝西省慶陽縣「隕石如雨， 擊死人數萬」，造成慘重傷亡，也是目前有史可查最嚴重的隕石撞地球事件。一九〇八年在西伯利亞通古斯上空六、七公里處曾發生大爆炸，也跟隕石墜落地球時高 溫燃燒爆炸有關。

葉永烜強調，美國等天文科學先進國家為防範地球遭受彗星或近地小行星攻擊，近幾年積極串連各國部署天文望遠鏡，聯 合展開「巡天計畫」，我國已先後加入美國主導的「泛星計畫」與加州理工學院主導「瞬時現象工廠」，共同執行「巡天計畫」，搜尋任何可能對地球產生撞擊威脅 的小型天體。

但他也直言，目前天文科學家僅能觀測追蹤直徑超過一百公尺的小型天體，對於小於一百公尺的微小型天體，還是無法事先掌握，美國國家科學基金會已計畫建造口徑八米的大型天文望遠鏡，搜捕可能在外太空流竄的微小型天體，我國也計畫加入這項「巡天任務」。
原文轉載自【2013-02-17/中國時報/A3 版/焦點新聞】

俄羅斯流星雨　隕石摩擦空氣　產生爆炸

不是首次發生　只是正好掉在人多的地方
【記者陳幸萱／台北報導】

昨天有流星雨進入俄羅斯並爆炸，傳出近千人受傷；國立自然科學博物館館長、台大天文所教授孫維新表示，這是「太空物質與空氣摩擦爆炸」的典型案例，不是首次發生，只是這次正好掉落在人煙較多的地方。

孫維新指出，隕石掉落地球上是正常現象，事實上，每天都有六十噸至一百噸的物質從太空掉到地球，「對人類沒有太大的威脅」。

他解釋，隕石分為兩種，密度較高的隕石會直接撞擊地表，在地面留下「隕石

坑」；另一種就像昨天在俄羅斯上空爆炸的隕石，密度較低，進入地球大氣層後與大氣摩擦生熱，由於物質鬆散，高溫加熱後就會爆炸。

另外，太空物質在空中劃過時，會因熱量穿透太空物質而發光，或是熱量使空氣中的粒子暫時電離，粒子重新結合時也會發出亮光。夜空中的流星就是太空物質進入地球大氣層後，與大氣摩擦後產生的發光軌跡。

昨天俄羅斯的隕石也在空中留下類似「飛機雲」或「飛機凝結尾」的軌跡，孫維新指出，產生軌跡原理與飛機雲相同，都是加熱空氣、使空氣中的水氣凝結成雲。

孫維新說，隕石掉落的機率「全球都差不多」，只是美國、俄羅斯等國的監控系統較完善，所以隕石被發現的機會較高。

中央大學天文所教授陳文屏也說，美國、俄羅斯占地較廣，因此發現隕石的數量也較多。

原文轉載自【2013-02-16/聯合報/A3 版/焦點】

科技遇上人文　巡天二十年　中大天文觀星記

作者：文與圖／張光祥

一九九二年中央大學成立天文研究所，開創國內天文學研究與教育的第一個機構，至今已二十年。如今好奇號在火星上探索人類未來，我們在這裡培育探索人類未來的科學家。

夜間白雲與浩瀚銀河

為了天文觀測的需要，早期校園的照明燈都罩上黑色半球的燈罩，目的在於避免光害直接影響星空。現今因光害影響，校內的觀測較少，因此對夜間照明的控制逐漸降低，校內的照明燈也就五花八門。

當初，半黑半白設計的照明燈只剩校史館前一盞，保留了校園早期原有照明的風味。如果您在中大校園內看到此類型的燈，或許能喚起您對建校初期校園的記憶。

談起天文所師生觀測星空與流星雨的有趣故事：蔡文祥教授回憶民國八十一年，帶著首屆天文研究所學生，到玉山國家公園進行觀測教學，在燦爛星空下，幾位不曾 見過「銀河」的都市小孩，陶然自得地感受宇宙浩瀚，忽然有人迸出一句「為什麼天上那一大片白雲都不動？」他定睛一看，原來那亮麗耀眼的「銀河」，被誤認為 「白雲」。也令人想起，一九九八年獅子座流星雨引領大家觀測星空的風潮，也曾經流傳一則冷笑話：「請問：看流星雨要用雨衣還是雨傘好？」

有「鹿」而沒「路」的天文台

天文所師生在鹿林山經過多年謹慎規畫、選址、地形地質勘查、氣象資料蒐集、土木興建、儀器設備架設等艱辛歷程，於民國九十一年設置了一部購自德國，

精度高、集光性佳，並配有自動導星系統、高靈敏度電子相機等設備的一公尺口徑望遠鏡，提供師生，以及台灣其他大學研究與教學。鹿林山天文台另安置了中美掩星計畫的四台五十公分口徑超廣角望遠鏡。由於台灣位於低緯度，占有可見天區大的優勢，鹿林山天文台已成為國際間小型望遠鏡觀測網的重要成員。

前往鹿林山天台是從台灣的平原直登三千公尺左右的大山，生態環境的改變就像從北回歸線到北極圈一樣，可體驗到豐富的生物多樣性。鹿林山，傳說是群鹿如林的地方，目前為台灣最高的天文台，也是國內天文學術的研究重鎮，天文台規模設備雖小，卻有著全世界極佳的觀測優勢。

其得天獨厚的觀測優勢不只在於台灣高山多，鹿林天文台設於海拔二八六二公尺的玉山國家公園旁，光害和塵害很少。接近赤道的低緯度，也可以觀測較寬廣的天域，尤其是南天球的天體，這是日本、韓國等高緯度國家所觀測不到的。再者，在經度上位於西太平洋重要觀測據點，沿夏威夷的大天文台群過來，下一次觀測站就是台灣，國際上扮演著舉足輕重的地位。在國際上沒有一處可以取代它。

披星戴月，篳路藍縷

台灣天文發展最早可追溯至日據時代，但是一九九〇年代，中央大學在鹿林山開始籌備建立一米望遠鏡的天文台，才真正起步。相較於國際知名天文台豐沛的資源，鹿林天文台籌建過程可說是披星戴月，篳路藍縷，建設十餘年了，由於法規的限制，至今尚未有公路通往鹿林天文台，是世上少數幾個沒有路的天文台。

在鹿林天文台的背後是許多在地住民的付出，鹿林海拔二千八百公尺，一般人很難在這麼高的地方工作生活。天文台建設之初，端賴布農族和鄒族朋友披荊斬棘，一磚一瓦揹上山頭。成立迄今，更有四位鄒族同仁全年三六五天二十四小時輪班守候，無論颱風來襲或除夕過年，在鹿林前山之巔堅守著崗位。他們是玉山的子民，守護著鹿林。

建設鹿林天文台的同時，我們亦同步見證台灣交通建設多處快速公路的完成，使得師生前往鹿林的時程大大縮短，從一天變半天。在賀伯颱風、九二一地震、桃芝颱風、八八風災等天然災害與環境的巨大變遷，重創山區的環境下我們，仍一日又一日，滿懷希望。希望在不久的將來，能在對環境衝擊最小的狀況下，完成二公尺望遠鏡天文台與道路設施。

兩個十年

透過天文望遠鏡看到的天空面積只有約月亮大小，用這月亮大小的視野逐一搜索整個天空稱為「巡天」，要從浩瀚星空找出會動的目標是一項大海撈針的工作。而且尋找彗星是跟全世界在競爭，每一萬個新發現的移動天體（小行星）裡

只有一個彗星，機率只有萬分之一；同時也是跟時間在賽跑，只要晚一秒鐘發現就是別人的，跟全球幾個大型巡天計畫相比，鹿林巡天的規模只是他們的千百分之一，要想以小博大，就必須策略正確，並持之以恆。

鹿林天文台正是這種策略下的計畫，第一個十年：從無到有，完成基礎建設。第二個十年：從一米到二米，有了更大更精良的望遠鏡之後，可以看得更多、看得更遠，培養更多的本土天文人才，在全球的天文學術研究上，讓台灣發光，站上更重要的一席之地。鹿林天文台在師生胼手胝足辛苦經營下，已有豐碩成果是國際上罕見的。

十月二十日邀集了百位以上校友來校，並邀請中大已命名的二十二顆小行星返校共襄盛舉；慶祝中大天文所成立二十周年，持續地一步一腳印，將小行星名遍布全台，帶領台灣人物、地名、山名及少數民族之名神遊宇宙。

原文轉載自【2013-01-23/人間福報/15 版/副刊】

隕石、火球毀滅地球　末日謠言版本多

2012/12/18 18:54
記者:廖宗慶　谷庭　　桃園　　報導

星期五就是 2012 年 12 月 21 日，根據所謂的末日傳說，當天隕石會撞地球、火山爆發，甚至海水倒灌，重大災情將毀滅地球，還有網友 KUSO 月曆，21 日當天將降下火球，溫度高達 999 度，更搞笑自製影片如何躲過隕石，而 7 名中央大學天文學的教授，就特地自拍影片駁斥謠言，以科學解釋世界末日，只是穿鑿附會的謠言。

2012 年 12 月 21 日世界末日，隕石撞地球，帶來毀滅性災難，民眾面露恐懼，屈膝蹲低。廣告對白：「只剩 1 分鐘，剩 1 分鐘了！」

大伙用力一跳，地球瞬間降一格，成功躲過隕石攻擊，泰國廣告 KUSO 末日謠言超爆笑，網友還畫可愛日曆說 21 日那天，美國會有外星人入侵，東京則是酷斯拉來搗亂，大陸僵屍大軍橫行，韓國則爆發核武戰爭，各國被摧毀的方式不同，而台灣的致命災難，竟然是總統馬英九，連查詢氣溫的手機 APP，21 日末日當天是降下火球，溫度飆高到 999 度，22、23 日也因為地球毀滅了，空空如也。

火山爆發、噴射岩漿，地底溫度破表，釀成毀滅性大地震，引發海水倒灌，各種末日謠言穿鑿附會，甚至太陽和地球和宇宙中心黑洞連成一線，地球將瞬間灰飛煙滅。中央大學天文所教授周翊：「(黑洞)它是地球到太陽距離的 17 億倍，因

此對我們的影響是微乎其微。」

　　中央大學 7 名天文所教授，用專業知識自拍影片闢謠，2012 年 12 月 21 日只是馬雅文化曆法「結束」，而非終結的那一天，加上電影渲染，穿插少部分科學事 實，就像撲克牌洗牌夾雜，讓人虛實難辨，但不代表劫難跟著來，各式 KUSO 災難，有人擔憂，有人覺得好笑，因為與其畏懼末日，不如珍惜當下。

原文轉載自【2012-12-18/TVBS 】

破除末日預言　中大音樂會為重生祈福

【記 者何侑霖、李岱桃園採訪報導】國立中央大學２１號晚間舉辦「末日重生」晚會活動。晚會從下午五點半開始，以「２０１２」這部末日電影正式揭開序幕。除了末 日電影院外，這次晚會也包含「觀末日星空」、「末日對談」與「末日宣言競賽」等活動，邀請學生一同參與，以科學的角度破除末日預言。

　整個晚會最受矚目的活動為「末日對談」，由中大天文所陳文屏教授主持，邀請六位來自不同領域的專家學者共同討論末日議題，除了研究地質學、人類學的教授，以科學的角度剖析末日預言外，也包含天主教與佛教的專家，以宗教的觀點闡述對末日的看法。

　末日宣言競賽邀請多位中大學生及校友參與比賽，參賽者用自己的方式將熱舞、樂團和雜耍與末日的概念結合，創造出帶有末日色彩的精采演出。其中身為台北市街頭藝人的徐開炫以一身超級瑪莉歐裝扮登場，專業的演出博得滿堂彩，也奪下個人組的冠軍。

　　活動在中場休息時發放彩色的氣球，邀請學生在氣球上寫下自己的末日願望，多位學生寫下「歐趴」與「嗨趴」，祈求大學課業順利。在晚會的尾聲，近百位學生拿 著寫有願望的氣球，聚集在校門口施放，將自己的願望升上天空，同時也為地球祈福。在午夜十二點整，學生們在校門口點燃仙女棒，象徵破除末日預言，一同慶祝 重生。

　活動負責人校友組專任助理李美儀表示，這場活動主要目的除了以科學的角度破除末日預言，藉此幫助社會大眾釐清關於末日錯誤的觀念外，也希望能夠凝聚中大學生，並達到宣傳中大專業師資的效果。

原文轉載自【2012-12-28/第 1538 期 大學報 12/28~1/11 > > 藝文 】